



Université  
de Toulouse

# THÈSE

En vue de l'obtention du

## DOCTORAT DE L'UNIVERSITÉ DE TOULOUSE

**Délivré par :**

Institut National Polytechnique de Toulouse (Toulouse INP)

**Discipline ou spécialité :**

Science et Génie des Matériaux

---

**Présentée et soutenue par :**

M. ADRIAN KORYCKI

le lundi 9 mars 2020

**Titre :**

Study of the selective laser sintering process: materials properties and effect of process parameters

---

**Ecole doctorale :**

Sciences de la Matière (SDM)

**Unité de recherche :**

Laboratoire de Génie de Productions de l'ENIT (E.N.I.T-L.G.P.)

**Directeur(s) de Thèse :**

MME VALERIE NASSIET

M. CHRISTIAN GARNIER

**Rapporteurs :**

M. DANIEL THERRIault, ECOLE POLYTECHNIQUE DE MONTREAL

M. FREDERIC LEONARDI, UNIVERSITE DE PAU ET DES PAYS DE L ADOUR

**Membre(s) du jury :**

M. FABRICE SCHMIDT, ECOLE NLE SUP DES MINES ALBI CARMAUX, Président

M. CHRISTIAN GARNIER, ECOLE NATIONALE D'INGENIEUR DE TARBES, Membre

Mme CLAIRE BARRES, INSA LYON, Membre

Mme ELISABETH LAURENT, CENTRE NATIONAL D'ETUDES SPATIALES CNES, Invité

Mme FRANCE CHABERT, ECOLE NATIONALE D'INGENIEUR DE TARBES, Membre

Mme VALERIE NASSIET, ECOLE NATIONALE D'INGENIEUR DE TARBES, Membre

M. YVES GROHENS, UNIVERSITE DE BRETAGNE SUD, Membre



## Résumé

La fabrication additive permet de répondre aux exigences de réactivité et de rapidité de création d'un produit industriel en réduisant les phases de développement et d'industrialisation. Parmi les technologies prometteuses pour les pièces en thermoplastiques, le procédé de fusion sur lit de poudre (SLS : Selective Laser Sintering) se distingue en raison de sa capacité de réalisation des géométries à faibles tolérances dimensionnelles. Ce procédé est basé sur le déplacement d'un faisceau laser qui interagit avec le lit de poudre. L'attractivité de la fabrication additive contrebalance cependant avec le choix des matériaux actuellement utilisables : ce sont principalement les polyamides. Les polyaryléthercétone (PAEK) adaptés au procédé SLS sont encore rares sur le marché et coûteux. Dans ces travaux, différentes poudres ont été caractérisées pour mieux comprendre les propriétés nécessaires à leur utilisation en SLS et définir leur fenêtre de température de processabilité. L'absence de poudre de PEEK adaptée nous a conduit à élaborer un nouveau matériau en mélangeant le PEEK à un thermoplastique amorphe, le polyethersulfone (PESU). Les mélanges initialement immiscibles ont été compatibilisés dans l'objectif d'améliorer leurs propriétés mécaniques et pour retarder leur cristallisation au refroidissement.

Pendant la fabrication, de nombreux paramètres du procédé contrôlent la fusion de la poudre, et ainsi les propriétés des pièces et leur précision dimensionnelle. Ainsi, l'analyse statistique de la réponse de l'ensemble des paramètres a fait l'objet d'un plan d'expériences pour en extraire les paramètres les plus influant. L'étude paramétrique, conduite avec la poudre polyamide, a été réalisée en faisant varier cinq paramètres et en regardant leur influence sur cinq groupes de réponses relatives aux propriétés physico-chimiques, physiques, mécaniques et thermiques ainsi qu'aux durées d'impression des pièces. Le plan d'expériences a permis d'établir les modèles mathématiques des surfaces de réponses liant les réponses aux facteurs et à leurs interactions. Ces modèles statistiques ont été utilisés pour définir un jeu de paramètres optimal. Enfin, une approche combinant expérimental et simulation numérique a été menée pour estimer l'influence de chaque passage du laser sur le taux de cristallinité et les propriétés mécaniques de chaque couche. Les résultats montrent que l'échauffement dû aux passages successifs du laser couvre une épaisseur équivalente à 14 couches déposées. Cependant, seules les 4 couches supérieures sont affectées thermiquement de manière significative par le lasage d'une couche de poudre et montrent ainsi une évolution de leur taux de cristallinité.

**Mots clefs :** fabrication additive, fusion sur lit de poudre, thermoplastique haute performance, mélanges de polymères, paramètres de procédé, adhérence entre couches

## Abstract

Additive manufacturing is attractive because it allows to reduce significantly the development and industrialization phases of part design. Among the promising technologies for thermoplastic parts, the SLS (Selective Laser Sintering) process stands out because of its ability to produce geometries with low dimensional tolerances. This process is based on the displacement of a laser beam that interacts with the powder bed. The attractiveness of additive manufacturing counterbalances, however, with the choice of currently available materials: these are mainly polyamides. Polyaryletherketones (PAEK) suitable to SLS process are still rare on the market and expensive. In this work, various powders have been characterized to deeper understand the properties necessary for their use in SLS and to define their processability temperature window. The absence of suitable PEEK powder led us to develop a new material by blending PEEK with an amorphous thermoplastic, polyethersulfone (PESU). The initially immiscible blends have been compatibilized in order to improve their mechanical properties and to delay their crystallization on cooling.

During manufacturing, many process parameters control the melting of the powder, and thus the properties of the parts and their dimensional accuracy. Thus, a statistical analysis of the response of the parameters was led by a design of experiments to extract the most influential parameters. The parametric study, done with the polyamide powder, was carried out by varying five parameters and by looking at their influence on five groups of responses relating to the physical, mechanical and thermal properties as well as to the printing duration of the parts. The design of experiments made it possible to establish the mathematical models of the response surfaces linking the responses to factors and their interactions. These statistical models were used to define an optimal set of parameters. Finally, a combined experimental and numerical simulation approach was conducted to estimate the influence of each laser pass on the degree of crystallinity and the mechanical properties of each layer. The results show that the heating due to the successive laser passes cover a thickness equivalent to 14 deposited layers. However, only the 4 upper layers are significantly thermally affected by the laser pass on a powder layer and thus show an evolution of their degree of crystallinity.

**Key words:** additive manufacturing, selective laser sintering, high-performance thermoplastic, polymer blends, process parameters, interlayer adhesion



## Streszczenie

Produkcja przyrostowa jest atrakcyjna, ponieważ pozwala znacznie ograniczyć etapy projektowania i uprzemysłowienia projektowanych części. Spośród obiecujących technologii dla części termoplastycznych, proces SLS (selektywne spiekanie laserowe) wyróżnia się zdolnością do wytwarzania geometrii o niskich tolerancjach wymiarowych. Proces ten opiera się na przesunięciu wiązki laserowej, która oddziałuje ze złożem proszku. Jednak atrakcyjność produkcji przyrostowej stanowi przeciwwagę przy wyborze obecnie dostępnych materiałów: są to głównie poliamidy. Poliaryloeteroketony (PAEK) odpowiednie do procesu SLS są nadal rzadkie na rynku i drogie. W tej pracy scharakteryzowano różne proszki, aby lepiej zrozumieć właściwości niezbędne do ich zastosowania w procesie SLS i zdefiniować ich okno temperatur przetwarzania. Brak odpowiedniego proszku PEEK doprowadził nas do opracowania nowego materiału przez zmieszanie PEEK z amorficznym termoplastycznym polieterosulfonem (PESU). Początkowo niemieszalne mieszanki zostały skompatybilizowane w celu poprawy ich właściwości mechanicznych i opóźnienia ich krystalizacji podczas chłodzenia.

Podczas produkcji wiele parametrów procesu kontroluje topienie proszku, a tym samym właściwości części i ich dokładność wymiarową. Tak więc analiza statystyczna odpowiedzi parametrów została przeprowadzona przez projekt eksperymentów w celu wyodrębnienia najbardziej wpływowych parametrów. Badanie parametryczne dla proszku poliamidu przeprowadzono poprzez zmianę pięciu parametrów i przyjrzenie się ich wpływowi na pięć grup odpowiedzi związanych z właściwościami fizycznymi, mechanicznymi i termicznymi, a także z czasem drukowania części. Projekt eksperymentów umożliwił wyznaczenie modeli matematycznych łączących odpowiedzi na czynniki i ich interakcje. Te statystyczne modele wykorzystano do zdefiniowania optymalnego zestawu parametrów. Na koniec przeprowadzono połączone eksperymentalne i numeryczne podejście symulacyjne w celu oszacowania wpływu każdego przejścia lasera na stopień krystaliczności i właściwości mechaniczne każdej warstwy. Wyniki pokazują, że ogrzewanie w wyniku kolejnych przejść laserowych pokrywa grubość równą 14 osadzonym warstwom. Jednak tylko 4 górne warstwy bezpośrednio podlegają znacznemu termicznemu oddziaływaniu lasera na warstwę proszkową, a zatem wykazują zmianę stopnia krystaliczności.

**Słowa kluczowe:** wytwarzanie przyrostowe, selektywne spiekanie laserowe, wysokowydajne tworzywa termoplastyczne, mieszanki polimerów, parametry procesu, przyczepność między warstwami

## Acknowledgements

This research work was carried out within the Interfaces and Functional Materials (IMF) and Mechanics of Materials and Structures Processes (M2SP) teams at Laboratoire Génie de Production at École Nationale d'Ingénieurs (Tarbes, 65). This study was set up within the framework of a tripartite CIFRE agreement between the Company Prismadd (Montauban, 82), the Laboratoire Génie de Production and the Agence Nationale Recherche et Technologie.

This thesis is the result of research during three years. This work could not have happened without many people, who supported me. For that, I am extremely grateful to all of them.

First, I thank my thesis director, Madam Valérie Nassiet, who accepted to welcome me to her research group, trusted me during these few years and gave me the freedom to work. I wish to express my deep sense of gratitude to my supervisors Madam France Chabert and Mister Christian Garnier for their kindness, understanding, guidance and valuable comments provided during the preparation of this work. I appreciate the opportunity to work in such a professional and friendly environment.

I am also grateful to Mister Charles Tarek Sultan, my industrial supervisor, for his wise advice, his advanced scientific discussions and especially for his scientific and human qualities. He was of valuable support for me from the side of the company. I would like to thank Madam Elisabeth Laurent who provided me with very useful projects and ideas to improve the quality of my research.

I would like to thank my two thesis rapporteurs, Mister Daniel Therriault and Mister Frederic Leonardi, who accepted to read, correct and evaluate my work. I also warmly thank the president of my jury, Mister Fabrice Schmidt, who made me this honour. I would like to extend my sincere gratitude to Mister Yves Grohens and Madam Claire Barres for accepting desire to participate in my defence of doctorate.

My deepest gratitude goes to my parents (Danuta and Marian), who supported me throughout my work and gave me the strength necessary to implement my life plans. I would like to thank my sisters (Dominika and Klaudia) and brother (Konrad), who have always been there for me. Their love, support and protection have allowed me to be here today. I cannot forget of course all my relatives, especially Ula, Sylwek, Romek, and friends who, near and far, have always supported me tirelessly.

# Table of Contents

Résumé.....	3
Abstract.....	4
Streszczenie.....	5
Acknowledgements .....	6
RÉSUMÉ EN FRANCAIS .....	11
Introduction .....	12
État de l'art.....	14
Caractérisation des poudres disponibles sur le marché : PEEK & PA .....	18
Elaboration d'un nouveau matériau : mélanges PEEK/PES .....	22
Effet des paramètres du procédé de fabrication sur les pièces imprimées.....	25
Influence de l'histoire thermique sur les paramètres matériaux .....	29
Conclusion et perspectives .....	31
<b>INTRODUCTION.....</b>	<b>33</b>
Research context and objectives.....	34
Thesis outline .....	38
<b>1. STATE OF THE ART .....</b>	<b>39</b>
<b>1.1. The basic concept of additive manufacturing of polymers.....</b>	<b>41</b>
<b>1.2. The selective laser sintering process.....</b>	<b>45</b>
1.2.1. The parameters of the SLS process.....	46
1.2.2. Studying the effect of parameters on the properties of printed parts .....	57
1.2.3. Main disadvantages of SLS printed parts.....	59
1.2.4. Post-processing of SLS printed parts .....	60
1.2.5. Conclusion on the selective laser sintering process .....	61
<b>1.3. Thermoplastic powders for SLS process .....</b>	<b>62</b>
1.3.1. General information on thermoplastics.....	62
1.3.2. Commercially available powders.....	63
1.3.3. Structure and properties of polyamides.....	66
1.3.4. Structure and properties of polyaryletherketones.....	72
1.3.5. Conclusion on the thermoplastic powders for the SLS process .....	79
<b>1.4. Properties of polymer powders required in the SLS process.....</b>	<b>80</b>
1.4.1. Shape, surface and size distribution of particles .....	81
1.4.2. Flowability .....	84
1.4.3. Optical properties.....	85
1.4.4. Thermal properties and transitions.....	87
1.4.5. Rheological properties .....	89
1.4.6. Molecular weight .....	96
1.4.7. Recycling of powders used in the SLS process .....	98
1.4.8. Conclusion on the properties of polymer powders required in the SLS process.....	100
<b>1.5. The theoretical basis of coalescence .....</b>	<b>101</b>
1.5.1. Diffusion of macromolecular chains: reptation theory .....	101
1.5.2. Diffusion at interfaces.....	105
1.5.3. Coalescence mechanisms and densification.....	106
1.5.4. Influence of surface tension and viscosity .....	110
1.5.5. Conclusion on the theoretical bases of coalescence.....	112
<b>1.6. Conclusion .....</b>	<b>113</b>

<b>2.</b>	<b>CHARACTERIZATION OF POWDERS AVAILABLE ON THE MARKET: PEEK &amp; PA.....</b>	<b>115</b>
2.1.	Presentation of suppliers and materials.....	117
2.2.	Morphology of powder particles .....	120
2.2.1.	Particle shape analysis by SEM imaging .....	120
2.2.2.	Analysis of particle size distribution by laser granulometry.....	128
2.2.3.	Conclusion on the morphology of powder particles .....	131
2.3.	Flowability of powders .....	132
2.3.1.	Angular measurements .....	132
2.3.2.	Aptitude for settlement .....	134
2.3.3.	Packing fraction .....	136
2.3.4.	Modification of flowability of PEEK powders .....	138
2.3.5.	Conclusion on the flowability of powders .....	140
2.4.	Thermal properties of powders .....	141
2.4.1.	Thermal transitions .....	141
2.4.2.	Thermal conductivity and heat capacity .....	149
2.4.3.	Conclusion on the thermal properties of powders.....	151
2.5.	Rheological properties in the molten state.....	153
2.5.1.	Dynamic viscosity of PEEK powders .....	153
2.5.2.	Calculation of relaxation times .....	158
2.5.3.	Conclusion on the rheological properties in the molten state .....	164
2.6.	Effect of recycling on the properties of PA12.....	165
2.6.1.	Qualitative study of the degradation of PA12.....	165
2.6.2.	Moisture content .....	166
2.6.3.	Observation of the recycling effect.....	167
2.6.4.	Conclusion on the effect of recycling of PA12.....	170
2.7.	Conclusion.....	171
<b>3.</b>	<b>ELABORATION OF A NEW MATERIAL: PEEK/PES BLENDS.....</b>	<b>173</b>
3.1.	Theory of blends .....	175
3.2.	Choice of polymers for blends .....	178
3.2.1.	PEEK / PES blends .....	179
3.2.2.	Compatibilization.....	182
3.2.3.	Conclusion on the choice of polymers for blends .....	183
3.3.	Characterization of uncompatibilized blends .....	184
3.3.1.	Preparation of blends .....	184
3.3.2.	Study of miscibility by DSC and DMTA.....	185
3.3.3.	Morphological analysis of PEEK/PES bends .....	193
3.3.4.	Effect of PES on thermal stability by TGA .....	195
3.3.5.	Conclusion on the characterization of uncompatibilized blends.....	197
3.4.	Characterization of blends with compatibilizer .....	198
3.4.1.	Preparation of blends with compatibilizer .....	198
3.4.2.	Study of miscibility by DSC and DMTA.....	199
3.4.3.	Morphological analysis of blends with compatibilizer .....	205
3.4.4.	Conclusion on the characterization of blends with compatibilizer .....	207
3.5.	Conclusion .....	208
<b>4.</b>	<b>EFFECT OF PROCESS PARAMETERS ON THE PRINTED PARTS .....</b>	<b>209</b>
4.1.	High temperature laser sintering (HT-LS) machines and materials.....	211
4.2.	Influence of manufacturing on material performance .....	212
4.2.1.	Manufacturing of specimens .....	215

4.2.2.	Effect of specimen size .....	217
4.2.3.	Effect of specimen orientation .....	221
4.2.4.	Conclusion on the influence of manufacturing on material performance .....	224
<b>4.3.</b>	<b>Design of experiments on the SLS materials .....</b>	<b>226</b>
4.3.1.	Set-up of designs o experiments .....	227
4.3.2.	Characterization methods and results .....	231
4.3.3.	Conclusion on the design of experiments on the SLS materials .....	243
<b>4.4.</b>	<b>Statistical analysis of the impact on the SLS materials .....</b>	<b>244</b>
4.4.1.	Remarkable correlation .....	244
4.4.2.	Principle of visualization by the iconography of correlations.....	245
4.4.3.	Multiple regression models.....	250
4.4.4.	Effect of interaction between process parameters.....	251
4.4.5.	Optimization .....	254
4.4.6.	Single parameters effect on the properties .....	255
4.4.7.	Conclusion on the statistical analysis of the impact on the SLS materials .....	257
<b>4.5.</b>	<b>Conclusion .....</b>	<b>258</b>
<b>5.</b>	<b>EFFECT OF SLS THERMAL CYCLES ON THE MATERIAL PROPERTIES .....</b>	<b>259</b>
<b>5.1.</b>	<b>Monitoring of thermal field during SLS process .....</b>	<b>261</b>
<b>5.2.</b>	<b>Analytical and numerical studies .....</b>	<b>263</b>
5.2.1.	Continuum approach for the SLS process.....	263
5.2.2.	Discrete approach for the SLS process .....	264
5.2.3.	Conclusion on the analytical and numerical studies .....	265
<b>5.3.</b>	<b>Simulation of thermal profile for several layers .....</b>	<b>266</b>
5.3.1.	General hypothesis.....	266
5.3.2.	Results of the simulation.....	269
5.3.3.	Conclusion on the simulation of thermal profile for several layers .....	271
<b>5.4.</b>	<b>Influence of thermal cycles on the properties of layers .....</b>	<b>272</b>
5.4.1.	Manufacturing of the layers .....	272
5.4.2.	Thermal profile application.....	272
5.4.1.	Conclusion on the influence of thermal cycles on the properties of layers.....	276
<b>5.5.</b>	<b>Influence of annealing on the mechanical properties of PEEK .....</b>	<b>277</b>
5.5.1.	Manufacturing of the annealing samples .....	277
5.5.2.	Conclusion on the influence of annealing on the mechanical properties of PEEK.....	281
<b>5.6.</b>	<b>Conclusion .....</b>	<b>282</b>
	<b>CONCLUSION AND PERSPECTIVES.....</b>	<b>283</b>
	Purpose and scope of work.....	284
	General conclusion.....	285
	Future development.....	288
	<b>ADDITIONAL INFORMATION .....</b>	<b>289</b>
	List of abbreviations.....	290
	List of symbols .....	292
	List of figures .....	295
	List of tables.....	298
	List of literature.....	299
	<b>ANNEXES .....</b>	<b>311</b>
<b>A.1.</b>	<b>Technical specification .....</b>	<b>312</b>
A.1.1.	Duraform PA12.....	312
A.1.2.	Duraform FR1200.....	313

A.1.3.	ZYPEEK 330 PF and ZYPEEK 550 FP .....	314
A.1.4.	VESTAKEEP 2000 FP .....	315
A.1.5.	KATESPIRE KT-880 SFP.....	316
A.1.6.	VICTREX PEEK 450 G .....	317
A.1.7.	EOS PEEK HP3.....	318
A.1.8.	ULTRASON E 1010 PESU .....	319
A.1.9.	ULTRASON E 3010 PESU .....	320
A.1.10.	sPro 230 SLS .....	321
A.1.11.	ProX 500 SLS .....	322
A.1.12.	EOSINT P800.....	323
<b>A.2.</b>	<b>Research methodology .....</b>	<b>324</b>
A.2.1.	Morphology .....	324
A.2.2.	Flowability .....	328
A.2.3.	Chemical analysis by Fourier transform infrared spectroscopy (FT-IR) .....	331
A.2.4.	Thermal properties.....	331
A.2.5.	Rheological and dynamic mechanical properties.....	334
<b>A.3.</b>	<b>Preparation of blends .....</b>	<b>337</b>
A.3.1.	Process 11 parallel twin screw extruder.....	337
A.3.2.	Micro compounder 15 HT .....	339
<b>A.4.</b>	<b>Print of specimens (machine/material pairs).....</b>	<b>341</b>
A.4.1.	The sPro230 SLS and Duraform PA12.....	341
A.4.2.	The ProX500 SLS and Duraform FR1200.....	342
<b>A.5.</b>	<b>Engineering stress-engineering strain curves.....</b>	<b>344</b>
A.5.1.	Diagrams for long and small specimens in each direction of printing .....	344
A.5.2.	Diagrams for pairs machine/material in each direction of printing.....	345
<b>A.6.</b>	<b>Iconography of correlations.....</b>	<b>346</b>
A.6.1.	Positive (green) and negative (red) correlations of average data .....	346
A.6.2.	Positive (green) and negative (red) correlations of all the results .....	347
A.6.3.	Summary of CORICO and regression analysis.....	348
A.6.4.	Interactions of CORICO method .....	349

# **RÉSUMÉ EN FRANÇAIS**

## **Introduction**

Les technologies additives (impression 3D) ont créé une approche prospective du problème de la fabrication de produits à partir de divers matériaux. Des économies de matériaux élevées, une consommation d'énergie réduite, un temps de formation de produit réduit, l'infrastructure minimale nécessaire à la fabrication des produits, l'utilisation de systèmes informatiques modernes sont les avantages fondamentaux du développement futur de l'industrie. Cette thèse présente la technologie fusion laser sur lit de poudre, communément appelée SLS, et les matériaux polymères utilisés dans la fabrication de produits utilisant cette technologie.

Les exigences du marché actuel obligent les industriels à minimiser le cycle de développement des produits. La durée entre l'idée et le produit final doit donc être la plus faible possible. Pour répondre à ces exigences, la fabrication additive apparaît un moyen encourageant. Parmi les technologies les plus prometteuses, il se distingue le procédé de frittage sélectif laser (SLS) basé sur la fusion et la coalescence des poudres thermoplastiques. La famille des polyarylethercétone (PAEK), polymères les plus durables en environnement sévères parmi les thermoplastiques hautes performances, émerge comme étant incontournable dans les applications exigeantes. Malgré des progrès notables dans la maîtrise de sa mise en œuvre, l'impression de pièces en polyetherethercétone (PEEK) reste un défi en raison de sa température de fusion élevée (335 °C) et de la cristallisation rapide lors du refroidissement.

Les objectifs de cette thèse sont le développement de nouveaux polymères et la compréhension des différents mécanismes physiques impliqués au cours de sa fusion laser sur lit de poudre.

Dans le premier chapitre, une étude bibliographique est conduite sur les polymères utilisés communément en fabrication additive, sur les PAEK et les polyamides plus particulièrement. Dans le deuxième chapitre, l'adaptabilité des poudres de polyamide et de polyarylethercétone au procédé SLS est évaluée expérimentalement. Dans ces travaux, différentes poudres ont été caractérisées pour mieux comprendre les propriétés nécessaires à leur utilisation en SLS. Leur fenêtre de processabilité a ensuite définie.

L'absence de poudre de PEEK adaptée au procédé SLS conduit au développement d'un nouveau matériau en le mélangeant à un thermoplastique amorphe. La miscibilité des mélanges ayant de bonnes propriétés mécaniques et un retard de cristallisation est étudiée dans la troisième partie de ce mémoire.



Dans le quatrième chapitre, l'étude de l'influence des paramètres opératoires du procédé SLS sur les propriétés thermomécaniques des pièces est réalisée. Le quatrième chapitre vise à comprendre le rôle des différents paramètres du processus. De nombreux paramètres de procédé contrôlent la fusion de la poudre, et donc les propriétés des pièces et leur précision dimensionnelle. Ainsi, une analyse statistique de la réponse des paramètres a été conduite par un plan d'expériences pour en extraire les paramètres les plus influents. L'étude paramétrique, réalisée avec la poudre de polyamide en poudre Duraform FR1200, a été réalisée en variant cinq paramètres sur la machine ProX500 SLS et en étudiant leur influence sur cinq groupes de réponses relatives aux propriétés physiques, mécaniques et thermiques ainsi qu'à la durée d'impression des pièces. Le plan d'expériences a permis d'établir les modèles mathématiques des surfaces de réponse reliant les réponses aux facteurs et leurs interactions. Ces modèles statistiques ont été utilisés pour définir un ensemble optimal de paramètres.

Enfin, une approche combinant le numérique et l'expérimental est réalisée afin d'estimer l'influence de chaque cycle thermique sur la structure chimique et les propriétés mécaniques de chaque couche au cours du processus SLS. Les résultats montrent que l'échauffement dû aux passages successifs du laser couvre une épaisseur équivalente à 14 couches déposées. Cependant, seules les 4 couches supérieures sont affectées thermiquement de manière significative par le lasage d'une couche de poudre et montrent ainsi une évolution de leur taux de cristallinité.

## État de l'art

Le frittage laser sélectif est une technologie qui permet de produire des modèles 3D en combinant de fines particules de matériaux polymères, pour former, de façon successive, des couches minces. La formation de ces dernières se fait par l'utilisation d'un flux thermique généré par un laser. Dans le traitement des matériaux polymères, les lasers au CO<sub>2</sub> sont le plus souvent utilisés en raison de leur prix et de leur disponibilité. Ils conviennent à la plupart du spectre électromagnétique des polymères. En effet, le coefficient d'absorption dans cette gamme, pour la plupart des polymères, est suffisamment élevé pour que la poudre absorbe la quantité d'énergie nécessaire à la fusion des grains. Comme l'absorption des radiations n'atteint jamais son maximum, la plupart des polymères contiennent des additifs (métaux, titane ou oxyde de silicium, noir de carbone) qui l'augmente. Après le passage du laser, les grains de poudre de granulométrie appropriée (50-70 µm) fondent et coalescent : une couche uniforme est alors créée. Le fonctionnement du système laser et l'interaction avec la couche de poudre sont illustrés à la Figure 0.1.



**Figure 0.1. Circonstances optiques du processus SLS**

L'utilisation efficace de la technologie de fabrication additive, à partir de poudres de polymères, implique l'ajustement approprié d'un certain nombre de paramètres. Leur sélection correcte est un facteur clé pour obtenir des pièces imprimées de bonne qualité qui répondent aux exigences attendues. Dans les publications scientifiques, des informations sur l'impact des paramètres procédé sont disponibles. On peut trouver certaines combinaisons recommandées entre la puissance du laser et la vitesse de balayage pour un matériau spécifique, ce qui est extrêmement important pour contrecarrer les phénomènes indésirables : par exemple, une

pénétration insuffisante se produisant avec une puissance laser trop faible, une pénétration trop élevée étant la combinaison entre une vitesse de balayage faible et une puissance laser élevée, ou bien une fusion irrégulière ou un effet de bille (la formation de billes de matériau fondu). L'épaisseur de la couche peut également avoir un impact sur les propriétés mécaniques et la qualité de surface de la pièce fabriquée. Plus l'épaisseur de couche est faible, plus les propriétés mécaniques et la rugosité sont élevées. Lors de la fabrication d'une pièce prototype, des couches plus épaisses sont utilisées, ce qui réduit considérablement le temps et donc les coûts de production. Lors de la production correcte, il est également important de choisir l'épaisseur appropriée de la couche, non seulement en raison des caractéristiques nécessaires, mais également du temps et des coûts de production susmentionnés.

Les propriétés des matériaux utilisés ont un rôle direct sur le réglage des paramètres procédé et la qualité des pièces imprimées. La Figure 0.2 présente un aperçu des propriétés ayant un impact significatif sur le procédé SLS. Comme vous pouvez le constater, l'un des principaux est le type et les caractéristiques de la poudre. Par conséquent, un accent particulier est mis sur le développement de nouveaux matériaux et sur les modifications de matériaux déjà éprouvés, adaptés au SLS.

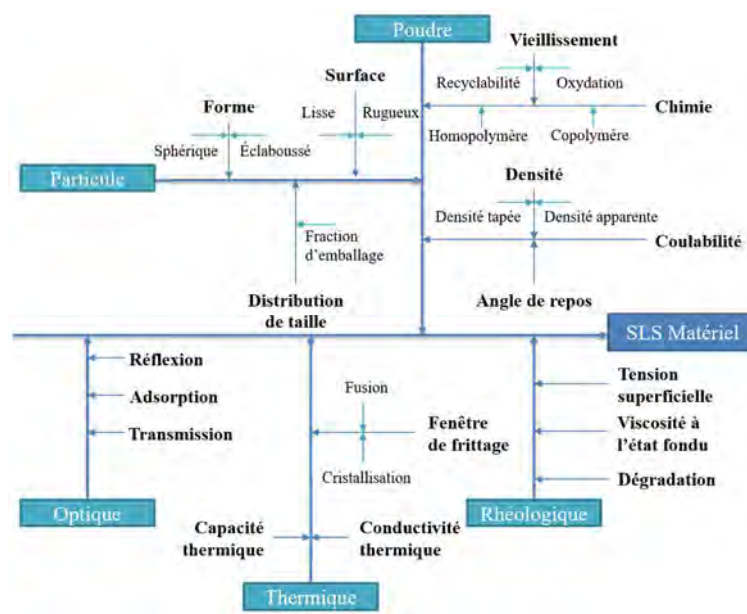


Figure 0.2. Combinaison de propriétés importantes de poudres pour le procédé SLS

Tous les thermoplastiques peuvent être assemblés par fusion laser. Cependant, il existe de grandes différences entre les polymères en termes d'interaction laser-matière (absorption du faisceau laser, tension superficielle, viscosité à l'état fondu, etc.). Pour chaque matériau, les paramètres du procédé doivent être déterminés expérimentalement pour éviter les défauts lors du balayage et minimiser la porosité. Pour cette raison, un nombre limité de matériaux sont

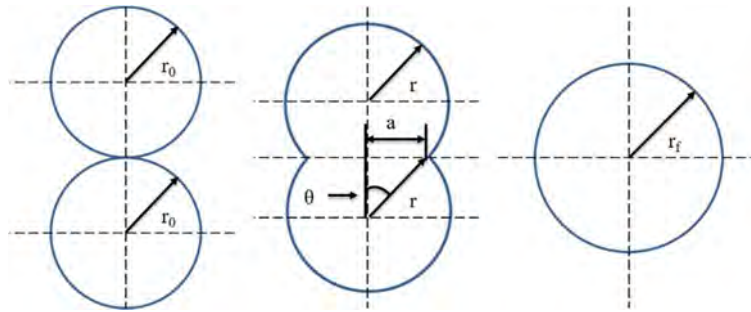
disponibles sur le marché, principalement des polyamides. Les poudres à base de polyarylethercétones constituent un autre groupe de matériaux pour la fabrication SLS. Le polyetherethercétonne est un polymère thermoplastique semi-cristallin à très haute résistance thermique et chimique. Ses propriétés mécaniques restent stables jusqu'à une température de 260 °C, tandis que sa température de fusion et donc de mise en œuvre varie de 370 °C à 400 °C. Les poudres peuvent avoir différentes propriétés, même si elles ont la même composition chimique. Ces différences peuvent être notables, entre autres, dans les propriétés thermophysiques de la poudre, conduisant ainsi à l'obtention de la densité, de la qualité de surface et des propriétés mécaniques. La densité et la conductivité thermique d'une couche de poudre uniformément répartie sont deux caractéristiques qui affectent considérablement le processus de frittage. Le processus de solidification et de consolidation des particules polymères en dépend, ce qui affecte directement la qualité de la pièce obtenue. Il est également possible d'ajouter des fibres ou d'autres additifs aux poudres, telles que des fibres de carbone, de verre ou d'aluminium, améliorant ainsi le comportement mécanique des pièces. Le mélange de polymères cristallins et amorphes peut aboutir à la création de nouveaux matériaux offrant de nouvelles propriétés.

Sur la base de recherches et d'expériences antérieures, plusieurs critères ont été définis en ce qui concerne les matériaux polymères utilisés dans le procédé de fusion laser sur lit de poudres. Il a été constaté que pour obtenir les meilleurs résultats, il est nécessaire que le matériau présente des propriétés spécifiques telles que :

- zone étroite du point de fusion du polymère (jusqu'à fusion complète);
- enthalpie de fusion élevée pour obtenir une séparation nette du matériau fondu de la poudre;
- grande plage de température entre le point de fusion et la cristallisation au refroidissement;
- cristallisation lente pour les semi-cristallins ou solidification lente pour les amorphes;
- distribution granulométrique étroite pour une absorption d'énergie homogène;
- viscosité à l'état fondu adéquate, car elle détermine la vitesse de coalescence du matériau.

Le processus de coalescence est considéré comme l'étape principale du procédé, au cours duquel les zones de contact entre les grains se développent, comme montré sur la Figure 0.3. Un temps de coalescence suffisant permet l'élargissement des zones de contact. En effet, une

haute porosité du produit est obtenue quand le temps de coalescence n'est pas suffisant. La diffusion des macromolécules est suivie de leur cristallisation. Il est nécessaire de maintenir la température de la chambre supérieure à la température de cristallisation pendant plusieurs heures après le balayage laser, afin de garantir la cristallisation complète et la relaxation des contraintes due au gradient de dilatation dans la pièce imprimée.



Le polymère fondu est un matériau viscoélastique typique. Par conséquent, le modèle de coalescence visqueux ne convient pas dans ce cas. Le modèle de diffusion à la limite des grains est capable de simuler le déplacement du grain dû à la coalescence. Cependant, ce modèle nécessite de nombreux paramètres (par exemple les propriétés du matériau) difficiles à obtenir. Ainsi, le modèle de coalescence viscoélastique est présenté comme le plus approprié pour le frittage laser sélectif, car il peut décrire le changement de géométrie du lit de poudre de polymère.

## Caractérisation des poudres disponibles sur le marché : PEEK & PA

Le deuxième chapitre de ce manuscrit porte sur l'adaptabilité des poudres de polymères au frittage sélectif au laser. Dans cette partie, la réutilisation de la poudre non exposée au faisceau laser a été également une question essentielle. Jusqu'à présent, aucune étude détaillée n'a été réalisée sur la dégradation des poudres au cours du procédé et sur l'influence de la dégradation sur les propriétés des pièces.

La possibilité de mettre en œuvre le matériau et les propriétés des composants fabriqués à partir de celui-ci dépendent principalement de paramètres de base tels que :

- forme du matériau: taille des particules, forme, etc.;
- propriétés thermiques du matériau: température de transition vitreuse, fusion, cristallisation, chaleur spécifique, conductivité;
- changement d'état du matériau au cours du procédé: sous forme de poudre et de poudre fondue.

Les poudres utilisées en impression 3D doivent répondre à certains critères, en effet celles-ci doivent avoir une bonne coulabilité pour pouvoir être étalées de façon homogène par le rouleau sur le lit d'impression. Elles doivent aussi avoir une densité tapée suffisamment importante pour éviter une trop grande porosité des pièces imprimées.

Afin de faciliter la fusion de la poudre par le laser, la poudre est préchauffée à une température inférieure à la température de cristallisation ( $T_c$ ) puis est chauffée par le laser au-dessus de la température de cristallisation et en dessous de la température de fusion ( $T_m$ ) pour les polymères semi-cristallins. La fenêtre de frittage est généralement définie comme la plage de température entre les points caractérisant le début de la cristallisation (début  $T_c$ , pendant le refroidissement) et le début de la fusion (début  $T_m$ , pendant le chauffage) du matériau. Cette plage de température varie selon les polymères, elle est fournie par les fournisseurs de poudre et peut être mise en évidence grâce à un test de calorimétrie différentielle à balayage (DSC), comme sur la Figure 0.4.

Le choix de la température de préchauffage est très important car en maximisant la température du lit d'impression, la puissance du laser nécessaire pour faire fondre les grains diminue, le gradient de température au sein du bac d'impression et l'expansion thermique due à la chauffe du laser diminue aussi. Mais une trop haute température de préchauffage réduit la coulabilité de la poudre et entrainera la fusion de grains non souhaitée ce qui compliquera les opérations de post production et diminuera la quantité de poudre pouvant être recyclée.

Inversement une température d'impression trop basse diminuera la résistance des pièces. De plus, les propriétés de la poudre peuvent changer ou se dégrader durant l'impression. Pour ralentir la dégradation, la température de préchauffage doit être diminuée.

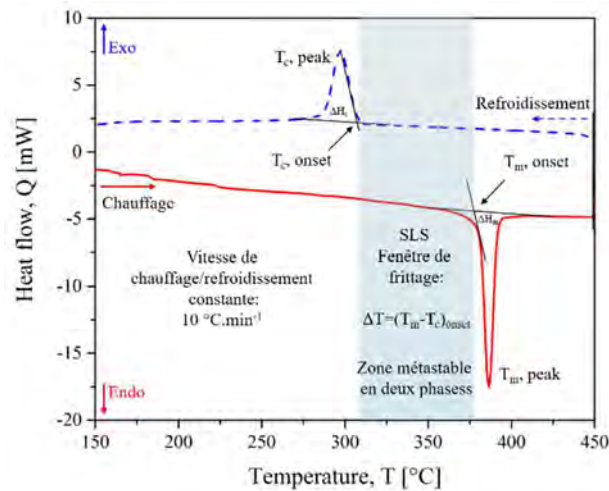


Figure 0.4. Thermogramme de DSC représentant la fenêtre de frittage pour un PEEK HP3

Les propriétés rhéologiques du matériau, comme présenté dans la Figure 0.5, sont un autre paramètre important pour le processus de frittage laser. Les propriétés du polymère fondu, en l'occurrence la viscosité à l'état fondu, ont un impact significatif sur les propriétés du produit final ainsi que sur les paramètres du procédé. La probabilité de fusion complète et de frittage des particules de poudre au cours du processus ne peut se produire que si le matériau est caractérisé par une faible viscosité à l'état fondu. Le gradient de cisaillement étant faible lors de la coalescence, la viscosité d'intérêt correspond à la viscosité au plateau Newtonien. Cette valeur est difficilement mesurable, comme indiqué sur la Figure 0.5 car le polymère se dégrade en raison des temps de mesure plus grands que pour les fréquences élevées.

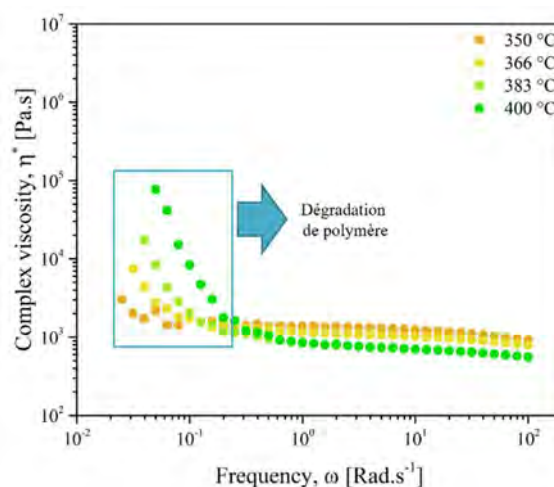


Figure 0.5. Viscosité complexe du PEEK 2000 FP déterminée par le rhéomètre

Les principales propriétés de la poudre nécessaires au SLS ont été étudiées. Tout d'abord, la forme et la taille sont étudiées par les images de microscopie électronique à balayage. Il a été possible de comparer les poudres de polyamide, déjà utilisées pour le procédé de frittage sélectif au laser, avec des poudres de polyétheréthércétone. Le PA12 n'est pas parfaitement sphérique, il n'a que 0.61 de circularité moyenne, et les polyétheréthércétones ont une circularité moyenne comprise entre 0.30 et 0.45. Le PEEK 2000 FP et le PEEK 880 SFP ont un rapport de forme comparable à celui du polyamide 12, aux alentours de 1.67. La distribution de la taille des particules a été vérifiée pour les poudres de polyétheréthércétone et il a été noté que les résultats sont proches des données commerciales. Le grade PEEK HP3 est déjà utilisé pour le procédé de frittage sélectif au laser et la taille moyenne des particules est de 77.8  $\mu\text{m}$ , de sorte que cette valeur se situe dans les limites de la littérature. Le grade le plus proche des poudres testées à cette valeur est le PEEK 2000 FP avec une taille de particule moyenne de 73.2  $\mu\text{m}$ .

Ensuite, la coulabilité des poudres a été réalisée par mesure de densité et angulaire. Le PA12 en tant que poudre appropriée pour le SLS se caractérise par un bon et excellent comportement en écoulement, contrairement aux poudres de polyétheréthércétone. Dans le groupe des poudres de polyétheréthércétone, on distingue le PEEK 2000 FP avec son angle de repos de 49.4° et son indice de Hausner de 1.49, qui sont les plus proches. Cependant, la réduction de l'aptitude à l'écoulement de la poudre peut probablement affecter négativement la stabilité et la reproductibilité du procédé. Les poudres les plus compactes sont le PA12 et le PEEK 450 G, ce qui peut être dû à sa taille supérieure à celle des autres PEEK.

La calorimétrie à balayage différentiel a été utilisée pour vérifier la température de fusion et de cristallisation, qui définissent la fenêtre de frittage. La fenêtre la plus large concerne le PEEK HP3, qui se situe autour de 72 °C. Dans le cas d'autres poudres de polyétheréthércétone et de polyamide, les fenêtres sont assez étroites et il peut être difficile de contrôler le procédé à des températures très élevées. Le degré de cristallinité du grade PEEK HP3 est d'environ 40 %. Des recherches plus approfondies ont révélé que le PEEK HP3 peut être un copolymère de polyéthércétone et de polyéthersulfone. Deux températures de transition vitreuse d'environ 165 °C et 185 °C indiquent respectivement du PEK et PES. De plus, les spectres de spectroscopie infrarouge à transformée de Fourier montrent un pic supplémentaire à 1240 nm comme caractéristique de l'étirement des liaisons sulfones. La conductivité thermique a été trouvée pour le PEEK 2000 FP à l'état consolidé et en poudre tapée de 0.24  $\text{W}\cdot\text{m}^{-1}\cdot\text{K}^{-1}$  et 0.15  $\text{W}\cdot\text{m}^{-1}\cdot\text{K}^{-1}$ , respectivement.



La viscosité et le temps de relaxation ont été mesurés au rhéomètre. Le facteur de dégradation de la poudre sans l'oxydation et la température. Le procédé doit donc être effectué dans une atmosphère d'azote et à des températures qui impose une plage de température d'impression étroite pour le processus. Les temps de diffusion sont compris entre 0.8 ms et 1.4 ms pour les chaînes courtes et entre 0.5 s et 1.0 s pour les chaînes longues, ce qui signifie qu'il est nécessaire de maintenir la température est suffisamment élevée pour permettre la diffusion des chaînes polymères pendant cette durée.

Les propriétés de la poudre PA12 se détériorent lors du processus de frittage sélectif au laser et la poudre recyclée doit être mélangée avec une nouvelle poudre. Il n'y a pas assez d'informations pour savoir comment traiter le matériau recyclé. Le temps de fabrication, la position dans la chambre de travail, ainsi que le type de machine de frittage laser sélectif doivent être pris en compte.

Les résultats de ce chapitre montrent qu'il manque sur le marché des poudres de polyétheréthercétone appropriées au SLS. Ainsi, dans la prochaine étape, l'élaboration d'un nouveau matériau composé de polyétheréthercétone et de polymères amorphes a été étudiée. Sur la base des résultats de ce chapitre, les polymères suivants ont été sélectionnés : PEEK 450 G (granulés) et Vestakeep 2000 FP (poudres), de Victrex et Evonik, respectivement. Le premier polymère sélectionné représentera le matériau avec de longues chaînes et le second avec des chaînes courtes.

## Elaboration d'un nouveau matériau : mélanges PEEK/PES

Les poudres de polymères hautes performances disponibles actuellement sur le marché ne sont pas adaptées au procédé SLS en raison de différentes caractéristiques déjà identifiées. L'objectif principal de ce chapitre a donc été d'élaborer de nouveaux matériaux à propriétés contrôlées dans le but de la fabrication additive par SLS.

Il a fallu réaliser les mélanges PEEK et PES par extrusion bivis puis effectuer les tests de caractérisation sur ces mélanges. Le but était d'obtenir des mélanges miscibles, avec de bonnes propriétés mécaniques, un retard à la cristallisation pour avoir une fenêtre de processabilité large. Il a été décidé de travailler avec deux types de polymère PES. L'un avec une chaîne longue, le PES 3010 G, et l'autre avec une chaîne courte, le PES 1010 G. En effet, un mélange avec des chaînes longues sera susceptible de donner un matériau non miscible (ou partiellement miscible) mais avec une rigidité élevée, tandis qu'un mélange avec des chaînes courtes donnera un matériau moins rigide mais une meilleure miscibilité.

Deux types de PEEK et de PES ont été mélangés à l'état fondu et examinés pour déterminer leurs propriétés. L'analyse par DSC et rhéométrie en torsion rectangulaire permet de déterminer leur miscibilité. Deux températures de transition vitreuse correspondant au PEEK à environ 160 °C, associées à la phase riche en PEEK, et au PES à environ 227 °C (PES 1010 G) ou à 230 °C (PES 3010 G), associées au PES phase riche. En considérant uniquement les mélanges, on observe un léger retard de la température de cristallisation avec une augmentation de la teneur en PES pour tous les mélanges, à l'exception des mélanges PEEK 450 G et PES 3010 G. La Figure 0.6 montre que les fenêtres de processabilité sont peu modifiées.

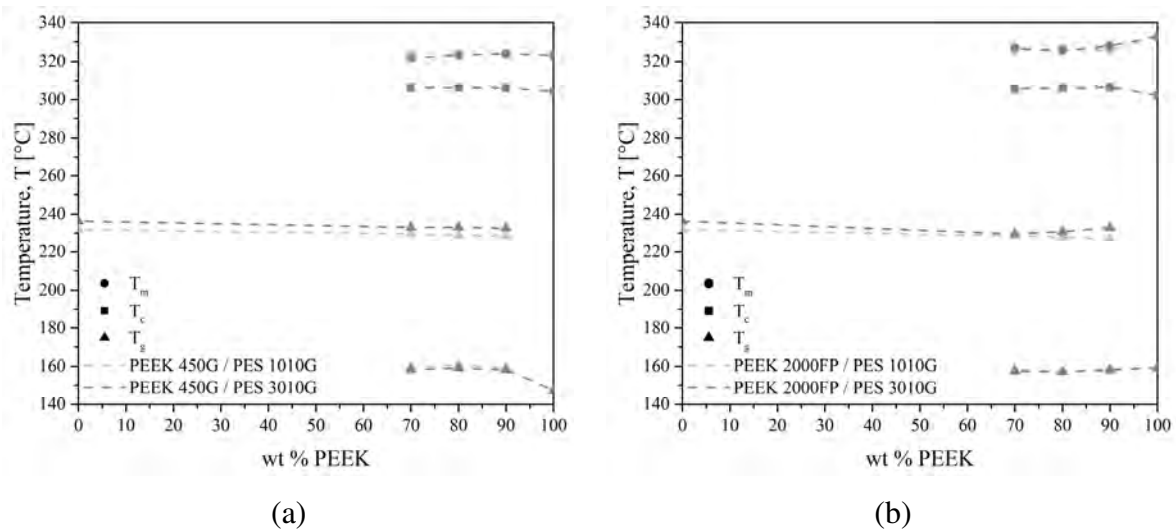
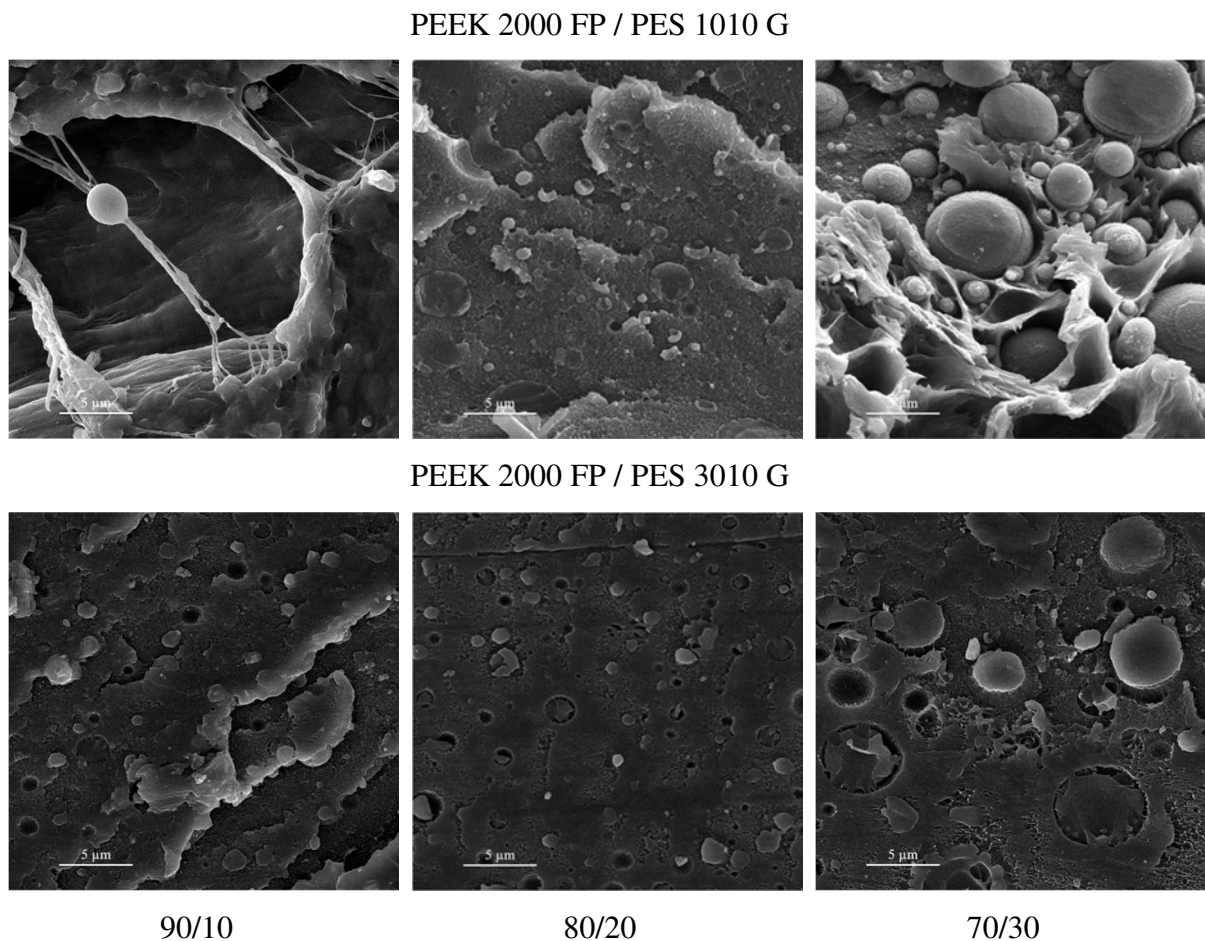


Figure 0.6. Transitions thermiques des mélanges PEEK/PES

Le module d'élasticité de tous les mélanges avec PEEK 450 G est compris entre 1313 MPa et 1850 MPa, la valeur la plus élevée correspondant à 90/10 wt.% de PEEK 450 G et PES 1010 G. Dans le cas de mélanges avec PEEK 2000 PF, le module est dans la plage de 1440-1637 MPa, ce qui le rend plus stable pour toutes les compositions et moins dépendant de la teneur en PES.

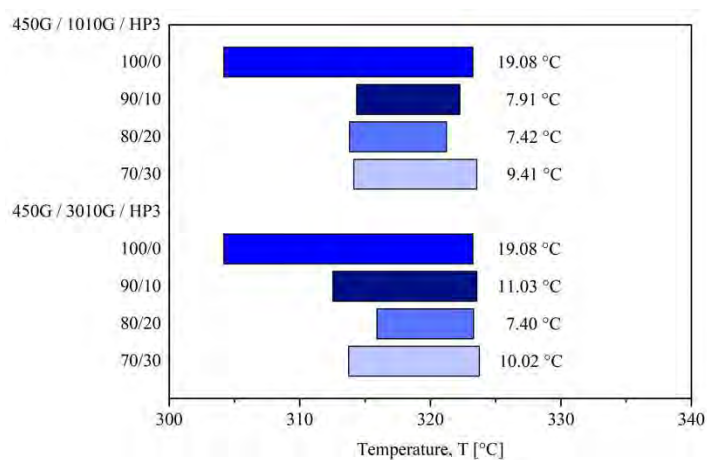
Les mélanges PEEK/PES résultants présentent une immiscibilité ou une faible miscibilité. L'objectif de retarder la cristallisation n'a pas été atteint. La morphologie des mélanges montre une nette séparation de phases caractérisée par des domaines sphériques de PES sur la Figure 0.7. De plus, une faible adhérence interfaciale dans toutes les compositions conduit à l'idée d'ajouter un troisième composant pour compatibiliser les deux phases.



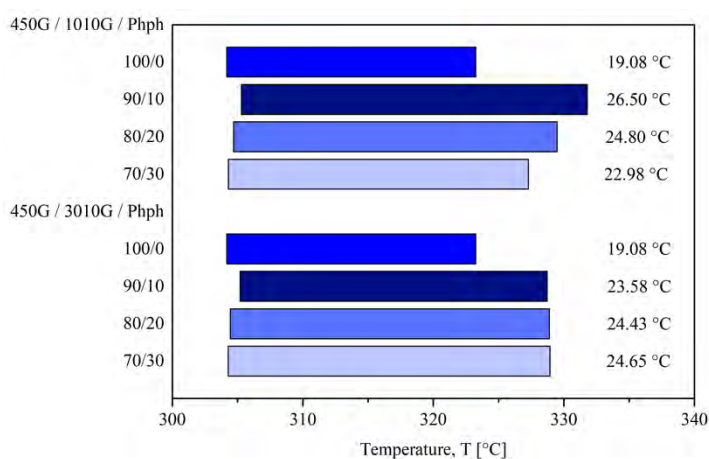
**Figure 0.7. Les images SEM des mélanges PEEK 2000 FP et PES [wt. %]**

Deux types de compatibilisants ont été choisis, le copolymère HP3 et la phénolphtaléine. Les mélanges de polymères présentent une immiscibilité avec HP3, cependant, la phénolphtaléine ressemble à un plastifiant. Pour les mélanges de PEEK et de PES avec des groupes cardo-latéraux de phénolphtaléine la fenêtre de frittage est agrandie, comme le montre la Figure 0.8 en augmentant le point de fusion et en diminuant le degré de cristallinité du PEEK.

L'analyse morphologique montre des domaines sphériques PES nanométriques à micrométriques.



(a)



(b)

**Figure 0.8. Fenetre de processabilité des mélanges PEEK and PES avec (a) HP3 et (b) phenolphtaleine**

Ces résultats prometteurs devront être approfondis pour anticiper le comportement du matériau au cours du procédé SLS.

## Effet des paramètres du procédé de fabrication sur les pièces imprimées

L'un des aspects de cette thèse est la détermination des paramètres d'impression optimum du PA12. Cette étude nécessite l'impression de nombreuses éprouvettes de test, or les coûts d'impression étant fonction de la taille des pièces, la possibilité de faire cette étude en réduisant la taille des pièces, moins onéreuses à fabriquer, a été étudiée. Pour cela, deux sets de 5 lots d'éprouvettes en Duraform PA12 ont été imprimés sur la machine sPRO230. Un set de grandes éprouvettes (170 mm de long) et un set de petites éprouvettes (85 mm de long). Couplée à cette étude sur la taille des éprouvettes, une étude sur l'orientation des éprouvettes a été réalisée. Des essais de traction uniaxiale ont été réalisés afin d'obtenir le comportement mécanique des pièces réalisées.

L'étude a mis en avant que le module d'élasticité est plus élevé dans le cas des grands échantillons, de 16 % à 23 % par rapport aux petits échantillons. Pour les échantillons de grandes dimensions, le module d'élasticité varie entre 1702 MPa et 1855 MPa, selon la direction de fabrication, avec la valeur la plus faible pour la direction YZ/Y. Pour les petits échantillons, il varie entre 1349 MPa et 1502 MPa, selon la direction de fabrication, avec la valeur la plus faible pour la direction XY/Y. Dans ces 2 cas d'étude, les modules d'élasticité, dans les 3 directions sont quasi-identiques, ce qui ne discrimine pas la fabrication sur la réponse élastique du matériau dans la direction Z. Dans le cas des 2 configurations, petites et grandes éprouvettes, les meilleurs résultats ont été obtenus pour la fabrication suivant l'axe X. De plus, les valeurs maximales du module d'élasticité obtenues sont plus élevées de 15 % en comparaison avec les valeurs présentes dans la fiche technique du matériau.

En ce qui concerne la résistance à la traction, la différence de valeurs entre les grands et les petits échantillons est significative pour les orientations XY/X et XZ/Z. Cet écart atteint 10 MPa pour une valeur de résistance mécanique de l'ordre de 40 MPa. Si l'on ne considère que les échantillons de grande taille, la résistance à la traction se situe entre 38 MPa et 44 MPa, la valeur la plus faible étant celle de la direction XZ/Z. La résistance à la traction varie entre 27 MPa et 38 MPa pour les petits échantillons, la valeur la plus faible pour l'axe Z. Ainsi, la résistance à la traction montre des résultats similaires à la fiche technique du matériau, pour les grands échantillons. Cependant, la fabrication suivant l'axe Z est discriminante avec des valeurs de résistance mécaniques plus faibles, représentant un écart pouvant atteindre les 43 % et pouvant s'expliquer par une faible liaison entre couches. Les échantillons fabriqués le long de l'axe Z révèlent aussi un allongement à la rupture inférieur dans chaque cas.

L'étude sur l'orientation des couches a été renouvelée pour la comparaison de 2 couples matériaux-machines : Duraform PA12/sPro230 et FR1200/xPro500. Il n'a pu être mis en avant qu'un couple matériau-machine était plus adapté que l'autre. Le matériau utilisé dans les 2 cas est du PA12 mais qu'il est modifié pour le FR1200. Cependant, il est essentiel de noter qu'avec l'utilisation des 2 couples, les propriétés mécaniques ne varient pas de façon significative. L'exception est l'allongement à la rupture qui présente des valeurs inférieures sur le ProX500 SLS, mais il est dû aux propriétés du matériau.

Ces études montrent que les propriétés mécaniques dépendent beaucoup des paramètres du procédé et en particulier de la stratégie de lasage. Ainsi, une étude de plus grande ampleur a été réalisée en prenant en compte une gamme plus importante de paramètres pouvant agir sur les propriétés finales des pièces. Nous nous sommes intéressés, entre autres, à la puissance du laser, en mode contour LPo et en mode remplissage LPf, le pas de lasage SS, le nombre de passage du laser sur la même couche, en mode contour SCo et en mode remplissage SCf. Les niveaux choisis pour chacun de ces facteurs sont présentés dans le Table 0.1. Cette étude expérimentale s'est appuyée sur une analyse statistique afin de comprendre les relations entre chacun des paramètres et chacune des réponses associées.

**Table 0.1. Facteurs et niveaux choisis pour l'analyse statistique**

Paramètres de procédé	Paramètres étudiés				
	1	2	3	4	5
Puissance laser en mode remplissage, LPf [W]	15	20	30	40	45
Nombre de passage laser en mode remplissage, SCf [-]	1	2			
Puissance laser en mode contour, LPo [W]	10	13	15	/	/
Nombre de passage laser en mode contour, SCo [-]	1	2			
Pas de lasage, SS [mm]	0.15	0.20	0.25	/	/

Lors de cette étude, nous avons voulu voir l'influence de ces facteurs sur les réponses relatives à la géométrie, aux propriétés physico-chimiques et mécaniques, ainsi qu'au temps de production. Celles-ci sont répertoriées dans le Table 0.2.

**Table 0.2. Réponses choisies pour l'analyse statistique**

Réponses étudiées					
Densité et porosité	Géométrie et dimensions	Propriétés mécaniques en traction	Propriétés mécaniques en flexion	Transitions thermiques	Temps de production

Pour chaque jeu de paramètres du plan d'expériences, 40 au total, 5 éprouvettes de traction et 5 éprouvettes de flexion ont été réalisées. En se basant sur les résultats des expériences réalisées, nous pouvons affirmer que de bonnes pièces ont été fabriquées avec succès par procédé SLS à différentes puissances laser en utilisant le moyen commercial ProX500 SLS avec une densité d'énergie allant de  $0.015 \text{ J.mm}^{-2}$  à  $0.043 \text{ J.mm}^{-2}$ .

La faible porosité des échantillons imprimés, de l'ordre de 8 %, est observée pour une masse volumique presque stable sur l'ensemble des jeux de paramètres, pour une valeur comprise entre  $0.97 \text{ g.cm}^{-3}$  et  $1.04 \text{ g.cm}^{-3}$ . Un léger retrait, en longueur et en largeur, a été mis en avant. Le volume des pièces frittées augmente avec l'augmentation de la densité d'énergie du laser : cela est dû à la croissance de l'épaisseur des pièces. En comparant les propriétés mécaniques et le temps de production, en fonction de l'ensemble des paramètres, le jeu de paramètre n°9, proposé par le fournisseur du couple matériau/machine, ne sembla pas être optimum. De meilleures propriétés mécaniques ont été observées pour les jeux de paramètres n°11 et n°13. Les valeurs maximales de module et de résistance en flexion sont 1989 MPa et 68 MPa, respectivement. Tandis que pour la traction, le module d'élasticité, la résistance mécanique et l'allongement à la rupture ont des valeurs maximales de 2142 MPa, 44 MPa et 4.6 %, respectivement. On observe que le temps de production diminue avec une augmentation de la puissance du laser et une diminution du nombre de balayages. Les propriétés thermiques et la cristallinité restent inchangées quel que soit le jeu de paramètres utilisés.

La sphère globale de tous les résultats, Figure 0.9, fournit des corrélations plus précises.

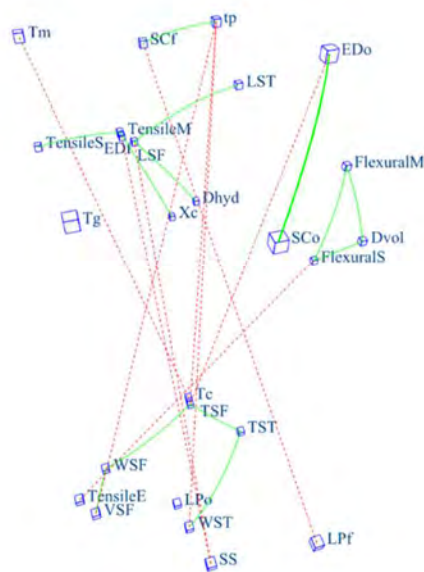


Figure 0.9. Sphère globale de tous les résultats au seuil de 0.3

L'étude montre que la méthode de l'iconographie des corrélations est adaptée à quarante configurations différentes d'un ensemble de paramètres avec un grand nombre de variables et de réponses. Malgré son apparente complexité, la méthode représentant l'organisation globale des variables met rapidement en évidence toutes les corrélations remarquables, qu'elles soient statistiquement significatives ou non, dont certaines peuvent être inattendues.

La méthode de l'iconographie des corrélations, en utilisant l'entièreté et l'unicité des données, peut permettre de définir les paramètres appropriés pour obtenir une pièce désirée. Suite à la détermination des surfaces de réponses et à leur optimisation, un jeu de paramètres optimisé a été défini. Les valeurs des facteurs à utiliser sont les suivantes : nombre de passage et puissance laser, en mode contour, 1.17 et 28.20 W, nombre de passage et puissance laser, en mode remplissage, de 1 et 15 W et un pas de lasage de 0.16 mm.



## Influence de l'histoire thermique sur les paramètres matériaux

Une approche numérique/expérimentale combinée permet d'estimer l'influence de chaque cycle thermique sur la cristallinité et les propriétés mécaniques des couches imprimées au cours de la technologie de frittage laser. L'objectif de ce chapitre est de comprendre l'impact thermique du laser lors d'un procédé de fabrication additive (SLS) sur les propriétés et la structure du matériau utilisé.

Pour la réalisation de la simulation, il a été choisi d'utiliser le logiciel Abaqus de Dassault Systèmes. L'objectif de cette simulation est d'obtenir l'histoire thermique de chaque couche suite aux passages successifs du laser. Un modèle de conduction 2D a été réalisé. Les profils thermiques de toutes les couches de 250  $\mu\text{m}$  ont été extraits. Il s'avère qu'un passage laser affecte thermiquement 14 couches. Seules les deux premières couches sont thermiquement affectées instantanément. Les quatre premières couches sont sensiblement affectées. Leurs profils thermiques sont donc réalisés en prenant en compte que le laser irradie la matière toutes les 4 secondes.

Etant donné qu'aucun PEEK n'existe pour le procédé SLS et qu'aucune machine n'existe pour la fabrication des pièces en PEEK, le profil assemblé pour la quatrième couche, Figure 0.10, est linéarisé afin de l'affecter au PEEK 2000 FP par l'intermédiaire d'un four de rhéomètre.

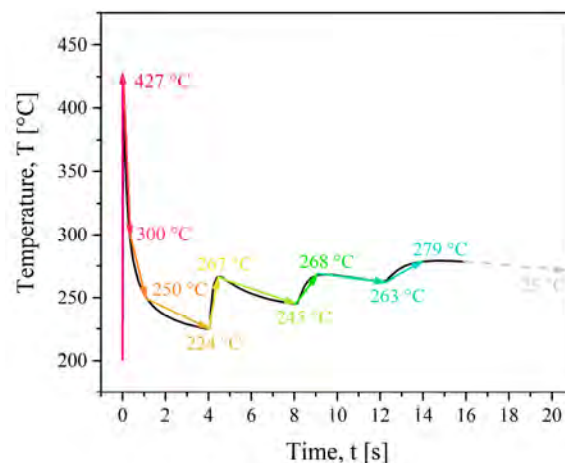


Figure 0.10. Linéarisation du profil thermique lors de 4 passages laser

L'étude sur le taux de cristallinité des différentes couches créées souligne que le taux de cristallinité est différent d'une couche à l'autre. Cela souligne que les pièces PEEK créées par le procédé SLS auront un gradient de cristallinité. Ainsi, pour mesurer le taux de cristallinité d'une pièce imprimée, la calorimétrie différentielle à balayage n'est pas un outil évident car elle donne une valeur moyenne en volume. La DRX semble donc plus adaptée. En outre, il a été

souligné que chaque couche reste à une température supérieure à 200 °C pendant toute la durée du lot. On peut supposer qu'il correspond à un temps de recuit.

Une étude sur le recuit des pièces a donc été réalisée pour des cycles de recuit de 2 heures et 4 heures à 204 °C. L'influence du recuit a donc été évaluée sur les propriétés mécaniques. Cette étude a prouvé que le recuit agit sur les propriétés mécaniques du PEEK 2000 FP. Plus le temps de recuit est long, meilleure est la résistance mécanique en traction et l'allongement, + 60 % et + 81 % pour 4 heures de recuit à 204 °C, respectivement. Le temps de recuit permet la diminution de l'écart-type qui indique une diminution des contraintes internes. Néanmoins, pour le PEEK 2000 FP, le recuit ne modifie pas son module d'élasticité.

## Conclusion et perspectives

Ces travaux mettent en lumière différents points et des efforts sont encore nécessaires pour optimiser les propriétés des pièces imprimées et améliorer la fiabilité du procédé.

Concernant l'élaboration d'un matériau aux propriétés adaptées pour répondre aux exigences SLS, nous avons proposé un nouveau matériau à base de PEEK et PES compatibilisé avec la phénolphtaléine. Les nouveaux mélanges présentent des propriétés mécaniques améliorées et une fenêtre de frittage étendue. Cependant, il serait intéressant de poursuivre. Un problème restant sera le traitement de ce mélange en particules sphériques et lisses et régulières. Il n'y a pas encore de procédé disponible pour obtenir de telles particules de 50 microns de diamètre moyen à partir de thermoplastiques.

Lors de la fabrication, de nombreux paramètres du procédé contrôlent la fusion de la poudre, et donc les propriétés des pièces et leur précision dimensionnelle. Ainsi, une analyse statistique de la réponse des paramètres a été conduite par un plan d'expériences pour en extraire les paramètres les plus influents. L'étude paramétrique, réalisée avec la poudre de polyamide, a été réalisée en faisant varier cinq paramètres et en examinant leur influence sur cinq groupes de réponses relatives aux propriétés physiques, mécaniques et thermiques ainsi qu'à la durée d'impression des pièces. Le plan d'expériences a permis d'établir les modèles mathématiques des surfaces de réponse reliant les réponses aux facteurs et leurs interactions. Ces modèles statistiques ont été utilisés pour définir un ensemble optimal de paramètres. Les résultats et l'optimisation des paramètres laser du procédé SLS ont montré comment ils influençaient le temps de production. Les résultats des essais sur la géométrie et la densité des éprouvettes en polyamide 12 ont confirmé que l'augmentation de la distance entre les passages successifs du faisceau laser permet une réduction significative du temps de fabrication. De plus, on observe une légère augmentation de la porosité du matériau avec des pores présentant un caractère stochastique. Par l'optimisation des paramètres laser, il est possible d'obtenir des propriétés mécaniques équivalentes, voire supérieures aux exigences actuelles, avec une réduction du temps de production de plus de 33 %. La méthode de l'iconographie des corrélations, en utilisant chaque spécimen comme donnée unitaire, peut donner les corrélations entre paramètres et les réponses ou bien même entre réponses. L'analyse d'optimisation par régression multiples permet d'obtenir les paramètres appropriés pour obtenir la pièce désirée. Dans cette étude, l'ensemble optimisé des paramètres nécessite une puissance laser de remplissage de 1.17 x 28.20 W, une puissance laser de contour de 1 x 15 W et un espacement de balayage de 0.16 mm. Il serait intéressant d'utiliser cet

ensemble pour récupérer des échantillons et un objet en taille réelle pour une analyse plus approfondie.

Enfin, une approche combinée expérimental/numérique a été réalisées pour estimer l'influence de chaque passage du laser sur le degré de cristallinité et les propriétés mécaniques de chaque couche. Les résultats montrent que l'échauffement dû aux passages successifs du laser couvre une épaisseur équivalente à 14 couches déposées. Cependant, seules les 4 couches supérieures sont significativement affectées thermiquement par le passage du laser sur une couche de poudre et montrent donc une évolution de leur degré de cristallinité. Il serait intéressant de passer à un modèle 3D multi-échelle et multi-physique plus avancé. Un modèle couplé DEM/FEM peut être utilisé en prenant en compte les phénomènes multi-physiques à différentes échelles : source de chaleur volumique à l'échelle de la poudre/bain de fusion, diffusion du laser au contact de la poudre et changements de phase et taux de cristallinité à l'échelle de la poudre/bain de fusion, conduction thermique à l'échelle de la poudre et à l'échelle de la pièce consolidée, déplacement du laser à l'échelle consolidée. Cela permettrait de prendre en compte des champs thermiques plus réalistes, de mieux intégrer les effets de bord sur les pièces, l'interaction entre le faisceau laser et la poudre, d'analyser le taux de cristallinité, l'évolution des porosités ouvertes et la création de porosités fermées dans le lit de poudre et d'intégrer les phénomènes de diffusion. Ensuite, ces champs thermiques plus précis pourraient être appliqués expérimentalement aux polyamides et aux polyétheréthércétones modifiés.

# **INTRODUCTION**

## **Research context and objectives**

The requirements of industrial market pose a challenging task to minimize the time from the idea to the final version of the product. To meet such requirements, additive manufacturing (AM) is attractive because it allows reducing significantly the development and industrialization phases of part design. Initially intended to facilitate and accelerate the fabrication of prototypes, additive manufacturing has become these five last years a very flexible method of tool production (rapid tooling) and short series product manufacturing. Such methods give the ability to quickly modify the part shapes and dimensions without having to change the tools. In addition, it allows quickly building a prototype model, which significantly reduces the time needed to launch a new product on the market. The high flexibility of additive technologies allows easy adaptation of product features to the needs and requirements of customers. As the machines production throughput has increased these last five years, AM is now beginning to extend in the industry to short and medium batch production. In the case of polymeric parts and polymer-based composites, these manufacturing processes compete effectively with injection moulding, extrusion, thermoforming and others for small series. In such processes, each change of product features requires modification of tools (mould, die head and other), which are usually expensive and time-consuming. Most of the additive processes do not require any mould. Finally, additive manufacturing gives the opportunity to virtually create any three-dimension complex shape such as hollow parts, lattices, foams with controlled porosity rate and any ideas that were previously impossible to manufacture. Indeed, the cost and time reduction associated with weight and topological optimization allow AM technologies to be adopted in several industrial segments.

Among the promising technologies for thermoplastic parts, the SLS (selective laser sintering) process stands out because of its ability to produce geometries with low dimensional tolerances. Industrial SLS applications are begun to widespread in aerospace, automotive and medical industries. This process is based on the displacement of a laser beam that interacts with the powder bed. It consists of the even application of thin layers of polymeric powder on a movable table of the machine on which the part is created. The table lowers by the thickness of the powder layer, applied each time before the laser beam passes through the powder layer.

A part of the laser energy is absorbed by the powder and melts the thermoplastic grains, the latter coalesce to connect the polymer particles. Several types of laser are used in additive manufacturing. Due to the high absorption coefficient of polymers in this wavelength range, the CO<sub>2</sub> lasers at 9.4 μm and 10.6 μm are the most used for polymer additive manufacturing. The unsintered powder inside the building chamber serves as natural support of the part under

the building. The procedure is repeated layer by layer until the whole part is obtained. After sintering the entire number of layers needed, the building chamber is cooled down to room temperature before removing the part and the unsintered powder. Then, the post-processing steps include coating and surface finishing. For example, some parts are treated with plating vacuum metallization and automated painting.

Theoretically, all thermoplastics can be assembled by sintering (or properly melting). However, there are large differences between polymers in their ability to be heated by a laser (wavelength range absorption, reflection and transmission coefficient) and their ability to be assembled by heat (melt viscosity, surface tension, the kinetics of crystallization). For each polymer, the process parameters must be determined in correlation with a thorough knowledge of the polymer properties to prevent defects in the scanning paths and high porosity. Some thermoplastics are not suitable for laser processing or their melt viscosity is too high to be assembled by heat. For this reason, limited polymeric materials are suitable for the SLS process. Due to the novelty of the process, few materials are available on the market, mostly polyamides.

The currently available polymers constitute a hurdle limiting widespread adoption of these key technologies in industry: The segments of aeronautics, space and military equipment require high-performance polymers, that is to say, thermal resistance higher than 250 °C in continuous use, elastic moduli of some GPa and low sensitivity to thermo-oxidative ageing. However, these high-performance polymers, tuned to be suitable to the SLS process, are still rare on the market. The cost of these powders is very high and their supply is limited. In addition, the powders and processes are often protected by international patents which limit the scope of action of companies. Polyaryletherketone (PAEK) are potential candidates for SLS printing. Polyetheretherketone (PEEK) is a semi-crystalline, thermoplastic polymer with very high thermal and chemical resistance. Its mechanical properties remain stable up to a temperature of 260 °C, while the processing temperature is from 370 °C to 400 °C. Moreover, the powders can have different properties depending on their size distribution, roughness and particle shape, even if they have the same chemical composition. These differences may be noticeable, among others, in the physical properties of the powder, thus resulting in different densities, surface quality and mechanical properties of the printed parts. The density and thermal conductivity of an evenly distributed powder layer are two features that significantly affect the sintering process. The course of solidification and consolidation of polymeric particles depends on them, which directly affects the quality of the obtained part. It is also possible to add fillers and other additives to the polymeric powders such as glass, aluminium and carbon fibres, thus improving the mechanical behaviour of the printed parts.

The effective use of SLS involves the appropriate adjustment of several process parameters. Their proper selection is a key factor in obtaining good quality printed components that meet the requirements. Some information about the impact of the individual process on the properties of the printed parts are available in scientific publications. However, the effect of combined parameters is rarely described. For example, the energy density is a combination of laser power and scanning speed. Their effect will be specific to each polymer, so it is extremely important in counteracting undesirable phenomena such as an insufficient penetration with too low laser power, a too high penetration with a low scanning speed and high laser power would lead to an irregular melting and “balling effect”, the formation of balls of melted material. The thickness of the layer also may have an impact on the mechanical properties and surface quality of the manufactured part. The lower its value, the higher the mechanical properties and lower roughness. When producing a prototype part, thicker layers are used, which measurably saves time and production costs. During proper production, the appropriate layer thickness must be chosen to reach the utility features in balance with the production time and costs.

This project was launched and driven by the company Prismadd (Montauban, France), specialized in additive manufacturing. It received funding from ANRT through a CIFRE agreement and was supported by Occitanie Region through a Pile-CIFRE. Additionally, this work was partly supported and driven by Centre National d’Etudes Spatiales (CNES), Sous-direction Assurance Qualité, Service Technologies, Matériaux et Procédés (Toulouse, France).

The work was carried out at Laboratoire Génie de Production (EA1905) at Ecole Nationale d’Ingénieurs de Tarbes (ENIT) in the research teams Interfaces and Functional Materials (IMF) and Mechanics of Materials and Structures Processes (M2SP). The company Prismadd, offers high-tech polymer or metal parts and subassemblies. As a part of WeAre Group, the company is situated in the additive business unit. The group builds competitive solutions tailored to the needs of its customers in the aeronautics, space, defence, energy, transportation and medical sectors. Focusing on polymeric parts, Prismadd manufactures aircraft parts (for example, tablet holder), prototypes and small series (air duct or steering ball joint, case prototype and more), tooling (drilling tool or positioning tool for welding, setting tool), maintenance parts (for example, conveyor clamps for a bottle filling line). In addition, the desire to maintain an active position in the aerospace industry motivates many of the research and development programs developed by WeAre Tech.



At the beginning of this PhD thesis in 2016, only a few studies on SLS processes were available in the literature. It is worth citing the three PhD thesis defended in France in 2012 and 2013:

- Dupin [1] contributed to a better understanding of the different physical mechanisms involved during the laser sintering of polyamide 12 powders. For that, he specified the relations between powder parameters, process variables and final properties of parts. Many recommendations for the optimization of powder properties can be derived from his work to develop new polymeric materials adapted to selective laser sintering process;
- Defauchy [2] proposed a model of the selective laser sintering process for high-temperature polymers like PEEK. He used numerical simulation at a microscopic level of the melting and the grain coalescence. For that, he used C-NEM method (Constrained Natural Element method) implemented on Matlab applied to preheated polymer powder bed. Then, the thermal study of the additional powder layer spread on the melted layer was performed on a commercial finite element software. During his study, he determined the spreading conditions allowing the melted material to keep the temperature above its crystallization temperature to enhance the material densification;
- Dumoulin [3] investigated the physical-chemical properties of seven high-performance polymer powders and studied their influences on the process steps and the quality of sintered/melted materials. Further, he studied the influence of the process parameters to obtain parts with good material quality, taking into account the evolution of the powder after each fabrication cycle. Finally, he determined and implemented a finite element subroutine for the mechanical behaviour in terms of the geometry of laser-sintered polyamide 12.

This PhD thesis follows on from the previous works, with new scopes to be taken up:

- studying the properties of some polymers to be used for SLS like polyamide 12 and polyetheretherketone available on the international market in 2016;
- formulating of new material with tuned properties to be suitable for SLS;
- optimizing the parameter sets on the ProX500 SLS printer to obtain the best mechanical characteristics;
- understanding the effect of the process parameters on the heat distribution in the part during printing.

## **Thesis outline**

This manuscript is divided into five chapters. The first chapter is a literature review on the SLS process: it is devoted to the general description of the process, the process parameters affecting the properties of 3D parts are presented as well as the properties of the polymeric materials playing a crucial role in the properties of the final parts. Also, the coalescence models are described, with an emphasis on the role of viscoelastic properties of polymers.

The second chapter presents the selection and characterization of two families of selected thermoplastic powders, polyamides and polyaryletherketones. The adaptability of these powders to the selective laser sintering process is evaluated experimentally. The recyclability issue of polyamides powders is also discussed at the end of the chapter.

The third chapter is dedicated to the elaboration of a new thermoplastics for the SLS process. The absence of suitable PEEK powder led us to develop a new material by blending PEEK with an amorphous thermoplastic, polyethersulfone (PESU). The initially immiscible blends have been compatibilized to improve their mechanical properties and to delay their crystallization on cooling. The influence of compatibilizers on the thermomechanical properties and morphology of the blends is highlighted.

The fourth chapter aims to understand the role of the different process parameters. Many process parameters control the melting of the powder, and thus the properties of the parts and their dimensional accuracy. Thus, a statistical analysis of the response of the parameters was led by a design of experiments to extract the most influential parameters. The parametric study, done with polyamide powder, was carried out by varying five parameters on the SLS machine and by looking at their influence on five groups of responses relating to the physical, mechanical and thermal properties as well as to the printing duration of the parts. The design of experiments made it possible to establish the mathematical models of the response surfaces linking the responses to factors and their interactions. These statistical models were used to define an optimal set of parameters.

In the last chapter, a combined experimental and numerical simulation approach was conducted to estimate the influence of each laser pass on the degree of crystallinity and the mechanical properties of each layer. The influence of the thermal cycles during the printing process, by simulating the heat transfer on the structure and mechanical properties are investigated. This study points out the evolution of temperature for a layer as a function of the number for layers below it, to determine the thickness affected by each laser pass.

# **1. STATE OF THE ART**

The literature review discusses three main issues, the understanding of which is crucial in the case of this research. First of all, the selective laser sintering process with special attention to the processing parameters has been investigated. The properties and structure of materials used for the research, with a particular accent on polyamides and polyaryletherketones, are the second part that explains their meaning and in which their main classifications are presented. The third part, which deals with the issue of physical phenomena of diffusion and coalescence, explains the theoretical basis and it is an introduction to the research objectives of this work.

## 1.1. The basic concept of additive manufacturing of polymers

To a new branch of technology which uses the incremental model, the building belongs to rapid prototyping (RP) technologies. This concept also called additive manufacturing (AM) or solid freeform fabrication (SFF) has gained popularity worldwide. In the industry, the devices are commonly called as three-dimension (3D) printing. By comparison with subtractive processes such as machining, small amounts of waste material are generated during a solid freeform fabrication. These technologies allow producing prototypes, patterns, models, and low volume parts in a very short time, which is associated with a wide range of applications thus producing models at reduced costs compared to traditional manufacturing processes. Layer upon layer, machines fabricate plastic, composite, ceramic and metal parts using thin and horizontal cross-sections. Raw materials may be in the form of a liquid, powder, sheet or filament. The 3D printing technique is used to make a physical copy of an object based on 3D models made with any computer-aided design (CAD) data, computer-based medical imaging techniques and other computer-based technologies. The models are made based on electronic 3D documentation provided in the following file formats: standard triangulation language (STL), virtual reality modelling language, and others [4]. The advantages of rapid prototyping include:

- reduction of cost up to 50 %;
- processing time reduction up to 75 %. Physical models from computer-aided design data files can be manufactured in a matter of hours to allow design effectiveness and rapid evaluation of manufacturability;
- better concept verification and visualization;
- high design flexibility to allow short-term component modifications;
- usage of a prototype in the next manufacturing operations gives final parts;
- cost-effective component production for demonstration purposes, and functional test samples.

Wohlers Association's report as an independent consulting firm provides technical, market and strategic advice on the new developments and trends in rapid product development, additive manufacturing, and 3D printing. According to the Wohlers report from 2019 [5], the additive manufacturing industry came within about \$ 200 million from producing \$ 10 billion in products and services in 2018. Moreover, it grew by nearly 62 % over the past two years, Figure 1.1.a. The significant share of this growth is the production based on the production of metal parts related to laser sintering technologies such as:

- electron beam melting (EBM) uses a beam of electrons to melt the metal powder;
- direct metal laser sintering (DMLS) or selective laser melting (SLM) to create complex shapes by selective melting of metal powders.

Many factors are contributing to strong additive manufacturing growth worldwide. Among them are industrial and business machines (20 %), aerospace (19 %), and motor vehicles (16 %), which constitute the largest share in additive manufacturing on the market, Figure 1.1.b.

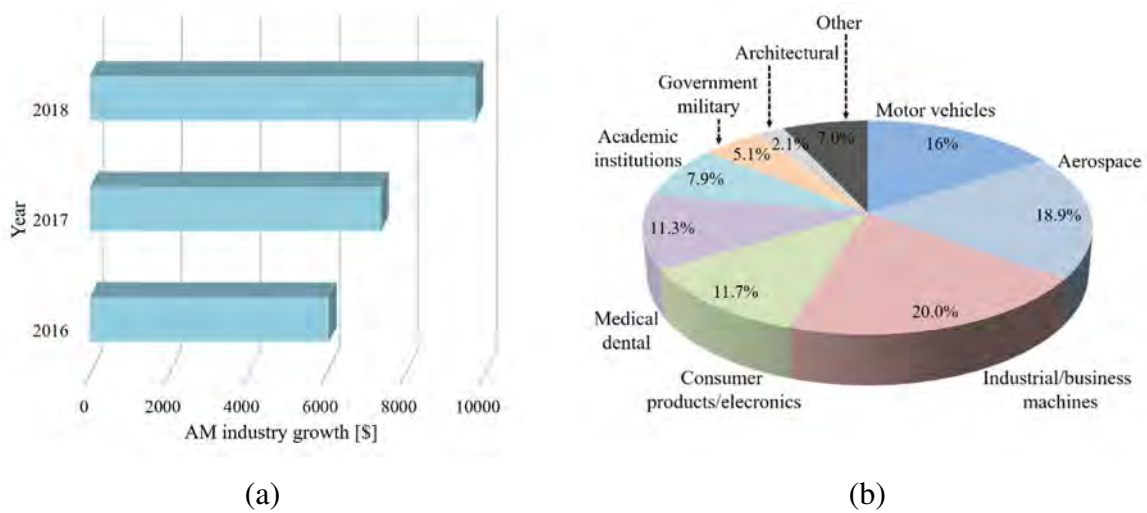


Figure 1.1. The Wohlers report 2019 of (a) AM industry growth (b) industrial activities of AM

In the area of rapid prototyping, there are always new or modified methods and techniques [6,7]. Most of the available processes for additive manufacturing work by sharing models for a horizontal layer by layer, which is built by using different techniques and materials. Moreover, 3D parts are highly effective in the production unit or implemented in small series [8]. The processes are designed to accelerate the preparation of a product, to improve its quality and to minimize costs to form a physical object. Currently, in mechanical engineering, architecture, medicine, and aerospace, the most common methods of additive manufacturing by using polymer powders are:

1. These based on curing of ultraviolet (UV) sensitive resins:

- material jetting (MJ), which creates parts by jetting tiny droplets of liquid photopolymer and instantly cured with ultraviolet light. The inkjet printer deposits only a single layer of hundreds of tiny droplets at a time, then the printing head cures the deposited material, solidifying it and creating the first layer. After the layer is complete, the build platform moves downwards one-layer height and the process repeats until the whole part is complete. After printing, it is necessary to remove the support gel by rinsing it with a water jet in a special pressure washer. Depending on the type of material used, it is possible to print transparent elements.

- stereolithography (SLA), which moves a lower power ultraviolet laser beam across an entire vat filled with liquid photopolymer. During the build cycle, the platform on which the part is placed, lowering by single layer thickness and selectively cured by the laser, Figure 1.2. The process repeats until the part is complete. Supports are also made of building material and they are removed mechanically after printing.

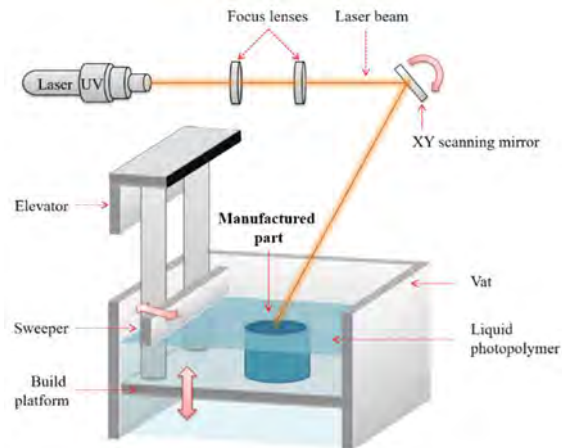


**Figure 1.2. Schematic of SLA process**

2. These based on melting of thermoplastic material:

- fused filament fabrication (FFF), which injects material through extrusion nozzles onto a build platform. Nozzles trace the cross-section pattern for each particular layer with a thermoplastic material hardening before applying the next layer.

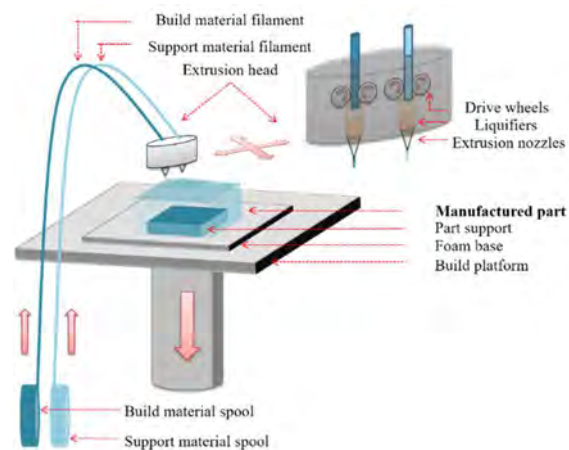


**Figure 1.3. Schematic of FFF process**

An extrusion head moves in two dimensions to deposit one horizontal plane at a time, the build platform or the print head is then moved vertically by a small offset from actual position to begin a new layer, Figure 1.3. The part is ready with the deposition of the last layer. Supports are built of the same material as the element being made and removed mechanically, or from special material and dissolved in water. Products assumed to be

manufactured with an accuracy of 0.13 mm in the X-axis and Y-axis, accuracy in Z-axis depends on the thickness of the applied layer.

- selective laser sintering (SLS), Figure 1.4, which applies a high powered laser to fuse small particles of material. During the build cycle, the platform on which the build is repositioned, lowering by single-layer thickness. After each laser sweep, a new layer of powder is added until the resulting workpiece [9].

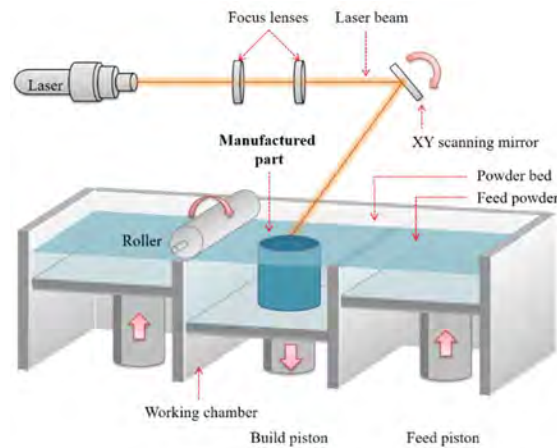


Figure 1.4. Schematic of SLS process

Considering all current automated manufacturing technology layer by layer, selective laser sintering has the greatest production potential. This is due to several very important advantages such as high accuracy, no need for support material and a high construction rate. The main advantage of the selective laser sintering process is the ability to rapidly produce net-shape or near-net-shape parts with varying geometries by using a single machine without any specific tool. The process exhibits very high freedom of design currently available and many industrial sectors such as jewellery, fashion and consumer goods, have started to use it. Moreover, freedom of design allows patient-specific customised implants in the medical sector, whereas the aerospace, defence and automotive industries have been utilising selective laser sintering process for the production of design optimised lightweight components. Nevertheless, some drawbacks can be specified like a narrow range of materials (mostly polyamides) and high material prices for other high-performance polymers on the market (polyaryletherketones). Most polymeric grades exhibit mechanical and material properties that are not suited to applications requiring high material performance such as tensile strength, wear resistance, thermal stability, and chemical neutrality.



## 1.2. The selective laser sintering process

The selective laser sintering process produces small prototypes, for example, jewellery, fashion, consumer goods and others. It was first developed and patented by Deckard and Beaman [10] from the University of Texas at Austin (USA) in the mid of 1980s. It was commercialized by Desktop Manufacturing Corporation from the USA in 1987 [11].

The manufactured part in the selective laser sintering process is executed based on the geometry of the 3D model saved in a format standard triangulation language. The prepared model is transferred to the system by the use of software and is divided into layers [12]. The nomenclature involved in laser sintering technology is presented in Figure 1.5. There is laser beam power (applied power of laser as it scans the area of each layer), scan count (number of times the laser beam goes through a scan vector per layer), scan speed (velocity at which the laser beam travels as it traverses a scan vector), scan spacing (distance between parallel laser scans) and powder layer thickness, which determine the laser energy input into the part bed. Moreover, exposure time (length of time when laser spots in a single point) and point distance (distance between laser spots) can be taken into account.

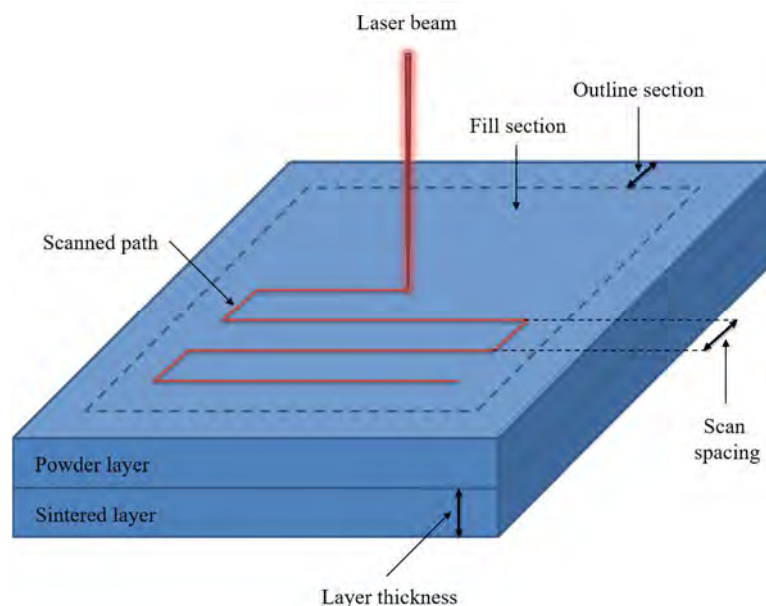


**Figure 1.5. Schematic diagram of the SLS process showing the relevant nomenclature**

The process consists of sintering the surface of the layer with a laser beam, such as carbon dioxide (CO<sub>2</sub>) laser or neodymium: yttrium aluminium garnet (Nd:YAG) laser. The powder from a feed chamber is distributed by a roller layer by layer on a build piston.

Before starting the process, the entire bed temperature is increased below the melting point of material by infrared heating lamps. The laser beam enters a layer (generally the order of 100  $\mu\text{m}$ ), first the outline of the section, then fills the inside of the section layer. The parts are built layer by layer where the powder is scanned by the laser beam tracing upon the platform. The height of the next layers makes the platform lowered and the powder is reapplied. This process continues and it is repeated until the object is complete. Thus, the duration of manufacturing a part depends on its height and surface, and it is almost identical regardless of the number of parts to be manufactured in the volume of the build chamber.

The powder in excess in each layer supports the structure during the building of a part. Therefore, the parts do not require separate support structures during manufacturing. This fact allows this method to perform even the most complex shapes and spatial structures with a minimum wall thickness at the level of a millimetre. In the end, when the part is complete, the non-fused powder can be removed by shaking the object manually or using a compressed air jet as well as sandblasting [13].

Selective laser sintering technology enables high part accuracy, flexible and low-cost production of small series and individual parts. Also, the selective laser sintering process is carried out in a protective atmosphere of inert gas and proceeds without using crucibles moulding element to give free of impurities and side effects of combustion. A significant disadvantage of this process is a long time to cool before removing the part from the workspace and removing the unused powder.

### **1.2.1. The parameters of the SLS process**

Evaluation of parameters that could influence the optimisation of quality characteristic was carried out. Previous studies [1–3] indicate that preheating and part bed temperature, energy density, layer cooling time, powder base and layer thickness, as well as part location, position and orientation, have an influence on a manufactured part in the selective laser sintering process.

Besides parameters, which can be controlled, there are also uncontrolled factors that may affect the selective laser sintering technology. The controllable and uncontrollable factors can generate signals, in favour of sintering process performance, and noises that work against sintering process performance. It is necessary to increase the signal and reduce noise from uncontrollable factors [14].

**Table 1.1. Processing parameters that may affect the SLS process**

Controlled parameters	Uncontrolled parameters
Preheating temperature, $T_p$ [°C]	Chamber temperature variation
Part bed temperature, $T_b$ [°C]	Composite homogeneity
Energy density, ED [J.mm <sup>-2</sup> ]	Moisture in the material
Laser power, LP [W]	Optical properties
Scan speed, LS [mm.s <sup>-1</sup> ]	Layer cooling time
Scan spacing, SS [mm]	
Scan count, SC [-]	
Layer thickness, PLT [mm]	
Orientation, $\theta$ [°]	
Post add powder layer delay, $t_{pl}$ [s]	

During the selective laser sintering process, there are many parameters which control the powder fusion and edge definition, as presented in Table 1.1. Those parameters may have an impact on the final properties of parts [15]. Two types of essential parameters can intervene:

- preheating temperatures of powder and part bed temperature;
- energy density calculated from the parameters of the laser.

### 1.2.1.1. Preheating temperature

The main goal of preheating the powder bed is to make easier for the laser to raise the temperature and obtain melting of polymer. The powder bed needs to be heated during the selective laser sintering process for a sufficient duration before the parts are built and also after they have been completed. It minimises shrinkage that occurs during cooling and recrystallization. The improved dimensional accuracy and reduced distortion can be obtained by controlling the rate of crystallisation temperature ( $T_c$ ) [16]. The feed chamber temperature should be above the glass transition temperature ( $T_g$ ) and just below the melting temperature ( $T_m$ ) of semi-crystalline polymers or in the case of amorphous polymers, approximately equal or less than the glass transition. Maximising the part bed temperature can minimise the amount of laser energy needed for consolidation, lower the thermal gradient between a consolidated and unconsolidated powder and decrease the thermal expansion due to heating by the laser. Thus, it is very important to choose the right temperature of preheating the powder materials. Too high bed temperature may reduce the flow of material or unsintered powders (known as the “powder cake”) can partly fuse with the sintered structure, which can make it more difficult

to remove after the process and reduce the degree of recyclability of powder. On the other hand, incorrect part bed temperature may lower the mechanical strength of sintered products and created objects may fall apart during the post-treatment [17].

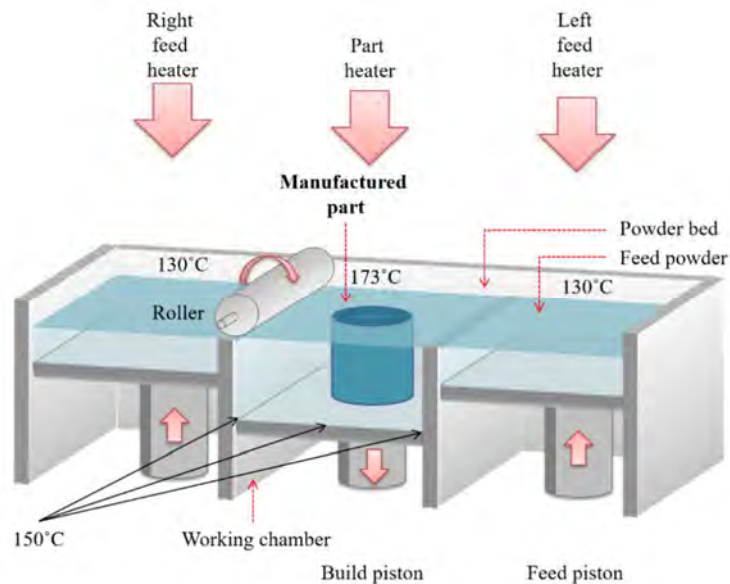


**Figure 1.6. Schematic of preheating temperature during the SLS process (3D Systems, Sinterstation HiQ)**

In Figure 1.6, it can be seen that the system can preheat the powder in feed chambers that are surrounded by heaters. The build chamber has a piston heater under the part bed, a cylinder heater encompassed it and the heater above the build area is divided into two, an inner and outer ratio. Thermal control, real-time monitoring and calibration are controlled by the machine. Other kinds of machines can have an exchangeable frame that contains heaters in the walls and base. There is also a process chamber heater that flash heats the powder bed between layers (EOS, P3 and P7 series). The heater can be larger than the build area, where the radiant heater is above and two convector heaters at the side of the removal build frame, at an angle (EOS, P100 series) [18]. The part quality and material recyclability are strongly affected by different methods of preheating. Moreover, the expense of powder requires reusing unconsolidated powder.

### 1.2.1.2. Part bed temperature

The main stages of the selective laser sintering process depend on heating the powder from room temperature to above the melting point to allow melting. Then, the material is cooled in the machine until the temperature allows opening the build chamber, next until the ambient temperature in a nitrogen atmosphere at a breakdown station. The processing temperature range for a polymeric material can be determined by the differential scanning calorimetry (DSC) curves.

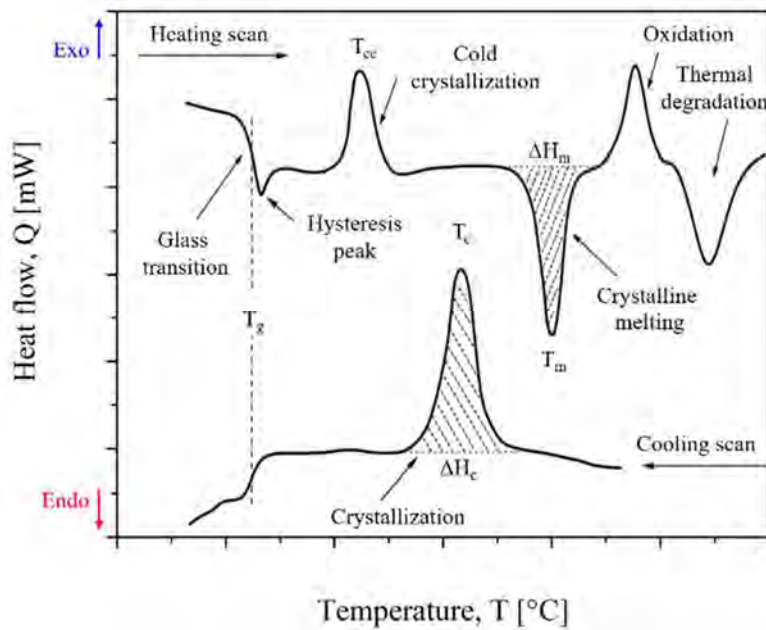


**Figure 1.7. The DSC curves of different transitions and reactions of the typical polymer [19]**

Figure 1.7 shows the phase transitions for different phases of matter, which can be changed under the right conditions, wherein its properties also change in a distinctive and readily apparent manner. There are two reactions observed such as an exothermic reaction that releases energy through light or heat, and an endothermic process which requires or absorbs energy from its surroundings, usually heat. Usage of a differential scanning calorimetry technique makes possible to observe melting and crystallization phases as well as glass transition temperatures.

The temperature and heat are highly related to the motion of molecules, which is the dynamic behaviour of them, intramolecular and intermolecular interactions on a certain time scale. All molecules are in constant motion. For example, molecules of liquid have more freedom of movement than those in solid, molecules in a gas have the greatest degree of motion. Temperature is a measure of the average kinetic energy of molecules in a material. Heat is the energy transferred between materials that have different temperatures. Increase of temperature increases the translational motion of molecules energy [20].

The glass transition temperature is the one for which a rapid decrease in storage modulus occurs. It is varying for each polymer and it takes place in an amorphous region of semi-crystalline polymers. Glass transition occurs due to an increase in the motion of large segments of molecular chains caused by heating from below glass transition temperature. There is a point where the behaviour of polymer rapidly changes and the van der Waal bonds break, caused by the application of a certain amount of heat. The mechanical behaviour

changes from glassy and brittle to become less rigid and rubbery. The crystalline regions are maintained, because of stronger covalence bonds, so melting does not occur until a higher temperature is applied.

The melting point is the temperature at which the polymer changes state from solid to liquid by loss of order in the crystalline zones. When the temperature rises above the glass transition, the molecular motion starts to increase, because the elastic modulus goes down. The process continues in temperature rising to just above the melting point. After the polymer becomes liquid and the chains are all tangled up with their neighbours. The melting temperature is the one where the materials eventually obtain sufficient thermal energy as the temperature rises to enable its chains to move freely enough and to behave like a viscous liquid.

The crystallisation takes place between the melting point and the glass transition. At temperatures close to the melting point, large crystal sizes can be obtained, because of the low crystallisation rate. While at temperatures near to glass transition, the melt is so viscous that molecular motion is extremely slow, thus leading to a faster crystallisation rate.

Distance between onset melting point and onset crystallization temperature is called the “SLS sintering window” [21]. Thus, a wider window allows to semi-crystalline powders during the cooling phase to stay in its liquid state for at least the addition of several layers. It is important for interlayer welding and maintaining accurate part geometry. On the other hand, when the peaks are very close or superimposed each other, the material may quickly crystallise undercooling, making shrinkage and distortion more likely. Because melting temperature and re-crystallization (temperature below the melting point where semi-crystalline polymers solidify) are first-order phase transitions, enthalpies are associated with the transitions. Ideally, both enthalpies would be equal in magnitude and opposite in sign. A narrow melting peak is desirable because the part bed temperature can be raised closer to the average melting temperature, thus minimizing the laser power required for melting. The enthalpy of melting is endothermic, thus it acts as an energy barrier to melting. The enthalpy of crystallization is exothermic thus it slows down solidification from the liquid state.

In the case of an amorphous polymer, a physical change occurs at the glass transition which is a quasi-second order phase transition. The enthalpy is not changed at this transition, so it is more difficult to control the amount of sintered powder in the powder bed. Compared to semi-crystalline polymers, the temperature dependence of viscosity above the glass transition makes using amorphous polymers more difficult for the selective laser sintering process. More heat is required to decrease the viscosity in comparison to semi-crystalline polymers [22].

Furthermore, some behaviour can lead to deleterious effects on the mechanical properties of sintered parts. If part bed temperature is lower than the material onset crystallisation temperature, major and localized shrinkage may occur during and just after the laser exposure. While this temperature is higher than the material onset melting temperature, uncontrolled melting may occur all across the powder bed without even laser exposure [23]. Any selective laser sintering temperature inside the processing window can lead to a controlled and effective process.

During the selective laser sintering technology, to achieve fluidity without the need for excess energy, the desired thermal properties such as a narrow melting temperature range combined with a low melt viscosity are necessary. A lower viscosity tends to lead to greater shrinkage and lower accuracy. Thus, the bed temperature can be raised closer to the melting temperature of the polymer, minimising the power of the laser beam that is used to selectively melt the polymeric particles. For several sintered layers, the crystallization should be inhibited during processing as long as possible. A full coalescence of particles in the top powder layer and adhesion on the previously sintered layers are required [24].

### **1.2.1.3. Energy density**

Sintering of polymers or other materials with low melting temperatures usually requires using CO<sub>2</sub> lasers with a wavelength of 10.6 µm. However, for selective laser sintering process lasers, with a short wavelength of 1.06 µm named Nd:YAG, can also be used. They may outperform CO<sub>2</sub> lasers for sintering metallic and ceramic materials, which absorb much better at short wavelengths. It was found that for the CO<sub>2</sub> laser, the processing window is larger than for the Nd:YAG laser. Furthermore, for both kinds of laser, the processing windows are affected by the particle size of materials [25].

During the selective laser sintering technology, a laser beam hits a polymer material with three effects [21]. Besides the absorption of energy, it is possible to see the reflection and transmission presented in Figure 1.8. The energy absorption gives sufficient capability of the material to absorb radiation of laser wavelength. This is apparent for most polymers as they consist of aliphatic compounds (C-H). These polymers have some group vibrations in the “fingerprint” infrared (IR) region, sufficient to absorb relevant portions of 10.6 µm with CO<sub>2</sub> laser radiation.

However, during the selective laser sintering technology, the effects of reflection and transmission become relevant as well. Transmission is desired to direct a sufficient portion of

radiation energy into deeper regions of a powder bed to induce melting and adequate layer adhesion. Only when the current powder layer is connected with the previously sintered layer, the sintered part can be generated without layer delamination. In case of poor absorption and transmission capability, an increase of laser energy power can compensate to a certain amount the effect. An increase of laser power must be limited in order not to degrade the polymer with too much energy.

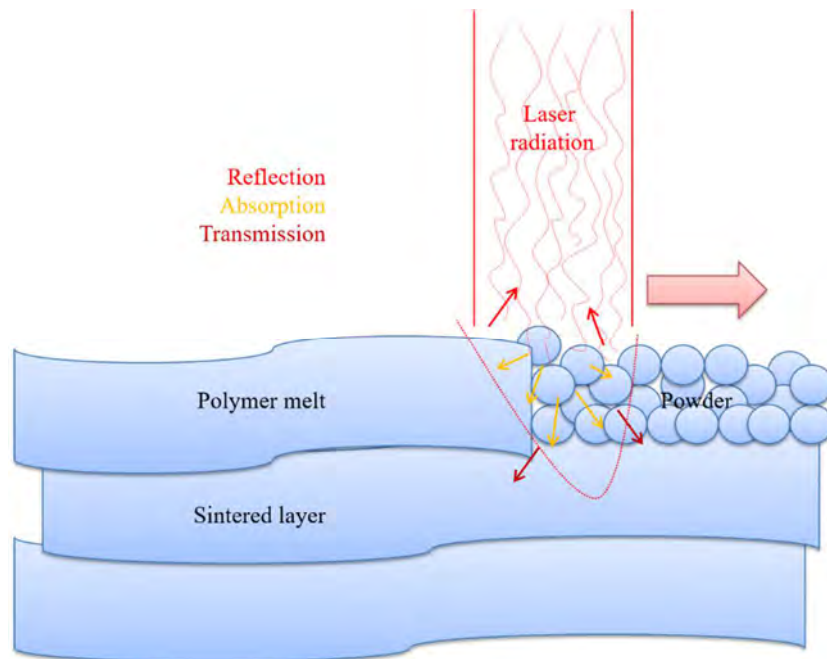


Figure 1.8. Optical circumstances of the SLS process

The value which describes the laser parameters is an energy density. Equation 1.1 determines the energy density as a function of laser power, scan spacing and laser scan speed [26]. The energy density level is the amount of energy supplied to the powder particles per unit area of the powder bed surface.

$$ED = \frac{LP}{SS \times LS} \quad (1.1)$$

where:

- ED - energy density [ $J \cdot mm^{-2}$ ];
- LP - laser power [W];
- SS - laser scan spacing [mm];
- LS - laser beam speed [ $mm \cdot s^{-1}$ ].

There is an optimum energy density for each material, which generally needs to be determined on an empirical basis, although some general rules apply. For the same energy



density level, it is possible to increase part density and tensile strength by increasing laser power, and at the same time decreasing scan speed and scan spacing [27]. On the other hand, if the laser power is too high, shear stresses between layers are formed as a result of increased liquid flow and the parts may curl or become distorted [28]. The higher energy density can improve particle fusion and mechanical properties, but if exceeded to the safe point, it results in degradation and deterioration of mechanical properties.

The range of energy density suggested for polyamide 12 should be between  $0.01 \text{ J.mm}^{-2}$  and  $0.048 \text{ J.mm}^{-2}$ . When the value of energy density is below  $0.01 \text{ J.mm}^{-2}$ , the sintering may not be proper, and if the value is above  $0.048 \text{ J.mm}^{-2}$  it was noticed that the degradation of the polymer occurs [25]. The effect of energy density was examined by Gill and Hon [29], for example, the results for polyamide/SiC composites confirm that the maximum strength is obtained at  $0.04 \text{ J.mm}^{-2}$ . The incident energy was insufficient below this level, which results in partial melting of polyamide and structural porosity. Above  $0.04 \text{ J.mm}^{-2}$ , the energy was too high causing degradation of polyamide, increased porosity, and reduced strength of parts. According to Negi et al. [30] who have worked on polyamide powder with the increase of laser power, the strength of parts increased over 14 %, on contrary, in case of increase in scan speed and scan spacing, the ultimate tensile strength and yield strength of sintered parts decreased over 85 % and 64 %, respectively.

Additionally, the layer thickness of part has been added in the energy density equation by Usher et al. [31], as presented in Equation 1.2. The addition of powder layer thickness (PLT) in the denominator of this equation provides the volume energy density [32]:

$$ED_{\text{vol}} = \frac{LP}{SS \times LS \times PLT} \text{ [J. mm}^{-3}\text{]} \quad (1.2)$$

The layer thickness is one of the important factors which indicates the properties of the sintered part. The common layer thickness for the selective laser sintering process is 0.1 mm or 0.15 mm, equating to two or three times the average recommended particle size. In this case, the majority of particles receive direct contact from the laser. Using a too-thin layer, equivalent to the average particle size, can cause the particles to segregate during deposition [18]. In the research of Pereira et al. [33], the powder layer thickness caused more alterations to scaffold properties than the scan spacing. The surface properties of scaffolds (substrates in tissue engineering) have an important role in stem cells of biomaterials interactions, ultimately controlling the stem cell adhesion, proliferation and differentiation after its

attachment on the surface [34]. Thus, the first slices deposited were significantly affected due to severe curling of these slices when the lowest value of powder layer thickness was used. The decrease of the values for layer thickness or scan spacing increased the compressive mechanical properties of the part. Stwora and Skrabalak [35] have investigated the parameters of laser sintering technology such as laser power, scan speed, exposure time and point distance on direct steel. The results show that the most important influence for hardness, density and compression strength of sintered samples are: laser power of 200 W, point distance of 50  $\mu\text{m}$  and exposure time of 100  $\mu\text{s}$  (EOS 250xt, SLS machine, and Renishaw AM250, SLM machine). With lower laser power and exposure time, the samples were not sintered properly. Scanning speed did not influence the sample properties, however, it might be possible to reduce the time of machining by maximising scan speed, in case of building large elements.

There is a different way to present the previous equation which can be used to approximately calculate the laser power required for a given material depending on its thermal properties [29].

$$LP = \frac{LS \times \rho \times D_{lb} \times PLT \times [C_p \times (T_m - T_b) + L_m]}{(1 - R_\lambda)} \quad (1.3)$$

where:

- LP - laser power [W];
- LS - laser beam speed [ $\text{mm}\cdot\text{s}^{-1}$ ];
- $\rho$  - powder bed density [ $\text{g}\cdot\text{mm}^{-3}$ ];
- $D_{lb}$  - diameter of laser beam [mm];
- PLT - powder layer thickness [mm];
- $C_p$  - specific heat [ $\text{J}\cdot\text{kg}^{-1}\cdot\text{K}^{-1}$ ];
- $T_m$  - melting temperature [K];
- $T_b$  - part bed temperature [K];
- $L_m$  - latent melting heat [ $\text{J}\cdot\text{K}^{-1}$ ];
- $R_\lambda$  - reflectance [-].

From Equation 1.3, the main fabrication parameters concerning the energy delivered are laser power, laser beam speed, scan spacing, and powder layer thickness.

Characterising the state of polyetheretherketone, due to process boundaries of laser sintering, showed a narrow process window of around 10  $^\circ\text{C}$  [36]. First of all, the preheating

temperature should be maintained within a range of 343-357 °C, near the melting temperature of polyetheretherketone (350 °C) and the surface energy is rapidly limited. A strong dependence of relative density with the surface roughness is shown. Furthermore, poor adhesion between layers and high porosity of 15 % is observed in the case of too low energy density. Distortions are visible in case of too high energy input [37]. However, the final part density also depends on the initial density of powder. These typical dimensional variations are due to inhomogeneous shrinkage during the building and cooling process.

In the selective laser sintering process, a standard print mode is characterised also by scanning strategy. This could be a “fill” or “fill and outline” option. It allows the laser beam to scan the entire cross-section with outlines its contour as shown in Figure 1.9.

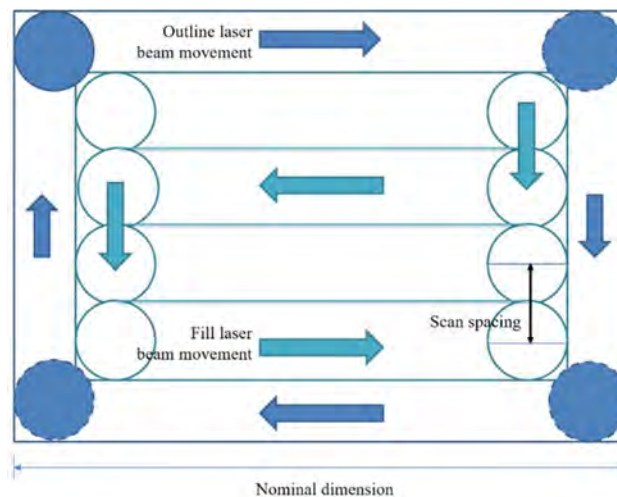


**Figure 1.9. Laser scanning strategy of the SLS process [28]**

In general, the fill and outline laser beam movement used to set the process parameters came from configuration files developed by the manufacturers. Usually, these offset values cannot be modified, except for small changes in the range from one to two. It can have a significant impact on dimensions of the part, as well as on build profiles [28].

Mentioned earlier scan spacing decides the beam overlap area of continually sintering scan lines that is relevant to the energy distribution. Moreover, sinter scan selects and sets the scan vectors to alternate in the X-axis and Y-axis every other layer.

#### **1.2.1.4. Other SLS parameters**

The other important selective laser sintering process parameters are layer thickness, the orientation of parts and post add powder layer delay [38]. These parameters determine the energy that the parts being sintered absorb, therefore, they can significantly affect the quality of sintered products.

**1.2.1.4.1. Layer thickness**

The thickness of spread layers has a direct influence on the productivity of sintering machines. Indeed, if the layers are thinner the duration of the manufacturing cycle is longer. Moreover, the energy supplied to the surface of powder layer depends only on parameters relating to the laser, but from a volume point of view, the energy received by the powder may also depend on the thickness of spread layer [39,40] and to the penetration depth of laser [41]. Thus, for the same energy density applied to the surface of the powder layer, the energy supplied to the unit volume of material in each new layer deposited may increase as the thickness of these layers may decrease. It is evident that the greater the thickness of the spread layer, the higher the energy required to allow the powder grains to melt over the entire thickness and thus to avoid problems of sintering between the layers which would drastically reduce the mechanical properties in the direction perpendicular thereto.



**Figure 1.10. Influence of thickness for spread layers on the surface appearance of parts**

The thickness of layers also has an influence on a surface appearance, roughness and on dimensional accuracy. Figure 1.10 shows that for an inclined plane, the surface appearance is better if the thickness of layers is low.

**1.2.1.4.2. Orientation**

The orientation of the 3D digital model is defined as a normal direction of sliced layers. Due to the layer by layer manufacturing mode, an anisotropy of mechanical properties of parts is expected. A part orientation is important because it affects most of the final properties.

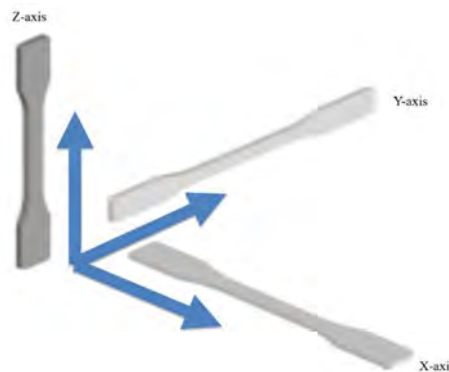


**Figure 1.11. Build orientation of parts**

Figure 1.11 presents the building orientations of parts. Some studies [26,28,42,43] have shown that the mechanical properties along the Z-axis, perpendicular to the powder layers are 20-30 % lower for tensile strength and 5-10 % lower for elongation at break than in a plane parallel to them. This anisotropy is explained by a lower adhesion between powder grains located at an interface of two layers than of neighbouring grains in the same layer, the latter receiving more energy. Ajoku et al. [44] also showed an anisotropy in the plane XY parallel to the powder bed. Indeed, by using a machine whose scanning direction of the laser remains parallel to the X-axis throughout the manufacturing, mechanical properties were improved along this axis were obtained concerning the Y-axis. They suggest that this phenomenon is due to a reduced adhesion between the sintered layers parallel to the X-axis. However, the spacing between each scan of the laser does not seem to have been taken into consideration in this study.

#### **1.2.1.4.3. Post add powder layer delay**

After the laser scans each layer, there is a delay time between the sintering of a new layer of powder over the build area and scanning of the next layer. This time may be imposed by the sintering machine but is also related to the surface to be scanned by the laser and hence to the quantity of sintered parts. According to Goodridge et al. [18], when this time increases, the mechanical properties of the parts can decrease and the phenomenon of “curling” grow. Jain et al. [45] showed that the delay between two successive sweeps of two adjacent points of the same part also influenced the tensile strength. They were able to determine an optimum delay between 0.007 s and 0.014 s for polyamide powder (PA2200) for which the tensile strength was maximum at around 44 MPa.

### **1.2.2. Studying the effect of parameters on the properties of printed parts**

It is possible to manufacture numerous products in the same build chamber at the same time according to the requirements of final users. The processing parameters can be chosen for each printed part during one process. Many parameters are affecting the properties of printed parts, and these parameters are interdependent. Understanding the effect of parameters requires the use of mathematical methods such as the design of experiments.

An extensive review has been carried out by Varia and Goyal [46] on the process parameters of surface quality and properties of printed parts. According to them to study the effect of processing parameters the Taguchi technique and an orthogonal array of experiments with analysis of variance (ANOVA) are mostly used. The review presents that optimisation of process parameters and the working accuracy of optical units were crucial for improving part

quality and accuracy. The influence of a particle size distribution, lower layer thickness, reduction of scan spacing, scanning speed and sensitive to build direction have been observed.

Principal component analysis (PCA) is a multivariate statistical method that is useful when a large number of quantitative variables are studied. It makes it possible to understand the structure of the cloud of data and to determine the links on all the variables considered. This calculation method is based on the projection of a set of quantitative data belonging to a multidimensional space on a 2D space. The principal component analysis is used to study the relationships between several variables whose values are known for every statistical unit. The principal component analysis consists of representing the data in the X-axis and Y-axis coordinate system to identify the main directions or principal components in which the data varies. Thus, non-viewable relationships in a space whose number of dimensions is greater than two are highlighted on the projection plane.

To analyse the variation of data, the variance can be used to characterise the dispersion of a sample or a distribution. One of the starting hypotheses is that the highest variances are found in the larger, called principal directions [47]. Thus, the amount of variance explained by each principal component is quantified by an eigenvalue.

It should be noted that the principal component analysis is particularly useful when the variables in the dataset are highly correlated. In probability and statistics, studying the correlation between two or more random variables or numerical statistics leads to study the intensity of the connection that can exist between these variables. The fact that two variables are “strongly correlated” does not demonstrate that there is a causal relationship between one and the other. The correlation indicates that there is redundancy in the data. Because of this, the principal component analysis can be used to reduce the number of original principal component variables, the latter accounting for most of the variance contained in the original variables [48]. Principal component analysis can also be useful for identifying correlated variables as well as “hidden profiles” in a dataset [49].

Another mathematical method is software, an iconography of correlations (CORICO) [50]. A commercial software, having the same name of the method, integrating the iconography of correlations and logical interactions, designed for large multivariate analyses. It also incorporates a predictive modelling technique based on postulated and unposted multiple regression models.

This method performs the experiments prescribed in the plan and based on results obtained, it eliminates the uninfluential factors. According to the desired response, the

iconography of correlations indicates the optimal configuration of the remaining factors. It can also take into consideration conditional similarity [51], possibly weighted, in a function of “desirability”, in order to find a configuration of factors giving the best compromise for all answers.

### **1.2.3. Main disadvantages of SLS printed parts**

The selective laser sintering technique is well mastered for polyamides 11 and 12 in thesis work from 2012 [1] and make them possible to manufacture prototyping parts. On the other hand, for the high-performance polymers and in particular polyaryletherketones (PAEK), the manufacture by selective laser sintering is not yet mature. The previous thesis works from 2012 and 2013 [2,3] helped to identify the most important parameters to achieve progress on the quality of a final part and robustness of the process. However, according to these works, the following points remain problematic:

#### 1. Effect of process parameters on the mechanical properties:

The modulus of elasticity of specimens manufactured in the XY-axis is generally 30 % higher than for an injected specimen, because of a larger crystalline phase. Indeed, slow cooling allows a larger organization of molecules. A high degree of crystallinity makes the materials brittle, so it is necessary to master this crystallinity rate according to desired mechanical properties. For the stresses at rupture, they are identical to that of a specimen injected in direction XY-axis, but on average 40 % lower in the Z-axis direction. The break-in tension is due to the loss of cohesion between two successive layers. This break always starts on a pore situated between two layers. The elongation at break is four times higher in the XY-axis or the XZ-axis than in the Z-axis production direction. The origin of this anisotropy is mainly due to the gradients of thermal fields during consolidation. In other words, the microstructure of parts from the selective laser sintering process is complex and heterogeneous. For instance, some particles absorbing sufficient energy are fully melted, other particles absorbing non-sufficient energy are partially or even not melted.

#### 2. Producing time of parts:

Reducing the production time of parts is essential to increase productivity. The manufacture of complex parts can last more than 24 hrs. During this time, the polyaryletherketones are degraded in the presence of oxygen at high temperature. Also, a record of temperature and thermal gradients are essential. In parallel, the good knowledge of thermal and rheometric properties of the material, by measurements of melting enthalpy, thermal

conductivity, viscosity as a function of temperature, may allow reducing the manufacturing time of parts while preserving a duration in a molten state. Thus, the mobility of molecules may sufficient interlayer cohesion.

### 3. Recyclability of powder:

The unconsolidated powder properties can change or degrade during the process, for example, polyamide 12 undergoes both solid-state polymerization and powder agglomeration where melt viscosity and part roughness increase, respectively [22]. To slow down the degradation, a lower part bed temperature can be used. In practice, a balance has to be struck between making parts and extending the life of used powder.

The recycling of powder which has not undergone the insolation of laser is a major challenge, knowing that the cost of polyaryletherketone powders is up to 1000 € per kilogram. Moreover, the cost of powder associated with that of the occupation of the machine makes the final price prohibitive for the moment. It is necessary to evaluate the influence of temperature of powder on its flowability. As a result, an increase of the amount of material used due to conditions may enable to propose a maximum recycling rate of powder for re-use in a new manufacturing cycle mixed with new powder.

#### **1.2.4. Post-processing of SLS printed parts**

Materials in laser sintering technology are ideal for the production of low mass from a few to a thousand parts, and an additional advantage of selective laser sintering process is much greater freedom of design complex parts than in the case of products designed for injection moulds. Unfortunately, as long as parts of selective laser sintering technology are far from the quality of surface obtained by injection and in the case of aesthetic detail is almost always required, laborious post-processing is needed. Despite this, there are more and more companies using the selective laser sintering process to produce fashion accessories as a complement to the art plating, vacuum metallization and automated painting.

Moreover, during the selective laser sintering, it is not always possible to achieve the best mechanical properties joined with the best quality. Because of that, some post-processing may be required. In selective laser sintering technology, the post-processing includes coating and surface finishing. Thus, the coating can improve tensile strength and surface hardness while surface finishing can improve dimensional and surface precision. According to Gibson and Shi [26], tensile strength with coating was increased by around 5 % compared to no coating specimens. The dominating factors determining tensile strength are powder material and



fabrication parameters. After coating, the hardness increases from 7 % to 13 % with each layer. Moreover, the hardness for the part with coating has the same value for each layer and therefore fully dependent on a coating material.

Post-processing of selective laser sintering parts is common practice with a range of techniques and finishes available. First of all, parts are removed from the build chamber and all powder is removed with compressed air. The surface is also cleaned by bead blasting to remove any unsintered powder stuck to the surface. This finish is inherently rough, similar to medium grit sandpaper.

For a smoother surface texture, the polyamide parts can be polished in media tumblers or vibration machines. A tumbler that contains small ceramic chips, that vibrate against the object, gradually erodes the outer surface down to a polished finish. As a result, this process has a small effect on part dimensions and results in rounding sharp edges. Tumbling is not recommended for parts with fine details and intricate features.

The porosity of selective laser sintering parts makes them ideal for dyeing. The part is immersed in a hot colour bath with a large range of colours available. Using a colour bath ensures full coverage of all internal and external surfaces. Typically, the dye only penetrates the part down to a depth of around 0.5 mm meaning continued to wear to the surface may expose the original powder colour.

For example, the lacquer coatings can improve wear resistance, surface hardness, water tightness and limit marks and smudges on the surface of the part. Silicones and vinyl-acrylates have been shown to provide an improvement in water resistance. Stainless steel, copper, nickel, gold and chrome can be deposited on the surface of parts to increase strength or electrical conductivity in shielding applications. Plastic can be retained as structural support or removed to create thin-walled parts of 25  $\mu\text{m}$  to 125  $\mu\text{m}$  thick [17].

### **1.2.5. Conclusion on the selective laser sintering process**

Rapid prototyping has created a forward-looking approach to the problem of manufacturing products from various materials. High material savings, lower energy consumption, shorter product creation time, a minimal infrastructure needed to manufacture products, use of modern information technology systems are basic attributes of future industry. The dynamic development of rapid prototyping methods means that more and more often selective laser sintering is widely used in various industries and is an alternative production method for the implementation of complex, time-consuming and demanding large financial outlays

### 1.3. Thermoplastic powders for SLS process

Among three types of polymers (thermoplastics, thermosetting resins, and elastomers), only thermoplastics are used in selective laser sintering, because they can be melted. They turn to liquid when heated and freeze to glassy state when cooled.

#### 1.3.1. General information on thermoplastics

The thermoplastics are lightweight and insulating materials, easy to handle and safe, non-toxic, as well as, flexible at high temperatures. They are formed with long macromolecular chains made of carbon to carbon bonds (C-C). These chains are formed by monomers linked by covalent (strong) bonds. The intermolecular bonds between polymeric chains are weak, secondary bonds named van der Waals forces. Upon heat or a small amount of force, these bonds are broken, which helps the motion of macromolecules and changing the shape of samples. If the polymer is cooled it may become stiffer, and eventually brittle. The temperature at which the material becomes brittle is its glass transition temperature. At lower temperatures, the polymer chains may not slide past each other because they do not have enough energy to overcome the secondary bonds.

Thermoplastics are also classified into two kinds: amorphous and semi-crystalline polymers presented in Figure 1.12. Amorphous material has macromolecules arranged in random directions. Semi-crystalline material has part of macromolecules arranged in an orderly structure with parts disordered [52].

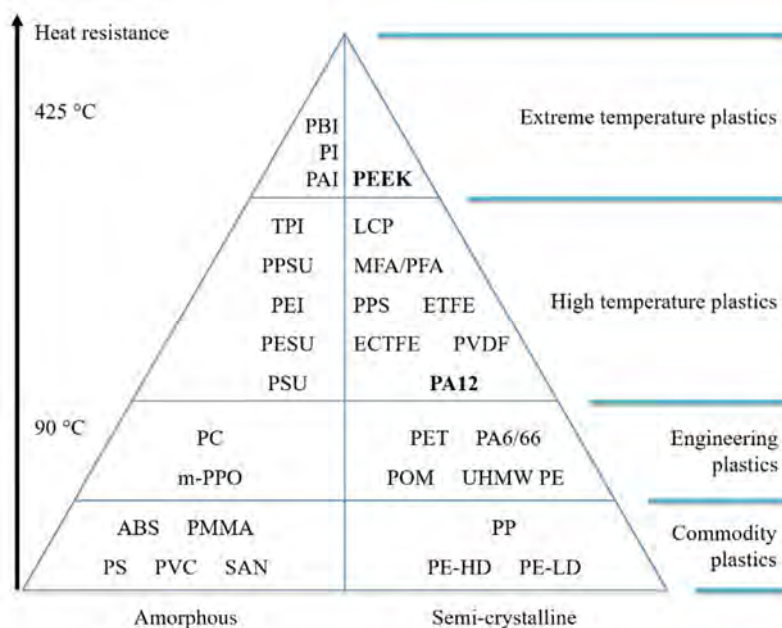
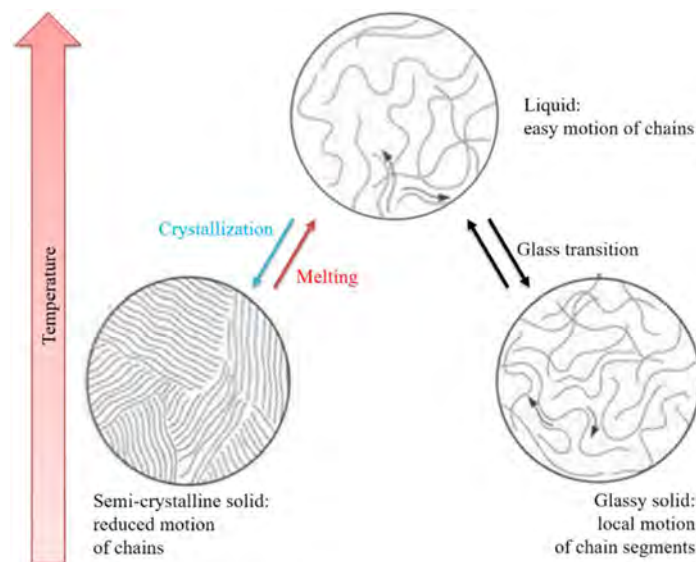


Figure 1.12. Thermoplastic polymers

Both semi-crystalline and amorphous thermoplastics are used for the selective laser sintering process [53]. In practice, the best thermoplastic materials suitable for laser sintering technology are those having a semi-crystalline polymer due to some orderly structures.

When the thermoplastic materials are heated up from low temperatures to higher ones during a melting process, they may change their structure from hard to softer, and finally, turn into a liquid with easy motion of chains. The process of crystallisation occurs by forming a solid, where the atoms or molecules are highly organized into a structure known as a crystal with a reduced motion of chains, Figure 1.13. Semi-crystalline polymers have a glass transition temperature below or around room temperature or higher ( $-100\text{ }^{\circ}\text{C}$  to  $150\text{ }^{\circ}\text{C}$ ) and a distinct melting temperature above  $100\text{ }^{\circ}\text{C}$  (between  $100\text{ }^{\circ}\text{C}$  and  $400\text{ }^{\circ}\text{C}$ ) at which its volume significantly changes.



**Figure 1.13. Solid-state properties of thermoplastic polymers**

It is important to control the cooling of polymers during manufacturing because it can lead to distortion of parts. The anisotropic shrinkage of material can be reduced by preheating of powders to temperature a little below the melting point and keeping it for a time after consolidation. While in the case of amorphous polymers, there is no melting temperature. Their glass transition is around  $100\text{ }^{\circ}\text{C}$  or higher, above which the material may gradually expand to a leathery, rubbery and finally viscous liquid state as temperature increases, without clear transitions [54].

### 1.3.2. Commercially available powders

The field of polymer materials for additive manufacturing is very competitive internationally. Dissemination of knowledge is rarely done by scientific journals, although some works are cited there. In 2016, 85 % of commercial powders were polyamide 12 and its composites obtained by dry blends. Polyaryletherketones represent only 1 % of available

powders. Since then, the situation has changed a little. Indeed, few of these powders meet both the geometric criteria and also in terms of intrinsic properties such as their melting temperature and their kinetics of crystallization.

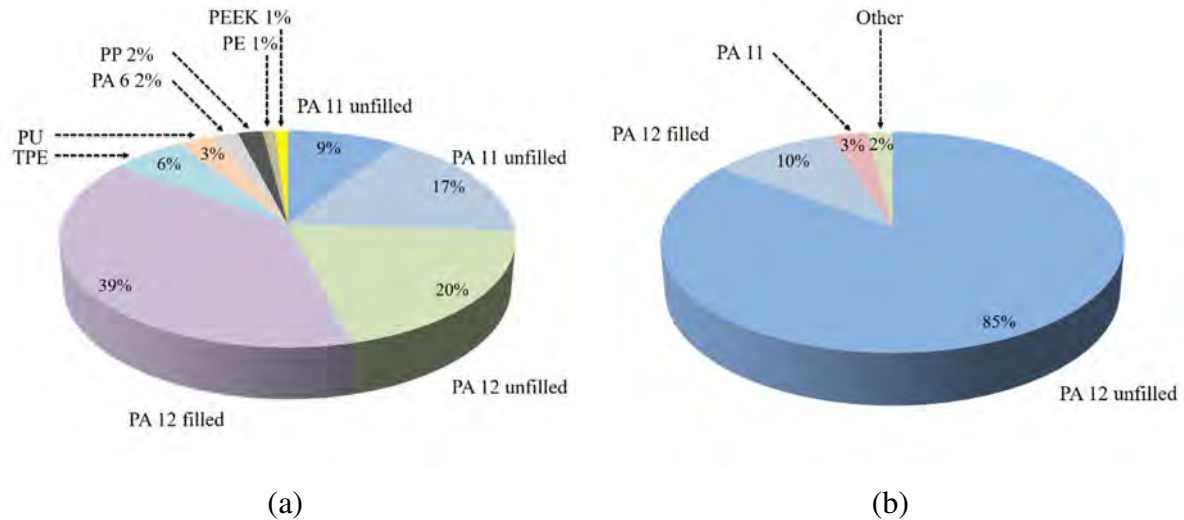


Figure 1.14. The Wohlers report 2017 of (a) material distribution (b) real consumption in SLS process [55]

The polymers of polyaryletherketone family are of application interest because of their chemical resistance and temperature stability. The behaviour of these polymers, which have been on the market since the 1990s, is still not well known. The study of their durability has shown that the polymers of polyaryletherketone family are the most durable. They retain longer their mechanical properties during exposure to a temperature close to their glass transition. Selective laser sintering powders based on polyaryletherketones are marketed by the German company Electro Optical Systems (EOS, HP3 and HT-23 which is a carbon fibre grade) and the American company Oxford Performance Materials (OPM), bought in 2017 by Hexcel which offers three grades of powders based on polyetherketoneketone (OXFAB, OXFAB-ESD with 15 % carbon fibre and OXFAB-Ni, a composite with nickel). About twenty patents concern the formulation of powders for additive manufacturing processes, in particular, deposited by Electro Optical Systems and Oxford Performance Materials.

In the selective laser sintering process, the most commonly used polyamides, PA11 or PA12, offered by key manufacturers under the trade names PA2200 (company EOS), Duraform PA and Duraform ProX PA (company 3D Systems) and mixtures thereof with dyes, flour glass or aluminium, or even the addition of carbon fibre. Due to the large heat shrinkage of polyamide (2-4 %), the laser sintering process is carried out at temperatures of 173 °C, near the melting point of 190 °C. The material which is not sintered can be partly degraded and cannot be used at 100 % again. Generally, the mixtures of “recycled” and “fresh” powder are

used. Selective laser sintering equipment manufacturers are trying to reduce the proportion of fresh powders so final parts could be cheaper. Nowadays in the case of materials such as PA11 or PA12 can be used successfully ratio of 50/50 wt.%, and in some applications, even ratios of 70/30 wt.% recycled to fresh powders.

According to the Wiseguy report from 2019 [56], in 2016, Europe was the largest production area of polyamide 12 with 76.4 % in share. The USA and Japan each took 13.5 % and 10.1 % of the total production share. Europe was also the largest consumption area of polyamide 12 in 2016 with 34.4 % in share. North America, China, and Japan are other major consumption regions took 23.4 %, 15.7 % and 9.2 % of total consumption share, respectively.

The worldwide market for polyamide 12 is expected to grow roughly 3.6 % over the next five years, may reach \$ 1690 million in 2023, from \$ 1360 million in 2017, according to Global Info Research study.

One of the newest materials that can be processed by selective laser sintering are polyaryletherketones. The most known on the market is polyetherketone (PEK) protected by a patent [57] and under commercial name HP3 with a melting point of 372 °C and processing temperature of 385 °C. In laser sintering technology, a powder, a process and a machine have to match perfectly. The machines are mostly designed for a special powder, especially the EOSINT P800 [58] for HP3 copolymer. The system is designed to use a layering process on high-performance polymers at temperatures of up to 385 °C and producing parts for medicine, aerospace industry or motorsports. Most machines and parameter settings are therefore compromised so they are able to produce all kind of parts if they are thin and small or thick and large. In medical applications, the properties make this material an ideal replacement for stainless steel and titanium. In the aerospace industry and motorsports where lightweight and fire resistance are of paramount importance, HP3 copolymer has developed to be the metal replacement. Moreover, the HP3 copolymer is characterised by high mechanical strength up to 95 MPa and elastic modulus up to 4400 MPa. The temperature resistance within 180 °C (mechanical dynamic), 240 °C (mechanical static) and 260 °C (electrical) depend on the applications.

The polyaryletherketone family can offer also polyetherketoneketone (PEKK) with a wider processing window from 350 °C to 380 °C. This thermoplastic polymer is mainly used as medical implants, known under commercial name OXFAB with mechanical strength up to 62 MPa and high elastic modulus up to 4826 MPa.

Besides the above-mentioned materials on the market, the commodity powder materials such as polystyrene (PS, for example, Primecast 101 from EOS), polypropylene (PP) and high-density polyethylene (HDPE) powders are known in selective laser sintering. These materials are characterised by a much lower price (0.5 € per kilogram) than high-temperature plastics. The price per kilogram of PA12 powder is approximately 50-60 € and for extreme temperature plastics around 200 € per kilogram. In the foundry industry, polystyrene is used because of its low processing temperature of 82-90 °C [59] and a low amount of ash after burning of 0.002 %. Polystyrene is characterised by a glass transition of 105 °C. The typical application by using the laser sintering technology is the production of lost patterns for the plaster casting process and of master patterns for vacuum casting. The sieved, recycled powder can be completely reused because it does not undergo thermal degradation. Powders of polypropylene and polyethylene in contrast to polyamides, which use recycled powder at 30/70 wt.%, may use again recycled powder almost at 100 % what significantly reduced production costs. In order to increase the rigidity of polypropylene may also be used mineral supplements type glass powder, metal oxides or aramid fibres [60].

### 1.3.3. Structure and properties of polyamides

Polyamides are the polymers comprising amide bonds (-C(O)-NH-) in their main chains. They are semi-crystalline materials, additionally reinforced by the formation of hydrogen bonds with the oxygen and nitrogen of two different amide groups. As a result, polyamides are more rigid and with a higher melting point than thermoplastic polyesters, significantly exceed those of vinyl polymers.

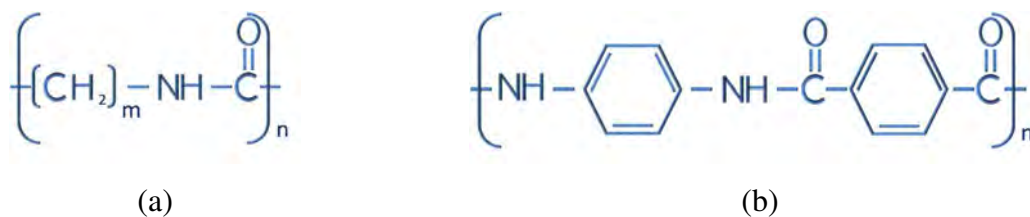


**Figure 1.15. Structure of (a) aliphatic polyamide (b) aromatic polyamide**

Polyamides are either aliphatic or aromatic. The aliphatic polyamides, Figure 1.15.a, are produced on a much larger scale and are the most important class of engineering thermoplastics. They are amorphous or with moderately crystallinity when injection moulded. The degree of crystallinity can be much increased for fibres and film applications by orientation via mechanical stretching (such as nylon 6 and nylon 6.6). The aromatic polyamides, Figure 1.15.b, are called aramids, they have a density of 1.44 g.cm<sup>-3</sup>, higher strength of 2900-3000 MPa, better solvent, flame and heat resistance and greater

dimensional stability than aliphatic amides. Wholly aromatic polyamides are synthetic polyamides in which at least 85 % of amide groups are bound directly to two aromatic rings. They are more difficult to produce so more expensive. The fully aromatic structure and the strong hydrogen bonds between the aramid chains results in high melting points at 500 °C, ultrahigh tensile strength at a low weight, even 3400 MPa, and flammability of 29 % (for example Kevlar and Nomex from DuPont) [61]. Major manufacturers worldwide of unfilled and filled aliphatic PAs are presented below:

**Table 1.2. Names and brands of manufacturers worldwide for polyamides**

Polymer	Country	Manufacturer	Trade names
Polyamide 6 Polyamide 6.6	Belgium	Solvay	Technylstar
	Germany	BASF	Ultramid, Nypel
		Lanxess	Durathan
	Italy	Radici	Radilon, Radistrong, Heramid, Torzen
	Switzerland	EMS-Grivory	Grilon
Polyamide 11	USA	Dupont	Zytel, Minlon
		Honeywell	Aegis
Polyamide 12	France	Arkema	Rilsan
	Germany	EOS	PA1100 Series
Polyamide 12	France	Arkema	Rilsamid, Orgalloy, Platamid, Orgasol
		Exceltec	Innov PA1550
	Germany	EOS	PA2100, PA2200, PA3200 Series
		Evonik	Vestamid, Vestosint
	Japan	UBE	UBESTA
	Switzerland	EMS-Grivory	Grilamid
	USA	3D Systems	Duraform

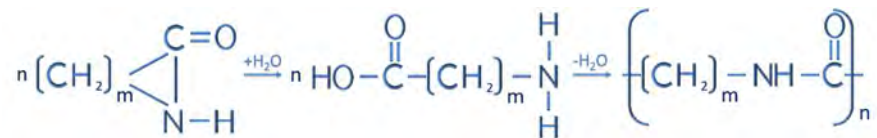
The main producers of polymer powders based on polyamide 12 are EOS, 3D Systems, and Arkema. The companies EOS and 3D Systems use the material of company Evonik Vestosint and a process of precipitation from solution (indirect method), while Arkema produces its product called Orgasol, which is obtained directly during polymerization.

It can be distinguished many types of polyamides, including those reinforced with glass fiber, which raises the density to  $1.6 \text{ g.cm}^{-3}$ , stiffness and creep resistance. It also enhances dimensional stability. The average continuous temperature range for PAs are from  $-30 \text{ }^\circ\text{C}$  to  $100 \text{ }^\circ\text{C}$ . Polyamides have several advantages over other classes of engineering polymers. For example, they are more resistant to alkaline hydrolysis than polyesters but not as resistant to acid hydrolysis. They also have better solvent resistance to many organic liquids when compared with polyethylene terephthalate (PET) and polycarbonate (PC).

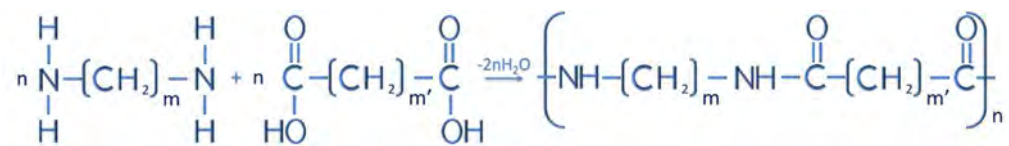
### 1.3.3.1. Polyamides 11 and 12 (PAs) for the SLS process

Polyamides are synthesized through step-growth polymerisation or polycondensation from small molecule compounds. The polyamides are obtained by the following methods:

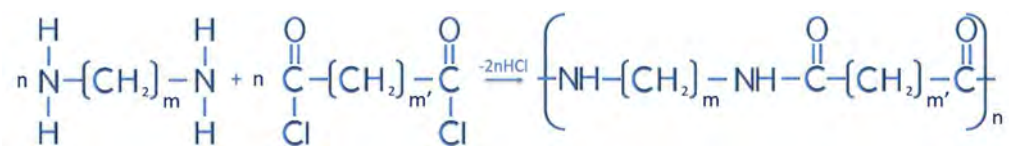
1. Lactam polymerisation:



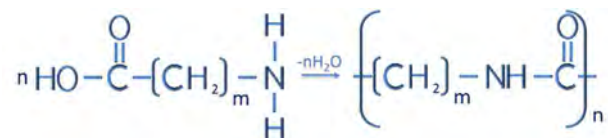
2. Polycondensation of diamines with dicarboxylic acid:



3. Polycondensation of diamines with dicarboxylic acid chlorides:



4. Homopolycondensation of  $\omega$ -amino acids:



Thus, a condensation reaction is mostly used to synthetically produce polyamide polymers in industry. Polyamides must specifically include a straight aliphatic chain monomer. The amide linkage is produced from the amine group and the terminal carboxylic component of the functional group. The hydroxyl from the carboxylic acid combines with hydrogen from the amine and gives rise to water, the elimination by-product. For example, polymerisation of polyamide 12



from lauryllactam ( $C_{12}H_{23}NO$ ) allows obtaining Duraform PA with open chain ends. The same reaction with termination X gives Orgasol invent smooth with blocked chain ends [62].

The polyamides have possessed a layer-like structure formed by hydrogen-bonded sheets. Two basic crystalline modifications designated as  $\alpha$  and  $\gamma$  forms were established. For polyamide (2n), where  $2n \leq 6$ , the  $\alpha$  crystal structure (with all-trans  $CH_2$  chains nearly coplanar with the hydrogen bonding plane) is more stable, while for  $2n > 6$ ,  $\gamma$  (with the alkane plane twisted by  $70^\circ$ ) is more stable. The lattice parameter refers to the physical dimension of unit cells in the crystal lattice.

**Table 1.3. Crystal structure of PA materials**

Polymer	Crystalline form	Crystal structure	Lattice parameters [Å] [63,64]
Polyamide 11	$\alpha$ -form	Triclinic cell	a = 4.94 b = 2.55
	$\gamma$ -form	Monoclinic cell	c = 14.1
Polyamide 12	$\gamma$ -form	Monoclinic cell	a = 9.38 b = 32.2
			c = 4.87

The crystallization kinetic study allows simulating during the building and cooling process of the selective laser sintering process. The crystallization of polyamide 12 has been investigated by Zhao et al. [65,66] in isothermal and non-isothermal conditions and presented in Equation 1.4 and Equation 1.5, respectively.

The isothermal crystallization is characterised by induction time and crystallization halftime. The model is based on the Avrami theory which describes the macroscopic nucleation and growth of any crystal structure as a function of time [67].

$$X(t) = 1 - \exp(-k(T)t^n) \quad (1.4)$$

where:

- X(t) - isothermal crystallization kinetic [-];
- k(T) - Avrami crystallization rate parameter depends on temperature [ $\text{min}^{-1}$ ];
- t - time [min];
- n - Avrami exponent, nucleation mode and dimensionality of crystal growth [-].

The non-isothermal crystallization model has been extended from Avrami theory by Ozawa [68]. The degree of crystallization can be written as a function of heating or cooling rate according to the equation:

$$X(t) = 1 - \exp\left(\frac{-k(T)}{f^m}\right) \quad (1.5)$$

where:

- X(t) - non-isothermal crystallization kinetic [-];
- k(T) - Ozawa crystallization rate parameter depends on temperature [ $\text{min}^{-1}$ ];
- f - heating or cooling rate [ $^{\circ}\text{C} \cdot \text{min}^{-1}$ ];
- m - Ozawa exponent, nucleation mode and dimensionality of crystal growth [-].

The crystallization kinetic of polyamide for the selective laser sintering process shows that the higher the isothermal holding temperature, the longer the crystallization takes. Moreover, for smaller cooling rate the initial temperature is higher and the crystallization time is longer. Between measurement and modelling, a small deviation of less than 5 % is seen before  $X(t) \leq 0.7$ . In the case of non-isothermal crystallization, the relative deviations plot of time between measurement and modelling up to  $X(t) = 0.9$  are within  $\pm 10\%$ . A minimum deviation plot of the temperature of all the curves up to  $X(t) < 0.9$  is only  $\pm 1\%$ .

For selective laser sintering treatment, stands out a several dozen basic polymers, where almost all of them are based on two basic polymers: polyamide 11 and polyamide 12 [69,70]. Figure 1.16 presents the chemical formula of two basic polymer structures.

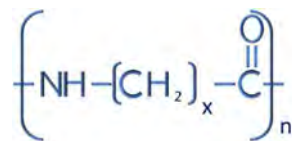


Figure 1.16. Chemical formula of PA11 (x = 10) and PA12 (x = 11)

The density of polyamides 11 and 12 in the basic form is approximately  $0.99 \text{ g} \cdot \text{cm}^{-3}$  and  $1.01 \text{ g} \cdot \text{cm}^{-3}$ , while the melting point is around  $201^{\circ}\text{C}$  and  $172\text{-}180^{\circ}\text{C}$ , respectively. Polyamides are distinguished by a tensile strength of 41 MPa, tension modulus of 1380 MPa, abrasion resistance of  $0.8 \mu\text{m} \cdot \text{km}^{-1}$  and low coefficient of friction of 0.32. It is also worth mentioning their resistance to gasoline and various types of solvents, while high humidity absorbance, around 1.6 %, prevents it to be used in direct contact with water. The moisture content depends on the electrical properties of the material [71].

The size distribution and morphology of polyamides 11 and 12 have been investigated by Verbelen et al. [72]. The powders consist of relatively spherical particles and narrow size distribution between 40  $\mu\text{m}$  and 60  $\mu\text{m}$ . The polyamide 12 obtained by the polymerization process is characterised by rather smooth particles in a cauliflower shape. While the polyamide 11 consists of rough particles with sharp edges, which is probably the result of the milling process.

The flowability of all powders is high without layer defects. The resulting flow behaviour is given by a value of packing density, 47 % and 58 % for polyamide 12 and 11, respectively [72]. The packing density of polyamide 12 is smaller compared to polyamide 11 which probably results from its higher sphericity and smaller particle size. Surprisingly, the rough polyamide 11 powder has a significantly higher packing density. The flowability of this powder is very high, which could appear from additives, like carbon black or silica, reducing interparticle friction.

### 1.3.3.2. Degradation mechanism of polyamide 12

During the selective laser sintering process, polyamides are essentially concerned with thermal and oxidative degradations. Indeed, the powder is exposed for a long time at high temperatures. A nitrogen sweep takes place within the machines but a certain quantity of oxygen is always present during the manufacturing process, machines were designed to operate with a quantity of oxygen up to 5.5 % in the atmosphere for the polyamide 12.

The thermal degradation of polyamide 12 under an inert atmosphere takes place between 350 °C and 450 °C [73] in a single step. However, a measurement with a low-temperature ramp of 1 °C.min<sup>-1</sup> shows that there may be at least two stages of degradation between 350 °C and 475 °C [74]. In the air, the last step occurs between 475 °C and 600 °C.

The mass spectroscopy detection of CO<sub>2</sub> during this last step shows that this is due to the degradation of ash from the first stage. The degradation of polyamide 12 releases a large number of chemical compounds such as:

- lactam 12, detected by Mailhos-Lefievre et al. [73], Herrera et al. [74] and Levchik et al. [75];
- olefin nitriles as well as unsaturated nitriles including benzonitrile (single unsaturated nitrile detected [74]);
- toluene mentioned [74] as the second most abundant product during pyrolysis at 950 °C under nitrogen;
- saturated and olefin hydrocarbons [73,75];

- carbon dioxide as well as hydrogen cyanide, detected by all authors;
- water and ammonia [74];
- ethylene and propylene [75];
- polycyclic aromatic hydrocarbons demonstrated [74] in quantities more abundant for polyamide 12 than for polyamides 6, 6.6 and 6.12.

Thermo-oxidation occurs when the polyamides are heated in the presence of oxygen. Karsten and Rossbach [76] have reported that a primary radical is formed following the extraction of the hydrogen atom from the amino ethylene group. In the presence of oxygen, this group leads to the formation of peroxide radicals.

#### 1.3.4. Structure and properties of polyaryletherketones

The polyaryletherketones are high-performance thermoplastics with semi-crystalline character and molecular rigidity of its repeating units. They demonstrate high-temperature stability, chemical resistance, and high mechanical strength over a wide temperature range. Polyetherketone (PEK), polyetheretherketone (PEEK), polyetherketoneketone (PEKK) and others have similar crystal structures of two-chain orthorhombic packing [77,78], but not the same ether/ketone content [79].

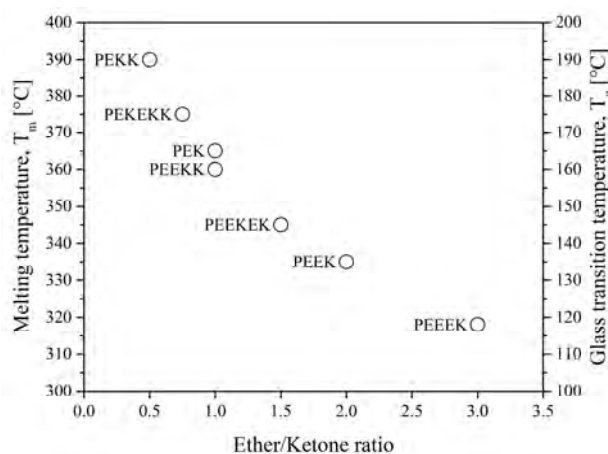


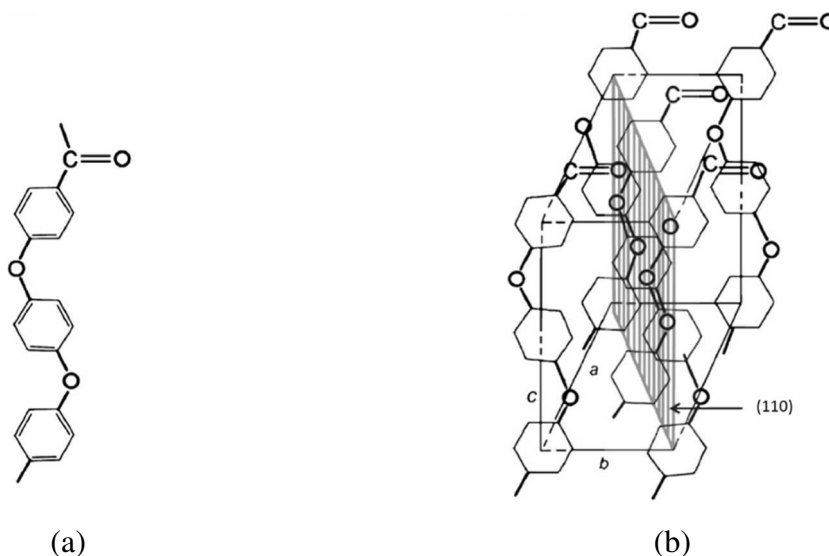
Figure 1.17. The  $T_m$  and  $T_g$  of PAEK powders as a function of ether/ketone ratio [80]

The properties of polyaryletherketones are due to the occurrence of phenylene rings linked via oxygen bridges (ether, R-O-R) and carbonyl groups (ketone, R-CO-R) in different configurations and proportions. The glass transition temperature and the melting point of the polymer depend on the ratio and sequence of ethers and ketones. They also affect its heat resistance and processing temperature. The lower the ratio of ether/ketone, the more rigid the polymer chain is, the higher the glass transition temperature and melting point as seen in Figure 1.17. As a consequence, the processing temperatures range is from 350 °C to 430 °C.

**Table 1.4. Crystal structure of PAEK materials**

Polymer	Ketone content [81]	Crystal structure	Lattice parameters [10 <sup>-10</sup> m] [82–84]
PEEK	33 %	Orthorhombic cell	a = 7.75 – 7.83 b = 5.86 – 5.94 c = 9.86 – 10.06
PEK	50 %	Orthorhombic cell	a = 7.63 – 7.65 b = 5.96 – 5.97 c = 10.00 – 10.09
PEKK	67 %	Orthorhombic cell	a = 4.17 b = 11.34 c = 10.08

According to Vasconcelos et al. [85] evaluation of crystallization kinetics based on the Avrami model for polyetheretherketone and polyetherketoneketone allows the study of crystal growth geometry in their regions. It was observed that the crystallization time for polyetheretherketone is between about 5-15 min. In order to promote crystallization, it is not necessary to maintain it at high temperatures for too long. It was also observed that the growth geometry of the disc type is promoted by lower cooling rates. The heterogeneous nucleation was observed with a growth type of disc geometry for polyetherketoneketone.

**Figure 1.18. Structure of (a) chain conformation (b) orthorhombic crystal unit cell of PEEK [86]**

Dawson and Blundell [83] reported that high similarity found in the crystal units of polyaryletherketones is due to the ability of ketone and ether links to be interchanged with

a minimum of distortion of chain packing and an only slight variation of lattice parameters. As the ketone content increases, the a-axis and b-axis of a crystal cell decreases and increases, respectively. The polyetheretherketone chain configuration and the orthorhombic crystal cell is shown in Figure 1.18.

The interest in a crystal cell and relative lattice parameters arises from the need to understand the crystallization mechanism and thermal behaviour of polyaryletherketones, which affect the final properties of the manufactured part.

#### 1.3.4.1. Polyetheretherketone (PEEK)

Polyetheretherketone is obtained by step-growth polymerization by the dialkylation of bisphenolate salts. It involves the reaction of compounds such as 4,4'-difluorobenzophenone or 1,4-bis(4-fluorobenzoyl) benzene with the disodium salt of hydroquinone, which is generated in situ by deprotonation with sodium carbonate. The polymer is then isolated by removal of alkali metal fluoride. The reaction is conducted around 300 °C in polar aprotic solvents such as diphenyl sulphone. The polyetheretherketone polymer supplied by Victrex is understood to be synthesised by high-temperature nucleophilic process [87] as depicted in Figure 1.19.

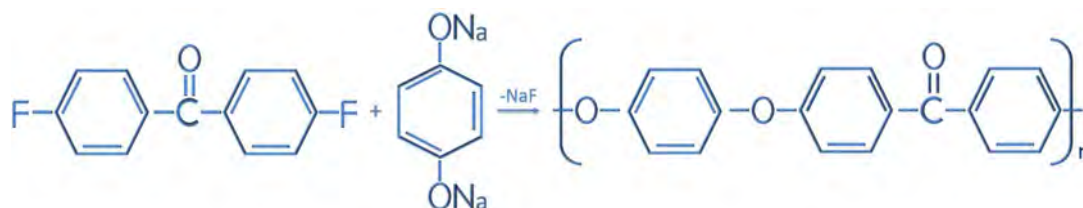


Figure 1.19. Scheme of the formation of PEEK

Polyetheretherketone has been commercially available from imperial chemical industries (ICI) since the early 1980s. Nowadays, there are many producers, the major manufacturers worldwide are:

Table 1.5. Names and brands of manufacturers worldwide for PEEK

Polymer	Country	Manufacturer	Trade names
PEEK	Belgium	Solvay	Ketaspire, Solviva, Zeniva, Tribocomp
	France	RTP Company	RTP 2200 Series
	Germany	Evonik	Vestakeep
		Lehmann & Voss	Luvocom
	United Kingdom	Victrex	Victrex
Saudi Arabia	Sabic	LNP Series	

Polyetheretherketone has a melting point at a temperature of 343 °C and a glass transition temperature at 143 °C, its melt viscosity is 350 Pa.s at a temperature of 400 °C. Polyetheretherketone combines the strength of 98 MPa and stiffness of 125 MPa with a very good tensile fatigue of 97 MPa, thermal and chemical resistance (including the majority of organic solvents, oils and acids). Its mechanical properties remain stable up to temperatures of about 240 °C. The density of polymer is 1.3 g.cm<sup>-3</sup> with low water absorption of 0.45 % [36].

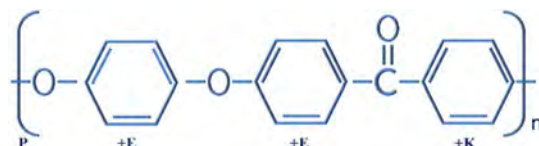


**Figure 1.20. Structure of PEEK**

This polymer has a maximum temperature to continues uses of 250 °C and a processing temperature of 370 °C to 400 °C [88]. The maximum achievable crystallinity of PEEK is about 48 % [89]. It is used for the production of high precision dimensional and materials for the bearings. Also, polyetheretherketone is a fire retardant material with a small amount of smoke during its combustion [90]. It has been reported that the amorphous state of pure polyetheretherketone can be obtained only when it is cooled at very high cooling rates of 1000 °C.min<sup>-1</sup> [91].

#### 1.3.4.2. Polyetherketone (PEK)

The polyetherketone polymer can be obtained by reaction of a component of the 4,4'-difluorobenzophenone with 4,4'-dihydroxybenzophenone in the presence of potassium carbonate, using diphenyl sulfone as solvent at temperatures of up to 340 °C, as seen in Figure 1.21. This very high reaction-temperature is required, not to overcome any energy-barriers to etherification but to prevent the PEK from crystallising from solution before high molar mass has been achieved [92]. The industrial reaction of polymerization:

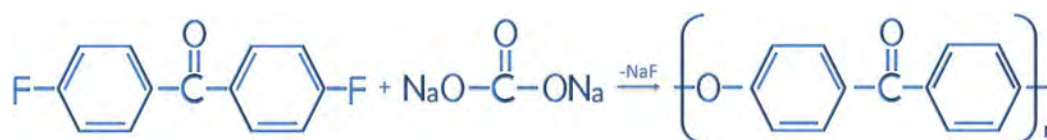


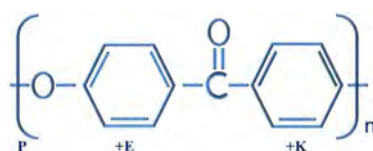
**Figure 1.21. Scheme of the formation of PEK**

The major manufacturers worldwide for polyetherketone are:

**Table 1.6. Names and brands of manufacturers worldwide for PEK**

Polymer	Country	Manufacturer	Trade names
PEK	France	RTP Company	RTP 2200 A Series
	Germany	Ensinger	Ultraprek
		Lehmann & Voss	Luvocom 1100 Series
	United Kingdom	Victrex	Victrex
India	Gharda	G-PAEK	

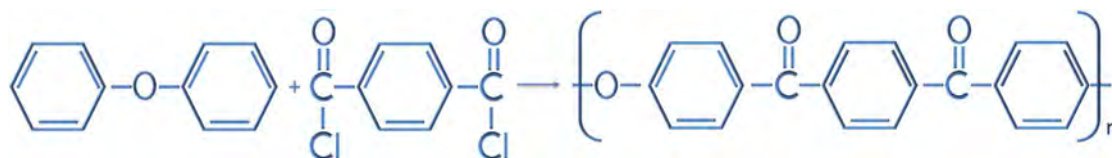
Polyetherketone is a high-performance material for applications demanding higher temperature resistance than other ketone polymers. The density of polymer is  $1.3 \text{ g.cm}^{-3}$  with low water absorption of 0.1 % [93].

**Figure 1.22. Structure of PEK**

It has a melting point at  $373 \text{ }^\circ\text{C}$  and a glass transition temperature at  $152 \text{ }^\circ\text{C}$ , its melt viscosity is  $350 \text{ Pa.s}$  at  $400 \text{ }^\circ\text{C}$ . Polyetherketone is characterised by very good material properties such as tensile strength of  $110 \text{ MPa}$ , the elastic modulus of  $4200 \text{ MPa}$  and elongation at break  $35 \%$ . It has a high resistance to abrasion and increased compression strength of  $180 \text{ MPa}$  at higher temperatures.

#### 1.3.4.3. Polyetherketoneketone (PEKK)

Aromatic polyetherketones are commonly prepared by either nucleophilic or electrophilic polymerisation. Polyetherketoneketone is formed using electrophilic polymerisation [87], as seen in Figure 1.23. This is also commonly referred to as the Friedel-Crafts method.

**Figure 1.23. Scheme of the formation of PEKK**

Polyetherketoneketone is a polymer with high heat resistance above  $300 \text{ }^\circ\text{C}$ , chemical resistance and an ability to withstand high mechanical loads from  $88 \text{ MPa}$  to  $112 \text{ MPa}$ . Polyetherketoneketone glass transition temperature is  $170 \text{ }^\circ\text{C}$  and a melting point of



approximately 390 °C depending on the grade. The density of the polymer is 1.3 g.cm<sup>-3</sup> with low water absorption of 0.1 % [94–96].

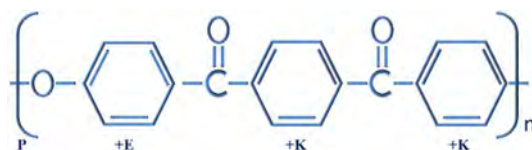


Figure 1.24. Structure of PEKK

The major manufacturers worldwide for polyetherketoneketone are:

Table 1.7. Names and brands of manufacturers worldwide for PEKK

Polymer	Country	Manufacturer	Trade names
PEKK	Belgium	Solvay	Cypek
	France	Arkema	Kepstan
		RTP Company	RTP 4100 Series
		United Kingdom	Victrex
	India	Gharda	GAPEKK
	USA	OPM	OXFAB

This polymer is synthesized in various formulations with individually unique properties. The polyetherketoneketone formulations are expressed by the ratio of percent terephthaloyl (T) to isophthaloyl (I) moieties used during the synthesis that created the polymer. The temperature dependence on T/I ratio is presented in Figure 1.25.

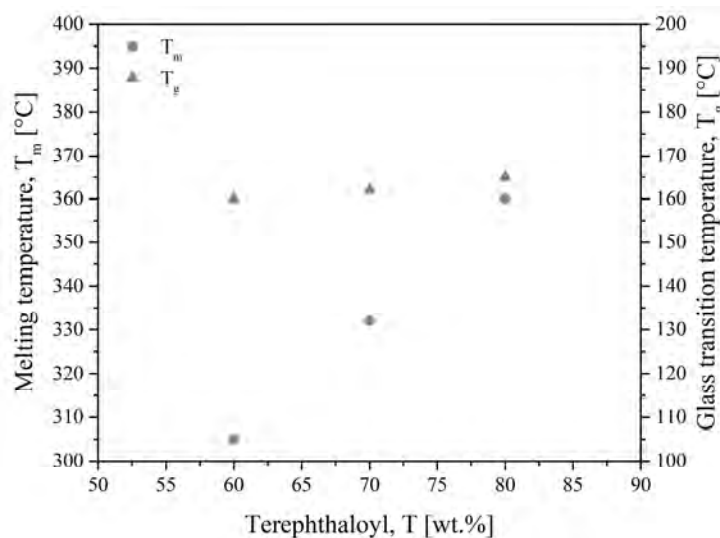


Figure 1.25. The T<sub>m</sub> and T<sub>g</sub> of PEKK as a function of T/I ratio [113]

The terephthaloyl moieties are straight and rigid represented by para (keto) linkage. The isophthaloyl moieties create a structural variation in the chain, that affects chain flexibility, mobility

and crystallization, it is represented by meta linkage. The T/I ratio affects the melting point ranging from 305 °C to 360 °C, glass transition temperature from 160 °C to 165 °C and crystallization kinetics. Increasing the isophthaloyl moieties decreases a melting temperature and crystallization rate, while increases chain flexibility and retain glass transition temperature at a high level.

#### 1.3.4.4. Degradation mechanisms of PAEK

Polyaryletherketone parts are operated in a severe environment, especially at high temperatures. For this reason, thermal stability and thermal degradation of polyaryletherketones have been the focus of many research works. It is important to understand thermal decomposition mechanisms of aromatic polyketone, consisting of ketone and aromatic moieties. The kinetic parameters of the mechanism involved during decompositions have been studied by Day et al. [97,98]. An isothermal weight-loss method in air and nitrogen atmosphere have been investigated and observed between 575 °C and 580 °C. Char yields of this polymer are above 40 % [99]. The PEEK occurs in different thermal degradation in both oxygen and nitrogen environments, nevertheless, both show two-step decomposition. The first step of decomposition is a random chain scission of the ether and ketone bonds [100]. Carbonyl bond creates more stable radical intermediates which would be expected to predominate. The second step is due to the oxidation of the carbonaceous char formed. Oxidation of pure PEEK occurs at around 700 °C.

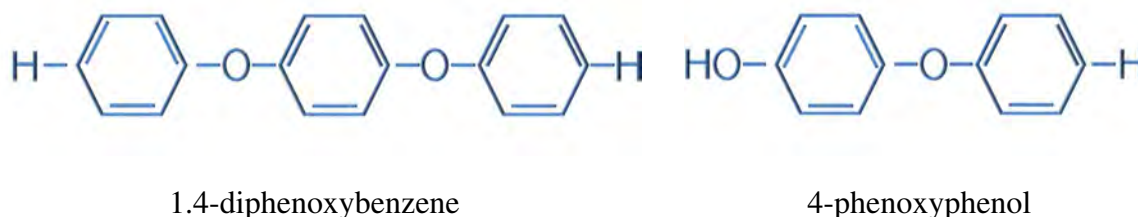


Figure 1.26. The PEEK degradation products at 450 °C

Competing mechanisms of decomposition of polyetheretherketone have been presented in the review article of Patel et al. [101]. It is known that different products are created at various temperatures from 450 °C (Figure 1.26), major polyetheretherketone degradation components are 1,4-diphenoxybenzene and 4-phenoxyphenol, by 650 °C with CO, CO<sub>2</sub> and 750 °C with phenols, some aromatic ethers (low molecular weight, such as benzene and toluene) to 1100 °C, the final products are 4-hydroxybenzophenone, 1,4-diphenoxybenzene and 4-phenylphenol [102]. Thus, the chain scission (volatile fuel formation) and crosslinking (char formation) are observed. Polyetheretherketone decomposition is initiated by random homolytic scission of either ether or carbonyl bonds in the polymer chain [103].

### **1.3.5. Conclusion on the thermoplastic powders for the SLS process**

New additive technologies successively based on the use of polymeric materials have a significant share in replace traditional ways of manufacturing products. With rapidly growing industry demand for services in this area (global growth dynamics of 22 % per year), new materials with special properties may be needed for applications in various fields “from medicine to space”. Currently, there are not many producers of materials that meet high requirements for usage in the selective laser sintering technology. Hence, the price of some materials, for example, in medicine reaches a value above \$ 2000. An important limitation in large-scale industrial production of products by the 3D printing is too low speed of production of elements and a small working chamber limiting a small size. Because of this science and industry face a challenge to improve the technological process and search for new materials increasing the application characteristics.

## 1.4. Properties of polymer powders required in the SLS process

In the selective laser sintering process, the surface quality and accuracy in the final parts depend on the powder so finer powders are selected. Schmid et al. [24] propose an Ishikawa diagram of different polymer properties for providing promising selective laser sintering material, as seen in Figure 1.27. They divide the properties into five main factors: powder and particle (extrinsic properties) as well as optics, thermal and rheology (intrinsic properties). Extrinsic properties are controlled by manufacturing processes (co-extrusion, precipitation and cryogenic milling) to achieve a higher powder packing and a homogeneous layer spreading. However, intrinsic properties are given from the molecular structure of the polymer itself and they cannot be influenced easily, otherwise by changing the powder.

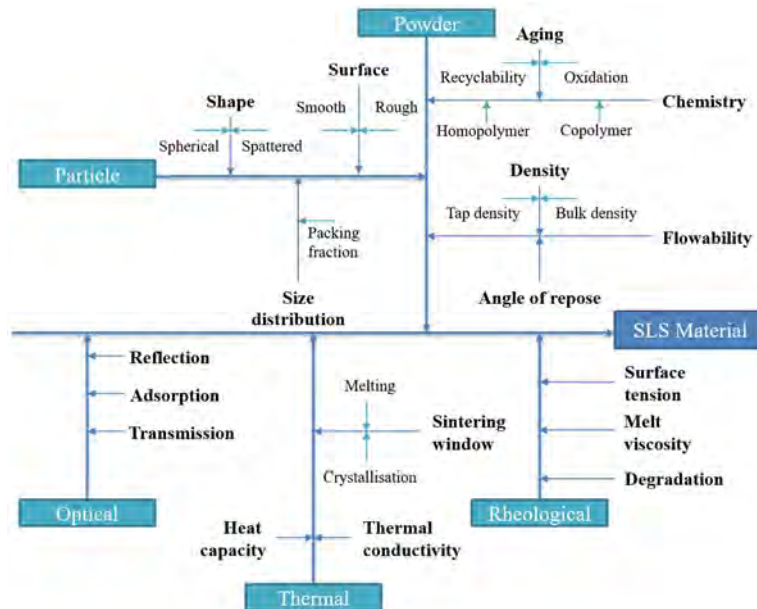


Figure 1.27. Combination of important properties of powders for SLS process [21]

In the literature, extrinsic properties are barely reported or simply left out except particle size distribution (PSD), whereas the characterization of intrinsic properties constitutes a standard practice, such as thermal and rheological measurements conducted by differential scanning calorimetry, thermos-gravimetric analysis, melt flow index analysis (MFI) and rheometer testing methods [104].

The size distribution and geometry of particles are important for sintered parts porosity. The smaller particles can help to increase the powder density and consequently a part density, dimensional accuracy and strength in sintered parts, but it may as well deteriorate a flow behaviour.

There are several properties which make thermoplastic polymers easier to process in laser sintering technology such as:

- relatively high viscosity in the liquid state;
- relatively low surface energy;
- low reactivity with most gases;
- low thermal conductivity.

Objects created by the selective laser sintering process require materials in a powder form. Ideally, polymer powders should have high sphericity to facilitate their flow, reduced surface area to volume ratio and improved packing efficiency. The surface theory of Brunauer-Emmett-Teller (BET) explains the physical adsorption of gas molecules on a solid surface and serves as the basis for the measurement of a specific surface area of materials. Thus, low BET-surface porosity to increase the density of powder bed and to decrease the likelihood of causing a reaction or ageing of powder is required [18].

#### **1.4.1. Shape, surface and size distribution of particles**

Powder generation processes lead to basic powder particle shapes: co-extrusion, precipitation and cryogenic milling [21]:

- the most desirable, spherical particles are usually received from co-extrusion processes with soluble or non-soluble material mixtures, such as oil droplets in water;
- the second shape which can be used for selective laser sintering process can have potato form, particles are available in a commercial polyamide powder obtained from precipitation process;
- particles obtained from cryogenic milling are inadequate and fail for the selective laser sintering process. The poorer powder flowability generates poor part bed surface in selective laser sintering machine and a reduced powder density. Thus, cryogenic milled powders finally end in weak, less condensed parts with a low density and poor properties usually.

To quantify the shape of particles two ways can be used: the circularity and the shape ratio. Shape index is relating to a particle surface area and particle volume, by comparing that to a sphere, the lowest circularity is required. Shape ratio is the ratio between the greatest and the smallest particle dimensions of a powder. A perfect sphere has a shape ratio of 1, a rounded particle has a shape ratio of 1.5, while flaky, cylindrical or acicular particles may easily have shape ratios of 3.5 or 10.

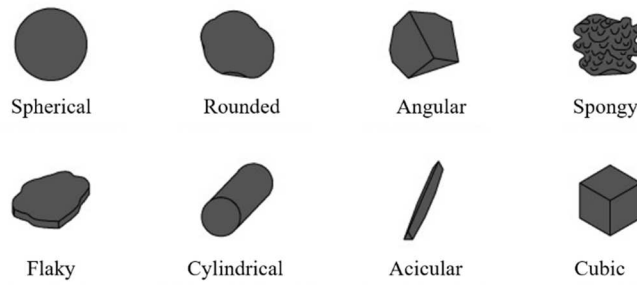


**Figure 1.28. Shape of powder particle**

The flow behaviour of powder is regulated by the shape and surface of single particles. For the selective laser sintering powders, the spherical shape of particles is expected. This is necessary to keep a free-flowing behaviour of laser sintering powders. The material can be distributed on the part bed of machine by roller or blade systems, what will protect from compaction. According to patent US 007601422 B2 [105], to provide high precision in detail and quality of the surface of parts, plastic powders are required to have an upper grain size limit of 100  $\mu\text{m}$ . Moreover, 90 % of fraction should be below 90  $\mu\text{m}$  and 10 % of fraction less than 32  $\mu\text{m}$  to provide a stable application of layers. Furthermore, the particles should have a spherical grain shape. By considering plastic powders for laser sintering technology, low porosity of particles, expressed as BET-surface, is required. The density of powder bed can be increased and the reaction tendency and ageing of powder are strongly decreased.

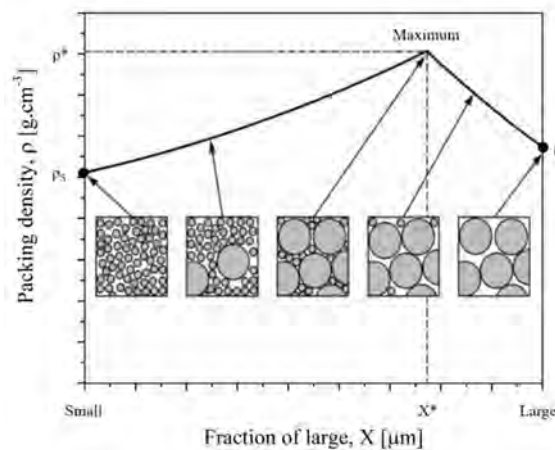


**Figure 1.29. Size of powder particle**

For selective laser sintering powders, a certain particle size distribution is necessary to be able to process on laser sintering machines. Small particles of 0.1-5.0  $\mu\text{m}$  tend to form clusters and prevent uniform recoating during the selective laser sintering process. Large particles of 90-120  $\mu\text{m}$  reduce the maximum layer packing density available [106] and it is different from typical bulk and tap densities. A mixture of small and larger particles is best suited for the laser sintering technology, where the smaller particles percolate through the larger particles and

suitably fill the void to achieve higher density in thin layers used in the selective laser sintering [107]. The layer thickness in the selective laser sintering process is approximately 100-150  $\mu\text{m}$  [18], thus it is recommended to be at least two times the size of the average particle size. The powder fusion occurs at direct contact of laser on the particle rather than relying on the particle to particle conduction. According to Chung and Das [108] who used layer thickness in the range 100-200  $\mu\text{m}$  (Sinterstation 2000, 3D Systems) and based on the powder size distribution which has to be slightly smaller than the layer thickness of selective laser sintering equipment used, decided that the most suitable range of particles is 10-150  $\mu\text{m}$ . Other authors agreed that good flowing powders should have an average particle size of 60  $\mu\text{m}$  and a low presence of particles of diameter equal to or less than 10  $\mu\text{m}$  [109]. Goodridge et al. [18] report as ideal size range for selective laser sintering process is 44-90  $\mu\text{m}$  and they suggest to avoid particles smaller than 45  $\mu\text{m}$ , but no experimental data are provided to support it. Mechanical properties, the surface roughness and porosity of investigated parts give information that larger particles led to the higher surface roughness, and larger and more surface pores in the sintered parts than in the ones sintered with smaller particles [10]. Consequently, the amount of internal pores increases with higher particle size.

The particle size of powder affects the precision and the density of selective laser sintering parts. Larger particle size may lead to a lower density. Considering the precision and density of selective laser sintering part and the difficulty of spreading powder, a particle size of 75-100  $\mu\text{m}$  is thought to be more suitable for the selective laser sintering process [16].

In the conclusion of this part, the various polyamide powders have been investigated by Dupin [1]. It is possible to note the strong similarities in terms of morphology and particle size distribution between the Duraform PA and PA2200 powders. The Innov PA1550 powder is distinguished mainly by its greater regularity of shape and tightening of its particle size distribution of 42.7  $\mu\text{m}$ . The Duraform PA and PA2200 powders have a wider distribution of 58.9  $\mu\text{m}$  and 58.4  $\mu\text{m}$ , respectively. Moreover, a bimodal distribution is observed for the Duraform PA powder, with a part of its distribution of average size around 60  $\mu\text{m}$  and another around 8  $\mu\text{m}$ . The shape analysis shows that the particles of Innov PA1550 have a more spherical shape than the particles constituting the two other powders. The values obtained for the particles constituting the Innov PA1550, Duraform PA and PA2200 powders are respectively  $1.17 \pm 0.05$ ,  $1.29 \pm 0.12$  and  $1.27 \pm 0.10$ . It may, therefore, be thought that the modes of synthesis of these polymers as well as the processes for obtaining these powders are identical.

The analyses carried out by Dumoulin [3] on polyamide, polyetheretherketones and polyetherketoneketones show the effort provided during the synthesis of polyamide 12 to obtain particles with the highest circularity  $0.79 \pm 0.09$  and a small dispersion of particle size of 2.1. It has also been shown that it is not possible to determine the presence of interparticle porosity by measurements of absolute density. The average circularity of polyetheretherketones and polyetherketoneketones is 0.62 and 0.57, respectively. The average size distribution is 58  $\mu\text{m}$  and 73  $\mu\text{m}$  for polyamide 12 and polyetherketoneketone, respectively. In the case of polyetheretherketone, for three different grades, a very wide range is observed of 20  $\mu\text{m}$ , 61  $\mu\text{m}$  and 95  $\mu\text{m}$ , but the dispersion of particle size is the same of 4.2.

### 1.4.2. Flowability

An appropriate particle size distribution leads to good powder spreading performance and a particle packing. More dense parts and less porosity are obtained [16]. Two kinds of density can be used for the calculation of flow behaviour of powders. The bulk density is the ratio of the mass of untapped powder sample and its volume including the contribution of interparticulate void volume. Hence, the bulk density depends on both the density of powder particles and the spatial arrangement of particles in the powder bed. The tapped density is an increase in bulk density obtained after tapping a container containing the powder sample. The flowability may be calculated by Hausner ratio (HR), Equation 1.6. According to the literature  $\text{HR} < 1.25$  gives free-flowing powder behaviour and  $\text{HR} > 1.40$  gives cohesive and non-flowing powders [21,110].

$$\text{HR} = \frac{\rho_{\text{tap}}}{\rho_{\text{bulk}}} \quad (1.6)$$

where:

- HR - Hausner ratio [-];
- $\rho_{\text{tap}}$  - tapped density [ $\text{g}\cdot\text{cm}^{-3}$ ];
- $\rho_{\text{bulk}}$  - bulk/apparent density [ $\text{g}\cdot\text{cm}^{-3}$ ].

Another method is the measurement by the angle of repose, where powder flows freely through a funnel onto a plate and the slope angle of the developed cone to the base plate is the angle of repose and considered as a measure for powder flowability.

The selective laser sintering part density achieved during processing is linked to powder density in part bed and is thus coupled to a shape of particles and their free-flowing behaviour.



Flowability depends on several factors: the environmental conditions such as temperature and moisture, the powder itself (shape, surface and particle size distribution) and even the flow test adopted (like the angle of repose). According to Schulze [111] and his wide research on flow properties of powders and bulk solids, adhesive strength and wall friction are the main physical factors affecting flowability.

Dupin [1] studied two types of polyamide 12 with small differences in particle morphology and particle size and they characterised their effect on the extent and morphology of porosity in the laser-sintered parts. He reported that the flow time of 60 s for Duraform PA powder is significantly higher than for PA2200 and PA1550. Moreover, in some cases the powder agglomerates and no longer flows. Thus, in the same way as for apparent density, sphericity probably plays a preponderant role on this property. In addition, the lower flow time of 52 s measured for the PA2200 powder shows that a greater amount of fine particles tends to reduce flowability. The Innov PA1550 is characterised by 49 s of flow time. Thus, rounder and bigger particles were believed to lead to better results with higher density, in reality, broader size distributions with a significant content of particle of size 8  $\mu\text{m}$  led to less part porosity even at lower manufacturing energy densities.

According to Dumoulin [3] who analysed three indices such as Carr index, Hausner ratio and compressibility, based on bulk and tapped density, are equivalent and lead to the same classification ability of powders to densify. The polyamide 12 powder comes off the other six powders with Carr index of 9.2 %, Hausner ratio of 1.11 and compressibility of 9.4 %. The polyetheretherketone and polyetherketoneketone powders are classified into three distinct groups. The PEKK\_A and PEEK\_C with Hausner ratio of 1.41, the PEKK\_B and PEEK\_B with Hausner ratio of 1.52, and PEEK\_A powder having no coating with Hausner ratio of 1.68. By regarding the cohesion constant, the uncertainty is such that only two groups can be distinguished. Thus, the first group is composed of polyamide 12 with a cohesive constant of 3 and the second group contains the other powders of study with cohesive constants between 9 and 15.

### **1.4.3. Optical properties**

Optical properties such as absorptivity, transmissivity, and reflectivity also are one of the factors influencing the sintering of polymer materials. These properties are dependent on the wavelength of the laser, the temperature of the powder bed, surface condition, incidence direction, the composition of materials and size of grains. These three properties are related to the intensity of light flux:

$$A_{\lambda} + T_{\lambda} + R_{\lambda} = 1 \quad (1.7)$$

$$T_{\lambda} = \frac{\varphi_{\lambda}^t}{\varphi_{\lambda}^i} \cdot 100 \% \quad (1.8)$$

$$R_{\lambda} = \frac{\varphi_{\lambda}^r}{\varphi_{\lambda}^i} \cdot 100 \% \quad (1.9)$$

where:

- $A_{\lambda}$  - absorbance [%];
- $T_{\lambda}$  - transmittance [%];
- $R_{\lambda}$  - reflectance [%];
- $\varphi$  - light flux [lm];
- $\lambda$  - wavelength [nm].

The three main optical properties are then determined by the ratios of absorbed transmitted and reflected fluxes. The optical characterization of the material consists of measuring these three parameters as a function of incident wavelength and then calculating the optical quantities:  $A_{\lambda}$ ,  $T_{\lambda}$ , and  $R_{\lambda}$ . This is achieved through spectrophotometry, which measures the amount of radiation or intensity of flux transmitted or reflected concerning the intensity of incident flux that is sent by the light source controlled by the device.

In the selective laser sintering process, the laser beam is commonly used as a radiation heat source. In industrial manufacturing, most polymers used for the selective laser sintering process are assumed to be opaque in case of CO<sub>2</sub> laser with a wavelength of 10.6 μm. The transmissivity is zero and non-reflected radiation energy is completely absorbed by a thin layer of material [112]. On the other hand, amorphous polymers are not opaque to all wavelengths, such as amorphous polyetherketoneketone investigated by Villar Montoya [113]. A part of the incident laser can transmit through a layer polyetherketoneketone with a thickness of 2 mm and a wavelength of 808 nm. The transmission of amorphous PEKK 6002 is about 63 %, while for the semi-crystalline state, the transmission is around 3 %. The total reflection of semi-crystalline PEKK 6002 substrate is 40 %, and it is 12 % for the amorphous state. Considering Equation 1.7, this allows calculating the optical absorption. The absorbance is 39 % in the case of the semi-crystalline substrate, while it is 27 % for the amorphous element. However, in applications, it is always assumed that all radiation energy is non-reflected and absorbed because the powder bed is much thicker than 0.25 mm.

Nevertheless, some semi-crystalline polymers, such as polyamide, are opaque in the solid phase and transparent when melting. So these materials absorb radiation energy differently depending on their state [2].

#### 1.4.4. Thermal properties and transitions

In laser sintering system essentially a CO<sub>2</sub> laser beam is used to selectively melt the polymer particles deposited in a thin layer, it introduces the energy that is necessary for the material to exceed the point of phase transition. However, the temperature increase in the powder bed should be as small as possible. Locally full coalescence of polymer particles in the top powder layer and adhesion with previously sintered layers are necessary.

##### 1.4.4.1. Sintering window

For semi-crystalline polymers usually used in the selective laser sintering process, this implies that crystallization temperature should be inhibited during processing as long as possible, at least for several sintered layers. If the processing temperature decreases below onset crystallization temperature, a major and localized shrinkage may occur during and just after the laser exposure. It can lead to undesirable effects on the mechanical properties of sintered parts. In the case, when the processing temperature is higher than the onset melting point uncontrolled melting may occur all across the powder bed without even the laser exposure. Powder particles in the proximity of laser trace stick to the molten surfaces and prevent the desired resolution of part topography [53,114].

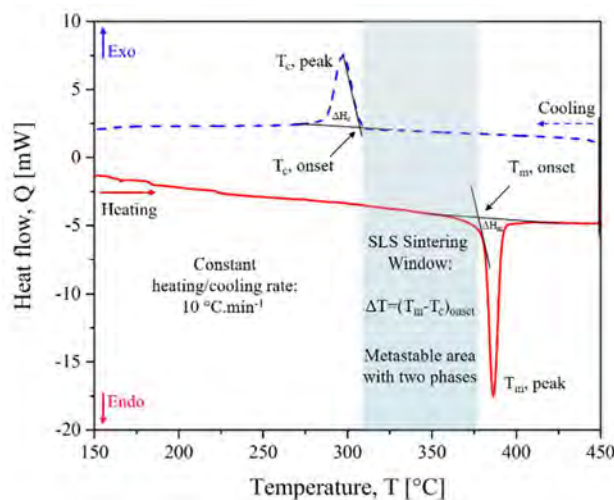


Figure 1.30. The DSC thermogram with nature of “sintering window” as SLS process temperature [21]

Thus, processing temperature must be precisely controlled in between melting and crystallization temperatures of the given polymer. Figure 1.30 shows a differential scanning calorimetry run for commercial HP3 copolymer powder. The sintering window

occurs between onset points of crystallization and melting point. For a good controlling of the selective laser sintering process, wide sintering window, sharp and narrow crystallization and melting region are required. These conditions may allow more uniform crystallization and melting mechanisms while avoiding the overlapping of these two thermal events [114].

However, fixed heating and cooling rates at  $10\text{ }^{\circ}\text{C}\cdot\text{min}^{-1}$  are just an idealised representation, it is far from the reality of the selective laser sintering process. There are undefined and hardly controllable temperature change rates during the process. The temperature between melting and crystallization along with the melting peak should be high with a narrow temperature range for the melting process itself.

#### **1.4.4.2. Thermal conductivity and heat capacity**

The selective laser sintering process is a complex thermal process which contains heat absorption, heat transfer and phase change. The thermal conductivity of materials is considered a measure of its ability to conduct the heat. Transfer of heat may occur at a lower rate in materials of low thermal conductivity than in materials of high thermal conductivity. Heat capacity is the amount of heat to be supplied to a given mass of a material to produce a unit change in its temperature. Heat capacity is an extensive property. The corresponding intensive property is the specific heat capacity.

For the thermo-physical properties of the powder bed during the selective laser sintering process, the effective density and specific heat depend on the gas fraction or the porosity and the liquid fraction of polymer. Mokrane et al. [115] have explained that modelling of thermal conductivity was complicated because it was an intensive quantity, with tensorial representation. The thermal conductivity of the powder bed is mainly dictated by the thermal conductivity of the gas present within the voids between grains.

According to Thümmeler and Oberacker [116], the thermal conductivity depends on porosity and pore geometries and it can be controlled by the amount of gas content inside the pore. Rombouts et al. [117] during their studies on light extinction in powder beds demonstrated that the effective thermal conductivity of powder is essentially independent of material but depends on the size and morphology of particles and the void fraction, as well as on the thermal conductivity of gaseous environment. The density and heat capacity of powder can be described as the mean of individual components [118].

### 1.4.5. Rheological properties

The flow and deformation of materials in the laws of elasticity and viscosity represent the rheological properties. It is the science of mechanical properties of real materials. These properties are determined by the relationship between external interactions (forces loading the body) and internal reactions of material (body deformations). In other words, rheology deals with issues related to deformation and flow of materials. The rheological properties of polymers are between these of melted state and solid-state over a time scale. The liquid flow consists of moving its particles under the influence of applied forces. The force that resists the movement of liquids is internal friction, the greater the speed of mutual displacement of particles.

The law of Newton expresses the linear relationship between shear stress and shear rate. It applies to many liquids, such as air (and all gases), water, gasoline, and liquid metals. Generally, it can be stated that this relationship is valid for all gases as well as liquids and low molecular weight solutions. The plot of  $\tau = f(\dot{\gamma})$  was called the flow curve, as seen in Figure 1.31.a. In the case of a Newtonian fluid, this relationship is rectilinear, passing through the origin of the coordinate system. However, many liquids do not show such a straight-line relationship between shear stress and shear rate, for example, melted polymers, paints, varnishes, building materials or food. These types of systems are called non-Newtonian fluids.

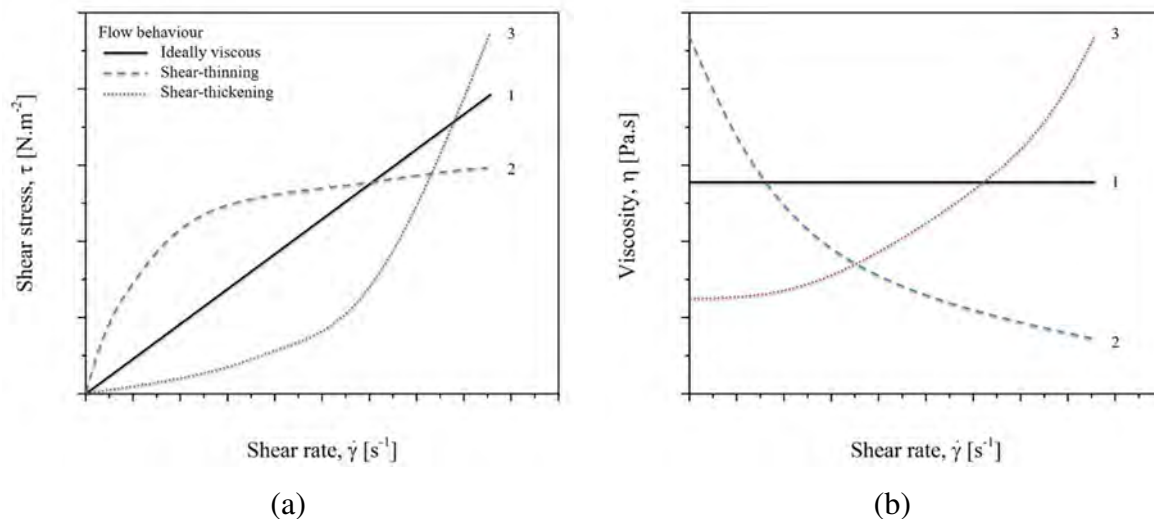


Figure 1.31. Diagram of (a) flow curves (b) viscosity curves [119]

Ideally, viscous or Newtonian flow behaviour means that the measured viscosity is independent of shear rate (Figure 1.31.b.1). Typical materials from this group include water, mineral oil, silicone oil, salad oil, solvents such as acetone, as well as viscosity standards (such as calibration oils). Shear-thinning or pseudoplastic flow behaviour is characterised by

decreasing viscosity with increasing shear rates (Figure 1.31.b.2). Typical materials that show this behaviour are coatings, glues, shampoos, polymer solutions and polymer melts. Shear-thickening or dilatant flow behaviour means increasing viscosity with increasing shear rates (Figure 1.31.b.3). Materials that typically display such behaviour include highly filled dispersions, such as ceramic suspensions (casting slurries), starch dispersions, plastisol pastes that lack a sufficient amount of plasticizer, dental filling masses (dental composites) as well as special composite materials for protective clothing.

#### 1.4.5.1. Shear stress

The shear stress is the component of stress coplanar with a material cross-section. In this modelling, shear stress arises from the force vector component parallel to the cross-section of material. It is assumed that other stresses are neglected due to their smaller value compared to shear stress. The state of pure shear stress is applicable.

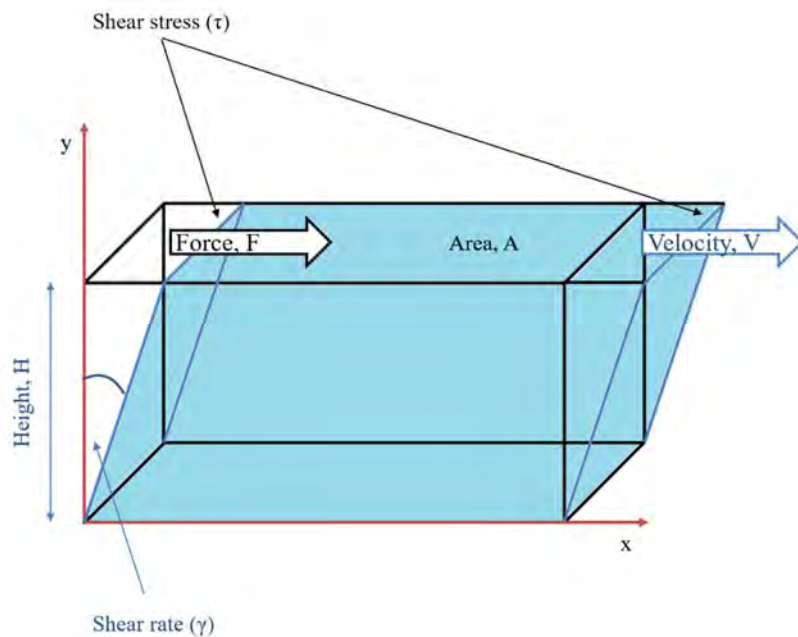


Figure 1.32. Simple mean shear stress and shear rate between two parallel plates

$$\tau_{\text{mean}} = \frac{F}{A} \quad (1.10)$$

where:

- $\tau_{\text{mean}}$  - mean shear stress in the cross-section [ $\text{N.m}^{-2}$ ];
- F - applied force [N];
- A - cross-sectional area of material with area parallel to applied force vector [ $\text{m}^2$ ].

### 1.4.5.2. Shear rate

The shear rate is defined as the rate at which a progressive shearing deformation is applied to the material, as seen in Figure 1.32.

$$\dot{\gamma} = \frac{V}{H} \quad (1.11)$$

where:

- $\dot{\gamma}$  - shear rate [ $s^{-1}$ ];
- $V$  - velocity of moving plate [ $m.s^{-1}$ ];
- $H$  - distance between the two parallel plates [m].

In the selective laser sintering process, the shear rate is very low compared to other processes to mould thermoplastics. Indeed, the shear rate is about  $10^3 s^{-1}$  and  $10^4 s^{-1}$  for extrusion and injection moulding, the melted polymer is under a high shear because of rotation and translation of screw. Oppositely, the melted grains are not under any pressure during the coalescence step. In the fused filament fabrication process, the shear rate was determined to be from  $1200 s^{-1}$  to more than  $5000 s^{-1}$ . Bakrani Balani [119] has reported that the limit for poly(lactic acid) appeared to be approximately  $4000 s^{-1}$ . Haworth et al. [120] have studied shear viscosity of polyamide 12 for laser sintering. They found that the valid measurements are probably restricted to the shear rate range  $10^2-10^3 s^{-1}$  because the shear viscosity of polymers is known to tend towards a limiting value at low stress (zero shear viscosity).

### 1.4.5.3. Melt viscosity

Viscosity is related to the resistance of the fluid to flow. Thus, the viscosity of melted thermoplastics depends on its chemical structure, composition and processing conditions, as well as, on temperature, shear rate and pressure. When the viscosity is higher, it implies a higher resistance of flow to shear rate. The viscosity behaviour of thermoplastics is defined below:

$$\eta = \frac{\tau}{\dot{\gamma}} \quad (1.12)$$

where:

- $\eta$  - viscosity [Pa.s];
- $\tau$  - shear stress [ $N.m^{-2}$ ];
- $\dot{\gamma}$  - shear rate [ $s^{-1}$ ];

It is important to keep the viscosity of melted grains low enough so material melt flow characteristics can lead to a good particle coalescence by fast and high neck growth. This is needed to allow complete coalescence of polymer particles and to obtain fully dense parts. Especially a low melt viscosity is of high importance, as unlike injection moulding, selective laser sintering process does not provide additional compaction during part generation. A low viscosity promotes good interdiffusion of polymer chains, high particle necking and satisfying layer to layer adhesion [18]. It was reported that low viscosity also allows a fast and more efficient sintering dynamics that lead to more fully dense parts [121]. However, too low polymer viscosity leads to rapid particle sintering but creates parts of low mechanical performance and with a higher occurrence of shrinkage in the geometry [122]. On the other hand, high molecular weight polymers have a high melt viscosity, which leads to slow particle sintering and potentially reduced neck growth and thus improves the dimensional accuracy [53].

Semi-crystalline polymers are characterised by a first-order melting transition which causes a very drastic decrease in viscosity at the phase transition, as seen in Figure 1.33. According to Schultz [22], this drastic decrease in viscosity results in better tolerances observed for parts fabricated from semi-crystalline polymers results from the enthalpy of melting which acts as an energy barrier, thus limiting the liquid volume.

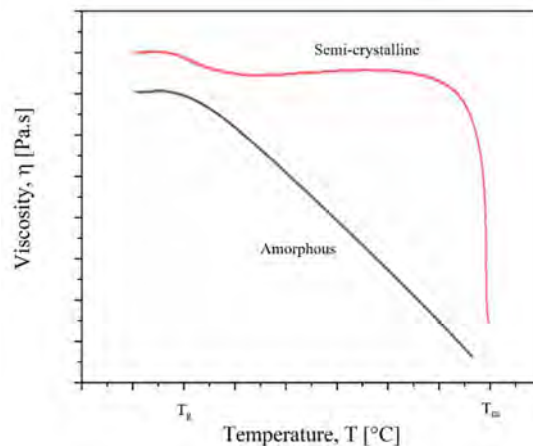


**Figure 1.33.** The viscosity as a function of temperature for amorphous and semi-crystalline polymers [22]

However, the viscosity of amorphous polymers above glass transition temperature is still very high and generally, a proper coalescence does not take place causing higher residual porosity. According to Schmid et al. [24], it is important to use materials with low melt viscosity, in another case attempts to process amorphous polymers with selective laser sintering process usually ends with brittle and unstable parts. Thus, when the temperature increases the viscosity of the polymer decreases considerably. According to the Arrhenius equation, the viscosity is dependent on the polymer temperature:



$$\eta = A \exp\left(\frac{E}{k_B T}\right) \quad (1.13)$$

where:

- $\eta$  - viscosity [Pa.s];
- A - constant frequency factor for a given material [mPa.s];
- E - energy of viscous flow [J];
- $k_B$  - Boltzmann's constant [=  $1.380649 \cdot 10^{-23}$  J.K<sup>-1</sup>];
- T - temperature [K].

Liu [123] suggested that the balling effect is an important consequence of melt viscosity in the selective laser sintering process. Very high melt viscosity at low energy input generates a severe balling effect, and high energy input with very low melt viscosity results in melt spreading [124]. The precise control of melt temperature and the melt viscosity is very critical to improve the quality of parts.

#### 1.4.5.4. Surface tension

Surface tension is a physical phenomenon occurring at the interface of liquid from the solid, gas or other liquid so that this surface acts as a resilient membrane. The surface tension is also called the physical size of engaging this phenomenon quantitatively, it is the force per unit of length, which is equivalent to the work required to expand the surface of this unit, in Equation 1.14. For example, a liquid film unbuttoned on a wireframe with a sliding side length, enabling the surface to be reduced or increased depending on the value of force.

$$\gamma = \frac{F}{2L} \quad (1.14)$$

where:

- $\gamma$  - surface tension [N.m<sup>-1</sup>];
- F - force [N];
- L - length [m].

The force value is divided by two lengths because the liquid span on the frame has two surfaces.

The work carried out at a constant temperature causes the process of surface change. Thus, the second definition of surface tension is got as the energy needed to create a new surface. It is also related to such items as work of adhesion, work of cohesion, wetting and contact angle.

$$G = \gamma A \rightarrow \gamma = \frac{G}{A} \quad (1.15)$$

where:

- $\gamma$  - surface tension [ $J.m^{-2}$ ];
- $G$  - potential energy [J];
- $A$  - frame offset by  $dx$  and multiplied by  $L$  [ $m^2$ ].

Adhesion is a phenomenon where the two surfaces of different bodies are combined. To the adhesion may participate in chemical forces, electrostatic dispersion, the strength of hydrogen bonds. The measure of interaction forces between the surfaces is the work of adhesion. In the macroscopic description of the phase boundary, there are considered two immiscible phases  $\alpha$ - $\beta$  and the process of their distribution for  $\alpha$ -phase and  $\beta$ -phase. In the case of liquid  $\alpha$ -phase consisting of molecules of the same type, the formation of two new surfaces is also related to the change of free energy for a smooth-running operation called cohesive.

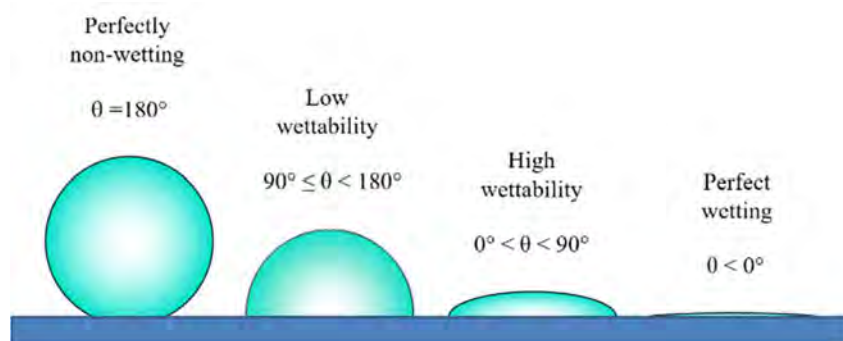


Figure 1.34. Wetting of different fluids [125]

A drop on the solid surface can be more or less spread out, as in Figure 1.34. It will depend on intermolecular forces between the solid and liquid. If the liquid particles are more strongly attracted to the solid particles, the liquid will be more prone to dissolve the solid surface. It is said that the liquid wets the solid. This process is called wetting [125].

A quantitative measure of wetting for both solids and liquids is the contact angle. It is the angle formed by the solid surface and a plane tangent to the surface of the liquid at the contact point of solid or to the surface of the two contact liquids, as presented in Figure 1.35.

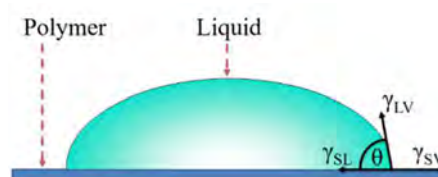


Figure 1.35. Liquid droplet remaining in an equilibrium state with the flat solid surface [125]

The surface energy of polymer is thus determined by the elastic equation in the transformed form, which considers the equilibrium of forces between the polymer and its vapour, polymer and substrate and substrate and vapour [126]. Standard liquid phase sintering is divided into three overlapping stages, but only the first stage of liquid phase sintering is expected to play a significant role in the selective laser sintering process. The wetting characteristics of the solid phase by the liquid phase are crucial in selective laser sintering processing. The wetting of solid by liquid is related to the surface tension of three interfaces and can be defined by the contact angle.

$$\gamma_{SV} = \gamma_{SL} + \gamma_{LV}\cos\theta \quad (1.16)$$

where:

- $\gamma_{SV}$  - free surface energy between solid-vapour [ $\text{J}\cdot\text{m}^{-2}$ ];
- $\gamma_{SL}$  - free surface energy between solid-liquid [ $\text{J}\cdot\text{m}^{-2}$ ];
- $\gamma_{LV}$  - free surface energy between liquid-vapour [ $\text{J}\cdot\text{m}^{-2}$ ];
- $\theta$  - equilibrium contact angle or wettability [ $^{\circ}$ ].

The value is influenced also by the material temperature, impurities in solid and liquid phases and the atmosphere. The wettability higher than  $90^{\circ}$  is limited, but when it decreases below  $90^{\circ}$ , wetting improves and complete wetting occurs as contact angle approaches zero.

The surface tension between the solid-liquid interface of particles defined as the free surface energy holds the particles together to minimize the superficial energy of powders. During the selective laser sintering process, the material is partially melted. If the surface tension between the liquid-vapour interface is higher than that between the solid-liquid interface, increases and the liquid retracts by spheroidization to minimize the superficial energy. On the other hand, if the surface tension between the solid-liquid interface is higher than that between the liquid-vapour interface, the liquid spreads around particles and joins them together [112].

During the selective laser sintering process of polymeric materials, sintering behaviour occurs at the interface of particles. The powder is partly melted by the laser, and then viscosity flow takes place so that the particles gather. Because the powder is partly melted, the dimensional precision of selective laser sintering parts, especially small parts, such as the size of the right angle, can be retained [16].

#### 1.4.5.5. Degradation

The degradation of polymer usually begins with a covalent bond cut due to thermal, oxidative, chemical, mechanical, radiative, hydrolytic, photolytic or biological degradation. Thus the stability of polymer depends on its chemical structure, the types of bonds constituting the macromolecular chain. The physical state of the polymer also influences its stability. For example, oxidation always begins in the amorphous phase [127]. Finally, the presence of additives in the commercial polymers modifies their kinetics of degradation. These additives may especially consist of stabilizers whose role is to reduce the factors responsible for degradation.

Phillips et al. [128] have studied the thermal stability of carbon-fibre-reinforced polyetheretherketone composite using rheological measurements in air and differential scanning calorimetry measurements on samples held for several minutes at temperatures between 360 °C and 420 °C. They observed an increase in complex modulus as temperature increased and melting and glass transition temperatures decreased melting enthalpy. The consolidation of the composite is deteriorated due to the degradation phenomenon. Nevertheless, the limit of fall in the quality of consolidation is set at 350 s at 420 °C.

#### 1.4.6. Molecular weight

The molecular weight is one of the important factors for describing the characteristics of polymers. The thermal properties of polymers through the melting viscosity are directly affected by the average molecular weight. The shear viscosity is directly proportional to the average molecular weight above the critical molar mass, they depend on a greater power. The molecular weight and the melting viscosity can obey the relationship applies to the intrinsic viscosity of the polymer is given by equation [16]:

$$\eta = K(M_w)^n \quad (1.17)$$

where:

- $\eta$  - viscosity [Pa.s];
- $K$  - constant that depends upon the type of polymer [mL.g<sup>-1</sup>];
- $n$  - constants exponent for a particular polymer [-];
- $M_w$  - molecular weight [g.mol<sup>-1</sup>].

For the polymer material, the melting viscosity depends on the molecular weight. Every polymer material has a critical molecular weight. Equation 1.17 indicates that the melting viscosity varies largely with a change in the molecular weight. Shi et al. [108] reported that the molecular

weight by affecting directly the melt viscosity of melted material, have a strong impact on the quality of sintered parts. The components of polystyrene built with the grade with lower melting viscosity exhibited higher densities than the specimens built with the higher viscous grade.

Moreover, molecular weight influences the maximum rate of crystallisation. The sample with lower molecular weight crystallises faster. There are two types of nucleation: homogeneous (or primary) nucleation and heterogeneous (or secondary) nucleation. Nucleation is the stage where the polymer chains organize themselves in alignment to form nuclei or crystallization seeds. The presence of nuclei affects the overall crystallisation rate by facilitating the initial nucleation step [129]. Some of the hydrogen bonds remain fixed and result in effective nucleation sites on cooling. The thermal history should, therefore, be erased and all homogeneous nuclei destroyed by holding the polymer for a sufficient time in the melt before crystallisation can take place.

The Avrami kinetic model [67] describes the nucleation and growth until the crystals collision. Any crystal structure as a function of time can be described by macroscopic nucleation and growth. In general development, it is assumed that the time of nucleation and crystal growth are interdependent and depend on the distribution of material to areas of growth of crystallites [130,131]. The transformed volume fraction is expressed concerning the fraction occupied if all the seeds were activated. The final expression for isothermal crystallization is given by Equation 1.18:

$$X(t) = 1 - \exp(-kt^n) \quad (1.18)$$

where:

- X(t) - fraction of substance that has not yet crystallized by time t [-];
- k - crystallization rate constant [s<sup>-1</sup>];
- t - time [s];
- n - Avrami exponent [-].

Two kinetics of crystallization have been identified and modelled by the Avrami and Kissinger equations. The analysis of Avrami exponents obtained for polyetheretherketone and polyetherketoneketone indicates that the two polymers show the formation of two crystalline phases with a heterogeneous geometry of nucleation and growth of sticks or disks depending on the cooling conditions [85,130]. The existence of these different crystalline forms was reported by Villar Montoya [113], which have been reflected by the appearance of three main melting peaks for polyaryletherketones.

The density of the crystalline phase is always higher than the density of the amorphous phase. For instance, for polyetheretherketone, Giants [132] reported that the density of the crystalline phase is  $1.378 \text{ g.cm}^{-1}$ , while Hay et al. [133] measured that of the amorphous phase is  $1.264 \text{ g.cm}^{-1}$ . The different measurements of the density of the amorphous phase are constant from one publication to another. Conversely, the density of the crystalline phase depends on crystallization conditions and densities between  $1.36 \text{ g.cm}^{-1}$  to  $1.41 \text{ g.cm}^{-1}$  were identified by Nicodeau [134]. The density of the crystalline phase of polyamide 12 depends on the cooling conditions and values ranging from  $1.034 \text{ g.cm}^{-1}$  to  $1.106 \text{ g.cm}^{-1}$  have been reported by Gogolewski et al. [64]. As for the density of the amorphous phase, three publications indicate the same value of  $0.990 \text{ g.cm}^{-1}$ , this density being less dependent on the operating conditions.

According to Shi et al. [16], the crystalline shrinkage largely affects the precision of selective laser sintering parts. For this reason, when a part is under printing, a gradient of shrinkage rate along the Z-axis could evolve to distortion of the part. The shrinkage can become more serious with increasing crystallinity. The crystallization rate which is closely correlated with crystallinity greatly affects the precision of objects. A polymer material whose melting point is far from the crystalline peak is not easily warped when sintered. It keeps the liquid state which cannot transfer the stress during the cooling process.

The glass transition and melting point values depend also on the molecular weight of the polymer. This can explain why there might be a significant difference in selective laser sintering process ability between the low and high molecular weight of any thermoplastic. To obtain functionally and strong parts, polymers need to have a molecular weight as high as possible. Above the critical molecular weight, the good mechanical properties can be obtained. Too high molecular weight can cause degradation, because of increasing in melt viscosity. On the other hand, for good interdiffusion of polymer chains, particle necking and layer to layer adhesion, low melt viscosity is indicated.

#### **1.4.7. Recycling of powders used in the SLS process**

Recovery of materials in a manufacturing process has become a necessity infiltrating not only from economic aspects but also from the broader environment. It forces producers of each industry to minimize plastic waste generated during the manufacturing process. The minimization of waste has also found its reflection in modern manufacturing techniques such as a selective laser sintering process.

In the selective laser sintering process, the volume part is less than 10-15 % of the building chamber, therefore about 85-90 % of material in the build remains unsintered and it is considered as a waste. Recycling and reusing waste powder are necessary due to the high cost of purchasing material and it is necessary to minimize the amount of waste.

This huge amount of powder could be recycled. Because of very long manufacturing times, the powder is kept for several hours at a temperature below the crystalline point. At the end of the selective laser sintering process, the unsintered, but thermally affected powder is separated from the sintered part and if possible, it may be recycled. For that, the material has to be particularly resistant to thermal degradation. Moreover, some grains are agglomerated due to heat in the building chamber. To be recycled, only the non-agglomerated powder is desirable to keep a particle size and distribution close to the initial powder. In the industry, the current powder recycling practices do not control the quality of already used material. The used powder is mixed with up to 50 wt.% of virgin one [135]. At this rate, the properties of powders are considered unchanged, thus the powder keeps the properties needed to be sintered.

The fresh and recycled powders have been compared by studying the microstructure of selective laser sintering parts by Zarringhalam et al. [136]. Recycled and fresh polyamide 12 (Duraform and PA2200), as well as a refreshed powder (mix of 67 wt.% recycled and 33 wt.% fresh powder), were compared by thermal and molecular weight analysis. The refreshed powder showed a slight increase in the melt temperature of 1 °C indicating more perfect crystals due to a crystalline reorganisation. Degree of crystallinity for fresh and refresh powders was measured of 55 % and 51 %, respectively. The decrease in crystallinity instead of increase gives the information that the increase in the melt temperature was due to a crystalline reorganization rather than increased crystallinity. The molecular weight of recycled powder significantly increased from 70.000 g.mol<sup>-1</sup> to 170.000 g.mol<sup>-1</sup>. The polydispersity index is 2.84 for recycled powder and 2.34 for fresh polyamide 12. This indicates that polymerization occurs in the solid-state powder. The authors explain that reduced molecular motion due to increased molecular weight might hinder crystallization. Aged in laboratory conditions, PA2200 powder was also studied by Pham et al. [137]. The samples of recycled and fresh powders were tested by differential scanning calorimetry, melt flow rate indexer and gel permeation chromatography. It was confirmed that degradation mainly depends on the laser temperature and processing time. Next, Dotchev and Yusoff [135] have investigated the percentage of fresh powder mixed with recycled powder to improve the quality of recycled powders. They declared that the refreshed rate powder can change shrinkage and rough surface of finish parts that is commonly called

“orange peel”. It was noted that the more times the powder is recycled decreased the melt flow rate from 17 g.10min<sup>-1</sup> to 13 g.10min<sup>-1</sup> for two and three recycled times, respectively, because of bad deterioration. Nevertheless, the melt viscosity has improved and the powder was less degraded when the fresh powder was mixed in different ratios. As a result of improving the melt flow rate, the “orange peel” also appeared less frequently.

To improve the quality and to reduce the cost of fabricated parts, more efficient recycling of powdered material is required. It was reported [135] that the temperature is different in each area of the building chamber, thus the powder occurs a specific thermal history depending on its location in the building chamber. The results indicate that the unsintered powder should be collected selectively and graded accordingly which would allow a better powder utilisation and control, more efficient recycling, and saving of new materials.

#### **1.4.8. Conclusion on the properties of polymer powders required in the SLS process**

Based on previous research and experiments, several criteria have been defined concerning polymeric materials used in the selective laser sintering process. It was found that for the best results it is required that the material has specific properties such as:

- the narrow area of polymer melting point (until complete melting);
- high melting enthalpy to achieve sharp separation of melted material from powder;
- large temperature ranges between melting point and crystallization;
- slow crystallization or amorphous solidification rate;
- the specific value of a surface tension force needed to melt powder particles;
- the largest possible difference between the surface energy of powder and the surface energy of alloy for high edge sharpness;
- narrow particle size distribution for homogeneous energy absorption;
- adequate melt viscosity, because it determines the melting (sintering) speed of material.

For the above criteria to be 100 % met, the polymer material must be very homogeneous, which in practice is virtually impossible to achieve for technological and financial reasons.



## 1.5. The theoretical basis of coalescence

The main principle of the selective laser sintering is based on the coalescence of polymeric particles. In material science, the word “sintering” often refers to compaction and forming by heat or pressure without reaching melting of the material. Despite the name of the selective laser sintering process, the polymeric grains are brought to a melted state to merge into each other. Another definition of sintering is when two liquid droplets are drawn together by capillary forces, for example, by a reduction in interfacial energy that accompanies the merging of two droplets [138]. Sintering is the physical phenomenon occurring in many manufacturing processes of polymer parts such as rotomoulding and selective laser sintering process. For the sintering droplets of Newtonian fluids, the driving force is the reduction in interfacial energy:

$$\Delta\gamma = \gamma_{LV} \quad (1.19)$$

where:

$\Delta\gamma$  - interfacial energy [ $\text{J}\cdot\text{m}^{-2}$ ];

$\gamma_{LV}$  - energy of interface between the liquid droplet and surrounding vapor [ $\text{J}\cdot\text{m}^{-2}$ ];

However, melted polymers exhibit a non-Newtonian flow behaviour with a high viscosity. The capillary forces are much lower compared to the viscosity forces, as a consequence, the contact or mutual wetting is not sufficient to ensure the coalescence of polymeric grains. The coalescence or wetting at that interface is assisted by the flow and deformation of particles.

The theoretical basis of all sintering techniques of polymer grains is based on the phenomenon of interdiffusion of macromolecules. From these theoretical bases of interdiffusion, the concepts of coalescence are explained. Thus, diffusion of chains across the interface and establishment of the equilibrium distribution of a chain is required to recover a homogeneous bulk properties [139].

### 1.5.1. Diffusion of macromolecular chains: reptation theory

The rheological properties of polymers in both solid and melted states are largely determined by intermolecular interactions. These include energetic interactions related to van der Waals forces and dispersion forces in a system of densely packed macromolecules. Typical interactions in condensed polymer systems are also entanglement. The essence of entanglement

is shaped by two types of interactions: elastic and sticky. The elastic effects accompany the shifting of chains in the normal direction to the plane of entanglement, and the sticky effects, the slip of one chain against the other without moving their contact [140].

The molecular entanglements in very long linear polymer systems affect the molecular motion, which has an influence on the rheological properties of bulk polymers in a melted state. Research on the translational diffusion of macromolecules in bulk was deeply analysed [141–144]. First of all, Rouse [141] describes the conformational dynamics of an ideal chain. The Rouse model assumes the movement of the idealized bead-spring chain (Figure 1.36) consisting of segments in a solvent environment. During movement, the beads experience a resistance force proportional to their speed.

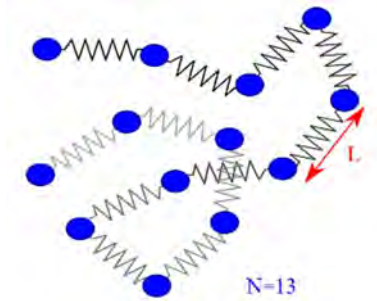


**Figure 1.36. The bead (fraction factor) and spring (Gaussian entropy) molecular model**

Next, the classical entanglement coupling model has been proposed by Bueche [142], which predicts the translational diffusion coefficient for the centre of mass motion of polymer molecules in a bulk. Then, de Gennes [143] introduced the new concept of “reptation” to explain the dependence of the mobility of macromolecule on its length in a hypothetical tube reflecting the potential associated with both adjacent chains as well as with the occurring impediments in the form of entanglement [145], as seen in Figure 1.37.

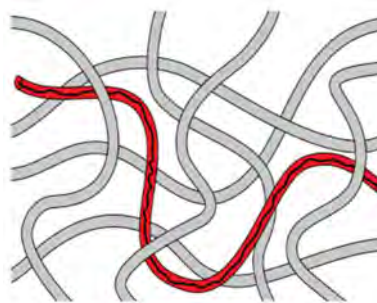


**Figure 1.37. Polymer chain located in a fixed network with representing obstacles**

The reptation theory is used as a mechanism to describe the motion of the amorphous polymer chain. It was reported that the delay of relaxation at low frequencies is related to the fact that entanglements are created all along the chain so that the longer the chain is considered,

the longer is the relaxation time (characterised at macroscale by the zero-shear viscosity of polymer). In the case of short chains, the viscosity of polymer melt increases linearly with increasing molecular weight. For long chains, the viscosity starts to increase more rapidly as a result of the emergence of a network of tangles. For instance, during the selective laser sintering process of polycaprolactone with the molecular weight of  $50.000 \text{ g.mol}^{-1}$ , the part demonstrated good laser processability [146], while polycaprolactone with the molecular weight of  $40.000 \text{ g.mol}^{-1}$  could not be laser sintered well [147] due to big distortions caused by the shrinkage.

Afterwards, the theory of molecular dynamics of polymers was refined by Doi and Edwards [144] into a full description of linear and nonlinear rheology of monodisperse entangled melts. The assumptions of this model concern chain movement, which consists of two mechanisms. Relatively free, winding a thermal movement of a chain along the tube with a defined coefficient of friction and a continuous process of decay and formation of a new tube section due to disentanglement and becoming entangled in the existing entanglement network. The tube thickness of the repetition process is a constant of the model and is determined by a network of entanglements that create obstacles to chain movement.

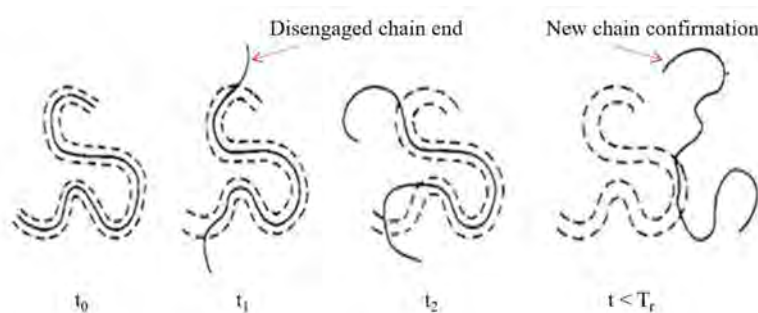


**Figure 1.38. Reptation theory,  $t_0 < t_1 < t_2 < T_r$  (the tube renewal time) [148]**

Over time, in the process of self-diffusion along its contour, the chain gradually disentangles from the original tube to find itself in a new environment, like in a new tube, as illustrated in Figure 1.38.

To describe the movement of the polymer, the Rouse model [141] is considered. Thus, the model interprets chain displacements by scattering mechanisms, estimates of total chain motion can be made from the unidimensional diffusion coefficient and then it can be described by Equation 1.20.

$$D_{\text{tube}} = \frac{k_B T}{\mu N} \quad (1.20)$$

where:

- $D_{\text{tube}}$  - unidimensional diffusion coefficient [ $\text{m}^2 \cdot \text{s}^{-1}$ ];
- $k_B$  - Boltzmann's constant [ $= 1.38 \cdot 10^{-23} \text{ J} \cdot \text{K}^{-1}$ ];
- $T$  - absolute temperature [K];
- $\mu$  - coefficient of monomer-monomer friction [-];
- $N$  - average number of segments in a chain [-].

The time it takes the chain to disentangle itself from the original tube is called the reptation time or the disequilibrium time. To describe the movement of polymer, the polymer self-diffusion constant can be determined by the time of the unidimensional diffusion of a chain on the primary road due to Brownian motion.

$$\tau_{\text{rep}} = \frac{L^2}{2D_{\text{tube}}} \quad (1.21)$$

where:

- $\tau_{\text{rep}}$  - reptation time [s];
- $L$  - length of primitive path [m];
- $D_{\text{tube}}$  - unidimensional diffusion coefficient [ $\text{m}^2 \cdot \text{s}^{-1}$ ].

This reptation time can be approximated as the product of time scale of diffusion, and the ratio of number of monomers of the chain, on the number of monomers between entanglements (Equation 1.21). From experimental measurements, the dependence of disentangling time on the molecular weight takes the form  $\tau \sim (M_w)^n$ , with the exponent in the range from 3.2 to 3.6. The presented Doi-Edwards model [149] predicts the value of  $n = 3$ .

$$\tau_{\text{rep}} \cong \tau_0 \frac{N^3}{N_e} \quad (1.22)$$

where:

- $\tau_{\text{rep}}$  - reptation time [s];
- $\tau_0$  - time scale of diffusion [s];
- $N$  - number of monomers of the chain [-] ;
- $N_e$  - number of monomers between entanglements [-].

The time scale of molecular motions is characteristic of monomers considered. For a melted polymer, the order of magnitude is between nanoseconds and picoseconds. Like all

scattering mechanisms, the reptation is a temperature activated phenomenon. Moreover, Doi and Edwards [149] have established a relation between time scale of diffusion, temperature, and coefficients of friction between monomers.

$$\tau_0 \cong \frac{\mu L^2}{\pi^2 k_B T} \quad (1.23)$$

where:

- $\tau_0$  - time scale of diffusion [s];
- $\mu$  - coefficient of monomer-monomer friction [-];
- $L$  - length of primitive path [m];
- $k_B$  - Boltzmann's constant [=  $1.38 \cdot 10^{-23}$  J.K<sup>-1</sup>];
- $T$  - absolute temperature [K].

The compatibility of experimental measurements with the predictions of model is therefore not ideal. The theory of polymer creeping has limitations:

- it predicts a variation in the limiting viscosity in the order of  $(M_w)^3$ , but experimentally it varies according to  $(M_w)^{3.4}$ ;
- it predicts a self-diffusion coefficient in the order of  $N^{-2}$ , but there is a variation of  $N^{-2.3}$ ;
- the tube that surrounds the chain is formed by other entangled molecules that move in turn. As a result, the tube has a limited lifetime.

Nevertheless, the reptation theory correctly indicates the order of molecular weight effects and entanglement in the rheological properties of condensed polymers.

### 1.5.2. Diffusion at interfaces

In contrast to interdiffusion in simple liquids, interdiffusion of polymeric chains is dominated by their intertangement and their large size.

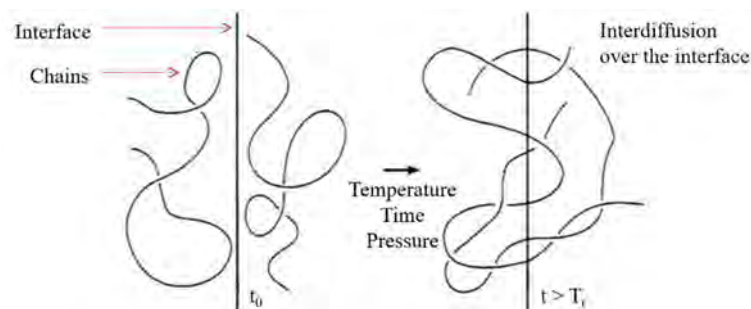


Figure 1.39. Interdiffusion of chains across an interface [148]

From the previously commented concepts of reptation theory and the dynamics of polymers, it can be established that the adhesion of polymer interface represented by a resistant module is proportional to the length of the interpenetration of polymer chains. At the time, this interpenetration length is a function of the square root of the interdiffusion time [150,151].

$$\frac{G(t)}{G(\infty)} \sim \frac{L(t)}{L} \sim \left( \frac{t}{\tau_{\text{rep}}} \right)^{\frac{1}{2}} \quad (1.24)$$

where:

- $G(t)$  - energy of interfacial separation (fracture toughness) [J.cm<sup>-2</sup>];
- $G(\infty)$  - restitution rate of energy for an infinite time [J.cm<sup>-2</sup>];
- $L(t)$  - length searched by the chain on the other side of interface [m];
- $L$  - length needed to completely renew the tube [m];
- $t$  - interdiffusion time [s];
- $\tau_{\text{rep}}$  - reptation time of polymer [s].

The interdiffusion time is the time at which the diffusion of macromolecule is possible, according to the processing parameters. Energy depends on the density of macromolecular links across the interface. Equation 1.24 allows understanding how the interdiffusion time can influence the fraction of length of interpenetrating polymer chains at the interface. In a second step, it is important to know the relation between the adhesion of interdiffusion interface and interdiffusion time. Under ideal conditions, the adhesion of the amorphous polymer interface increases with the square root of interdiffusion time.

### 1.5.3. Coalescence mechanisms and densification

The selective laser sintering process involves two physical phenomena: the coalescence of grains which leads to the densification of powder by evacuation of air trapped between the grains. For polymers, these phenomena have been widely studied for the rotomoulding.

The reduction of system interfacial energy during the selective laser sintering process is related to the growth of neck joining particles in thermodynamic equilibrium, which causes a microstructural evolution. According to Coble [152] who reported the formation of porosity, the sintering consists of three stages. In the initial stage of sintering, particles are assumed to be in point contact. The first stage includes the formation and growth of necks between particles. In the second stage, the volume of the network of pores is reduced gradually. Finally, the third stage eliminates spherical and isolated pores.

The first works addressing the coalescence of grains are proposed by Frenkel [153], quickly corrected by Eshelby [154], and later Mackenzie and Shuttleworth [155]. They were interested in the study of fluid flowing. Since then, different models were proposed to represent the evolution of coalescence of grains. The validity of classical sintering models is well established for sintering of amorphous materials. In past years, a new model was developed by Hopper [156,157], based on the Kolosoff-Muskhelishvili equations and complex function theory. Analytical solution of Hopper is only limited to two-dimensional and Newtonian flow problems. To predict the coalescence kinetics, it has also been developed numerical simulations of sintering process by Jagota and Dawson [158], van de Vorst and Mattheij [159], Martinez-Herrera and Derby [160,161].

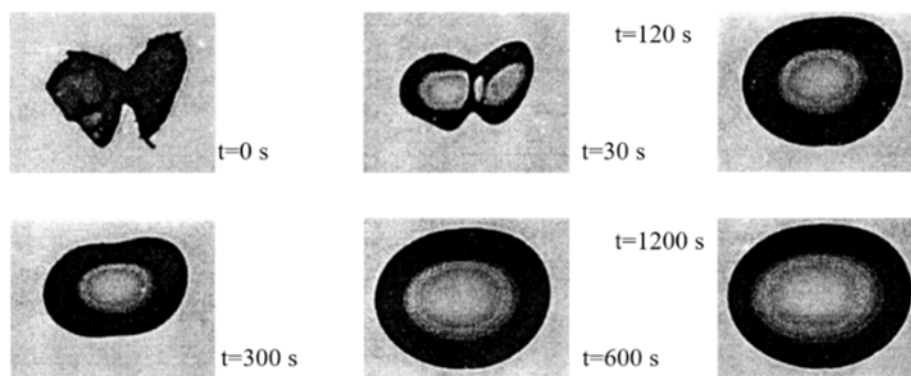


**Figure 1.40. Sintering sequence for PP-XP1 powder particles at 190 °C [162]**

Above, Figure 1.40 shows the isothermal coalescence over time of two grains of polypropylene at 190 °C. The process takes more than 120 s from the melting of grains to obtain a larger one. The coalescence is a phenomenon whose relatively slow kinetics involves various parameters. In the case of the selective laser sintering process which is not isothermal the effective time of coalescence of polymer grains is very insufficient in the printing process. According to the work of Schultz [22] who simulated the temperature evolution of polyetheretherketone powder bed, the grains last less than 1 s in the molten state.

The mechanisms of sintering are generally classified such as viscous model, viscoelastic model, and grain diffusion model [163]. The coalescence models have been widely studied and can be seen in the work of Schultz [22] and Liu [123].

The theory of viscous sintering of polymer was modelled by Frenkel in 1945 [153] using the isothermal coalescence of two identical spheres in its first moments. This model is interesting because it allows for understanding the influential parameters in the coalescence process. The results are consistent with experimental measurements. In this model, a neck of radius grows between two adjacent particles.

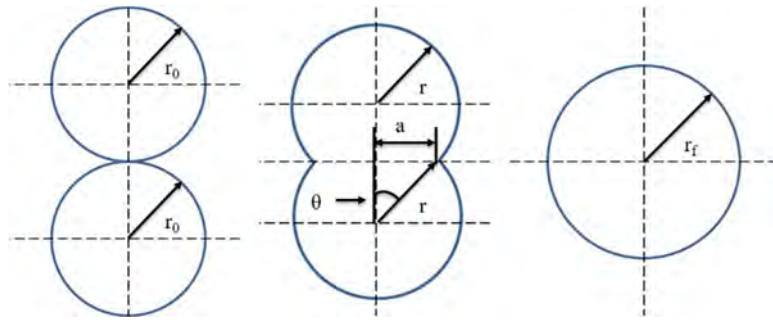


Figure 1.41. Schematic sintering sequence for two spheres [162]

Sintering model of Frenkel predicts that neck growth is based on equating the rate of energy dissipation by viscous flow to the rate of energy release from surface area reduction. Frenkel proposed to represent coalescence using two parameters, the radius of sphere and fillet radius. The angle of coalescence is represented by the ratio of sintering neck radius and sphere radius, defined in Figure 1.41.

Applying the correction proposed by Eshelby [154], the model of Frenkel can be described by the equation:

$$\frac{a}{r} = \left( \frac{\gamma t}{r_0 \eta_0} \right)^{\frac{1}{2}} \quad (1.25)$$

where:

- a - sintering neck radius [m];
- r - sphere radius [m];
- r<sub>0</sub> - initial sphere radius [m];
- γ - surface tension [J.m<sup>-2</sup>];
- t - sintering time [s];
- η<sub>0</sub> - zero-shear viscosity [Pa.s].

The equation says that neck growth is proportional to the square root of surface energy and sintering time and inversely proportional to the square root of zero-shear viscosity. Surface tension is the engine of coalescence, while the viscosity controls the flow. Following this theory, it is possible to calculate the theoretical value of melting viscosity. When the ratio of  $a/r = 0.5$  it means that the sintering process between two spheres is finished [16].

Pokluda et al. [164] by modifying the Frenkel model have been solved numerically and show that this approximation is good at zero. They found the model predictions to be in relatively good agreement with the sintering process between two spheres is finished model of Hopper [156] and numerical results proposed by Jagota et al. [158] for viscoelastic spheres.



$$\frac{d\theta}{dt} = \frac{\gamma}{r_0 \eta} \frac{2^{-\frac{5}{3}} \cos(\theta) \sin(\theta) [2 - \cos(\theta)]^{\frac{1}{3}}}{[1 - \cos(\theta)][1 + \cos(\theta)]^{\frac{1}{3}}} \quad (1.26)$$

where:

- $\theta$  - angle of coalescence [°];
- $t$  - sintering time [s];
- $\gamma$  - surface tension [J.m<sup>-2</sup>];
- $r_0$  - initial sphere radius [m];
- $\eta$  - viscosity [Pa.s].

The surface tension (Equation 1.27) at melting point by Parachor equation to approximate the surface tension at the melted state and viscosity (Equation 1.28) are described below:

$$\gamma = \left(\frac{P_s}{V}\right)^4 \quad (1.27)$$

with  $V = f(T)$  represents the molar volume and variable temperature. The molecular volume is the ratio between molecular weight and density of the polymer. The molecular Parachor ( $P_s$ ) is an additive, constitutive, property of the material [165]. The molecular Parachor is independent of the temperature [166].

$$\eta_0(T) = \eta_0(T_0) \exp \left[ \frac{E_a}{R} \left( \frac{1}{T} - \frac{1}{T_0} \right) \right] \quad (1.28)$$

The above model (Equation 1.26) is the most interesting because it allows understanding the influential parameters like surface tension and viscosity in the coalescence process [164]. this model has been successfully applied by Bakrani Balani [119] to study coalescence of PEEK filament.

The experimental and theoretical work presented in the literature shows that the predictions of classic sintering models for amorphous materials underestimate the contact growth observed in polymeric powders for times less than the characteristic relaxation time because these models only consider curvature-based forces and assume deformation occurs by viscous flow. When a large critical separation distance is assumed, the long-time viscoelastic contact growth equation presented by Lin et al. [167] has been shown to describe the contact behaviour of viscoelastic spheres before the characteristic relaxation time. The author of this work hypothesizes that viscoelastic contact growth can be a significant densification mechanism during the selective laser sintering process of polymers. The magnitude of contact

growth which occurs by viscoelastic deformation may depend on the particle size and the characteristics of creep compliance.

The objective of sintering models is to develop a closed-form analytical formulation that accounts for viscoelastic and viscous contact growth, a combined-mechanism sintering model. The closed-form analytical model of viscoelastic contact growth most applicable to modelling the selective laser sintering process is the long-time viscoelastic limit presented by Lin et al. [167]. As previously discussed, a large critical separation distance should be assumed to account for the contributions of curvature-based forces to zipping contact growth and stretching mode contact growth by viscoelastic deformation.

Sintering in practice is the control of both densification and grain growth. Densification is the act of reducing porosity in a sample thereby making it denser. The phenomena of densification can be distinguished into two different stages [168]. In the first stage, the fast increase in density is observed. The grains are not stuck yet, and the air between them can escape rapidly through the freeways because of the high mobility of particles in the liquid phase. This stage is controlled by the coalescence phenomena and its kinetic depends on the viscosity and surface tension of the material. In the second stage, the formation and release of entrapped gases are considered. The interfaces between grains are not free and the air cannot escape this way anymore. Thus, the air is trapped in the melted polymer and forms bubbles. The migration of air towards outside may be performed by the diffusion of gas in melted grains.

#### **1.5.4. Influence of surface tension and viscosity**

As seen in the sintering models, the coalescence is mostly driven by the surface tension and the viscosity. As mentioned before, the viscosity of powder during the selective laser sintering process includes the viscosity of both solid and liquid phase, which is dependent on characters of solid and liquid.

The selective laser sintering process causes that the material is partially molten. Wetting characteristics are very important as they are bonding the solid particles by the molten liquid. When choosing materials for selective laser sintering processing, it has to be ensured that the surface tension of the liquid phase can be lower than that of the solid phase. It should be chosen by right binary material systems, including trace alloying of low melting point material, or by varying the processing conditions such as temperatures and atmosphere. Wetting properties can be improved by using in situ deoxidizers or fluxing agents. Small quantities of these additives are added to the powder mix to aid sintering by lowering the wetting angle between a liquid and solid phase.

The rheological properties of melted liquid in conjunction with solid particles play an important role in determining a successful selective laser sintering process. The liquid phase can be presented by the following equation:

$$\eta = \eta_0 \left[ 1 - \frac{\Phi}{\Phi_m} \right]^{-2} \quad (1.29)$$

where:

- $\eta$  - viscosity of a solid-liquid mixture [Pa.s];
- $\eta_0$  - viscosity of the liquid phase without any solids (melt viscosity) [Pa.s];
- $\Phi$  - volume fraction of solids in liquid [-];
- $\Phi_m$  - critical volume fraction above which mixture has infinite viscosity [-].

The melt viscosity controls the particle bonding. Thus, it should be low enough that liquid surrounds the solid particles. However, the mixture viscosity should be high enough to prevent the formation of small spheres approximately the diameter of the laser beam during the selective laser sintering process. The combination of low melt viscosity and controlled of mixture viscosity can be best achieved by the right solid-liquid ratio and controlling the degree of superheat of low melting phase to influence the melt viscosity. Agarwala et al. [169] demonstrated that the viscosity of the solid-liquid mixture increases with the volume fraction of solid-phase and decreases when the particle size increases. Moreover, the viscosity of the mixture is directly proportional to the volume fraction of the liquid phase.

Taking into concertation the material viscosity described earlier, a low value is more desirable because it is responsible for good interdiffusion of polymeric chains, as well as, high particle necking and satisfying layer to layer adhesion [18]. The fully dense parts during the fast and more efficient sintering dynamics are more possible to obtain with a fairly low viscosity. On the other side, a high viscosity determined by the possible highest molecular weight allows manufacturing parts with the highest mechanical properties. Indeed, there is a dependency on mechanical strength (elastic modulus) with molecular weight. Berretta et al. [23] reported the differences in the chemical structure and crystallinity due to the molecular weights. These could cause a slightly higher storage modulus in HP3 copolymer than for PEEK 150 PF and PEEK 450 PF (83.000 g.mol<sup>-1</sup> and 115.000 g.mol<sup>-1</sup>, respectively) with similar storage modulus values. Also, as polyetherketone has a higher glass transition temperature than polyetheretherketone, storage and loss moduli were shifted towards higher temperature values.

However, when the viscosity is too low, higher shrinkage and poor part accuracy in the sintered parts may occur. According to Kruth et al. [53] the ratio between surface tension and melt viscosity gives a velocity parameter that defines the limit for a successful selective laser sintering process of polymers. For example, the PA12 with a melt viscosity of 100 Pa.s can be fully sintered under surface tension of 30 mN.m<sup>-1</sup> thanks to a velocity equal of 3·10<sup>-4</sup> m.s<sup>-1</sup>. Polymers like polycarbonate, with melt viscosity of 5000 Pa.s and dissimilar surface tension are not allowed.

### **1.5.5. Conclusion on the theoretical bases of coalescence**

To conclude, the coalescence process can be regarded as the first stage of sintering, in which contact areas between grains are expanding and necks begin to grow. The lack of effective time of coalescence may constrain the growing of necks and expand of contact areas resulting in a high porosity of a product. Thus, extra post-processing is required in case of selective laser sintering process in polymer powder bed [170]. It is necessary to maintain the chamber temperature higher than crystallization temperature for hours after laser scanning, to guarantee enough time for sintering.

The melted polymer is a typical viscoelastic material. Therefore, the viscous coalescence model is not suitable in this case. According to Liu [123], the grain-boundary diffusion model is capable to simulate the displacement of a melted grain due to the coalescence. However, this model requires many parameters (for example material properties) which are difficult to obtain. Thus, the viscoelastic coalescence model is presented as the most suitable for the selective laser sintering process, because it can describe the change of geometry of polymer powder bed.

Liu [123] by the comparison between numerical and experimental results confirmed that the viscoelastic coalescence model function well. It has a great potential in modelling the physical phenomena of grains inside powder bed and optimizing parameters of the selective laser sintering process.

## 1.6. Conclusion

Over the past years, the development of several additive techniques (MJ, SLA, FFF, SLS) can be observed. These techniques may differ due to the production of parts, quality of products, kind, and form of materials (liquid, solid powders, filament wire), purpose, availability, etc. In many aspects, the development of additive manufacturing is associated with process economics such as equipment, material and service costs. Recently the progress of the selective laser sintering process has enabled the development of polyamide parts for applications with high added value and for small quantities of identical parts which are very useful in many areas such as medicine, aerospace, aeronautics, automobile racing and others.

Due to the survey of Lawrence Livermore National Laboratory, 47 % [171] of manufactures in the USA do not yet trust the selective laser sintering process because of non-reproducibility of performances obtained. Thus, there is an urgent need to improve understanding of multiple mechanisms involved in a selective laser sintering process. A path to increase the number of materials for a selective laser sintering process should include the development of analytical and empirical models which include relevant sintering mechanisms and material properties. Such models could then be used to guide a material selection and determination of laser sintering technology parameters.

Simultaneously with the progress in the construction of devices, the materials market developed dynamically, which in turn allowed the development of new types (PA, ABS/PC, PA/GF, PEEK). Nowadays, polymeric materials are widely used in many different fields of technology, these materials are an integral part of the daily routine. Polymer materials are increasingly replacing traditional construction materials, they can also be used to make machine and mechanism elements or to use them as functional materials.

The way to increase the opportunities for the selective laser sintering process may include the development of analytical and empirical models which include relevant sintering mechanisms and material properties. The bibliography to understand the mechanical behaviour of the consolidated materials has been done.

The selective laser sintering technique is well mastered for polyamides and make them possible to manufacture prototyping parts. On the contrary, for the high-performance polymers and in particular polyaryletherketones, the manufacture by selective laser sintering is not yet mature. Effect of process parameters on the mechanical properties, the producing time of parts, recyclability of powder plays an essential role.

This state of the art made it possible to divide this study into four main chapters. First of all, the understanding of the behaviour of input material (thermoplastic powders) was carried out. Secondly, with the knowledge of material properties, the elaboration of new material for selective laser sintering was proposed and investigated, which today are restricted almost exclusively to polyamides 11 and 12. The blend between polyetheretherketone and amorphous thermoplastic was considered. Then, the different phenomena involved in manufacturing were verified by the production of polyamide 12 samples by the 3D printer. Effect of process parameters on the printed parts was studied. Finally, by the determination and the application of numerical models of materials behaviour in mechanics. Numerical and experimental analysis of the thermal profile of printed layers during the selective laser sintering process of polyetheretherketone was proposed.

The second chapter of this manuscript focuses on the adaptability of new polymer powders to the selective laser sintering process. In this part, the reuse of powder not exposed to the laser beam was also an essential issue. So far, no detailed study has been carried out on the degradation of powders during the process and the influence of these degradations on the properties of parts.

## **2. CHARACTERIZATION OF POWDERS AVAILABLE ON THE MARKET: PEEK & PA**

The second part of the thesis consists of characterizing several polyetheretherketones and polyamide 12 (as reference material) in powder form to compare their properties and choose the most suitable grade for the selective laser sintering process. For this, the bibliographic work has been completed by the expertise on material accumulated by Prismadd company/WeAre group and the Laboratoire Génie de Production (LGP-ENIT). At the beginning of the project, wide research of materials available has been carried out to select PEEK and PA powders.

Then, a board characterization of the chosen polyetheretherketone and polyamide materials has been done to specify the morphology and flowability of powder particles, their thermal properties (expansion coefficient, heat capacity, heat conductivity, etc.) and the flow properties with temperature. Most of the grades are not suitable for SLS since their flowability in the solid-state is too low. So, some attempts to improve the flowability of PEEK powders are proposed.

The objective of this chapter is to highlight the differences or similarities between the powders, in order to explain the different behaviour of powders. From this, we would be able to predict the properties of the printed parts.



## 2.1. Presentation of suppliers and materials

There are only a few manufacturers of polyaryletherketone (PAEK) powders on the market, whereas plenty of manufacturers of standard thermoplastics such as polyethylene, polypropylene, styrenics and polyvinyl chloride. Polyaryletherketones are supplied in pellets, for injection moulding and extrusion, or in powders for compression moulding or coating of metallic parts. Several types of PAEK materials are available, with PEEK outshining the others. The manufacturers of polyaryletherketones are Daicel, Evonik, Lehmann & Voss, Polymics, Sabic, Solvay, Victrex, Jilin Zhongyan High Performance Plastic, Gharda, RTP, Arkema, Velox and Cytec.

Compounds, long fiber composites and other PAEK-based semi-finished products are commercially available in the form of tubes, round rods, sheets and complex shapes. Driven by the development of AM these last years, many suppliers propose PAEK-based filaments for fused filament fabrication. Besides, PAEK powders suitable for SLS are rare on the market. When this work has begun in 2016, only one polyetherketone (PEK) powder was sold as a powder for selective laser sintering process, which is PEEK HP3 by EOS company. So, we decide to broaden our research of materials to all PAEK powders commercially available in the range 30-100  $\mu\text{m}$ , based on previous works done on the SLS process [1–3]. The PEEK 450 is by far the most used PAEK in the industry worldwide. This grade has been widely studied from 80<sup>ies</sup> when it was launched on the market. These last years, some research projects were carried out or they are currently running at LGP-ENIT with this polymer: PEEK/carbon nanotubes compounds for embedded electronic applications, (FUI WASPE: lightening aeronautical structures: power and control electronics packaging in 2013-2017), on fused filament fabrication (PhD thesis by Shahriar Bakrani Balani in 2015-2019 [119]), on tribological properties of PEEK-based composites (PhD thesis by Marie Doumeng in 2017-2020). Because of the knowledge gathered on this grade, this polymer, available in pellets in our laboratory, was included in our list.

The PAEK powders are generally devoted to compression moulding, electrostatic powder spraying, flame spraying, and scattering. They can also be used as a suspension in aqueous as well as solvent-based systems. The sectors are as electrical, electronics, communications engineering, automotive and food industries, aerospace and oil and gas. These PAEK products favour industrial companies in developing and delivering high-value, sustainable products and solutions which consume less energy and reduce CO<sub>2</sub> emissions, optimizing the use of resources. Lightweight polyetheretherketone thermoplastics count

towards more fuel-efficient and environmentally friendly aircraft, faster assembly times, greater reliability and lower operating and manufacturing costs.

The Electro Optical Systems (EOS) is a company founded in Germany by dr. Hans J. Langer in 1989. This is the only company in Europe that performs three-dimensional printing process using selective laser sintering. They sell the machine EOSINT P800, described in Annex A.1.12. The EOS machines type P are plastic laser-sintering machines with a CO<sub>2</sub> laser with an infrared wavelength of 10.6 μm. For the production of small series, the type FORMIGA P110 is suitable. The recommend EOS P396 and EOS P760 for flexible series and EOS P800 for large series. EOS deposited several patents in 2009, 2010 and 2013 [57,58,105], in which the process is described: the invention relates to a process for manufacturing a three-dimensional object from a powder by selective sintering by means of electromagnetic radiation of the powder. Also, the patents refer to a new powder for the SLS process developed by EOS, namely HP3. The HP3 powder is made of a polyaryletherketone/polyarylethersulfone copolymer. The patent mention that the powder may be a composite powder that comprises one or more fillers and/or additives besides a matrix of the respective blend.

The parts made of HP3 by laser sintering can achieve a tensile strength of 95 MPa and elastic modulus of 4400 MPa. These values are 100 % higher than the materials PA11 and PA12 prevailing on the market. The temperature range for HP3 in uses is 180 °C under dynamic mechanical load, 240 °C under static mechanical load and 260 °C under electrical load.

All the manufacturers cited above have been contacted. After long discussions to justify our interest to collaborate with them, some manufacturers sent us their products for free, others proposed to buy it, and some decline the proposition. The latter argued their PAEK powder was not suitable for SLS and they were conducting (in 2016) their own research to develop PAEK powder for this manufacturing process. So, four commercial powders of polyetheretherketone have been selected to carry out this work. It was not possible to get supplies from EOS due to the minimum quantity of 20 kg they ask to buy and the corresponding price of 6160 € (excl. VAT/delivery cost). To circumvent this drawback, we got recycled HP3 powder (meaning the powder remaining in the SLS chamber after a production cycle) from Centre National d'Etudes Spatiales (CNES).

Moreover, as mentioned earlier, polyamide is the main polymer currently used in laser sintering technology, in particular, because of its thermal properties. For this reason, one grade of polyamide 12 has been retained for our study.

The full list of polymer materials is presented below:

- Duraform PA12 from 3D Systems (USA)
- Duraform PA12 from 3D Systems (USA) after selective laser sintering process (recycled) from Prismadd (France)
- ZYPEEK 330 PF, from Jilin Zhongyan High Performance Plastic (China);
- ZYPEEK 550 PF, from Jilin Zhongyan High Performance Plastic (China);
- VESTAKEEP 2000 FP, from Evonik (Germany);
- KATESPIRE KT-880 SFP, from Solvay (Belgium)
- PEEK 450 G from Victrex (United Kingdom); The pellets were milled to 250  $\mu\text{m}$  particles at LGP-ENIT
- PEEK HP3 after selective laser sintering process (recycled) from Electro Optical Systems (Germany) delivered by Centre National d'Etudes Spatiales (France).

The technical specification of each polymeric material is presented in the Annex A.1. The recycled PA12 powders were submitted to one manufacturing cycle (preheating temperature of 130 °C and bed temperature of 174 °C). The recycled HP3 PEEK powders have been submitted to one manufacturing cycle (preheating temperature of 336 °C, bed temperature of 385 °C).

The study of recycled polymers aims to understand the effect of manufacturing cycles on the properties of the powder. Indeed, it would be useful to re-use the remaining powder after extracting the sintered part out the powder bed, for saving resources and money.

## 2.2. Morphology of powder particles

The morphological analysis is divided into two parts. The first part is devoted to the observation of powder particles by scanning electron microscopy (SEM) and image analysis to extract meaningful information. In the second part, laser diffraction particle size analysis was carried out to obtain a size distribution of the particles. The methodologies for morphology analysis are presented in the Annex A.2.1.

### 2.2.1. Particle shape analysis by SEM imaging

It is interesting to quantify the morphology of polymer particles for several reasons. The first one is to know the particle size distribution to control the layer thickness, this property determines the precision of the printed part. The second reason is that the shape of the particles is directly linked to the flowability: spherical and smooth particles roll easily one upon another, on the contrary, rough particles come into solid contact through one or a few asperities, resulting in high friction between particles. In this case, the layer thickness would not be homogeneous.

The morphology, size, and shape of polyamide grains have been measured by scanning electron microscopy observation. The images are presented in different magnifications x100 and x1200 in Figure 2.1 for fresh PA12 and Figure 2.2 for recycled PA12.

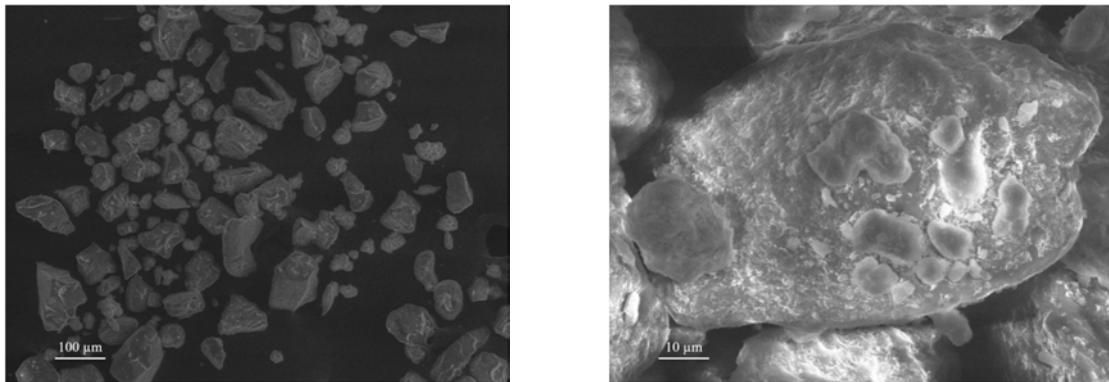


Figure 2.1. The SEM of fresh PA12 powder

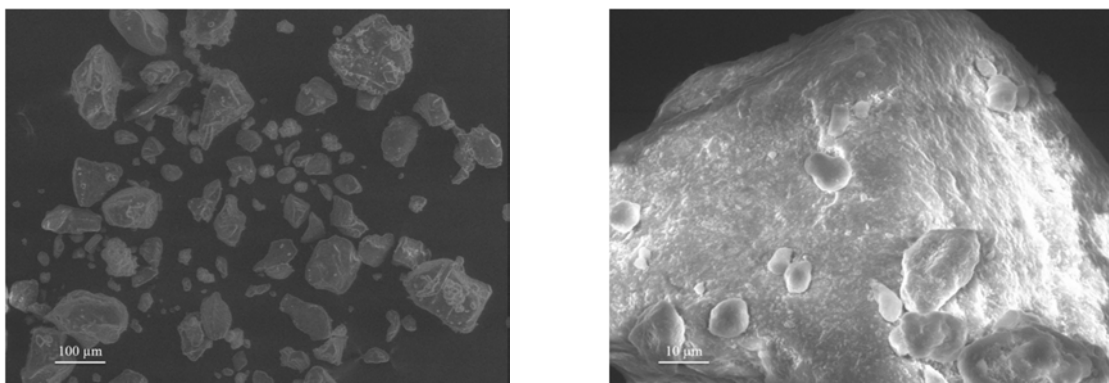


Figure 2.2. The SEM of recycled PA12 powder

The polyamide 12 powders have a quite irregular shape, with coarse surface and disparate sizes. There is no obvious difference between the fresh and recycled powder with a magnification of x100. A closer look with a magnification of x1200 at the surface of particles reveals a small difference between the two powders: the particle surface of recycled PA12 looks smoother. This could be due to the thermomechanical cycle seen by the recycled powder: the friction between particles when the powder is spread to form a layer and the exposure to a temperature near the glass transition for several hours, the particle surface could become smoother.

It is worth noticing that on the surface of the particles, some finer particles appear. Dupin [1] explains that Duraform PA12 powder for selective laser sintering process contains flowing agent such as fumed silica. It is noticed that the fine particles appear more clearly than the large ones, suggesting that these particles consist of chemical elements with a higher atomic number. The EDX analysis allowed detecting of a great concentration of silicon and oxygen elements for the fine particles, confirming the presence of silica in larger amounts in these particles. The fine particles of silica enhance flowability and generate higher bulk density for sintered parts [24]. The fumed silica bonded on the particle surface reduces the adhesion force between the polymeric particles.

Thus, scanning electron microscopy analysis, therefore, revealed a strong similarity in terms of morphology and particle size between fresh and recycled PA12. The polyamide 12 particles represent a well-established material for selective laser sintering, therefore its morphology was used as a reference material to be compared to the potential polyetheretherketone powders.

The images of polyetheretherketone grains are presented in different magnifications of x100 and x400 in Figure 2.3-2.8. The polyetheretherketone particles seem smaller than polyamide particles.

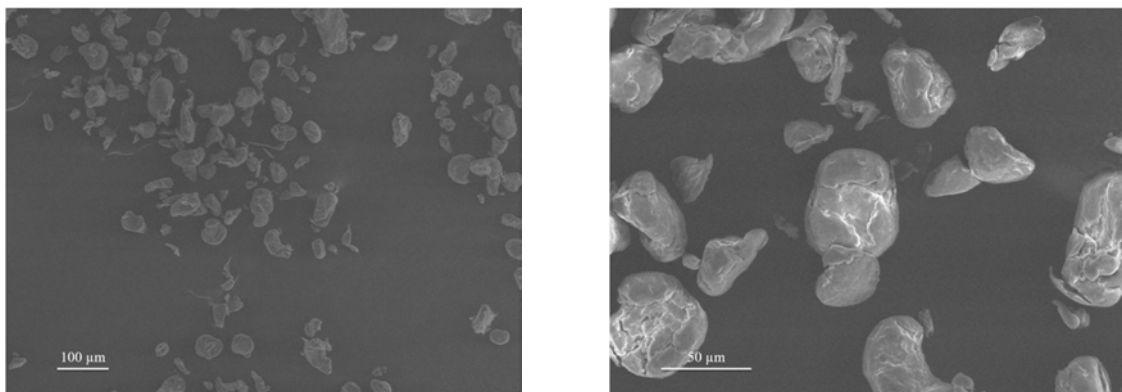


**Figure 2.3. The SEM images of PEEK 330 PF**

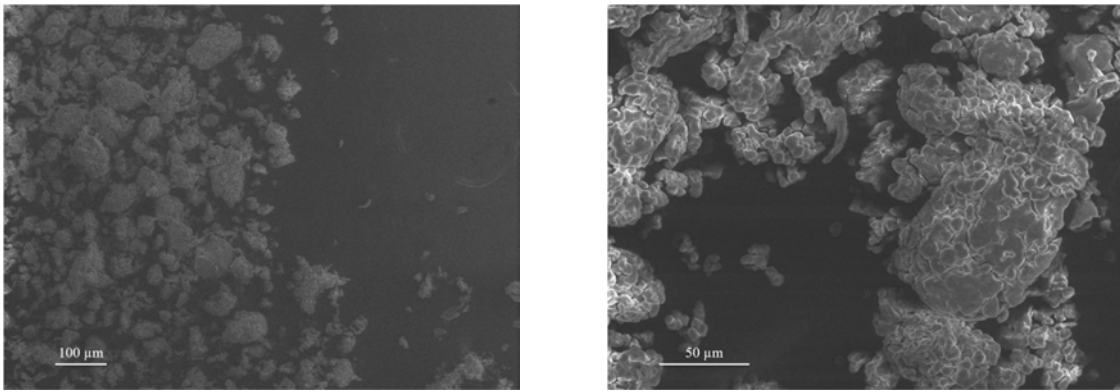


Figure 2.4. The SEM images of PEEK 550 PF

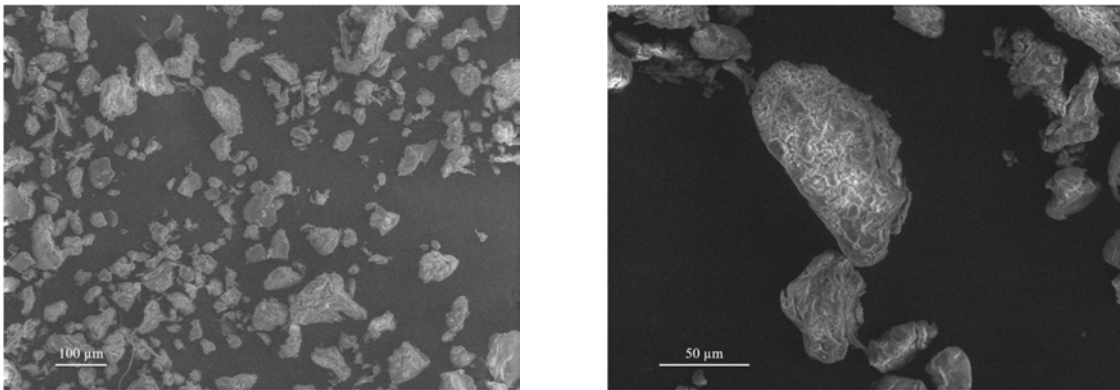


Figure 2.5. The SEM images of PEEK 2000 FP

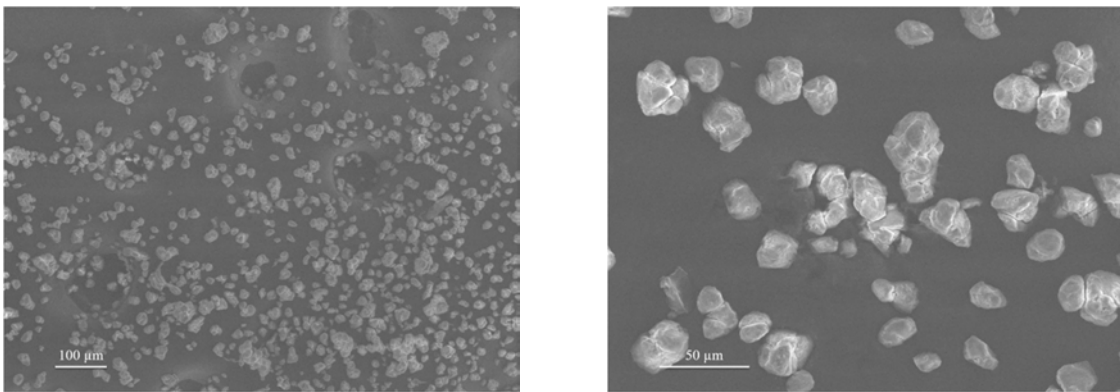


Figure 2.6. The SEM images of PEEK 880 SFP

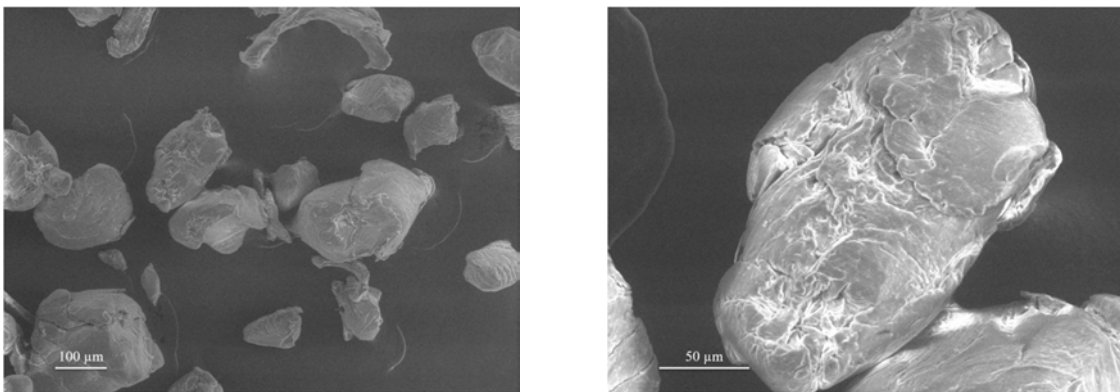
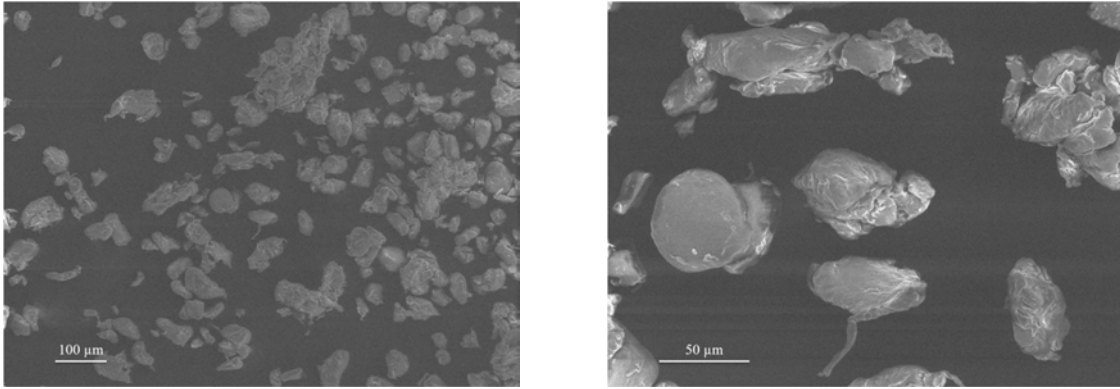


Figure 2.7. The SEM images of PEEK 450 G



**Figure 2.8. The SEM images of PEEK HP3**

The polyetheretherketone powders consist of irregular shapes and they are characterized by the presence of highly irregular flaky structures on the surface. These structures could cause friction and mechanical interlocking between the particles, decreasing their flowability. As seen on SEM images, the particle size is in the range 10-150  $\mu\text{m}$ . According to Chung and Das [108], this size is suitable for the selective laser sintering process. These particles are mixed with the finest ones present in bigger amount. To look closer, it can be seen that PEEK 330 PF and PEEK 880 SFP are smoother and more spherical than PEEK 550 PF and PEEK 2000 FP, they look created by aggregated very small particles. It is interesting to note that those materials could be classified into two types: the first ones (PEEK 330 PF and PEEK 880 SFP) are characterized by round protuberances composed by sub-structural fibrils and second ones (PEEK 550 PF and PEEK 2000 FP) are similar to flaky particles.

The powder milled from the PEEK 450 G granules has been obtained by micronization by Micronis company. It is performed using liquid nitrogen gas, to prevent heating. These low cryogenic micronization temperatures create an atmosphere in which the jet-milled powder becomes more brittle than it would be at ambient temperature. The powder size is around 250  $\mu\text{m}$  and it serves as a comparison with the other polyetheretherketone powders. It is not suitable for the selective laser sintering process because of the too big size of particles, but as it will be shown later, this powder is characterized by a good flowability.

The particles of PEEK HP3 are shown in Figure 2.8. The particles are not spherical shaped; however, they have smooth surfaces and they look fully dense structures at high magnification. The same observations have been done by Beretta et al. [172] who confirms the lack of alternative polyetheretherketone powders suitable for the SLS process.

The previous observation is not quantitative ones, that is why image analysis has been performed on the same images and more to extract quantitative meaningful data.

### 2.2.1.1. Image analysis

The shape and the size of powder particles play an essential role in the flowability and bulk density of powder. A smooth and spherical shaped particle promotes flowability and improves bulk density. The measurement of the circularity index and the shape ratio was chosen to characterize the shape of the particles. This measurement was carried out by analysing the SEM images with ImageJ software.

For precise measurements of circularity index and shape ratio from the images, a procedure was defined and it is presented in Annex A.2.1.2. The circularity is a dimensionless ratio between 0 and 1 characterizing the geometrical resemblance of a grain with a circle. It is possible to evaluate the morphological state of the particles, the closer it gets to 1, that means the particle is circular in shape. The shape ratio is defined as the ratio between the maximal and minimal fiber diameters. The diameters of fiber are obtained by surrounding the grain by two parallel straight lines. When the lines are rotated around the grain, the maximum value and minimum value are defined. The area and diameters of grains needed for calculation are exported in an Excel file to allow data processing. The results are as follows in Table 2.1. The average values of circularity and shape ratio with their standard deviations are presented.

**Table 2.1. Circularity and shape ratio of PA and PEEK particles**

Powder	PA12 (fresh)	PA12 (recycled)	PEEK 330 PF	PEEK 550 PF	PEEK 2000 FP	PEEK 880 SFP	PEEK 450 G	PEEK HP3
Circularity [-]	0.59	0.63	0.41	0.30	0.45	0.42	0.39	0.40
Standard deviation	0.20	0.22	0.21	0.14	0.18	0.20	0.25	0.26
Shape ratio [-]	1.67	1.65	2.03	1.87	1.68	1.67	1.91	1.95
Standard deviation	0.75	0.73	1.06	0.69	0.60	0.54	0.82	0.78

The PA12 powder developed specifically for SLS has the highest circularity of 0.59 and the lower shape ratio of 1.67. When comparing fresh and recycled PA12 powders, in Figure 2.9 and Figure 2.10 in terms of circularity and shape ratio, respectively, it looks that the printing cycle affects increasing the circularity and decreasing the shape ratio of PA12 grains. This confirms the variation in the particle shape or surface observed on SEM images. After the sintering process, PA12 particles are more spherical: the maximum circularity is shifted from 0.60 to 0.75 and a maximum shape ratio initially at 1.20 for the fresh one is broadened from 1.10 to 1.40 for the recycled one.



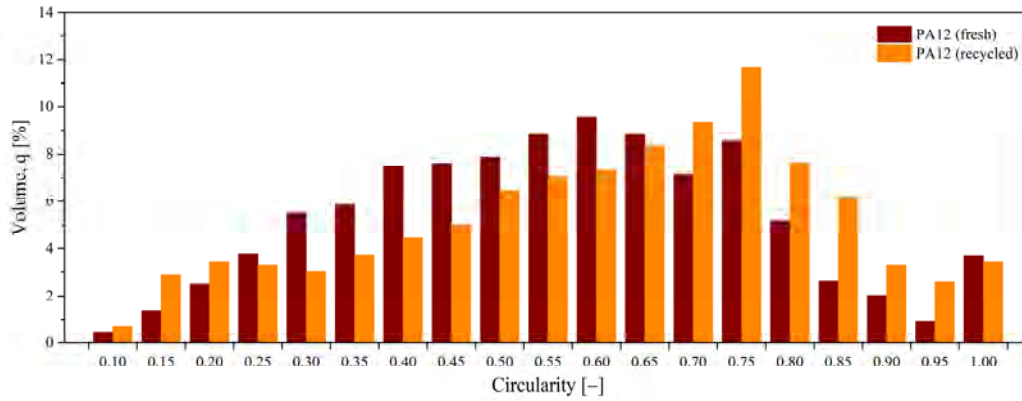


Figure 2.9. Distribution of circularity for fresh and recycled PA12

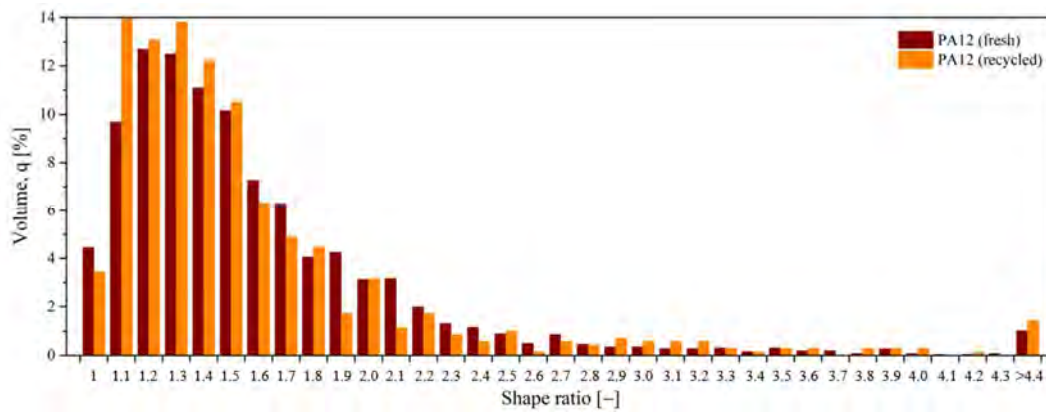
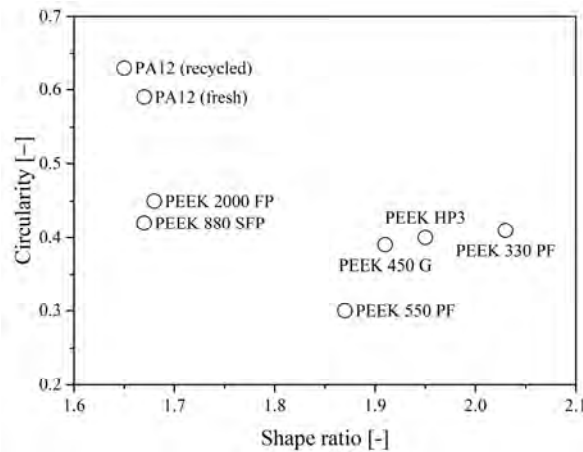


Figure 2.10. Distribution of shape ratio for fresh and recycled PA12

All PEEK particles present similar values of circularity around 0.40, which is lower in comparison with the values of PA12. The lowest value of circularity of 0.30 is obtained for PEEK 550 PF, it stems from the powder morphology: it seems to be created from aggregated very small particles, implying then the presence of sharper, elongated and irregular particles. The highest circularity (meaning the closest to 1) for PEEK particles is observed for PEEK 2000 FP. Dumoulin [3] confirms these results: he measured the sphericity of Primepart PA12 powder, his results show a circularity of 0.79 and shape ratio of 1.40, which are higher than PEEK particles with the circularity around  $0.62 \pm 0.03$  (PEEK\_A, PEEK\_B and PEEK\_C in Dumoulin's PhD thesis). Moreover, he investigated PEKK particles for which he obtained similar results as our PEEK with a circularity around 0.57. Berretta [172] also confirms these results, she obtained 0.61 of circularity and 1.82 of shape ratio for PEEK HP3.

The circularity-shape ratio diagram is a way to quantify the shape anisotropy of particles, that is to say if they are more or less elongated. The circularity is 1 when the particle is spherical in the shape. The shape ratio close to 1 indicates the presence of equated particles that can correspond to different shapes such as circles, squares, overall circular polygons, while higher values identify highly elongated particles.



**Figure 2.11. The circularity-shape ratio diagram of polymer powders**

The ratio obtained for our powders is plotted in Figure 2.11. The shape ratio values between 1.65 and 2.03 for PA12 and PEEK particles are all greater than 1. The PA12, PEEK 2000 FP and PEEK 880 SFP grades present lower shape ratio among all the materials with 1.66, 1.68 and 1.67, respectively. It means that the majority of particles are circular or slightly elongated. The PEEK 550 PF, PEEK 450 G and PEEK HP3 show slightly higher shape ratio of 1.87, 1.91 and 1.95, respectively. The PEEK 330 PF covers the highest value of shape ratio, 2.03, an indication of the presence of highly elongated and sharper particles compared to other grades.

The most widely used method for describing particle size distributions are D values. For this, it was chosen to select the average Feret diameter defined as the maximum and minimum diameter of the particle. The  $D_{10}$ ,  $D_{50}$  and  $D_{90}$  are commonly used to represent the midpoint and range of particle sizes from a cumulative distribution in many particles. The first of these diameters correspond to the fact that 10 % of particles have an average Feret diameter of less than  $D_{10}$ , the second corresponds to 50 % of particles which have a diameter less than  $D_{50}$  and the last corresponds to 90 % of particles which have a diameter less than  $D_{90}$ . The scheme in Figure 2.12 could help to understand the meaning of these diameters.

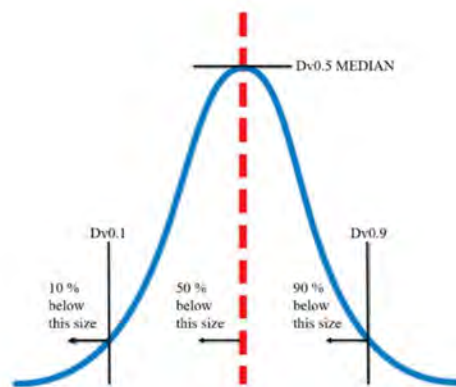


**Figure 2.12. Three x-axis values  $D_{10}$ ,  $D_{50}$ , and  $D_{90}$  [173]**

The results are obtained by image analysis of SEM images of PA12 and PEEK powders. The procedure of image analysis is explained in Annex A.2.1.2. The results are reported in Table 2.2. The relative standard deviation of these results is 10 % for this method.

**Table 2.2. The particle size distributions by ImageJ analysis**

Powder	PA12 (fresh)	PA12 (recycled)	PEEK 330 PF	PEEK 550 PF	PEEK 2000 FP	PEEK 880 SFP	PEEK 450 G	PEEK HP3
D <sub>10</sub> [μm]	7.0	15.3	17.6	12.7	7.9	8.3	61.6	7.9
Standard deviation	1.4	2.2	2.7	1.3	0.9	0.9	1.3	1.2
D <sub>50</sub> [μm]	28.1	42.0	42.2	33.9	20.5	19.9	230.8	44.1
Standard deviation	7.3	9.5	9.7	7.1	4.4	4.2	8.1	13.0
D <sub>90</sub> [μm]	76.1	110.5	80.1	104.7	78.9	49.1	395.9	174.5
Standard deviation	18.4	25.9	19.0	23.0	18.5	10.5	25.4	37.2

Our results range from 7.0 μm to 17.6 μm for D<sub>10</sub>, from 19.9 μm to 44.1 μm for D<sub>50</sub> and from 49.1 μm to 174.5 μm for D<sub>90</sub>.

The particles of fresh PA12 have D<sub>50</sub> of 28 μm. Dumoulin [3] has obtained for Primepart PA12 a diameter D<sub>50</sub> of 44 μm. By laser granulometry, Dupin [1] has observed a wide bimodal distribution with a D<sub>50</sub> equal to around 59 μm for Duraform PA12 powder, with a part of its distribution of average size around 60 μm and another around 8 μm. From his data, we deduce that the powder Duraform PA12 contains a very large number of fine particles.

The results show that the particles of recycled PA12 are bigger than for the fresh PA12 for each diameter, up to is 33 % higher for D<sub>50</sub>. This may be due to the formation of agglomerates between particles after the selective laser sintering process. In opposite, Mielicki [174] reports that with increasing ageing time, which may correspond to the time that the powder is in the building chamber, the particle size distribution of PA12 powder is unchanged. He confirms that for powder oven aged at a temperature of 174 °C, neither the particle size nor the particle shape change with increasing storage time. Beside unchanged particle sizes, its curves show a narrow particle size distribution, which is favoured for high bulk and thus high component densities. Nevertheless, it is difficult to trust such results because the analysis of particle shape shows high deviations, particularly for long ageing times. The heat brought by the laser beam causes the particles to coalesce and thus to form agglomerates increasing the particles size distribution.

The analysis of particle size distribution showed high standard deviations, particularly for  $D_{90}$ . The image analysis is not the most commonly used technique for particle size distribution analysis of powders, because an image is a small fraction of the powder, a few micrograms so the analysed zone could be not representative of the whole sample.

### 2.2.2. Analysis of particle size distribution by laser granulometry

The technique of laser diffraction granulometry makes possible to analyse the particle size distribution by volume of a large number of particles and it is easy to implement. The granulometry analysis can be represented in terms of sample volume or terms of many particles in the sample. The results obtained for  $D_{10}$ ,  $D_{50}$  and  $D_{90}$  are very different depending on the technique used. The reasons for these differences, when comparing image analysis and laser diffraction granulometry are:

**Table 2.3. Differences between image analysis and laser granulometry**

ImageJ analysis	Laser granulometry
Number analysis (the $D_{10}$ always lower)	Volume analysis (minimizing the influence of small particles)
No cluster counted	Cluster counted
Average of Feret diameter	Approximation of spherical particles
Sampling from 100 to 600 particles	Sampling of several thousand particles

Despite these differences, both measurements remain to be perfectly exploitable.

The description of the technique is given in Annex A.2.1.2 for ImageJ and Annex A.2.1.3 for laser granulometry. The polymeric particles were suspended in water or ethanol as media with 1 min of ultrasonic waves. The particle size detected ranges are from 100 nm to 3000  $\mu\text{m}$ .

The results are presented below:

**Table 2.4. The particle size distributions by laser granulometry in water**

Powder	PEEK 330 PF	PEEK 550 PF	PEEK 2000 FP	PEEK 880 SFP	PEEK 450 G	PEEK HP3
$D_{10}$ [ $\mu\text{m}$ ]	27.0	26.4	34.7	24.3	130.1	44.4
$D_{50}$ [ $\mu\text{m}$ ]	50.0	48.8	73.2	80.2	271.6	77.8
$D_{90}$ [ $\mu\text{m}$ ]	88.2	85.3	152.5	211.4	462.3	149.5
Uncertainty [ $\mu\text{m}$ ]	$\pm 1.6$	$\pm 1.6$	$\pm 1.8$	$\pm 2.3$	$\pm 1.7$	$\pm 1.6$

The  $D_{50}$  values of  $50\ \mu\text{m}$  for PEEK 330 PF and  $50.75\ \mu\text{m}$  for PEEK 550 PF obtained, agree with the commercial datasheet. The result of PEEK 2000 FP is 32 % higher than the value given by Evonik. The EOS reports the average grain size as  $60\ \mu\text{m}$  for HP3, it is 23 % lower than the value from obtained results. It must be emphasised that our PEEK HP3 is the powder after the SLS cycle, then it is considered as recycled powder. This difference could stem from the increase of particle size with the manufacturing cycle, comparable to our observation for PA12 powders.

The PEEK 450 G is provided in pellets, for this project, it was milled to size  $250\ \mu\text{m}$  and provided by the company Micronis, what is confirmed with a result of  $271.6\ \mu\text{m}$  for the average particle size.

In the case of PEEK 880 SPF, the results are twice higher than the one given by the commercial datasheet, which is  $30\ \mu\text{m}$ . This result was obtained in water. For comparison, the powders were dispersed in ethanol and sonicated in a bath. The results are only significant for PEEK 880 SFP and they are presented in Figure 2.13. It probably comes from a poor deagglomeration of very small particles in the water medium. Moreover, small size powders are very light so it floats on the surface of the water during the measurement. On the contrary, the particles with a size bigger than  $50\ \mu\text{m}$  are well desagglomerated and do not float in the water medium.

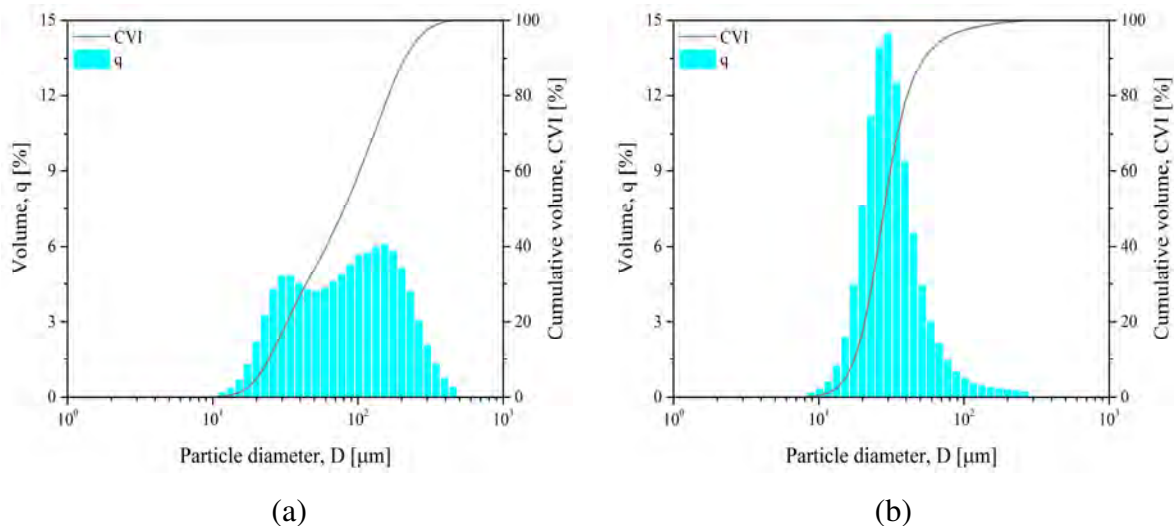


**Figure 2.13. The PSD by laser granulometry for PEEK 880 SFP at (a) water (b) ethanol**

Wide and bimodal distribution of particles is observed when water was used as a media, with a part of its distribution of average size around  $142\ \mu\text{m}$  and another around  $32\ \mu\text{m}$ . In contrary, for the measurements made in ethanol, a narrow peak is obtained, which perfectly fits the commercial data of  $30\ \mu\text{m}$ . Ethanol and water give different results, especially for PEEK 880 SPF. An explanation is a solvent-particle interaction: polymeric particles have more

affinity with ethanol than water. Indeed, the relative polarity of ethanol is 0.654 [175] over 1 for water. Polymers such as PEEK and PA contains some polar groups: amide, carbonyl (ketone) and ether groups, but also non-polar aliphatic chains and aromatic groups. So, the polymeric particles stay aggregated in water to minimize the solvent-particle contact surface, resulting in higher apparent diameters.

In Table 2.5, the diameters  $D_{10}$ ,  $D_{50}$  and  $D_{90}$  measured in ethanol for PEEK powder are presented. PA12 powder was not measured in ethanol. The  $D_{50}$  of PEEK HP3 in ethanol is closer to the commercial value of 60  $\mu\text{m}$  than the one obtained in the water of 78  $\mu\text{m}$ .

**Table 2.5. The particle size distributions by laser granulometry in ethanol**

Powder	PEEK 330 PF	PEEK 550 PF	PEEK 2000 FP	PEEK 880 SFP	PEEK 450 G	PEEK HP3
$D_{10}$ [ $\mu\text{m}$ ]	24.8	23.7	27.0	17.6	165.7	36.6
$D_{50}$ [ $\mu\text{m}$ ]	45.5	61.6	67.2	28.2	298.0	58.2
$D_{90}$ [ $\mu\text{m}$ ]	76.2	132.0	144.5	53.3	480.7	91.9
Uncertainty [ $\mu\text{m}$ ]	$\pm 1.7$	$\pm 2.1$	$\pm 2.0$	$\pm 1.6$	$\pm 1.5$	$\pm 1.5$

Figure 2.14 presents the particle size distribution by laser granulometry in water, except for PEEK 880 SFP, for which the value in ethanol was taken.

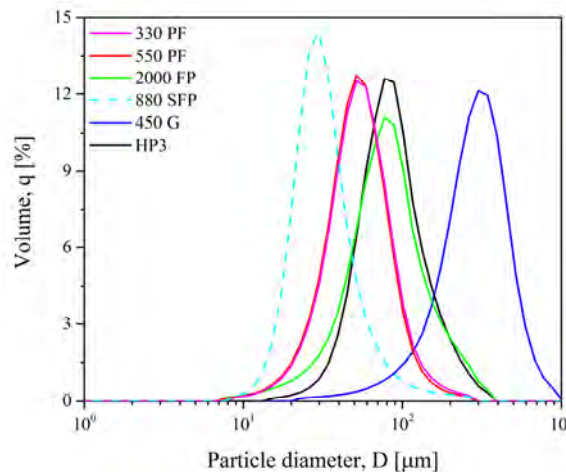


**Figure 2.14. The PSD by laser granulometry (solid line - water, dash line - ethanol)**

The PEEK HP3 is the only powder suitable for the SLS process, it is investigated as a reference to compare with other powders. Figure 2.14 shows that the particle size for PEEK HP3 is around 80  $\mu\text{m}$ . The closest one to this value is PEEK 2000 FP, approximately covering the same diameter range. However, PEEK HP3 shows a higher content of particles having a diameter in the 68-89  $\mu\text{m}$  range. Berretta [176] reports that PEEK HP3 has been found

in the 37.5-63.0  $\mu\text{m}$  range, which is close to data given by the supplier. The PEEK 330 PF and PEEK 550 PF curves are slightly shifted to the left (peak in the 45-59  $\mu\text{m}$  range), indicating the presence of particles with smaller diameters than HP3. The particle size of PEEK 880 SFP is away from other PEEK powders and its peak is in the 26-34  $\mu\text{m}$  range. The diameters of PEEK 450 G are too large (peak of 266-344  $\mu\text{m}$  range) and not suitable for the selective laser sintering process.

To sum up this part, the results of image analysis and laser granulometry in water and ethanol of particle size distribution are presented below:

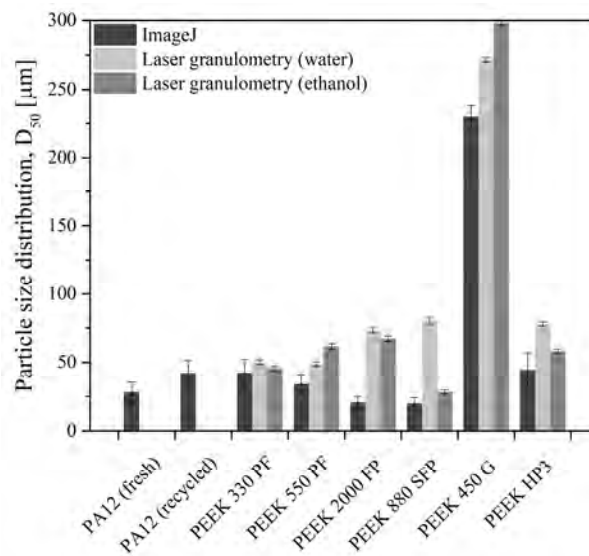


Figure 2.15. Particles size distribution comparison for  $D_{50}$  of PA and PEEK powders

First of all, it can be seen that the measurement error is much greater in the case of image analysis. Nevertheless, the results are comparable, the biggest difference occurs for PEEK 2000 FP and PEEK 880 SFP. As mentioned earlier, the laser granulometry measurement in water and ethanol media does not show major changes except for PEEK 880 SFP.

### 2.2.3. Conclusion on the morphology of powder particles

To conclude, PEEK 2000 FP has been found as the most suitable among the characterized polymer powders for the selective laser sintering process. It is described with the circularity level of  $0.45 \pm 0.18$  and the ratio shape of  $1.68 \pm 0.60$ , the closest values to the expected value of 1. Its average particle size distribution of  $80.2 \pm 2.3 \mu\text{m}$  perfectly fits in the expected range of 10-150  $\mu\text{m}$  [108] for the selective laser sintering process.

Particles of size equal to or less than 10  $\mu\text{m}$  have to be avoided because they are considered to be difficult to spread and separate, especially at high temperatures due to their high interparticular friction [108].



## 2.3. Flowability of powders

It has been specified in the previous chapter that the necessary condition for using powders in the framework of selective laser sintering process is to be able to form layers of compactness and homogeneous thickness of approximately 100  $\mu\text{m}$  to 200  $\mu\text{m}$  [108].

During the selective laser sintering process, the step of loading the powder into the machine, as well as, the spreading phase require the use of powder having good flow properties. Moreover, the density of powder bed before laser passes through plays an important role in the final properties of sintered parts. Thus, it is important to characterize the bulk and tapped density of powders and their behaviour during the flow.

The measurement of powder flowability was carried out by two categories: angular measurement and settlement measurement. The principles and procedures for flowability of powders are described in Annex A.2.2. These methods are considered as the closest to the machine spreading conditions. They were only carried out at ambient temperature; however, it is known that the flowability changes with the temperature.

### 2.3.1. Angular measurements

The first method chosen to compare the flowability of powders was the angle of repose also named as the angle of slide slope. The test was performed three times to be able to measure the average angle of repose for each type of powder. The results presented in Table 2.6 are as follows:

**Table 2.6. Angle of repose for the different powders**

Powder	PA12 (fresh)	PA12 (recycled)	PEEK 330 PF	PEEK 550 PF	PEEK 2000 FP	PEEK 880 SFP	PEEK 450 G	PEEK HP3
Angle of repose [°]	33.6	34.7	49.7	53.3	49.4	48.6	38.1	38.3
Standard deviation	2.0	1.1	1.0	0.4	3.2	2.4	0.3	2.3

Although there is some variation in the qualitative description of powder flow using the angle of repose, much of the literature appears to be consistent with the classification by Carr [177], shown in Table 2.7. When the angle of repose is in the range of 25° to 40°, the powder is well suited for SLS manufacturing, but when the angle exceeds 40° the flow is rarely acceptable for laser sintering purposes. It means the powder cannot be spread properly in the building chamber.



**Table 2.7. Flow properties and corresponding angles of repose [177]**

Flow property	Angle of repose [°]
Excellent	25-30
Good	31-35
Fair - aid not needed	36-40
Passable - may hang up	41-45
Poor - must agitate	46-55
Very poor	56-65
Very, very poor	>66

Duraform PA12 presents the smallest values of angle of repose of 33.6° indicating a good flow performance. The polyamide 12 powders (fresh and recycled) are very distinct from the other powders in terms of its flowability. This is not surprising, as PA12 has been already optimized for the selective laser sintering process. Dumoulin [3] obtained a maximum angle of repose for Primepart PA12 of 32°, and the PEKK powders he studied are in the range between 45-61°, indicating poor or very poor flow. A dynamic angle of rotation, which is especially the method that comes the closest to the mechanical action performed during the layering of powder bed in the SLS machine was also reported [3]. During layering, a roller pushes a pile of powder that forms and collapses successively to form a layer under it. This method also confirms the results obtained by Dumoulin, the angle of rapture (when the particles slide down) for Primepart PA12 is 33° and for PEEK powders is in the range of 43-68°.

The angle of repose of PEEK HP3, currently used in SLS manufacturing, was found to increase slightly to 38.3°, indicating a fair flow performance. The same level of angle has been achieved for PEEK 450 G of 38.1°. The PEEK 450 G demonstrate a better flow because of the bigger size of particles and therefore their higher weight. The above Table 2.6 shows that measurements of the angle of repose give poor flow level for PEEK 330 PF, PEEK 550 PF, PEEK 2000 FP and PEEK 880 SFP powders, which are in the range of 46-55°. Berretta [176] reports the angle of repose for PEEK HP3 as 42.4°, which allows broadening the values of angle of repose still leading to good flow behaviour.

The measurement of the angle of repose allows distinguishing three different behaviours as good flow, fair flow and poor flow. The PA12 powder is very different from the other powders in terms of flow properties, as well as, PEEK HP3. They both have the lowest angles of repose and therefore the best flowability. These measurements are supplemented by measurements of powder density and deposition ability.

### 2.3.2. Aptitude for settlement

The ability of a granular medium to reduce its volume, and thus to increase its density or compactness, is directly related to the way the particles can be interwoven with each other. The mechanical resistance of this medium is directly related to interparticle forces. The higher these forces are, the more they are opposed to the rearrangement and the more the system needs to supply energy. These indices quantify the capacity of powder to densify and they are consequences of properties such as bulk and tapped density. The Carr index is sometimes called “index of flowability” or “compressibility index”. The Carr index is defined as a difference between the tapped density to the bulk density to the tapped density. As for the Hausner ratio defined as the ratio of the tapped density to the bulk density, it gives an account of state for interparticle friction. The closer it is to 1, the better the flowability. The results of the tests are shown in Table 2.8.

**Table 2.8. Carr and Hausner indices of different powders**

Powder	PA12 (fresh)	PA12 (recycled)	PEEK 330 PF	PEEK 550 PF	PEEK 2000 FP	PEEK 880 SFP	PEEK 450 G	PEEK HP3
Bulk density [g.cm <sup>-3</sup> ]	0.518	0.570	0.360	0.227	0.274	0.291	0.553	0.368
Standard deviation	0.005	0.050	0.006	0.004	0.002	0.000	0.004	0.000
Tapped density [g.cm <sup>-3</sup> ]	0.636	0.630	0.546	0.343	0.401	0.472	0.713	0.584
Standard deviation	0.014	0.020	0.035	0.003	0.019	0.040	0.007	0.005
Carr Index [%]	19	10	34	34	32	38	22	37
Uncertainty	± 5 %							
Hausner Ratio [-]	1.23	1.11	1.52	1.51	1.46	1.62	1.29	1.59
Uncertainty	± 0.05							

The results obtained for the bulk and tapped density are in continuity with those previously found. In all powders, the tapped density is always higher than the bulk one. This result is expected as a powder should pack more closely together when it has been put under some force.

The rate of consolidation is sometimes measured in addition to the change in volume that occurs on tapping. For the indicators of Carr index and the Hausner ratio, the generally accepted scale of flowability is given in Table 2.9, as the classification proposed by Carr [177].

**Table 2.9. Scale of flowability [177]**

Flow character	Compressibility index [%]	Hausner ratio [-]
Excellent	≤10	1.00-1.11
Good	11-15	1.12-1.18
Fair	16-20	1.19-1.25
Passable	21-25	1.26-1.34
Poor	26-31	1.35-1.45
Very poor	32-37	1.46-1.59
Very, very poor	>38	>1.60

Two different behaviours emerged: the first one is a low Carr and Hausner indices for the fresh PA12 powder of 19 % and 1.23, respectively, indicating fair flow character. These results agree with those reported by Dumoulin [3] for fresh PA12 with Carr index of 9.2 % and the same Hausner ratio. The recycled PA12 is indicating with good flow for Carr index of 10 % and Hausner ratio of 1.11. In our case, the bulk density increases when the PA12 powder is submitted to one manufacturing cycle. According to the literature [178,179], the bulk density decreases for recycled polyamide powders. However, Bajric [178] reports that the Hausner ratio does not change significantly, while Wudy and Drummer [179] observed that the bulk density decreases with rising heating time, whereby the Hausner ratio shows an inverse trend. A consequence of lower bulk density will be a reduced specimen density. The rise of Hausner ratio goes along with reduced powder flowability. Both mechanisms might influence the density of the sintered parts because of the presence of porosity, and then, their mechanical properties. In this work, the higher bulk density for recycled PA12 can be explained by getting better sphericity remarked in a change of particle surface or higher measuring error of 0.05 g.cm<sup>-3</sup> compared to other powders with a standard deviation of 0.005 g.cm<sup>-3</sup>.

The second behaviour leads to high indices for all PEEK powders (except PEEK 450 G) with Carr index in the range of 32-37 % indicating very poor flow character, even for recycled HP3. PEEK 450 G has a Carr index of 22 % indicating passable flow, which can be the result of a bigger size of particles and therefore higher particles weight.

Dupin [1] reported that sphericity plays a more important role in the bulk density than the particle size distribution, by reducing the interparticular friction and thus facilitating the rearrangement of grains. In this case, it can be observed that the circularity of 0.45 for PEEK 2000 PF decrease the angle of repose, but the opposite is seen for PEEK 880 SFP with

a similar circularity of 0.42. While, the size distribution is around 70  $\mu\text{m}$  and 30  $\mu\text{m}$ , respectively. It means that the flowability might also depend on the particle size distribution. A larger number of fine particles tends to decrease flowability. It can be also observed that the energy stored before each angle of the rapture is lower in the case of powder flowing well compared to powder flowing with difficulty [1]. This leads to decreasing the entropy variations of the system and leads to more continuous and less chaotic phenomena.

To sum up this part, the results of two categories of measurements of powders flowability are presented below:

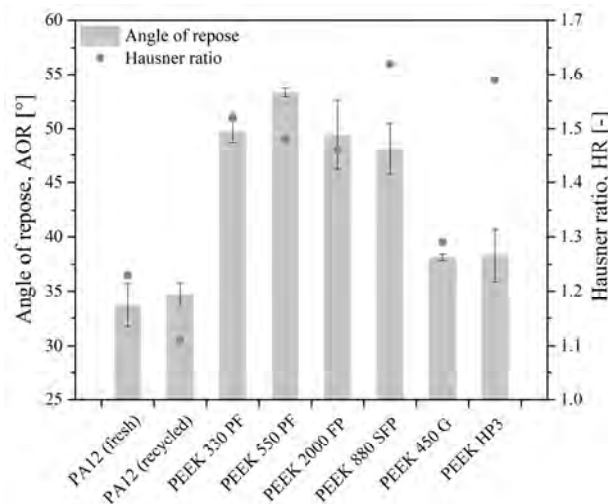


**Figure 2.16. Flowability of powders**

The expected values for an optimized powder are: for the angle of repose is under 40° and less than 1.25 for the Hausner ratio [177]. Figure 2.16 shows that PA12 is the most suitable material for the SLS process with the angle of repose of 33.6° and Hausner ratio of 1.23. In the case of polyetheretherketone powders, the suitable ones would be PEEK 450 G (despite its size distribution) and PEEK HP3. From the group of tested polyetheretherketone powders, the PEEK 2000 FP can be distinguished with the angle of repose 49.4° and Hausner ratio of 1.49, which are the closest to the expected one. However, the reduction of powder flowability may presumably affect the process stability and reproducibility negatively.

### 2.3.3. Packing fraction

The packing fraction is another parameter that indicates how well a powder material can compact. In other words, occupying the smallest volume with the highest number of particles. When this value is small (it tends to zero), it indicates that material has poor packing behaviour with many voids within the unit volume.

In the case of non-deformable spherical particles, the spheres organize in three different manners, as seen in Figure 2.17 below. Gauss [180] proved that the highest packing density for spherical particles amongst all possible lattice packing is around 0.74048.

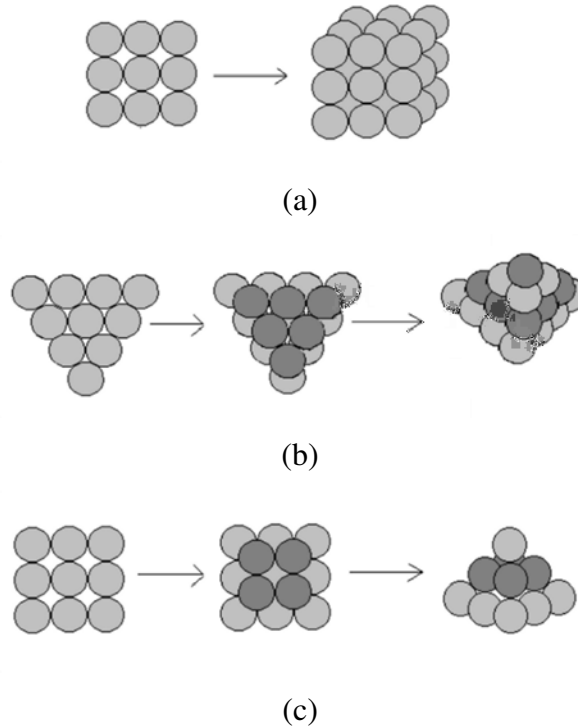


**Figure 2.17. Cell aggregation and sphere packing (a) simple cubic (b) face-centred cubic (c) hexagonal**

Thus, when the packing fraction is close to 0.74048 the material has good packing properties with a large number of particles occupying the unit volume. This parameter represents a key property in the selective laser sintering process where a good degree of compaction in the powder bed is necessary for creating fully dense parts. The packing fraction has been calculated according to the following equation:

$$\Phi = \frac{\rho_{\text{bulk}}}{\rho_{\text{true}}} \quad (2.1)$$

where:

- $\Phi$  - packing fraction [-];
- $\rho_{\text{bulk}}$  - bulk density [ $\text{g}\cdot\text{cm}^{-3}$ ];
- $\rho_{\text{true}}$  - true density [ $\text{g}\cdot\text{cm}^{-3}$ ].

with:

- $\rho_{\text{true}} = 1.095 \text{ g}\cdot\text{cm}^{-3}$  for PA12
- $\rho_{\text{true}} = 1.320 \text{ g}\cdot\text{cm}^{-3}$  for PEEK

The results of packing fraction for our polymeric powders are presented in Table 2.10 below:

**Table 2.10. Packing fraction for the different powders**

Powder	PA12 (fresh)	PA12 (recycled)	PEEK 330 PF	PEEK 550 PF	PEEK 2000 FP	PEEK 880 SFP	PEEK 450 G	PEEK HP3
Fraction packing [-]	0.473	0.521	0.273	0.172	0.208	0.221	0.419	0.279
Standard deviation	0.003	0.030	0.003	0.002	0.001	0.000	0.002	0.000

Our particles have non-spherical shape, as calculated by the shape ratio comprised between 1.65 and 2.03 (it equals to 1 for a perfect sphere). Nevertheless, the packing fraction may bring a qualitative comparison of the final density of the parts. Moreover, the density measurements have been done at room temperature for technical reasons, and it is known that the density changes with temperature.

The best packing fraction is observed for fresh PA12 with 0.473. When comparing fresh and recycled PA12 powder, the packing fraction increases: it is shifted to 0.521 for recycled PA12. These results are presumably due to the increase of the particle size, as seen for  $D_{90}$ , initially 76.1  $\mu\text{m}$  it goes to 110.5  $\mu\text{m}$  for recycled PA12. The highest value is obtained for PEEK 450 G of 0.419. The PEEK HP3 has a low packing fraction of 0.279. It can be assumed that during the process, particles are randomly added to the work chamber and they are compressed by the roller. They generally form what is known as an “irregular” or “jammed” packing configuration when they cannot be more compressed. This irregular packing generally has a density of less than 0.634 [181]. In the work of Berretta, the packing fraction of particle for polyetheretherketone powder thermally conditioned is 0.29 [176]. Nevertheless, she did not give the conditioning temperature.

#### 2.3.4. Modification of flowability of PEEK powders

Nowadays, the powders constitute about 75 % of raw materials that are used in the industry [56]. It is described that their main interest is their high surface to volume ratio. Thus, modifying the surface properties of polymeric materials is a great scientific and industrial challenge [182]. Surface modification such as coating usually should be thin to affect only the topmost layer of the surface. Indeed, too thick layer can lead to delamination caused by lack of adhesion of the coating to the particle surface, and so undesirably alter the bulk properties which. On the other side, overly thin layers can be eroded. Considering these requirements, there are several ways to tune the surface properties of polymeric materials to enhance their

functionality [183]. The main groups are chemical treatment, physical treatment and coating of another material.

As seen below, most of the studied powder has low flowability. That is why some attempts have been done to improve their flowability. The flowability is linked to several parameters such as Carr index, Hausner ratio and angle of repose, but the first ones we consider are the shape ratio and the interparticular forces. For metallic particles, plasma treatment at high temperature gives very nice results to improve the sphericity, as seen in Figure 2.18. For instance, the thermal plasma system at a temperature of around 3025 °C and nitrogen atmosphere can treat titanium powder. Once the plasma is stable, the as-received powder is fed near the tail flame operated by the plasma torch at 150 A and 200 V with a rate of 5 g.min<sup>-1</sup> [184].

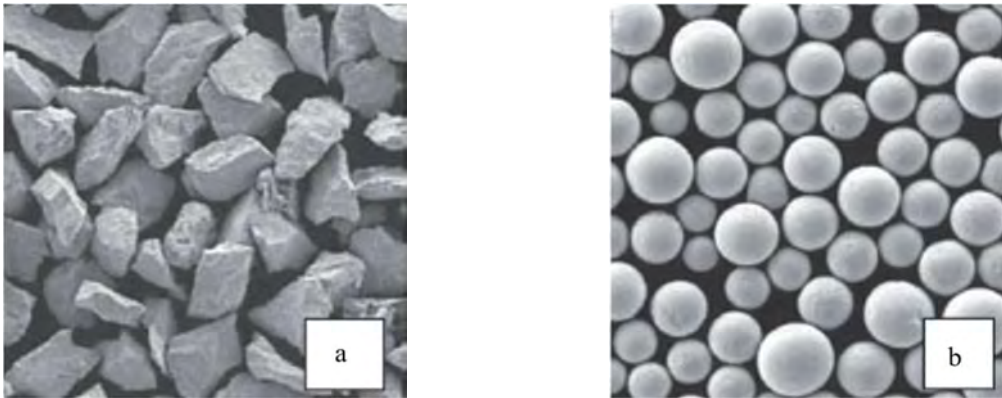


**Figure 2.18.** The SEM images of titanium powder (a) before (b) after plasma treatment [184]

Unfortunately, it is not possible to apply such plasma treatment to polymers, due to their heat sensitivity (they would degrade) and their high melt viscosity (the polymeric particle keep its shape unless a shear is applied).

So, other methods have been tested to change the morphology and surface tension of powders, to achieve greater sphericity and smoothness. Polymer particles were modified by chemical treatment to partially dissolve or swell the surface of them. Besides, nano and microsize materials have been added to improve their flow performance.

As expected, the impact of solvent on the flowability is quite insignificant. According to Cogswell [185] toluene, acetone and ethanol do not have a significant effect on PEEK powders even after seven days of exposure at 23 °C.

The tribological properties of a polymeric material can be tailored by the addition of nano or microparticles, small moieties, oligomers, and by grafting other polymers or copolymers onto the surface. Likewise, in bulk materials, adding small particles in a powder made of bigger

particles could reduce friction and so, improve flowability. The incorporation of nanosilica inside commercial PA12 powder for SLS has been attested by Dupin [1].

The tribological properties are greatly influenced by the chemical structure of the particles. Hexagonal boron nitride (h-BN) presents a layered structure, in which BN nanosheets, corresponding to a hexagonal network consisting of an alternation of boron and nitrogen atoms covalently bonded, are stacked together thanks to van der Waals interactions in such a way that in neighbouring sheets, atoms follow this sequence BNB... on top of each other. Due to this structure, hexagonal boron nitride demonstrates a low friction coefficient and it is used as a solid lubricant [186]. This material has been widely studied at LGP-ENIT [187] that is why we have chosen it.

Like the previous results of the solvent impact, a slight increasing in bulk and tapped densities has been observed, which can be also an influence of ethanol used in the protocol on the surface of PEEK powder. The calculation of Carr index and Hausner ratio has changed for nanosilver particles and indicate the flow behaviour as “poor” instead of “very poor”. The angle of repose is modified as well, where the flow behaviour is shifted from “poor” to “passable” in the case of boron nitride, and “fair” for microsilver particles.

### **2.3.5. Conclusion on the flowability of powders**

In the group of polyetheretherketone powders, the PEEK 2000 FP can be distinguished with the angle of repose  $49.4^\circ$  and Hausner ratio of 1.49, which are the closest to the expected values. The most compact powders are polyamide 12 and PEEK 450 G which may be due to its bigger size compared to other polyetheretherketones.

The incorporation of nano and microparticles is a promising way to improve the flowability of powders. The best results have been obtained with nanosilver particles, this powder flows with a “fair” or “poor” behaviour, indicated by an angle of repose at  $35.7^\circ$  and Hausner ratio of 1.45, respectively. To sum up, the surface treatments that we have performed until now have not enough improved the flowability to fit the requirements of the selective laser sintering process for this moment. The principle is promising, nevertheless, it requires further trials.



## 2.4. Thermal properties of powders

Printing thermoplastics by the selective laser sintering process involves a complex thermal cycle. The polymer powder is first placed in a supply tank where it is heated to avoid a thermal shock when depositing the powder bed in the manufacturing tank. The powder is then spread out in the manufacturing tank where it is brought close to its melting temperature, generally 30 °C below its melting point. The thermoplastic may then be brought to its melting point “very rapidly” during the passage of the laser beam and then cooled “slowly” in the manufacturing tank. To evaluate the heating speed instead of the term “very rapidly”, the study made by Villar Montoya [188] is worth to be cited: the temperature at the surface of a PEKK specimen has been measured by infrared thermography when a laser beam with a wavelength of 808 nm goes through. The heating speed is 600 °C.min<sup>-1</sup>. Even if the conditions are different (wavelength, material, laser speed and power), it gives an idea of the heating speed underwent by the powder.

It is necessary to get a deep knowledge of the thermal properties of the powders to explain the behaviour of the powder all along the manufacturing cycle and to choose the process parameters to get the best properties of the printed parts.

Therefore, differential scanning calorimetry was selected to measure glass transition range, melting or crystallization temperatures and enthalpies. Concerning the thermal stability of powders, the thermogravimetric analysis was chosen. Finally, for measurements of thermal conductivity and heat capacity, the hot disk was selected, by coupling with the X-ray tomography to measure the compaction of the powders. All these techniques are described in Annex A.2.4.

### 2.4.1. Thermal transitions

The differential scanning calorimetry is a thermal analysis technique that measures the differences in heat exchange between a sample to be analysed and referenced. It makes it possible to determine transitions such as glass transition temperature of the amorphous phase in thermoplastics, crystallization, melting and recrystallization ranges. The enthalpies of fusion and crystallization are also determined. In the SLS process, it is important because they are directly related to the energy the laser may have to provide to melt the particles. Indeed, the powder is kept in the building chamber at a temperature just below the starting of melting.

Polymeric materials have a microstructural state specific to the way they have been transformed, called the “thermomechanical history”. It means that one polymer may have

various microstructural states depending on the thermomechanical stresses undergone. In the case of semi-crystalline thermoplastics, the crystalline morphology and the degree of crystallinity are fixed during their processing.

First of all, the DSC runs were carried out under a nitrogen sweep, the polymer is heated at a rate of  $10\text{ }^{\circ}\text{C}\cdot\text{min}^{-1}$  from room temperature until complete melting, next it is cooled at a rate of  $10\text{ }^{\circ}\text{C}\cdot\text{min}^{-1}$  until room temperature. This cycle is representative of the cycle underwent by the powder, except in terms of heating and cooling speed.

The purpose of these analyses is to provide the information required to predict the processing temperature. Also, the sintering window of polyamide and polyetheretherketone powders will be deduced from the results. PA12 and PEEK HP3 were used as comparative materials.

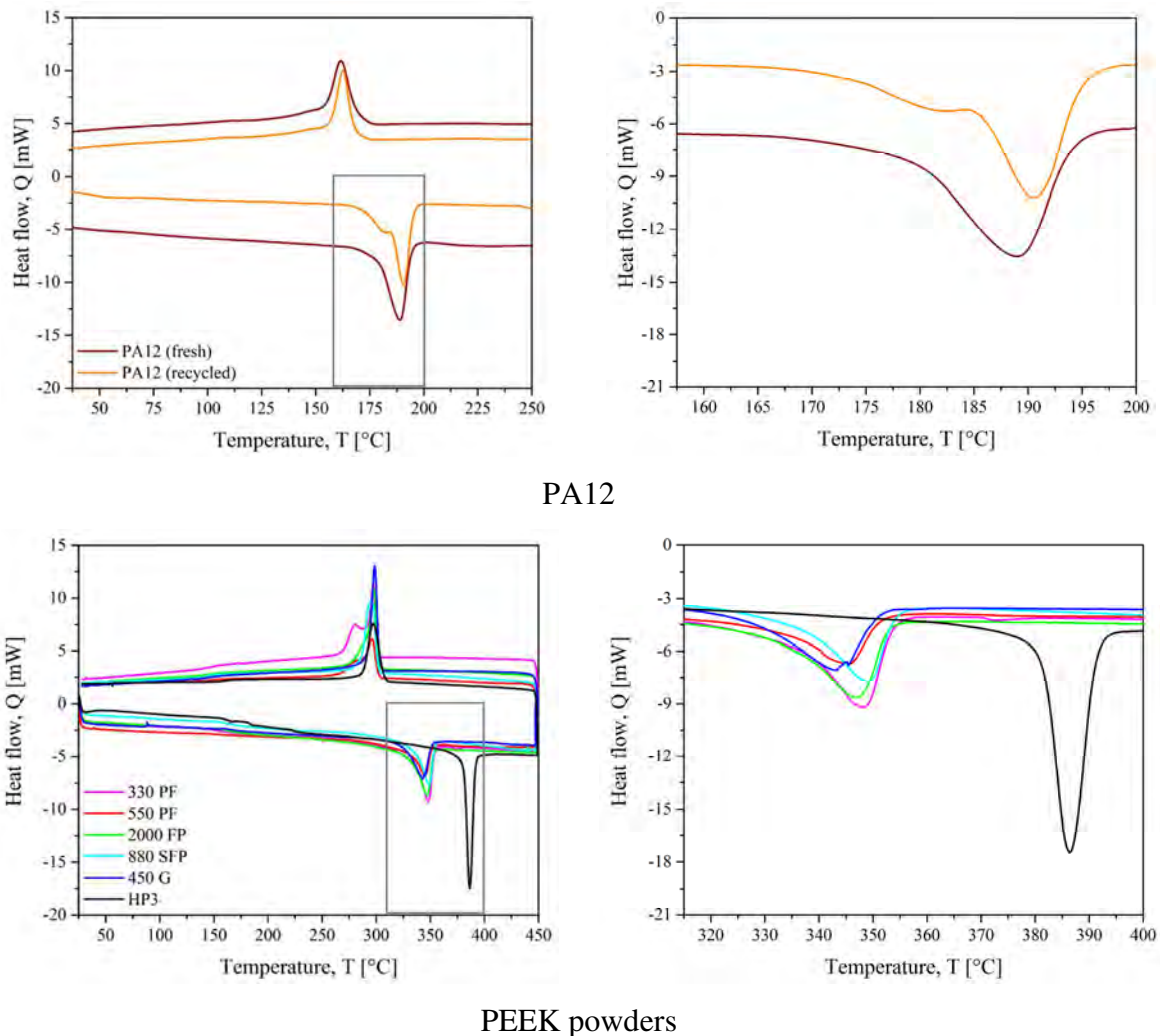


Figure 2.19. The DSC thermogram obtained at  $10\text{ }^{\circ}\text{C}\cdot\text{min}^{-1}$

Typical thermograms obtained for PA12 and PEEK powders are shown in Figure 2.19. As observed, the polymer powders show sharp and clear melting and crystallization peaks. The

melting peaks occur at 189 °C and 191 °C for fresh and recycled PA12, respectively. The crystallization temperature is observed at around 162 °C for both polyamide powders. In the case of PEEK powders, the melting point occurs between 345 °C and 349 °C, besides PEEK HP3 which is 386 °C. While the crystallization peaks are in the range of 396 °C to 300 °C for all polyetheretherketone powders. The PEEK HP3 is the only one with a higher melting temperature.

The mass fraction of the crystalline phase is calculated from the melting enthalpy measured by differential scanning calorimetry and the theoretical melting enthalpy of 100 % crystalline phase with the following formula:

$$X_c = \frac{\Delta H_m}{\Delta H_{th}} \times 100 \% \quad (2.2)$$

where:

- $X_c$  - degrees of crystallinity [%];
- $\Delta H_m$  - melting enthalpy [J.g<sup>-1</sup>];
- $\Delta H_{th}$  - theoretical melting enthalpy of 100 % crystalline phase [J.g<sup>-1</sup>].

with:

- $\Delta H_{th}$  = 209.3 J.g<sup>-1</sup> for PA12 of 100 % crystalline phase [64];
- = 130.0 J.g<sup>-1</sup> for PEEK of 100% crystalline phase [189].

These two values are the most commonly accepted because they are representative of crystalline forms the most frequently encountered in the case of these two polymers. The results of melting and crystallization temperatures in the onset point, as well as, melting enthalpy and degrees of crystallinity, are shown in Table 2.11.

No significant temperature shifts and enthalpy change seems to occur between fresh and recycled polyamide 12, providing a further indication of high recyclability of this material. The degree of crystallinity in the recycled PA12 powder showed a slight decreasing. It can be noticed that polyamide 12 presents higher melting enthalpy than polyetheretherketones over 30 %. This is due to their chemical structure: the structure of polyetheretherketone is made of aromatic groups, ketones and ethers, they provide rigidity to the macromolecular chain, thus preventing the chain to move to self-organize into crystallites. On the contrary, the chain of polyamide 12 is more flexible with possible rotation under simple C-C bonds along the aliphatic chain.

**Table 2.11. The DSC results for PA and PEEK powders**

Powder	Melting		Crystallization		$\Delta H_m$ [J.g <sup>-1</sup> ]	$X_c$ [%]
	temperature		temperature			
	$T_{onset}$ [°C]	$T_{max}$ [°C]	$T_{onset}$ [°C]	$T_{max}$ [°C]		
PA12 (fresh)	178.21	188.96	169.27	161.64	49.31	23.56
PA12 (recycled)	183.91	190.56	167.69	162.74	47.48	22.69
PEEK 330 PF	335.26	348.38	301.03	297.35	32.43	24.95
PEEK 550 PF	333.47	345.48	301.63	295.94	33.80	26.00
PEEK 2000 FP	333.76	346.99	302.21	297.86	32.64	25.11
PEEK 880 SFP	335.83	349.02	301.32	295.51	31.93	24.56
PEEK 450 G	323.60	342.17	304.34	300.18	35.37	27.21
PEEK HP3	381.39	386.36	309.80	297.29	51.35	39.50
Uncertainty			± 1 %		± 5 %	

The degree of crystallinity is almost identical for fresh and recycled PA12 of 23.6 % and 22.7 %, respectively. Interestingly, Dupin [1] reports for Primepart PA12 the degree of crystallization 52.4 % considering the first DSC heating ramp and 24.4 % for the second one. He explains this results by changing in crystalline structure from unknown form to  $\gamma$  crystalline form. Similarly, Dumoulin [3] obtained 49 % for Primepart PA12 for the first heating ramp.

Taking into consideration PEEK powders, the melting and crystallization occur in the same range: between 324 °C and 336 °C for melting onset temperature and from 301 °C to 304 °C for crystallization onset temperature. Among polyetheretherketone powders, the exception is PEEK HP3 which has a melting enthalpy of 51.3 J.g<sup>-1</sup> compared from 32 J.g<sup>-1</sup> to 35 J.g<sup>-1</sup> for other PEEK grades. Unlike other powders, PEEK HP3 has a much higher melting point at 386 °C and crystallization at temperatures of 310 °C. The degrees of crystallinity for all PEEK powders are very similar and in the range of 24 % to 27 %, besides PEEK HP3 at 39 %. Interestingly, Ghita et al. [190] report for recycled HP3 a higher crystallinity of 52.1 %. Also, she measured crystallization onset, melting onset and melting point at around 315 °C, 375 °C and 397 °C, respectively. In our study, we measured similar results: the onset temperatures and melting point at 310 °C, 381 °C and 386 °C, respectively.

The sintering window is a selective laser sintering processing window, which is defined as the difference between the melting and crystallization onset temperatures. The processing window can be calculated with Equation 2.3.

$$\Delta T = (T_m - T_c)_{\text{onset}} \quad (2.3)$$

where:

- $\Delta T$  - range of temperature for sintering window [°C];
- $T_m$  - melt temperature onset [°C];
- $T_c$  - crystallization temperature onset [°C].

It is necessary to have a temperature range as wide as possible to facilitate the processing inside the selective laser sintering system for successful manufacturing. A large temperature range enables the powder to be spread out in the powder bed without melting before laser exposure and to avoid crystallization during laser exposure or just after. The results are presented in Figure 2.20.

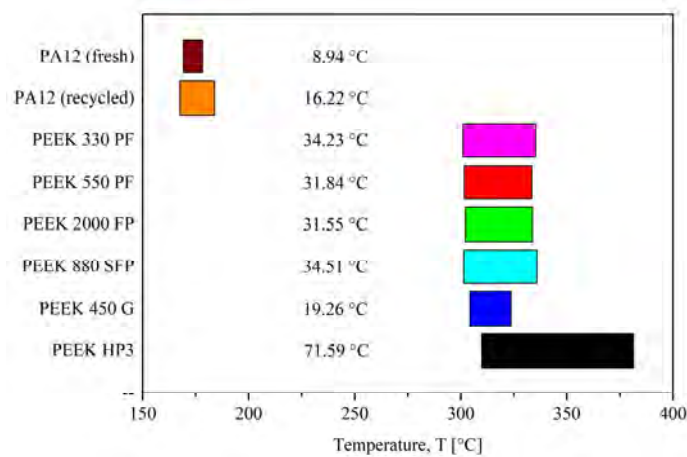


**Figure 2.20. Sintering windows of PA12 and PEEK powders**

For each material, the sintering window is displayed. Surprisingly, the narrowest processing window of 9 °C is obtained for fresh PA12. The recycled PA12 magnified the sintering window twice with 16 °C. The fresh and recycled PA12 also shows sharp and clear melting and crystallization peaks, as seen in Figure 2.19. These characteristics are well-known for thermoplastics suitable for the SLS process and they are considered to be the reason why polyamide 12 is successful in the SLS process. Bajric [178] has observed smaller changes in the sintering windows between fresh and recycled polyamide powders. Nevertheless, he reports a wider processing window  $20.7 \pm 0.2$  °C and  $19.5 \pm 0.4$  °C for fresh and recycled powders, respectively.

In the case of polyetheretherketones, the narrower sintering window is observed for PEEK 450 G and the widest for PEEK HP3, 19 °C and 72 °C, respectively. The other grades exhibit a processing window between 32 °C and 35 °C. Our results for polyetheretherketones

agree with the work of Dumoulin [3] who obtained sintering windows of 42 °C, 43 °C and 54 °C for his PAEK. In contrast, Berretta [176] reports that the sintering window cannot be defined for high-temperature polymers. The latter show fairly wide melting and crystallization regions that overlap. She proposed to use the sintering window as help to select a new low-temperature polymer based on material properties and offers the possibility to approximately estimate processing temperatures of new materials before a series of the trial-and-error building process.

The most interesting polyetheretherketone turned out to be PEEK HP3 from EOS because it is already used for selective laser sintering process and it is the only one available on the market. This powder has been tuned to fit the SLS requirements. From the previous DSC results, investigations to understand its chemical structure was done. To obtain more information, differential scanning calorimetry analysis has been applied to recycled powder and printed parts, both made of HP3 copolymer.

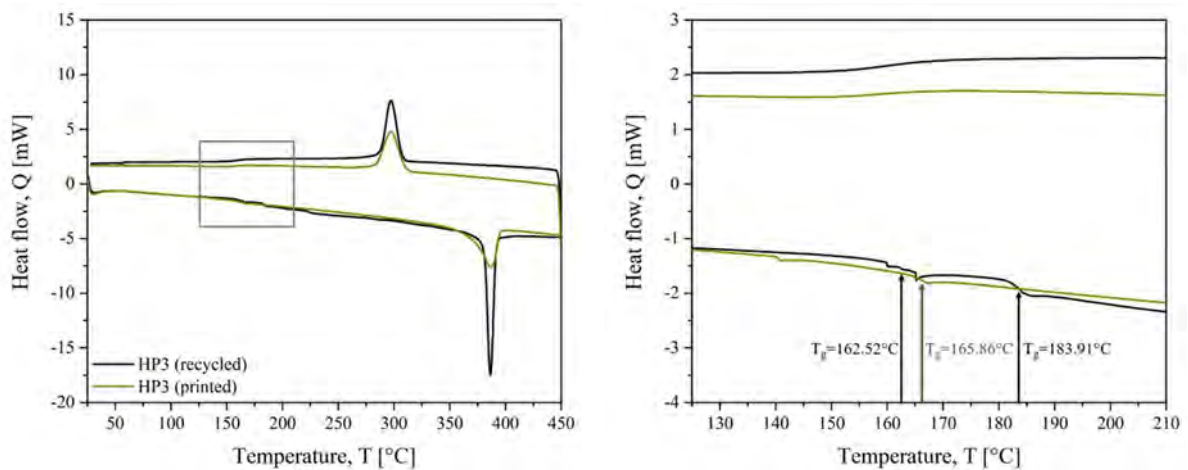


**Figure 2.21. The DSC thermogram obtained for PEEK HP3**

The thermograms in Figure 2.21 for recycled powder and printed part of PEEK HP3 are very similar, nevertheless, some differences are observed: the recycled powder shows sharp and clear peaks corresponding to melting and crystallization, whereas the peaks are smaller and wider for printed parts. This could be attributed to different crystalline forms.

The melting points are around 386 °C. Their crystallinity does not change significantly, 39.5 % for recycled HP3 and 38.1 % for printed HP3. A very interesting phenomenon was noted: in Figure 2.21 on the right, two different glass transition temperatures are visible. Several tests were repeated on recycled powder and printed part of PEEK HP3. The first glass transition temperature is observed between 160 °C and 170 °C, it is more intense for the printed part. The second one appears around 185 °C and mainly in the recycled powder. According to the

US 8420001 B2 patent [58] from 2013, HP3 is described as “copolymer PEK/PES preferably has a glass transition higher than 180 °C”. This is a confirmation of the composition of HP3: the glass transition at 160-170 °C corresponds to polyetherketone (PEK) and the one at 185 °C corresponds to polyethersulfone (PES).

The FTIR spectroscopy has been used to assess the chemical composition of HP3. The procedure is explained in Annex A.2.3. The spectra of PEEK 2000 FP and PEEK HP3 powders has been registered and compared, as seen in Figure 2.22.

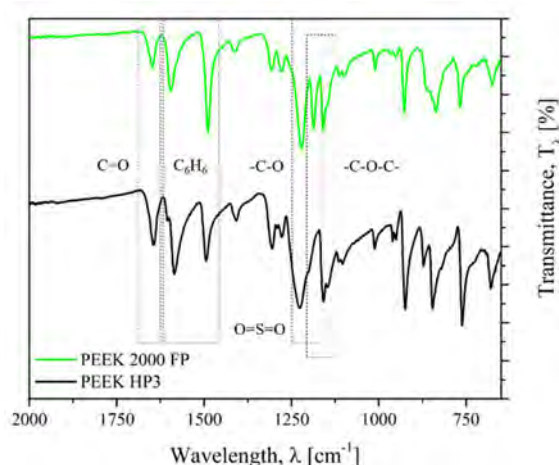


**Figure 2.22. The FTIR spectrum of PEEK 2000 FP and PEEK HP3**

For PEEK 2000 FP, a strong absorption band characteristic of carbonyl stretching bond is seen at 1650  $\text{cm}^{-1}$ , which is attributed to the aliphatic ketone. The peaks at 1620  $\text{cm}^{-1}$  and 1490  $\text{cm}^{-1}$  are characteristic of ring absorption, which identifies the sample as an aromatic thermoplastic. Next, the absorption band characteristic of the carbonyl stretching structure is seen at 1150  $\text{cm}^{-1}$ , which is attributed to aliphatic ether. Carbon-oxygen-carbon stretching is observed at 1130  $\text{cm}^{-1}$ . The peaks showed at around 900  $\text{cm}^{-1}$ , 860  $\text{cm}^{-1}$  and 750  $\text{cm}^{-1}$  are common to most aromatic thermoplastics. Similar results of FTIR spectra of amorphous polyetheretherketone were reported by Harris [191]. For PEEK HP3, a strong band characteristic of sulfones stretching is seen at 1240  $\text{cm}^{-1}$ .

Despite its composition, made of PEK and PES, we will continue to name it PEEK HP3 or HP3 copolymer. The material has been analysed by thermogravimetric analysis to evaluate its heat resistance. The test was carried out with a temperature ramp at 10  $^{\circ}\text{C}\cdot\text{min}^{-1}$  up to 850  $^{\circ}\text{C}$  under air.

The thermogravimetric plots show a two-step decomposition for PEEK HP3. In the first decomposition step, random chain scission of ether and ketone bonds is the main mechanism, with phenol being the predominant degradation product with smaller amounts of other



compounds like benzene and dibenzofuran. However, cleavage of the carbonyl bond will lead to radical intermediates that are more stable due to resonance effects and would be expected to predominate. The second decomposition stage, occurs slower volatilization of residue, with about 52 % to 55 % of residue remaining at 850 °C [101].

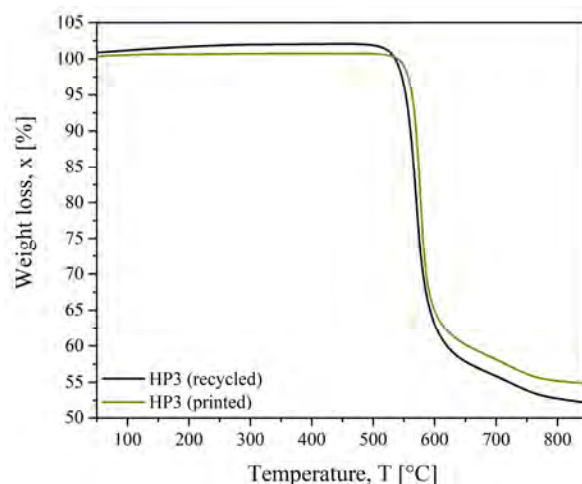


**Figure 2.23. The TGA thermogram obtained for PEEK HP3**

It is observed that the powder increases its weight of 2 % for recycled HP3 and 0.75 % for printed HP3 until 470 °C. This could be due to the oxidation mechanisms, which fix O<sub>2</sub> from the air onto the chemical structure of the polymer.

Later, the temperature when the copolymer starts its thermal decomposition is about  $538 \pm 2$  °C. Rapid and significant mass loss occurs just below 600 °C resulting in the volatilization of around 45 % of polymer weight, the remaining polymer weight appears to be carbonaceous char. Finally, it can be observed that the polyetheretherketone left a great amount of residue, more than 50 %. The similar results have been observed by Vasconcelos et al. for different PEEK [85]. They reported that polyetheretherketone in a slower process of volatilization under the nitrogen atmosphere has over 45 % of residue still present even at 1000 °C. Summarizing, our results on PEEK HP3 show a stable sintering region finishing at around 535 °C. Berreta [176] has reported that conditioned PEEK shows a stable sintering region starting at 380 °C and finishing at around 530 °C. This wide range of possible stable sintering temperatures is due to the high onset material degradation temperature, a known characteristic of polyetheretherketone materials.

The mechanical, shrinkage and degradation characteristics of PEEK HP3 has been examined by Ghita et al. [192]. The samples were manufactured along the X-axis, Y-axis and Z-axis of the EOSINT P 800 system. They report a higher shrinkage for samples built in the middle of the building chamber of the system and a drop of the tensile properties for samples



built along the Z direction. In a later work, Ghita et al. [190] studied fresh PEEK HP3 samples blended with recycled PEEK HP3 powder. Both powders and sintered specimens were analysed. The recycled powder shows a higher melting point at 397 °C and delayed crystallisation temperature at 294 °C, over 6 % and 13 %, respectively, compared to fresh powder. Interestingly, the specimens incorporating recycled PEEK HP3 powder (30/70 wt.% recycled/fresh PEEK HP3 powder) showed a drop of the tensile strength values of only 17 % from around 90 MPa to 75 MPa.

#### 2.4.2. Thermal conductivity and heat capacity

The thermal conductivity and heat capacity has been measured for PEEK 2000 FP powder. Low thermal conductivity is required in the selective laser sintering process to avoid undesired melting of particles surrounding a part under manufacturing and to guarantee a good separation between molten and solid phases [109].

The density of the powder may greatly influence the thermal properties, because of the presence of air. Indeed, the thermal conductivity of air is very low compared to those of thermoplastics. We know from the previous section that tapping powder results in increasing its density. So, we want to link the density to the thermal properties. The methodology is to prepare powder samples with the different compacting state, to measure the volume ratio of polymer/air in each by X-ray tomography and to measure the thermal properties by hot disk technique.

Thermography uses X-ray to create cross-sections of physical objects that are used to recreate a virtual model without destroying the original object. The X-ray tomography tests allow to obtain the percentage of air in specific density states such as apparent, tapped and pressed. Likewise, the tests carried out with the hot disk on PEEK 2000 FP powder allowed to get the thermal conductivity in each of these densities as well as the specific heat.

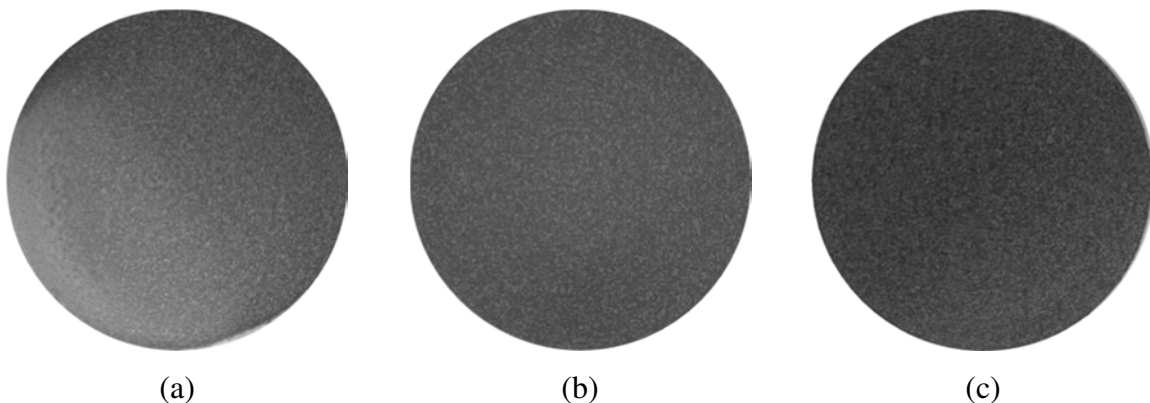


Figure 2.24. Images of X-ray tomography of (a) apparent (b) tapped (c) pressed density

The images obtained for the three samples of different densities are presented in Figure 2.24. The measurements of thermal conductivity of PEEK 2000 FP powder were combined with the results of volume fraction of air. The calculations were made assuming the temperature of 20 °C, the theoretical trend for the thermal conductivity was obtained by Equation 2.4 and the theoretical trend for density, by Equation 2.5.

$$\lambda = \lambda_{\text{air}}u_{\text{air}} + \lambda_{2000\text{FP}}u_{2000\text{FP}} \quad (2.4)$$

$$\rho = \rho_{\text{air}}u_{\text{air}} + \rho_{2000\text{FP}}u_{2000\text{FP}} \quad (2.5)$$

where:

- $\lambda$  - thermal conductivity [ $\text{W}\cdot\text{m}^{-1}\cdot\text{K}^{-1}$ ];
- $\rho$  - density [ $\text{kg}\cdot\text{m}^{-3}$ ];
- $u$  - fraction of air [%].

with:

- $\lambda_{\text{air}} = 0.025 \text{ W}\cdot\text{m}^{-1}\cdot\text{K}^{-1}$  [193];
- $\lambda_{2000\text{FP}} = 0.240 \text{ W}\cdot\text{m}^{-1}\cdot\text{K}^{-1}$ , measured by hot disc method in consolidated state;
- $\rho_{\text{air}} = 1225 \text{ kg}\cdot\text{m}^{-3}$  [193];
- $\rho_{2000\text{FP}} = 1300 \text{ kg}\cdot\text{m}^{-3}$  [Annex A.1.4].

The powder can be assimilated to a composite material composed of air and polymer, the thermal conductivity of air is  $0.025 \text{ W}\cdot\text{m}^{-1}\cdot\text{K}^{-1}$ , being almost 10 times lower than that of polyetheretherketone. The experimental results are presented in Table 2.12.

**Table 2.12. Experimental results of PEEK 2000 FP powder properties**

Density	Density [ $\text{kg}\cdot\text{m}^{-3}$ ]	Fraction of air [%]	Thermal conductivity [ $\text{W}\cdot\text{m}^{-1}\cdot\text{K}^{-1}$ ]
Apparent	280	79	0.07
Tapped	1007	29	0.15
Pressed	1027	21	0.19
Uncertainty	$\pm 1 \%$	$\pm 1 \%$	$\pm 0.01 \%$

Figure 2.25 compares these experimental results to the line calculated by additivity laws. A fairly good correlation of the experimental points with the theoretical trends is observed. The results of tapped density will be used in the fifth chapter to develop the numerical simulation of thermal history during the selective laser sintering process.

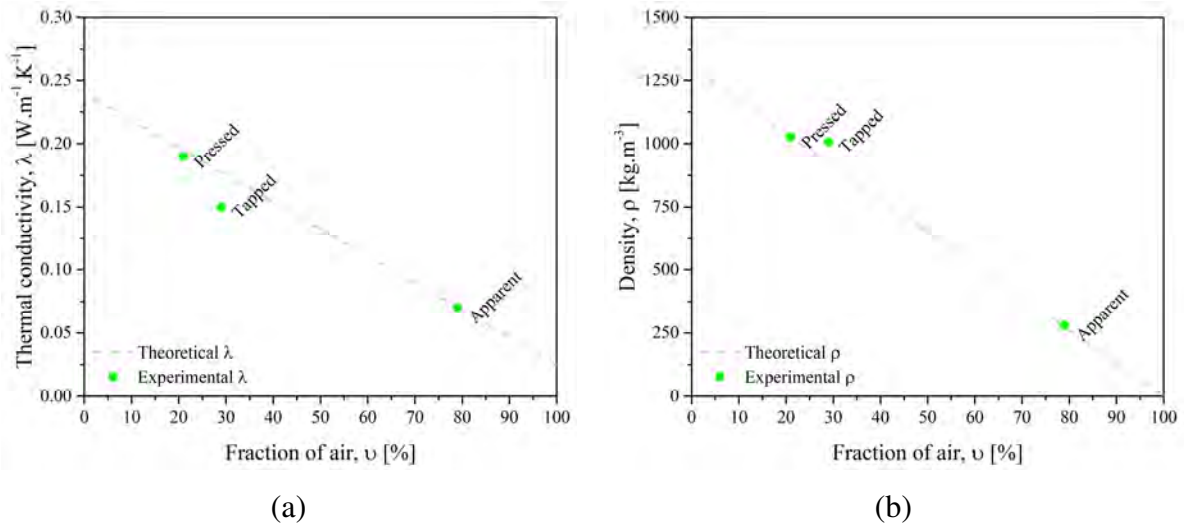


**Figure 2.25. Diagrams of (a) thermal conductivity (b) density as a function of air fraction**

As expected, the thermal conductivity and density increase while the percentage of air decreases. This is due to a higher packing level of particles. The measured thermal conductivity of PEEK 2000 FP is  $0.19 \text{ W}\cdot\text{m}^{-1}\cdot\text{K}^{-1}$  for pressed density. It is assumed that pressed density is the closest one to the selective laser sintering process when the roller distributes the powder. This value is confirmed with results of some research: Choy et al. [194] found out that the thermal conductivity of PEEK is  $0.26 \text{ W}\cdot\text{m}^{-1}\cdot\text{K}^{-1}$  on solid sample measured by Laser Flash technique at  $25 \text{ }^\circ\text{C}$  and Diez-Pascual et al. [195] at  $0.22 \text{ W}\cdot\text{m}^{-1}\cdot\text{K}^{-1}$ . Defauchy [2] also chooses for the development of a microscopic model for the selective laser sintering process the thermal conductivity of  $0.25 \text{ W}\cdot\text{m}^{-1}\cdot\text{K}^{-1}$  and the density of  $1072 \text{ kg}\cdot\text{m}^{-3}$ , which are close to the results of this work. The thermal conductivity of bulk PEEK 2000 FP was measured by Rivière et al. [196,197]. They reported the thermal conductivity of  $0.26 \text{ W}\cdot\text{m}^{-1}\cdot\text{K}^{-1}$  for the density of  $1280 \text{ kg}\cdot\text{m}^{-3}$ . These values are comparable to our results obtained for the same material in the consolidated state:  $0.24 \text{ W}\cdot\text{m}^{-1}\cdot\text{K}^{-1}$  for a density of  $1300 \text{ kg}\cdot\text{m}^{-3}$ .

The specific heat capacity of bulk PEEK 2000 FP was measured by Rivière et al. [196,197] at  $1053 \pm 30 \text{ J}\cdot\text{kg}^{-1}\cdot\text{K}^{-1}$ . Besides, Cheng et al. [198] studied heat capacities of high melting polymers containing phenylene groups. They reported the heat capacity of  $1090 \text{ J}\cdot\text{kg}^{-1}\cdot\text{K}^{-1}$  for PEEK in the solid-state. It was also observed that specific heat increases with increase in the temperature [198]. Thus, Defauchy [2] has reported the specific heat of  $1600 \text{ J}\cdot\text{kg}^{-1}\cdot\text{K}^{-1}$  at  $400 \text{ }^\circ\text{C}$ .

### 2.4.3. Conclusion on the thermal properties of powders

The widest sintering window was noted for PEEK HP3, which is around  $72 \text{ }^\circ\text{C}$ . In the case of other polyetheretherketone and polyamide powders, the windows are quite narrow, and controlling the process at very high temperatures might be difficult. The degree of crystallinity

of around 40 % is higher for PEEK HP3 grade, compared to other PEEK. Thermal conductivity and heat capacity have been found for PEEK 2000 FP in the consolidated state and tapped powder of  $0.24 \text{ W.m}^{-1}.\text{K}^{-1}$  and  $0.15 \text{ W.m}^{-1}.\text{K}^{-1}$ , respectively.

To sum up this part, all PEEK powders tested have the sintering window between  $32 \text{ }^\circ\text{C}$  and  $35 \text{ }^\circ\text{C}$ . It should be noticed that the DSC analyses were made at heating and cooling rates of  $10 \text{ }^\circ\text{C.min}^{-1}$ . This speed is very frequently used in differential scanning calorimetry because it allows a good compromise between the observation of temperature transition and melting ranges. It would be interesting to evaluate the thermal cycle of powder when submitted to the selective laser sintering process. Indeed, it can be already assumed that during the passage of the laser beam, a rapid temperature rise occurs at the surface of the powder bed. Knowing the real thermal cycle of powder, it would be possible to measure the thermal properties of powders in conditions closer to the real sintering cycle. This idea will be developed in chapter 5 about heat management during the selective laser sintering process.

## 2.5. Rheological properties in the molten state

The viscosity of the polymer in the molten state is an indication of the resistance to its flow. The rheological properties of molten polymers are accurately measured as a function of temperature and shear rate with a rheometer. For this purpose, the fluid is sheared between two disks or more generally between a stator and a rotor and its resistance is calculated by measuring the torque required for moving the rotor.

The rheological measurements have been carried out to evaluate the macromolecular diffusion times. Indeed, the coalescence of grains is driven by the macromolecular diffusion at the interface of two grains. The viscosity is a macroscale indication of the macromolecular diffusion.

For that, a strain-controlled rheometer was used in oscillatory mode. The full description of the procedure is seen in Annex A.2.5. The rheological tests have been done under air flow conditions using 25 mm diameter parallel plate configuration. All experiments were done in an oscillatory mode, within the viscoelastic linear domain, determined from strain sweep tests.

### 2.5.1. Dynamic viscosity of PEEK powders

The flowing ability is associated with the viscosity of molten polymers [164]. The viscosity is highly influenced by the temperature and shear rate for molten polymers [199]. The storage  $G'$  and loss  $G''$  moduli and the complex viscosity of polyetheretherketone in their molten state have been measured in oscillatory mode.

Isothermal tests were made under air atmosphere in the range of 350 °C to 400 °C. Frequency sweeps are between  $\omega = 100 \text{ rad.s}^{-1}$  and  $\omega = 0.01 \text{ rad.s}^{-1}$  at 0.5 % of strain within the viscoelastic linear domain..

The complex viscosity is calculated from  $G'$ ,  $G''$  and  $\omega$  by the equation:

$$\eta^* = \frac{\sqrt{(G')^2 + (G'')^2}}{\omega} \quad (2.6)$$

where:

- $\eta^*$  - complex viscosity [Pa.s];
- $G'$  - storage modulus [Pa];
- $G''$  - loss modulus [Pa];
- $\omega$  - angular frequency [ $\text{rad.s}^{-1}$ ].

Molten polymers generally exhibit shear-thinning behaviour with a Newtonian plateau at low shear rate. The involved shear rates in the SLS process are very low due to the absence of pressure when the coalescence takes place. It is assumed that the shear rates correspond to the Newtonian plateau, meaning the highest viscosity of the flow curve. On the contrary, standard polymer processing such as injection or extrusion involves shear rates above  $1000 \text{ s}^{-1}$ . The complex viscosity versus angular frequency is presented in Figure 2.26. The graphs of the corresponding  $G'$  and  $G''$  with angular frequency are presented in Figure 2.34.

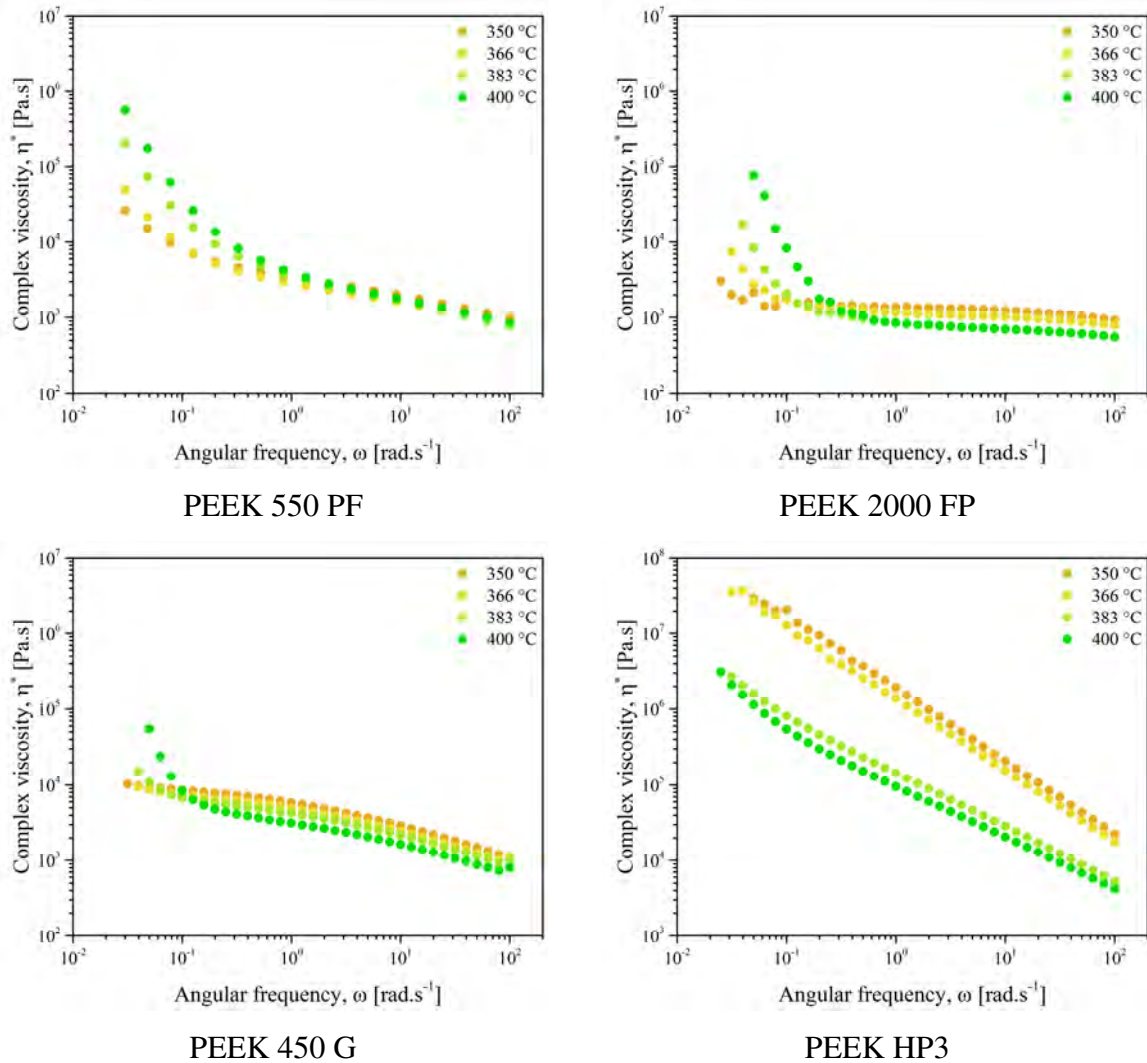
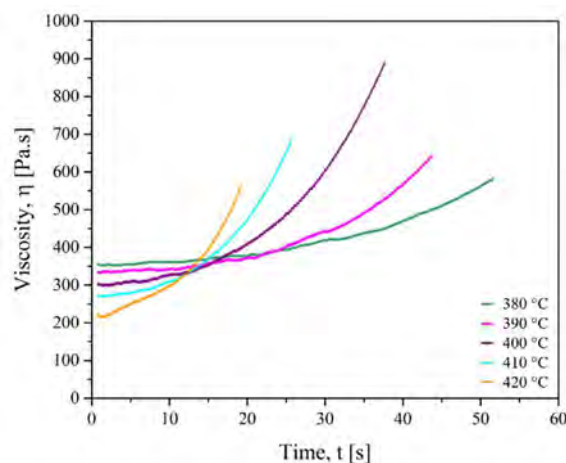


Figure 2.26. Dynamic viscosity of PEEK powders for different temperatures

The general behaviour of the flow curves obtained for PEEK powders is not typical of molten polymers. Despite a shear-thinning behaviour for the highest angular frequencies, only the flow curve for PEEK 450 G at  $350 \text{ °C}$  shows a Newtonian plateau at low shear rates associated with a shear-thinning behaviour. The other curves exhibit a rapid rise at the lowest frequency, a typical explanation is the evolution of the material with time. Indeed, the acquisition times are very fast for the highest frequencies, but it takes some minutes to get the

points at  $\omega = 0.1 \text{ rad.s}^{-1}$  and below. It is known that polyaryletherketones are sensitive to thermo-oxidative degradation at high temperature.

To confirm this hypothesis, the evolution of the complex viscosity is presented with time at a fixed angular frequency and fixed strain. The graph in Figure 2.27 shows that the viscosity is doubled in a few minutes.



**Figure 2.27. Viscosity as a function of time for different temperatures [200]**

As seen above, Bessard et al. [200] have reported that at 400 °C the thermal degradation occurs after 15 min and the viscosity, initially of about 350 Pa.s, reaches 800 Pa.s after 35 min. The processing conditions in the conventional compression moulding process are limited by thermal degradation. Thus, the uses of processing temperature over 400 °C is impossible. However, the high heating and cooling kinetics allow controlling the time of exposure of PEEK to a high temperature by induction technology. Processing temperatures of about 420 °C may thus be used but the processing time must be limited to a few minutes.

At temperatures between 350 °C and 400 °C, the molecular chains of PEEK undergo recombination of a random chain scission of the ether and ketone bonds [98]. Moreover, the air atmosphere has a large influence on the stability of PEEK in the melt state and its thermal degradation. The results show that PEEK viscosity remains mostly constant during a few minutes but quickly increase for a longer time of exposure due to crosslinking. Day et al. [98,201] reported that the prime decomposition mechanism leads to the production of phenol, which is the major gaseous product of the pyrolysis. This would imply that the primary chain scission reaction involves the ether linkages rather than the carbonyl linkage, as seen in Figure 2.38;

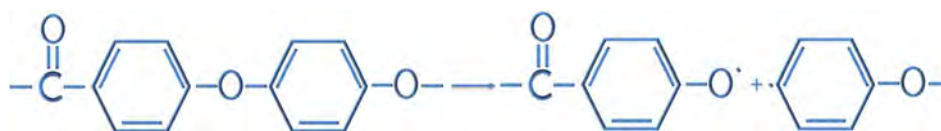


**Figure 2.38. Scheme of the degradation mechanism of PEEK**

Hydrogen abstraction from adjacent polymer chains can then lead to the following stable chain ends, as seen in Figure 2.29.

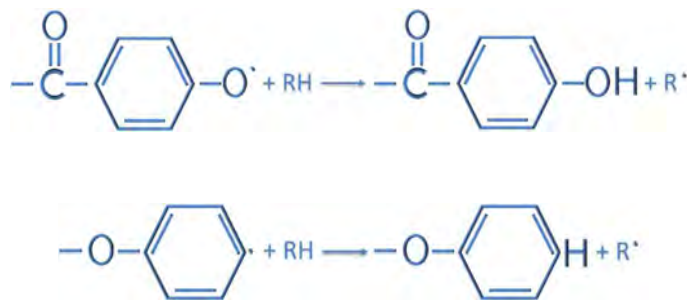


Figure 2.29. Scheme of the radicals propagation

Subsequent cleavage of these chain ends will then give rise to species capable of forming phenol, the major volatile pyrolysis product, as seen in Figure 2.30.

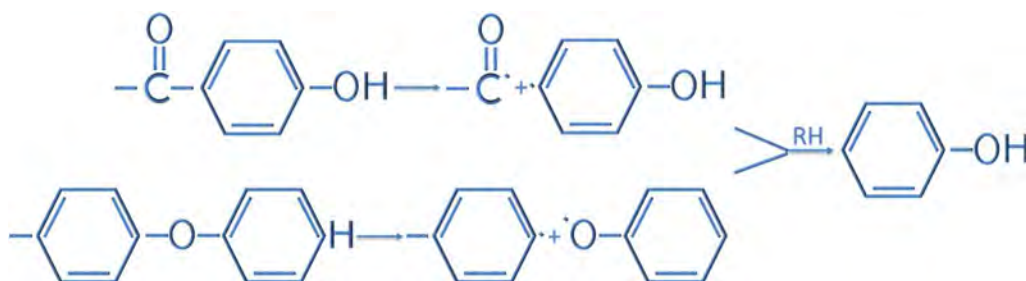


Figure 2.30. Scheme of the formation of phenolic species

It would appear that the degradation of polyetheretherketone is initiated by homolytic chain cleavage at the ether bond. In the result, the phenolic end groups, produced on subsequent hydrogen abstraction, are cleaved to produce phenol as the initial and major pyrolysis product.

The PEEK 550 PF, PEEK 2000 FP and PEEK 450 G present a similar sensitivity to degradation. Considering the acquisition time is the same for each experiment, the degradation appears faster in the case of PEEK 550 PF than the other polymers. The complex viscosity of PEEK 2000 FP and PEEK 450 G remain constant over the frequency range of 100 rad.s<sup>-1</sup> to 0.1 rad.s<sup>-1</sup>.

The PEEK HP3 did not reach a Newtonian plateau in the experimental frequency range with a continuous increasing with decreasing frequency. This may be due to the morphological organization of immiscible domains [202]. Like any copolymer, it self-organizes into spheres, cylinders, lamellae or network-like morphology, depending on the relative polymer-block chain lengths. Such morphologies strongly impede the flow behaviour and relaxation characteristics of the material. For homopolymer, the loss modulus slope in the terminal region is 1 whereas for triblock copolymer the slope is about 0.2 [203]. In Figure 2.31 the slope for G'' is calculated at 0.25, so HP3 could be a triblock copolymer. The loss factor represents a stable behaviour



with a decrease at a low angular frequency, which may originate from the shape relaxation of dispersed droplets of one component when sheared. In Figure 2.26 for PEEK HP3, we see that the complex viscosity is typical of a triblock copolymer with high shear-thinning behaviour.

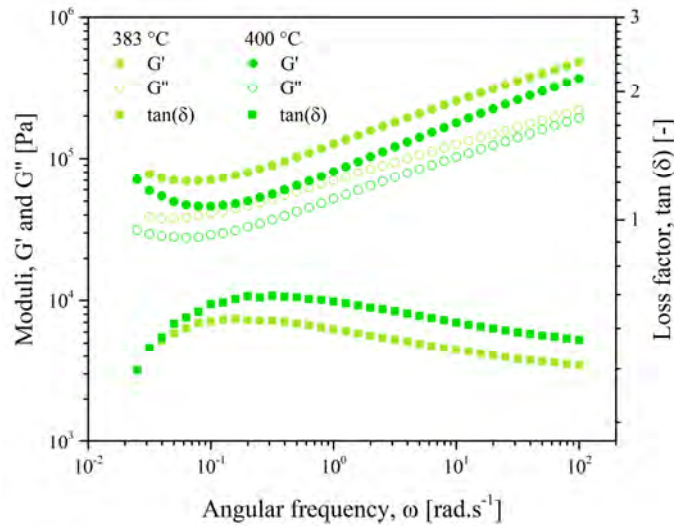


Figure 2.31. Rheological behaviour of PEEK HP3 at 383 °C and 400 °C

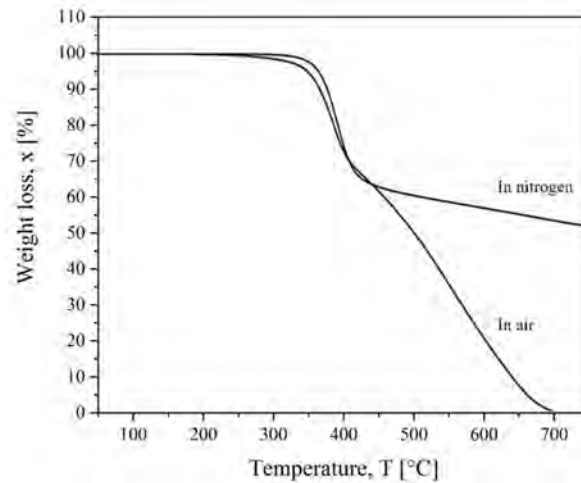
The complex viscosity at 1 rad.s<sup>-1</sup> of all PEEK powders is reported in Table 2.13. As expected, a temperature increase results in decreasing the melt viscosity. The PEEK 2000 FP exhibits the lowest viscosity with 840 Pa.s at 400 °C compared to above 3000 Pa.s at 400 °C for PEEK 550 PF and nearly 96000 Pa.s at 400 °C for HP3 copolymer.

Table 2.13. Complex viscosity for 1 rad.s<sup>-1</sup> of PEEK powders

Powder	PEEK 550 PF	PEEK 2000 FP	PEEK 450 G	PEEK HP3
350 °C	3159 Pa.s	1375 Pa.s	5841 Pa.s	1918979 Pa.s
366 °C	2635 Pa.s	1146 Pa.s	4880 Pa.s	1374774 Pa.s
383 °C	3178 Pa.s	854 Pa.s	4214 Pa.s	144620 Pa.s
400 °C	3415 Pa.s	842 Pa.s	3139 Pa.s	95876 Pa.s
Uncertainty	± 2 % [204]			

The rheological experiments have been carried out under airflow. Some authors [98,201,205–207] demonstrate that degradation is slower in the inert gas environment, as seen in Figure 2.32.

The thermogravimetric analysis reported by Shabaev et al. [207] showed that in an inert atmosphere, 2 % and 5 % of the mass loss occurred at temperatures of 550 °C and 560 °C, respectively. The decomposition of the polymer occurred in one stage with the formation of a residue accounting for approximately 50 % of the original polymer weight.



**Figure 2.32. Degradation of PEEK under air and nitrogen [207]**

That is why the bed powder is under inert gas during the fabrication. Indeed, in machines of 3D Systems such as sPro230 and ProX500 uses nitrogen. The same inert atmosphere is applied to the powder cake during cooling in the breakout station.

Bakrani-Balani [208] reported that the increase of viscosity due to degradation strongly influences the kinetics of interdiffusion of polymeric chains. This interdiffusion may impact the mechanical properties of printed parts. The mechanical strength of printed parts stems from the interlayer adhesion. The latter is due to interdiffusion of polymeric chains in adjacent filaments. This interdiffusion is directly linked to the viscosity of the polymer. If the interdiffusion is not done at most, the interlayer adherence can be weak, resulting in low fracture resistance of parts.

### 2.5.2. Calculation of relaxation times

To determine relaxation time relative to the reptation phenomenon, several analyses are possible by using experimental results:

- from the intersection of an elastic and viscous component of complex modulus tangents when frequency tends to 0 [209].
- from the viscosity values, it is a transition between Newtonian state characteristic of intermolecular friction and which is obtained when each macromolecule is relaxed and the shear-thinning regime for which the viscosity follows the power-law model [210].
- from generalized Maxwell's model that well describes terminal zone behaviour. The relaxation spectrum can be deduced from the complex modulus [211].

The first method has been chosen. The terminal relaxation time has been determined directly from the projection of the intersection point, as seen in Figure 2.34, and extrapolation to the zero-shear rate viscosity.

It is admitted that the relaxation time fits the Arrhenius law [212], as the Newtonian viscosity:

$$\tau = Ae^{\frac{-E_a}{RT}} \quad (2.7)$$

$$\ln\tau (T) = -\frac{E_a}{RT} + \ln A \quad (2.8)$$

where:

- $\tau (T)$  - relaxation time [ $s^{-1}$ ];
- $A$  - pre-exponential factor, a constant value for each chemical reaction or physical phenomena [ $s^{-1}$ ];
- $E_a$  - activation energy [ $J.mol^{-1}$ ];
- $R$  - universal gas constant [= 8.314  $J.K^{-1}.mol^{-1}$ ];
- $T$  - temperature [K].

K. S. Cole and R. H. Cole [213] proposed the following dynamic viscosity expression, the Cross model, according to the following equation (Equation 2.9), to calculate the characteristic relaxation time. The Newtonian viscosity refers to the asymptotic value of the complex viscosity at very low shear-rate (or zero shear viscosity).

$$\eta^*(\omega) = \frac{\eta_0}{1 + (j\omega\lambda_0)^{1-h}} \quad (2.9)$$

where:

- $\eta^*$  - dynamic viscosity [Pa.s];
- $\eta_0$  - Newtonian viscosity [Pa.s];
- $\omega$  - angular frequency [ $Rad.s^{-1}$ ];
- $\lambda_0$  - characteristic relaxation time [s];
- $h$  - relaxation time distribution parameter [ $0 \leq h < 1$ , the larger the distribution and the more  $h$  tends towards 1].

The plot of Cole-Cole diagram consists in representing the imaginary part of viscosity  $\eta''(\omega)$  as a function of real part  $\eta'(\omega)$  of dynamic viscosity  $\eta^*(\omega)$ . The curve obtained has an arc shape from which the following three parameters can be derived:

- the Newtonian viscosity corresponds to the greater of two values of intersection between the arc of the circle and the axis of abscissa and it is calculated with the following equation:

$$\eta_0 = x_c + \sqrt{(R^2 - y_c^2)} \quad (2.10)$$

where:

- $\eta_0$  - Newtonian viscosity [Pa.s];
- R - radius of arc [-].

- the characteristic relaxation time corresponds to the inverse of frequency obtained for the maximum value of loss viscosity;
- the relaxation time distribution parameter can be determined graphically by measuring the angle between the radius of the circle passing through the coordinate point (0.0) and the abscissa axis. This angle is equal to  $h(\pi/2)$  [213].

A graphical determination of Newtonian viscosity determined from the Cole-Cole diagram for different temperatures is presented below. Figure 2.33 shows that the experimental dots follow quite well the expected arc shape for PEEK 450 G, whereas it is less proper for PEEK 2000 FP. The data corresponding to the highest frequencies satisfies the Cole-Cole theory for both. Once the degradation begins, the values leave the arc shape, the Cole-Cole theory is not yet suitable.

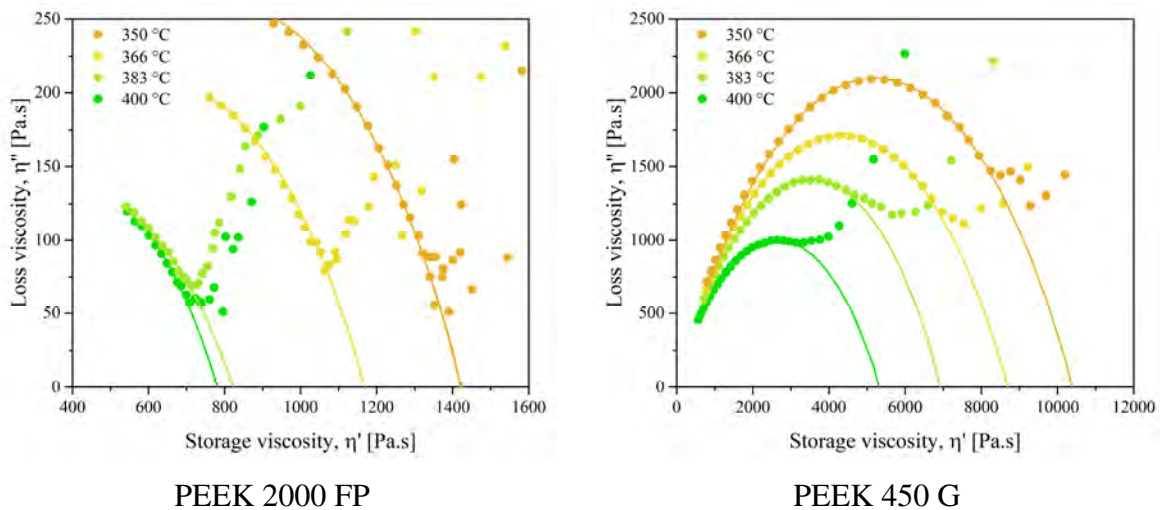


Figure 2.33. Cole-Cole representation from frequency sweep for PEEK powders

The Newtonian viscosity is much lower for PEEK 2000 FP than for PEEK 450 G. At 350 °C, 366 °C, 383 °C and 400 °C for PEEK 2000 FP, the zero-shear viscosity is 1425 Pa.s, 1160 Pa.s, 825 Pa.s and 780 Pa.s, respectively. For PEEK 450 G, the zero-shear viscosity is 10400 Pa.s, 8800 Pa.s, 7000 Pa.s and 5300 Pa.s, respectively.

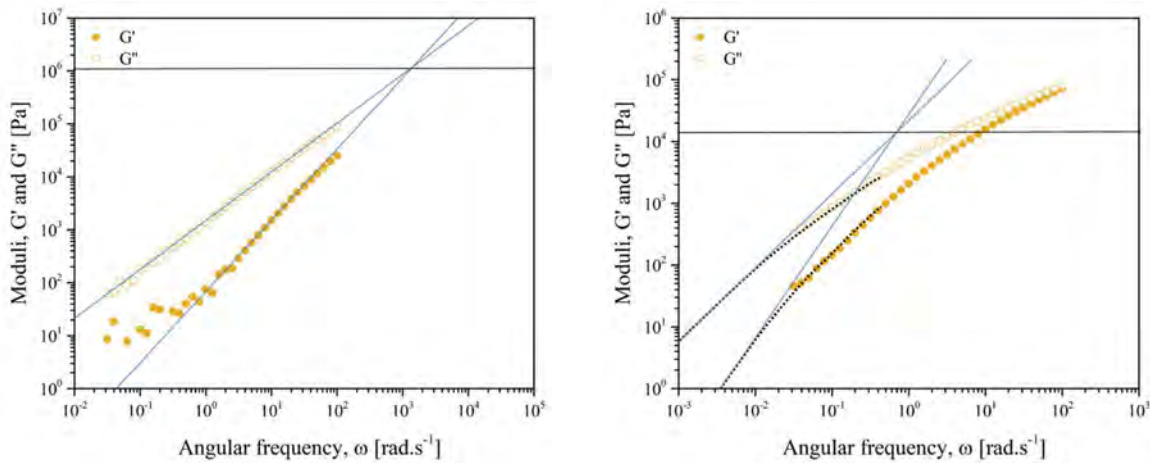
The limited elastic complacency ( $J_e^0$ ) reflects the residual internal elasticity of macromolecules. It corresponds to the inverse of the intersection of slopes of elastic and viscous modulus at low frequencies and given by the inverse of modules:

$$G^* = \frac{1}{J_e^0} \quad (2.11)$$

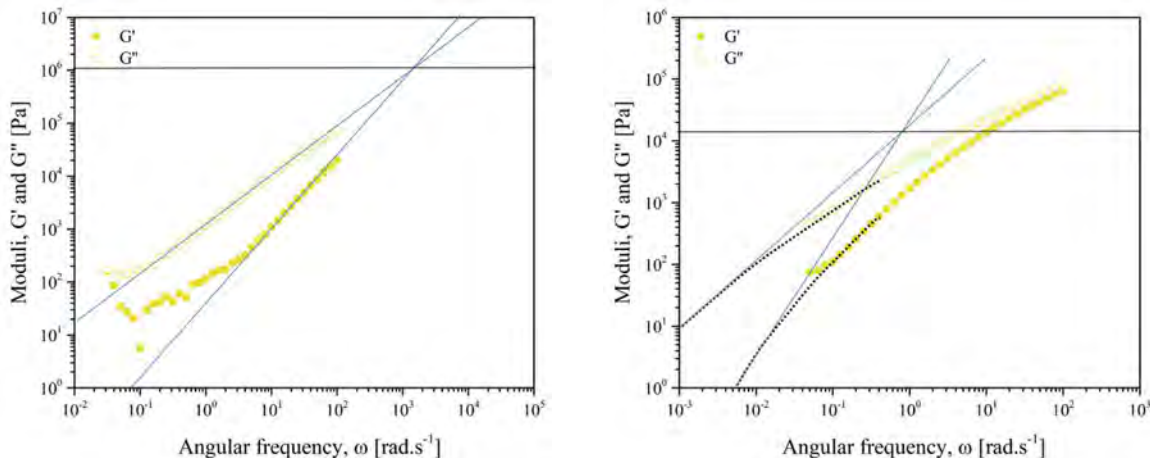
The curves of storage  $G'$  and loss  $G''$  moduli are presented in Figure 2.34. In the terminal regime or longest relaxation time, the slope of  $G'$  and  $G''$  are expected to be 2 and 1 respectively for a model entangled polymer in its melted state. As shown by Lamethe [150] and Nicodeau [134], the terminal regime cannot be reached because of the degradation of PAEK in the melted state, even when the rheological measurements are carried out under nitrogen flow. For this reason, we have extrapolated the curves of storage  $G'$  and loss  $G''$  moduli at low frequencies, then their intersection is identified as  $J_e^0$ .

For PEEK 2000 FP, the values of both moduli give suitable slopes to be extrapolated to high frequencies. For PEEK 450 G, the curves of moduli have been extrapolated to low frequencies to reach the expected slopes. The results are presented for four temperatures in the melted state: 350 °C, 366 °C, 383 °C and 400 °C.

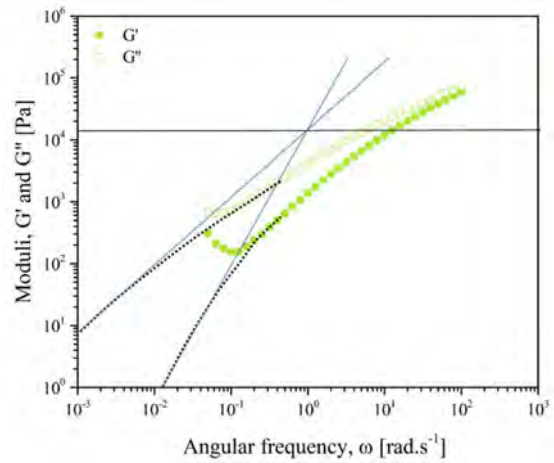
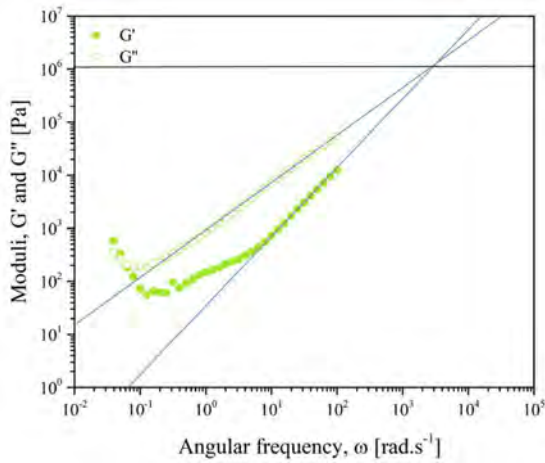
350 °C



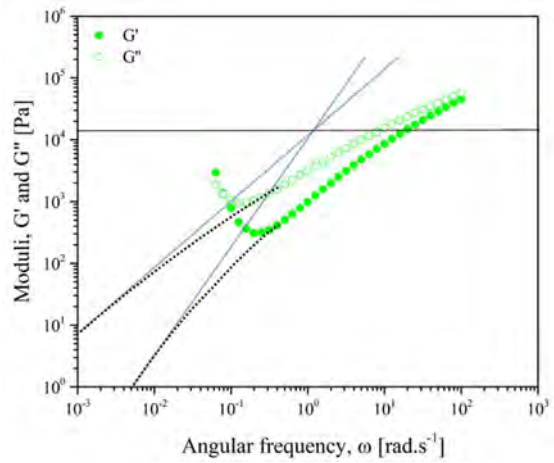
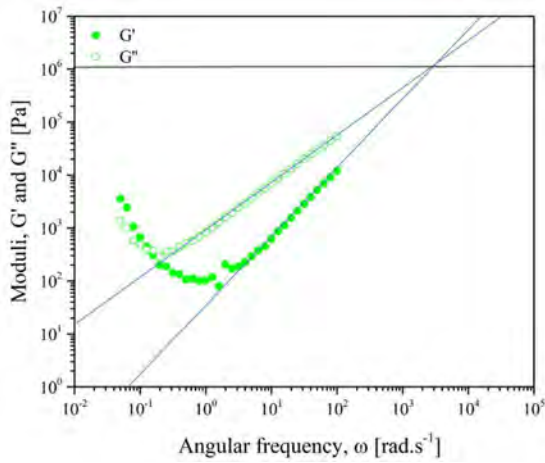
366 °C



383 °C



400 °C



PEEK 2000 FP

PEEK 450 G

**Figure 2.34. Determination of limited elastic complacency for PEEK powders**

The value of limited elastic complacency obtained for PEEK 2000 FP and PEEK 450 G are  $1.00 \cdot 10^{-6} \text{ Pa}^{-1}$  and  $9.52 \cdot 10^{-5} \text{ Pa}^{-1}$ , respectively, at each studied temperature. According to Graessley [214], the final relaxation, meaning the relaxation time for the longest macromolecules is given by:

$$\lambda_w = \eta_0 J_e^0 \quad (2.12)$$

where:

- $\lambda_w$  - final relaxation time [s];
- $\eta_0$  - Newtonian viscosity [Pa.s];
- $J_e^0$  - limit elastic compliance [ $\text{Pa}^{-1}$ ].

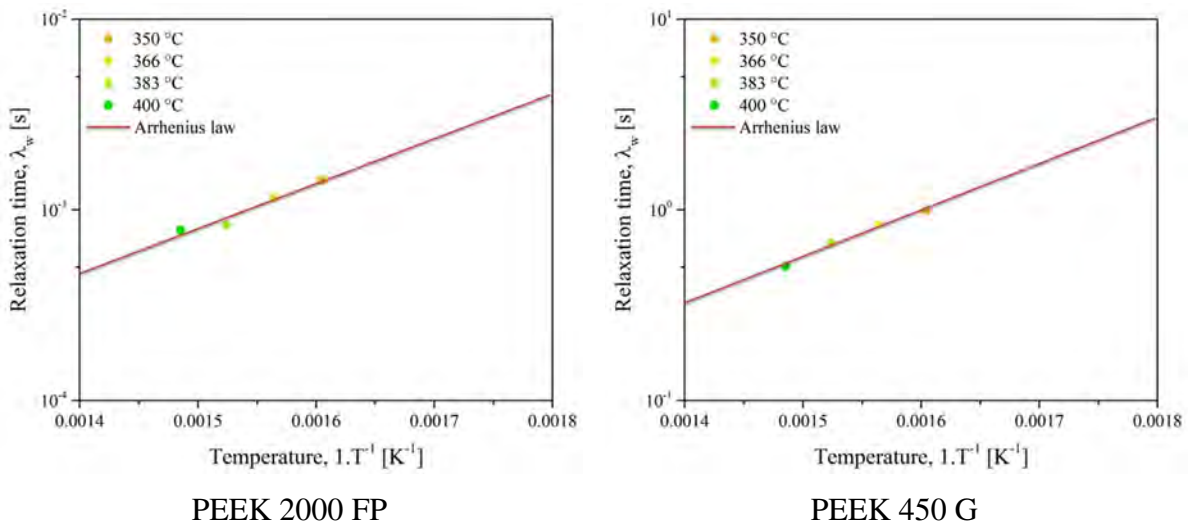
This method made it possible to calculate  $\lambda_w$  for different temperatures. The terminal relaxation times are presented in Table 2.14.

**Table 2.14. Relaxation time for PEEK powders**

Powder	PEEK 2000 FP	PEEK 450 G
350 °C	1.43 ms	0.99 s
366 °C	1.16 ms	0.84 s
383 °C	0.83 ms	0.67 s
400 °C	0.78 ms	0.50 s

In the SLS process, it is necessary to maintain the temperature high enough while the polymer is in its melted state to allow interdiffusion of polymeric chains, ensuring coalescence of powder grains. The longest macromolecules give relaxation times from 0.8 ms to 1.4 ms for PEEK 2000 FP and from 0.5 s to 1.0 s for PEEK 450 G. For example, Coulson et al. [215] reported the relaxation time of 9.0 ms and zero shear-rate of 710 Pa.s at 355 °C for PEKK. In the case of PEEK 450 G, the results are comparable with obtained by Régnier et al. [216].

As expected, the results show longer relaxation times for lower temperatures. The agreement of these results with Arrhenius law (Equation 2.7) is presented in Figure 2.35. The relaxation times are an Arrhenius activated phenomenon. The activation energy  $E_a$  is equal to 45 kJ.mol<sup>-1</sup> for PEEK 2000 FP compared to 47 kJ.mol<sup>-1</sup> for PEEK 450 G. As can be seen in Figure 2.35, the thermal variations of the relaxation time are very identical for the two PEEK samples.


**Figure 2.35. Relaxation time with extrapolation according to the Arrhenius law**

It is worth noticing that even if the straight line has been extrapolated in these graphs, the reptation theory is no longer valid neither when the polymer degrades at high temperature nor when it crystallizes at low temperature.



### 2.5.3. Conclusion on the rheological properties in the molten state

To sum up, in this section, the rheological behaviour of polyetheretherketones is studied in their melted state. Because of their melting point around 350 °C, their rheological study has been performed between 350 °C and 400 °C. In this temperature range, they demonstrate a complex behaviour because of high sensibility to thermo-oxidative degradation. Hence, it is necessary to make the experiments under nitrogen to slow down the degradation process. Nevertheless, some results have been extracted from our experiments: among PEEK we characterized, the lowest viscosity is observed for PEEK 2000 FP. The viscosity of PEEK HP3 is much higher than that of other polyetheretherketones. This is due to the morphological organization of the copolymer. We deduced from rheological measurements that PEEK HP3 could be a triblock copolymer.

The degradation at high temperatures and the crystallization at the low temperature limit the exploration of the temperature window. Moreover, the limitation in frequency is determined by the apparatus, between 0.001 rad.s<sup>-1</sup> and 100 rad.s<sup>-1</sup>. In the SLS process, the shear rate involved for the coalescence step is considered under 1 s<sup>-1</sup>, so our experiments are useful to give information on the flow behaviour of polymers in the melted state.

Nevertheless, the relaxation times for PEEK 2000 FP and PEEK 450 G has been calculated. The other PEEK and HP3 do not fit the Cole-Cole theory. The relaxation time for PEEK 2000 FP is in the range from 0.8 ms to 1.4 ms, thus, it is therefore much shorter than those of PEEK 450 G of 0.5-1.0 s. This difference is probably due to their molecular weight. The melted polymers exhibit viscoelastic behaviour. This behaviour is, in fact, the translation of molecular motions within the material whose characteristic times are in order of magnitude of those obtained by experiments. Thus, there is a one-to-one relationship between the macroscopic response of the material and the molecular characteristic times of polymers. The molecular weight of PEEK 450 G is supposed to be 115.000 g.mol<sup>-1</sup> [217], while PEEK 2000 FP could have shorter chains with the molecular weight assumed to be 33.000 g.mol<sup>-1</sup>. Those values are in agreement with those obtained by Lamethe [150] on another PEEK grade. He reported that the relaxation times of shortest chains are very much less than the second, the times associated with the longest chains are of the order of 4 s.

The difference of relaxation times was expected, as PEEK 450 G is a grade intended for extrusion and injection purpose in the form of pellets. In these processes, the viscosity must be high to avoid the melted polymer flowing between the two parts of the injection mould or at the exit of the die in extrusion. On the contrary, PEEK 2000 FP is designed for manufacturing compression moulding parts that is why lower viscosity is necessary.



## 2.6. Effect of recycling on the properties of PA12

After fabrication, the printed part is removed from the powder bed, and a big amount of unsintered powder is lost. In some cases, this powder is salvaged to be re-used. In practice, a small fraction of 50 wt.% and in some applications, even of 70 wt.% of PA12 powder is mixed with virgin powder for a new batch of fabrication.

The purpose of this section is to investigate the evolution of the properties of polyamide 12 powder used in the selective laser sintering process. The aim is to quantify the potential degradation of the powder to increase the ratio of recycled powder. The main goals are: to compare the powder before and after the printing process and to advise a rate of recycling powder to minimize the consumption of fresh material.

To observe the effect of the printing cycle on the powder, a set of values was measured on fresh and recycled PA12 powder. Some of these results are presented earlier in comparison with polyetheretherketone powders. The morphology (particle shape by scanning electron microscopy and image analysis), flowability (angular measurement and densities), thermal properties and crystallinity, moisture content, and rheological properties in the molten state have been taken into account.

### 2.6.1. Qualitative study of the degradation of PA12

The fresh and recycled PA12 powders have been studied regarding mass loss by thermogravimetric analysis. It consists of continuous measurement of the mass of the sample while the temperature is changed over time. During the test, the polymer degrades by reacting with dioxygen when the experiment is done under air flow. The successive phases of the degradation are analysed from the weight loss curve. Moreover, the remaining mass corresponds to the quantity of inorganic fillers added to modify the polymer properties or its cost of production.

About 10 mg of powder is placed in a thermogravimetric analyser and heated between 25 °C and 750 °C at 10 °C.min<sup>-1</sup> under air flow. The thermograms obtained for fresh and recycled (having undergone a printing cycle) PA12 are shown in Figure 2.36.

The two curves show similar behaviours with four distinct steps, which indicates the same degradation mechanism. In the first step below 280 °C, a slight loss is measured, it corresponds to the volatilization of lightest products, water, and then, monomers and oligomers. The second region, between 270 °C and 350 °C, corresponds to the beginning of the degradation, which is

considered when the polymer loses 5 % of its mass. Between 350 °C and 550 °C, around 85 % of polymer degrades: the polymer undergoes one or more reactions leading to the volatilization of unsaturated nitriles, and vinyl groups [75]. Finally, the last step is beyond 550 °C until carbon residues are obtained. In the end, the residual mass is about 5 %. The results obtained are comparable with those from previous studies of Dupin [1] and Levchik et al. [75] on PA 2200 from EOS company.

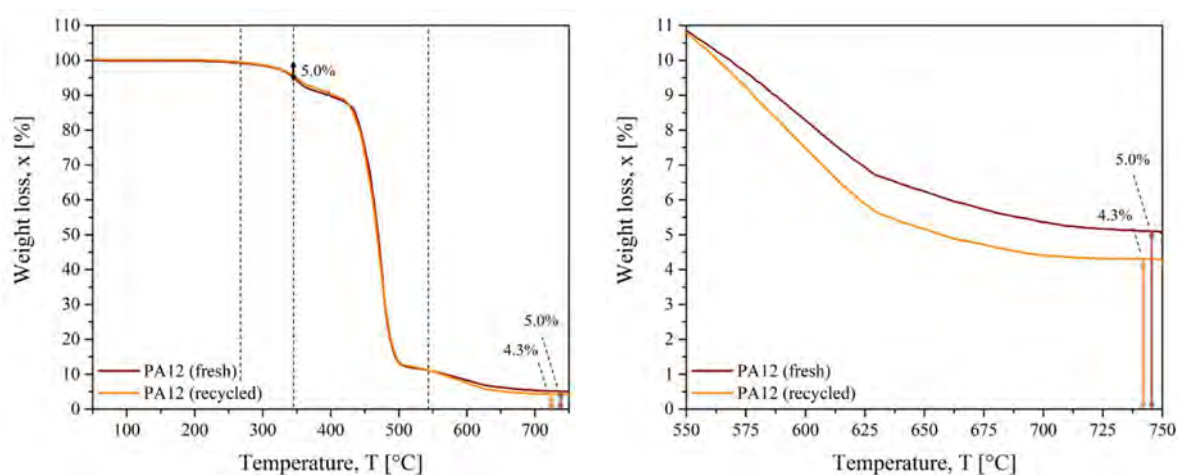


Figure 2.36. The TGA thermogram obtained for PA12 powders

The measurement of residual mass is done on the final asymptote of the weight loss curve. The results of fresh and recycled PA12 and presented in Table 2.15 below:

Table 2.15. The weight loss of PA12 at 750 °C

Powder	PA12 (fresh)	PA12 (recycled)
Residual mass [%]	5.040	4.293
Standard deviation	0.001	0.001

Thus, the temperature inside the chamber is at 173 °C, so it is much lower than when the degradation occurs: the chemical changes could not be significant even if the powder stays at this temperature.

### 2.6.2. Moisture content

The absorption rate of water for fresh and recycled PA12 powders has been investigated. To measure the water content, the NFP-94050 standard was used. Three samples of more than 20 g were put in aluminium cups and weighed with a laboratory scale. After 4 hrs, 24 hrs and 48 hrs at 105 °C in the oven, the powders were removed and put in a desiccator for 30 min to allow them to cool down. They were then weighed and put back in the oven to finish the cycle of three measurements.

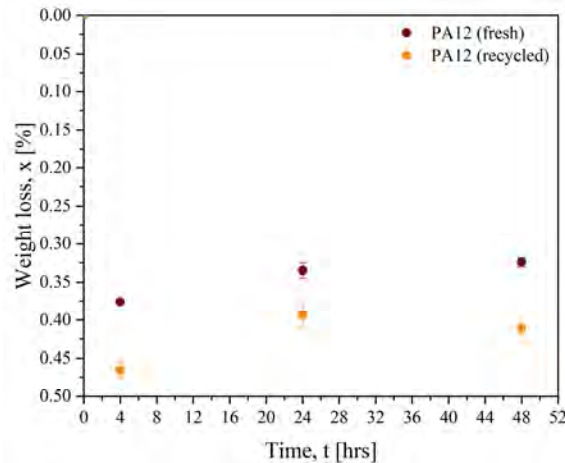


**Figure 2.37. Evolution of the percentage of weight loss from  $t_0$**

The weight difference corresponding to the water loss during the drying process is plotted in Figure 2.37. Surprisingly, the weight loss reaches around 0.38 % and 0.46 % after 4 hrs for fresh and recycled PA12. Then, the mass slightly increases and the weight loss is stabilized at around 0.33 % and 0.40 %, respectively since the moisture absorption of fresh PA12 powder is supposed to be 0.07 % according to the datasheet (Annex A.1.1).

Thus, the recycled powder is more susceptible to water absorption than fresh PA12. According to Ha [218], the water content is around 0.1 % after 4 hrs of drying for recycled polyamide 12, while the moisture absorption of fresh PA12 powder is 1 % to 2 %.

The difference of water absorption of fresh and recycled powder is possibly due to slight chemical changes towards more hydroxyl (-OH) groups onto the surface of the powders that undertook the thermal cycle inside the printer. With more (-OH) groups onto the surface, the powder grains would be more prone to making hydrogen bonds with  $H_2O$ .

### 2.6.3. Observation of the recycling effect

The rheological tests were done to measure the evolution of storage  $G'$  and loss  $G''$  moduli with time at 200 °C with parallel plate geometry. During printing, the temperature of the chamber is 173 °C, while the laser heats the powder to 265 °C [115].

The thermal stability under the condition of air flow of fresh PA12 was characterized at the frequency of 1  $\text{rad}\cdot\text{s}^{-1}$  and strain of 1 % within the viscoelastic linear domain. The results are presented in Figure 2.38.

The time sweep shows that the  $G'$ ,  $G''$  and thus the complex viscosity are quite stable for 100 s. After that, a progressive increase with time is registered. An increase in viscosity would mean an increase in molecular weight arising from further polycondensation, which would release additional

water molecules. A similar observation has been made by Dijkstra [219] on PA6 during the measurement at 240 °C under nitrogen atmosphere. On the contrary, Dupin [1] has reported a slight increase in  $G'$  observed at 250 °C on Innov PA12, but it remains insignificant after 5 min stays stable. He assumed that at the processing temperature range, the polymer remains stable throughout tests between 5 min and 10 min. Drummer et al. [220,221] reported investigations on a recycled polyamide 12 (PA 2200) powder: it reveals a decrease of melt volume rate due to thermally induced post-condensation reaction under nitrogen and vacuum atmosphere for short periods of storage time near the beginning of melting. The storage under dioxygen at  $T = 175$  °C for short periods leads to increase and afterwards to decrease of average molecular weight due to competing for chain branching and scission mechanisms.

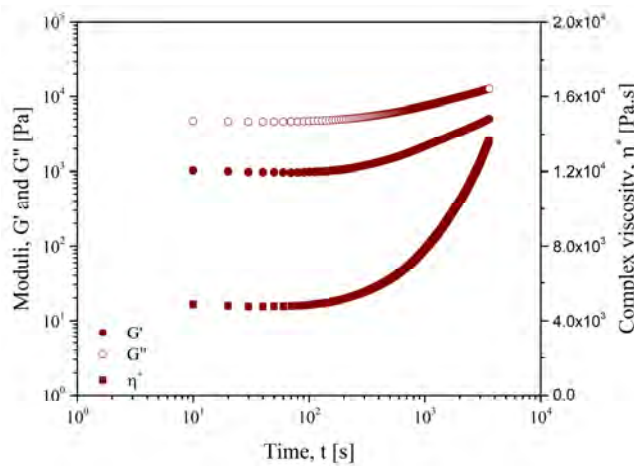


Figure 2.38. Evolution of  $G'$  and  $G''$  with time at constant angular frequency and 200 °C for fresh PA12

In the second step, the rheological behaviour of fresh and recycled PA12 powder was compared. Still, within the viscoelastic linear domain, the tests have been performed at 0.3 % of strain and temperature of 200 °C, 220 °C and 240 °C. Figure 2.39 compares the frequency sweeps for fresh and recycled PA12 powder.

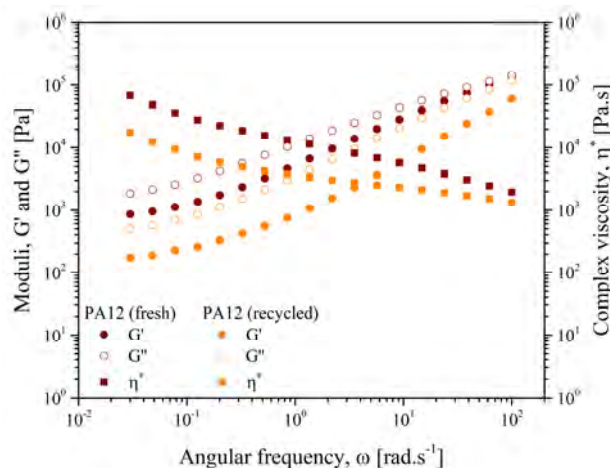
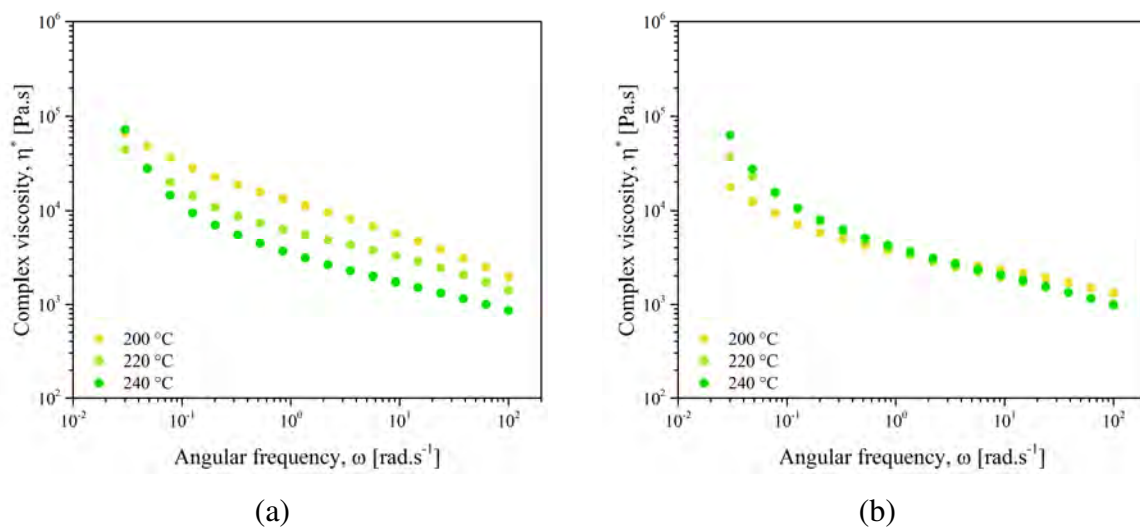


Figure 2.39. Comparison of rheological properties of fresh PA12 and recycled PA12 at 200 °C

The melted PA12 demonstrate a shear-thinning behaviour on the whole range of angular frequencies. The  $G'$  and  $G''$  moduli and thus the complex viscosity are lower for recycled powder compared to fresh powder. The complex viscosity for  $1 \text{ rad.s}^{-1}$  is  $11340 \text{ Pa.s}$  and  $3360 \text{ Pa.s}$  for fresh and recycled PA12, respectively. As an explanation, the recycled powders spend a long time over 24 hrs very close to their melting point in the printing bed. They undertake chemical degradation and oxidation, which could increase the molecular weight of polyamide 12, thus viscosity of polyamide 12 powder increases [218].

The effect of temperature on the complex viscosity of fresh and recycled PA12 is pointed out in Figure 2.40.



**Figure 2.40. Rheological properties of (a) fresh (b) recycled PA12 for different temperatures**

As expected, temperature increase results in a decrease of complex viscosity of PA12 for fresh powder. At low frequencies, the viscosity increases drastically at  $240 \text{ °C}$  for both. The frequency range demonstrates a shear-thinning behaviour and continuous increase with decreasing frequency. The complex viscosity of recycled PA12 is slightly higher at  $240 \text{ °C}$  than those of the fresh one. It means that the degradation of fresh PA12 powder is much faster at  $240 \text{ °C}$  than at  $200 \text{ °C}$ .

While the effect of temperature on viscosity is significant for fresh powder, it is not anymore for recycled powder, which has already seen thermal cycles during the previous production batch. Indeed, the values reported in Table 2.16 show that the complex viscosity of recycled PA12 is quite constant for  $200 \text{ °C}$  and  $220 \text{ °C}$  and a slight increase is noticed at  $240 \text{ °C}$ . This indicates that the powder has undergone post condensation reactions [222]. It is an effect of unblocked chain ends of PA12, which occurs during ageing. After this reaction, the chemical structure is almost stabilized, this could explain the stability of the viscosity with temperature for the recycled PA12.

**Table 2.16. Complex viscosity for 1 rad.s<sup>-1</sup> of PA12**

Powder	PA12 (fresh)	PA12 (recycled)
200 °C	11337 Pa.s	3360 Pa.s
220 °C	5511 Pa.s	3310 Pa.s
240 °C	3092 Pa.s	3605 Pa.s
Uncertainty	± 2 % [204]	

With a higher viscosity, the sintering behaviour may change. According to Frenkel's theory of sintering, with increasing viscosity the time for particle coalescence rises [57]. Additionally, the bubble removal time in a polymer melt increases for rising viscosity, which is known from rotational moulding [58]. Both effects affect the time necessary to reach a homogeneous melted layer is formed. Thus, it would influence the density of the SLS printed parts.

Under dioxygen and nitrogen atmosphere, in the first hours of SLS process, cross-linking of PA12 dominates whereas chain scission occurs at long storage times under O<sub>2</sub> [223]. Cross-linking of PA12 material is the dominant effect during the SLS process. Wudy et al. [223] reported that mixing fresh and recycled powder may improve the flowability of melt. Due to the cross-linking effect the average molecular mass of the polymer increases, which influences the melt flow behaviour. Nevertheless, using recycled powder can decrease the mechanical properties. Wudy et al. [223] showed that tensile strength decreases with an increasing number of processing cycles at 175 °C. The tensile strength is 35 MPa after the first cycle, while during the second one it decreases up to 5 MPa and even less with the next cycles.

#### **2.6.4. Conclusion on the effect of recycling of PA12**

From an economic perspective, it was investigated if the powders that have gone through a printing cycle can be used again to make new parts. The properties of recycled and fresh PA12 powders have been compared. No drastic chemical change is revealed when comparing fresh and recycled powder by TGA. The residual mass is higher for fresh PA12 powder. It could be an indication of a previous degradation inside the recycled PA12 sample. The water absorption is higher for recycled powder than for fresh powder: more hydroxyl (-OH) groups could be onto the surface of the recycled powders, resulting in more hydrogen bonds with H<sub>2</sub>O.

The time sweep for fresh PA12 shows that the  $G'$ ,  $G''$  and thus the  $\eta^*$  are quite stable for 100 s, then, they progressively increase with time. This increase in  $M_w$  arising from further polycondensation. When studying the rheological properties of recycled PA12, there is almost no further evolution of the complex viscosity with temperature, it looks that the chemical structure is almost stabilized. On the contrary, the  $\eta^*$  of fresh PA12 changes with temperature from 200 °C to 240 °C.

## 2.7. Conclusion

Some polyamide and polyetheretherketone powders have been selected for this study. A few of them are suitable for SLS, the others are intended for other purposes. Nevertheless, they all have been characterized to get a deeper knowledge of the properties required for SLS.

First of all, the shape and size of powders have been studied by SEM images. It was possible to compare polyamide powder, already used for selective laser sintering process with polyetheretherketone powders. The PA12 powder is not perfectly spherical, their average circularity is  $0.61 \pm 0.21$ , while polyetheretherketones have the average circularity between 0.30 and 0.45. The PEEK 2000 FP and PEEK 880 SFP have a comparable shape ratio as PA12, of around 1.66. The particle size distribution of powders has been checked by image analysis and laser diffraction granulometry: it was noted that the results are close to commercial data. The PEEK HP3 grade is already used for selective laser sintering process and the average particle size is  $77.8 \pm 1.6 \mu\text{m}$ . The closest grade to this value among the tested powders is PEEK 2000 FP with an average particle size of  $73.2 \mu\text{m}$ .

Next, the flowability of powders was carried out by density and angular measurement. PA12 as a suitable powder for selective laser sintering process is characterized by a “good” and “excellent” flow behaviour, in contrast to polyetheretherketone powders. In the group of polyetheretherketone powders, PEEK 2000 FP can be distinguished with the angle of repose  $49.4^\circ$  and Hausner ratio of 1.49, which are the closest to the expected ones. However, the reduction of powder flowability may presumably affect the process stability and reproducibility negatively. The most compact powders are polyamide 12 and PEEK 450 G, for the latter, it may be due to its bigger size compare to other polyetheretherketones. Incorporation of nano and microparticles can slightly improve the flowability of powders. The surface modifications by chemical treatments do not improve enough the flowability to make them suitable for the selective laser sintering process.

Differential scanning calorimetry has been used to measure the melting and crystallization temperature, which define the sintering window for the selective laser sintering process. The widest window was noted for PEEK HP3, which is around  $72^\circ\text{C}$ . In the case of other polyetheretherketone and polyamide powders, the windows are quite narrow, and controlling the process can be difficult. The degree of crystallinity of around 40 % is measured for PEEK HP3 grade whereas for others PEEK powders, it is around 25 %. PEEK HP3 is a copolymer of polyetherketone and polyethersulfone. Two glass transition temperatures have

been measured at around 165 °C and 185 °C, which indicate PEK and PES, respectively. The composition was confirmed by FTIR spectroscopy. Moreover, the thermal conductivity of PEEK 2000 FP has been measured on the consolidated state at  $0.24 \text{ W}\cdot\text{m}^{-1}\cdot\text{K}^{-1}$  for the density of  $1300 \text{ kg}\cdot\text{m}^{-3}$  and was calculated for tapped powder at  $0.15 \text{ W}\cdot\text{m}^{-1}\cdot\text{K}^{-1}$  for the density of  $1007 \text{ kg}\cdot\text{m}^{-3}$ .

The rheological properties in the molten state have been measured by rheometry. It was noted that the thermal degradation of the powders is a problem for the selective laser sintering process and it occurs faster with the increase in temperature. An accelerating factor of degradation for powder is oxidation and temperature. thus the process must be done in a nitrogen atmosphere to avoid dioxygen. The process must, therefore, be carried out in a nitrogen atmosphere and at temperatures that impose a narrow printing temperature range for the process. The terminal relaxation times have been calculated from the rheological measurements. They correspond to the time needed by the longest macromolecules to move out the tube in the reptation theory. This time is from 0.8 ms to 1.4 ms, which means that the temperature must be maintained high enough to allow inter-diffusion of polymeric chains this duration.

The properties of PA12 powders that have gone through a printing cycle, namely recycled powder, have been compared with fresh powder to estimate the possibility to re-use them. No significant change in the chemical structure has been shown in our work. We have highlighted a slight degradation increasing viscosity, and so, increase in relaxation times. Further investigations are necessary to judge how much recycled material could be mixed with a fresh one to be processed. Also, the build time, the position in the work chamber, as well as, the type of selective laser sintering machine should be considered. For example, Pham et al. [137] reported that the powder collected from the building periphery, where the temperature was high only for a short period, is less damaged than the material collected from the building centre.

The results of this chapter show that there is a lack of polyetheretherketone powders suitable for the selective laser sintering process on the market. Even the copolymer HP3 has been identified with some unrequired properties which may affect the properties of printed parts. Thus, in the next step of our work, we intend to elaborate on new material based on the melt blending of polyetheretherketone with an amorphous polymer. Based on the results of this chapter, the following polymers were selected PEEK 450 G (granules) and Vestakeep 2000 FP (powders), purchased from Victrex and Evonik, respectively. The first polymer selected will represent the material with long chains and the second with short ones.



### **3. ELABORATION OF A NEW MATERIAL: PEEK/PES BLENDS**

The polyetheretherketone-based powders currently available on the market are not adapted to the selective laser sintering process because of various characteristics already identified, except HP3 from EOS. Because of the monopoly, the cost and availability of this powder are still an impediment to the large use of this material. The main objective of this chapter is to develop new material with controlled properties to fit the requirements of SLS.

Our strategy is to elaborate a polyetheretherketone-based blend. With regards to the composition of HP3 made of PES/PEK copolymer, the polyethersulfone was chosen to be mixed with PEEK. The polyetheretherketone and polyethersulfone blends have been prepared by melt mixing using an extruder. The resulting blends have been characterized for various relative weight ratio.

The main requirement was to obtain miscible blends with a large sintering window, that is to say with a delayed crystallization on cooling while keeping high mechanical strength at the glassy state. It was decided to work with two types of polyethersulfone and two types of polyetheretherketone in granules (PEEK 450 G) and powders (PEEK 2000 FP) form. One with a long chain, PES 3010 G, and the other with a short chain, PES 1010 G have been chosen. The datasheet of each material can be found in Annex A.1. Indeed, a blend with longer chains would give an immiscible material or partially miscible, but with high mechanical rigidity, while a blend with shorter chains would result in a material with better miscibility but lower rigidity. After presenting the theory of blends, the properties of PEEK/PES blends are exposed. In the last section of this chapter, the properties of PEEK/PES blends with a compatibilizer are shown. Finally, some advice for further work are presented.

### 3.1. Theory of blends

Polyaryletherketones offer a compromise between mechanical properties, chemical resistance and durability; however, cutting-edge applications require multifunctional materials. Ideally, one material should fit all the targeted properties. Blending two polymers may be the easiest option to design such materials. Indeed, two or more thermoplastics, often chosen such as their properties complement one another, yielding a new material with “best-of-both-world” properties.

The miscibility of the two polymers is often required, especially in load-carrying applications, since bad miscibility gives a weak interfacial adhesion, leading to a poor stress transfer from one to the other phase, up to fracture. In some specific cases, blends of immiscible polymers may be used to design a nano or microstructure. Polymeric blends are generally classified according to their homogeneity or heterogeneity (miscible or immiscible). Miscible blends are characterised by one phase, even if they may undergo phase separation due to temperature, pressure or composition changes. The miscibility of a polymeric blend depends on the Gibbs energy value of blend:

$$\Delta G_m = \Delta H_m - T\Delta S_m \quad (3.1)$$

where:

- $\Delta G_m$  - Gibbs free energy [J];
- $\Delta H_m$  - enthalpy of mixing, heat consumed (endothermic) or generated (exothermic) [J];
- T - temperature [K]
- $\Delta S_m$  - entropy factor [J.K<sup>-1</sup>].

During mixing, if the system is exothermic, the blend can be miscible. Phase separation in polymeric blends is either by nucleation or by growth or combination of them both and the most commonly observed phase diagrams display phase separation during heating and cooling. If there are strong interactions between the phases, the blend may be miscible [224].

The miscibility of polymer blends is most often checked by the measurement of glass transition temperature for the compositions [225,226]. An immiscible blend displays two distinct glass transitions ( $T_g$ ) while a miscible blend is characterized by only one  $T_g$ . From thermodynamically considerations, such as developed by Couchman [227], the glass transition temperature was found to depends on the composition of miscible blend, and usually increases with it. Several equations have been developed on those assumptions, to describe the glass

transition temperature dependence over the composition. The well-known Fox equation [228] may be the most widely used for polymer blends.

$$\frac{1}{T_{g,mix}} = \frac{\sum_i w_i}{T_{g,i}} \quad (3.2)$$

where:

- $T_{g,mix}$  - glass transition temperature of blend [K];
- $T_{g,i}$  - glass transition temperature of components [K];
- $w_i$  - mass fraction of component [g].

while more sophisticated equations, as the Gordon-Taylor equation [229], have been developed based on the same theoretical basis, but with a different hypothesis:

$$T_g = \frac{w_1 T_{g1} + K w_2 T_{g2}}{w_1 + K w_2} \quad (3.3)$$

where:

- $T_g$  - glass transition temperature [K];
- $T_{g,i}$  - glass transition temperature of components [K];
- $w_i$  - mass fraction of component [g];
- $K$  - adjustable fitting parameter which can be variable [-] [18].

More equations derived from those considerations may be found in the report by Aubin and Prud'homme [230].

Depending on the processing conditions and blend compositions, immiscible polymer blends can form various phase morphologies. However, immiscible polymer blends may be divided into two main categories: one component forms a continuous phase and the other component forms a dispersed phase, and the second category presents each component as a continuous phase, giving rise to an interlocked or interpenetrated state of dispersion [231].

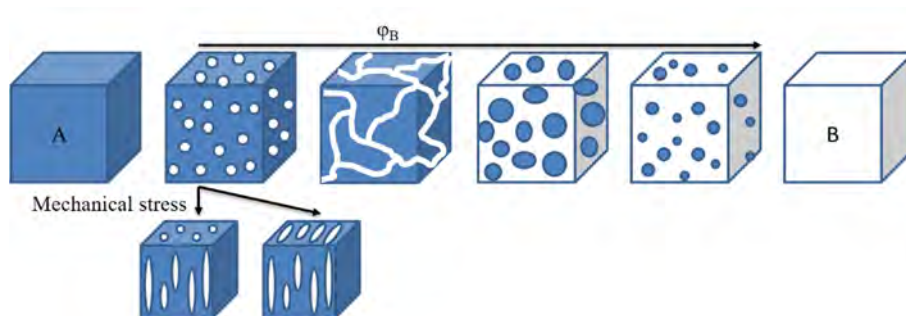
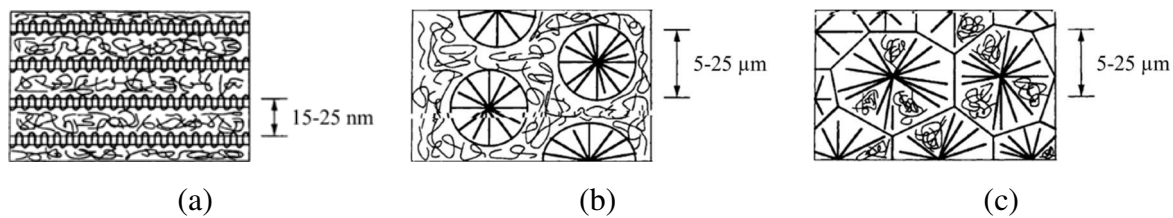


Figure 3.1. Basic types of phase structures in polymer blends

The vast majority of polymer blends can be classified as a blend with either a depressed or continuous morphology, as shown schematically in Figure 3.1. The low amount of component B allows to form dispersed particles surrounded by a matrix of component A. By increasing the amount of phase B, the size of dispersed domains grows and the first continuous structure appears by approaching the threshold of geometric percolation. With the further increase in the concentration of phase B, the structure of phase A disintegrates and finally, the phases invert. To minimize the free surface energy of the system, the dispersed particles tend to achieve a spherical shape. Nevertheless, many anisotropic particle shapes, such as ellipsoids, fibrils or platelets can be observed in polymer blends, as a final morphology is often quenched immediately after melt processing. Thus, any particles deformed by mechanical stress applied in the blending devices are solidified before they can obtain a spherical shape [232].



**Figure 3.2. Morphology of (a) interlamellar (b) interspherulitic (c) interfibrillar in blends [233]**

The semi-crystalline/amorphous blends may develop three types of no-crystalline segregation morphology [233–236] such as

- interlamellar, where the semi-crystalline polymer form pure lamellae, alternating with amorphous rich phase;
- interspherulitic segregation, where spherulites develop in an amorphous rich matrix;
- interfibrillar (interlamellar-bundle), where the amorphous polymer may be trapped between bundles of the semi-crystalline polymer.

Competition between diffusion of amorphous component out of crystal domains and crystal growth is the controlling factor, while strong segmental interactions may hinder the former competition. In the case of weak interactions, interlamellar (first and third morphologies cases may be favoured if the amorphous component diffuses fast and that crystal growth is slow. Conversely, trapping of amorphous components may occur, leading to spherulitic morphologies.

In any case, immiscible polymers may be compatibilized. It helps to bond the two phases to each other more tightly. The addition of compatibilizer is the main route to obtain melt-mixed polymer blends [237]. Compatibilizers may be classified into two categories: under the form of nanoparticles or the form of block copolymers. Thus, the length of blocks and the number of copolymers may control the stability and the final morphology of blends.

### 3.2. Choice of polymers for blends

Polymer blends are homogeneous mutual solutions or colloidal blends of two or more polymers of varying chemical structure, to create a new material with different physical properties for commercial applications [224]. Usually, the blends are produced by their direct mechanical stirring in a liquid (solution blending) or by melt-mixing with twin screw extruder.

One possible option is the blending of polyaryletherketones with high-performance amorphous polymers. Incorporation of an amorphous polymer in a semi-crystalline matrix induces an increase of the amorphous phase, thus reducing the distribution of the crystalline phase. The amorphous phase is considered as a diluent for the crystalline phase. Thus, the more amorphous content the more difficult it is the crystallization of the crystalline phase. It is then possible to delay the crystallization by blending an amorphous polymer with the targeted semi-crystalline polymer. A wide review considering this topic has been done during this thesis on polyaryletherketones-based polymeric blends with high-performance polymers. The article will be submitted soon. It is the basis for choosing the right polymer blend to obtain a new material suitable for the selective laser sintering process.

To fit the requirements of the selective laser sintering process, the polymeric material should have to follow properties:

- thermal properties: for semi-crystalline polymers, the sintering temperature should be between the initial crystallization temperature ( $T_c$ , onset) and the initial melting temperature ( $T_m$ , onset). This area is named “sintering window” and it is one of the indicators characterizing the applicability of a given polymer in the selective laser sintering technique [238]. The theory of quasi-isothermal laser sintering signifies that polymer melt and powder coexist during the whole building process [239];
- degree of crystallinity: the lower the degree of crystallinity, the less the polymeric part shrinks, and thus the part may be characterized by greater dimensional accuracy of model [240];
- viscosity and surface tension: low values of both properties are necessary for the proper combination of macromolecules. This is of particular importance in the sintering process, as there are no additional shearing forces, compared to injection moulding or extrusion. The polymeric particles coalescence is mainly driven by viscosity and surface tension of melt [24];

- shape and size of particles: individual powder particles should be as close as possible to spherical shape. Such a powder has good flow properties so that even thin layers can be obtained. At the same time, models obtained from spherical granules have the highest density. The literature shows that the optimal diameter of powder granules should be in the range of 20-150  $\mu\text{m}$  or with an average particle size of approximately 60  $\mu\text{m}$ . Also, the grain size distribution should be fairly even and narrow [172]. After exposure, the building chamber is lowered by the thickness of one layer, usually between 0.08 mm and 0.15 mm and a new layer of powder is applied.

To control the above properties for the selective laser sintering process, the opportunities offered by blending polyetheretherketone and polyethersulfone have been investigated. Generally, blending semi-crystalline and amorphous polymers can lead to improved processing properties while enhancing shape accuracy and geometric fidelity [241,242].

Based on the results obtained in chapter 2, the characterization of powders available on the market: PEEK and PA, it is known that HP3 copolymer is suitable for the selective laser sintering process. The HP3 copolymer composition includes, among others, polyetherketone and polyethersulfone. This composition has motivated more research work on polyetheretherketone and polyethersulfone blends, the latter is explained in the following subsections.

### **3.2.1. PEEK / PES blends**

Polyetheretherketone and polyethersulfone blends were found to be compatible when prepared by solution blending in diphenyl sulfone at 310 °C, with a single glass transition temperature reported by Yu et al. [243] for the various compositions. It has to be noted that the films processed by compression moulding at 310 °C have been found with one glass transition temperatures for each composition. However, when the films are processed at 350 °C, it was found that there exist two glass transition temperatures for each blend. It indicates that phase separation occurs in this case. Therefore, it means that the phase diagram would reveal a low critical soluble temperature behaviour with the cloud point located between 310 °C and 350 °C when the fraction of PES is in the range from 70 wt.% to 30 wt.%. Besides, partially miscible polyetheretherketone and polyethersulfone blends have been investigated by Malik [244]. For more than 30 wt.% of PEEK in the blend, an amorphous behaviour with glass transition temperature close to the pure polyethersulfone is showed. The degree of crystallinity and melting peak significantly decrease with the amount of PES in the blend, from 42 % to 27 % and from 342 °C to 325 °C, respectively.

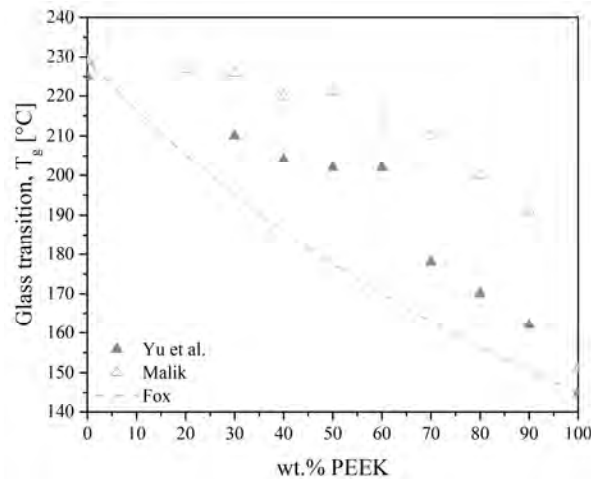


**Figure 3.3.** The  $T_g$  of PEEK/PES blends versus PEEK composition of different authors [243, 244]

The glass transition temperature of each blend progressively changes between the glass transition temperatures of homopolymers in the amorphous blends, according to the Fox equation within experimental error. In his work, Ni [245] prepared the blends by solvent mixing in sulphuric acid,  $H_2SO_4$  (98 %). The 50/50 PEEK/PES blend has two glass transition temperatures at 146 °C and 230 °C, the crystallization peak is at 180 °C and the melting point at 333 °C. The presence of two separated phases was indicated. The partial compatibility between PEEK and PES is obtained, while the PES component reduces the degree of crystallinity of PEEK in the blend. Investigated by Arzak et al. [246] a quenched 50/50 PEEK/PES blend was immiscible with two glass transition temperatures at 144 °C and 220 °C, the crystallization temperature at 180 °C and the melting point at 335 °C. Similar results were obtained for almost all PEEK fractions.

The values of  $T_g$  measured for PEEK/PES blends are reported in Figure 3.3. Other authors have studied some properties of PEEK/PES blends, mainly thermal stability and mechanical properties.

The thermodegradative behaviour of blends has been studied by Nandan et al. [247] up to 700 °C under a nitrogen atmosphere. The results show that PEEK is more stable than PES, but the degradation is faster in PEEK. Both exhibit thermal degradation below 700 °C with the degradation occurring between 450 °C and 650 °C for PES. They also show that the presence of one component affects the thermal degradation behaviour of other component and that the blend has lower thermal stability compared to each component. This is due to the chemical interactions between the degradation products of PES and PEEK and the reduction of viscosity of the medium.

According to Yu et al. [243], the elastic modulus of PEEK at a range of 150-180 °C drops dramatically from around 1200 MPa at room temperature, while for PES the modulus decreases at 240 °C. The addition of PES can remarkably improve the dynamic mechanical properties at elevated



temperature. For the blend 40/60 PEEK/PES, the elastic modulus is about ten times of those for pure PEEK at temperatures 180-220 °C. Malik [244] has reported that tensile strength and tensile modulus also significantly increase with PES addition from 77 MPa to 135 MPa and from 2550 MPa to 4650 MPa, respectively. An irregular enhancement of mechanical properties is observed with increasing PEEK amount to a max of around 60 %, then drops and follow the linear rule of blending.

The morphology of 20/80 PEEK/PES blend shows the spherical and well distributed, in the PES matrix, domains of PEEK, as results from phase separation. The good interfacial adhesion between both components was also observed by Malik [244].

To sum up, PEEK and PES are not miscible from a thermodynamic point of view. However, some compatibility may be achieved for particular blending conditions. Compatibility arises from specific interaction between sulfonated PES and PEEK backbone, hence mechanical properties slightly deviating from additivity rules.

### 3.2.1.1. Structure and properties of polyethersulfone (PES)

The polysulfones are a family of amorphous engineering thermoplastic polymers. They are known for their toughness and stability at high temperatures. Their glass transition is 225 °C [243], with a tensile modulus of 2650 MPa at 23 °C. The density of polyethersulfone is 1.37 g.cm<sup>-3</sup>. It has good hydrolytic stability with water absorption of 0.8 % and thermo-oxidative stability up to 190 °C [246].

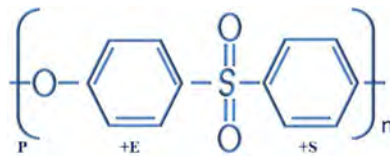


Figure 3.4. Structure of PES

The structure of the PES is presented in Figure 3.4. The polyphenylene sulfone when heated, it remains rigid with no melted state until it decomposes at around 500 °C. This implies an impossibility of processing. For this, it is necessary to make the chain more flexible so that the polymer softens at a reasonable temperature. This is where the ether groups come in because of their flexibilities.

Comparatively to polyaryletherketones, this family of polymers has very interesting properties and characteristics explained below:

- good tensile strength and elastic modulus of 85 MPa and 2650 MPa at 23 °C, respectively, while it is 98 MPa and 4000 MPa at 23 °C for PEEK.

- good creep resistance, retaining between -100 °C and 150 °C, while PEEK has a maximum temperature to continues uses of 250 °C and a processing temperature of 370 °C to 400 °C [88].
- good dielectric constant and high transverse resistivity at temperatures above 200 °C. The dielectric constant of polyethersulfone at 20 °C is 3.5, while at 23 °C for polyetheretherketone is 3.0;

Because of its fire behaviour, the polyethersulfone is used as a composite with laminated sheets and expanded polystyrene for interior aircraft coatings. More details of these materials are available in Annex A.1.8 about Ultrason E 1010 PESU and Annex A.1.9 about Ultrason E 3010 PESU. It is important to note that this application is approved by Airbus Industries and Federal Aviation Regulation. Other applications of polyethersulfone are the air conditioning ducts and radar overlay materials due to the radio wave transparency of PES.

### **3.2.2. Compatibilization**

Compatibilization is an addition of a substance to an immiscible blend of polymers that increase its compatibility and stability. Polymeric blends are typically described by coarse, unstable phase morphologies. This results in poor mechanical properties. Compatibilizing the system makes a more stable and better-blended phase morphology by creating interactions between the two previously immiscible polymers. This not only enhances the mechanical properties of blend, but it often yields properties that are generally not attainable in a single pure component.

#### **3.2.2.1. PEEK / PES blends with compatibilizer**

Ternary blends may be relevant as hinted in the previous sections. Indeed, the third component in this particular family of the blend may act as a link between two immiscible materials, provided it is miscible with the both.

One of the mechanisms for the compatibilization of immiscible blends is the addition of segmented block copolymers of the type (A-B)<sub>n</sub> consisting of segments chemically comparable to the parent homopolymers [248]. Properties of segmented block copolymers in PEEK/PSU blends were studied by Hoffmann et al. [249]. Summarizing the mechanical properties, improved strength and toughness were reached, but the effectiveness of the segmented block copolymers was hindered by the missing phase separation between the PEEK and PSU segments.

Mitschang et al. [250] reported a blend of PEEK/PEI/PES used as composite matrices. The tensile strength, modulus and elongation have been reported as 92 MPa, 3400 MPa and 5.4 %, respectively. While the mechanical properties for neat PEEK were 100 MPa, 3500 MPa and

5.0 %, for neat PEI were 105 MPa, 3200 MPa, and 6.0 % and for neat PES were 90 MPa, 2700 MPa and 6.7 %, respectively. It can be already observed that three different polymers may be successfully blended with a slight lowering in mechanical properties. Looking at the reachable laminates qualities, the blend obtained the maximum bending strength of 1096 MPa with bending stiffness of 49 GPa, while the maximum is 62 GPa with a crystallinity of 12 %.

Blends of PEEK/PEK-C (PEK with cardo side groups) or PEEK/PES-C (PES with cardo side groups) have high operating temperature and good mechanical properties. They are partially miscible with a slower crystallization, lower melting point and lower PEEK degree of crystallinity [251–253]. The cardo side group may be created by phenolphthalein, Figure 3.5. Polymers with cardo side groups are a subgroup of polymers where carbons in the backbone of the polymer chain are also incorporated into ring structures.

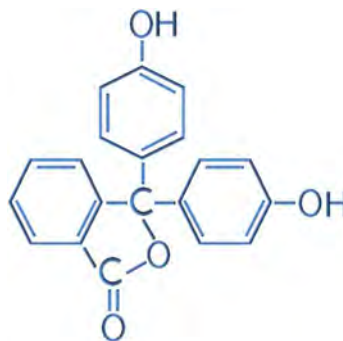


**Figure 3.5. Structure of phenolphthalein**

The process of preparing PEK-C or PES-C is through the aromatic nucleophilic substitution reaction of phenolphthalein (Phph) with 4,4'-dichlorobenzophenone or 4,4'-dichlorodiphenyl sulfone in sulfolane in the presence of potassium carbonate. However, these polymers, as well as other polyarylethers, suffer greatly from the high softening temperatures and especially the high melt viscosities, which combine to limit the application of these materials in areas such as fiber impregnation and microscale fabrication. An alternative route to produce PEK-C and PES-C is through ring-opening polymerization of macrocyclic precursors [254,255].

### **3.2.3. Conclusion on the choice of polymers for blends**

The polyethersulfone is a good candidate to be blended with polyetheretherketone as it may enhance the polyetheretherketone thermal stability. Polyetheretherketone and polyethersulfone were found to be poorly or only partially miscible, but some degree of compatibility may be achieved depending on the method chosen to prepare the blends. In this work, two kinds of compatibilizers have been chosen, the first one is HP3 copolymer considered as triblock copolymers and the second one is phenolphthalein.

### 3.3. Characterization of uncompatibilized blends

In this work, the effect of blend ratio and compatibilizer on thermo-mechanical properties of PEEK/PES blends were investigated. Then, dynamic mechanical properties have been correlated with the morphology of the blends observed by scanning electron microscopy.

#### 3.3.1. Preparation of blends

Two types of polymeric material can be specified. The matrix of each blend are high-temperature polymers, the main base is polyetheretherketone, while polyethersulfone is up to 30 wt.% of the blends

The polymers used are commercial products. Their properties are shown in Table 3.1. The selected polyetheretherketones were PEEK 450 G (granules) and Vestakeep 2000 FP (powders) to cover two molecular weight, purchased from Victrex and Evonik, respectively. Polyethersulfones were Ultrason E1010 G and Ultrason E3010 G from BASF. PES 1010 G represents short chains, while PES 3010 G longer chains. The molecular weight of polyethersulfones has been provided by the supplier.

**Table 3.1. Properties of the blend components**

Polymer	Melt flow index [g.10min <sup>-1</sup> ]	Molecular weight [g.mol <sup>-1</sup> ]	Density [g.cm <sup>-3</sup> ]
PEEK 450 G	5	115.000 [217]	1.30
PEEK 2000 FP	70	33.000	1.30
Ultrason E1010 G	150	35.000	1.37
Ultrason E3010 G	35	58.000	1.37

##### 3.3.1.1. Realization of blends

The PEEK and PES polymers were blended in ratios of 100/0, 90/10, 80/20, 70/30 and 0/100 (wt.%), respectively. Before blending, the neat polymers were completely dried in a vacuum oven at 120 °C for at least 48 hrs. Melt mixing was carried out in the parallel-twin screw microextruder, Process 11, described in Annex A.3.1. Before extrusion, the two chosen polymers were physically blended with appropriate weight ratios in small batches of 10 g and then fed into the feeder of the twin-screw extruder. The temperature of the rotors and die zone were kept at 350 °C and the rotor speed of 70 rpm was used for all blend compositions. In our conditions, the residence time of material (time during which the polymer fall from the

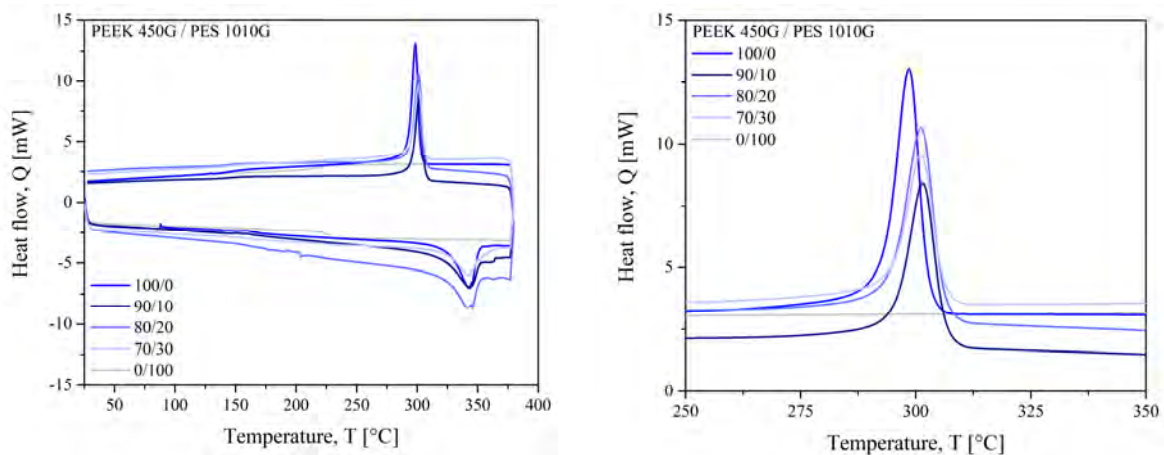
dispenser until it is extruded by the die) inside the blending zone was measured at 2.20 min. This residence time is short enough to prevent degradation. The blend is extruded into filaments through a 2 mm diameter die. The filaments are cooled under air. Further, the filaments were chopped into small granules.

### 3.3.1.2. Production of plates by compression

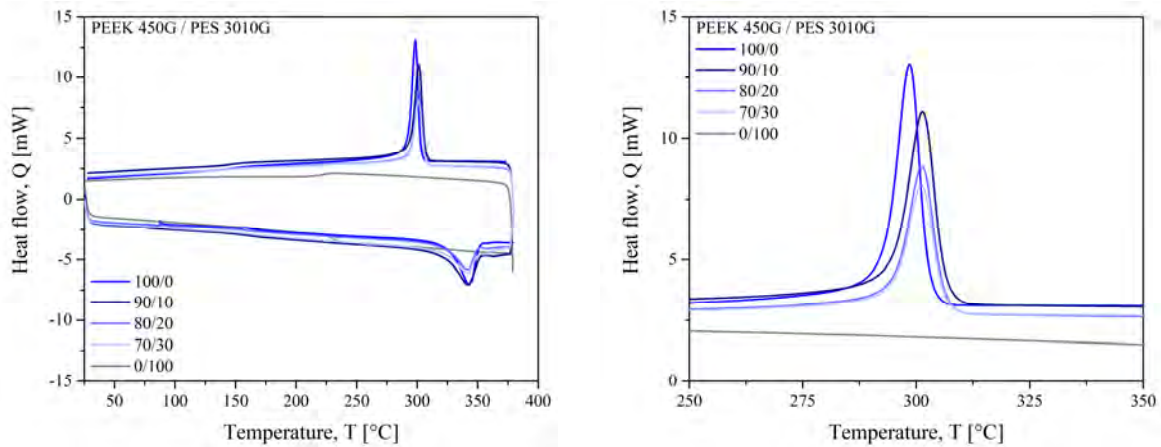
For further testing, the blends were processed by compression moulding. A hydraulic press LAB 800P PEI from Pinette Emidecau Industries was used for preparing 2 mm thick plates. The granules were dried in a vacuum oven at 150 °C for at least 3 hrs. A steel mould with a 149 mm x 76 mm x 2 mm cavity has been used. Granules of blends were kept in the cavity between two steel foils and placed between the plateau of the press, which was preheated at 200 °C. Next, the temperature was increased at 10 °C.min<sup>-1</sup> until 360 °C and a pressure of 50 kN was applied for 5 min. Then, the moulded samples were cooled down at the speed of 4 °C.min<sup>-1</sup> inside the press under pressure up to 200 °C, separated from steel foils and left at room temperature to slowly cool down.

### 3.3.2. Study of miscibility by DSC and DMTA

Differential scanning calorimetry tests have been done, for which the samples were cut from plates produced by compression moulding. The procedure is explained in Annex A.2.4.1. Glass transition, crystallization, melting point and miscibility of blends have been determined with the precision more or less 1 %. All tests were carried out at a scan rate of 10 °C.min<sup>-1</sup> under nitrogen from room temperature to 380 °C and cooled down at the same ramp up to 25 °C. The specimens have been previously dried for at least 3 hrs at 150 °C. The mass of samples was approximately 10 mg.



(a)



(b)

**Figure 3.6. The DSC of (a) long-short (b) long-long chains for PEEK 450 G and PES blends**

Typical thermograms obtained for PEEK 450 G and PES blends are shown in Figure 3.6. Two  $T_g$  associated to PEEK 450 G at 147.4 °C and to PES 1010 G at 231.8 °C and PES 3010 G at 236.4 °C appear in the samples. The melting endotherm of PEEK is observed at around 340 °C. On cooling, an exothermic peak is seen at around 300 °C which corresponds to the crystallization of PEEK. When comparing PEEK 450 G and PES 1010 G blends in Figure 3.6.a on the right the crystallization onset temperature slightly increases with the amount of PES from 304 °C to 306 °C.

As expected, the blends are partially miscible in all compositions. Indeed, more the blends are miscible, more the glass transition temperature is tending to get closer between the glass transition temperature of PEEK and that of PES. This indicates the presence of two virtually pure phases in the blends.

The thermomechanical properties of blends were performed by dynamic mechanical analysis, explained in Annex A.2.5. The 45 mm x 10 mm x 2 mm rectangular specimens were dried for at least 3 hrs at 150 °C. The tests were carried out in torsion mode at a frequency of 1 Hz within the viscoelastic linear domain at a heating rate of 3 °C.min<sup>-1</sup> from 25 °C to 325 °C. The uncertainty is considered at more or less 2 %. The shear storage modulus ( $E'$ ) characterizing the elastic behaviour of the blend, the shear loss modulus ( $E''$ ) characterizing the viscous behaviour of the blend, and loss factor ( $\tan \delta = E''/E'$ ) were determined.

The DMTA responses are presented in Figure 3.7. for PEEK, PES and their blends. The curves of PEEK and PES represent the typical behaviour of their respective structures. They both display a  $T_\alpha$  that represents the onset of molecular motion in the amorphous region. In PES, the mechanical strength decreases after the  $T_\alpha$ . However, in PEEK, the decline in modulus is around 50 % compared to those at room temperature, due to the contribution of the rigidity of the crystalline structure.

The dynamic mechanical analysis gives information on the mechanical properties and the compatibility of the blends. The value of storage modulus  $E'$  signifies the stiffness of the material. The curves with PEEK show three distinct regions: a high modulus glassy region where the segmental mobility is restricted, a transition zone where a substantial decrease in the storage modulus with the increase in temperature and a rubbery region (the flow region) where a drastic decay in the modulus with temperature is seen. The storage modulus curve of PES shows the typical behaviour of an amorphous polymer, which migrates from energy-elastic to entropy-elastic state after reaching the glass transition temperature.

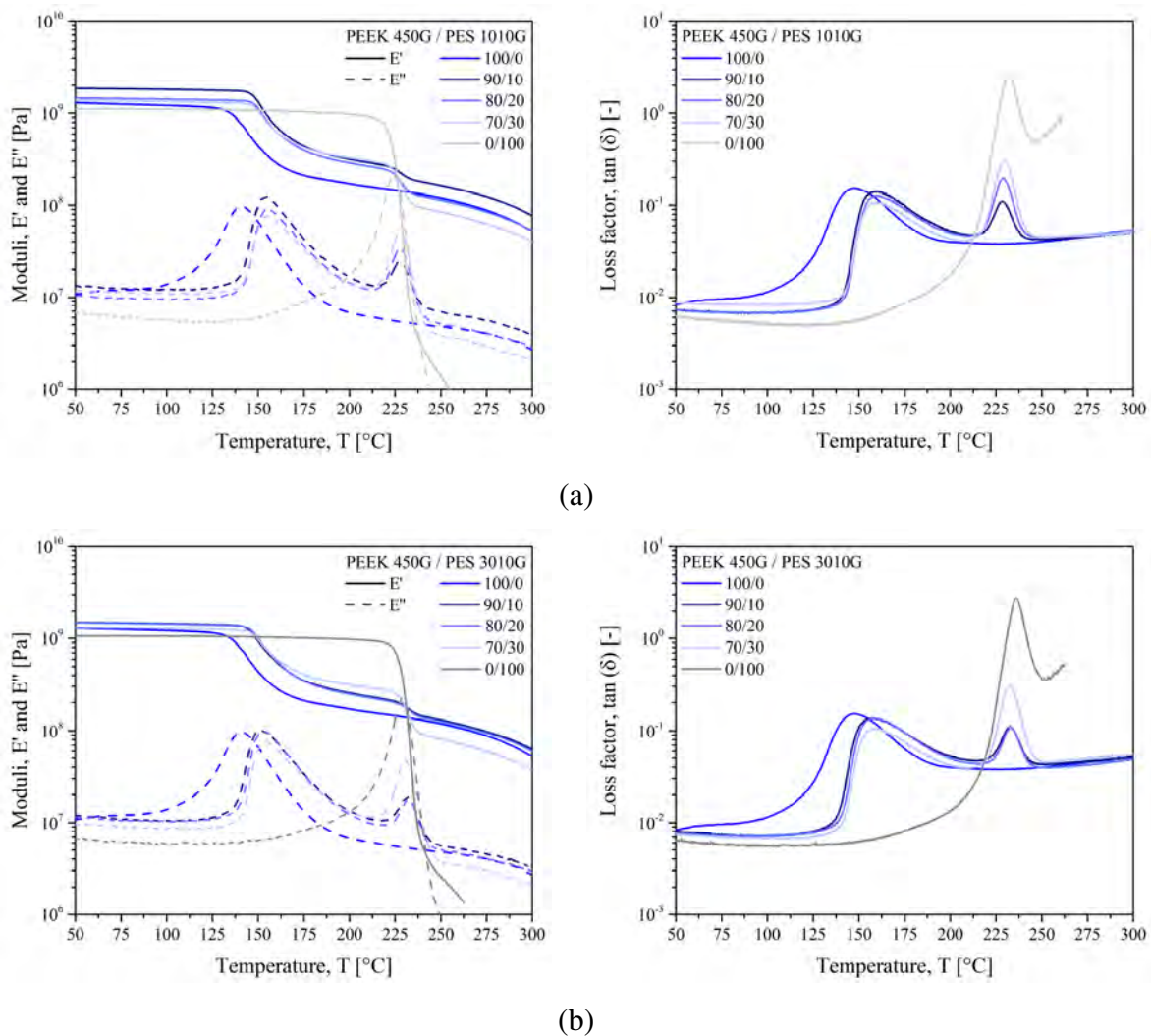


**Figure 3.7.** The DMTA of (a) long-short (b) long-long chains for PEEK 450 G and PES blends

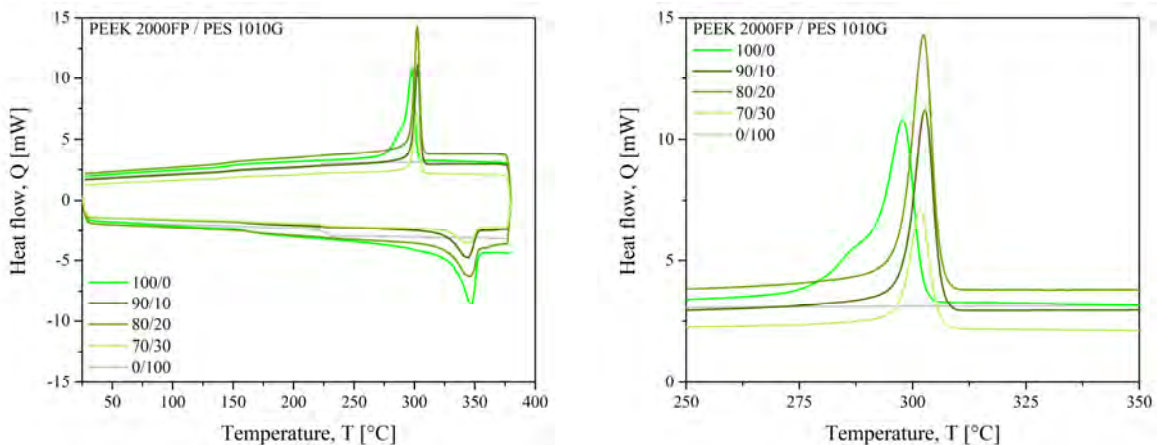
All the blends show a clear dependency on PES content. The storage modulus is presented from 50 °C to 300 °C. It can be observed that the elastic modulus increases for all the blends compare to neat thermoplastics. The storage modulus at 50 °C is 1294 MPa, 1109 MPa and 1057 MPa for PEEK 450 G, PES 1010 G, and PES 3010 G, respectively. The highest modulus of 1850 MPa has been obtained for 90/10 wt.% blend of PEEK 450 G and



PES 1010 G. It can also be noted that the storage modulus decreases with increasing the amount of PES content. Once heated above the glass transition point of PEEK (147 °C) the storage modulus dropped to a significantly lower level for each composition around 160 °C. The glass transition temperature of the PES portion (above 225 °C) limits the relevant stability of the blends. However, the presence of PES led to a plateau of elastic modulus at high temperatures. All blends show a storage modulus of around 300 MPa at 200 °C. The presence of PES significantly elevates the thermal stability of all blends while lowering the modulus at moderate temperatures.

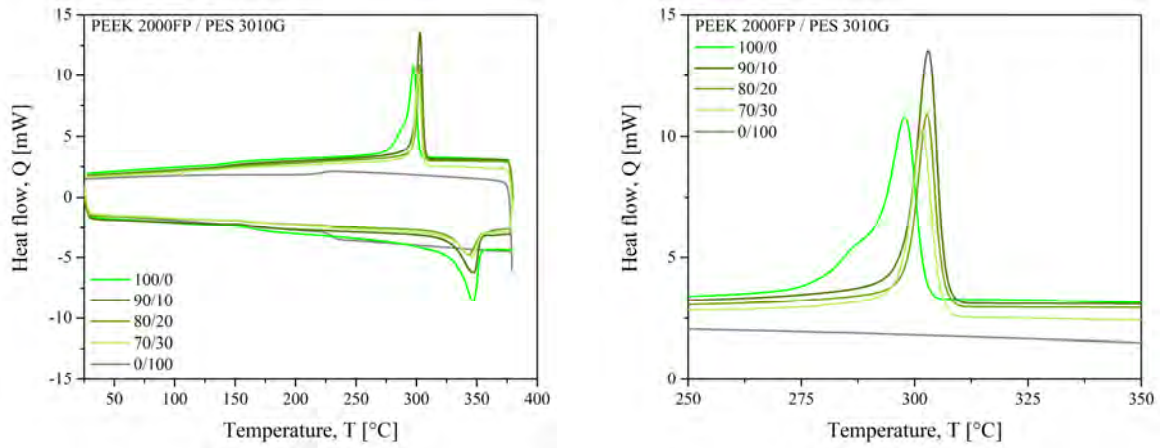
Then, Figure 3.7 presents the loss factor versus temperature curves for PEEK/PES blends. It can be seen the characteristic immiscible behaviour with two peaks corresponding to the glass transition temperature of PEEK and PES phases. The highest transition for PEEK is measured at 160 °C in the blends. The glass transition of pure PEEK is 147 °C, which means that there is a shift towards the higher temperatures due to the presence of the PES phase. Similarly, the  $T_g$  of PES is shifted towards lower temperatures. This indicates that some PES segments are dissolved in the PEEK phase, whereas some PEEK segments are dissolved in the PES phase. Hence there is an existence of PEEK-rich and PES-rich phase in each blend composition, also observed by Nandan et al. [27] with differences of glass transition temperature for PEEK from 164.2 °C to 171.3 °C and PES from 234.5 °C to 225.7 °C in the composition of 75 wt.% of PEEK.

One important goal of this study is to delay the crystallization on cooling. Recall that these blends are intended for the SLS process and that PES was chosen to delay the crystallization of PEEK on cooling. After analysis, it was found that there is no significant delay in the crystallization point. It was decided to make other blends with the PEEK 2000 FP which represents shorter chains than PEEK 450 G, with expected better miscibility. DSC thermograms for PEEK 2000FP/PES are presented in Figure 3.8.



(a)



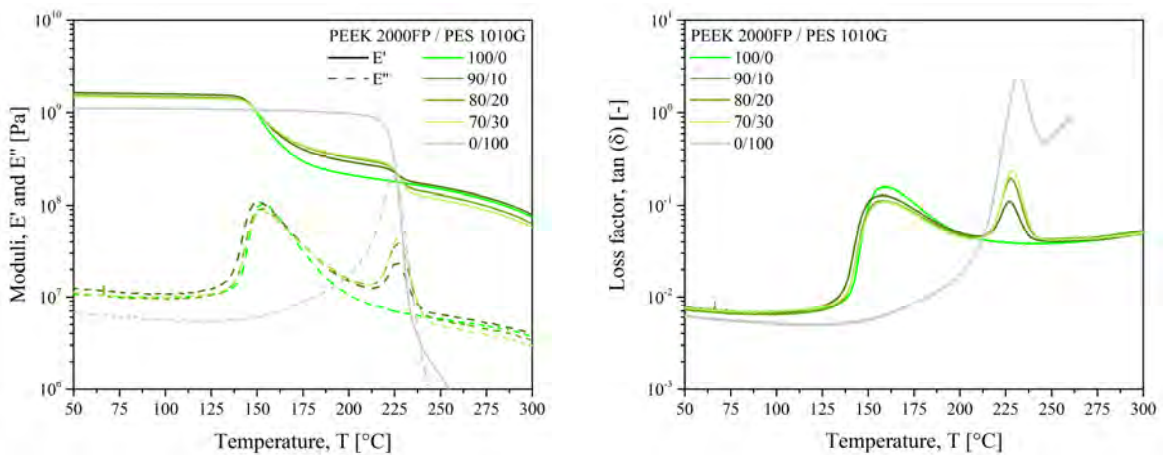


(b)

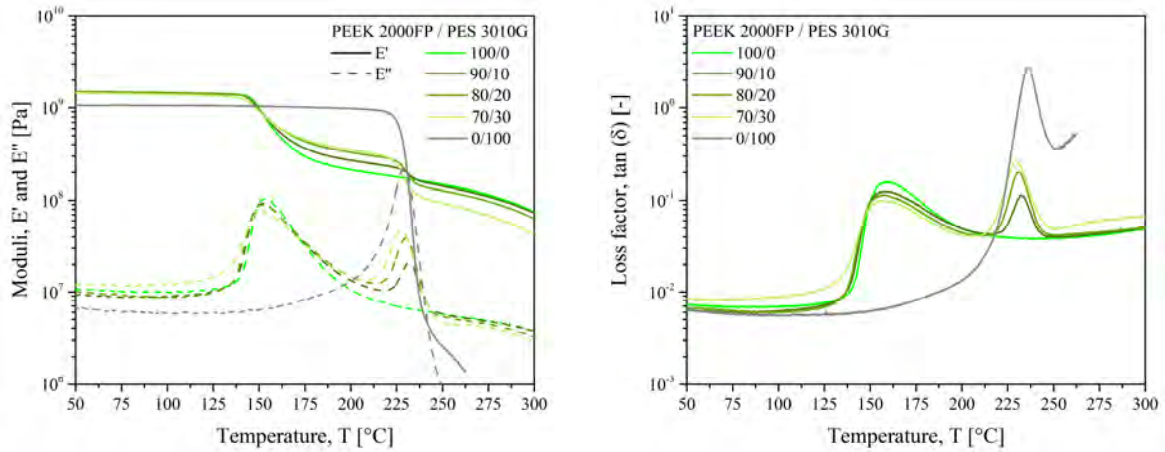
Figure 3.8. The DSC of (a) short-short (b) short-long chains for PEEK 2000 FP and PES blends

The blends of PEEK 2000 FP with PES display acceleration of crystallization. The crystallization onset temperature slightly increases with the amount of PES from 302 °C to 305 °C and the melting point decreases with the amount of PES from 332 °C to 326 °C. Moreover, the glass transition temperature stays stable at 157 °C for PEEK and decrease of 5 °C for PES 1010 G and 3 °C for PES 3010 G.

Storage modulus, loss modulus and loss factor versus temperature plots for PEEK/PES blends are reported in Figure 3.9. It can be observed that the  $E'$  is almost equal for PEEK 2000 FP and all the blends. The storage modulus obtained at 50 °C is 1496 MPa for PEEK 2000 FP. The highest modulus of 1637 MPa has been observed for 90/10 wt.% blend of PEEK and PES 1010 G. Two  $T_{\alpha}$  at around 157 °C for PEEK and 227 °C (PES 1010 G) or 230 °C (PES 3010 G) for each blend confirms the immiscibility for each ratio. It indicates that phase separation occurs in this case, but it is less than in the blends with PEEK 450 G. The curves of PEEK 2000 FP, PES and their blends show the same behaviour as previously observed for PEEK 450 G and its blends.



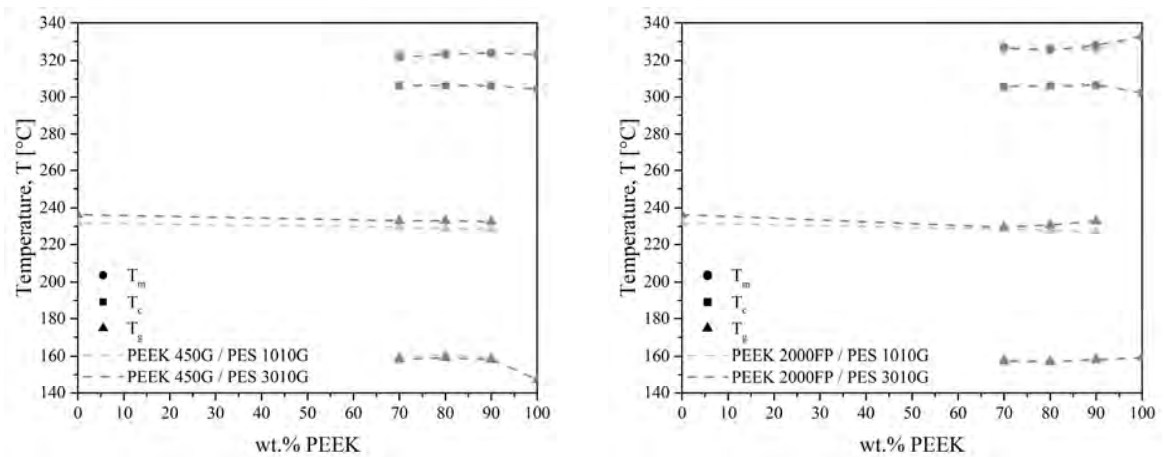
(a)



(b)

Figure 3.9. The DMTA of (a) short-short (b) short-long chains for PEEK 2000 FP and PES blends

All the thermal transitions measured for PEEK/PES blends are presented in Figure 3.10. For blends with PEEK 2000 FP, the partial miscibility is less obvious than for PEEK 450 G.



(a)

(b)

Figure 3.10. Thermal transitions of PEEK/PES blends

Considering these results determined by differential scanning calorimetry and dynamic mechanical thermal analysis, and the small variations observed with increasing the PES content, no clear conclusions can be obtained. For this reason, these results have been further correlated with the morphology of the blends.

### 3.3.2.1. Effect of PES on sintering window

An important factor that ensures successful processing by SLS is a wide sintering window. The sintering window is defined as the temperature range between the onset of crystallization temperature and the onset of melting temperature. The sintering windows obtained from DSC thermograms are displayed in Figure 3.11 for blends with PEEK 450 G and

Figure 3.12 for ones with PEEK 2000 FP. They show a narrow window of 19 °C and a wider window of 30 °C for pure PEEK 450 G and 2000 FP, respectively. The windows are however narrowed considerably when the material is blended with PES. The crystallization onset is shifted to higher temperatures by 2-4 °C, resulting in sintering windows between 15-18 °C wide for blends with PEEK 450 G. Nevertheless, the delay of crystallization can be observed with an increase of PES content in the composition of blends. In the case of blends with PEEK 2000 FP, a significant decrease of melting temperatures is observed, the latter gives sintering windows between 19-21 °C. This could lead to problems during the selective laser sintering process, because of non-uniform temperature distribution. Indeed, the thermal gradient into the powder bed could be in the order of 10-15 °C [257], especially when processing high-performance polymers for which higher temperatures are required. So, a narrow sintering window may complexify the control of the process.

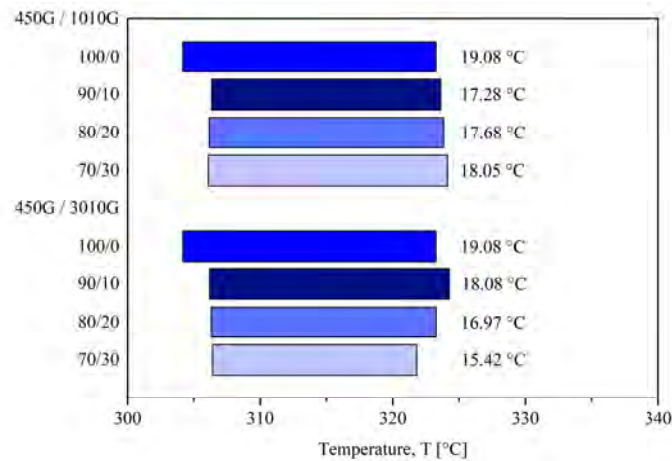


Figure 3.11. Sintering windows of PEEK 450 G and PES blends

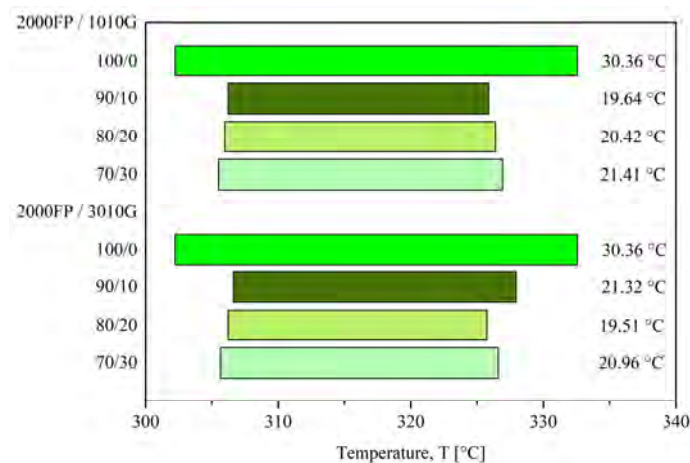


Figure 3.12. Sintering windows of PEEK 2000 FP and PES blends

The issues of a narrow sintering window have been observed by Kleijnen and al. [257]. Due to the high crystallization rate and associated shrinkage, the polymer parts showed an

increasing degree of curling as they were built. This caused the parts to be shifted on the powder bed by the roller. By comparing all the blends, we see that PEEK 450 G and PES 1010 G in the composition of 70/30 wt.% could provide a slight delay of crystallization and increases of a melting point compared to pure polyetheretherketone.

### 3.3.2.2. Effect of PES on crystallization

The degree of crystallinity of blends can be estimated from the differential scanning calorimetry results. It was calculated by dividing the fraction of PEEK of the melting enthalpy for blend by the melting enthalpy of 100 % crystalline polyetheretherketone of  $130 \text{ J.g}^{-1}$ , so the PES does not contribute to the melting peak of blend [189]. The results are presented in Figure 3.13.

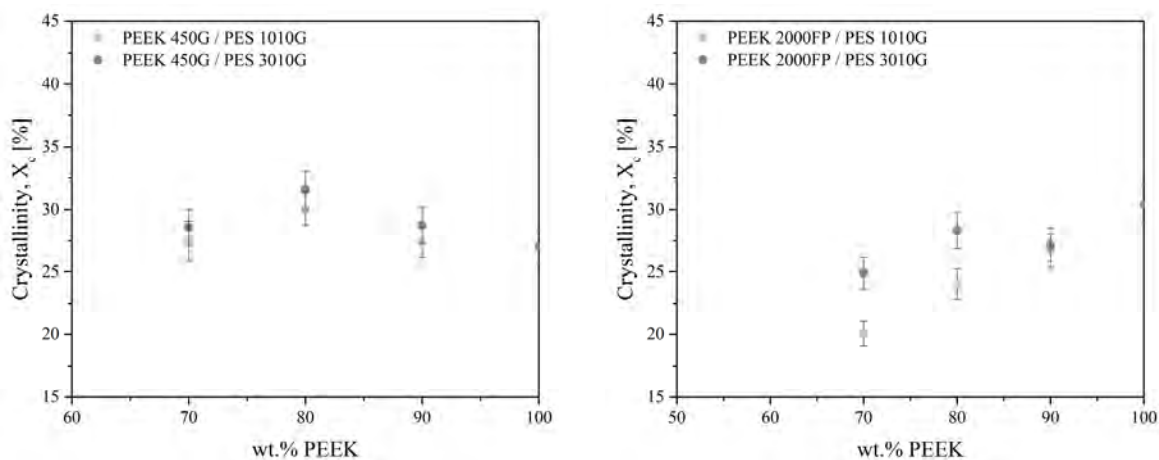


Figure 3.13. Degree of crystallinity ( $\pm 5 \%$ ) for PEEK/PES blends

The degree of crystallinity of PEEK in the blends with both PES remains close to the degree of crystallinity of pure PEEK for blends with PEEK 450 G. The degree of crystallinity is initially of 27 % for pure PEEK, for blends of PEEK 450 G (70 wt.%) and PES it is 27 % with PES 1010 G and 29 % with PES 3010 G. As expected, the degree of crystallinity does not significantly change in the immiscible blends. It looks that there is no effect of adding longer or shorter PES chains on the mobility of PEEK. Nevertheless, a higher degree of crystallinity can be observed for blends with longer PES chains.

In contrast, the degree of crystallinity of PEEK in the blends with PEEK 2000 FP decreases with increasing PES content. The degree of crystallinity for neat PEEK 2000 FP is 30 %. It can be observed that the crystallinity decreases for blends with PEEK 2000 FP and 70 wt.% of PEEK it is 20 % with PES 1010 G and 25 % with PES 3010 G. It has been shown that the introduction of PES segments into PEEK 2000 FP molecular chain disturbs the packing of PEEK repeating units so that the degree of crystallinity becomes smaller and thus the melting points and the crystallinity of blends are reduced.

Very similar results on quenched PEEK/PES blends are presented by Arzak et al. [246]. The value for 70 wt.% of PEEK in the blends is 16.6 %. Moreover, they reported that the degree of crystallinity of PEEK calculated from density values are almost none for slowly cooled blends in all compositions. Their results confirm that PEEK crystallization is hindered by the presence of PES. Malik [244] has reported the PEEK/PES blends containing up to 40 wt.% PEEK are amorphous, and beyond this concentration, semi-crystalline.

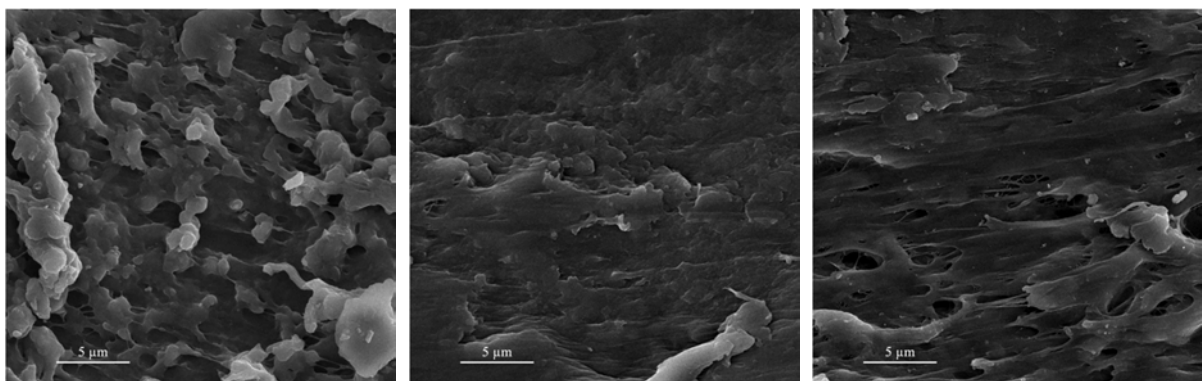
The influence of processing temperature on the crystallinity has been studied by Wu et al. [258]. It was seen that in the films formed at 340 °C, the degree of crystallinity of PEEK is about 30 %, while in the film formed at 300 °C, it is about 46 %. The second value corresponds to the maximum crystallinity of PEEK. It can be due to viscoelastic behaviours where transition regions of PEEK and PES are separately exhibited. It seems that the PEEK component was in the molten state while the blend was formed into a film at 340 °C (higher than the melting point of PEEK). The PEEK crystallize during the spontaneous cooling without the influence of the PES phase.

### 3.3.3. Morphological analysis of PEEK/PES blends

The morphology of PEEK/PES blends was studied on cryogenic fractured surfaces using a scanning electron microscopy performed with Inspect S by the FEI Company (Laboratorio de Microscopias Avanzadas, Universidad Zaragoza).

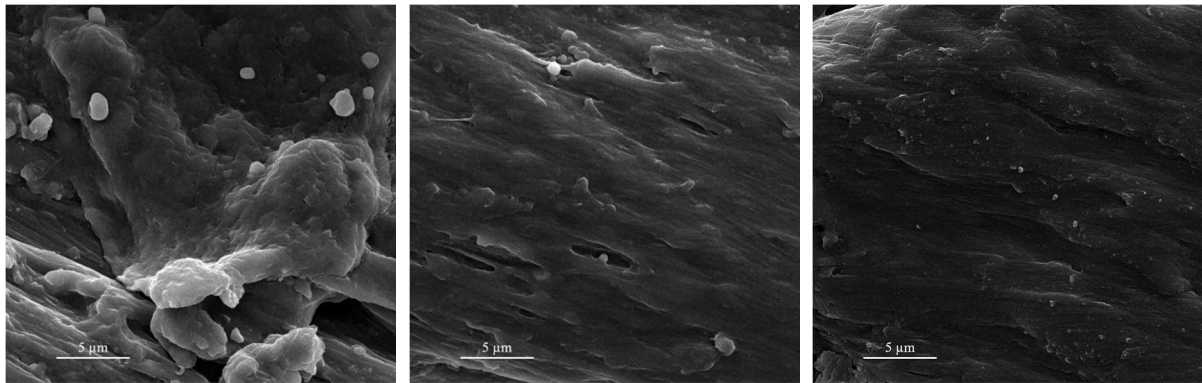
The micrographs of blends with PEEK 450 G or PEEK 2000 FP and PES in all compositions are shown in Figure 3.14 and Figure 3.15. The images have been registered in a gradient vacuum with an accelerating voltage of 10 kV and in analysis mode with a magnification of x10000.

PEEK 450 G / PES 1010 G





PEEK 450 G / PES 3010 G



90/10

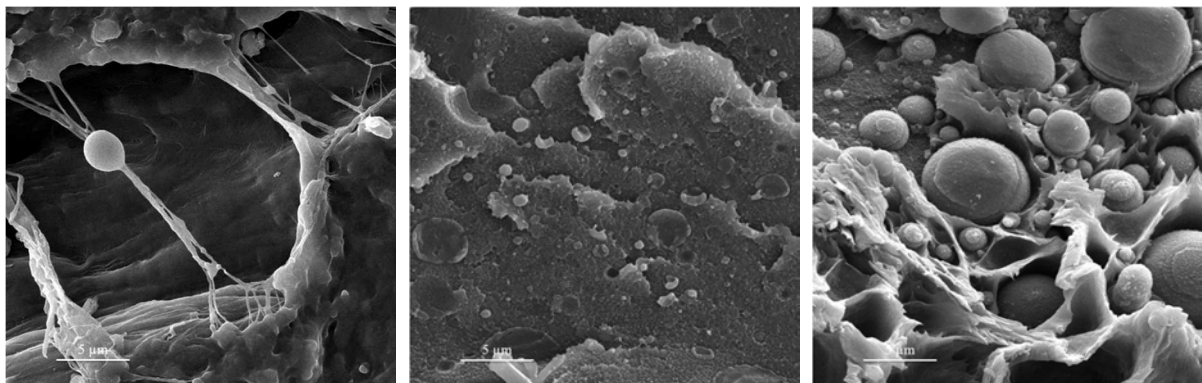
80/20

70/30

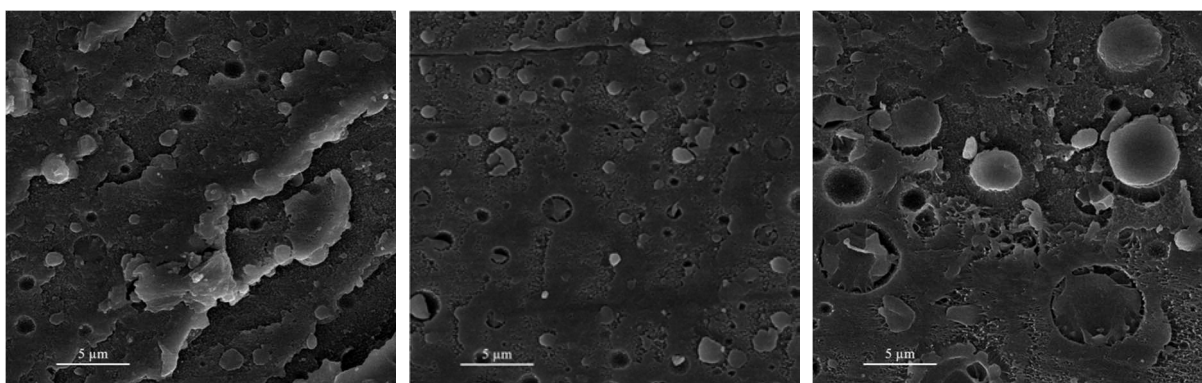
**Figure 3.14. The SEM images of microstructure of PEEK 450 G and PES blends [wt.%]**

In the case of PEEK 450 G and PES, all the compositions show a quasi-single phase morphology that may have a dispersed phase of PES made of very small dimensions.

PEEK 2000 FP / PES 1010 G



PEEK 2000 FP / PES 3010 G



90/10

80/20

70/30

**Figure 3.15. The SEM images of microstructure of PEEK 2000 FP and PES blends [wt.%]**

The SEM images confirm the immiscibility of PEEK 2000 FP and PES blends at all compositions. The PES forms spherical domains, the droplets dispersed within the PEEK matrix can be observed. Some of the particles are very close to each other and droplet-droplet

interactions occur during blending at these concentrations. The images of blends of PEEK 2000 FP and PES 3010 G illustrate in a very clear way the dispersed morphology. For blends with 10 wt.% PES, a fine dispersion is found: the size of the PES droplets is around 1  $\mu\text{m}$  or less. In the 80/20 PEEK/PES composition, the size of the droplets become around 1  $\mu\text{m}$ . A higher amount of PES (30 wt.%) supports the coalescence of PES droplets. These phenomena cause an increase of PES spherical domains from 1  $\mu\text{m}$  to even 5  $\mu\text{m}$ . The presence of black spaces around PES droplets indicates low adhesion between the two phases. However, some half-cut spheres are observed on images at 30 wt.% PES, it shows that adhesion forces are quite high. Also, the SEM of these compositions demonstrates that although the interface between the matrix and the dispersed phase is quite sharp, there seems to be good adhesion between the two phases.

The morphology is identified to be more homogeneous and better dispersed for blends with PEEK 450 G compared to samples prepared with PEEK 2000 FP. This agrees with the rheological results discussed in the previous section, where better dispersion results in higher elastic modulus.

Nandan et al. [259,260] studied the morphology of PEEK/PES blends. For PEEK-rich blends before the phase inversion point (which is assumed to be at a 75/25 PEEK/PES composition), the PES is dispersed within the PEEK matrix in the form of sub-micron droplets. As the PES content increases, the morphology changes to a two phases structure, with PEEK droplet larger than micron forming the dispersion. At the phase inversion point, an almost co-continuous phase was observed. Arzak et al. [246,261] noted a few differences in the structure between slowly cooled and quenched blends. However, the structure of the quenched blend seems to account for a better phase adhesion than the slowly cooled blends, as fewer PEEK droplets deboned from the PES matrix are seen in the structure of the latter.

### 3.3.4. Effect of PES on thermal stability by TGA

thermogravimetric analysis of PEEK/PES blends was carried out in TGA 1 STAR System from Mettler Toledo. The flow rate of nitrogen was kept constant at 50  $\text{ml}\cdot\text{min}^{-1}$ . A heating rate of 10  $^{\circ}\text{C}\cdot\text{min}^{-1}$  from 25  $^{\circ}\text{C}$  to 900  $^{\circ}\text{C}$  was performed on 10 mg of each different composition of PEEK 2000 FP and PES. Figure 3.16. shows the TGA traces for various blends compositions.

Both component homopolymers show a single-stage thermal degradation at temperatures lower than 700  $^{\circ}\text{C}$ . The mechanism of thermal degradation of PEEK has been described before. The PES degrades mainly between 450-650  $^{\circ}\text{C}$ . This degradation mechanism has been studied

by Hale et al. [262]. The sulphur dioxide has been found as the first decomposition product as the temperature increases beyond 400 °C. The degradation starts by chain scission at the carbon-sulphur bond between the aromatic ring and the sulfone group, as the weakest link in the polysulfone repeat unit.

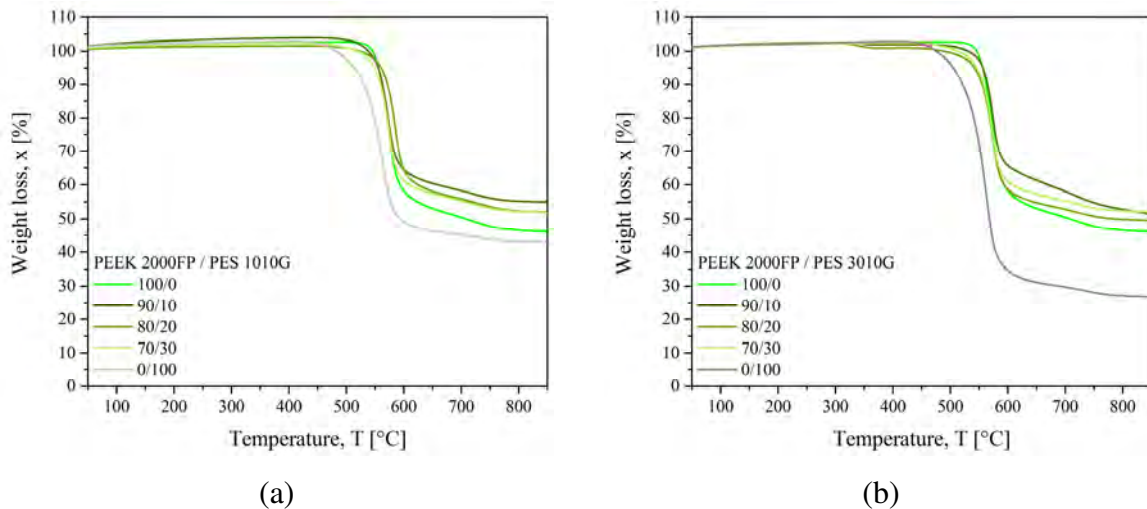


**Figure 3.16. The TGA curves of PEEK 2000 FP and PES blends**

The results show that neat PES starts degrading at a lower temperature than neat PEEK, however, the rate of degradation is faster for PEEK. The decomposition temperatures at which a weight loss reaches 5 % of the original sample weight, were 556 °C, 514 °C and 505 °C for samples of PEEK 2000 FP, PES 1010 G and PES 3010 G, respectively. Moreover, PES 3010 G is characterized by 16 % of weight loss more than PES 1010 G at 900 °C.

The thermal stability of the blends is slightly reduced by the incorporation of PES segments to neat PEEK and the decomposition temperature values decrease with increasing PES content. Nevertheless, the degradation pattern of blends follows an unusual way. Normally the weight loss curves of blends should fall between pure component, but in this case, the weight loss curves of PEEK/PES blends are over each homopolymer in the final part of the degradation range. Moreover, the weight of neat components degrades below 50 % while the weight of blends stays over 50 %. This indicates that PEEK and PES have a destabilizing effect on the degradation process when they are blended. Those variations can be explained considering the morphology of the blends and depend upon the thermal degradation characteristics of the component, which forms the matrix phases.

Nandan et al. [247] have reported that the temperature difference between temperature for 5% weight loss and the temperature corresponding to maximum degradation rate, can be taken as a measure of the degradation rate. The reported value of degradation rate is about 63 °C in PES, whereas in PEEK it is only around 10 °C.



### 3.3.5. Conclusion on the characterization of uncompatibilized blends

Two kinds of PEEK and PES were melt-blended and examined for their miscibility. Two glass transition temperatures were found corresponding to PEEK at around 160 °C, associated with the PEEK-rich phase, and PES at around 227 °C (PES 1010 G) or 230 °C (PES 3010 G), associated with the PES-rich phase. Considering only blends, a slight delay of crystallization temperature is observed with increase in PES content. The values for crystallinity of blends with PEEK 450 G increase with an increasing PES content causing better mobility to PEEK macromolecules to crystallize. In contrast, the degree of crystallinity of PEEK in the blends with PEEK 2000 FP decreases with increasing PES content. The degree of crystallinity becomes smaller and thus the melting points and the crystallinity of blends are reduced. Higher thermal stability is observed for blends with PES 1010 G. The PES 3010 G is characterised by 16 % of weight loss more than PES 1010 G at 900 °C.

The elastic modulus for all blends with PEEK 450 G is in the range of 1313-1850 MPa with the highest value for 90/10 wt.% of PEEK 450 G and PES 1010 G. In the case of blends with PEEK 2000 PF, the modulus is in the range of 1440-1637 MPa, which makes it more stable for all the compositions and less dependent on PES content.

The PEEK/PES blends show the morphology of partially compatible system with clear phase separation characterized by spherical domains of PES. Hence, the properties measured by DSC, thermomechanical analysis and TGA are in agreement with the morphology of the blends.

Nevertheless, a moderate interfacial adhesion in all compositions leads to the idea of adding a third component to enhance the miscibility between the two phases. Considering the previous results, PEEK 450 G have been chosen to elaborate the blends with compatibilizer.

### 3.4. Characterization of blends with compatibilizer

As discussed in the above section, the polyetheretherketone/polyethersulfone blends are immiscible. Thus, the incorporation of a compatibilizer into an immiscible blend reduces the interfacial energy of the phases, stabilizes the morphology against coalescence and improves the interfacial adhesion. As a result, systems with improved and reproducible properties are obtained.

#### 3.4.1. Preparation of blends with compatibilizer

Like presented previously, the matrix of each blend are high-temperature polymers, the main base is polyetheretherketone, while polyethersulfone is up to 30 wt.% of the blends, and the compatibilizer is block copolymer (HP3 copolymer) or nanoparticle (phenolphthalein).

The structure of HP3 copolymer has been investigated earlier. It has a semi-crystalline structure. Its tensile strength is up to 95 MPa, its elastic modulus is in the range up to 4400 MPa. The HP3 copolymer has its melting point at 372 °C. It can be used under temperature conditions up to 180 °C with dynamic mechanical stress, up to 240 °C under static load and up to 260 °C under electric load.

Phenolphthalein (C<sub>20</sub>H<sub>14</sub>O<sub>4</sub>) is slightly soluble in water and usually is soluble in alcohol. It is a weak acid, which can lose hydrogen ions (H<sup>+</sup>) in solution. The phenolphthalein molecule is colourless, and the phenolphthalein ion is pink. Phenolphthalein is usually used as an indicator in acid-base titrations. For this application, it turns colourless in acidic solutions and pink in basic solutions. It belongs to the class of dyes known as phthalein dyes.

##### 3.4.1.1. Realization of blends

The blends with compatibilizers were blended in ratios of 100/0, 90/10, 80/20, 70/30 and 0/100 (wt.%), PEEK 450 G and PES respectively. The HP3 copolymer and phenolphthalein were added as 10 % of volume for the entire blend. The micro-compounder 15 HT, described in Annex A.3.2, were used to prepare the blends in several batches. For each batch, the ingredients were weighed and blended manually in a beaker. The resulting blend was introduced gradually into the micro-compounder at a temperature of 375 °C and speed of screws of 100 rpm. After the complete introduction of materials, the blend was homogenized for 2.30 min at constant conditions. Phenolphthalein appears to be a plasticizer, as the torque significantly decreases during mixing and the melt looks less viscous compared to other blends. Four batches of 11 g each were prepared for each blend. After the residence time, the sample was obtained in the form of the filament. The blend was cooled and then granulated.

Production of plates was performed as described previously for uncompatibilized blends.

### 3.4.2. Study of miscibility by DSC and DMTA

The procedure of differential scanning calorimetry tests is the same as previously, it is explained in Annex A.2.4.1.

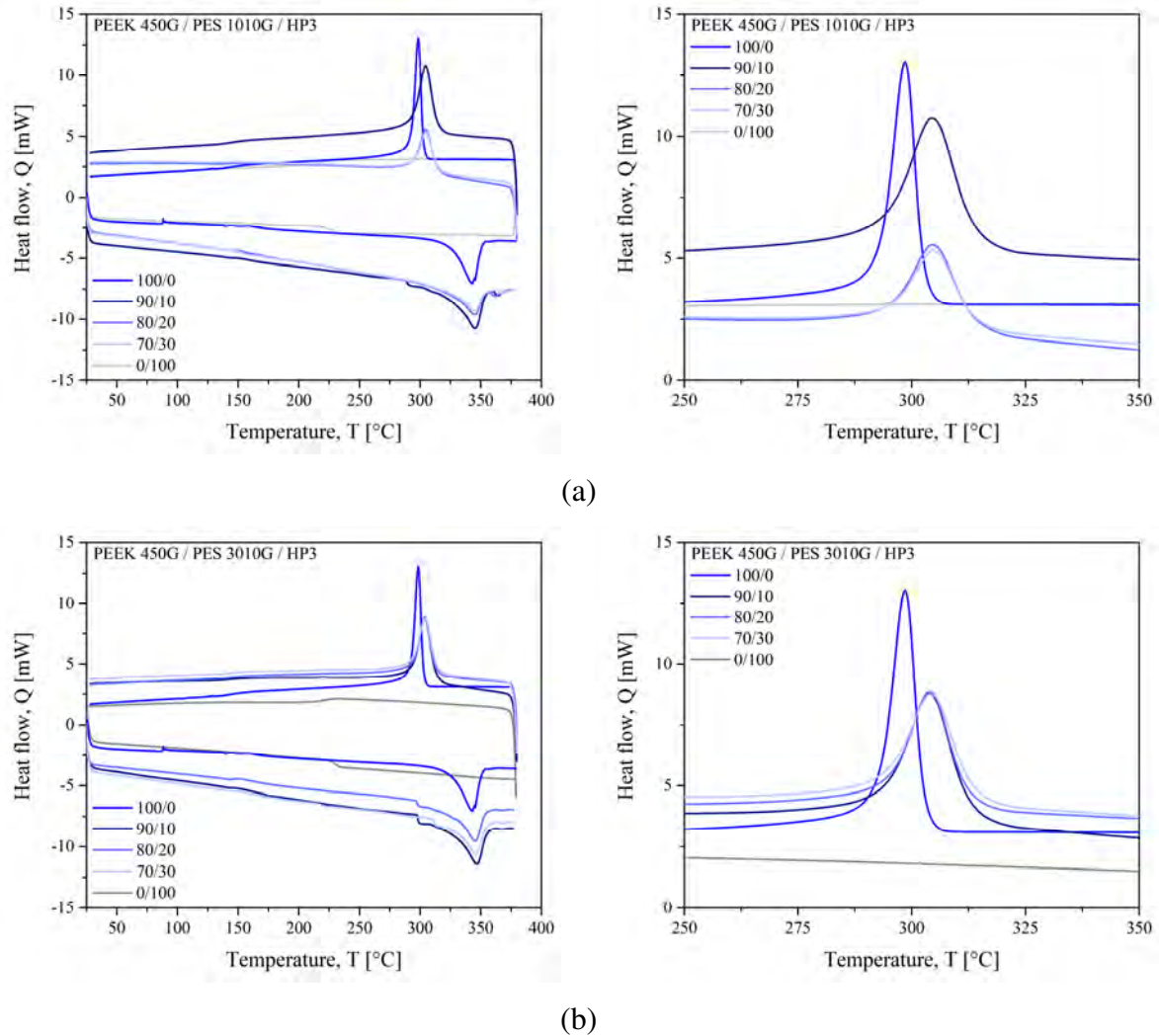


**Figure 3.17. The DSC of PEEK 450 G and PES blends with HP3**

The DSC thermograms of blends of PEEK/PES with HP3 copolymer are presented in Figure 3.17. As it was observed before, two glass transition temperatures, for PEEK 450 G at 147 °C and PES 1010 G at 232 °C or PES 3010 G at 236 °C appear in the samples. The glass transition temperature corresponding to PEEK increases above 160 °C for each blend. The second glass transition remains unchanged and close to the one of PES. The crystallization exotherm appears at around 304 °C for pure PEEK while for blends it is observed at 314 °C. The graphs on the right in Figure 3.17. show that crystallization peaks occur faster of around 10 °C. Finally, the melting endotherm of PEEK is also observed at around 345 °C for all blend compositions. The blends remain partially miscible in all compositions.

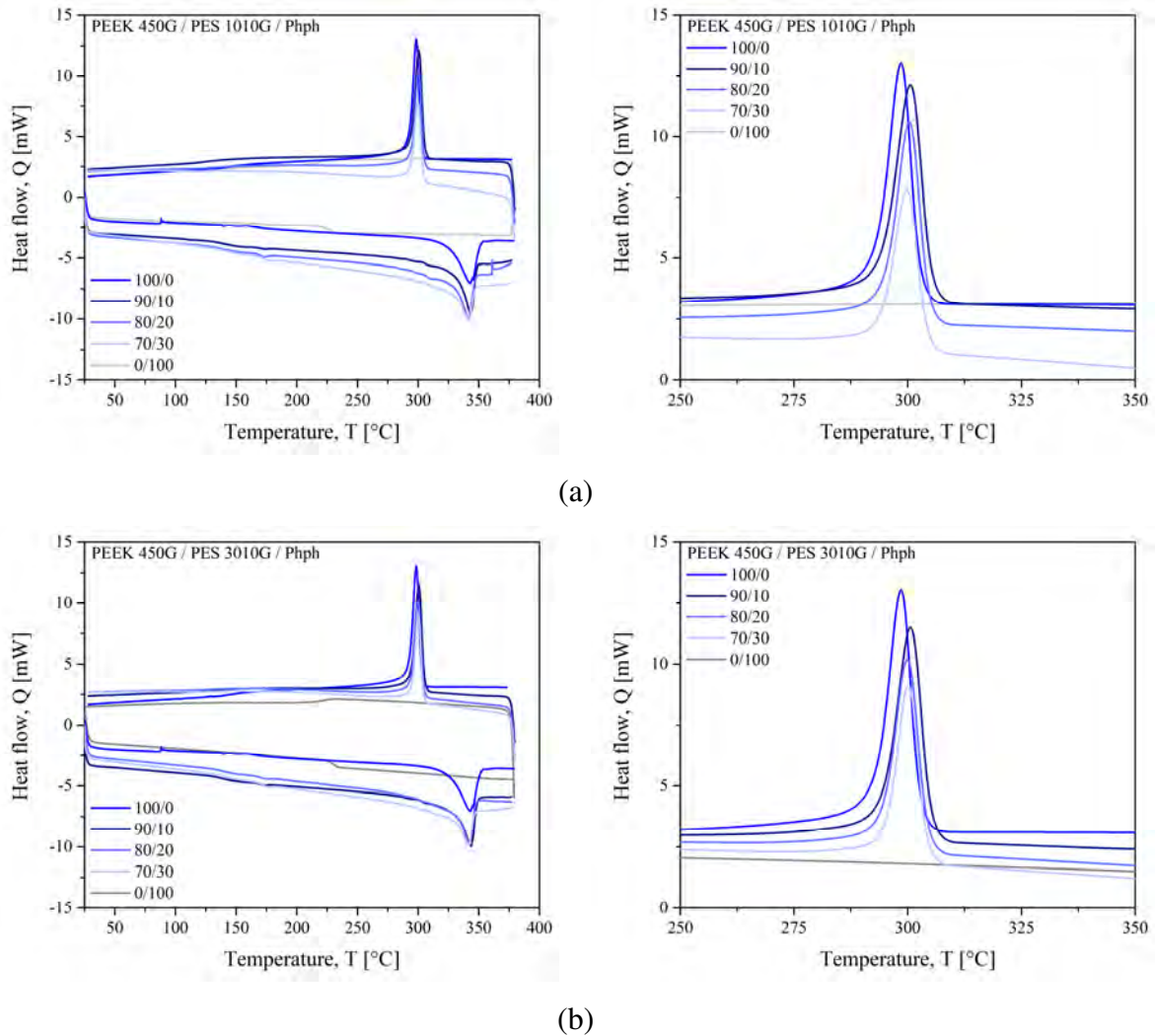


**Figure 3.18. The DSC of PEEK 450 G and PES blends with Phph**

In the case of blends with phenolphthalein, Figure 3.18 shows that PEEK and PES glass transition temperatures are very close one to each other, the first proof of the plasticizing effect of phenolphthalein. The gap between the two glass transition temperatures has been registered at 25 °C to 30 °C. The better miscibility is attached to PES content because mainly its glass transition temperature lowers from 232 °C to 173 °C for blends with PES 1010 G and from 236 °C to 174 °C for blends with PES 3010 G. Moreover, it is noticed that with the increase of PES content in the blends, the miscibility increases. The glass transition temperature that corresponds to PEEK increases with the decrease of PES, it is from 147 °C to 154 °C for PES 1010 G and to 155 °C for PES 3010 G. The crystallization and melting peaks do not show significant changes in the blends.

The thermomechanical properties are presented in Figure 3.19 for blends with HP3 and in Figure 3.20 for blends with Phph. The procedure of DMTA is explained in Annex A.2.5.

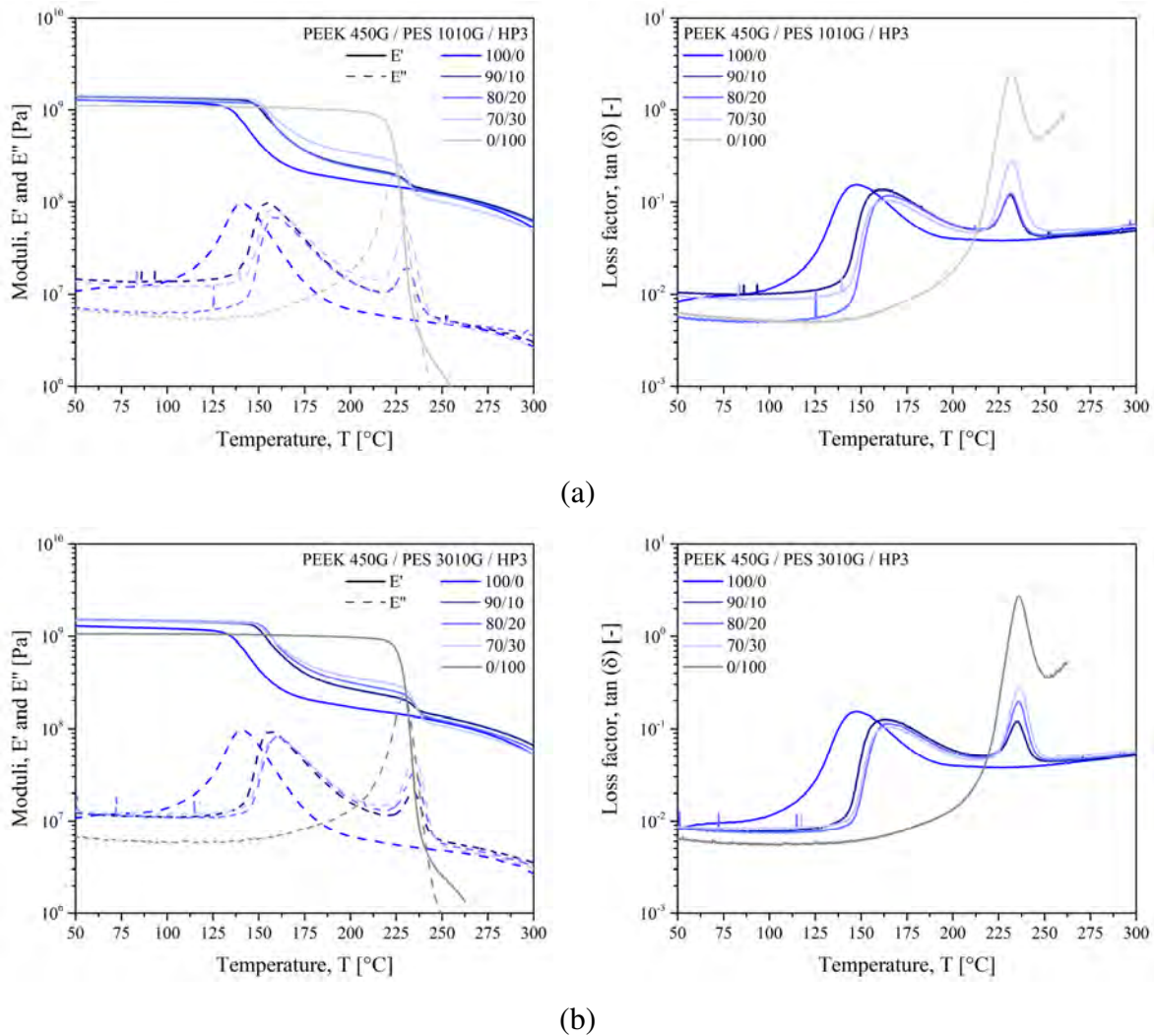


Figure 3.19. The DMTA of PEEK 450 G and PES blends with HP3

The PEEK/PES blends with HP3 represent the same mechanical behaviour as blends without compatibilizer. Two glass transitions that represent the onset of molecular motion in the amorphous regions of the structure is observed. The storage modulus increases for all the blends compare to neat thermoplastics. The highest modulus  $E'$  of 1517 MPa has been obtained for 80/20 wt.% blend of PEEK and PES 3010 G. The lowest modulus of 1279 MPa was obtained with blend with 20 wt.% of PES 1010 G. The other blends show similarity with the storage modulus between 1400 MPa and 1500 MPa. However, the modulus is lower than for blends without compatibilizer. The highest modulus of 1850 MPa has been obtained for 90/10 wt.% blend of PEEK 450 G and PES 1010 G.

The mechanical behaviour represented by the curves is explained in the previous section for blends of PEEK 450 G with both PES. To sum up, the addition of HP3 as compatibilizer does not change significantly the properties of blends.

In opposite, the addition of phenolphthalein significantly improves the plasticization of blends. This is proved by the Figure 3.20, where the peaks corresponding to the glass transition temperature approach one to each other at 25 °C for blends with 10 wt.% of PES 3010 G. It is observed that for the blend, the second peak of glass transition almost disappears. The storage modulus curves of blends with PES 3010 G are much closer to the shape of pure PEEK curve. The storage modulus is in the range 1384 MPa to 1757 MPa for blends with PES 1010 G and from 1534 MPa to 1757 MPa for blends with PES 3010 G. The highest modulus corresponds to blends of 90/10 wt.% of PEEK/PES 1010 G and 80/20 wt.% of PEEK/PES3010 G.

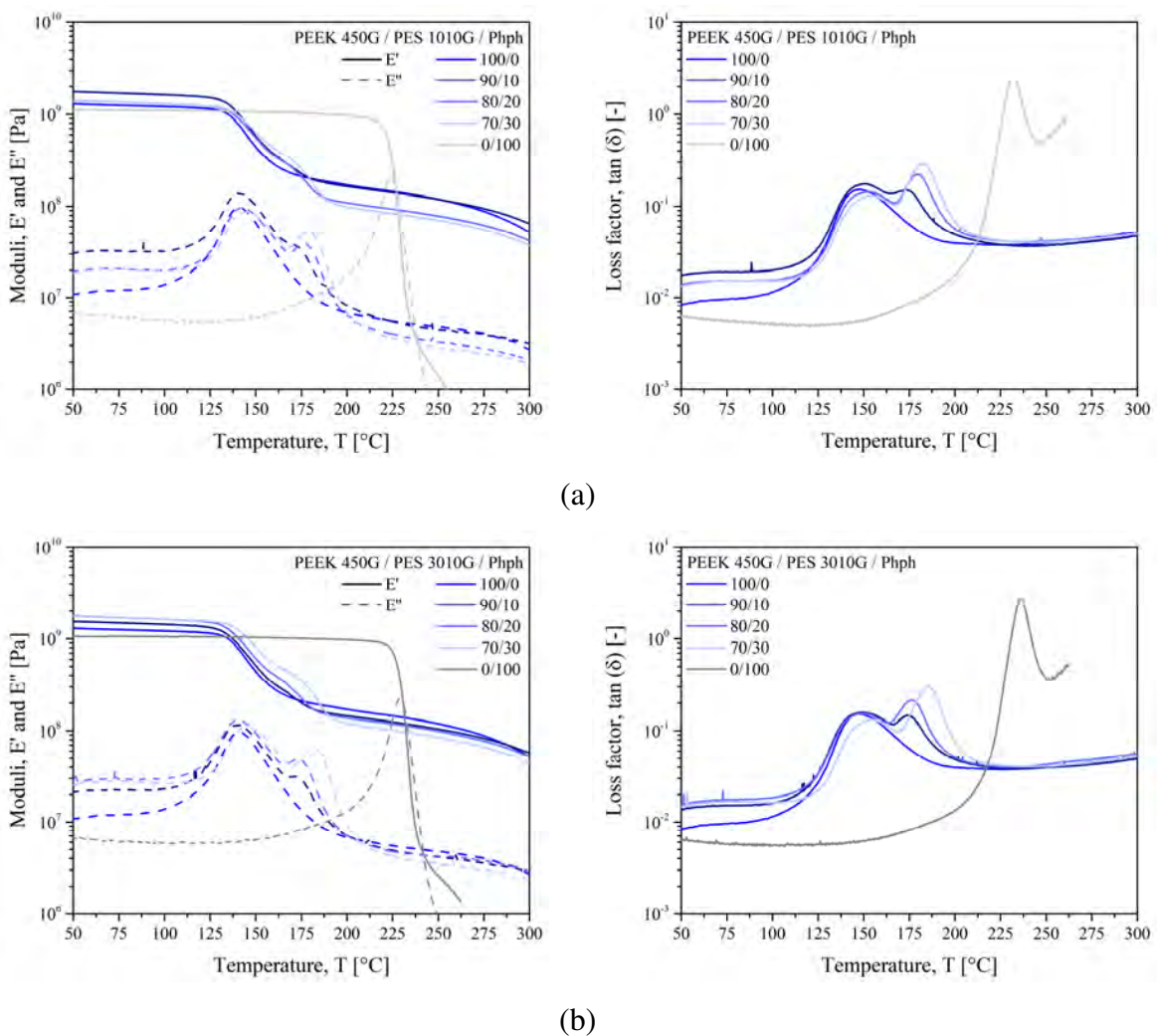
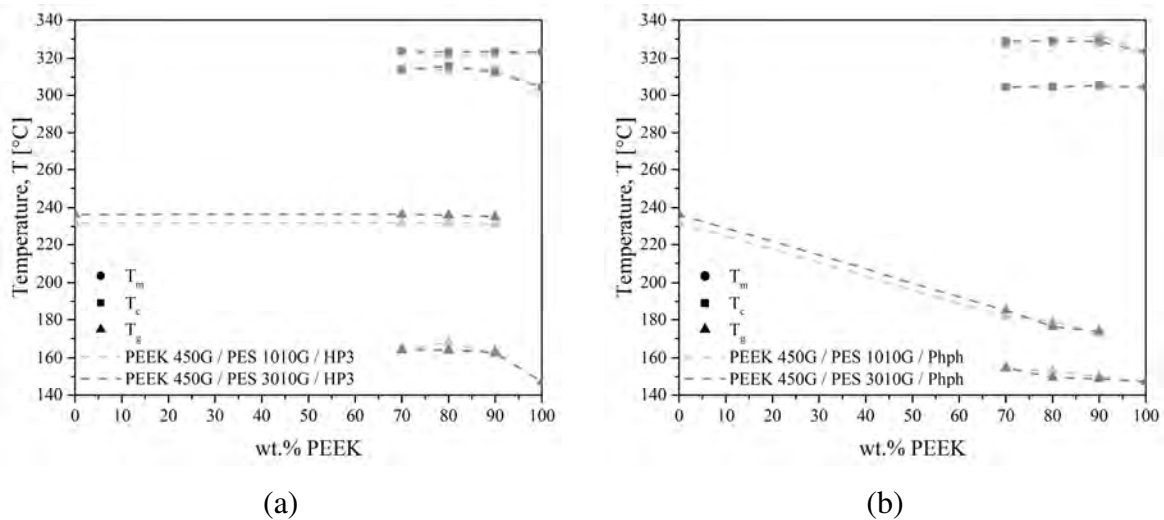


Figure 3.20. The DMTA of PEEK 450 G and PES blends with Phph

All the results of thermal transitions of PEEK/PES blends with compatibilizers are presented in Figure 3.21.

The HP3 causes an increase of crystallization temperature, while phenolphthalein increases the melting point of the blends.





**Figure 3.21. Thermal transitions of PEEK 450 G and PES blends with (a) HP3 (b) Phph**

The degree of crystallinity for blends of PEEK and PES-C has been measured by wide-angle X-ray diffraction (WAXS) by Zhang and Zeng [251]. The C in the name represents cardo side groups obtained by synthesis of PES and phenolphthalein. They also report a decrease in the degree of crystallization with increasing PES-C content. The value of 28.4 % has been observed for blends with 80 wt.% of PEEK.

### 3.4.2.1. Effect of compatibilizer on sintering window

In this section, the width of the sintering window is studied. The processing window is situated between the onset of crystallization temperature and the onset of melting temperature. The sintering windows obtained from differential scanning calorimetry thermograms for blends with compatibilizers are presented in Figure 3.22 and Figure 3.23.

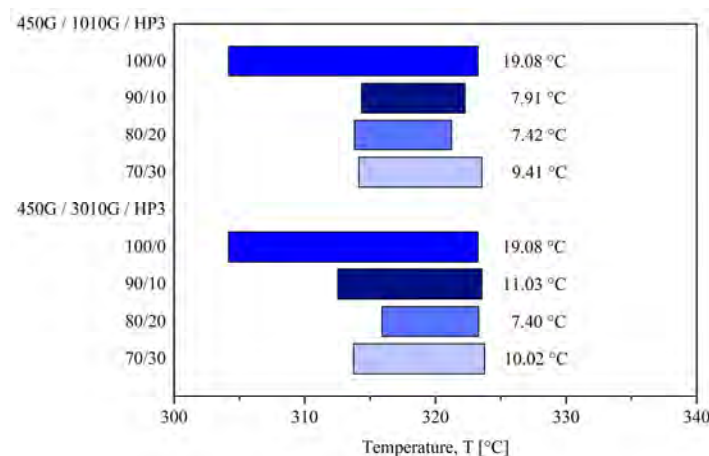


**Figure 3.22. Sintering windows of PEEK 450 G and PES blends with HP3**

The blends with HP3 show decrease of sintering window in each composition. The narrowest window of 7 °C and the widest window of 11 °C are obtained for 20 wt.% and 10 wt.% of PES 3010 G, respectively. It is due to the shifting of crystallization to higher temperatures.

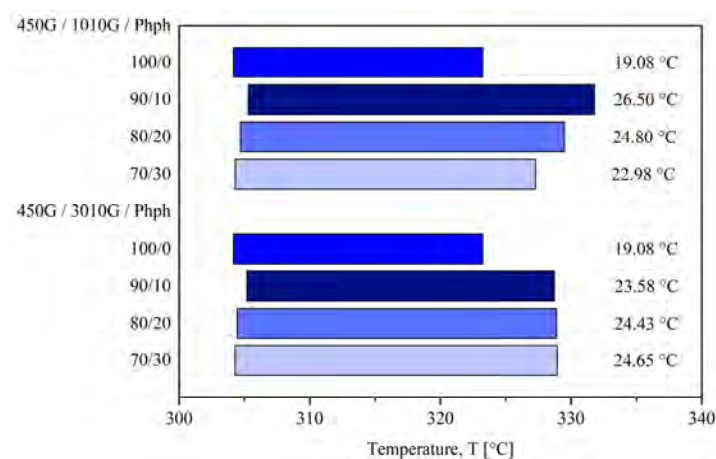


Figure 3.23. Sintering windows of PEEK 2000 FP and PES blends with Phph

On the contrary, the blends with phenolphthalein show a broadening of the processing window in all blends, which is caused by a delay by 4-9 °C in the melting point. The narrowest window of 23 °C and the widest window of 26 °C are obtained for 30 wt.% and 10 wt.% of PES 1010 G, respectively. The delay of crystallization can be observed with an increase of PES in the composition of all blends.

### 3.4.2.2. Effect of compatibilizer on crystallization

Blends of a semi-crystalline polymer and an amorphous one with compatibilizers could change the degree of crystallinity and the crystalline morphology. The degree of crystallinity of blends was estimated from differential scanning calorimetry results and calculated by dividing the fraction of PEEK of the melting enthalpy for blend and the heat fusion of 100 % crystalline polyetheretherketone of 130 J.g<sup>-1</sup> [189]. The results are presented in Figure 3.24.

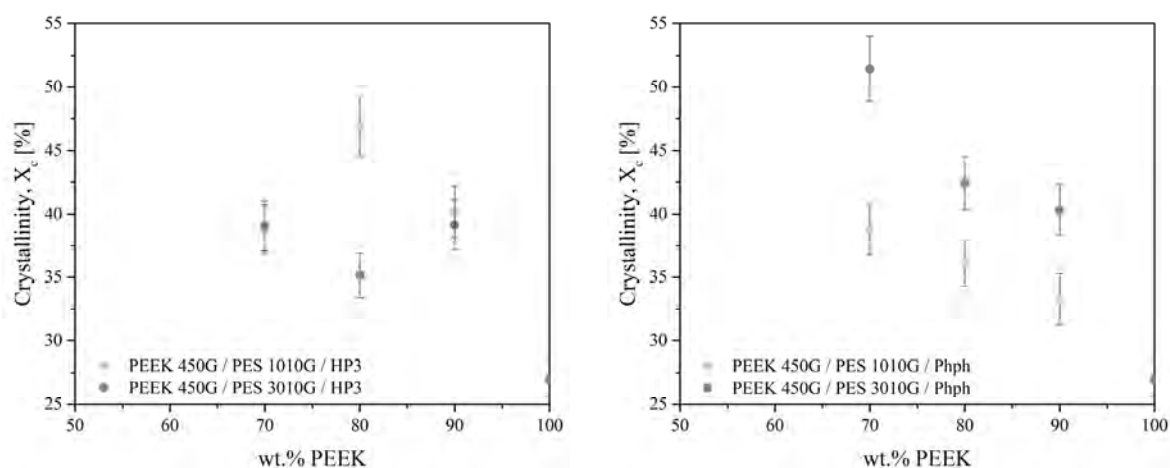


Figure 3.24. Degree of crystallinity ( $\pm 5\%$ ) for blends

As in the case of PEEK 450 G and PES blends without phenolphthalein, the degree of crystallinity of PEEK in the blends increases. For the blends with HP3, the crystallinity



remains to be stable around 40 % and the same for both PES with variation at 20 wt.% of PES. Thus, for PES 1010 G the value is 47 % and for PES 3010 G it is 33 %. HP3 copolymer causes the same mobility to PEEK macromolecules to crystallize for both PES. Nevertheless, the addition of phenolphthalein leads to a linear increase of crystallinity with increasing of the PES content. The maximum degree of crystallinity for blends with 70 wt.% PES 1010 G is 39 %, while for 70 wt.% PES 3010 G it reaches 51 %. It means that when adding phenolphthalein into blends of PES and PEEK gives more mobility to PEEK macromolecules to crystallize. It has to be noted that long PES chains increase the mobility of PEEK macromolecules over 50 %.

### 3.4.3. Morphological analysis of blends with compatibilizer

The morphology of PEEK/PES blends with compatibilizer (10 wt.% in each composition) was studied on the fracture surfaces using a scanning electron microscope performed with Inspect S by the FEI Company (Laboratorio de Microscopias Avanzadas, Universidad Zaragoza).

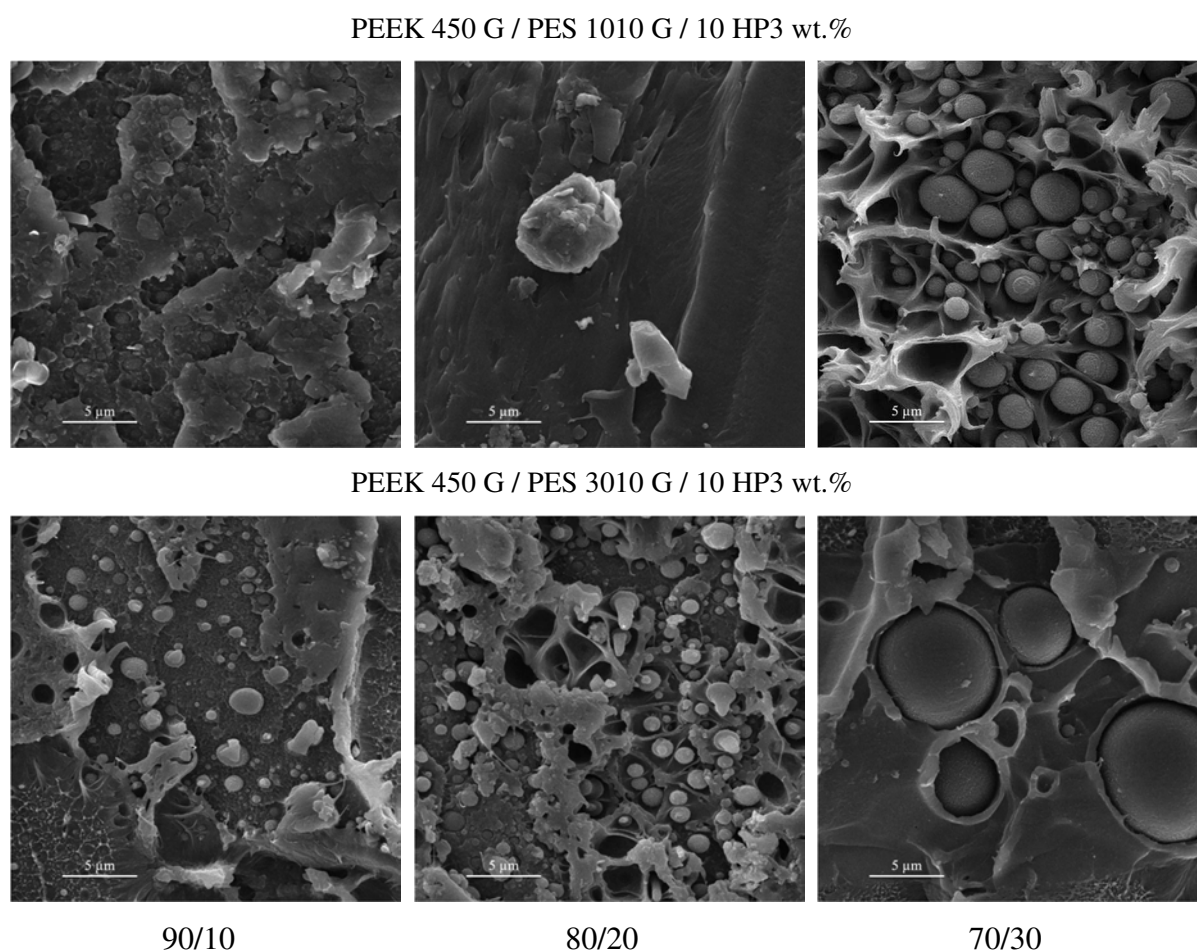


**Figure 3.25.** The SEM of the microstructure of PEEK 450 G and PES blends [wt.%] with HP3 copolymer



In this work, phenolphthalein was added into the PEEK/PES matrix. Phenolphthalein is chemically bonded with PEEK or PES monomers, causing the appearance of the cardo-side groups. Zhang and Zeng [251] have investigated blends of polyetheretherketone with polyethersulfone with cardo side groups obtained in the  $\alpha$ -chloronaphthalene solution blending at 250-260 °C. The morphologies of the blends crystallized at 290°C from the melt of different compositions show birefringent spherulites of PEEK. The samples of the blends were filled with spherulites in which there were no large separated domains of PES-C. With increasing the PES-C content, the size of the spherulites increases, and the texture of the spherulites becomes open, which means a relatively small overall crystallinity of a spherulite and is related to the presence of an amorphous component. In our case, it would be necessary to observe the crystalline morphology of the compatibilized blends to check if we confirm the result of Zhang and Zeng [251].

#### **3.4.4. Conclusion on the characterization of blends with compatibilizer**

Two kinds of compatibilizers in a matrix of PEEK and PES have been chosen, HP3 copolymer and phenolphthalein, to prepare blends by melt mixing. The polymer blends display immiscibility, however, with the plasticizing effect of phenolphthalein occurred. As previously, two glass transition temperatures were found, corresponding to PEEK between 147 °C and 168 °C, associated with the PEEK-rich phase, and PES between 231 °C and 236 °C for blends with HP3 and between 173 °C and 185 °C for blends with phenolphthalein, associated with the PES-rich phase.

For blends of PEEK and PES with cardo side groups from phenolphthalein, the sintering window is expended, by increasing the melting point and decreasing the degree of crystallinity of PEEK.

### 3.5. Conclusion

The main goal of this chapter was to elaborate a new high-performance thermoplastic material suitable for the SLS process. For that, we target a miscible blend with a large sintering window, that is to say with a delayed crystallization on cooling while keeping high mechanical strength at the glassy state. Two types of polyethersulfone and two types of polyetheretherketone have been chosen.

The resulting PEEK/PES blends demonstrate immiscibility or plasticization. The goal of delaying the crystallization was not reached. The morphology of blends shows a clear phase separation characterized by PES spherical domains. Moreover, a weak interfacial adhesion in all compositions leads to the idea of adding a third component to compatibilized the two phases.

Two kinds of compatibilizers have been chosen, HP3 copolymer and phenolphthalein. The polymer blends display immiscibility with HP3, however, phenolphthalein looks like a plasticizer. For blends of PEEK and PES with cardo side groups from phenolphthalein, the sintering window is expended, by increasing the melting point and increasing the degree of crystallinity of PEEK. The morphological analysis displays nano to microsized PES spherical domains.

The results obtained for PES/PEEK/phenolphthalein blends are promising, however, some further work would be necessary:

- a wider study of the crystallization of this blend is required to link the cooling rate to the crystallization kinetics and the PEEK crystalline morphology;
- the rheological behaviour of the blend in the melted state and the calculation of the interdiffusion times would be useful, as done in chapter 2 for commercial materials;
- its thermal stability would be measured to ensure the phenolphthalein does not fasten the degradation;
- then, if the results are still promising, a remaining issue would be to process the blend into regular and spherical 50  $\mu\text{m}$  diameter particles to fit the SLS requirement.

So, the effect of the laser beam on the properties of this new material would be studied by performing laser passes onto the powder bed.

## **4. EFFECT OF PROCESS PARAMETERS ON THE PRINTED PARTS**

This chapter is closely related to the use of polymer materials and additive manufacturing in the industry. One of the aspects of this chapter is the determination of optimum polyamide 12 print parameters. This study usually requires the printing of many test specimens, and the cost of printing depends on the size and orientation of parts. It has been investigated if the same tests on smaller specimens (cheaper to manufacture) and larger specimens are comparable. For this, two sets of five batches of test pieces were printed: a set of large test specimens of 170 mm long and a set of small test ones of 85 mm long. Each set of test specimens contains as well as five different orientations. In this research, the specimens of Duraform PA12 powder on the sPro230 SLS machine were performed.

The next aspect considers the recommendation of the level of input polyamide 12 powder properties which could guarantee acceptable part quality in the selective laser sintering process. For this study, the specimens of Duraform FR1200 on the ProX500 were investigated.

#### 4.1. High temperature laser sintering (HT-LS) machines and materials

The selective laser sintering process having an operating temperature-higher than 200 °C is called high-temperature laser sintering. This process allows using some polymers with higher melting temperatures and higher mechanical performances compared to polymers of the traditional selective laser sintering process. They can replace metals for some applications that require operating temperatures up to 250 °C and can provide a lower material density than metals. In past years, the only available high-temperature laser sintering printer for polyaryletherketones, as PEEK HP3, was commercial EOSINT P800 from Electro Optical Systems (EOS, Germany). The processing of machine takes place at temperatures higher than 200 °C and applies an additional heating phase at the end of laser exposure of every layer, called “post sintering”. The EOSINT P800 system also offers the possibility to manufacture components in variable building chamber size.

The selective laser sintering process of high-temperature HP3 copolymer has been widely studied by Ghita et al. [23,190,192,263,264]. The HP3 copolymer has a melting point at 372 °C and crystallization temperature around 300 °C, more details are presented in Annex A.1.7, while the melting temperature of standard PA12 is 172 °C. First of all, Beard et al. [263] analysed standard-shaped dog bones printed with a preheating temperature of approximately 366 °C. They have reported high thermal (glass transition temperature around 180 °C) and mechanical properties (tensile strength above 90 MPa) and density-independent from the building position of specimens within the building chamber. In a later work, Ghita et al. [190,192] have investigated the mechanical properties, shrinkage and degradation of samples manufactured along the X-axis, Y-axis and Z-axis. A higher shrinkage for samples built in the middle of the building chamber and decrease of tensile properties of 50 % for samples built along the Z-axis direction was presented. The specimens incorporating recycled powder (30 wt.% of recycled and 70 wt.% of fresh HP3 copolymer) showed a decrease of tensile strength values of up to 17 % from around 90 MPa to 75 MPa.

This thesis work is supported with two selective laser sintering machines, facilities of Prismadd, with high-powered CO<sub>2</sub> laser to selectively melt and fuse powdered thermoplastics such as sPro230 and ProX500 by 3D Systems. Each machine was adapted to the specific polyamide 12 material like Duraform PA12 and Duraform FR1200, respectively. The machine/material pairs are presented in Annex A.4 for the printing of specimens. The mechanical and physicochemical properties on the printed part were investigated on polyamide 12 powders because of their availability in the company.

## 4.2. Influence of manufacturing on material performance

Up to the recent works [265–267], the most important build parameters that may have an influence on the SLS process and thereby affect the resulting part properties are:

- supplied energy density and absorption;
- part bed orientation;
- feed and bed temperature;
- layer thickness and width;
- material type and its powder consistency.

The supplied laser energy and absorption, as well as, part orientation in the build chamber are part dependent and can be different for each part in the build chamber. The preheating and processing temperature, rate temperature, thickness and width of the sintered layer, material type and its consistency are more build or layer dependent, the parameters are the same for all parts within a single layer of build and they can be changed with the height of the build chamber.

Thus, supplied laser energy density is a key factor that affects the sintered structure. The temperature obtained during the sintering process depends on it. The energy density is characterised by the total (maximum) power provided by the laser, the speed of laser moving and the spacing between laser scans. As the speed of movement of laser in the working chamber increases, the time of irradiation of a given space is reduced. It can affect the thickness of the sintered layer. The range of energy density should be between  $0.01 \text{ J.mm}^{-2}$  and  $0.048 \text{ J.mm}^{-2}$  [29,264]. When the value is below  $0.01 \text{ J.mm}^{-2}$ , the sintering may not be proper, when the value is above  $0.048 \text{ J.mm}^{-2}$  the degradation of the polymer occurs. Thus, in the case of polymer parts, Caulfield et al. [28] studied the influence of energy density in the selective laser sintering process on the mechanical properties of polyamide. It was reported that parts manufactured at high energy density levels (around  $0.028 \text{ J.mm}^{-2}$ ) have more ductile behaviour than the samples manufactured at low energy density levels (around  $0.008 \text{ J.mm}^{-2}$ ). The tensile strength, elastic modulus and yield strength also increase with an increase in energy density. They have found for Duraform PA12 a maximum tensile strength of 48 MPa for horizontally printed samples and 44 MPa for vertically printed samples. According to the datasheet, a tensile strength of Duraform PA12 is 43 MPa. It means that maximum strength may be obtained with a relatively low energy density. However, the elastic modulus has been found extremely low maximum values of 1100 MPa and 900 MPa for horizontal and vertical printed samples, respectively. In more recent work, Khalil et al. [37] studied the influence of energy density range between



0.016 J.mm<sup>-2</sup> and 0.032 J.mm<sup>-2</sup> on flexural properties of ultra-high molecular weight polyethylene. The average elastic modulus and flexural strength of printed parts increased with an increase in laser energy density up to 0.027 J.mm<sup>-2</sup>. The maximum values of elastic modulus and flexural strength are  $46.86 \pm 3.07$  MPa and  $2.12 \pm 0.05$  MPa when the laser density was maintained at about 0.027 J.mm<sup>-2</sup>.

The laser energy absorption is a parameter dependent on the absorbance of structure used for sintering. Due to the very short exposure times (in the order of few milliseconds) the sintering process can be facilitated by using the appropriate type of CO<sub>2</sub> laser with a wavelength of 10.6 μm. Laumer et al. [268] have reported that polyamide 12 has an absorbance of 31 % from room temperature until 168 °C. At this temperature, the transmittance increases sharply until a value of 88 % at 200 °C, whereas the reflectance decreases to 7 % and the absorbance to 5 %. It is due to the melting of crystalline areas of material.

The part orientation in the build chamber allows printing the designed part in various settings, for example, parallel or perpendicular to the working table. Appropriate selection of its position, depending on the shape in the chamber, allows obtaining optimal properties. Design of experiment approach used by Wegner and Witt [42] has shown the correlation models demonstrate the complex correlations of process parameters in laser sintering, in most cases showing a non-linear nature with multiple parameter interactions. The mechanical properties such as elastic modulus, tensile strength and elongation at break increase with increasing the energy density. However, the parts printed in the Z-axis obtained lower values than the parts printed in other orientations. Maximum tensile strength of 51.3 MPa for horizontally printed samples and 48.9 MPa for vertically printed samples were obtained for a volumetric energy input of 0.52 J.mm<sup>-3</sup>. For elastic modulus and tensile strength, the values are worse of approximately 25 % and 46 %, respectively, at 0.25 J.mm<sup>-3</sup> energy density volume. The biggest difference has been observed for elongation at break, the value for parts printed in the Z-axis is worse of around 87 % than for parts printed in the X-axis for the volumetric energy density of 0.25 J.mm<sup>-3</sup>. In the opposite, Caulfield et al. [28] have found values of elongation at break of 0.15 (X-axis direction) and 0.18 (Z-axis direction), which means that the elongation values for vertically printed samples are higher than for horizontally printed samples. Thus, Hofland et al. [43] reported that the elongation at break does not depend on the energy input, but it is related to the crystallinity of polymer and another process parameter such as cooling rate. They obtained maximum values with polyamide of horizontally printed samples for the tensile strength, elastic modulus and elongation at break were, respectively, 50.1MPa, 2239MPa and

25.9 %. The maximum obtained values of vertical printed samples were 51.2MPa, 2171MPa and 15.6 %, respectively.

The feed and bed temperature, which are the temperature of preheating powder and build chamber, respectively, are used to reduce laser energy density and avoid curling and distortion. Negi et al. [269] used response surface methodology to determine the effect of sintering conditions on mechanical properties of glass-filled polyamide. They have observed that the mechanical properties of sintered parts increase with increasing of laser power and preheating temperature and decrease with an increase in scan speed and scan spacing. Thus, the low level of bed temperature and laser power decreases the energy affecting the powder, which causes poor strength of sintered parts. High bed temperature results in the formation of the dense structure of powder particles with less porosity [270], which results in improving the mechanical strength. However, too high bed temperature may provide distortion of powder, which restricts the recyclability of powder. Kumar et al. [266] investigated the physical build process parameters such as laser power, bed temperature and part orientation in three levels, which governs the final part quality. They have reported that optimal parameters for better dimensional accuracy and micro-hardness are laser power of 18.5 kW (level 1), bed temperature of 171 °C (level 1) and part orientation at the Z-axis (level 3). Among these parameters the laser power and temperature influence the dimensional accuracy and temperature influences the micro-hardness of selective laser sintering prototype.

The thickness and width of the sintered layer affect the dimensional accuracy. These parameters depend on the energy density of the laser and the diameter of the laser beam. Caulfield et al. [28] have observed that the part width increased with increasing the energy density in the range of 0.008-0.028 J.mm<sup>-2</sup>. However, all parts were smaller than expected due to the shrinkage of parts during the cooling process. They assumed that the variation in the width may have been due to a difference in build accuracy in the horizontal (within a layer) and vertical (perpendicular to a layer) directions for SLS process. On the other hand, the desired thickness of 3 mm was reached and exceeded by the majority of parts. Based on the finding by Khalil et al. [37] presented above, shrinkage in the length and width was evident. The volume of the sintered parts increased with increasing of laser energy density due to the growth in the thickness of the parts.

Material type and its powder consistency, usually consider thermoplastics, which are classified such as semi-crystalline and amorphous polymers. The wide research on this point has been presented in the second chapter about the characterization of powders.

To conclude, the correlation of process parameters with mechanical properties of laser-sintered polyamide 12 parts was studied by Hofland et al. [43]. Their design parameters were the laser power, scan speed, scan spacing, part build orientation, preheating temperature and layer thickness. Sensitivity analysis shows the uncertainty in the output of a mathematical model. It was calculated that the most important process variables were scan spacing of 30 % and 23 % for horizontal and vertical printed samples, respectively. Then, the layer thickness of 29 % for horizontal printed samples and 28 % for vertical printed samples. Scan speed has the third largest impact on the part properties, followed by preheating temperature and laser power. All the authors agreed that the mechanical properties are worse for parts printed in the Z-axis.

#### 4.2.1. Manufacturing of specimens

The sintering experiments were carried out by using a commercial selective laser sintering machines using polyamide 12 materials, with the melting temperature of 180 °C. The tensile specimens on sPro230 SLS (high capacity machine) were manufactured in two sizes such as  $L = 170$  mm and  $L = 85$  mm, with five orientations mentioned in Figure 4.1 such as XY axis X, XZ axis X, XY axis Y, YZ axis Y and XZ axis Z. On ProX500 SLS (small capacity machine) the tensile parts were fabricated in normalized size of 170 mm with three orientations: XZ axis X, YZ axis Y and XZ axis Z. The directions in the build chamber are as follows:

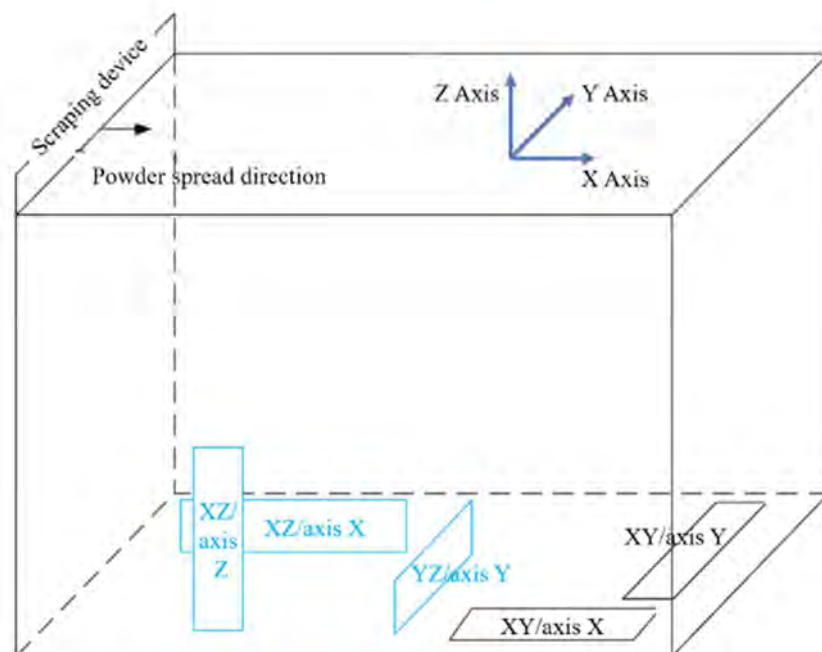


Figure 4.1. Samples orientation in build chamber

All test samples were dog-bone tensile samples as defined in ISO 20753 and ISO 527. The main processing parameters that have been used to manufacture the specimens are the

optimal parameters used by the manufacturer, 3D Systems. The processing parameters are presented in Table 4.1.

**Table 4.1. Processing parameters for tensile specimens**

Process parameters	sPro230 /Duraform PA12	ProX500 /Duraform FR1200
Preheating temperature, $T_p$	130 °C	130 °C
Bed temperature, $T_b$	174 °C	173 °C
Layer thickness, PLT	0.1 mm	0.1 mm
Fill energy density, $ED_f$	0.021 J.mm <sup>-2</sup>	0.017 J.mm <sup>-2</sup>
Laser power, LP	42 W	20 W
Scan speed, LS	10160 mm.s <sup>-1</sup>	12000 mm.s <sup>-1</sup>
Scan spacing, SS	0.2 mm	0.2 mm
Scan count, SC	1	2
Outline ED, $ED_o$	/	0.029 J.mm <sup>-2</sup>
Laser power, LP	/	10 W
Scan speed, LS	/	3500 mm.s <sup>-1</sup>
Scan spacing, SS	/	0.2 mm
Scan count, SC	/	2

During the selective laser sintering process, the preheating temperature is adjusted at least 30 °C less than the melting point to reduce the warm-up time of powder in the build chamber. The bed temperature is always between crystallization temperature onset and melting temperature onset, it is so-called sintering windows of processing temperatures. Layer thickness can be set between 0.08 mm and 0.25 mm, and usually makes up two or three times of average particle size. The laser parameters such as laser power, scan speed, spacing and count depend on the capabilities of the machine. Moreover, two kinds of laser scanning strategy like “fill” or “fill and outline” options are available.

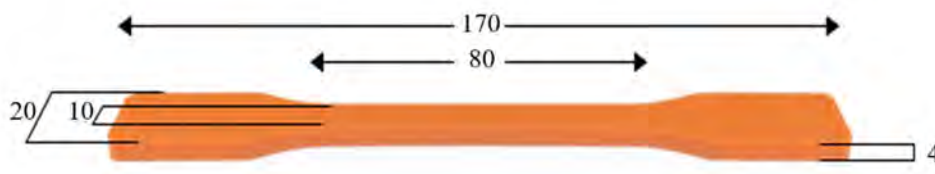
In this work, the optimal processing parameters for polyamide 12 differ slightly from each other for two kinds of selective laser sintering machines. This is due to the use of two different laser scanning strategies. In the first machine only fill laser beam scan is considering, while in the second machine laser beam scans the entire cross-section with outlines its contour. The preheating temperature and layer thickness remain unchanged. Further, the bed temperature during the selective laser sintering process always varies more or less than 1 °C. Nevertheless, the reduced temperature in the second machine is regulated by increasing the average energy density to 0.023 J.mm<sup>-2</sup> instead of 0.021 J.mm<sup>-2</sup> in the first machine.

## 4.2.2. Effect of specimen size

The effect of the relative size of the specimen structure on the macrostructure is important. It may induce the size impact on mechanical properties of the material and the change in the deformation mechanism depending on the shape of the macrostructure. In the present study, the effect of the specimen size and orientation in the build chamber on the mechanical properties are investigated. In this section, all the manufactured parts are based on Duraform PA12 powder sintered by the sPro230 SLS machine.

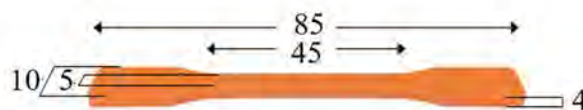
### 4.2.2.1. Geometry of specimens

The research on new powder for additive manufacturing requires many test specimens and the cost of printing depends on the size and orientation of parts. It could be interesting to decrease the amount of powder needed to print test specimens by reducing their size compared to standards and defining if scale factor exists in the mechanical response of samples.



All dimensions are in millimeters and are approximate

(a)



All dimensions are in millimeters and are approximate

(b)

**Figure 4.2. Dog-bone tensile test specimen (a) L = 170 mm (b) L = 85 mm**

Test specimens were designed to the ISO 527 tensile dog-bone geometry standard for longer samples and half of the dimensions for small samples. The most important dimensions of these samples are summarised in Figure 4.2.

### 4.2.2.2. Tensile test method

The mechanical properties of selective laser sintering parts were determined according to the ISO 527. They were carried out with an Instron Universal Testing System 33R4204

computer-controlled electromechanical testing system, capable of performing a variety of tests based on tension and compression. The load frame is a tension/compression type employing a moving (screw-driven) crosshead. It is rated for loading capacity up to 50 kN, crosshead speeds range from 0.05 mm.min<sup>-1</sup> to 500 mm.min<sup>-1</sup> and maximum crosshead travel of 1.17 m. The system is controlled from the control panel and a computer. The computer provides automated control, data acquisition and analysis. During tests, samples are equipped by an external mechanical extensometer in a controlled room. Tensile tests were performed using five samples type 1 for each of the specimens tested. The test parameters are as follow:

- displacement rate: 2 mm.min<sup>-1</sup>;
- 5 kN force cell (Instron 2525-805);
- Instron 2620 series extensometer;
- end of the test criterion: the rupture of the test specimen.

During measurement of the tensile specimens, the X-axis and Y-axis printed samples are loaded parallel to the layer interfaces, while the Z-axis printed samples are loaded perpendicularly to the layers. During all the tests, load, cross-head displacement and elongation are recorded to post-treat the behaviour of the materials.

#### 4.2.2.3. Results and discussion

Engineering stress-engineering strain curves in Figure 4.3 were used to calculate the elastic modulus of the material. Engineering stress was defined as the force divided by the initial cross-section areas measured per sample. The strain was defined as the measured displacement divided by the initial length of the sample. The resulting force-displacement data was used to calculate the ultimate tensile strength (maximum resistance or stress) and elongation at break.

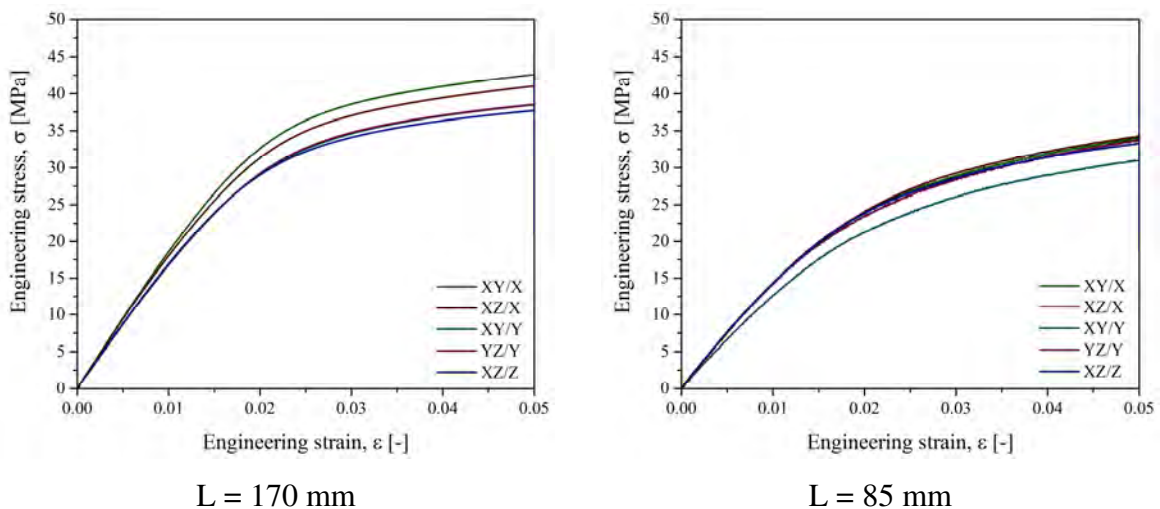


Figure 4.3. Stress-strain diagrams for long and small specimens in all directions of printing

First of all, for all the configuration, length and orientation, the reproducibility of the test is outline by the fact that all the curves have the same trend and there is no major difference between all the curves of the same configuration. A comparison of stress-strain curves obtained for long and small printed samples in each configuration shows a similar profile. All the diagrams in each direction of printing are presented in Annex A.5.1. The behaviour of printed samples has a non-linear global profile which can be cut in two distinct parts. The beginning of the linear curve presents elastic behaviour, then a macroscopic hardening of the curve appears. This represents an elastic linear initial behaviour, then in a second time, a viscoelastic behaviour. The behaviour of the material is non-linear viscoelastic. The rate at which stress increases with strain reduces faster after an initial rapid increase, the stress-strain curves become nearly flat as the failure strain is approached. It can be due to strong bonds between the powder particles after the sintering process. There is no significant difference in the trend between the long and small specimens. Similar results on polyamide 12 have been reported by Hofland et al. [43] and Jain et al. [270].

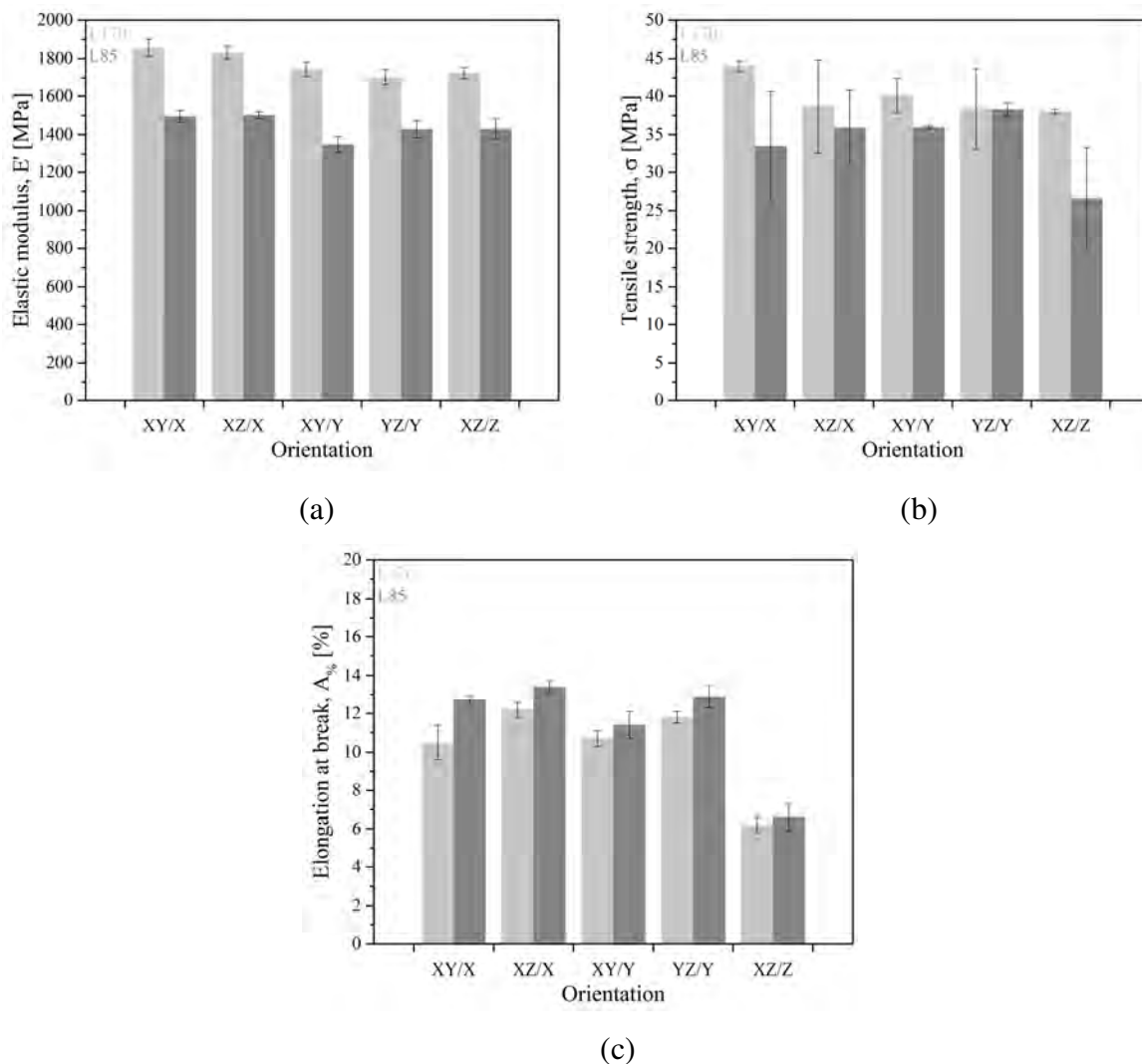


Figure 4.4. Mechanical properties for 2 different length specimens

Elastic moduli  $E'$ , to respect the ISO 527 standard, have been calculated for a deformation between 0.0005 and 0.0025. The elastic moduli (a), tensile strength (b) and elongation at break (c) of Duraform PA12 parts are presented above, in Figure 4.4.

Elastic modulus is always higher for large specimens, from 16 % to 23 % compared to small ones. For large specimens, the modulus is between 1702 MPa and 1855 MPa, with the lowest value for the YZ/Y direction. The modulus varies between 1349 MPa and 1502 MPa for small specimens, with the lowest value for the XY/Y direction. These results are close to each other, indicating that for elastic modulus the Z direction is not distinguishable for large and small specimens. The best results have been obtained for samples printed in the X-axis for both, large and small specimens. Moreover, the maximum obtained values of elastic modulus found for large specimens are much higher than the values presented in material datasheet. By considering the elastic modulus of 1586 MPa based on the technical specification of Duraform PA12, the value is higher of 15 %, 9 % and 8 % for the highest values in the X-axis, Y-axis and Z-axis, respectively. In the case of small specimens, the elastic modulus obtained is smaller of 6 %, 18 % and 11 % for the highest values in the X-axis, Y-axis and Z-axis, respectively. The most comparable result has been obtained for small specimen printed in the XZ/X direction with the elastic modulus of 1502 MPa.

Concerning the ultimate tensile strength, the difference between large and small specimens is significant for the XY/X and XZ/Z orientations. The difference reaches up to 10 MPa between the two types of test samples. For the XZ/X and XY/Y orientations, the results are different up to 4 MPa for large and small specimens, an average of 39 MPa and 36 MPa, respectively. The YZ/Y direction presents the same tensile strength of 38 MPa for both sizes. Ultimate tensile strength is always higher for large specimens, up to 43 % compared to small ones. Considering only large specimens, the tensile strength is between 38 MPa and 44 MPa, with the lowest value for the XZ/Z direction. The tensile strength varies between 27 MPa and 38 MPa for the small specimens, with the lowest value for the Z-axis. Thus, the tensile strength shows similar results for large specimens in all directions, while there is a greater dispersion of 43 % on small specimens made in Z-axis. In contrast to elastic modulus, the values of ultimate tensile strength are closer to the values presented in material datasheet. The tensile strength of 43 MPa based on the technical specification of Duraform PA12 is the same for large specimens printed in XY/X direction and differs only up to 13 % for the lowest values for all orientations. In this case, the tensile strength is much lower for small specimens from 13 % to 62 %.

The elongation at break of large and small test pieces are similar, however, the elongation is always higher for small specimens. Large test specimens elongate less, by a maximum of



12.7 %, except that with the smaller value for XZ/Z orientation of 6.6 %. Small specimens are more deformable, with an elongation rate up to 13.4 % maximum, and only 6.2 % for XZ/Z orientation. This result is also explained by a larger volume on the large specimens increasing the risk of the presence of defect decreasing the properties to failure. For both types of specimens, the deformation does not depend on the orientation, except for the XZ/Z, for which deformation is lower, probably due to interlayer delamination. Moreover, based on the technical specification of Duraform PA12, the elongation at break is 14 %, thus, the values are lower for large and small specimens. Nevertheless, the elongation at break is close for large and small specimens up to 25 % and 19 %, respectively. The best value of elongation (13.4 %) has been obtained for small specimens in XZ/X orientation.

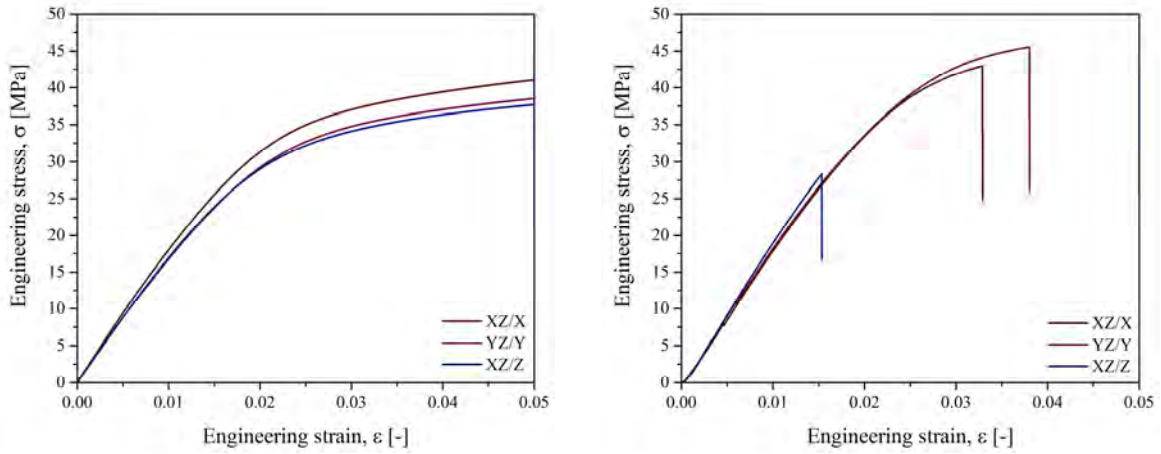
The differences in mechanical properties between large and small specimens could be explained by the process strategy. It has been to be considered that if the dimensions of the large specimens are larger than the small ones, the laser will spend more time to come-back at the same position, for the large specimen, to irradiate the following layer. That is to say that the large specimen has more time to cool before the second pass of the laser compared to the small ones. So, the thermal history of the material for large specimens and small specimens is different, that is conducted to the difference in thermo-physical properties such as crystallinity rate and so on, mechanical properties.

In the next section, the obtained results are compared for the effect of specimen orientation with another machine/material pair.

#### **4.2.3. Effect of specimen orientation**

In all the traditional manufacturing processes, orientation is a parameter which has an impact on the feasibility of part. The orientation choice can make the part complicated to produce, and it can raise the cost of the final part. Usually, the AM processes are not impacted by orientation when it comes to the feasibility of part, mainly in the case for powder-based technologies such as selective laser sintering. The part orientation mainly has an impact on the quality of the final part, and often the printing in the Z-axis makes the problems [271].

Wide research on two pairs of selective laser sintering machine and polyamide material is presented. First of all, the pair of sPro230/ Duraform PA12 was observed, then the pair of ProX500/ Duraform FR1200 has been studied as a pair used in the next part of this chapter. According to the geometry and tensile test method from the previous section, the following results are obtained.



sPro230 /Duraform PA12

ProX500 / Duraform FR1200

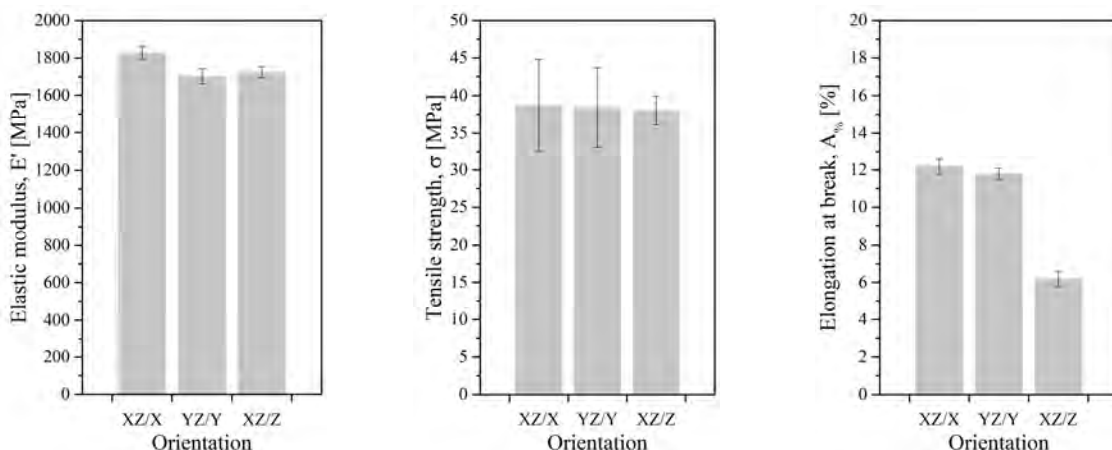
**Figure 4.5. Stress-strain diagrams for pairs machine/material for all directions of printing**

The same trend of stress-strain curves for each direction and each pair of material/machine is obtained. So, it gives a good reproducibility for each configuration. All the diagrams in each direction of printing are presented in Annex A.5.2. The curves represent elastic behaviour on the beginning, and then a macroscopic hardening of the behaviour takes place. Non-linear viscoelastic behaviour is identified. The profile is similar for the X-axis and Y-axis, while for the Z-axis turns out that the deformation threshold involving the inflexion of the curves is smaller. It is due to worse mechanical properties.

The stress-strain curves, as seen in Figure 4.5, allow the description of the behaviour of the material. In all direction, the curves show a similar trend with close values for all directions of the samples.

For the two machine/material pairs, the validity of the tests had resulted in a break in the useful area of the test specimens. It may follow a calculation of an elastic modulus of elasticity, maximum resistance or stress and elongation at break.

sPro230 /Duraform PA12



## ProX500 / Duraform FR1200

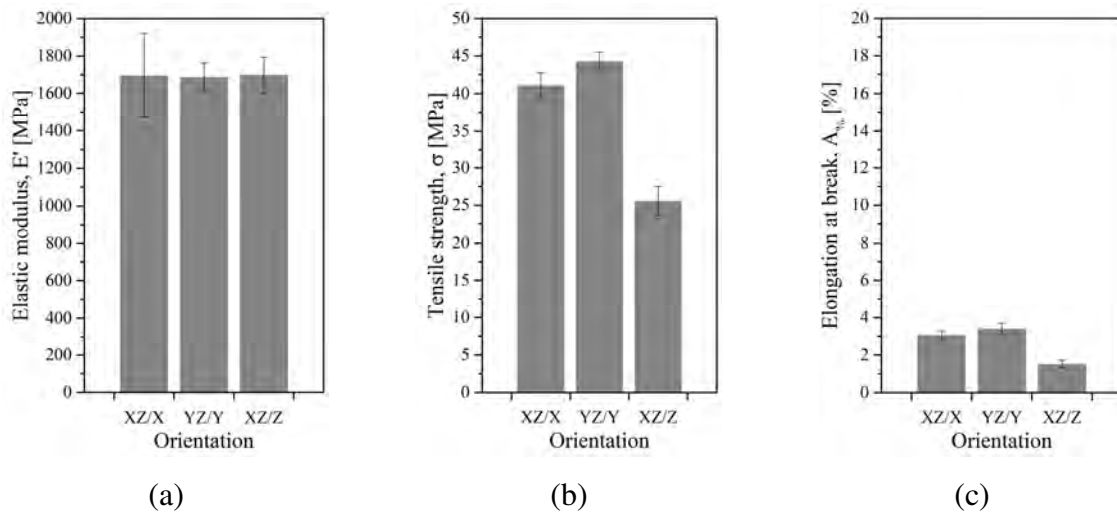


**Figure 4.6. Mechanical properties of (a) elastic modulus (b) tensile strength (c) elongation at break**

As in the previous section, elastic moduli, to respect the ISO 527 standard, has been calculated for a deformation between 0.0005 and 0.0025. Elastic modulus, tensile strength and elongation at break of pairs machine/material parts are presented above.

Taking into consideration that two different machines and polyamides were used, the elastic modulus maintains similar values between 1688 MPa and 1829 MPa. However, the elastic modulus is always higher for Duraform PA12. This is an unexpected result because according to the technical specification of powders, Duraform FR1200 has an elastic modulus of 2040 MPa, which is 29 % higher than for Duraform P12. The ultimate tensile strength is observed to be also similar for both pairs of machine/material and it is between 38 MPa and 44 MPa. In contrast to elastic modulus, the values of tensile strength are higher for Duraform FR1200 in the X-axis and Y-axis. In this case, the tensile strength in XZ/Z orientation on ProX500 SLS is 41 % less than for the specimens printed in the Y-axis. Generally, the values are close to expected from technical specifications, 43 MPa and 41 MPa for Duraform PA12 and Duraform FR1200, respectively. The elongation at break of test samples shows significant differences. This is not a surprise because according to datasheets, the elongation at break is 14 for Duraform PA12 and 5.9 % for Duraform FR1200. Of course, the results are lower than expected. In both cases, the results are quite similar in the X-axis and Y-axis direction, around 12 % and 3 % for Duraform PA12 and Duraform FR1200, respectively. The specimens printed in XZ/Z direction are two times smaller. The results obtained from parts printed in the Z-axis orientation were due to weak layer-layer bonding. This offered little resistance to the load applied, which was perpendicular to the layer-layer bonding. This is in contrast with the test specimens built in the X-axis orientation, where the loading was applied parallel to the layer-layer bonding.

The orientation of printed specimens in the X-axis and Z-axis of Duraform PA12 has been also studied by mentioned before Caulfield et al. [28]. They used the pair machine/material as DTM Sinterstation 2500 and Duraform PA12 by 3D Systems. For the laser energy density of  $0.020 \text{ J.mm}^{-2}$ , the laser power of 15 W, scan spacing of 0.15 mm, as well as, a scan speed of  $5080 \text{ mm.s}^{-1}$  have been applied. They found extremely low elastic modulus of 1050 MPa and 850 MPa for the X-axis and Z-axis directions. However, obtained values of tensile strength were found around the maximum of 48 MPa for horizontally printed specimens and 44 MPa for vertically printed specimens. They reported higher elongation at break of 17 % for Z-axis. The elongation at break in the X-axis was found 14 %, which perfectly corresponds to the technical specification of this material.

The results on the orientation of printed parts in the X-axis, Y-axis and Z-axis have been reported by Ajoku et al. [272]. They used the pair machine/material as Vanguard and polyamide 12 by 3D Systems. In this case, the machine has filled and outline laser strategy. The sintering process parameters were filled laser power of 11 W, outline laser power of 5 W, scan spacing of 0.15 mm and scan speed of  $5000 \text{ mm.s}^{-1}$ . They have found the highest elastic modulus, ultimate tensile strength and elongation at break of 2047 MPa, 50 MPa and 11 %, respectively, in the X-axis. The lowest obtained values for the elastic modulus of 1830 MPa, tensile strength of 42 MPa and elongation at break of 8.6 % were found in the Z-axis.

#### **4.2.4. Conclusion on the influence of manufacturing on material performance**

The size of printed samples has a direct impact on the mechanical properties, which are lower for small specimens. In the case of samples orientation, there is almost no difference between them, the exception is the XZ/Z direction where the area between sintered layers was the smallest one, caused by weak layer-layer bonding. The specimen manufactured along the Z-axis reveal a lower elongation at break in each case.

It cannot lead to pointing which of the machine is better as it is known that different polyamides were used. However, it is essential to note that usage of one machine or the other does not significantly affect mechanical properties. However, it has to be noticed that the Duraform FR1200 processes on the ProX500 SLS show a brittle behaviour compared to the Duraform PA12 processes on the sPro230. Regarding the elongation at break, it shows lower values on ProX500 SLS, but it is due to the fire retardant added material in the polyamide. It is therefore advisable thoroughly observe properties along the Z-axis when manufacturing the part.

This research shows that mechanical properties very much depend on sintering process parameters, in particular, laser properties, which define the laser energy density. Thus, laser power, scan spacing and scan speed play an essential role in the selective laser sintering process. The results of this work led to understanding the consequences of varying these parameters in the selective laser sintering process on quality of parts (strength) and processing time.

### 4.3. Design of experiments on the SLS materials

The design of experiments is the design of any task that aims to describe or explain the variation of information under conditions that are hypothesized to reflect the variation. The term is generally associated with experiments in which the design introduces conditions that directly affect the variation, but may also refer to the design of quasi-experiments, in which natural conditions influence the variation which is selected for an object of the research.

The classical method is to give a constant value to almost all the variables (S) except one and to vary it, the number of experimental points (n) is then chosen. When all the defined experiments are done, the answer is plotted according to the variable. If the totality of variables is studied, the number of experiments to realize (N) is then:

$$N = S^n \quad (4.1)$$

Besides, to be sure that the measured answer is correct, each experiment must be repeated to have several similar results. The number of experiences then grows multiplicatively. This approach is not viable. There are two solutions for the experimenter: to reduce the number of experimental points or to reduce the number of variables. Whether in the first case or the second, a significant amount of data is lost and the understanding of the system is biased. Thus, the experimental design method was developed to overcome the experimental method.

The crucial difference between the two methods is that, for experimental designs, the levels of all factors vary for each experiment. This change is still done in a programmed and reasoned way. The incessant change of all the factors at once seems to be a disadvantage but it brings many advantages [273]:

- decrease in the number of tests;
- very large number of factors studied;
- detection of interactions between factors;
- detection of optimal;
- better precision on results;
- optimization of results;
- modelling of results.

Experimental designs then make it possible to study many factors (discrete or continuous) at different levels and to determine the most influential ones. Thus, additional tests can be

performed on the variables identified previously. Also, they allow achieving a complete study by limiting the budget and time consumption.

#### 4.3.1. Set-up of designs o experiments

The ProX500 SLS machine using only fresh Duraform FR1200 powder has been chosen to print tensile and flexural specimens for monitoring the quality of the printing process. The chosen 3D printer is a fully industrial machine. For the experimental work, the process parameters, such as fill laser power, fill scan count, outline laser power, outline scan count and scan spacing were selected due to their dominant influence on part quality. These process parameters are defined as follows:

- laser power, the amount of power or energy available from the laser beam at part bed surface during filling of laser in a slice;
- scan count, the number of laser movements on the surface of part on the part bed;
- scan spacing, the distance between two neighbouring parallel scan lines during a fill.

The ranges of factors were finalized based on energy density and opinions of experts [26]. The fill and outline energy density that affect the part quality have been calculated according to the given equation:

$$ED = \frac{LP \times SC}{SS \times LS} \quad (4.2)$$

where:

- ED - energy density [J.mm<sup>-2</sup>];  
 LP - laser power [W];  
 SC - scan count [-];  
 SS - laser scan spacing [mm];  
 LS - laser beam speed [mm.s<sup>-1</sup>].

with:

- LS<sub>fill</sub> = 12000 mm.s<sup>-1</sup>;  
 LS<sub>outline</sub> = 3500 mm.s<sup>-1</sup> [Annex A.1.11].

It was justified by Yusoff and Thomas [274] that the laser energy density depends mainly on three variables like laser power, scan count and laser scan spacing which can have a different

impact on the results. The laser speed is constant as invariable adjusted by 3D Systems. According to Stwora and Skrabalak [35], the scanning speed does not influence sample properties, however, it might be possible to reduce the time of machining by maximizing scan speed, in case of building large elements.

**Table 4.2. Production thermoplastic parts with ProX500 SLS printer**

Possibilities of process parameters	ProX 500 SLS
Preheating temperature, $T_p$	< 200 °C
Bed temperature, $T_b$	< 290 °C
Layer thickness, PLT	0.08 – 0.15 mm
Fill laser power, LPf	< 100 W
Fill scan speed, LSf	12000 mm.s <sup>-1</sup>
Outline laser power, LPo	< 50 W
Outline scan speed, LSo	3500 mm.s <sup>-1</sup> (2018) or 5000 mm.s <sup>-1</sup> (2019)
Scan spacing, SS	< 0.25 mm
Scan count, SC	1 or 2
Orientation, $\theta$	< 90°
Post add powder layer delay, $t_{pl}$	< 5 s

Literature suggests that the energy density for polyamide 12 should be between 0.01 J.mm<sup>-2</sup> and 0.048 J.mm<sup>-2</sup> [31]. A total of forty experiments were executed at five independent input variables which were varied up to five levels in the range of parameters available in the machine presented in Table 4.2. Different process parameters and their values which have been finalised for the experimental part are presented in Table 4.3. The rest of parameters despite the selected process were kept fix.

**Table 4.3. Different process parameters and their values**

Process parameters	Studied parameters				
	1	2	3	4	5
Fill laser power, LPf [W]	15	20	30	40	45
Fill scan count, SCf [-]	1	2			
Outline laser power, LPo [W]	10	13	15	/	/
Outline scan count, SCo [-]	1	2			
Scan spacing, SS [mm]	0.15	0.20	0.25	/	/



Any design of experiences is characterised by the factors and their influences but also by the desired answers. As the development of parameter sets on the ProX500 SLS is required, the answers concern the mechanical and geometrical characteristics in additive manufacturing. It has been added production time to evaluate some industrial parameters. The answers are presented below:

**Table 4.4. Studied answers for the design of experiments**

Studied answers					
Density and porosity	Geometry and dimensions	Tensile mechanical properties	Flexural mechanical properties	Production time	Thermal transitions

After calculations, forty sets of parameters have been selected according to the range of energy density to obtain proper and not degraded sintering parts. Tests were performed for the fixed preheating temperature of 130 °C, part bed temperature of 173 °C and powder layer of 0.1 mm. The inert gas atmosphere of nitrogen has been used for the sintering process. Experiment n°9 corresponds to standard parameters of fill laser power of 2 x 20 W, outline laser power of 2 x 10 W and scan spacing of 0.20 mm proposed by the supplier of machine and powder.

**Table 4.5. Duraform FR1200 experimental design with variable values**

Exp. n°	Fill laser power [W]	Fill scan count [-]	Outline laser power [W]	Outline scan count [-]	Scan spacing [mm]	Fill energy density [J.mm <sup>-2</sup> ]	Outline energy density [J.mm <sup>-2</sup> ]
1	15	2	10	2	0.15	0.017	0.038
2	15	2	10	1	0.15	0.017	0.019
3	15	2	13	1	0.15	0.017	0.025
4	15	2	15	1	0.15	0.017	0.029
5	20	2	10	2	0.15	0.022	0.038
6	20	2	10	1	0.15	0.022	0.019
7	20	2	13	1	0.15	0.022	0.025
8	20	2	15	1	0.15	0.022	0.029
9	20	2	10	2	0.20	0.017	0.029

10	20	2	13	2	0.20	0.017	0.037
11	20	2	13	1	0.20	0.017	0.019
12	20	2	15	2	0.20	0.017	0.043
13	20	2	15	1	0.20	0.017	0.021
14	30	1	10	2	0.15	0.017	0.038
15	30	1	10	1	0.15	0.017	0.019
16	30	1	13	1	0.15	0.017	0.025
17	30	1	15	1	0.15	0.017	0.029
18	40	1	10	2	0.15	0.022	0.038
19	40	1	10	1	0.15	0.022	0.019
20	40	1	13	1	0.15	0.022	0.025
21	40	1	15	1	0.15	0.022	0.029
22	40	1	10	2	0.20	0.017	0.029
23	40	1	13	2	0.20	0.017	0.037
24	40	1	13	1	0.20	0.017	0.019
25	40	1	15	2	0.20	0.017	0.043
26	40	1	15	1	0.20	0.017	0.021
27	45	1	10	2	0.15	0.025	0.038
28	45	1	10	1	0.15	0.025	0.019
29	45	1	13	1	0.15	0.025	0.025
30	45	1	15	1	0.15	0.025	0.029
31	45	1	10	2	0.20	0.019	0.029
32	45	1	13	2	0.20	0.019	0.037
33	45	1	13	1	0.20	0.019	0.019
34	45	1	15	2	0.20	0.019	0.043
35	45	1	15	1	0.20	0.019	0.021
36	45	1	10	2	0.25	0.015	0.023
37	45	1	13	2	0.25	0.015	0.030
38	45	1	13	1	0.25	0.015	0.015
39	45	1	15	2	0.25	0.015	0.034
40	45	1	15	1	0.25	0.015	0.017

Five standardised tensile and flexural specimens were manufactured in YZ axis Y orientation with the length direct parallel to the Y-axis, width parallel to the Z-axis and

thickness parallel to the X-axis for each experiment set of parameters. The trajectory of the laser was perpendicular to the length of the specimens, which is presented and marked in the red circle in Figure 4.7.

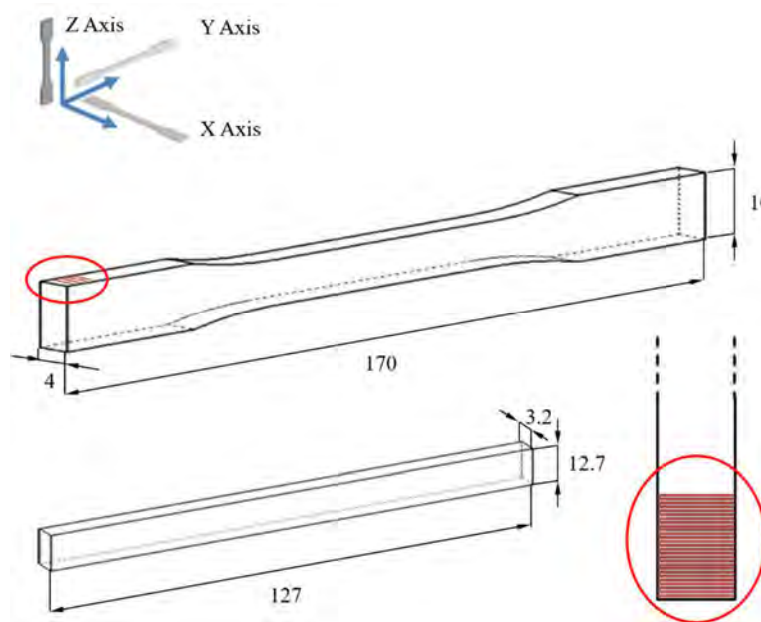


**Figure 4.7. Specimens for tensile and flexural testing**

A total of four hundred samples were prepared and tested as a designed plan presented in Table 4.5. Further, the iconography of correlations analysis was carried out on the collected data to obtain an optimized set of parameters.

## 4.3.2. Characterization methods and results

### 4.3.2.1. Density and porosity

The bulk and relative density of printed flexural parts was determined. First of all, the volumetric method, where the mass of samples was obtained by weighing on a digital scale and the volume was determined by using Vernier calliper measurement with the uncertainty on a single reading of 0.01 mm.

$$\rho_{\text{volumetric}} = \frac{\text{Mass [g]}}{\text{Volume [cm}^3\text{]}} \quad (4.3)$$

The fabricated parts contain pores, so the determination of actual density by hydrostatic weighing was done. Thus, the Archimedes principle [275], which states that a body immersed in a fluid is buoyed up by a force equal to the weight of the displaced fluid. This method can measure the density of the entire part with its pores. The measurement procedure for the bulk density of the sintered part is the following:

- measurement of the dry weight of part ( $M_1$ ), at least 3 hrs at 100 °C;
- a weight measurement of the water-saturated sample in water ( $M_2$ ). The density of water was quoted. The measured room temperature of the laboratory was 27 °C. The density of water according to the measured temperature is 0.9965 g.cm<sup>-3</sup>;
- a weight measurement of the water-saturated sample in the air ( $M_3$ ).

The determined  $M_1$ ,  $M_2$  and  $M_3$  are substituted in Equation 4.4.

$$\rho_{\text{hydrostatic}} = \frac{M_1}{M_1 - [M_2 - (M_3 - M_1)]} \left[ \frac{\text{g}}{\text{cm}^3} \right] \quad (4.4)$$

Moreover, the relative density characterised porosity was calculated from the ratio of hydrostatic density and theoretical density of fresh powder.

$$\rho_{\text{relative}} = \frac{\rho_{\text{hydrostatic}} \left[ \frac{\text{g}}{\text{cm}^3} \right]}{\rho_{\text{true}} \left[ \frac{\text{g}}{\text{cm}^3} \right]} \times 100 \% \quad (4.5)$$

The true density of Duraform FR1200 was measured by the pycnometer method measured in ethanol and it is equal to 1.095 g.cm<sup>-3</sup>. The results of density for Duraform FR1200 parts are presented in Figure 4.8.

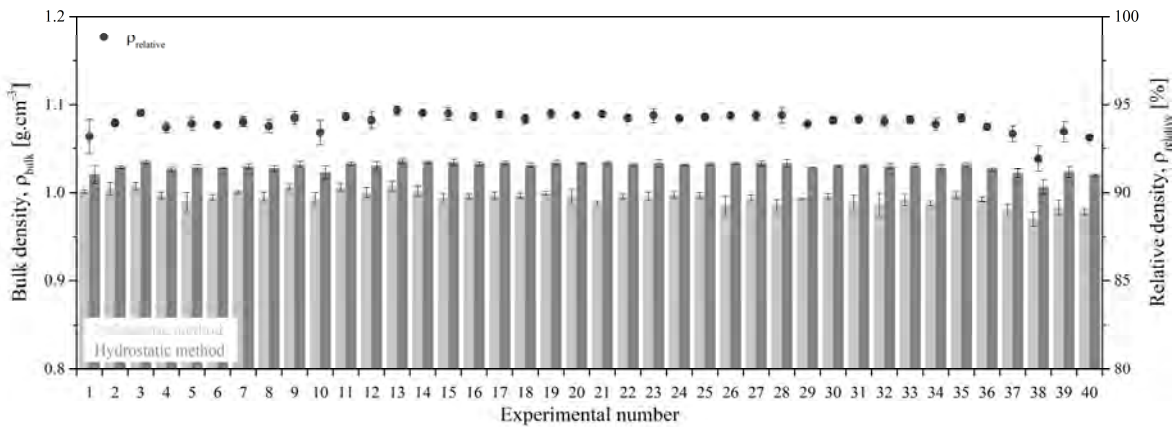


**Figure 4.8. Bulk and relative density of sintered parts**

During the selective laser sintering process, the powder particles are sintered by the heat of laser and therefore the part density and porosity depending on the energy density provided by the laser [276]. Sintered parts have achieved bulk density in the range from 0.970 g.cm<sup>-3</sup> to 1.007 g.cm<sup>-3</sup> and from 1.006 g.cm<sup>-3</sup> to 1.036 g.cm<sup>-3</sup> for volumetric method and Archimedes principle, respectively. The highest hydrostatic density was obtained for exp. n°13 while the lowest density had exp. n°38.

Wegner and Witt [42] reported maximum densities of PA12 approximately  $0.998 \text{ g.cm}^{-3}$ , while Caulfield et al. [28] found even higher values of  $1.050 \text{ g.cm}^{-3}$  for horizontally printed samples. The difference in density may be related to differently shaped density samples or different methods used. For example, Wegner and Witt [42] and Caulfield et al. [28] both used density cubes to determine the bulk density. According to the technical specification of Duraform FR1200, the bulk density of the sintered part is  $1.020 \text{ g.cm}^{-3}$ . Thus, the results of the second method, as closer to the datasheet, have been used for calculation of porosity.

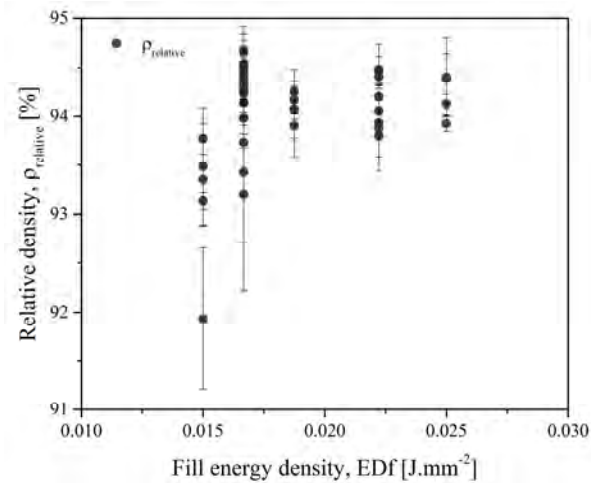


**Figure 4.9.** Effect of fill energy density upon the relative density of Duraform FR1200 samples

The relative density in the range of 92-95 % corresponds to a very small porosity of sintered parts around 8 %. The highest relative density of 94.67 % was achieved with a fill energy density of  $0.017 \text{ J.mm}^{-2}$  (LP = 20 W, SC = 2, exp. n°13). The highest porosity of 8.07 % was obtained with a fill energy density of  $0.015 \text{ J.mm}^{-2}$  (LP = 45 W, SC = 1, exp. n°38). In general, the high relative density of Duraform FR1200 parts has been observed for all sintered parts which indicate a small number of pores developed by the selective laser sintering process. In Figure 4.9 it can be seen that the less is the fill energy density, the higher is porosity. Ajoku et al. [272] have compared laser sintering and injection moulded polyamide 12 parts. The density of the sintered sample was measured of  $0.96 \text{ g.cm}^{-3}$ , while the density of injection moulded polyamide 12 was measured to be  $1.03 \text{ g.cm}^{-3}$ . This shows 7 % of porosity within the selective laser sintered polyamide 12.

#### 4.3.2.2. Geometry and dimensions

An analysis of the dimensionality control of specimens according to ISO 2768 [277,278] to discard the sets of parameters do not guarantee tolerated geometry of pieces. Medium tolerance class has been applied to linear dimensions of printed parts. Three individual measurements (length, thickness, and width) of each dimension were taken and an average

value was calculated. The dimensions were measured using Vernier calliper with a precision of 0.01 mm and compared to the dimensions of input drawing. The length of tensile samples was measured by a ruler with a precision of 0.1 mm. The results of each five samples per set of parameters are presented in Figure 4.10 and Figure 4.11. The tolerance is described by the area between green lines according to real dimensions.

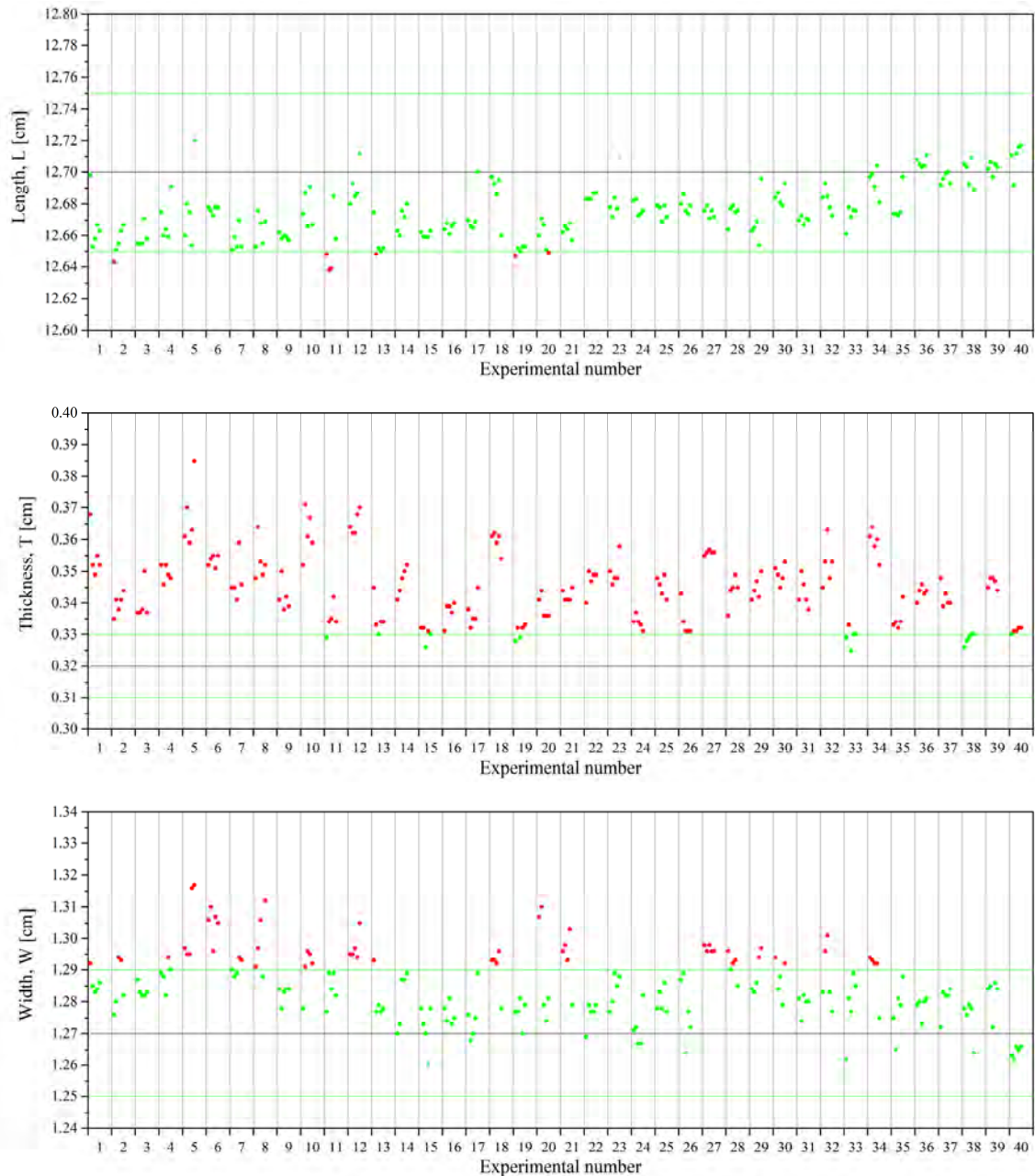
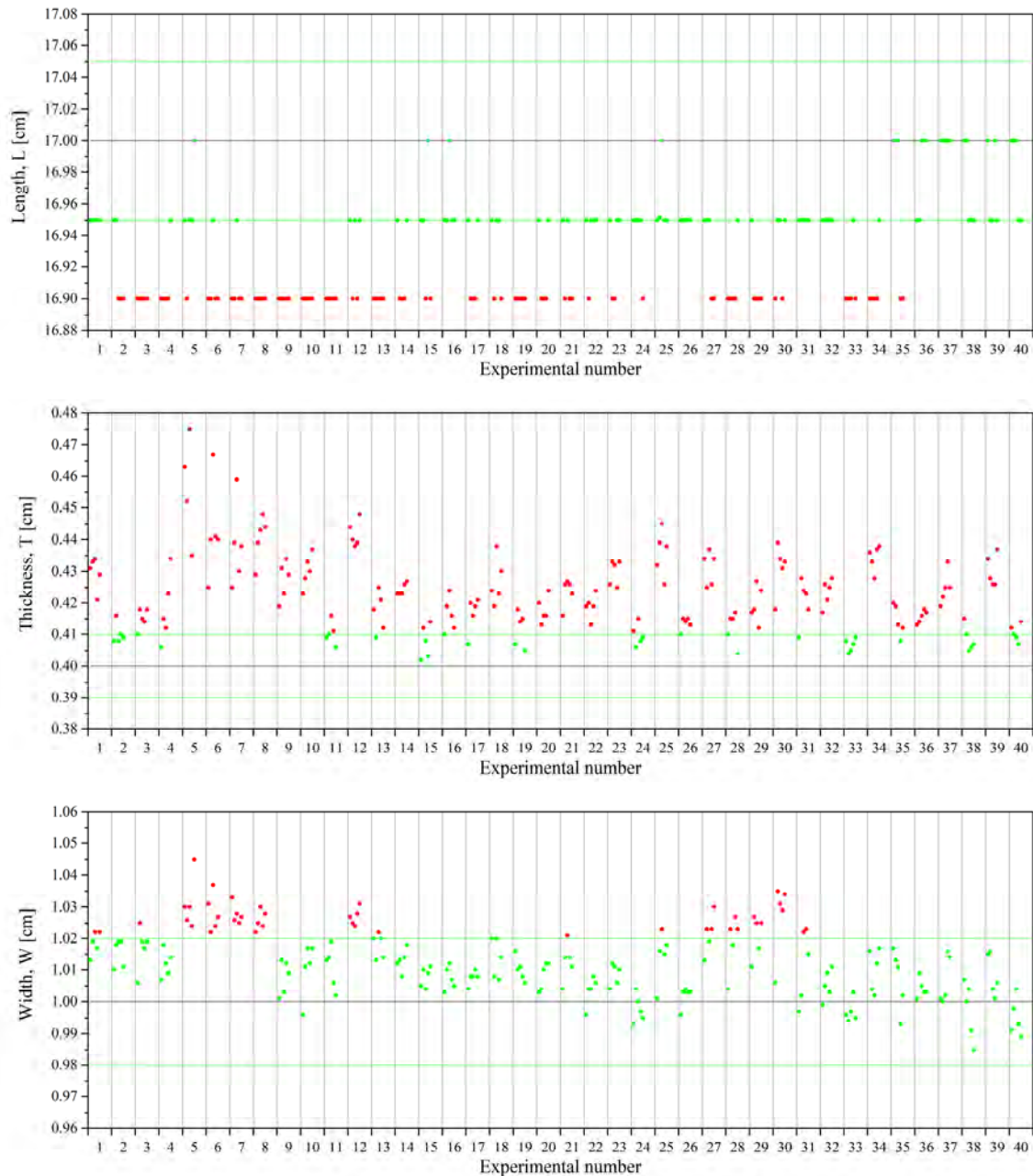


Figure 4.10. Tolerances for linear dimensions of sintered flexion samples

The sintered flexion samples represent better dimensions for length and width. Only 7 samples are over the tolerance for length and 3 of them come from exp. n°11. Most of the samples are below the expected size with the maximum error obtained of 0.5 %. The increase in the dimension of length can be observed for experiments with higher laser power. One-quarter of

samples is over the tolerance for width, consisting of 19 sets of parameters. Most of the samples are oversized with a maximum error of 3.7 % for exp. n°5. The width decrease for higher laser power. In the case of thickness almost all the samples are over the tolerance and oversize. The 16 samples have classified in the range of tolerance and those are exp. n°11, n°13, n°15, n°19, n°33, n°38 and n°40. The maximum error in the thickness is 20.3 % for exp. n°5.



**Figure 4.11. Tolerances for linear dimensions of sintered tensile samples**

The sintered tensile samples show similar results, nevertheless, the dimension of length is worse than in the case of flexion samples. Of course, this is due to the less accurate measurement method using the ruler with the uncertainty on a single reading of 0.1 mm, which makes it less comparable with other results. Half of the samples in the dimension of length is outside the



tolerances, moreover, the samples present the trend below the expected size. The best values of 170 mm long were obtained for higher laser powers. Considering the thickness, less than one-quarter of samples are found in the tolerances by consisting of 17 sets of parameters. The oversize in thickness is obvious and the maximum error of 22.0 % corresponds to exp. n°5. The results of width also show oversizing, but only one-quarter of samples is out of tolerance for 15 experiments. The maximum error in the width is 4.5 % for exp. n°5.

Concluding, the thickness and width grow in the sintered flexion and tensile samples while length decreases. This phenomenon can be explained by perpendicular to the length of the specimens trajectory of the laser. Thus, more energy is applied in a small area of thickness and width of samples. The higher grow corresponds to the scan spacing of 0.15 mm. The best dimensional results (medium tolerance in length, thickness and width for at least three samples) are seen for exp. n°33, n°38 and n°38, n°40 for flexion and tensile samples, respectively.

In this work, the linear shrinkage of sintered parts was calculated as follows:

$$L_{\text{shrinkage}} = \frac{(L_0 - L)}{L_0} [\%] \quad (4.6)$$

$$W_{\text{shrinkage}} = \frac{(W_0 - W)}{W_0} [\%] \quad (4.7)$$

$$T_{\text{shrinkage}} = \frac{(T_0 - T)}{T_0} [\%] \quad (4.8)$$

$$V_{\text{shrinkage}} = \frac{(V_0 - V)}{V_0} [\%] \quad (4.9)$$

where:

- $L_0$  - nominal length [cm];
- $W_0$  - nominal width [cm];
- $T_0$  - nominal thickness [cm];
- $V_0$  - nominal volume ( $L_0 \times W_0 \times T_0$ ) [cm<sup>3</sup>];
- $L$  - actual length [cm];
- $W$  - actual width [cm];
- $T$  - actual thickness [cm];
- $V$  - actual volume ( $L \times W \times T$ ) [cm<sup>3</sup>].



For shrinkage of part dimensions, five sintered parts were used for each set of parameters and then the average value for the sample length, thickness and width for each set was obtained.

The results of part dimension measurements are presented in Figure 4.12 and Figure 4.13 for flexion and tensile samples, respectively.

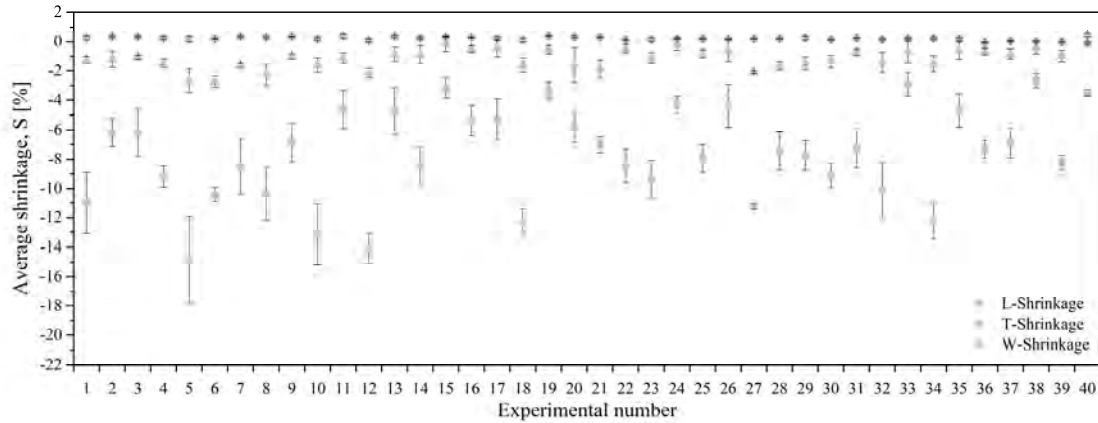


Figure 4.12. Average shrinkage of sintered flexion samples

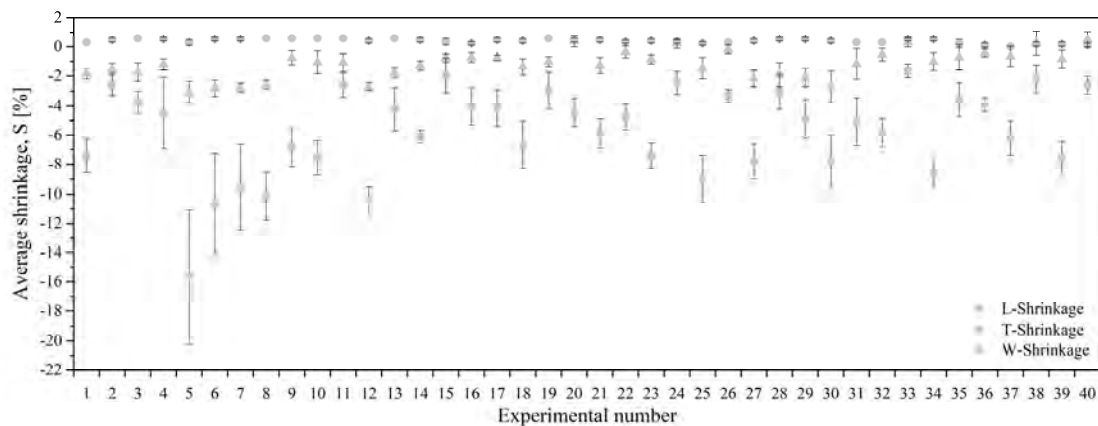
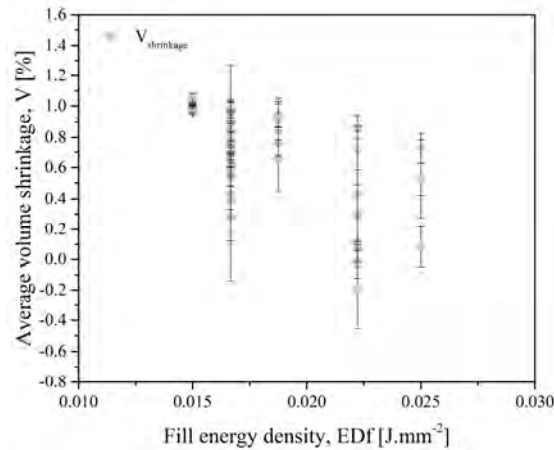


Figure 4.13. Average shrinkage of sintered tensile samples

The investigation shows that the shrinkage in the length and width is smaller than in the thickness of printed parts. The high growth in the thickness shrinkage is fluctuating in the range from -2.7 % to -14.9 % (exp. n°5) and from -1.6 % to -15.6 % (exp. n°5) for flexion and tensile samples, respectively. The maximum linear shrinkage was 0.4 % in both, length and width, for tensile parts. In the case of flexion parts, the maximum linear shrinkage was 0.6 % and 0.5 % in length and width, respectively. In general, the thickness depends on the outline scan count. For the outline scan count of 2, the thickness shrinkage represents lower values. It can be seen in Figure 4.14 that the volume of sintered samples was increasing with the increase of fill energy density which was due to high growth in the thickness of parts. Similar results on UHMWPE have been reported by Khalil et al. [37] who printed their samples in the XY-axis and the thickness was in the Z-axis.



**Figure 4.14. Average volume shrinkage of sintered flexion samples with different laser energy densities**

Distortion in the selective laser sintering process can be caused by stresses during the building and cooling processes [279]. Shrinkage may be caused by factors, such as the kind of materials, process parameters, and orientation of sintered parts. Moreover, growth in sintered parts may also occur due to thermal inconsistencies within the powder bed. Goodridge et al. [280] reported the influence of time the powder bed retains heat and the thickness of the powder layer. They were able to produce UHMWPE sintered parts with a dimensional accuracy of more or less 0.1 mm for parts being built in the Z-axis direction.

#### 4.3.2.3. Mechanical properties

The mechanical tests were performed on flexural specimens by three-point bending tests according to ISO 178. The bending samples were designed with a nominal dimension of 127 mm long, 12.7 mm wide and 3.2 mm thick. The tensile specimens were measured according to ISO 20753 and ISO 527. The samples were designed with a nominal dimension of 170 mm long, 10 mm wide and 4 mm thick. They were carried out on the Instron Universal 33R4204 traction machine. The test parameters are as follows:

- movement speed of 2 mm.min<sup>-1</sup>;
- 5 kN force cell (Instron 2525-805);
- span length of 56 mm for flexural specimens only;
- Instron 2620 series extensometer for tensile specimens only;
- end of the test criterion is the rupture of the test specimen.

As previously, the stress-strain curves allow to describe typical yield behaviour of the material. Strain-stress curves, as seen in Figure 4.15, are presented for exp. n°1, n°5, n°14, n°18 and n°27 which correspond to fill laser power of 15 W, 20 W, 30 W, 40 W and 45 W, respectively.

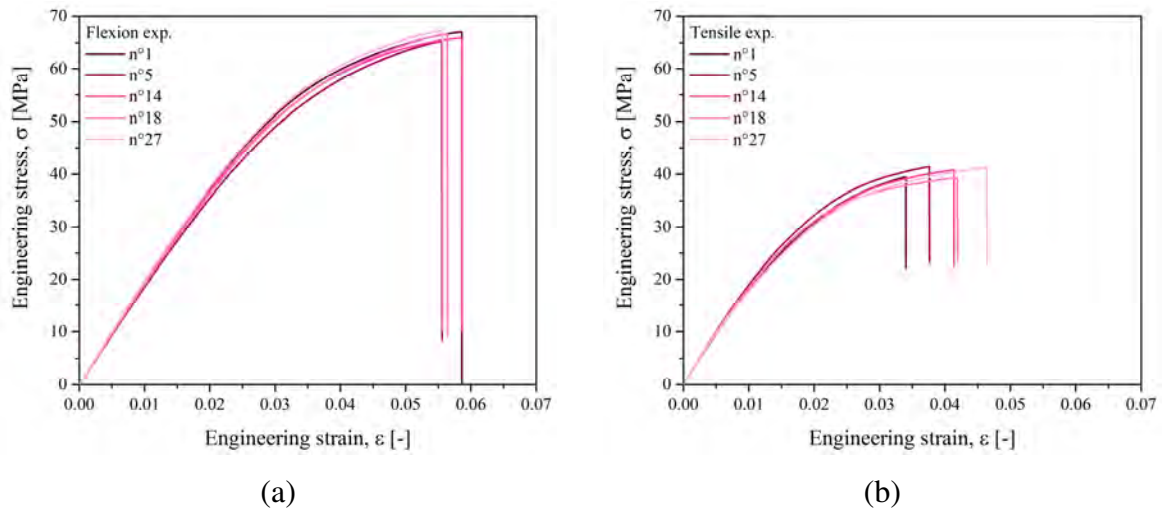


**Figure 4.15. Stress-strain diagrams for some (a) sintered flexion samples (b) sintered tensile samples**

The behaviour of a material is represented by a non-linear curve, first an elastic linear initial behaviour then a non-linear viscoelastic behaviour is observed. The shown curves are representative for all tests performed, and very little scatter was observed between different samples of the same set of parameters. Figure 4.15.b indicates a difference in mechanical response for tensile properties depending on the laser power. The effect of fill laser power on the stress-strain curves of tensile specimens shows that as the laser power increases so does the elastic modulus and the elongation at break.

The viscoelastic behaviour of semi-crystalline polyamide 12 can be determined by the deformation caused by straining the interlamellar amorphous regions enclosed by crystallites. That means that a low degree of crystallization may result in a low elastic modulus and the higher crystallinity in higher modulus as the molecular chains are packed closely and parallel. The viscoplastic behaviour is determined by the fine chain slip of amorphous regions and the large slip between the crystallites. It can be said that a low crystallinity may result in a larger elongation at break [17].

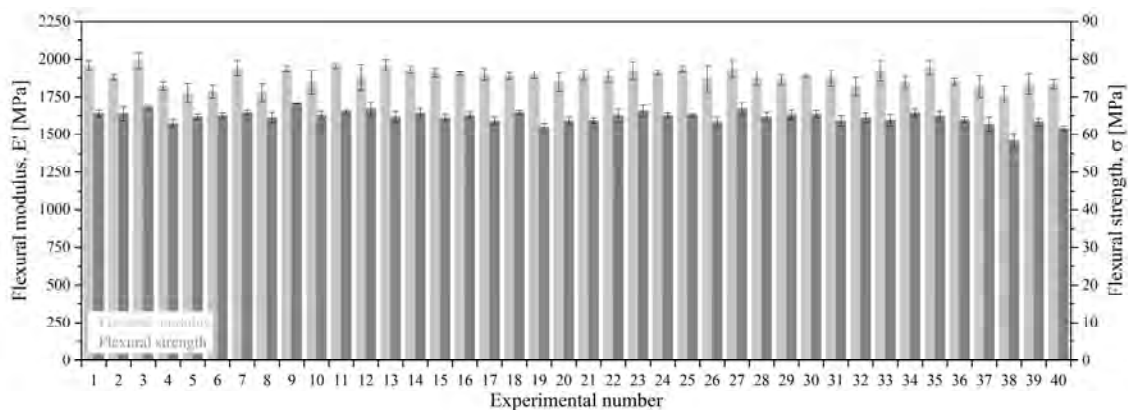
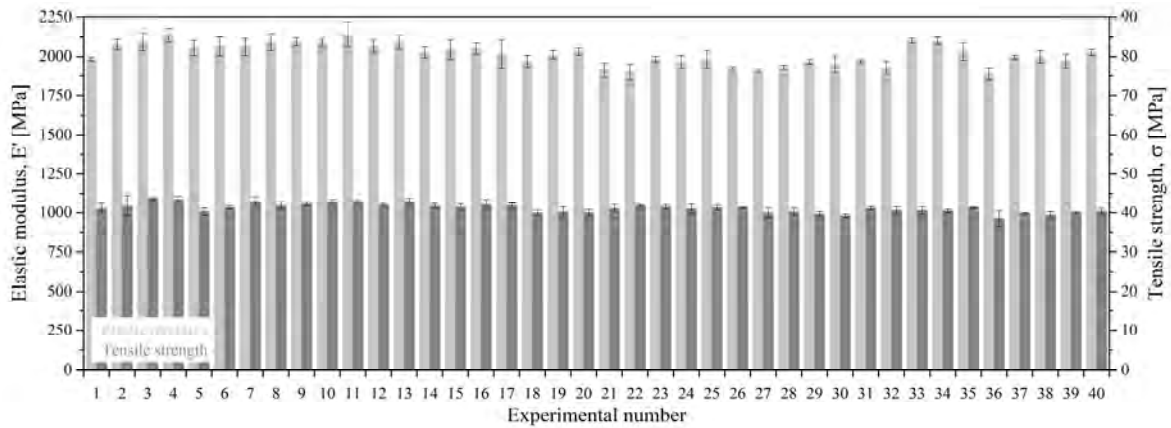


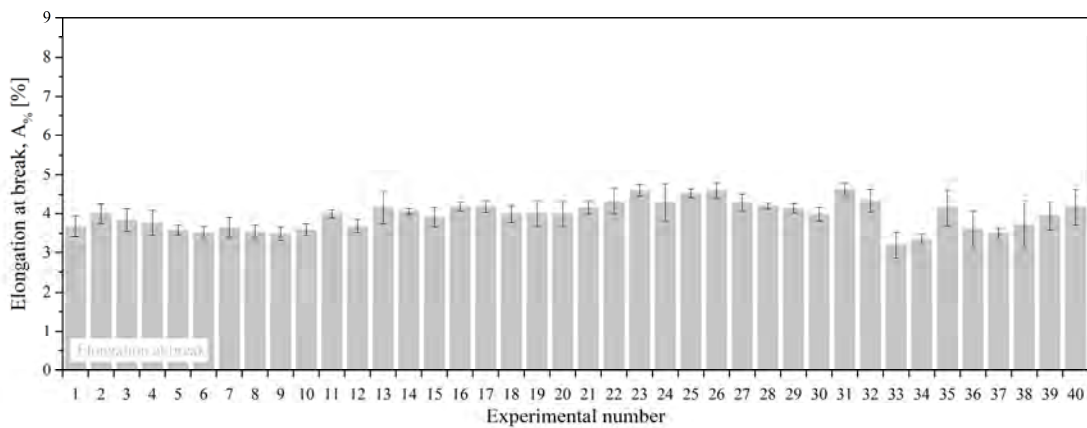
**Figure 4.16. Flexural properties of sintered parts**

According to Goodridge et al. [18] and Zarringhalam et al. [136], rapidly cooled products have a higher elongation at break than slowly cooled products. In addition to a different elongation at break, it is important to know that slow cooling (higher crystallinity) results in more shrinkage [16].

The results of the mechanical properties of various experiments do not reveal significant variations. The maximum flexural modulus and strength are 1989 MPa (exp. n°3) and 68 MPa (exp. n°9), while the minimum values are 1764 MPa (exp. n°38) and 58 MPa (exp. n°38), respectively. The differences between the highest and the lowest values are 11 % for flexural modulus and 15 % for flexural strength. According to the technical specification of Duraform FR1200, the flexural modulus and strength are 1770 MPa and 62 MPa, respectively. It means that almost all the sets of parameters have obtained higher values for flexural modulus and strength.



(a)



(b)

Figure 4.17. Tensile properties of sintered parts

The maximum and minimum elastic moduli are 2142 MPa (exp. n°11) and 1888 MPa (exp. n°36), respectively, with a difference of 12 %. The obtained values for tensile strength are

the maximum of 44 MPa (exp. n°3) and a minimum of 38 MPa (exp. n°36), which is 14 % of the difference. In the case of elongation at break, 4.6 % (exp. n°31) has been found as the highest value, while 3.2 % (exp. n°33) is the lowest one. Referring to the datasheet, the elastic modulus of 2040 MPa and tensile strength of 41 MPa have been found in the range of results, while the elongation at break of 5.9 % is higher of obtained values. The highest error for elongation at break is 46 %. Comparison of elastic modulus and tensile strength for PA2200 with literature studies showed that Wegner and Witt [42] found maximum values of 1758 MPa and 51.3 MPa (LP = 42.5 W, SC = 1, SS = 0.2 mm, LPT = 0.075 mm, ED = 0.33 J.mm<sup>-3</sup>) and Hofland et al. [43] have obtained the maximum of 2239 MPa (ED = 0.61 J.mm<sup>-3</sup>) and 50.1 MPa (ED = 0.52 J.mm<sup>-3</sup>), respectively. The obtained values for elongation at break are 21.2 % (Wegner and Witt) and 25.9 % (Hofland et al.), which corresponds to the value of 24 % verified with technical specification of material.

The exp. n°11 and n°13 seem to offer the best mechanical properties by comparing flexural and tensile results. The flexural modulus and strength are around 1957 MPa and 65 MPa, respectively. The elastic modulus, tensile strength and elongation at break are approximately 2118 MPa, 43 MPa and 4 %, respectively. It can be observed that the improvements made remain low (1-5 %) compare to exp. n°9.

#### 4.3.2.4. Thermal transitions

The apparatus used for thermal analysis is the DSC (Annex A.2.4.1), the measurements were carried out under nitrogen sweep 50 ml.min<sup>-1</sup> and for heating and cooling rates of 15 °C.min<sup>-1</sup> from ambient temperature to 300 °C. A mass from 8 mg to 16 mg of the solid part was placed in aluminium crucibles closed. The glass transition temperature ( $T_g$ ), crystallization temperature ( $T_c$ ) and melting temperature ( $T_m$ ) were determined and the apparent degree of crystallization ( $X_c$ ) was calculated for each set of parameters.

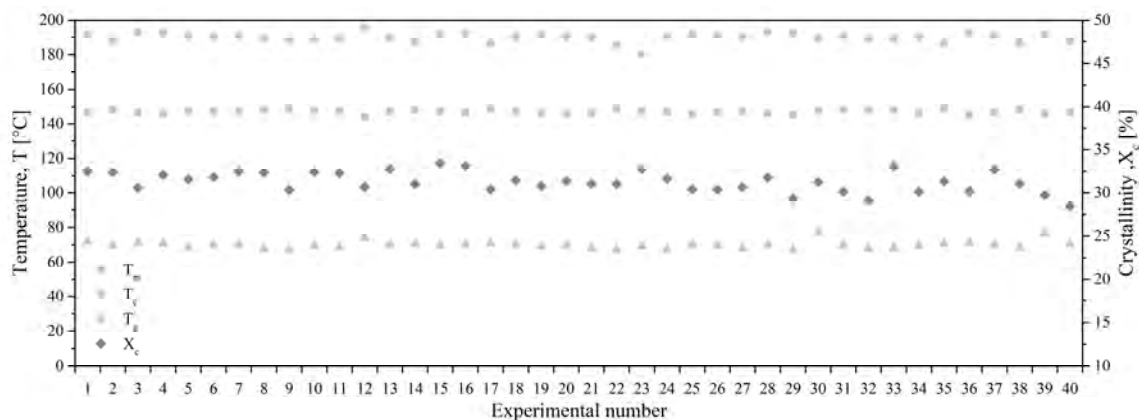


Figure 4.18. Thermal properties of sintered parts

As presented in Figure 4.18, the thermal properties and apparent crystallinity of various experiments do not show significant variations. The range of glass transition, apparent crystallization and melting temperatures are in the range of 67.05-76.95 °C, 143.95-148.93 °C and 180.30-195.59 °C, which is around 10 °C, 5 °C and 15 °C of differences, respectively. The apparent percentage of crystallinity varied from 28.49 % (exp. n°40) to 33.45 % (exp. n°15). The uncertainty of measurement by differential scanning calorimeter is more or less 1 %.

#### 4.3.2.5. Production time

One of the important factors for the industry is the production time of sintered parts. Gains in manufacturing performance can lead to gains in financial performance, which can result in increased access to capital, decreased cost of capital and increased investment in the manufacturing plant. An important measure of manufacturing performance is manufacturing efficiency. Minimizing production time can improve manufacturing efficiency.

The production time was calculated to obtain the time needed to print a single sample with a determined set of parameters.

$$t_p = \left( \frac{T}{SS} L \frac{SC_f}{LS_f} + (2T + 2L) \frac{SC_o}{LS_o} \frac{W}{LPT} \right) + 2 \frac{T}{SS} L \frac{SC_o}{LS_o} \quad (4.10)$$

where:

- $t_p$  - production time [s];
- $T$  - actual thickness [mm];
- $L$  - actual length [mm];
- $W$  - actual width [mm];
- $LPT$  - layer thickness, [mm];
- $SS$  - laser scan spacing [mm];
- $SC_f$  - fill scan count [-];
- $LS_f$  - fill laser beam speed [mm.s<sup>-1</sup>];
- $SC_o$  - outline scan count [-];
- $LS_o$  - outline laser beam speed [mm.s<sup>-1</sup>].

The results of production time are presented in Figure 4.19. It can be observed that the production time decreases with subsequent experiments, while the fill laser power increases. Nevertheless, production time is independent of the laser power as seen in Equation 4.10, so it may depend on scan count and scan spacing.

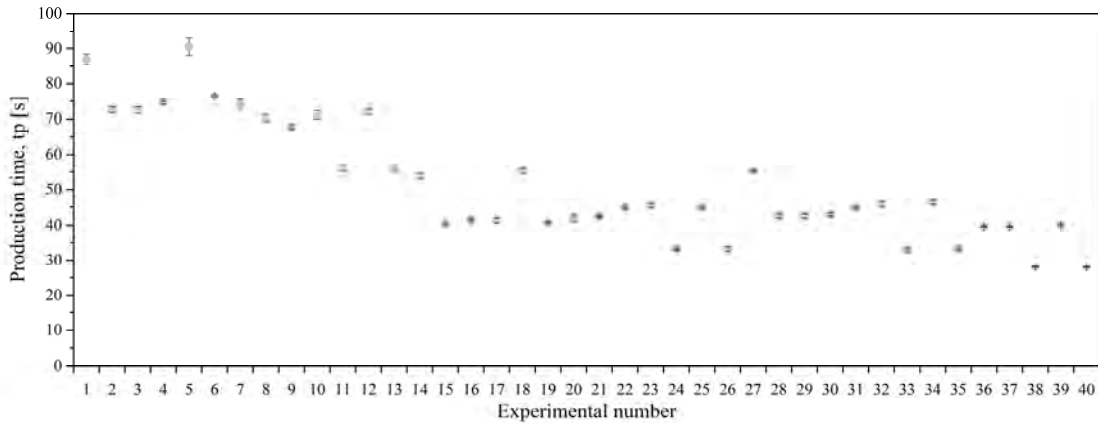


**Figure 4.19. Production time of flexural sintered parts**

The highest production time is 90.53 s for exp. n°5 (LPf = 2 x 15 W, LPo = 2 x 10 W, SS = 0.15 mm), while the lowest one is 28.13 s for exp. n°40 (LPf = 1 x 45 W, LPo = 1 x 15 W, SS = 0.25 mm). It can be observed that the production time is higher with twice scan count, which is caused by the double pass of the laser. Moreover, the higher scan spacing reduces the sintered area so it shortens production time. By comparing these results with the results of dimensional tolerances can draw the conclusions that the highest production time gives the best dimensions of samples.

### 4.3.3. Conclusion on the design of experiments on the SLS materials

Present work quantified the part properties of 200 tensile and 200 flexion samples produced with 40 different parameters sets. The design parameters were the laser power, scan count and scan spacing for both fill and outline region. According to the results of performed experiments, sintered parts were fabricated successfully at various laser power using a commercial machine ProX500 SLS with energy density range between 0.015-0.043 J.mm<sup>-2</sup>.

The small porosity of 8 % for printed samples is observed for almost stable density in a range of around 0.97-1.04 g.cm<sup>-3</sup>. Based on the findings of this study, small shrinkage in the length and width was evident. The volume of sintered parts increased with the increase in energy density due to the growth in the thickness of parts. By comparison of mechanical properties and production time, according to the set of parameters, exp. n°9, proposed by the supplier, better properties can be observed for exp. n°11 and n°13. The highest flexural modulus and strength values achieved were 1989 MPa and 68 MPa, respectively. Elastic modulus, tensile strength and elongation at break in the highest values were 2142 MPa, 44 MPa and 4.6 %, respectively. It is observed that production time decreases with the next set of parameters, thus with an increase of laser power and decrease of scan count. The thermal properties and apparent crystallinity of various experiments do not show significant variations.

#### 4.4. Statistical analysis of the impact on the SLS materials

To develop empirical models for mechanical properties and study the influence of selected parameters on it, a plan of experiments was prepared based on energy density and opinions of experts. The selected design consists of a combination of factors at two, three and five levels. Hence, planned forty experiments were performed to investigate the influence of selected parameters on the output parameters. This design allows the response to be analysed by using the iconography of correlations method (Version 4.00, Copyright Michel Lesty 1981-2019, France) and discussed in the next section and subsection as per output response.

The CORICO method [281,282] is characterised by an extension of interaction notion, of partial correlation as a factor selection tool, and a synthetic diagram including the chosen factors and conspicuous instances. The method simultaneously allows screening of factors and the construction of non-linear model by careful study of interactions. The response is expressed as multiple regressions. The algorithm is not based on a transformation as in the linear method, but initial variables are kept. In CORICO, selection of predictors takes place before the model is fitted and the calculation of coefficients is performed. There is no limitation on the number of variables, the CORICO discovers the model which fits the best with the actual data.

##### 4.4.1. Remarkable correlation

The correlation coefficient that allows the comparison of deviations around the mean of two variables  $x$  and  $y$  is the mathematical evaluation of what distinguishes their variations [50]. Let  $\bar{x}$  and  $\bar{y}$  be the means of  $x$  and  $y$ , and let  $X_i = x_i - \bar{x}$  and  $Y_i = y_i - \bar{y}$  be the deviations, for the  $i$  varying from 1 to  $n$ . The variation of each variable can be represented by a vector represented in  $n$ -dimensional space. The correlation coefficient is the cosine (in a space with  $n$  dimensions) of the angle that differentiates the “deviation vectors”  $X$  and  $Y$ , whose respective coordinates are  $X_i$  and  $Y_i$ :

$$r(x, y) = \cos(X, Y) = \frac{X_1 Y_1 + X_2 Y_2 + \dots + X_n Y_n}{\sqrt{X_1^2 + X_2^2 + \dots + X_n^2} \sqrt{Y_1^2 + Y_2^2 + \dots + Y_n^2}} \quad (4.11)$$

To respect the native discontinuity of observations, the CORICO method relies essentially on the calculation of total and partial correlations. Each observation pair corresponds to one moment and only one. If the vectors are collinear, the cos is equal to 1. If the cos is equal to 0, the two vectors are orthogonal. The correlation thus makes it possible to determine the phase shifts with great precision.



#### 4.4.2. Principle of visualization by the iconography of correlations

The indicator variable of line  $i$  of the data table is called “instant  $I$ ”. The instant bears the same name as the line it represents. The correlation link is named “remarkable” and therefore traced if it cannot be explained by any other variable or “instant”. Contrary to the principal component analysis, this is not a projection on a plane, and there is no axis to interpret. The points are placed on the surface of the sphere. Interpretation of the diagram is essentially based on links (or lack of link) and not on positions.

The link  $AB$  is considered as remarkable and therefore traced, only if the total correlation  $r(A, B)$  is greater than the chosen threshold, and if the partial correlations  $r(A, B)$  concerning all the other available variables are also greater than the threshold. Only the strongest links remain. The significant correlation in the sense of the classical statistic will not necessarily be retained. Conversely, the CORICO method may find a relationship worth of attention first even if it was considered statistically insignificant. The correlation link  $AB$  does not necessarily imply a causal relationship in the direction  $A \rightarrow B$  or in the direction  $B \rightarrow A$ .

The positions of the points on the diagram, on the one hand, and the links between these points, on the other hand, are completely decoupled. The position is chosen to maximize readability, but the interpretation depends first on links which, by definition, are unambiguous. The solid line announces a remarkable positive correlation between two variables (they grow and decay together). This resemblance is “remarkable” because it is not entirely explainable by the variations of the other available variables. The dashed line reflects a remarkable symmetry of variation (negative correlation: each variable increases when the other decreases).

Each variable (column of the table) is represented by a cube. The peak (or hollow) remarkable in the variation profile of variable is represented by a triangle, or its name is preceded by a “.” This peak (or hollow), which is not necessarily an extreme value, is called the “remarkable moment of analysis” because it is not entirely explicable by the variations of other variables available. The possible remarkable property  $P$  of variable  $A$  is represented by a small oblique cube (or its name is preceded by “:”). If it is related to  $A$ , it “explains” the similarities of other variables with  $A$ .

To get a wide range of results, the global spheres were obtained with average values and with all the results. The first option allows comparing all the variable with one value per set of parameters, while during the global sphere with all the results, missing data can occur for some samples in a given experiment.

**4.4.2.1. Global sphere with average data**

A lighten approach with average data has been illustrated in Figure 4.20, the iconography of correlations diagram for 40 sets of parameters, 27 variables (22 studied answers and 5 studied parameters). The threshold for the lines representing remarkable correlations is 0.3, which is the default value used in the iconography of correlations. Other values were tested without obtaining better information, so 0.3 is the threshold used in this study. The link between two variables is said “remarkable” (it is plotted) if this link subsists when any of the other variables are constant. Moreover, a link which is only due to one observation is not drawn.

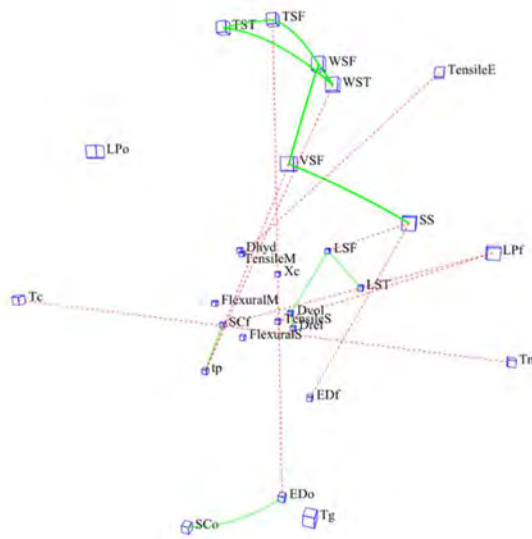


**Figure 4.20. CORICO diagram of average data at threshold 0.3**

The results obtained from average data and calculated by CORICO show positive and negative correlations between variables. The total correlations ( $R^2$ ), higher than 0.80, are presented according to variable A and B in Table 4.6.

**Table 4.6. Positive (green) and negative (red) correlations of average data**

A	B	$R^2$
LPf	-Scf	0.92
SCf	tp	0.88
SCo	EDo	0.80
EDo	-TSF	0.80
Dvol	Drel	0.96
TSF	TST	0.84
WSF	VSF	0.83

The isolated, variable without a link are: outline laser power, hydrostatic density, flexural modulus, flexural strength, glass transition temperature and crystallinity. These variables are considered by this method as not remarkable correlations.

In the global approach, diagram contraction involves two phases:

1. An analysis phase of each relationship, during which the attribute is tested to determine if the link remains without it.
2. A synthesis phase, which involves the global plotting of a simple relationship.

Thus, the results show some obvious and some interesting correlations. All the positive and negative correlations of average data are presented in Annex A.6.1. First of all, by considering positive correlations, when the fill scan counting passes more times the production time is longer. From the calculation is obvious that the outline energy density increases when the outline scan counting is higher because the laser passes more time with the same energy density in the same place. All links between shrinkage also make a sense because of using the same material with the same process parameters during the selective laser sintering process. The best correlation of 0.96 is indicated for volumetric and relative density, if one increases the second one will increase, this result is clear because it considers two densities which depend on each other. To go further, the correlation is 0.61 and 0.68 for scan spacing - volume shrinkage of sintered flexion samples and volumetric density - length shrinkage of sintered flexion samples, respectively. In the first case, it can be considered that the bigger scan spacing more important volume shrinkage of sintered flexion samples is, the smaller scan spacing the more consolidated material is (impact of temperature). Next, if the printed part is smaller the length shrinkage of sintered flexion samples increases, the bigger volumetric density may close the pores of the printed sample.

Like before, some negative correlations came from equations, the fill laser power increases when the fill scan counting decreases or the fill energy density increases if the scan spacing decreases. Next, it can be considered that the higher outline energy density the less thickness shrinkage of sintered flexion samples. Moreover, if the production time is longer the better dimensions of sintered parts are. The relation between the elastic modulus and elongation at break is normal and can be confirmed by mechanical results. The relation between temperatures is not considered, because they are not dependent on each other. A more interesting correlation is observed for the fill laser power - tensile strength and length shrinkage of sintered flexion samples – scan spacing of 0.76 and 0.68, respectively. In the first case,

several hypotheses may be considered, when the fill laser power increases the degradation of the printed sample takes place and the tensile strength decreases because of higher porosity or bad cohesion and interdiffusion. In the second case, if the scan spacing increases the length shrinkage of sintered flexion samples decreases what gives longer parts. The scan spacing increases in the direction perpendicular to the direction of laser pass, the length shrinkage of sintered flexion samples decreases in the direction of laser pass.

The approach with average data (one average result per set of parameters) gives some interesting correlations, but they do not significantly change the results. One possibility is the fact that the average values are used for responses and the correlation in averaging are lost. Nevertheless, in the next part of this study, the approach with all the experiments as a unique value (mostly five results per set of parameters) is considered. Thus, the statistical value is based on 400 results.

**4.4.2.2. Global sphere with all the results**

As previously, a lighten approach with all the results has been illustrated in Figure 4.21, the iconography of correlations diagram for 40 sets of parameters and 26 variables. In this case, hydrostatic density and relative density are considered as variables correlated positively or negatively. Thus, this method removed the redundant variable, which was relative density. The threshold for the lines representing remarkable correlations is 0.3. The abbreviations are explaining in the previous section.

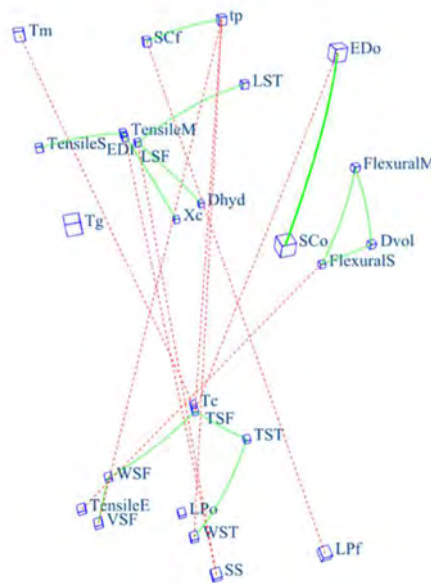


**Figure 4.21. CORICO diagram of all the results at threshold 0.3**

All the positive and negative correlations of all the results are presented in Annex A.6.2.

The geometric approach obtained from all the experiments as unique value produced by CORICO shows positive and negative correlations between variables. The total correlations, higher than 0.80, according to variable A and B are presented in Table 4.7.

**Table 4.7. Positive (green) and negative (red) correlations of all the results**

A	B	R <sup>2</sup> in all the results analysis	R <sup>2</sup> in average analysis
LPf	-SCf	0.92	0.92
SCf	tp	0.88	0.88
SCo	EDo	0.80	0.80
EDo	-TSF	0.79	0.80
TSF	TST	0.74	0.84
WSF	VSF	0.77	0.83

The isolated, variable without a link are outline laser power and glass transition temperature. Thus, the way to use unique value instead of averaging decreases the number of uncorrelated responses.

For positive correlations, it appears that increasing the volumetric density causes the increase of flexural modulus and strength. When the porosity of a part is smaller the resistant section is higher, so as the flexural modulus. Moreover, when cohesion of a part is higher, it delayed break initiation and increase the flexural strength. By considering the volumetric and hydrostatic density the same, it can be seen that if the printed part is smaller the length shrinkage of sintered flexion samples increases. The bigger hydrostatic density causes the closure of pores of the printed sample. Further, the positive correlation between flexural modulus and strength, and elastic modulus and tensile strength is observed, the correlation is 0.69 and 0.58, respectively. Thus, an increase in one property causes another to increase, which is correct. The elastic modulus linked to the crystallization is also observed. It means that better chains rearrangement, so less flexibility and mobility of chains increase the elastic modulus.

In the case of negative correlations, new interesting links were not observed besides the previous ones already explained.

The main conclusions of this research are that statistical analysis by CORICO method shows an increase in connections of correlations. Also, the changes in the total correlations for certain correlations are observed. In the first method, the maximal and minimal total correlations are 0.96 and 0.54, respectively, while in the second method the maximum is 0.92

and the minimum is 0.39. Moreover, the total correlations decrease in the connections between the higher number of experiments considered. It is an effect of non-averaging and the total correlations can be more precise. The new ones such as volumetric density and flexural modulus of 0.74 or strength of 0.68, flexural modulus and strength of 0.69, flexural strength and elongation at break of 0.39, tensile modulus and strength of 0.58, and tensile modulus and apparent crystallinity of 0.47 are all about mechanical properties. Thus, for industrial, the global sphere with all the results is more interesting because more information relating to mechanical properties can be obtained.

#### 4.4.3. Multiple regression models

The choice of regressors  $X_1, X_2 \dots X_n$  is determined in the following way. The factor or interaction best correlated to the response are formed. Then, the factor or interaction best correlated to the unexplained residue is looked at the previous correlation. This method aims are not taking into account twice the same influence when the factors are correlated, and to order them by decreasing importance. The “interactions” considered are not only the products or squares of factors but also the “logical” interactions defined above. No model is postulated priori.

The multiple regression models of CORICO were developed by analysing measured data. The analysis was used to estimate the effects of significant variables and their potential interactions on the studied answers. In the equation, the different terms are ranked by decreasing importance, each of them explaining the residue not explained by the preceding ones.

**Table 4.8. Summary of CORICO and regression analysis**

Models of CORICO for 5 regressors	
EDf	$= 1.9 \cdot 10^{-2} + 1.6 \cdot 10^{-2} \text{LPf-SS} + 1.5 \cdot 10^{-2} \text{SCf} \} \text{LPf} + 7.8 \cdot 10^{-3} \text{LPf\&-SS}$
<b>R<sup>2</sup></b>	<b>= 0.95</b>
EDo	$= 4.0 \cdot 10^{-3} + 3.1 \cdot 10^{-2} \text{LPo-SS} + 1.7 \cdot 10^{-2} \text{SCo} + 6.0 \cdot 10^{-3} \text{SCo} \} \text{SS} - 4.2 \cdot 10^{-3} \text{SS\&-LPo}$
<b>R<sup>2</sup></b>	<b>= 0.99</b>
tp	$= 51.4 + 93.2 \text{SCf\&-SS} + 41.6 \text{SCo-SS} + 17.6 \text{SS} \} \text{SCf} + 6.3 \text{SCf\&SCo} - 5.4 \text{LPo'SS}$
<b>R<sup>2</sup></b>	<b>= 0.99</b>

The adjusted  $R^2$  presents total coefficient correlation. The best correlations have been obtained for fill and outline energy density, and production time, 0.95, 0.99 and 0.99, respectively. These values were directly calculated from the laser properties, thus, it is confirmation that obtained models are correct.

#### 4.4.4. Effect of interaction between process parameters

The interactions of CORICO method are seen in Table 4.8 with the correlation over 0.80 for models. All the models of CORICO for 5 regressors are presented in Annex A.6.3. Several interactions were obtained. The interactions symbols are explained in Annex A.6.4. The regressors involve nonlinear functions of factors, the explanation of which is given as follow:

- high fill laser power and short scan spacing have a strong influence on fill energy density (LPf-SS). A similar situation occurs in the case of outline laser power, scan spacing and outline energy density (LPo-SS). It means that the higher energy density is required;
- high fill laser power if high scan spacing increase volumetric density (LPf]SS), but fill laser power which varies inversely as scan spacing influences hydrostatic and relative density (LPf#-SS);
- medium fill laser power if high scan spacing influences length shrinkage of sintered flexion samples (LPf{SS), but in the case of length shrinkage of sintered tensile samples high fill laser power if high scan spacing is more important. High outline scan count and short scan spacing have an influence on thickness shrinkage of sintered flexion and tensile samples (SCo-SS; SCo&-SS), for width/volume shrinkage of sintered flexion and tensile samples high fill scan count and short scan spacing is required;
- medium outline laser power if low fill laser power (LPo{-LPf) and high outline scan count while short scan spacing (SCo-SS) have a strong influence on flexural properties. Low fill laser power, high fill scan count and high outline scan count (LPf-SCf, SCf&SCo) influence tensile properties;
- high fill scan count and short scan spacing (SCf&-SS) have a strong influence on production time;
- high fill and outline laser power if high outline scan spacing (LPo]SCo, LPf#LPo) influence thermal properties.

When the number of factors is large, the number of response surface graphs becomes prohibitive. Moreover, to visualize the surface  $f(A, B)$  is of no help if the response depends on more than two variables:  $Y = f(A, B, C, D \dots)$ . The interactions and three-dimension plots among the most significant process parameters for densities (Figure 4.22), mechanical

properties (Figure 4.23 and Figure 4.24) and production time (Figure 4.25) are presented on the graphs below:

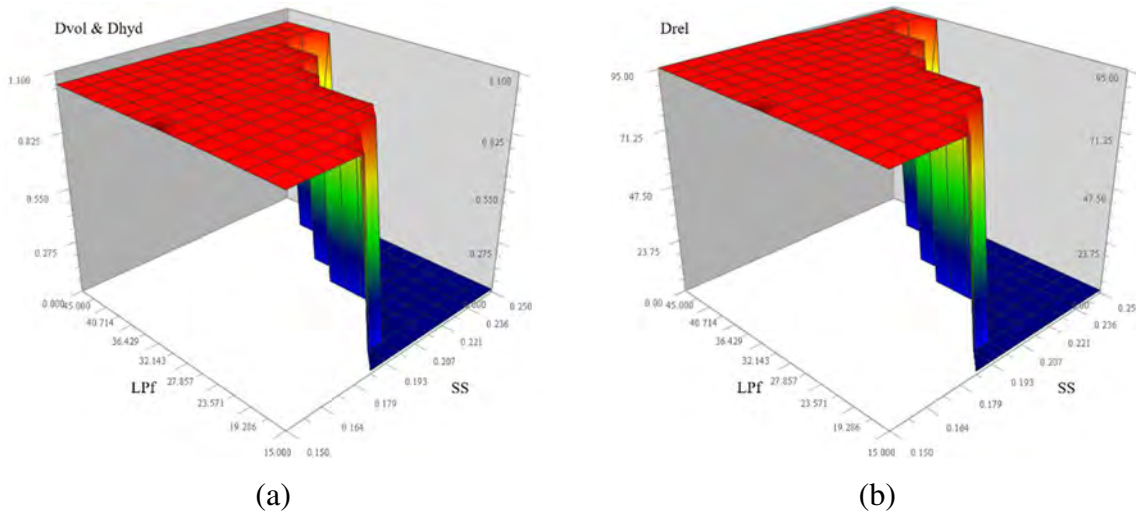


Figure 4.22. The 3D response surface plots between LPf and SS for (a) Dvol and Dhyd (b) Drel

The interaction plot displays the average of output variables obtained for specimens fabricated at the levels indicated independently of the setting of other variables. Figure 4.22 shows the three-dimensional plot for the interaction between the fill laser power and scan spacing for densities. It can be seen that at low fill laser power and high scan spacing the densities are very low. This is justified with the fact that at low fill laser power with a bigger distance between laser passes, the amount of energy delivered to the powder bed can be considered insufficient to sinter the part, resulting in poor densities and increasing the porosity. However, when scan spacing is low the fill laser power on each level may properly sinter the powder particles lead to a compact structure, which causes decreasing the porosity of part.

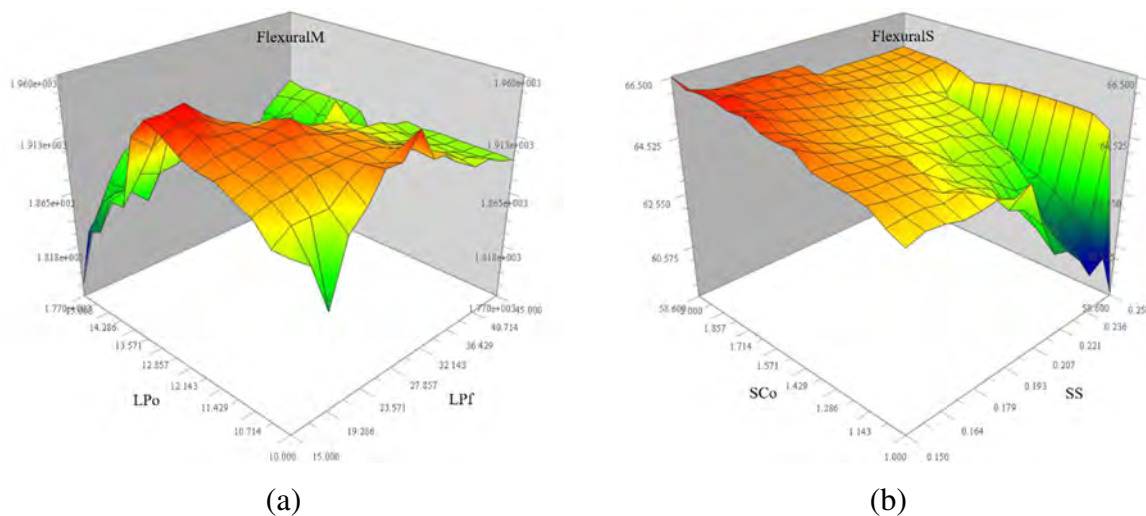
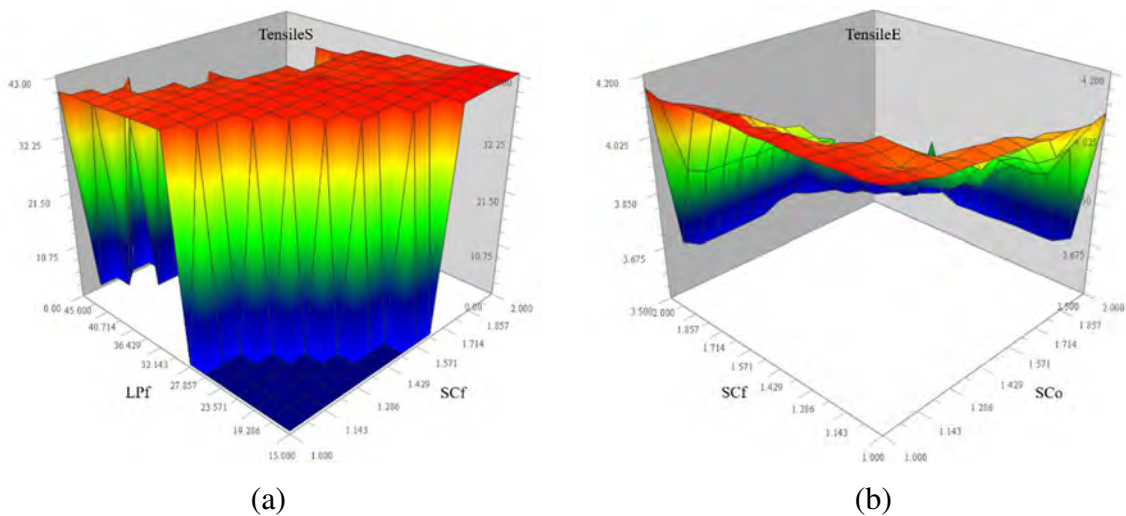


Figure 4.23. The 3D response surface plots between (a) LPo, LPf and FlexuralM (b) SCo, SS and FlexuralS



The flexural properties show significant interactions between outline laser power and fill laser power, as well as, outline scan count and scan spacing for flexural modulus and strength, respectively. Medium laser powers cause high flexural modulus, while high outline scan count and scan spacing increase the flexural strength. This is because at too high or too low laser power the delivered density may cause degradation of polymer or not proper sintering, respectively. High flexural strength can be obtained by double outline scan count with shorter scan spacing. This is linked to high density, while more laser power on smaller area causes a higher degree of sintering.



**Figure 4.24.** The 3D response surface plots between (a) LPf, SCf and TensileS (b) SCf, SCo and TensileE

High fill laser power and low fill scan count or the opposite cause high tensile strength, while low fill and outline scan count may give high elongation at break. In the first case, the medium of laser power is required instead of too high or too low impact of temperature which depends on it. The elongation at break gives information that one pass of the laser can increase its value.

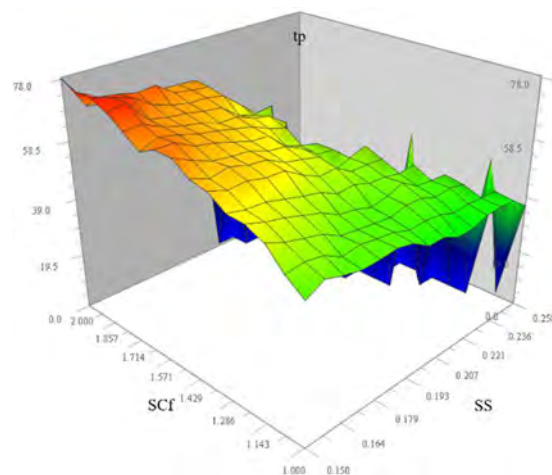


**Figure 4.25.** The 3D response surface plots on tp between SCf and SS

Graph for production time presents the interaction plots for fill scan count and scan spacing. It is observed that at a high level of fill scan count and the short distance between laser passes the production time is longer than the specimen sintered at double fill scan count and high scan spacing. This can be explained by the fact the part sintered with high scan spacing takes less time during printing. The production time is one of the most important parameters for the industrial point of view.

#### 4.4.5. Optimization

The above equation can be used to minimize or maximize the response (Monte Carlo method). The results may be subjected to one or more validation tests which, integrated with the previous results, will make it possible to refine the model. Therefore, the next step is to determine a set of working conditions by optimizing process parameters to achieve desirable properties. All densities and mechanical properties were maximized, while production time was minimized. It is expected that these goals may provide the best quality of printed parts for the industry. The responses independent of the process were averaged to decrease its impact. The optimization criteria for obtaining an acceptable set of parameters and the results are summarized in Table 4.9.

Optimal working conditions to maximize densities and mechanical properties, while minimizing production time rounded off are: fill laser power of 28.2 W, fill scan count of 1 (1.17), outline laser power of 15 W, outline scan count of 1 and scan spacing of 0.16, which is in reasonable agreement with predicted responses. For these parameters, the fill energy density is  $0.017 \text{ J.mm}^{-2}$  and for the outline, energy density is  $0.027 \text{ J.mm}^{-2}$ . The predicted mechanical properties for these set of parameters show an increase of tensile strength, tensile modulus, flexural strength and flexural modulus of 42 MPa, 2042 MPa, 64 MPa and 1868 MPa to the values in sheet data for Duraform FR1200 of 41 MPa, 2040 MPa, 62 MPa and 1770 MPa, respectively. In the case of elongation at break decrease from 5.9 % to 4.1 % is proposed. The production time is estimated at 45.41 s which is half the maximum time calculated to print one sample.

**Table 4.9. Proposed optimization criterion with results**

Conditions and response	Minimum	Maximum	Goal	Results	Unit
LPf	15.00	45.00	/	28.20	W
SCf	1.00	2.00	/	1.17	-
LPo	10.00	15.00	/	15.00	W
SCo	1.00	2.00	/	1.00	-
SS	0.15	0.25	/	0.16	mm

Conditions and response	Minimum	Maximum	Goal	Results	Unit
Dvol	0.96	1.01	Maximize	0.99	g.cm <sup>-3</sup>
Dhyd	1.00	1.04	Maximize	1.03	g.cm <sup>-3</sup>
Drel	91.13	94.78	Maximize	94.33	%
LSF	-0.87	0.45	Averaging	0.27	%
TSF	-15.00	-1.87	Averaging	-7.48	%
WSF	-2.91	0.63	Averaging	-0.51	%
VSF	-0.66	1.11	Averaging	0.85	%
LST	0	0.59	Averaging	0.33	%
TST	-15.75	-0.50	Averaging	-2.64	%
WST	-3.3	0.90	Averaging	-0.83	%
FlexuralM	1688.50	2021.20	Maximize	1867.69	MPa
FlexuralS	55.87	68.40	Maximize	64.50	MPa
TensileM	1819.00	2134.20	Maximize	2042.03	MPa
TensileS	37.94	44.85	Maximize	41.87	MPa
TensileE	3.11	5.06	Maximize	4.133	%
tp	28.03	89.93	Minimize	45.41	s
Tg	67.05	76.95	Averaging	70.38	°C
Tm	143.95	148.93	Averaging	147.01	°C
Tc	180.30	195.59	Averaging	189.68	°C
Xc	24.28	28.58	Averaging	27.15	%

It has been shown that the set of parameters n°17 is the closest one to the optimal set in order to obtain desirable properties of parts. To remain, the various values are sintered part density of 1.03 g.cm<sup>-3</sup>, the relative density of 94.44 %, the flexural modulus of 1897 MPa, the flexural strength of 64 MPa, the elastic modulus of 2015 MPa, the tensile strength of 42 MPa, the elongation at break of 4.2 % and the production time of 41.38 s.

#### 4.4.6. Single parameters effect on the properties

The purpose of this study is to provide a better understanding of the process parameters that have a significant influence on the properties of a sintered polyamide part. The selective laser sintering parameters, such as laser power, scan count and scan spacing have been found to play a significant role to optimize the process.

#### **4.4.6.1. Effect of laser power on the properties of printed parts**

First results on the iconography of correlations isolate outline laser power can be caused by the low impact of 8 % on the total volume of the sintered part. The effect of fill laser power on densities and mechanical properties as described in the previous subsection. It has been observed that sintered parts at the high level of outline laser power and a medium level of fill laser power have better flexural properties. To improve elastic modulus and tensile strength low level of fill laser power is required. It is important to remember that laser power is directly dependent on scan count. Moreover, the laser power influences the densities, which increase at each level of fill laser power with low scan spacing. The main reason behind this is that when sintering takes place at high laser power, the interdiffusion between the powder particles becomes stronger, increasing densities, thus in modulus and strength of specimens. Additionally, a higher level of energy density causes better fusion of particles, which results in better strength of parts. Similar results have also been reported by Negi et al. [269] and Singh et al. [283] using a polyamide material.

#### **4.4.6.2. Effect of scan count on the properties of printed parts**

Scan count affects all densities, mechanical properties and production time significantly. With double scan, the count increases volumetric density, while one scan count increases hydrostatic and relative density. Flexural properties can be improved with a double outline and fill scan count. In the case of elongation at break one pass of laser gives the best results, elastic modulus and tensile strength require double fill scan count and one pass of outline laser power for better properties. This might be because when the scan count increases the energy absorbed by the sintering material at a unit time and a unit area increases, which leads to better fusion of particles by energy delivered to the powder bed. Production time is longer when the laser passes twice than once which is confirmed with statistics.

#### **4.4.6.3. Effect of scan spacing on the properties of printed parts**

The influence of scan spacing on densities is demonstrated. It is observed that with increasing scan spacing from a low level to the high level, there is a decrease in all densities, thus in all mechanical properties. This can be easily confirmed with the fact that the large scan spacing causes poor packing of particles, due to which the problem of curling occurs more frequently. Consequently, poor sintering of successive layers of powder material is observed. Moreover, the strength of parts decreases with an increase in scan spacing, which was also presented in the work of Negi et al. [269].

#### **4.4.7. Conclusion on the statistical analysis of the impact on the SLS materials**

The study shows that the iconography of correlations method is suitable for forty different configurations of a set of parameters with large numbers of variables and responses. Five, three and two different levels of laser power, scan spacing and scan count, respectively, were used to create the experimental design. The three parameters were characterised to obtain a response to the impact on the sintered parts. Despite its apparent complexity, the method representing the overall organization of variables rapidly highlights all the remarkable correlations, whether statistically significant or not, some of which are unexpected.

The global sphere of all the results provides more precise correlations. Moreover, for industrial they are a valuable source of information because more mechanical information can be obtained. Interactions between process parameters show that scan spacing has a significant impact on all of the other parameters. Its changes can directly improve or worsen the influence of laser power and scan count.

The iconography of correlations method by using all the data can offer suitable parameters to obtain the desired part. In this study, the optimized set of parameters requires to fill laser power of 1.17 x 28.20 W, outline laser power of 1 x 15.00 W and scan spacing of 0.16 mm. This set of parameters is most similar to the exp. n°17.

## 4.5. Conclusion

First of all, the study of the size of specimens on mechanical properties outlines the existence of scale factor. When reducing the size of the sample, mechanical properties decrease. Taking into consideration elastic moduli and tensile strength, the orientation of the parts shows no significant effect on the values achieved, demonstrating that they are more robust to changes in build layout.

The tensile strength on the pair Duraform P12 and sPro230, no significant loss of resistance is outlined between directions. Regarding the pair Duraform FR1200 and ProX500, a major difference was an outline for the resistance in the Z-axis direction (- 41 %). The same is found for the elongation at break in the X-axis and Y-axis direction, with a decrease in the property when parts were produced in the Z-axis direction. It is also essential to note that from one machine to the next, mechanical properties do not significantly vary.

Present work quantified the part properties of four hundred samples produced with 40 different parameters sets. The design parameters were the laser power, scan count and scan spacing for both fill and outline region. Basing on the results of performed experiments, it can be stated that good sintered parts were fabricated successfully at various laser power using a commercial machine ProX500 SLS with energy density range between  $0.015 \text{ J.mm}^{-2}$  and  $0.043 \text{ J.mm}^{-2}$ . The small porosity of 8 % for printed samples is observed for stable density in the range of  $0.97\text{-}1.04 \text{ g.cm}^{-3}$ . Based on the findings of this study, small shrinkage in the length and width was evident. The volume of sintered parts increased with the increase in energy density due to the growth in the thickness of parts. By comparison of mechanical properties and production time, according to the set of parameters, exp. n°9, proposed by the supplier, better properties can be observed for exp. n°11 and n°13. The highest flexural modulus and strength values achieved were 1989 MPa and 68 MPa, respectively. Elastic modulus, tensile strength and elongation at break in the highest values were 2142 MPa, 44 MPa and 4.6 %, respectively. It is observed that production time decreases with the next set of parameters, thus with an increase of laser power and decrease of scan count. The thermal properties and crystallinity of various experiments do not show significant variations.

The presented results and optimization of the laser parameters of the selective laser sintering process showed how they influenced production time. The results of tests on the geometry and density of specimens made of the polyamide 12 confirmed that increasing the distance between successive laser beam transitions allows for a significant reduction in time of manufacture of the specimens. Moreover, it is observed that at the same time a slight increase in the porosity of the material, with pores presenting a stochastic character. By optimization of the laser parameters, it is possible to obtain desired mechanical properties with over 33 % of reduction in production time.

## **5. EFFECT OF SLS THERMAL CYCLES ON THE MATERIAL PROPERTIES**

The measurement of temperatures involved during the selective laser sintering process is of great importance for many reasons. First of all, to ensure that the temperature reached during the process is high enough to ensure sufficient mobility for the polymer chains interdiffusion to the interface. Secondly, to check that the temperature inside the polymer parts remains low enough to avoid material degradation. Finally, to know if the recycling of the powder which has not undergone the radiation of laser.

The knowledge of temperature distribution, and its temporal evolution, around the interface, makes it possible to know the coalescence behaviour of powders and the fraction of interdiffused interface. These thermal variations would cause a modification of physicochemical properties and dimensions of manufactured parts. In situ temperature measurements can allow a better understanding of the process of laser welding transmission to make it more reliable. During the selective laser sintering process, it turns out that temperature measurement becomes complicated, especially at the interdiffused interface.

In this chapter, the objective of the study is to understand the influence of thermal cycles during the printing process, by simulating the heat transfer during the selective laser sintering process of polyaryletherketone thermoplastics family on the structure and their mechanical properties. To simplify the development and validate the principles, 2D thermal conduction model has been chosen.



## 5.1. Monitoring of thermal field during SLS process

In laser sintering technology, the laser melting process is carried out in a protective atmosphere of inert gas and proceeds without the use of crucible as moulding element to give free of impurities and side effects of combustion parts [284]. During the selective laser sintering process, several parameters control the powder melting (preheating temperature, part bed temperature, energy density) which have an impact on the final density and mechanical behaviour of printed parts (elastic modulus, yield and fracture strength, elongation at break). Some printed parts demonstrate a lower rigidity in the Z-axis compared to X-axis and Y-axis [28]. It is assumed that this difference is due to the heat profile of the Z-axis. Indeed, in a layer by layer manufacturing, several layers in the Z-axis are impacted by the laser at each pass. Two types of parameters have an effect on the thermal profile in Z-axis such as the preheating temperature of powder and part bed temperature, as well as, the energy density calculated from properties of laser (power, scan speed, spacing, and count) [27].

Simulations of the thermal profile of layers in the Z-axis during the selective laser sintering process are not well known yet. Mostly, the laser and material interaction by the coalescence of a significant set of grains based on Frenkel-Eshelby physical model has been investigated [164,285]. Defauchy et al. [286,287] studied the conditions allowing the solidification of melted polymer in order to increase the density and to reduce parts distortions.

In the selective laser sintering process, each layer is heated up by the laser pass and re-heated by conduction several times when the laser beam melts the upper layers. For semi-crystalline polymers, these thermal cycles induce morphological changes [288] and the evolution of mechanical properties. To predict the mechanical properties, it is crucial to get a deeper knowledge of thermal cycle undergone by each layer.

The use of infrared thermography in different fields of technology is becoming very common now. It is used in ecology, medicine (cancer research), rescue, construction, observation of thermal processes. For example, to assess qualitative and quantitative, as well as, research materials or process monitoring, production and processing in the foundry. The infrared measurement methods are often complementary to other diagnostic methods, such as ultrasonic test or speckle shearing interferometry test [289]. Therefore, using a combination of several non-destructive methods allows obtaining all the relevant information concerning the defects affecting the structure and mechanical properties of parts quickly and precisely way.

Thermography and thermovision include testing methods involving the remote and contactless evaluation of temperature distribution on the surface of the test body. These methods are based on observation and recording of distribution of infrared radiation emitted by any object with a temperature higher than absolute zero which is  $-273.15\text{ }^{\circ}\text{C}$ . Figure 5.1 presents the range of infrared wavelength. Heat flux is thus on record by an infrared camera, which filters the radiation emitted by the blackbody (a surface that neither reflects nor transmits incident radiation), in the function of its wavelength, and then process it into a map of temperature. The thermography allows temperature measurement at any distance and at the same time over the entire surface, that confirms that infrared thermography is a non-contact method [290].

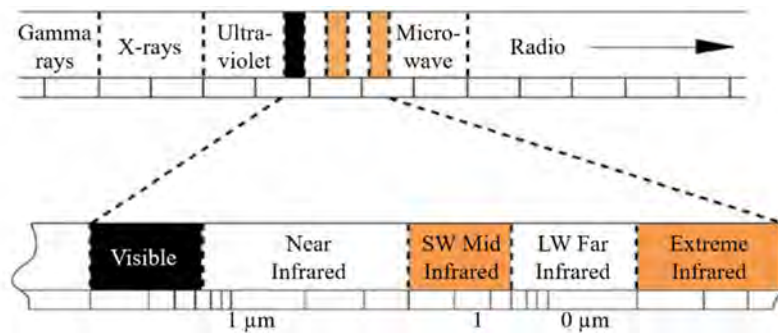


Figure 5.1. The electromagnetic spectrum

To understand more and more the SLS process, temperature measurement appears to be necessary. Moreover, thermal fields are needed to understand the evolution of temperature during all the process and overall the part, to understand the final properties of the materials. Infrared thermography method appears to be an interesting method, giving thermal information during the time on a surface without contact. It allows non-destructive thermal studies, thanks to which the optimal test parameters can also be determined. Unfortunately, in this study, it has not been possible to adopt this kind of measurement inside the closed chamber of the SLS machine, which is too small to receive this kind of IR device.

To replace it, the numerical method shall be the first step to generate thermal profile applicable to the material and representative of the real SLS process.

## **5.2. Analytical and numerical studies**

To manage heat conduction during the SLS process, two approaches can be used: continuous and discrete. Continuous methods are known as finite difference method (FDM), finite element method (FEM) and finite volume method (FVM) while the discrete method is known as discrete element method (DEM) and is used when discontinuous medium exists.

In the SLS process, two different phases are present at the same time: powder state corresponding to the powder to be fused and already fused material considered as a consolidated phase. The consolidated phase is used as a continuum medium while the powder layer can either be considered as a continuum or discrete medium.

### **5.2.1. Continuum approach for the SLS process**

For these studies, most of the authors consider the powder bed as a continuum medium. Most of the studies deal with the melting of metallic powder [291–297] but can be used for polymeric parts or composite materials based on polymeric parts [298–300]. Roberts et al. [297] have analysed the temperature field during laser melting of metal powder by using the 3D finite element model.

Childs et al. [293] have studied the heat conduction and powder densification of an amorphous polycarbonate using three approaches: analytical, finite difference method and finite element method. All three methods allow the temperature fields but are sensitive to the change of thermal properties during the SLS sintering of two metal powders, taking into account the shrinkage of the powder bed and the liquid flow. Two simulations were done with a stationary and the moving laser. They calculated the temperature fields numerically by the finite discrete method. Budega and Lombera [298] have developed a 3D simulation based on the FEM approach taking into consideration heat transfer and sintering. They considered that the transient analysis, due to the movement of the laser can be approximated as a steady analysis modifying the classical conduction equation. To take into account the porosity, they use the Yagui and Kunni (1989) formulation to calculate the effective conductivity in the powder bed. This simulation has been done on a polycarbonate track. The surface flux generated by the laser is evaluated around  $1 \cdot 10^8 \text{ W.m}^2$  and creates a surface temperature of 2530 K. Roberts et al. [297] have used a continuous approach to simulate the temperature fields for the process. Moreover, these properties are not so easy to be obtained a priori. Chen and Zhang [291] have developed an analytical 3D model for the laser melting of metal powders. They developed a new simulation technique known as element birth and death. When a new layer of powder is

dropped off, the simulation activates a new element. This technique can be considered as similar to the element progressive activation (EPA) implemented in Abaqus FEM software, as used by Favaloro et al. [299] for the simulation of the deposit of a new filament during the FFF process.

Taking into consideration the SLM process, Dai and Gu [294] have dealt with the temperature distribution of metal composite material. They used the finite volume method to simulate the transition from power to solid, the surface tension and the movement of the laser in order to obtain thermal fields. They studied the effect of the energy density, dimensions of the melt pool, densification with a Gaussian energy distribution laser. Ding et al. [295] have studied, by using a continuous approach, the difference between continuous exposure and point exposure for the SLM process. They compared the thermal fields and the molten volume. For the thermal fields, they pointed out that the point exposure method overestimates the maximum temperature compared to continuous exposure (2586 K against 2293 K). They also outlined that the shape of the heat-affected zone is like an ellipse for point exposure and as a comet for continuous exposure. Liu et al. [301] have investigated temperature distribution, thermal history, molten affected zones, and solidification during SLM of an aluminium alloy using the finite element method. They pointed out that the fourth layer is significantly heat affected by the laser pass.

Tian et al. [300] developed a model for the SLS process of composite material based on a polyamide matrix with carbon fiber and NaCl reinforcement. They used the finite element method using a volumetric heat source to simulate temperature fields. They outlined that for these composite materials, the heat transfer is mainly caused by the transmitted radiation. Moreover, the simulation is not so accurate regarding temperature fields and melting depth.

### **5.2.2. Discrete approach for the SLS process**

Moser et al. [302] have developed the SLS model based on the discrete element approach taking into account particle-particle contact conduction, particle-fluid conduction and scattering effects using a ray-tracing model. They tested the model with metallic and ceramics applications and they pointed out that this model is adapted when particles are spherical and its surfaces are smooth. For metals, there is no need to calibrate the model while for ceramics, it is the case. During his thesis, Liu [123] developed a 3D model to simulate the SLS process with a discrete approach with a multi-physical study. The power bed has been considered as a discrete media. Scattering effects, thermal conductivity, reflection and convection have been investigated. These simulated results have been compared [301,303] with the equivalent FEM model. He

pointed out that scattering effects and air between particles have an important impact on energy density. He outlines that DEM is more accurate for the simulation of the powder bed for the selective laser sintering process.

### **5.2.3. Conclusion on the analytical and numerical studies**

To conclude, the classical Fourier heat transfer equations are the most useful to describe the temperature distribution. Thus, various models have been studied by combining material thermal property nonlinear, latent heat, laser heat source distribution or even interaction between a laser beam and powder bed [115,300,304,305]. Moreover, the influence of sintered part shrinkage, molten pool liquid flow and coalescence mechanism have been considered in the models. Numerical methods are employed extensively to solve the temperature distribution problem where the finite element method has proven to be reliable using available commercial software. Thus, none of these models can be completely solved analytically. Finally, temperature measurement systems have been used to demonstrate the actual temperature distribution in selective laser sintering processes to compare against the models [306].

By considering the continuum approach, the laser beam energy input is very often modelled as a heat flux with density described by the Gaussian form of laser. The volumetric heat flux as a boundary heat source on the surface seems to be more realistic. It turned out to be possible to predict the temperature and energy density distribution in sintered amorphous polymer powders taking into account scattering effects, radiation, phase change when melting, convection, and heat conduction. It has been proved that not only one layer is affected by the pass of a laser source. The continuous approach is not enough accurate to simulate the process.

Most of the numerical studies about the selective laser sintering process only simulate the thermal diffusion inside a predefined powder bed [2,112,304,307]. However, in industrial manufacturing, the successive layers of powders are formed by laser sintering. Few studies have modelled the selective laser sintering process with successive layers and taking into account the effective heat conduction and the geometry of the powder. Liu [123] has proposed the numerical model based on the discrete element method and this approach seems to be interesting to simulate a model close to the real phenomenon taking place during the SLS process.

### 5.3. Simulation of thermal profile for several layers

The objective of this modelling is to give the thermal cycle that “undergoes” a layer after its printing, to determine from which layer [n-i] the laser does not affect layer [n]. Thus, by obtaining this cycle, the impact on the structure and mechanical properties of the material can be determined experimentally. As a result, the approximate form of evolution for the thermal cycle of the layer can be obtained. To achieve this goal, the simulation has been performed by the 2D model in which the conduction phenomenon through the material was studied. This model is intended to determine from which thickness the laser has no thermal influence on the material. Firstly, the evolution of temperature at different layers of powder bed is analysed. The thermal history of different layers is also studied.

#### 5.3.1. General hypothesis

It turns out that the time that the laser makes to travel the entire trajectory is negligible compared to the spreading time of the new powder. Thus, the 2D thermal transient analysis has been chosen to develop the simulation. It is possible to consider (to simplify hypothesis) that the heat flux transmitted by the laser (and perceived by the layer that will be melted) is homogeneous and constant over the entire surface and can be applied at the same time of  $7.89 \cdot 10^{-3}$  s. It is also considered that the 3D heat flux melts the first layer and because of that, instead of a volume flux, a temperature over the melting temperature of 680 K (407 °C) is used to heat-up the powder. Preheat of powder and convective exchanges are taken into account for this simulation. No scattering effects and no phase changes exist in this study.

With these hypotheses, the following parameters are used for the building of the model:

- physics: the thermal conduction model in 2D;
- initial conditions: the temperature of the chamber and powder bed is constant at 477 K (204 °C);
- convective exchanges are considered on the upper edge (the only surface in contact with the air of the chamber);
- heat source: the laser (surface heat flux) is represented by a contribution of temperature enough to melt the first layer;
- heat sources duration: the pass of the laser corresponds to the application of temperature previously described of  $7.89 \cdot 10^{-3}$  s on the upper surface;
- steps: one transient heat transfer step for “radiation” and one transient heat transfer for conduction;

- step time: after the passage of laser, a cooling time of 10 s is applied to the printed layer;
- the thickness of each layer is 250  $\mu\text{m}$ ;
- 39 layers have been printed before the current layer.

To carry out the simulation, the finite element method (FEM) commercial code Abaqus from Dassault System has been chosen. A heat transfer model has been built to determine the evolution of the temperature of a printed part through its thickness for multiple laser passes.

### 5.3.1.1. Process parameters

The parameters of the laser influence the other parameters of process printing such as preheating temperature. Thus, it is imperative to set laser parameters. First of all, the laser used in the selective laser sintering process is pulsed emission laser. Then, according to Peyre et al. [240], for the application of the SLS method to the polyetheretherketone, parameters needed to obtain homogeneous manufacturing are required and listed below. In our application, the following value for all parameters have been chosen:

- average power of the laser is 100 W;
- Gaussian laser shape (Figure 5.2);
- laser speed of 12.67  $\text{m}\cdot\text{s}^{-1}$ ;
- irradiation frequency of  $6\cdot 10^4$  Hz;
- preheating temperature of 477 K (204  $^{\circ}\text{C}$ );
- radius of the laser beam is  $60\cdot 10^{-6}$  m;
- laser pass spacing of  $0.2\cdot 10^{-3}$  m;
- time between two passes is 4 s.

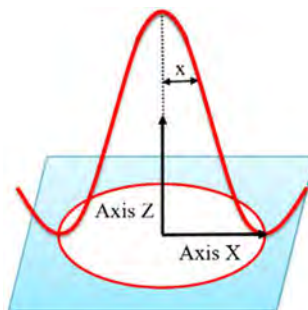


Figure 5.2. Gaussian shape of a laser

The parameters listed above allow the calculation of the surface flux generated by the laser. The following relation [308] (considering only the conduction) is considered as complementary to calculate the surface heat flux for a Gaussian form of the laser:

$$q_s = \frac{LP}{\pi r_{lb}^2} \exp\left[-\frac{2x^2}{r_{lb}^2}\right] \quad (5.1)$$

where:

- $q_s$  - surface heat flux [ $W \cdot m^{-2}$ ];
- $LP$  - power of laser [W];
- $r_{lb}$  - radius of laser beam [m];
- $x$  - distance from the centre [m].

After calculation, the heat surface flux generated by the laser is equal to  $1.44 \cdot 10^8 W \cdot m^{-2}$ .

### 5.3.1.2. Geometry of layers

It has been decided to use the dimensions (width/ length) of specimen central section defined by standard NF-EN 10002-2, as well as, the layer thickness of  $250 \mu m$  as shown in Figure 5.3.

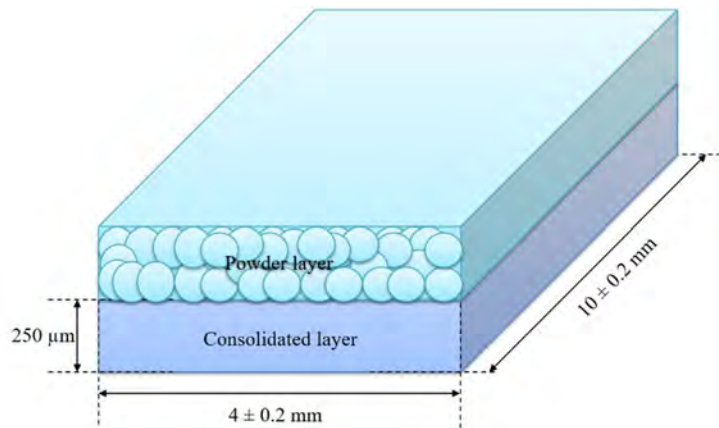


Figure 5.3. Dimensions of layer

The geometry is partitioned in two parts in order to consider different properties of the first layer (powder) and the rest of the sample (consolidated). No contact resistance has been taken into account between the two partitions. The contact is considered as perfect.

### 5.3.1.3. Material properties

To set up the simulation, properties of the material, PEEK 2000 FP in powder and consolidated state, are required. Indeed, it is imperative to hold the density, thermal conductivity and specific heat of the powder and consolidated material. It was decided to consider the powder in a tapped density state and the properties of the material used for this study are the ones determined in chapter 2 and summarized in Table 5.1.



**Table 5.1. Thermophysical properties of PEEK powder and consolidated PEEK**

Properties	Specific heat [J.kg <sup>-1</sup> .K <sup>-1</sup> ]	Density [kg.m <sup>-3</sup> ]	Thermal conductivity [W.m <sup>-1</sup> .K <sup>-1</sup> ]
Powder state	1053 [196]	1007	0.150
Standard deviation	30	10	0.001
Consolidated state	1053 [196]	1300	0.240
Standard deviation	30	13	0.002

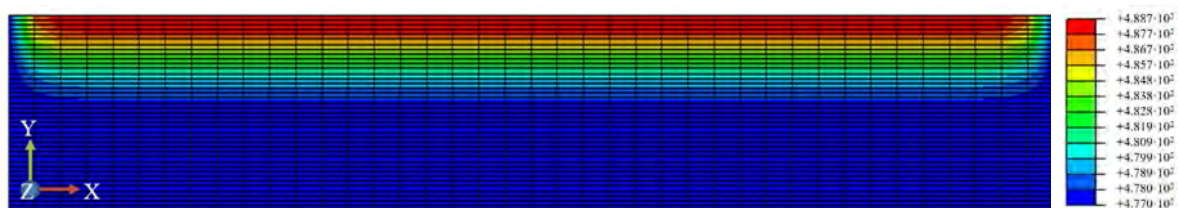
#### 5.3.1.4. Mesh properties

The 4-node linear heat transfer quadrilaterals (DC2D4) are used for the present work with 1 degree of freedom by node, the temperature T11. This element has 4 integration points.

The thickness of a layer is assumed to be 250  $\mu\text{m}$ . Each layer is meshed by 5 elements through the thickness, so the size of the element is 2.5 mm x 50  $\mu\text{m}$ . This model has a total of 8241 nodes and 8000 elements.

#### 5.3.2. Results of the simulation

An increase in temperature on the thickness during the time of 10 s is shown in the simulation. The temperature at the surface “irradiated” is transferred layer to layer during the time. At the end of the simulation, the temperature map, as seen in Figure 5.4, allows the measurement of the heat-affected zone. These results give a number of 14 layers affected thermally.

**Figure 5.4. Model mapping at 10 s**

The simulation has confirmed that the laser has a thermal influence not only on the first layer but on several layers. The laser affects quasi-instantaneously the two first layers. To explore wider the thermal effects of the laser on layers, the evolution of temperature as a function of time is plotted in Figure 5.5, for the fourteen thermally affected layers. The temperature of each layer corresponds to the middle position of the layer in the thickness, the Y-axis direction.

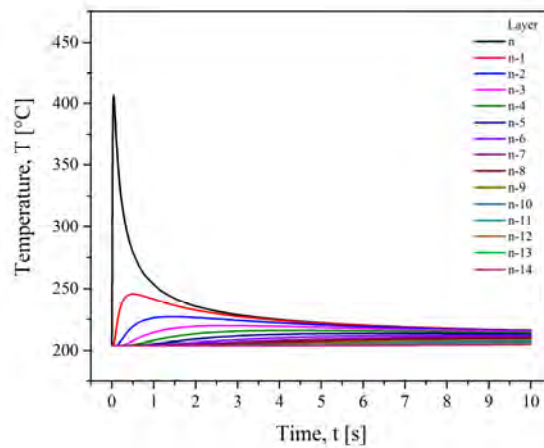


**Figure 5.5. Evolution of temperature as a function of time for layers from n to n-14**

With the results obtained, it was found that only the two first layers are almost instantaneously affected by one laser pass. The first layer reaches instantaneously 400 °C, over the melting temperature, to be molten by the heat flux. The material stands less than 0.15 s over the melting temperature. Then, its temperature decreases strongly to be under its crystallization temperature (around 290 °C) in less than 1 s. After that, its temperature still decreases following a trend of transient thermal profile. Within 10 s, the temperature of the first layer reaches 225 °C and can be considered as constant, the material temperature stays between glass transition and crystallization temperatures. Considering the second layer, the maximum temperature reached 246 °C after 0.5 s. Then, the temperature decreases slowly to reach 225 °C after 10 s. It has to be noted that the second layer, called n-1, is affected by heat but does not rise through the melting temperature. The third and fourth layers, called n-2 and n-3, respectively, have reached a maximum value of 227 °C and 220 °C at 1.4 s and 2.8 s, respectively. For other layers, it appears that the maximum rise in temperature is around 20 °C and their maximum temperature is 225 °C. They are considered not to be affected by the laser pass. Nevertheless, it has to be noticed that, during the manufacturing of a whole batch the layers stay over 200 °C during the ending of the batch.

By taking into account that the time between two laser passes is 4 s, it was possible to assemble the curves to get the thermal profile of layer n. Indeed, during several lasers passes, it can be noticed that the n layer necessarily undergoes the same temperature changes as the layers that precede it. For example, during the second pass of the laser, the layer n takes the place of layer n-1. Thus, by noting that only the temperature evolutions of layers n-1, n-2 and n-3 impact the thermal profile of layer n, it was obtained the following thermal profile, Figure 5.6.

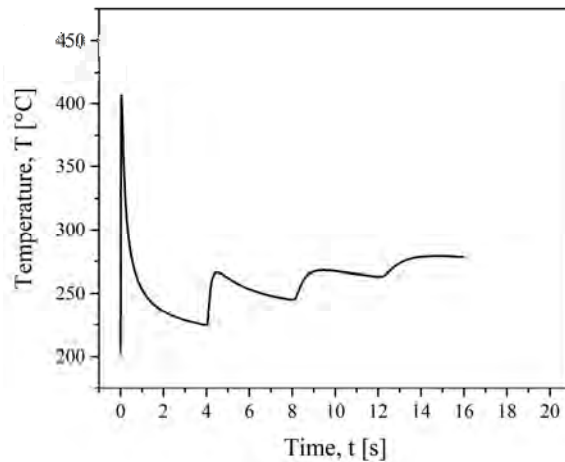


**Figure 5.6. Assembly of thermal profiles of each layer**

The assembly of the thermal profile for four laser passes shows the different cycles of heating and cooling due to the successive irradiation of the powder. After the 4<sup>th</sup> pass, the thermal evolution has no significant influence, less than 10 %, and the temperature is considered stabilized.

### **5.3.3. Conclusion on the simulation of thermal profile for several layers**

It has been confirmed that the layers undergo different thermal history during the selective laser sintering process. It can be outlining that after melting and cooling, the layer stays at a temperature between the glass transition temperature and the crystallization temperature. These results and the results of chapter 2, confirm that the SLS process results in a material with a gradient of properties.

The assembled thermal profile can be used experimentally to create each layer with the right thermal history. Thus, using differential scanning calorimetry and X-ray diffraction, it can determine the influence of the laser passes on the thermal transitions and crystallinity rate of the manufactured polyetheretherketone layers. It remains to be seen whether these changes are significant enough to have a major impact on the properties of plates and therefore a piece printed in the selective laser sintering process.

## **5.4. Influence of thermal cycles on the properties of layers**

The crystallinity of polyetheretherketone has been investigated on the properties of layers with differential scanning calorimetry and wide-angle X-ray diffraction (WAXS) techniques. The procedures are described in Annex A.2.4.1 and Annex A.2.1.4, respectively. The thermal cycle defined by numerical simulation has been applied to each layer. For that, a few layers of 250  $\mu\text{m}$  thickness have been prepared. To control the temperature, the oven of rheometer ARES LN2 has been chosen, as it is the fastest way to heat the sample without the laser. It has to be in mind that the physics used to heat-up the layer by rheometer is not the same as the physics required to heat-up the layer by the laser. In our experiment, conduction for the rheometer was applied instead of radiation for laser. Then the thermal history has been applied on each layer from the 1<sup>st</sup> to the 4<sup>th</sup>. It is not possible to follow exactly the temperature rates calculated by the numerical simulation because there are too fast for the rheometer. So, the profile has been linearized to be as close as possible to the calculation while being experimentally feasible.

### **5.4.1. Manufacturing of the layers**

The layers of 250  $\mu\text{m}$  thickness that have been used to apply the thermal profile obtained previously were manufactured in the oven of rheometer ARES LN2. First, the calculation of powder quantity to manufacture one layer was done. Then, the powder was dried at 120  $^{\circ}\text{C}$  for 72 hrs. To perform the rheometric tests, the PEEK plates of 39.80 mm diameter and 250  $\mu\text{m}$  thickness were prepared. The powder is placed on the lower plate of the rheometer oven which is heated up at a fixed temperature of 370  $^{\circ}\text{C}$ , corresponding to the melting temperature of the supplier. To have the desired thickness of the future plate, the gap between the two plates of the rheometer is adjusted. Once these steps have been completed, several parameters such as mass, duration at melting point and atmospheric medium (air or nitrogen) have been successively modified to obtain consolidated plates. Finally, to set up the correct thermal cycle, powder PEEK 2000 FP at the pressed mass of 202 mg was heated from 150  $^{\circ}\text{C}$  until 370  $^{\circ}\text{C}$  in the air atmosphere for 2 min in its melting point.

### **5.4.2. Thermal profile application**

Following the manufacture of plates, the thermal history has been applied on the layers. However, the ramps to be applied to achieve this thermal profile have too high values. Thus, it was decided to apply the fastest ramps that the rheometer can achieve and to be as close as possible to this profile. The linearization of the thermal profile of layer n has been managed,

Figure 5.7. Then, the oven of rheometer was preheated to 407 °C and then the cup containing the powder was placed for 2 min.

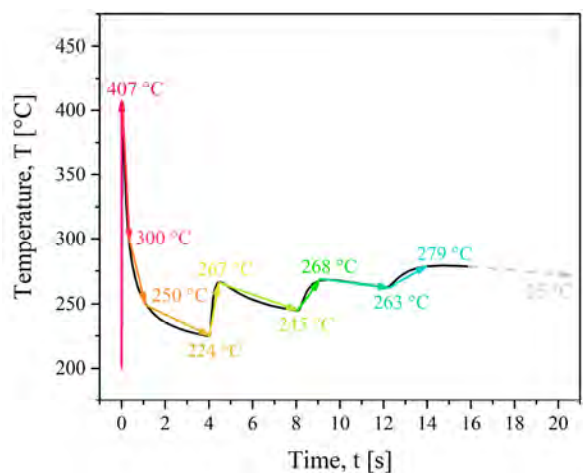


Figure 5.7. Linearization of thermal profile for the layer n

Moreover, to determine as precisely as possible, the influence of laser passes on the physicochemical properties of the material, each cycle of the thermal profile was applied on two different layers. Thus, the thermal profile containing four distinct cycles (each passage corresponds to one cycle), the eight layers having undergone different cycles have been formed.

This preparation allowed obtaining of PEEK plates as close as possible, experimentally, to layers manufactured using the selective laser sintering process.

#### 5.4.2.1. Influence on the crystallinity of PEEK

An understanding of the degree of crystallinity for a polymer is very important as crystallinity affects physical properties, such as storage modulus, permeability, density and melting temperature. A direct measure of the degree of crystallinity can provide fundamental property from which other physical properties can be predicted.

To determine the thermal transitions of samples, the differential scanning calorimetry tests were carried out. A thermal heating and cooling ramp of 10 °C.min<sup>-1</sup> at a temperature range from 25 °C to 450 °C with flushing gas being the dinitrogen and gas of sample being dioxygen have been applied.

The typical thermograms obtained for PEEK 2000 FP with four different cycles are presented in Figure 5.8. It can be observed that all cycles show sharp and clear melting peaks, while all crystalline peaks vary in the shape. It is confirmation of the impact on the microstructure of material by crystallization.

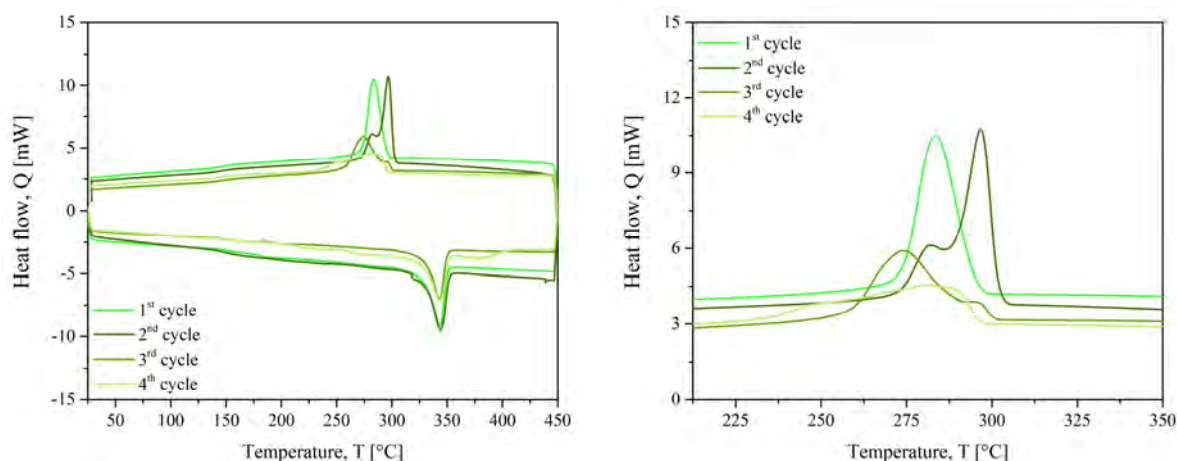


Figure 5.8. The DSC thermogram of four cycles

The results consisting of glass transition, melting and crystallization temperatures in the onset and maximum point, as well as, melting enthalpy and degrees of crystallinity, are shown in Table 5.2. The degree of crystallinity has been calculated from the ratio of melting enthalpy to theoretical one of 100 % crystalline phase of PEEK which is  $130 \text{ J.g}^{-1}$  [189].

Table 5.2. The DSC results for cycles of thermal profile

Passes	Glass	Melting		Crystallization			
	temp.	temperature		temperature			
	$T_g$ [°C]	$T_{\text{onset}}$ [°C]	$T_{\text{max}}$ [°C]	$T_{\text{onset}}$ [°C]	$T_{\text{max}}$ [°C]	$\Delta H_m$ [J.g <sup>-1</sup> ]	$X_c$ [%]
1 <sup>st</sup> cycle	155.14	329.58	343.40	294.92	283.30	35.48	27.29
2 <sup>nd</sup> cycle	145.14	330.10	344.37	301.84	296.67	34.16	26.28
3 <sup>rd</sup> cycle	153.46	333.21	341.45	291.97	273.66	35.77	27.51
4 <sup>th</sup> cycle	151.07	327.32	342.89	296.49	281.39	44.93	34.56
Uncertainty			$\pm 1 \%$				$\pm 5 \%$

In the view of these results, it can be deduced that the application of successive thermal cycles does not seem to have any dependence on the transition temperatures. Nevertheless, the glass transition, melting and crystallization temperatures vary within 10 °C, 3 °C and 23 °C, respectively. Indeed, it was noted that the melting temperature remains around 342 °C (despite the 370 °C given by the supplier) while the crystallization temperature remains around 284 °C. Considering the degree of crystallinity, a high increase is observed for the 4<sup>th</sup> cycle of 34 %, while the first three layers remain equal of around 27 %.

The technique of differential scanning calorimetry shows that there is no significant change in the crystalline rate for the first three cycles. However, this technique is not the most

appropriated to measure the crystalline rate for PEEK, because the sample is heated during the measurement. So, heat undergoes crystallisation of shorter chains within the melting peak, right after the same crystallites melt. For that, wide-angle X-ray diffraction at room temperature has been applied. The X-ray diffraction uses the total X-ray scattering of both the crystalline and amorphous phases to determine the crystallinity. The method provides a more accurate result than differential scanning calorimetry.

The diffraction scan is measured between  $2\theta$  values of  $5^\circ$  and  $40^\circ$  to subtract background radiation ( $\theta$  is the angle of incidence of the incoming X-ray beam). The area under the diffraction curve and above this line was then divided into the crystalline (green colours) and amorphous peaks (cyan colours), as seen in Figure 5.9. The ratio of the area of the crystalline peak to the area of the amorphous peak equals the weight ratio of crystalline to amorphous material.

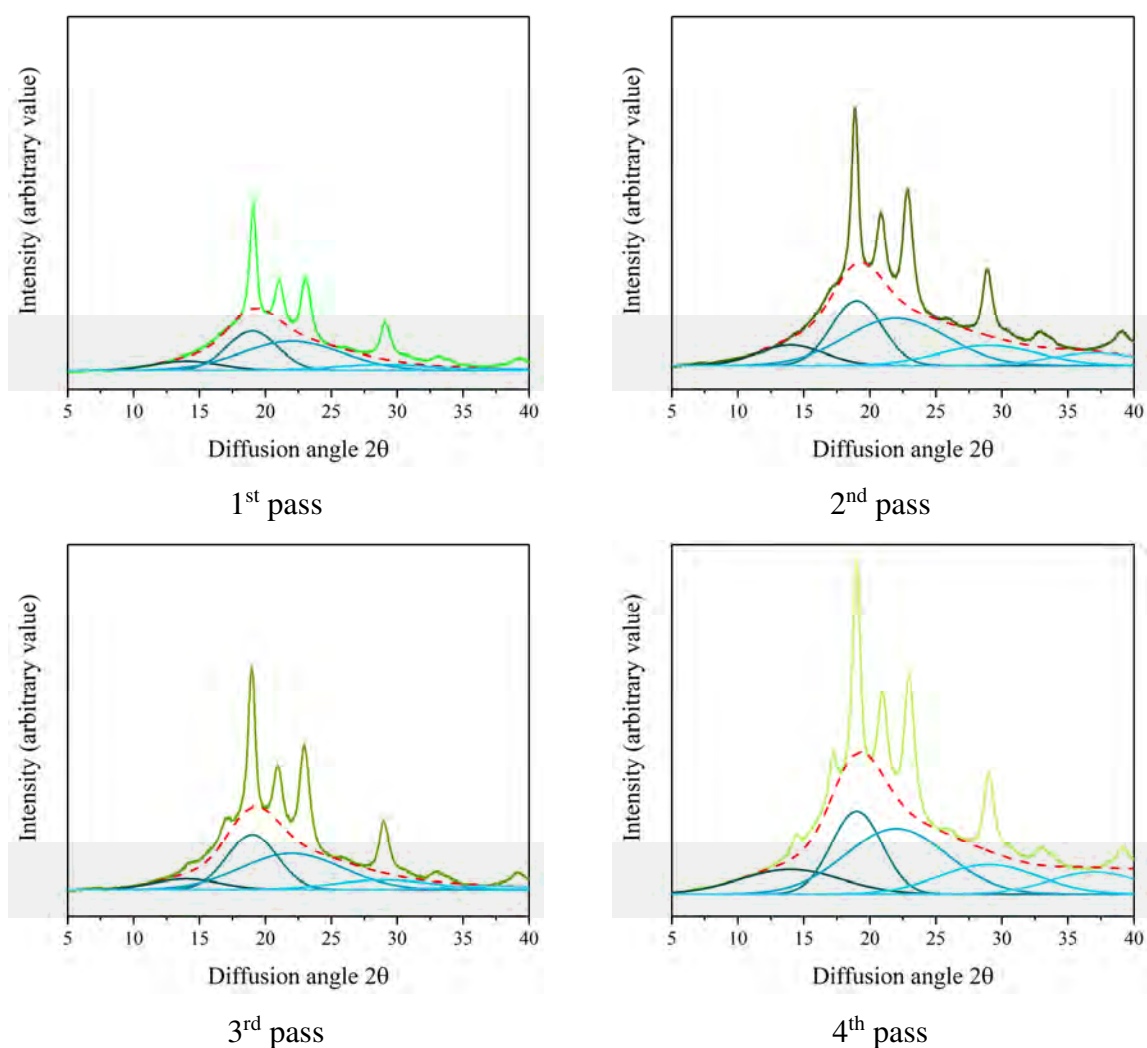


**Figure 5.9.** The WAXS diffractograms of four passes

The degree of crystallinity is determined by removing the amorphous halo (dashed red line), which is the sum of five amorphous functions (cyan colours) to fit well the signal of the



amorphous phase, as presented on the figure below. The crystallinity can be calculated by the following equation:

$$X_c = \frac{\text{Total area of crystalline peaks}}{\text{Total area of all peaks}} \cdot 100 \% \quad (5.2)$$

With these results, it is possible to determine the different levels of crystallinity as a function of a number of passes applied. These results are grouped in Figure 5.10.

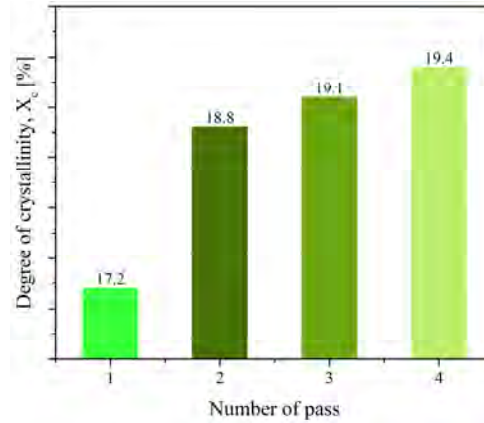


**Figure 5.10. Degree of crystallinity as a function of the number of passes applied**

An increase of 9.38 % between the application of the 1<sup>st</sup> cycle and that of the 2<sup>nd</sup> cycle has to be noted. Then, there are less significant increases (1.35 % and 1.38 %) but present. This increase in the degree of crystallinity reflects a change in the microstructure of the material.

#### **5.4.1. Conclusion on the influence of thermal cycles on the properties of layers**

Due to the lack of experimental data on the thermal history of the powder and printed part, numerical simulation was a good tool to predict the thermal history of each layer, with uncertainties due to hypotheses used to build the model. It has been shown that the four first layers are impacted by several laser passes. The simulated thermal history has been applied to the material and outlines that the crystallinity rate of each layer is different. That indicates that parts created by the SLS process have a gradient of crystallinity over their dimension. So, to measure the crystallinity rate of a printed part, differential scanning calorimetry is not the obvious tool because it gives a volume average value. The impact on the microstructure of a material has been observed, which leads to the need for investigation of mechanical properties. However, the standard mechanical tests are not possible on thin layers. Moreover, it has been pointed out that each layer stays at a temperature of over 200 °C during all the batch time. We can assume that it is corresponding to an annealing time.



## **5.5. Influence of annealing on the mechanical properties of PEEK**

Zimmermann and Könnecke [309] have reported that the increasing annealing temperatures can make materials rearrange with better packing, causing the cell volume to decrease and the crystallinity density to increase. Day et al. [98] analysed only PEEK 450 specimens thermally treated between 380 °C and 420 °C up to 120 min in air and nitrogen atmospheres. They have found that the longer the annealing time, the higher the temperature of the molten material may become. Thus, a smaller amount of powder can recrystallize, especially for the material treated in air. Samples of PEEK treated in the air, above the melting point crystallized at a slower rate than the corresponding samples treated in nitrogen. Rao and Sivadasan [310] also reported that when PEEK from ICI is subjected to an annealing treatment, the crystallinity increases as the annealing time increases. The grade of the material is not specified.

The effect of annealing on the properties of PEEK 450 has been also investigated by Arzak et al. [311]. In their study annealing of the specimens was carried out in an air oven at 100 °C, 150 °C, 200 °C, 250 °C and 300°C for 1 hr and 24 hrs. It was reported that annealing at temperatures higher than 150 °C caused an increase of mechanical properties with annealing time. For 200 °C the elastic modulus increase from around 3750 MPa to 4000 MPa, tensile strength from 93 MPa to 97 MPa. The differences in tensile properties can be attributed to the increased perfection of polyetheretherketone crystallites which seems to be obtained at the higher annealing time. However, the elongation at break is stable and equal around 50 % until 150 °C and drastically decrease to 20 % for higher temperatures. The effect of annealing time was reported by Kim et al. [312] on amorphous polystyrene. A similar phenomenon as in the case of these studies has been observed. The tensile strength increased with the longer annealing time from 10.3 MPa at ambient temperature, by 27.3 MPa at 2 hrs and 31.2 MPa at 4 hrs.

We can assume that annealing time results in changes in the degree of crystallinity of polyetheretherketone printed part. Thus, because of the relationship between mechanical properties and crystallinity, it is useful to characterize its impact on mechanical behaviour.

The purpose of mechanical tests carried out is to test three configurations of implementation for the same polymer grade PEEK 2000 FP and to evaluate the differences in mechanical properties induced.

### **5.5.1. Manufacturing of the annealing samples**

A laboratory hydraulic press LAB 800P PEI from the Pinette Emidecau Industries was used for preparing the moulded plates. The mass needed for the plate was calculated dried in a vacuum oven

at 120 °C for at least 3 hrs. The metal trays with a hole in the middle of 2 mm thick have been used. The powder was kept in the hole between two aluminium foils and placed between the platens of the press, which was already heated to 200 °C. Next, the temperature increases 10 °C.min<sup>-1</sup> until 370 °C and a pressure of 50 kN was applied for 5 min. Then, the moulded samples were cooled with the speed of 4 °C.min<sup>-1</sup> inside the press under pressure until 200 °C, separated from aluminium foils and left in room temperature to cool down. Further, the plates have undergone thermal treatment in the oven in two additional configurations. Finally, the three configurations can be specified:

- 370 °C for 5 min;
- 370 °C for 5 min + 204 °C for 2 hrs;
- 370 °C for 5 min + 204 °C for 4 hrs.

From the received plates were cut out the traction specimens. First of all, the dumbbell in the shape of a dog-bone tensile test specimen was heated in the oven at 450 °C for 20 min. The heated edges of the mould made it easier to cut the sample by positioning the plate and dumbbell punch under the compression press. Next, the test specimen was quickly removed from the punch to avoid melting the edges of the test sample. For each cut, the piece was heated again.

#### **5.5.1.1. Influence on the mechanical properties of PEEK**

The mechanical properties of annealing samples were determined according to the ISO 527. They were carried out with an Instron Universal Testing System 33R4204 with an external mechanical extensometer in a controlled room. Tensile tests were performed using at least six samples type 1 for each of the specimens tested. The test parameters are as follows:

- movement speed: 2 mm.min<sup>-1</sup>;
- 5 kN force cell (Instron 2525-805);
- Instron 2620 series extensometer.

The end of the test criterion was the rupture of the test specimen.

For the three configurations, including two effects of annealing, it was exposed the broken specimens, as well as, the stress-strain curves. The validity of the tests had resulted in a break in the useful area of the test piece. Thus, a calculation of the three following mechanical data is possible:

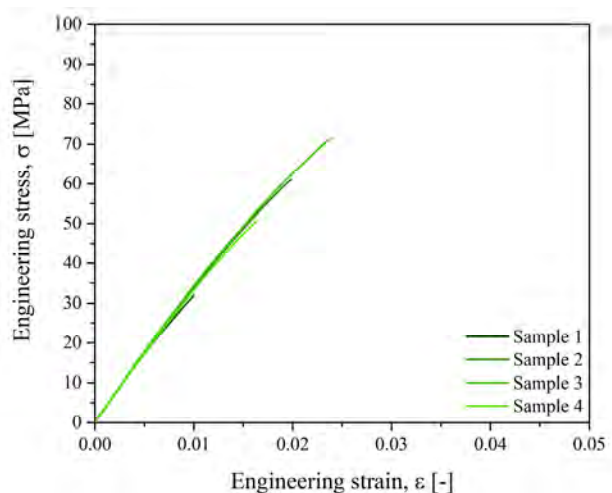
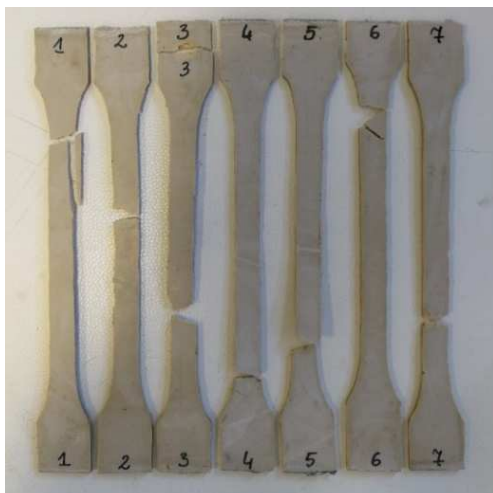
- the elastic modulus;
- the maximum resistance or stress;
- the elongation at break.

The elastic modulus, to respect the ISO 527 standard, has been calculated for a deformation between 0.0005 and 0.0025. The engineering stress-engineering strain curves allowed making statements about the mechanical behaviour of the material. In the first step, the broken test pieces of first, second and third configuration are presented in Figure 5.11.a and then, the engineering stress-engineering strain curves for the valid results are displayed in Figure 5.11.b.

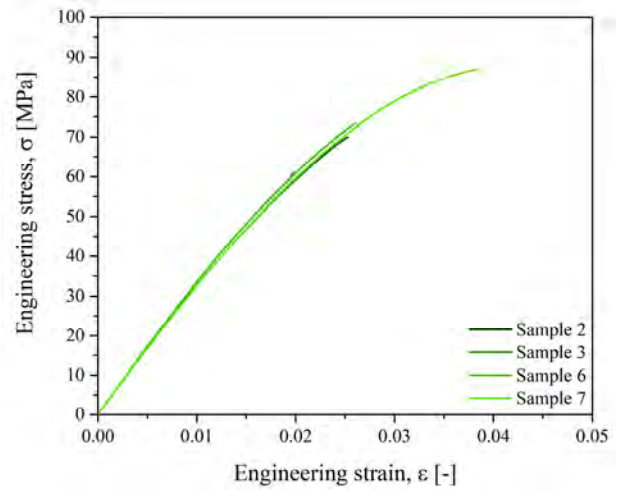
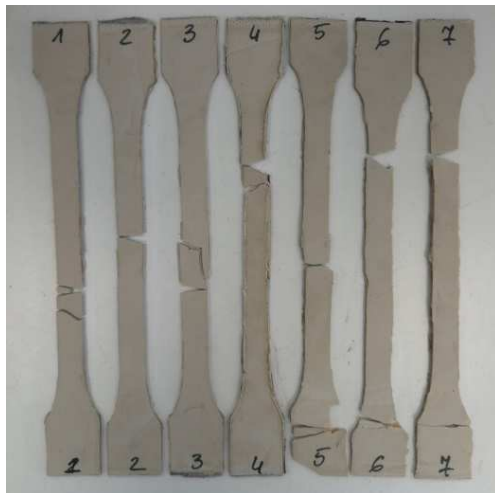
In all the tensile tests carried out, it can be noticed that all the breaks occurred in the useful zone of the specimens. In the case where the specimens exhibit multiple fractures, this is due to the propagation of the shock wave, due to the rupture of the specimen, which multiplies the broken areas. As a result of these tests, it was confirmed that all the tests are validated. This results in an exclusion of the specimens having a different traction profile from the others.

By looking at the tensile curves of the three configurations in Figure 5.11.b, the behaviour of the material in tension has a non-linear global profile which can be cut in two distinct parts, first, a beginning of the linear curve, then a hardening of the curve. This represents an elastic linear initial behaviour than in a second time, a viscoelastic behaviour. The point of inflexion of the curves is respectively 0.01 deformation, 0.012 deformation and 0.017 deformation for the configurations 1, 2 and 3, respectively. It turns out that the deformation threshold involving the inflexion of the curves is all the greater that the annealing time is long. What can also be put forward is that the softening is even greater than the annealing time is important. Kurtz and Devine [86] have studied the mechanical behaviour of PEEK by varying strain rates and testing temperature. They evaluated that at room temperature and for low strain rate PEEK shows a linear relationship between stress and strain in tensile and compression tests.

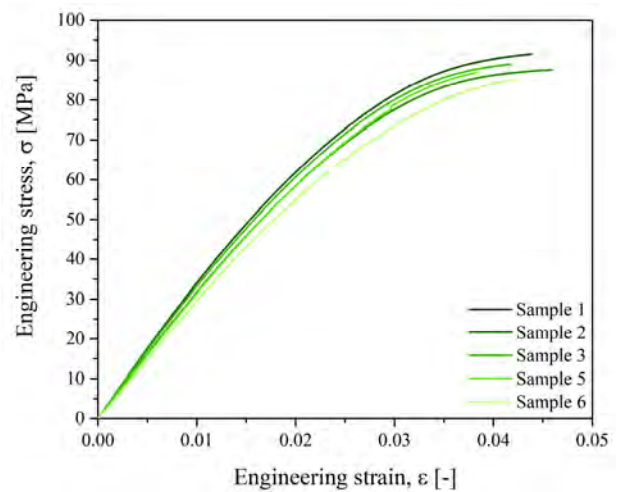
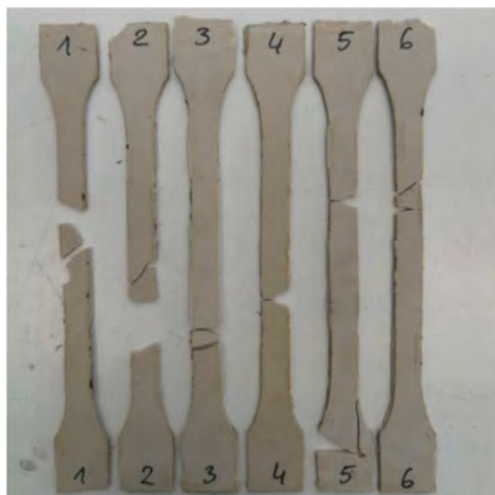
1<sup>st</sup> configuration, 370 °C for 5 min



2<sup>nd</sup> configuration, 370 °C for 5 min + 204 °C for 2 hrs



3<sup>rd</sup> configuration, 370 °C for 5 min + 204 °C for 4 hrs



(a)

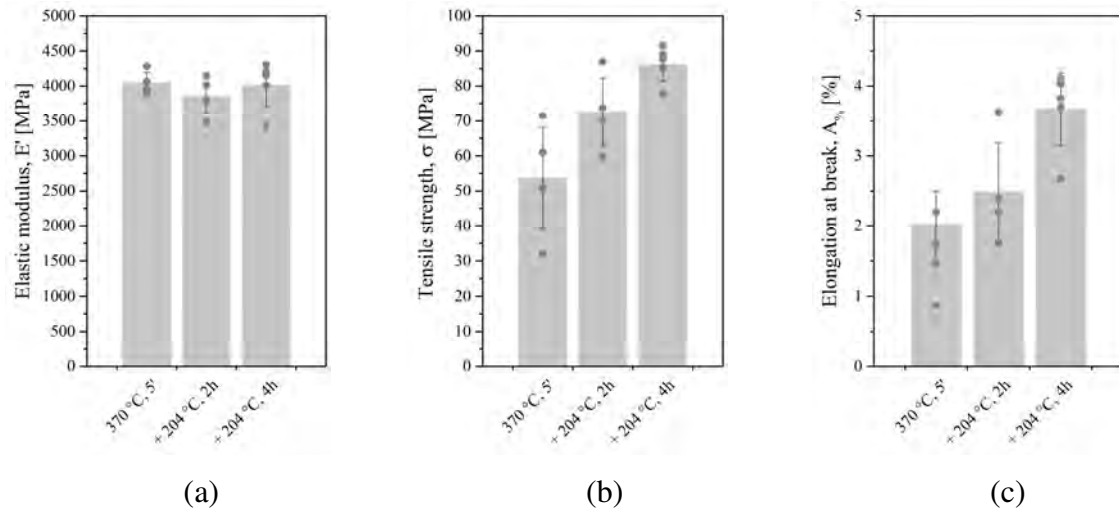
(b)

Figure 5.11. Broken samples and stress-strain curves for all configurations

The summary of mechanical results are presented in Table 5.3 and Figure 5.12.

Table 5.3. Summary of mechanical properties

Configuration	370 °C for 5 min	370 °C for 5 min	370 °C for 5 min
		204 °C for 2 hrs	204 °C for 4 hrs
Elastic modulus [MPa]	4045.4	3858.1	4016.3
Standard deviation	150.6	253.1	321.6
Tensile strength [MPa]	53.7	72.5	86.2
Standard deviation	14.6	9.8	4.8
Elongation [%]	2.0	2.5	3.7
Standard deviation	0.5	0.7	0.5



**Figure 5.12. Mechanical properties of (a) elastic modulus (b) tensile strength (c) elongation at break**

Regarding the elastic modulus of the PEEK 2000 FP, it remains constant regardless of the annealing time used and it reaches the average value of 4000 MPa, while the technical specification of PEEK gives a value of 3700 MPa. So, contrary to the results of Arzak et al. [311], the 204 °C annealing does not change the elastic modulus of the PEEK 2000 FP. It can be deduced that the 204 °C annealing does not act on an increase of the crystallinity of PEEK.

It can be outlined that annealing allows the increase of the mechanical strength. For samples without annealing, the average value of tensile strength is 53.7 MPa with a 14.6 MPa deviation. Considering samples with 2 hrs annealing, the strength value increases to 72.5 MPa (+ 35 %) with a decrease of the deviation, reaching a value of 9.8 MPa. For the samples with 4 hrs annealing, the tensile strength is 86.2 MPa (+ 60 % compared to 5 min annealing) with a deviation of 4.8 MPa.

For the elongation at break, the same trend emerges as the longer the 204 °C annealing time, the greater the value. This value for 5 min annealing is 2 % while for 2 hrs and 4 hrs it increases by + 23 % and + 81 %, respectively, to reach a maximum value of 3.7 %. For the deviation of elongation at break, it is quasi-constant for the three configurations with a value of 0.5 %. Annealing can promote better cohesion between powder grains.

### 5.5.2. Conclusion on the influence of annealing on the mechanical properties of PEEK

This study has proven that annealing act on mechanical properties. Longer is the annealing time better are the tensile strength and elongation, + 60 % and + 81 % for 4 hrs of 204 °C annealing time, respectively. The annealing time allows the diminution of the standard deviation that indicates a diminution of internal stresses. Nevertheless, for the PEEK 2000 FP, the elastic modulus does not change up to the annealing time.

## **5.6. Conclusion**

Thermal control during the selective laser sintering process for polyetheretherketone materials is hardly known due to high process temperatures. Thus, the lack of experimental data on the thermal history of the powder and printed part during the SLS process leads to the use of the numerical simulation. It was found that it is a good tool to predict the thermal history of each layer, with uncertainties due to hypotheses used to build the model.

The thermal profile was obtained based on the solution into conduction phenomena through the material using the finite element method. Abaqus software was used for calculations. The laser beam heat source was replaced by a surface temperature enough to melt the upper layer. The printing parameters dependent on laser and heat flux input were applied in the finite element method. As a result, the thermal history of each layer  $n$  has been calculated. The simulation shows that the heating due to the laser path spans length scales equivalent to 14 deposited layers. However, only the printing of the layers  $n$ ,  $n-1$ ,  $n-2$  and  $n-3$  are impacted by the laser pass.

Moreover, since the powder and printed layer stay at a temperature over 200 °C during the time of the batch, an annealing study was done. The results show that annealing can enhance significantly mechanical properties of polyetheretherketone. This enhancement probably results from the reorganization of the molecular chains between the major lamellae. It has been pointed out that annealing increases tensile strength and elongation at break without changing the elastic modulus.

Annealing allows the diminution of internal stresses due to the manufacturing process. As the internal stresses decrease, maximum stress increases. It has also to be noted that longer is the annealing, smaller is the standard deviation. That indicates that after manufacturing, the material has internal stresses not homogeneously diffused in the material. With time and temperature, this stresses decreases and are more diffused in the material.

# **CONCLUSION AND PERSPECTIVES**

## **Purpose and scope of work**

Initially intended to facilitate and accelerate the fabrication of prototypes, additive manufacturing has a great production potential. SLS (selective laser sintering) is one of the most promising processes for thermoplastic parts, because of its ability to produce geometries with low dimensional tolerances. Nevertheless, some issues remain to control the reliability of the manufacturing process and the properties of the printed parts. Moreover, the cost of the SLS process is several dozen times more expensive than other manufacturing processes. Another limitation of the SLS process is the lack of thermoplastics powder commercially available, mainly based on polyamides.

The aims of this thesis cover the four following topics:

- to give a deep knowledge of the requirement of the polymer powder properties to fit the SLS process;
- to stand out some orientations towards the formulation of new high-performance material with tuned properties to be suitable for SLS;
- to optimize the parameter sets on the ProX500 SLS printer to obtain the best mechanical and dimensional characteristics of the printed part;
- to understand the effect of the process parameters on the heat distribution in the part during printing.



## General conclusion

In the first part of this work, various commercial powders have been characterized to a deeper understanding of the properties necessary for their use in SLS and to define their processability temperature window. The results show that there is a lack of polyetheretherketone powders suitable for the selective laser sintering process on the market. Among the rare PEEK-based powders for SLS, we have chosen HP3 from EOS for our study. First of all, the shape and size of powders have been studied by SEM images and laser diffraction granulometry. It was possible to compare polyamide powder, already used for selective laser sintering process with polyetheretherketone powders. The powders shapes are far from spherical shape, with an average particle size of  $77.8 \pm 1.6 \mu\text{m}$  for PEEK HP3. The thermal transitions such as melting and crystallization temperature have been measured by DSC to define their sintering window. The widest window was noted for PEEK HP3, which is around  $72 \text{ }^\circ\text{C}$ . In the case of other polyetheretherketone and polyamide powders, the windows are quite narrow, and controlling the process would be difficult. Moreover, the thermal conductivity of PEEK 2000 FP has been measured on the consolidated state at  $0.24 \text{ W}\cdot\text{m}^{-1}\cdot\text{K}^{-1}$  for the density of  $1300 \text{ kg}\cdot\text{m}^{-3}$  and was calculated for tapped powder at  $0.15 \text{ W}\cdot\text{m}^{-1}\cdot\text{K}^{-1}$  for the density of  $1007 \text{ kg}\cdot\text{m}^{-3}$ .

The rheological properties in the molten state have been measured by rheometry. It was noted that the thermal degradation of the powders is a problem for the selective laser sintering process and it occurs faster with the increase in temperature. The terminal relaxation times have been calculated from the rheological measurements. They correspond to the time needed by the longest macromolecules to move out the tube in the reptation theory. This time is from 0.8 ms to 1.4 ms, which means that the temperature must be maintained high enough to allow inter-diffusion of polymeric chains this duration. Even HP3 has been identified with some unrequired properties which may affect the properties of printed parts. To complete these results, the powders could be additionally subjected to spectrophotometry to measure the reflection, absorption and transmission of the powders. These properties are dependent on the wavelength of the laser, temperature of the powder bed, surface roughness, incidence direction, chemical structure of the materials and size of grains.

At least, a few characterizations have been done to compare a recycled polyamide powder to a fresh one: We have highlighted a slight degradation increasing viscosity, and so, increase in relaxation times. Further investigations are necessary to quantify the fraction of recycled material to be mixed with a fresh one to be processed. Also, the build time, the position in the work chamber, as well as, the type of selective laser sintering machine should be considered.

The absence of suitable PEEK powder led us to develop new material in the second part of this work. For that, PEEK has been blended with an amorphous thermoplastic polymer, polyethersulfone (PES) by melt mixing. The PEEK/PES blends show the morphology of an immiscible system with clear phase separation observed. The SEM images are in agreement with the presence of two glass transitions, as attested by DSC and rheometry. The PES phase forms spherical nodules, for which the diameter increases with the PES content. The PEEK/PES interfacial adhesion looks weak. Nevertheless, the blends with PEEK 450 G show an improvement in storage modulus below the glass transition of PEEK. Thus, the initially immiscible blends have been compatibilized to delay their crystallization on cooling. Two kinds of compatibilizers have been chosen, HP3 copolymer and phenolphthalein. The polymer blends display immiscibility with HP3 and the phenolphthalein plasticizes the blends. It turned out that instead of delaying the crystallization, the melting point was increased, so we expended the sintering window by incorporation the phenolphthalein into the blends. The morphological analysis displays nano to microsized PES spherical domains. Moreover, phenolphthalein brings higher mobility to PEEK macromolecules, resulting in a higher degree of crystallinity.

To obtain relevant information for the material intended for the SLS process, these blends need deeper investigations: dynamic viscosity tests and interdiffusion times, thermal stability, crystallization kinetics and optical properties. To refine the analyses, the alone PEEK and PES will be extruded by following the same thermomechanical cycle than the different blends. Moreover, to better assess the compatibilizing effect of phenolphthalein, reference blends PEEK/phenolphthalein and PES/phenolphthalein will be performed at different phenolphthalein contents.

During manufacturing, many process parameters control the melting of the powder, and thus the properties of the parts and their dimensional accuracy. Thus, a statistical analysis of the response of the parameters was led by a design of experiments to extract the most influential parameters. The parametric study, done with the polyamide powder, was carried out by varying five parameters and by looking at their influence on five groups of responses relating to the physical, mechanical and thermal properties as well as to the printing duration of the parts. The design of experiments made it possible to establish the mathematical models of the response surfaces linking the responses to factors and their interactions. These statistical models were used to define an optimal set of parameters. The results and optimization of the laser parameters of the SLS process showed how they influenced production time. The results of tests on the geometry and density of specimens made of the polyamide 12 confirmed that increasing the

distance between successive laser beam transitions allows a significant manufacturing time reduction. Moreover, it is observed at the same time, a slight increase in material porosity with pores presenting a stochastic character. By optimization of the laser parameters, it is possible to obtain the targeted mechanical properties with over 33 % of reduction in production time. The iconography of correlations method by using all the data can offer suitable parameters to obtain the desired part. In this study, the optimized set of parameters requires to fill laser power of  $1.17 \times 28.20$  W, outline laser power of  $1 \times 15$  W and scan spacing of 0.16 mm.

Finally, a combined experimental and numerical simulation approach was conducted to estimate the influence of each laser pass on the degree of crystallinity and the mechanical properties of each layer. The results show that the heating due to the successive laser passes cover a thickness equivalent to 14 deposited layers. However, only the 4 upper layers are significantly thermally affected by the laser pass on a powder layer and thus show an evolution of their degree of crystallinity. The obtained model can be developed through the improvement of some parameters of temperature and laser to upgrade the simulation in 3D and simulate the whole process taking into account the movement of the laser with DFlux subroutine. Moreover, the model might be applied for polyamide 12 powder to be correlated with the results obtained in chapter 4.

## **Future development**

Considering the elaboration of material with tailored properties to fit the SLS requirement, we proposed a new material based on PEEK and PES, plasticized with phenolphthalein. The new blends show improved mechanical properties and an extended sintering window. However, it would be interesting to make more investigations. A remaining issue will be the processing of this blend into regular spherical and smooth particles. There is no available process yet to obtain such 50  $\mu\text{m}$  mean diameter particles from thermoplastics. It shall be interesting to measure the thermo-optical properties of this material such as reflection factor, absorption factor and transmission to perceive the interaction between laser and material in the wavelength range of the available laser. It should confirm the ability of this material to be used in additive manufacturing. Moreover, the simulated profile shall be simulated as done on PEEK 2000 FP and small layers should be created to verify if the use of this material will lead to the gradient of properties after additive manufacturing.

Taking into consideration the properties of the SLS process, an optimized set of parameters was presented for the Duraform FR1200 and ProX500 machine. The results obtained from the mathematical model have demonstrated improved mechanical properties and reduced production time. It would be interesting to use this set to retrieve samples and a full-size object for further analysis and to compare this optimized set of parameters with the tested parameters. This is a real challenge for the company. If these tests are satisfactory, the company shall change its parameters to obtain better parts, in terms of mechanical properties, geometry. Moreover, it will be a gain in time and productivity for it.

From a numerical point of view, it would be interesting to move to a more advanced multi-scale and multi-physics 3D model. A DEM/FEM coupled model can be used taking into account multi-physics phenomena at a different scale: volume heat source at the powder scale/bed fusion scale, scattering of the laser in contact with powder and phase changes at the powder/bed fusion scale, heat conduction at the powder scale and at the consolidated part scale, movement of the laser at the consolidated scale. This would take into account more realistic thermal fields, crystallinity rate, to better integrate the edge effects on the parts, the interaction between the laser beam and the powder, to analyse the evolution of open porosities and the creation of closed porosities in the powder bed and to integrate diffusion phenomena. Then, these more accurate thermal fields could be applied experimentally to polyamides and modified polyetheretherketone. Another important point to be solved is the unavailability of an SLS machine which can manufacture high-performance polymer. Two options are possible: the development of a laboratory bench to create our own machine or collaboration with the machine suppliers to draw-up a set of specifications. The latter will be the beginning of the development SLS machine able to manufacture high-performance polymers.

# **ADDITIONAL INFORMATION**

## List of abbreviations

2D	Two-dimension
3D	Three-dimension
ABS	Acrylonitrile butadiene styrene
AM	Additive manufacturing
ANRT	Association nationale recherche technologie
ASTM	American society for testing and materials
BASF	Badische anilin and sodafabric
BET	Brunauer-Emmett-Teller (names of scientists who published BET theory)
CIFRE	Conventions industrielles de formation par la recherche
CO <sub>2</sub>	Carbon dioxide
CORICO	Iconography of correlations
DEM	Discrete element method
DMTA	Dynamic mechanical analysis
DSC	Differential scanning calorimetry
ECTFE	Ethylene chlorotrifluoroethylene
ENIT	École nationale d'ingénieurs de Tarbes
EOS	Electro optical systems
ETFE	Ethylene tetrafluoroethylene
FEM	Finite element method
FFF	Fused filament fabrication
FP or PF	Fine powder
FR	Flame-retardant
FUI	Fonds unique interministériel
G	Granulate
GF	Glass fillers
HT	High torque
HT-LS	High-temperature laser sintering
ICI	Imperial chemical industries
IR	Infrared light
ISO	International organization for standardization
LCP	Liquid-crystal polymer
LGP	Laboratoire génie de production
MFA or PFA	Perfluoroalkoxy polymer
MJ	Material jetting
NaCl	Sodium chloride
Nd:YAG	Neodymium: yttrium aluminium garnet
OPM	Oxford performance materials
PA	Polyamide
PAEK	Polyaryletherketone
PAI	Polyamide-imide
PBI	Polybenzimidazole
PC	Polycarbonate
PE	Polyethylene
PE-HD	High-density polyethylene

PE-LD	Low-density polyethylene
PEG	Polyethylene glycol
PEI or ULTEM	Polyethylenimine
PEEEK	Polyetheretheretherketone
PEEK	Polyetheretherketone
PEEKEK	Polyetheretherketoneetherketone
PEEKK	Polyetheretherketoeketone
PEK	Polyetherketone
PEK-C	Polyetherketone with a cardo side group
PEKEKK	Polyetherketoneetherketoneketone
PEKK	Polyetherketoneketone
PES or PESU	Polyethersulfone
PES-C	Polyethersulfone with a cardo side group
PET	Polyethylene terephthalate
Phph	Phenolphthalein
PI	Polyimide
PMMA	Poly(methyl methacrylate)
POM	Polyoxymethylene
PP	Polypropylene
PPO	Poly(p-phenylene oxide)
PPS	Polyphenylene sulfide
PPSU	Polyphenylsulfone
PS	Polystyrene
PSU	Polysulfone
PU	Polyurethane
PVC	Polyvinyl chloride
PVDF	Polyvinylidene fluoride
RP	Rapid prototyping
SAN	Styrene-acrylonitrile
SEM	Scanning electron microscopy
SFP	Super-fine powder
SiC	Silicon carbide
SLA	Stereolithography
SLM	Selective laser melting
SLS	Selective laser sintering
O <sub>2</sub>	Oxygen
TGA	Thermogravimetric analysis
TPE	Thermoplastic elastomer
TPI	Thermoplastic polyimide
UHMWPE	Ultra-high molecular weight polyethylene
USA or US	United States of America
UV	Ultraviolet light
WASPE	Weight savings for aerospace packaging equipments
X, Y, Z	Manufacturing direction
XY	Axis parallel to deposited and consolidated layers of powder
XZ, YZ	Orthogonal plane to deposited and consolidated layers of powder

## List of symbols

\$	Dolar (currency in the USA)
€	Euro (currency in Europe)
a	Sintering neck radius [m] or thermal diffusivity of sample [ $\text{mm}^2.\text{s}^{-1}$ ]
a, b, c	Standard of the vectors defining a crystalline mesh [ $\text{\AA}$ ]
A	Area [ $\text{m}^2$ ]
$A_\lambda$	Absorbance [%]
AOR	Angle of repose [ $^\circ$ ]
$C_p$	Specific heat [ $\text{J}.\text{kg}^{-1}.\text{K}^{-1}$ ]
dF	Feret diameter [ $\mu\text{m}$ ]
D or d	Diameter [m]
$D_{10}$ , $D_{50}$ , $D_{90}$	Diameter of particle size distributions [ $\mu\text{m}$ ]
$D_{\text{lb}}$	Diameter of laser beam [ $\mu\text{m}$ ]
$D_{\text{tube}}$	Unidimensional diffusion coefficient [ $\text{m}^2.\text{s}^{-1}$ ]
$D_{\text{hyd}}$ or $\rho_{\text{hydrostatic}}$	Hydrostatic density [ $\text{g}.\text{cm}^{-3}$ ]
$D_{\text{rel}}$ or $\rho_{\text{relative}}$	Relative density [%]
$D_{\text{vol}}$ or $\rho_{\text{volumetric}}$	Volumetric density [ $\text{g}.\text{cm}^{-3}$ ]
E or G	Energy [J]
$E''$ or $G''$	Loss modulus [Pa]
$E_a$	Activation energy [ $\text{J}.\text{mol}^{-1}$ ]
ED	Energy density [ $\text{J}.\text{mm}^{-2}$ ]
$ED_{\text{vol}}$	Volumetric energy density [ $\text{J}.\text{mm}^{-3}$ ]
EDf	Fill energy density [ $\text{J}.\text{mm}^{-2}$ ]
EDo	Outline energy density [ $\text{J}.\text{mm}^{-2}$ ]
f	Heating or cooling rate [ $^\circ\text{C}.\text{mm}^{-1}$ ]
F	Force [N]
FlexuralM or $E'$	Flexural modulus [MPa]
FlexuralS or $\sigma$	Flexural strength or stress [MPa]
H or h	High [m] or relaxation time distribution parameter [-]
HR	Hausner ratio [-]
$J_e$	Elastic complacency [ $\text{Pa}^{-1}$ ]
k	Crystallization rate [ $\text{s}^{-1}$ ]
$k_B$	Boltzmann's constant [ $1.381 \cdot 10^{-23} \text{J}.\text{K}^{-1}$ ]
$k(T)$	Avrami or Ozawa crystallization rate [ $\text{min}^{-1}$ ]
K	Constant to calculate viscosity [ $\text{mL}.\text{g}^{-1}$ ]
L	Length [m]
$L_m$	Latent melting heat [ $\text{J}.\text{K}^{-1}$ ]
LP	Laser power [W]
LPf	Fill laser power [W]
LPo	Outline laser power [W]
LS	Scan speed [ $\text{mm}.\text{s}^{-1}$ ]
LSF	Length shrinkage of sintered flexion samples [%]
LST	Length shrinkage of sintered tensile samples [%]
m	Ozawa exponent [-]
$M_w$	Molecular weight [ $\text{g}.\text{mol}^{-1}$ ]



n	Avrami or constant exponent [-] or layer [-]
n°	Number [-]
N	Number of monomers in a chain [-]
N <sub>e</sub>	Number of monomers between entanglements [-]
p	Perimeter of analysed particle [μm]
P <sub>s</sub>	Molecular Parachor [-]
PLT	Layer thickness [mm]
PSD	Particle size distribution [μm]
q	Volume [%]
q <sub>s</sub>	Heat flux [W.m <sup>-2</sup> ]
Q	Heat flow [mW]
r or R	Radius [m]
rpm	Revolutions per minute [r.min <sup>-1</sup> ]
R	Gas constant [= 8.314 J.K <sup>-1</sup> .mol <sup>-1</sup> ]
R <sup>2</sup>	Total correlation [-]
R <sub>λ</sub>	Reflectance [%]
R(t)	Electrical resistance [Ω]
S	Shrinkage [%]
SC	Scan count [-]
SCf	Fill scan count [-]
SCo	Outline scan count [-]
SS	Scan spacing [mm]
t	Time [s]
t <sub>pl</sub>	Post add powder layer delay [s]
tp	Production time [s]
T	Temperature [°C or K] or thickness [m]
T <sub>b</sub>	Part bed temperature [°C]
T <sub>c</sub>	Crystallization temperature [°C]
T <sub>cc</sub>	Cold crystallization temperature [°C]
T <sub>g</sub> or T <sub>α</sub>	Glass transition temperature [°C]
T <sub>m</sub>	Melting point [°C]
T <sub>p</sub>	Preheating temperature [°C]
T <sub>r</sub>	Tube renewal time [s]
T <sub>λ</sub>	Transmittance [%]
tanδ	Loss factor [-]
TensileE or A%	Elongation at break [%]
TensileM or E' or G'	Tensile modulus or elastic modulus [MPa]
TensileS or σ	Tensile strength or stress [MPa]
TSF	Thickness shrinkage of sintered flexion samples [%]
TST	Thickness shrinkage of sintered tensile samples [%]
vol.%	Mass fraction by volume [%]
V	Velocity [m.s <sup>-1</sup> ] or volume [m <sup>3</sup> ] or molar volume [m <sup>3</sup> .mol <sup>-1</sup> ]
VSF	Volume shrinkage of sintered flexion samples [%]
w	Mass fraction [g]
wt.%	Mass fraction by weight [%]
W	Width [m] or work of adhesion [J.m <sup>-2</sup> ]

WSF	Width shrinkage of sintered flexion samples [%]
WST	Width shrinkage of sintered tensile samples [%]
x	Weight loss [%]
X	Fraction of particles large [ $\mu\text{m}$ ]
$X_c$	Degree of crystallization [%]
$X(t)$	Crystallization kinetic [-]
$\alpha, \beta, \gamma$	Physical transition of certain polymers, crystalline or phase form [-]
$\gamma$	Surface tension [ $\text{J.m}^{-2}$ or $\text{mN.m}^{-1}$ ]
$\dot{\gamma}$	Shear rate [ $\text{s}^{-1}$ ]
$\Delta H_c$	Crystallization enthalpy [ $\text{J.g}^{-1}$ ]
$\Delta H_m$	Melting enthalpy [ $\text{J.g}^{-1}$ ]
$\Delta H_{th}$	Theoretical melting enthalpy of 100 % crystalline phase [ $\text{J.g}^{-1}$ ]
$\Delta S_m$	Entropy factor [ $\text{J.K}^{-1}$ ]
$\varepsilon$	Strain or Deformation [-]
$\mu$	Friction [-]
$\eta$	Viscosity [ $\text{Pa.s}$ ]
$\eta^*$	Dynamic viscosity [ $\text{Pa.s}$ ]
$\eta'$	Loss viscosity [ $\text{Pa.s}$ ]
$\eta''$	Storage viscosity [ $\text{Pa.s}$ ]
$\theta$	Orientation or angle or wettability [ $^\circ$ ]
$\lambda$	Wavelength [ $\text{nm}$ ] or relaxation time [ $\text{s}$ ] or thermal conductivity [ $\text{W.m}^{-1}\text{.K}^{-1}$ ]
$\pi$	Ratio of the circle circumference to its diameter [= 3.141]
$\rho$	Density [ $\text{g.cm}^{-3}$ ]
$\rho_{\text{bulk}}$	Bulk density [ $\text{g.cm}^{-3}$ ]
$\rho_{\text{tap}}$	Tapped density [ $\text{g.cm}^{-3}$ ]
$\tau$	Shear stress [ $\text{N.m}^{-2}$ ]
$\tau_{\text{rep}}$	Reptation time [ $\text{s}$ ]
$v$	Fraction of air [%]
$\varphi$	Light flux [ $\text{lm}$ ]
$\Phi$	Packing fraction [-]
$\omega$	Angular frequency [ $\text{Rad.s}^{-1}$ ]
>	More than...
<	Less than...
$\pm$	More or less

## List of figures

Figure 0.1. Circonstances optiques du processus SLS .....	14
Figure 0.2. Combinaison de propriétés importantes de poudres pour le procédé SLS .....	15
Figure 0.3. Séquence de frittage schématique pour deux sphères .....	17
Figure 0.4. Thermogramme de DSC représentant la fenêtre de frittage pour un PEEK HP3 .....	19
Figure 0.5. Viscosité complexe du PEEK 2000 FP déterminée par le rhéomètre .....	19
Figure 0.6. Transitions thermiques des mélanges PEEK/PES.....	22
Figure 0.7. Les images SEM des mélanges PEEK 2000 FP et PES [wt.%] .....	23
Figure 0.8. Fenetre de processabilité des mélanges PEEK and PES avec (a) HP3 et (b) phenolphthaleine .....	24
Figure 0.9. Sphère globale de tous les résultats au seuil de 0.3.....	27
Figure 0.10. Linéarisation du profil thermique lors de 4 passages laser .....	29
Figure 1.1. The Wohlers report 2019 of (a) AM industry growth (b) industrial activities of AM .....	42
Figure 1.2. Schematic of SLA process.....	43
Figure 1.3. Schematic of FFF process.....	43
Figure 1.4. Schematic of SLS process.....	44
Figure 1.5. Schematic diagram of the SLS process showing the relevant nomenclature .....	45
Figure 1.6. Schematic of preheating temperature during the SLS process (3D Systems, Sinterstation HiQ) .....	48
Figure 1.7. The DSC curves of different transitions and reactions of the typical polymer [19].....	49
Figure 1.8. Optical circumstances of the SLS process .....	52
Figure 1.9. Laser scanning strategy of the SLS process [28] .....	55
Figure 1.10. Influence of thickness for spread layers on the surface appearance of parts.....	56
Figure 1.11. Build orientation of parts .....	56
Figure 1.12. Thermoplastic polymers .....	62
Figure 1.13. Solid-state properties of thermoplastic polymers.....	63
Figure 1.14. The Wohlers report 2017 of (a) material distribution (b) real consumption in SLS process [55].....	64
Figure 1.15. Structure of (a) aliphatic polyamide (b) aromatic polyamide .....	66
Figure 1.16. Chemical formula of PA11 (x = 10) and PA12 (x = 11).....	70
Figure 1.17. The $T_m$ and $T_g$ of PAEK powders as a function of ether/ketone ratio [80].....	72
Figure 1.18. Structure of (a) chain conformation (b) orthorhombic crystal unit cell of PEEK [86] .....	73
Figure 1.19. Scheme of the formation of PEEK.....	74
Figure 1.20. Structure of PEEK .....	75
Figure 1.21. Scheme of the formation of PEK.....	75
Figure 1.22. Structure of PEK.....	76
Figure 1.23. Scheme of the formation of PEKK .....	76
Figure 1.24. Structure of PEKK.....	77
Figure 1.25. The $T_m$ and $T_g$ of PEKK as a function of T/I ratio [113] .....	77
Figure 1.26. The PEEK degradation products at 450 °C.....	78
Figure 1.27. Combination of important properties of powders for SLS process [21] .....	80
Figure 1.28. Shape of powder particle .....	82
Figure 1.29. Size of powder particle .....	82
Figure 1.30. The DSC thermogram with nature of “sintering window” as SLS process temperature [21].....	87
Figure 1.31. Diagram of (a) flow curves (b) viscosity curves [119] .....	89
Figure 1.32. Simple mean shear stress and shear rate between two parallel plates.....	90
Figure 1.33. The viscosity as a function of temperature for amorphous and semi-crystalline polymers [22].....	92
Figure 1.34. Wetting of different fluids [125].....	94
Figure 1.35. Liquid droplet remaining in an equilibrium state with the flat solid surface [125].....	94
Figure 1.36. The bead (fraction factor) and spring (Gaussian entropy) molecular model.....	102
Figure 1.37. Polymer chain located in a fixed network with representing obstacles .....	102
Figure 1.38. Reptation theory, $t_0 < t_1 < t_2 < T_r$ (the tube renewal time) [148] .....	103
Figure 1.39. Interdiffusion of chains across an interface [148].....	105
Figure 1.40. Sintering sequence for PP-XP1 powder particles at 190 °C [162].....	107
Figure 1.41. Schematic sintering sequence for two spheres [162].....	108
Figure 2.1. The SEM of fresh PA12 powder.....	120
Figure 2.2. The SEM of recycled PA12 powder .....	120
Figure 2.3. The SEM images of PEEK 330 PF .....	121
Figure 2.4. The SEM images of PEEK 550 PF .....	122
Figure 2.5. The SEM images of PEEK 2000 FP .....	122
Figure 2.6. The SEM images of PEEK 880 SFP.....	122
Figure 2.7. The SEM images of PEEK 450 G.....	122

Figure 2.8. The SEM images of PEEK HP3 .....	123
Figure 2.9. Distribution of circularity for fresh and recycled PA12.....	125
Figure 2.10. Distribution of shape ratio for fresh and recycled PA12.....	125
Figure 2.11. The circularity-shape ratio diagram of polymer powders .....	126
Figure 2.12. Three x-axis values $D_{10}$ , $D_{50}$ , and $D_{90}$ [173] .....	126
Figure 2.13. The PSD by laser granulometry for PEEK 880 SFP at (a) water (b) ethanol .....	129
Figure 2.14. The PSD by laser granulometry (solid line - water, dash line - ethanol) .....	130
Figure 2.15. Particles size distribution comparison for $D_{50}$ of PA and PEEK powders .....	131
Figure 2.16. Flowability of powders .....	136
Figure 2.17. Cell aggregation and sphere packing (a) simple cubic (b) face-centred cubic (c) hexagonal .....	137
Figure 2.18. The SEM images of titanium powder (a) before (b) after plasma treatment [184].....	139
Figure 2.19. The DSC thermogram obtained at $10\text{ }^{\circ}\text{C}\cdot\text{min}^{-1}$ .....	142
Figure 2.20. Sintering windows of PA12 and PEEK powders.....	145
Figure 2.21. The DSC thermogram obtained for PEEK HP3.....	146
Figure 2.22. The FTIR spectrum of PEEK 2000 FP and PEEK HP3.....	147
Figure 2.23. The TGA thermogram obtained for PEEK HP3 .....	148
Figure 2.24. Images of X-ray tomography of (a) apparent (b) tapped (c) pressed density.....	149
Figure 2.25. Diagrams of (a) thermal conductivity (b) density as a function of air fraction .....	151
Figure 2.26. Dynamic viscosity of PEEK powders for different temperatures .....	154
Figure 2.27. Viscosity as a function of time for different temperatures [200] .....	155
Figure 2.28. Scheme of the degradation mechanism of PEEK .....	155
Figure 2.29. Scheme of the radicals propagation .....	156
Figure 2.30. Scheme of the formation of phenolic species .....	156
Figure 2.31. Rheological behaviour of PEEK HP3 at $383\text{ }^{\circ}\text{C}$ and $400\text{ }^{\circ}\text{C}$ .....	157
Figure 2.32. Degradation of PEEK under air and nitrogen [207].....	158
Figure 2.33. Cole-Cole representation from frequency sweep for PEEK powders.....	160
Figure 2.34. Determination of limited elastic complacency for PEEK powders.....	162
Figure 2.35. Relaxation time with extrapolation according to the Arrhenius law.....	163
Figure 2.36. The TGA thermogram obtained for PA12 powders.....	166
Figure 2.37. Evolution of the percentage of weight loss from $t_0$ .....	167
Figure 2.38. Evolution of $G'$ and $G''$ with time at constant angular frequency and $200\text{ }^{\circ}\text{C}$ for fresh PA12 .....	168
Figure 2.39. Comparison of rheological properties of fresh PA12 and recycled PA12 at $200\text{ }^{\circ}\text{C}$ .....	168
Figure 2.40. Rheological properties of (a) fresh (b) recycled PA12 for different temperatures.....	169
Figure 3.1. Basic types of phase structures in polymer blends.....	176
Figure 3.2. Morphology of (a) interlamellar (b) interspherulitic (c) interfibrillar in blends [233].....	177
Figure 3.3. The $T_g$ of PEEK/PES blends versus PEEK composition of different authors [243, 244].....	180
Figure 3.4. Structure of PES .....	181
Figure 3.5. Structure of phenolphthalein.....	183
Figure 3.6. The DSC of (a) long-short (b) long-long chains for PEEK 450 G and PES blends.....	186
Figure 3.7. The DMTA of (a) long-short (b) long-long chains for PEEK 450 G and PES blends.....	187
Figure 3.8. The DSC of (a) short-short (b) short-long chains for PEEK 2000 FP and PES blends.....	189
Figure 3.9. The DMTA of (a) short-short (b) short-long chains for PEEK 2000 FP and PES blends.....	190
Figure 3.10. Thermal transitions of PEEK/PES blends.....	190
Figure 3.11. Sintering windows of PEEK 450 G and PES blends .....	191
Figure 3.12. Sintering windows of PEEK 2000 FP and PES blends.....	191
Figure 3.13. Degree of crystallinity ( $\pm 5\%$ ) for PEEK/PES blends.....	192
Figure 3.14. The SEM images of microstructure of PEEK 450 G and PES blends [wt.%] .....	194
Figure 3.15. The SEM images of microstructure of PEEK 2000 FP and PES blends [wt.%].....	194
Figure 3.16. The TGA curves of PEEK 2000 FP and PES blends .....	196
Figure 3.17. The DSC of PEEK 450 G and PES blends with HP3 .....	199
Figure 3.18. The DSC of PEEK 450 G and PES blends with Phph .....	200
Figure 3.19. The DMTA of PEEK 450 G and PES blends with HP3 .....	201
Figure 3.20. The DMTA of PEEK 450 G and PES blends with Phph .....	202
Figure 3.21. Thermal transitions of PEEK 450 G and PES blends with (a) HP3 (b) Phph.....	203
Figure 3.22. Sintering windows of PEEK 450 G and PES blends with HP3 .....	203
Figure 3.23. Sintering windows of PEEK 2000 FP and PES blends with Phph.....	204
Figure 3.24. Degree of crystallinity ( $\pm 5\%$ ) for blends .....	204
Figure 3.25. The SEM of the microstructure of PEEK 450 G and PES blends [wt.%] with HP3 copolymer....	205
Figure 3.26. The SEM of the microstructure of PEEK 450 G and PES blends [wt.%] with phenolphthalein ....	206
Figure 4.1. Samples orientation in build chamber.....	215

Figure 4.2. Dog-bone tensile test specimen (a) L = 170 mm (b) L = 85 mm ..... 217

Figure 4.3. Stress-strain diagrams for long and small specimens in all directions of printing ..... 218

Figure 4.4. Mechanical properties for 2 different length specimens ..... 219

Figure 4.5. Stress-strain diagrams for pairs machine/material for all directions of printing ..... 222

Figure 4.6. Mechanical properties of (a) elastic modulus (b) tensile strength (c) elongation at break ..... 223

Figure 4.7. Specimens for tensile and flexural testing ..... 231

Figure 4.8. Bulk and relative density of sintered parts ..... 232

Figure 4.9. Effect of fill energy density upon the relative density of Duraform FR1200 samples ..... 233

Figure 4.10. Tolerances for linear dimensions of sintered flexion samples ..... 234

Figure 4.11. Tolerances for linear dimensions of sintered tensile samples ..... 235

Figure 4.12. Average shrinkage of sintered flexion samples ..... 237

Figure 4.13. Average shrinkage of sintered tensile samples ..... 237

Figure 4.14. Average volume shrinkage of sintered flexion samples with different laser energy densities ..... 238

Figure 4.15. Stress-strain diagrams for some (a) sintered flexion samples (b) sintered tensile samples ..... 239

Figure 4.16. Flexural properties of sintered parts ..... 239

Figure 4.17. Tensile properties of sintered parts ..... 240

Figure 4.18. Thermal properties of sintered parts ..... 241

Figure 4.19. Production time of flexural sintered parts ..... 243

Figure 4.20. CORICO diagram of average data at threshold 0.3 ..... 246

Figure 4.21. CORICO diagram of all the results at threshold 0.3 ..... 248

Figure 4.22. The 3D response surface plots between LPf and SS for (a) Dvol and Dhyd (b) Drel ..... 252

Figure 4.23. The 3D response surface plots between (a) LPo LPf and FlexuralM (b) SCo, SS and FlexuralS .. 252

Figure 4.24. The 3D response surface plots between (a) LPf, SCf and TensileS (b) SCf, SCo and TensileE .... 253

Figure 4.25. The 3D response surface plots on tp between SCf and SS ..... 253

Figure 5.1. The electromagnetic spectrum ..... 262

Figure 5.2. Gaussian shape of a laser ..... 267

Figure 5.3. Dimensions of layer ..... 268

Figure 5.4. Model mapping at 10 s ..... 269

Figure 5.5. Evolution of temperature as a function of time for layers from n to n-14 ..... 270

Figure 5.6. Assembly of thermal profiles of each layer ..... 271

Figure 5.7. Linearization of thermal profile for the layer n ..... 273

Figure 5.8. The DSC thermogram of four cycles ..... 274

Figure 5.9. The WAXS diffractograms of four passes ..... 275

Figure 5.10. Degree of crystallinity as a function of the number of passes applied ..... 276

Figure 5.11. Broken samples and stress-strain curves for all configurations ..... 280

Figure 5.12. Mechanical properties of (a) elastic modulus (b) tensile strength (c) elongation at break ..... 281

Figure A.1. Scanning electron microscopy scheme ..... 324

Figure A.2. The ImageJ processing using SEM images ..... 325

Figure A.3. Circularity of powder ..... 326

Figure A.4. Shape ratio of powder ..... 327

Figure A.5. Laser granulometry scheme ..... 327

Figure A.6. Measuring apparatus of (a) angle of repose (b) bulk density (c) tapped density ..... 329

Figure A.7. Differential scanning calorimetry scheme ..... 331

Figure A.8. Experimental device for measuring conductivity ..... 333

Figure A.9. Schematization of rheometer and sample in (a) molten state (b) solid-state ..... 335

Figure A.10. Twin-screw extruder Process 11 ..... 337

Figure A.11. Screw arrangement for PEEK ..... 338

Figure A.12. Micro compounder 15 HT ..... 339

Figure A.13. The sPro230 by 3D Systems ..... 341

Figure A.14. The ProX500 by 3D Systems (a) production machine (b) material quality control system ..... 343

## List of tables

Table 0.1. Facteurs et niveaux choisis pour l'analyse statistique.....	26
Table 0.2. Réponses choisies pour l'analyse statistique.....	26
Table 1.1. Processing parameters that may affect the SLS process .....	47
Table 1.2. Names and brands of manufacturers worldwide for polyamides .....	67
Table 1.3. Crystal structure of PA materials .....	69
Table 1.4. Crystal structure of PAEK materials.....	73
Table 1.5. Names and brands of manufacturers worldwide for PEEK.....	74
Table 1.6. Names and brands of manufacturers worldwide for PEK .....	76
Table 1.7. Names and brands of manufacturers worldwide for PEKK .....	77
Table 2.1. Circularity and shape ratio of PA and PEEK particles.....	124
Table 2.2. The particle size distributions by ImageJ analysis .....	127
Table 2.3. Differences between image analysis and laser granulometry.....	128
Table 2.4. The particle size distributions by laser granulometry in water.....	128
Table 2.5. The particle size distributions by laser granulometry in ethanol.....	130
Table 2.6. Angle of repose for the different powders.....	132
Table 2.7. Flow properties and corresponding angles of repose [177].....	133
Table 2.8. Carr and Hausner indices of different powders.....	134
Table 2.9. Scale of flowability [177].....	135
Table 2.10. Packing fraction for the different powders.....	138
Table 2.11. The DSC results for PA and PEEK powders .....	144
Table 2.12. Experimental results of PEEK 2000 FP powder properties .....	150
Table 2.13. Complex viscosity for 1 rad.s <sup>-1</sup> of PEEK powders.....	157
Table 2.14. Relaxation time for PEEK powders .....	163
Table 2.15. The weight loss of PA12 at 750 °C.....	166
Table 2.16. Complex viscosity for 1 rad.s <sup>-1</sup> of PA12 .....	170
Table 3.1. Properties of the blend components .....	184
Table 4.1. Processing parameters for tensile specimens .....	216
Table 4.2. Production thermoplastic parts with ProX500 SLS printer .....	228
Table 4.3. Different process parameters and their values .....	228
Table 4.4. Studied answers for the design of experiments .....	229
Table 4.5. Duraform FR1200 experimental design with variable values .....	229
Table 4.6. Positive (green) and negative (red) correlations of average data .....	246
Table 4.7. Positive (green) and negative (red) correlations of all the results .....	249
Table 4.8. Summary of CORICO and regression analysis.....	250
Table 4.9. Proposed optimization criterion with results.....	254
Table 5.1. Thermophysical properties of PEEK powder and consolidated PEEK.....	269
Table 5.2. The DSC results for cycles of thermal profile.....	274
Table 5.3. Summary of mechanical properties.....	280

## List of literature

- <sup>1</sup> S. Dupin, Etude fondamentale de la transformation du polyamide 12 par frittage laser : mécanismes physico-chimiques et relations microstructures/propriétés, Doctorat Dissertations, Institut National des Sciences Appliquées de Lyon, **2012**
- <sup>2</sup> D. Defauchy, Simulation du procede de fabrication directe de pieces thermoplastiques par fusion laser de poudre, Doctorat Dissertations, Institut des Sciences et Technologies de Paris, **2013**
- <sup>3</sup> E. Dumoulin, Fabrication additive de pièces en polymères thermoplastiques hautes performances et en polyamide 12 par le procédé de frittage sélectif par laser, Doctorat Dissertations, Institut des Sciences et Technologies de Paris, **2013**
- <sup>4</sup> G. Budzik, W. Budzik, M. Cygnar, K. Janisz, The possibilities of application of rapid prototyping in process of designing and manufacturing of elements of car vehicles, *Problemy Eksploatacji*, 1(1), 7–16, **2009**
- <sup>5</sup> T. Wohlers, Wohlers report 2019. 3D printing and additive manufacturing state of the industry, Wohlers Associates, **2019**
- <sup>6</sup> R.V. Rao, Advanced modeling and optimization of manufacturing processes: International research and development, Springer Science & Business Media, **2010**
- <sup>7</sup> A. Mazzoli, Selective laser sintering in biomedical engineering, *Medical & Biological Engineering & Computing*, 51(3), 245–256, **2013**
- <sup>8</sup> K.H. Lee, H. Woo, Direct integration of reverse engineering and rapid prototyping, *Computers & Industrial Engineering*, 38(1), 21–38, **2000**
- <sup>9</sup> N. Hopkinson, R. Hague, P. Dickens, Rapid manufacturing: an industrial revolution for the digital age, John Wiley & Sons, **2006**
- <sup>10</sup> C.R. Deckard, Methods and apparatus for producing parts by selective laser sintering, US4863538A, **1989**
- <sup>11</sup> T. Wohlers, T. Gornet, Wohlers report 2014. 3D printing and additive manufacturing state of the industry: history of additive manufacturing, Wohlers Associates, 1–34, **2014**
- <sup>12</sup> P. Zimniak, Recirculation of the plastics used in the art incremental SLS, *Inżynieria i Aparatura Chemiczna*, 49(5), 148–149, **2010**
- <sup>13</sup> V. Jaiganesh, A.C. Andrew, E. Mugilan, Manufacturing of PMMA cam shaft by rapid prototyping, *Procedia Engineering*, 97(1), 2127–2135, **2014**
- <sup>14</sup> R. Konda, K.P. Rajurkar, R.R. Bishu, A. Guha, M. Parson, Design of experiments to study and optimize process performance, *International Journal of Quality & Reliability Management*, 16(1), 56–71, **1999**
- <sup>15</sup> J.C. Nelson, S. Xue, J.W. Barlow, J.J. Beaman, H.L. Marcus, D.L. Bourell, Model of the selective laser sintering of bisphenol-A polycarbonate, *Industrial & Engineering Chemistry Research*, 32(10), 2306–2317, **1993**
- <sup>16</sup> Y. Shi, Z. Li, H. Sun, S. Huang, Effect of the properties of the polymer materials on the quality of selective laser sintering parts, *Journal of Materials: Design and Applications*, 218(3), 247–252, **2004**
- <sup>17</sup> B. Redwood, Post processing for SLS printed parts, *3D Hubs*, **2017**
- <sup>18</sup> R.D. Goodridge, C.J. Tuck, R.J.M. Hague, Laser sintering of polyamides and other polymers, *Progress in Materials Science*, 57(2), 229–267, **2012**
- <sup>19</sup> I.M. Kalogerias, Glass transition phenomena in polymer blends, in: I.I. Avraal, *Encyclopedia of Polymer Blends*, 1st ed., John Wiley & Sons, Arkom, OH, USA, **2016**
- <sup>20</sup> J. Jencyk, Badanie dynamiki molekularnej oraz struktury kopolimerów metodą NMR oraz spektroskopii dielektrycznej, Doctorat Dissertations, Adam Mickiewicz University Repository, **2011**
- <sup>21</sup> M. Schmid, K. Wegener, Additive manufacturing: polymers applicable for laser sintering (LS), *Procedia Engineering*, 149(1), 457–464, **2016**
- <sup>22</sup> J.P. Schultz, Modeling heat transfer and densification during laser sintering of viscoelastic polymers, Doctorat Dissertations, Virginia Polytechnic Institute and State University, **2003**
- <sup>23</sup> S. Berretta, Y. Wang, R. Davies, O.R. Ghita, Polymer viscosity, particle coalescence and mechanical performance in high-temperature laser sintering, *Journal of Materials Science*, 51(10), 4778–4794, **2016**
- <sup>24</sup> M. Schmid, A. Amado, K. Wegener, Polymer powders for selective laser sintering (SLS), in: *Proceedings of the 30th International Conference of the Polymer Processing Society*, AIP Publishing, Cleveland, OH, USA, 1–5, **2015**
- <sup>25</sup> M.M. Savalani, L. Hao, R.A. Harris, Evaluation of CO<sub>2</sub> and Nd:YAG lasers for the selective laser sintering of HAPEX®, *Proceedings of the Institution of Mechanical Engineers, Part B: Journal of Engineering Manufacture*, 220(2), 171–182, **2006**
- <sup>26</sup> I. Gibson, D. Shi, Material properties and fabrication parameters in selective laser sintering process, *Rapid Prototyping Journal*, 3(4), 129–136, **1997**
- <sup>27</sup> J.D. Williams, C.R. Deckard, Advances in modeling the effects of selected parameters on the SLS process, *Rapid Prototyping Journal*, 4(2), 90–100, **1998**

- <sup>28</sup> B. Caulfield, P.E. McHugh, S. Lohfeld, Dependence of mechanical properties of polyamide components on build parameters in the SLS process, *Journal of Materials Processing Technology*, 182(1–3), 477–488, **2007**
- <sup>29</sup> T. Gill, B. Hon, Selective laser sintering of SiC/polyamide composites, *CIRP Annals*, 52(1), 173–176, **2003**
- <sup>30</sup> S. Negi, S. Dhiman, R.K. Sharma, Influence of process parameters on mechanical properties of parts fabricated by selective laser sintering, 1–4, **2015**
- <sup>31</sup> J.S. Usher, T.J. Gornet, T.L. Starr, Weibull growth modeling of laser-sintered nylon 12, *Rapid Prototyping Journal*, 19(4), 300–306, **2013**
- <sup>32</sup> T.L. Starr, T.J. Gornet, J.S. Usher, The effect of process conditions on mechanical properties of laser-sintered nylon, *Rapid Prototyping Journal*, 17(6), 418–423, **2011**
- <sup>33</sup> T.F. Pereira, M.A.C. Silva, M.F. Oliveira, I.A. Maia, J.V.L. Silva, M.F. Costa, R.M.S.M. Thiré, Effect of process parameters on the properties of selective laser sintered poly(3-hydroxybutyrate) scaffolds for bone tissue engineering, *Virtual and Physical Prototyping*, 7(4), 275–285, **2012**
- <sup>34</sup> L. Ghasemi-Mobarakeh, M.P. Prabhakaran, L. Tian, E. Shamirzaei-Jeshvaghani, L. Dehghani, S. Ramakrishna, Structural properties of scaffolds: crucial parameters towards stem cells differentiation, *World Journal of Stem Cells*, 7(4), 728–744, **2015**
- <sup>35</sup> A. Stwora, G. Skrabalak, Influence of selected parameters of selective laser sintering process on properties of sintered materials, *Journal of Achievements in Materials and Manufacturing Engineering*, 61(2), 375–380, **2013**
- <sup>36</sup> M. Schmidt, D. Pohle, T. Rechtenwald, Selective laser sintering of PEEK, *CIRP Annals*, 56(1), 205–208, **2007**
- <sup>37</sup> Y. Khalil, A. Kowalski, N. Hopkinson, Influence of energy density on flexural properties of laser-sintered UHMWPE, *Additive Manufacturing*, 10(1), 67–75, **2016**
- <sup>38</sup> B. Duan, M. Wang, Selective laser sintering and its biomedical applications, in: V. Schmidt, M.R. Belegatis, *Laser Technology in Biomimetics*, Springer, Berlin, Germany, 83–109, **2013**
- <sup>39</sup> A. Simchi, Direct laser sintering of metal powders: mechanism, kinetics and microstructural features, *Materials Science and Engineering: A*, 428(1–2), 148–158, **2006**
- <sup>40</sup> T. Nakamoto, N. Shirakawa, Y. Miyata, H. Inui, Selective laser sintering of high carbon steel powders studied as a function of carbon content, *Journal of Materials Processing Technology*, 209(15–16), 5653–5660, **2009**
- <sup>41</sup> H. Chung, S. Das, Numerical modeling of scanning laser-induced melting, vaporization and resolidification in metals subjected to time-dependent heat flux inputs, *International Journal of Heat and Mass Transfer*, 47(19–20), 4165–4175, **2004**
- <sup>42</sup> A. Wegner, G. Witt, Correlation of process parameters and part properties in laser sintering using response surface modeling, *Physics Procedia*, 39(1), 480–490, **2012**
- <sup>43</sup> E.C. Hofland, I. Baran, D.A. Wismeijer, Correlation of process parameters with mechanical properties of laser sintered PA12 parts, *Advances in Materials Science and Engineering*, 2017(1), 1–11, **2017**
- <sup>44</sup> U. Ajoku, N. Saleh, N. Hopkinson, R. Hague, P. Erasenthiran, Investigating mechanical anisotropy and end-of-vector effect in laser-sintered nylon parts, *Proceedings of the Institution of Mechanical Engineers, Part B: Journal of Engineering Manufacture*, 220(7), 1077–1086, **2006**
- <sup>45</sup> P.K. Jain, P.M. Pandey, P.V.M. Rao, Effect of delay time on part strength in selective laser sintering, *International Journal of Advanced Manufacturing Technology*, 43(1–2), 117–126, **2009**
- <sup>46</sup> H. Varia, B. Goyal, A review on effect of process parameters on surface quality and properties of parts realized by selective laser sintering process, *International Journal on Recent and Innovation Trends in Computing and Communication*, 5(6), 45–51, **2017**
- <sup>47</sup> I.T. Jolliffe, Principal component analysis, in: M. Lovric, *International Encyclopedia of Statistical Science*, Springer, Heidelberg, Germany, **1986**
- <sup>48</sup> P.A. Cornillon, A. Guyader, F. Husson, N. Jégou, J. Josse, M. Kloareg, E. Matzner-Lober, L. Rouvière, *Statistiques avec R, 3rd, revue et augmentée ed.*, Presses Universitaires de Rennes, Rennes, France, **2012**
- <sup>49</sup> F. Husson, S. Lê, J. Pagès, *Exploratory multivariate analysis by example using R*, Chapman & Hall/CRC Computer Science and Data Analysis Series, Boca Raton, FL, USA, **2017**
- <sup>50</sup> M. Lesty, La recherche des harmoniques une nouvelle fonction du logiciel CORICO, *Revue Modulad*, 29(1), 34–74, **2002**
- <sup>51</sup> C. Engrand, J. Lespagnol, P. Martin, L. Thirkell, R. Thomas, Multi-correlation analyses of TOF-SIMS spectra for mineralogical studies, *Applied Surface Science*, 231–232(1), 883–887, **2004**
- <sup>52</sup> P.K. Jain, K. Senthikumar, P.M. Pandey, P.V.M. Rao, Advances in materials for powder based rapid prototyping, *International Journal of Manufacturing Technology and Management*, 27(1), 43–73, **2014**
- <sup>53</sup> J.P. Kruth, G. Levy, F. Klocke, T.H.C. Childs, Consolidation phenomena in laser and powder-bed based layered manufacturing, *CIRP Annals*, 56(2), 730–759, **2007**
- <sup>54</sup> D.T. Pham, S. Dimov, F. Lacan, Selective laser sintering: applications and technological capabilities, *Proceedings of the Institution of Mechanical Engineers, Part B: Journal of Engineering Manufacture*, 213(5), 435–449, **1999**



- <sup>55</sup> B. Kianian, Wohlers report 2017. 3D printing and additive manufacturing state of the industry: the middle east, and other countries, Wohlers Associates, **2017**
- <sup>56</sup> N. Trent, Polyamide 12 (PA 12/nylon 12) market 2019 global share, trends, demand, challenges and opportunities research report forecast to 2023, Wiseguy Reports, Pune, India, **2019**
- <sup>57</sup> F. Müller, A. Pfister, M. Leuterer, PAEK powder, in particular for the use in a method for a layer-wise manufacturing of a three-dimensional object, as well as method for producing it, US7847057B2, **2010**
- <sup>58</sup> M. Leuterer, A. Pfister, F. Müller, A. Wood, B. Wilson, H. Sandner, Influencing specific mechanical properties of three-dimensional objects manufactured by a selective sintering by means of electromagnetic radiation from a powder comprising at least one polymer or copolymer, US8420001B2, **2013**
- <sup>59</sup> C.Y. Wang, Q. Dong, X.X. Shen, Research on warpage of polystyrene in selective laser sintering, Applied Mechanics and Materials, 43(1), 578–582, **2010**
- <sup>60</sup> A. Wegner, New polymer materials for the laser sintering process: polypropylene and others, Physics Procedia, 83(1), 1003–1012, **2016**
- <sup>61</sup> J.M. García, F.C. García, F. Serna, J.L. de la Peña, High-performance aromatic polyamides, Progress in Polymer Science, 35(5), 623–686, **2010**
- <sup>62</sup> M. Schmid, Comparison of PA12 SLS-materials powders, parts and properties, **2016**
- <sup>63</sup> B.A. Newman, T.P. Sham, K.D. Pae, A high-pressure x-ray study of nylon 11, Journal of Applied Physics, 48(10), 4092–4098, **1977**
- <sup>64</sup> S. Gogolewski, K. Czerntawska, M. Gastorek, Effect of annealing on thermal properties and crystalline structure of polyamides. Nylon 12 (polylauro lactam), Colloid and Polymer Science, 258(10), 1130–1136, **1980**
- <sup>65</sup> M. Zhao, K. Wudy, D. Drummer, Crystallization kinetics of polyamide 12 during selective laser sintering, Polymers, 10(2), 168, **2018**
- <sup>66</sup> W.Y. Zhou, B. Duan, M. Wang, W.L. Cheung, Isothermal and non-isothermal crystallization kinetics of poly(l-lactide)/carbonated hydroxyapatite nanocomposite microspheres, in: B. Reddy, Advances in Diverse Industrial Applications of Nanocomposites, InTech, Rijeka, Croatia, 231–260, **2011**
- <sup>67</sup> M. Avrami, Kinetics of phase change. General theory, The Journal of Chemical Physics, 7(12), 1103–1112, **1939**
- <sup>68</sup> T. Ozawa, Kinetics of non-isothermal crystallization, Polymer, 12(3), 150–158, **1971**
- <sup>69</sup> M. Schmid, G. Levy, Lasersintermaterialien - aktueller stand und entwicklungspotential, in: Fachtagung Additive Fertigung, Erlangen, Germany, 43–55, **2009**
- <sup>70</sup> H. Scholten, W. Christoph, Use of a nylon-12 for selective laser sintering, US006245281 B1, **2001**
- <sup>71</sup> M. Gilbert, Aliphatic polyamides, in: Brydson's Plastics Materials, 8th ed., Butterworth-Heinemann, 487–511, **2017**
- <sup>72</sup> L. Verbelen, S. Dadbakhsh, M. van den Eynde, J.P. Kruth, B. Goderis, P. van Puyvelde, Characterization of polyamide powders for determination of laser sintering processability, European Polymer Journal, 75 163–174, **2016**
- <sup>73</sup> V. Mailhos-Lefievre, D. Sallet, B. Martel, Thermal degradation of pure and flame-retarded polyamides 11 and 12, Polymer Degradation and Stability, 23(4), 327–336, **1989**
- <sup>74</sup> M. Herrera, G. Matuschek, A. Kettrup, Main products and kinetics of the thermal degradation of polyamides, Chemosphere, 422(5–7), 601–607, **2001**
- <sup>75</sup> S.V. Levchik, L. Costa, G. Camino, Effect of the fire-retardant, ammonium polyphosphate, on the thermal decomposition of aliphatic polyamides: part II - polyamide 6, Polymer Degradation and Stability, 36(3), 229–237, **1992**
- <sup>76</sup> T. Karstens, V. Rossbach, Thermo-oxidative degradation of polyamide 6 and 6,6. Kinetics of the formation and inhibition of UV/VIS-active chromophores, Die Makromolekulare Chemie: Macromolecular Chemistry and Physics, 190(12), 3033–3053, **1989**
- <sup>77</sup> M. Dosière, D. Villers, M.G. Zolotukhin, M.H.J. Koch, Comparison of the structure and thermal properties of a poly(aryl ether ketone ether ketone naphthyl ketone) with those of poly(aryl ether ketone ether ketone), E-Polymers, 7(1), **2007**
- <sup>78</sup> R.M. Ho, S.Z.D. Cheng, B.S. Hsiao, K.H. Gardner, Crystal morphology and phase identifications in poly(aryl ether ketone)s and their copolymers. 1. Polymorphism in PEKK, Macromolecules, 27(8), 2136–2140, **1994**
- <sup>79</sup> A.P. Harsha, U.S. Tewari, Tribo performance of polyaryletherketone composites, Polymer Testing, 21(6), 697–709, **2002**
- <sup>80</sup> K. Friedrich, Z. Lu, A.M. Hager, Recent advances in polymer composites' tribology, Wear, 190(2), 139–144, **1995**
- <sup>81</sup> A.P. Harsha, U.S. Tewari, B. Venkatraman, Solid particle erosion behaviour of various polyaryletherketone composites, Wear, 254(1), 693–712, **2003**
- <sup>82</sup> R.J. Abraham, I.S. Haworth, Molecular modelling of poly(aryl ether ketones). 2. Chain packing in crystalline PEK and PEEK, Polymer, 32(1), 121–126, **1991**
- <sup>83</sup> P.C. Dawson, D.J. Blundell, X-ray data for poly (aryl ether ketones), Polymer, 21(5), 577–578, **1980**

- <sup>84</sup> D.J. Blundell, A.B. Newton, Variations in the crystal lattice of PEEK and related para-substituted aromatic polymers. 2. Effect of sequence and proportion of ether and ketone links, *Polymer*, 32(2), 308–313, **1991**
- <sup>85</sup> G. da C. Vasconcelos, R.L. Mazur, E.C. Botelho, M.C. Rezende, M.L. Costa, Evaluation of crystallization kinetics of polymer of poly (ether-ketone-ketone) and poly (ether-ether-ketone) by DSC, *Journal of Aerospace Technology and Management*, 2(2), 155–162, **2010**
- <sup>86</sup> S.M. Kurtz, J.N. Devine, PEEK biomaterials in trauma, orthopedic, and spinal implants, *Biomaterials*, 28(32), 4845–4869, **2007**
- <sup>87</sup> I. Towle, Method for preparing poly (ether ketone ketones), WO2011004164A2, **2011**
- <sup>88</sup> G. Petropoulos, F. Mata, J.P. Davim, Statistical study of surface roughness in turning of peek composites, *Materials & Design*, 29(1), 218–223, **2008**
- <sup>89</sup> R.B. Rigby, Polyetheretherketone PEEK, *Polymer News*, 9(1), 325, **1984**
- <sup>90</sup> M. Balsam, P. Barghoorn, U. Stebani, Trends in applied macromolecular chemistry, *Die Angewandte Makromolekulare Chemie*, 267(4681), 1–9, **1999**
- <sup>91</sup> C.N. Velisaris, J.C. Seferis, Crystallization kinetics of polyetheretherketone (PEEK) matrices, *Polymer Engineering and Science*, 26(22), 1574–1581, **1986**
- <sup>92</sup> A. Ben-Haida, H.M. Colquhoun, P. Hodge, D.J. Williams, Cyclic oligomers of poly(ether ketone) (PEK): synthesis, extraction from polymer, fractionation, and characterisation of the cyclic trimer, tetramer and pentamer, *Journal of Materials Chemistry*, 10(9), 2011–2016, **2000**
- <sup>93</sup> Victrex HT G45, **2014**
- <sup>94</sup> Kepstan 6000, **2013**
- <sup>95</sup> Kepstan 7000, **2012**
- <sup>96</sup> Kepstan 8000, **2013**
- <sup>97</sup> M. Day, J.D. Cooney, D.M. Wiles, The kinetics of the oxidative degradation of poly(aryl-ether-ether-ketone) (PEEK), *Thermochimica Acta*, 147(1), 189–197, **1989**
- <sup>98</sup> M. Day, D. Sally, D.M. Wiles, Thermal degradation of poly(aryl-ether-ether-ketone): experimental evaluation of crosslinking reactions, *Journal of Applied Polymer Science*, 40(910), 1615–1625, **1990**
- <sup>99</sup> H. Zhang, Fire-safe polymers and polymer composites, Doctorat Dissertations, University of Massachusetts Amherst, **2014**
- <sup>100</sup> L.H. Perng, C.J. Tsai, Y.C. Ling, Mechanism and kinetic modelling of PEEK pyrolysis by TG/MS, *Polymer*, 40(26), 7321–7329, **1999**
- <sup>101</sup> P. Patel, T.R. Hull, R.W. McCabe, D. Flath, J. Grasmeyer, M. Percy, Mechanism of thermal decomposition of poly(ether ether ketone) (PEEK) from a review of decomposition studies, *Polymer Degradation and Stability*, 95(5), 709–718, **2010**
- <sup>102</sup> C.J. Tsai, L.H. Perng, Y.C. Ling, A study of thermal degradation of poly(aryl-ether-ether-ketone) using stepwise pyrolysis/gas chromatography/mass spectrometry, *Rapid Communications in Mass Spectrometry*, 11(18), 1987–1995, **1997**
- <sup>103</sup> B. Nandan, L.D. Kandpal, G.N. Mathur, Poly(ether ether ketone)/poly(aryl ether sulphone) blends: thermal degradation behaviour, *European Polymer Journal*, 39(1), 193–198, **2003**
- <sup>104</sup> A. Amado, M. Schmid, G. Levy, K. Wegener, Advances in SLS powder characterization, *Group*, 7(10), 1–15, **2011**
- <sup>105</sup> M. Gersh, F. Müller, T. Mattes, P. Keller, Rounded-particle plastic powder in particular for application in laser sintering, method for production of such a powder and laser sintering process using such a powder, US007601422 B2, **2009**
- <sup>106</sup> R.K. McGeary, Mechanical packing of spherical particles, *Journal of the American Ceramic Society*, 44(10), 513–522, **1961**
- <sup>107</sup> R.M. German, S.J. Park, Handbook of mathematical relations in particulate materials processing, John Wiley & Sons, Canada, **2008**
- <sup>108</sup> H. Chung, S. Das, Processing and properties of glass bead particulate-filled functionally graded nylon-11 composites produced by selective laser sintering, *Materials Science and Engineering: A*, 437(2), 226–234, **2006**
- <sup>109</sup> D. Drummer, D. Rietzel, F. Kühnlein, Development of a characterization approach for the sintering behavior of new thermoplastics for selective laser sintering, *Physics Procedia*, 5(1), 533–542, **2010**
- <sup>110</sup> A.B. Spierings, M. Voegtlin, T. Bauer, K. Wegener, Powder flowability characterisation methodology for powder-bed-based metal additive manufacturing, *Progress in Additive Manufacturing*, 1(1–2), 9–20, **2016**
- <sup>111</sup> D. Schulze, Flow properties of powders and bulk solids, in: *Powders and Bulk Solids. Behavior, Characterization, Storage and Flow*, Springer, Wolfsburg, Germany, 35–74, **2008**
- <sup>112</sup> L. Dong, Simulation et modélisation du frittage sélectif par laser après la méthode des éléments finis, Doctorat Dissertations, Université Louis Pasteur, **2007**
- <sup>113</sup> M. Villar Montoya, Procédé de soudage laser de polymères haute performance: établissement des relations entre les paramètres du procédé, la structure et la morphologie du polymère et les propriétés mécaniques de l'assemblage, Doctorat Dissertations, Université de Toulouse, **2018**

- <sup>114</sup> B. Wendel, D. Rietzel, F. Kühnlein, R. Feulner, G. Hülner, Additive processing of polymers, *Macromolecular Materials and Engineering*, 293(10), 799–809, **2008**
- <sup>115</sup> A. Mokrane, M. Boutaous, S. Xin, Process of selective laser sintering of polymer powders: modeling, simulation, and validation, *Comptes Rendus Mécanique*, 346(11), 1087–1103, **2018**
- <sup>116</sup> F. Thümmeler, R. Oberacker, *An introduction to powder metallurgy*, Oxford Science Publications, London, GB, **1993**
- <sup>117</sup> M. Rombouts, L. Froyen, A.V. Gusarov, E.H. Bentefour, C. Glorieux, Light extinction in metallic powder beds: correlation with powder structure, *Journal of Applied Physics*, 98(1), **2005**
- <sup>118</sup> J.C. Nelson, N.K. Vail, J.W. Barlow, Laser sintering model for composite materials, in: *Proceedings of International Solid Freeform Fabrication Symposium*, 360–369, **1993**
- <sup>119</sup> S. Bakrani Balani, Additive manufacturing of the high-performance thermoplastic: Experimental study and numerical simulation of the fused filament fabrication, *Doctorat Dissertations, Université de Toulouse*, **2019**
- <sup>120</sup> B. Haworth, N. Hopkinson, D. Hitt, X. Zhong, Shear viscosity measurements on polyamide-12 polymers for laser sintering, *Rapid Prototyping Journal*, 19(1), 28–36, **2013**
- <sup>121</sup> J.J. Beaman, J.W. Barlow, D.L. Bourell, R.H. Crawford, H.L. Marcus, K.P. McAlea, *Solid freeform fabrication: a new direction in manufacturing*, Kluwer Academic Publishers, Norwell, MA, USA, **1997**
- <sup>122</sup> J.P. Kruth, G. Levy, R. Schindel, T. Craeghs, E. Yasa, Consolidation of polymer powders by selective laser sintering, in: *Proceedings of the 3rd International Conference on Polymers and Moulds Innovations*, 15–30, **2008**
- <sup>123</sup> X. Liu, Numerical modeling and simulation of selective laser sintering in polymer powder bed, *Doctorat Dissertations, Université de Lyon*, **2017**
- <sup>124</sup> I. Yadroitsev, I. Smurov, Selective laser melting technology: from the single laser melted track stability to 3D parts of complex shape, *Physics Procedia*, 5(1), 551–560, **2010**
- <sup>125</sup> A. Liber-Kneć, S. Łagan, The use of contact angle and the surface free energy as the surface characteristics of the polymers used in medicine, *Polimery w Medycynie*, 44(1), 29–37, **2014**
- <sup>126</sup> M. Żenkiewicz, *Adhezja i modyfikowanie warstwy wierzchniej tworzyw wielkocząsteczkowych*, Wydawnictwa Naukowo-Techniczne, Warsaw, Poland, **2000**
- <sup>127</sup> A. Tcharkhtchi, L. Audouin, J.M. Tremillon, J. Verdu, Oxyluminescence of polyamide 12, *Polymer Degradation and Stability*, 44(3), 335–341, **1994**
- <sup>128</sup> R. Phillips, T. Glauser, J.A.E. Manson, Thermal stability of PEEK/carbon fiber in air and its influence on consolidation, *Polymer Composites*, 18(4), 500–508, **1997**
- <sup>129</sup> K.C.H. Gardner, B.S. Hsiao, K.L. Faron, Polymorphism in poly(aryl ether ketone)s, *Polimer*, 35(11), 2290–2295, **1994**
- <sup>130</sup> B.S. Hsiao, I.Y. Chang, B.B. Sauer, Isothermal crystallization kinetics of poly(ether ketone ketone) and its carbon-fibre-reinforced composites, *Polimer*, 32(15), 2799–2805, **1991**
- <sup>131</sup> J.A. Ferrara, Manifestations of crystallization in the processing of high-performance thermoplastic composites, *Doctorat Dissertations, University of Washington*, **1995**
- <sup>132</sup> T.W. Giants, Crystallinity and dielectric properties of PEEK, poly (ether ether ketone), *IEEE Transactions on Dielectrics and Electrical Insulation*, 1(6), 991–999, **1994**
- <sup>133</sup> J.N. Hay, D.J. Kimmish, J.I. Langford, A.I.M. Rea, The structure of crystalline PEEK, *Polymer Communications*, 25(6), 175–178, **1984**
- <sup>134</sup> C. Nicodeau, *Modélisation du soudage en continu de composites à matrice thermoplastique*, Doctorat Dissertations, Institut des Sciences et Technologies de Paris, **2005**
- <sup>135</sup> K. Dotchev, W. Yusoff, Recycling of polyamide 12 based powders in the laser sintering process, *Rapid Prototyping Journal*, 15(3), 192–203, **2009**
- <sup>136</sup> H. Zarringhalam, N. Hopkinson, N.F. Kamperman, J.J. de Vlieger, Effects of processing on microstructure and properties of SLS nylon 12, *Materials Science and Engineering: A*, 435–436(1), 172–180, **2006**
- <sup>137</sup> D.T. Pham, K.D. Dotchev, W.A.Y. Yusoff, Deterioration of polyamide powder properties in the laser sintering process, *Proceedings of the Institution of Mechanical Engineers, Part C: Journal of Mechanical Engineering Science*, 222(11), 2163–2176, **2008**
- <sup>138</sup> S.T. Milner, Early stages of spreading and sintering, **2019**
- <sup>139</sup> S. Mazur, D.J. Plazek, Viscoelastic effects in the coalescence of polymer particles, *Progress in Organic Coatings*, 24(1–4), 225–236, **1994**
- <sup>140</sup> Z. Florjańczyk, S. Penczek, Makrocząsteczki i metody ich otrzymywania, in: A. Ziabicki, *Chemia Polimerów, Oficyna Wydawnicza Politechniki Warszawskiej*, Warsaw, Poland, 49–96, **1995**
- <sup>141</sup> P.E. Rouse Jr., A theory of the linear viscoelastic properties of dilute solutions of coiling polymers, *The Journal of Chemical Physics*, 21(7), 1272–1280, **1953**
- <sup>142</sup> F. Bueche, Viscosity of entangled polymers; theory of variation with shear rate, *The Journal of Chemical Physics*, 48(10), 4781–4784, **1968**

- <sup>143</sup> P.G. de Gennes, Reptation of a polymer chain in the presence of fixed obstacles, *The Journal of Chemical Physics*, 55(1), 572–579, **1971**
- <sup>144</sup> M. Doi, S.F. Edwards, Dynamics of concentrated polymer systems. 1. Brownian motion in the equilibrium state, *Journal of the Chemical Society, Faraday Transactions 2: Molecular and Chemical Physics*, 74(1), 1789–1801, **1978**
- <sup>145</sup> T. Hashimoto, Y. Tsukahara, H. Kawai, Dynamic small-angle x-ray scattering studies on diffusion of macromolecules in bulk. 2. Principle and preliminary experimental results, *Macromolecules*, 14(3), 708–715, **1981**
- <sup>146</sup> J.M. Williams, A. Adewunmi, R.M. Schek, C.L. Flanagan, P.H. Krebsbach, S.E. Feinberg, S. Das, Bone tissue engineering using polycaprolactone scaffolds fabricated via selective laser sintering, *Biomaterials*, 26(23), 4817–4827, **2005**
- <sup>147</sup> E.F. Wiria, C.K. Chua, Y. Liu, Poly- $\epsilon$ -caprolactone/hydroxyapatite for tissue engineering scaffold fabrication via selective laser sintering, *Acta Biomaterialia*, 3(1), 1–12, **2007**
- <sup>148</sup> A.B. Abibe, Friction-based injection clinching joining (F-ICJ): a new joining method for hybrid lightweight structures, Doctorat Dissertations, Technische Universität Hamburg, **2015**
- <sup>149</sup> M. Doi, S.F. Edwards, *The Theory of Polymer Dynamics*, Clarendon Press, **1988**
- <sup>150</sup> J.F. Lamethe, Etude de l'adhésion de composites thermoplastiques semi-cristallins; application à la mise en oeuvre par soudure, Doctorat Dissertations, Université Pierre et Marie Curie - Paris VI, **2004**
- <sup>151</sup> S.J. Whitlow, R.P. Wool, Diffusion of polymers at interfaces: a secondary ion mass spectroscopy study, *Macromolecules*, 24(22), 5926–5938, **1991**
- <sup>152</sup> R.L. Coble, Sintering crystalline solids. I. Intermediate and final state diffusion models, *Journal of Applied Physics*, 32(5), 787–792, **1961**
- <sup>153</sup> J.J. Frenkel, Viscous flow of crystalline bodies under the action of surface tension, *Journal of Physics*, 9(1), 385–391, **1945**
- <sup>154</sup> J.D. Eshelby, Uniformly moving dislocations, *Proceedings of the Physical Society. Section A*, 62(1), **1949**
- <sup>155</sup> J.K. Mackenzie, R. Shuttleworth, A phenomenological theory of sintering, *Proceedings of the Physical Society. Section B*, 62(12), 833–852, **1949**
- <sup>156</sup> R.W. Hopper, Coalescence of two equal cylinders: exact results for creeping viscous plane flow driven by capillarity, *Journal of the American Ceramic Society*, 67(12), 262–264, **1984**
- <sup>157</sup> R.W. Hopper, Stokes flow of a cylinder and half-space driven by capillarity, *Journal of Fluid Mechanics*, 243(1), 171–181, **1992**
- <sup>158</sup> A. Jagota, C. Argento, S. Mazur, Growth of adhesive contacts for Maxwell viscoelastic spheres, *Journal of Applied Physics*, 83(1), 250–259, **1998**
- <sup>159</sup> G.A.L. van der Vorst, R.M.M. Matheij, Numerical analysis of a 2-D viscous sintering problem with non-smooth boundaries, *Computing*, 49(3), 239–263, **1992**
- <sup>160</sup> J.I. Martinez Herrera, J.J. Derby, Analysis of capillary-driven viscous flows during the sintering of ceramic powders, *Journal of American Institute of Chemical Engineers*, 40(11), 1794–1803, **1994**
- <sup>161</sup> J.I. Martinez Herrera, J.J. Derby, Viscous sintering of spherical particles via finite element analysis, *Journal of American Ceramic Society*, 78(3), 645–649, **1995**
- <sup>162</sup> C.T. Bellehumeur, M. Kontopoulou, J. Vlachopoulos, The role of viscoelasticity in polymer sintering, *Rheologica Acta*, 37(3), 270–278, **1998**
- <sup>163</sup> D. Bouvard, R.M. McMeeking, Deformation of interparticle necks by diffusion-controlled creep, *Journal of the American Chemical Society*, 79(3), 666–672, **1996**
- <sup>164</sup> O. Pokluda, C.T. Bellehumeur, J. Vlachopoulos, Modification of Frenkel's model for sintering, *Journal of American Institute of Chemical Engineers*, 43(12), 3253–3256, **1997**
- <sup>165</sup> A. Williams, *Free energy relationships in organic and bio-organic chemistry*, Royal Society of Chemistry, Canterbury, UK, **2003**
- <sup>166</sup> J. Escobedo, G.A. Mansoori, Surface tension prediction for pure fluids, *Journal of American Institute of Chemical Engineers*, 42(5), 1425–1433, **1996**
- <sup>167</sup> Y.Y. Lin, C.Y. Hui, A. Jagota, The role of viscoelastic adhesive contact in the sintering of polymeric particles, *Journal of Colloid and Interface Science*, 237(2), 267–282, **2001**
- <sup>168</sup> S.J.L. Kang, *Sintering: densification, grain growth and microstructure*, Elsevier, **2005**
- <sup>169</sup> M. Agarwala, D. Bourell, J. Beaman, H. Marcus, J. Barlow, Direct selective laser sintering of metals, *Rapid Prototyping Journal*, 1(1), 26–36, **1995**
- <sup>170</sup> G.N. Labeas, G.A. Moraitis, C.V. Katsiropoulos, Optimization of laser transmission welding process for thermoplastic composite parts using thermo-mechanical simulation, *Journal of Composite Materials*, 44(1), 113–130, **2010**
- <sup>171</sup> M. Deborah, W. Marsden, S. Warde, Overview of additive manufacturing informatics: a digital thread, *Integrating Materials and Manufacturing Innovation*, 5(1), 114–142, **2016**

- <sup>172</sup> S. Berretta, O. Ghita, K.E. Evans, Morphology of polymeric powders in laser sintering (LS): from polyamide to new PEEK powders, *European Polymer Journal*, 59(1), 218–229, **2014**
- <sup>173</sup> HORIBA, Understanding and interpreting particle size distribution calculations, Horiba.Com, **2019**
- <sup>174</sup> C. Mielicki, B. Gronhoff, J. Wortberg, Effects of laser sintering processing time and temperature on changes in polyamide 12 powder particle size, shape and distribution, in: *Proceedings of the 29th International Conference of the Polymer Processing Society*, AIP Publishing, Nuremberg, Germany, 728–731, **2014**
- <sup>175</sup> C. Reichardt, The values for relative polarity are normalized from measurements of solvent shifts of absorption spectra, in: *Solvents and Solvent Effects in Organic Chemistry*, 3rd ed., Wiley-VCH Verlag, Weinheim, Germany, **2003**
- <sup>176</sup> S. Berretta, Poly ether ether ketone (PEEK) polymers for high temperature laser sintering (HT-LS), Doctorat Dissertations, University of Exeter, **2015**
- <sup>177</sup> R.L. Carr, Evaluating flow properties of solids, *Chemical Engineering Science*, 72(2), 163–168, **1965**
- <sup>178</sup> S. Bajric, Developing characterization procedures for qualifying both novel selective laser sintering polymer powders and recycled powders, University of Oregon, OR, USA, 1–11, **2017**
- <sup>179</sup> K. Wudy, D. Drummer, Aging behavior of polyamide 12: interrelation between bulk characteristics and part properties, in: *Proceedings of the 27th International Solid Freeform Fabrication Symposium*, 770–781, **2016**
- <sup>180</sup> C.F. Gauss, Besprechung des buchs von la seeber: untersuchungen uber die eigenschaften der positiven ternaren quadratischen formen usw, *Gottingensche Gelehrte Anzeigen*, 2(1), 188–196, **1876**
- <sup>181</sup> C. Song, P. Wang, H.A. Makse, A phase diagram for jammed matter, *Nature*, 453(7195), 629–632, **2008**
- <sup>182</sup> H.M. Alfaro-López, L. Aiche, H. Vergnes, B. Despax, B. Caussat, H. Caquineau, Surface modification of polymer powders by a far cold remote nitrogen plasma in fluidized bed, in: *Interface Controlled Porganic Thin Films*, Springer, Berlin, Germany, 79–83, **2009**
- <sup>183</sup> T. Govindarajan, R. Shandas, A survey of surface modification techniques for next-generation shape memory polymer stent devices, *Polymers*, 6(9), 2309–2331, **2014**
- <sup>184</sup> H. Bissett, I.J. van der Walt, J.L. Havenga, J.T. Nel, Titanium and zirconium metal powder spheroidization by thermal plasma processes, *Journal of the Southern African Institute of Mining and Metallurgy*, 115(10), 937–942, **2015**
- <sup>185</sup> F.N. Cogswell, Thermoplastic aromatic polymer composites: a study of the structure, processing and properties of carbon fibre reinforced polyetheretherketone and related materials, Butterworth-Heinemann, **2013**
- <sup>186</sup> Solid lubricants, *Tribology-Abc*, **2019**
- <sup>187</sup> A. Korycki, F. Chabert, T. Mérian, V. Nassiet, Probing wettability alteration of the boron nitride surface through rheometry, *Langmuir*, 35(1), 128–140, **2019**
- <sup>188</sup> M. Villar Montoya, C. Garnier, F. Chabert, V. Nassiet, D. Samélor, J.C. Diez, A. Sotelo, M.A. Madre, In-situ infrared thermography measurements to master transmission laser welding process parameters of PEKK, *Optics and Lasers in Engineering*, 106(1), 94–104, **2018**
- <sup>189</sup> J. Audoit, L. Rivière, J. Dandurand, A. Lonjon, E. Dantras, C. Lacabanne, Thermal, mechanical and dielectric behaviour of poly(aryl ether ketone) with low melting temperature, *Journal of Thermal Analysis and Calorimetry*, 135(4), 2147–2157, **2019**
- <sup>190</sup> O.R. Ghita, E. James, R. Trimble, K.E. Evans, Physico-chemical behaviour of poly (ether ketone) (PEK) in high temperature laser sintering (HT-LS), *Journal of Materials Processing Technology*, 214(4), 969–978, **2014**
- <sup>191</sup> L. Harris, A study of the crystallisation kinetics in PEEK and PEEK composites, Doctorat Dissertations, University of Birmingham, **2011**
- <sup>192</sup> O. Ghita, E. James, R. Davies, S. Berretta, B. Singh, S. Flint, K.E. Evans, High temperature laser sintering (HT-LS): an investigation into mechanical properties and shrinkage characteristics of poly (ether ketone) (PEK) structures, *Materials & Design*, 61(1), 124–132, **2014**
- <sup>193</sup> Air - thermophysical properties, *Engineering ToolBox*, **2003**
- <sup>194</sup> C.L. Choy, K.W. Kwok, W.P. Leung, F.P. Lau, Thermal conductivity of poly (ether ether ketone) and its short-fiber composites, *Journal of Polymer Science Part B: Polymer Physics*, 32(8), 1389–1397, **1994**
- <sup>195</sup> A.M. Diez-Pascual, J. Guan, B. Simard, A.A. Gomez-Fatou, Poly(phenylene sulphide) and poly(ether ether ketone) composites reinforced with single-walled carbon nanotube buckypaper. 2. Mechanical properties, electrical and thermal conductivity, *Composites Part A: Applied Science and Manufacturing*, 43(6), 1007–1015, **2012**
- <sup>196</sup> L. Rivière, N. Caussé, A. Lonjon, E. Dantras, C. Lacabanne, Specific heat capacity and thermal conductivity of PEEK/Ag nanoparticles composites determined by modulated-temperature differential scanning calorimetry, *Polymer Degradation and Stability*, 127(1), 98–104, **2016**
- <sup>197</sup> L. Rivière, A. Lonjon, E. Dantras, C. Lacabanne, P. Olivier, N.R. Gleizes, Silver fillers aspect ratio influence on electrical and thermal conductivity in PEEK/Ag nanocomposites, *European Polymer Journal*, 85 115–125, **2016**
- <sup>198</sup> S.Z.D. Cheng, S. Lim, L.H. Judovits, B. Wunderlich, Heat capacities of high melting polymers containing phenylene groups, *Polymer*, 28(1), 10–22, **1987**

- <sup>199</sup> R.G. Larson, The structure and rheology of complex fluids, Oxford University Press, New York, NY, USA, **1990**
- <sup>200</sup> E. Bessard, O. De Almeida, G. Bernhart, F. Chinesta, Y. Chastel, M. El Mansori, Melt state behaviour of PEEK and processing window interpretation for fast compression moulding process, in: Proceedings of International Conference on Advances in Materials and Processing Technologies, AIP Publishing, Paris, France, 167–172, **2011**
- <sup>201</sup> M. Day, J.D. Cooney, D.M. Wiles, The thermal degradation of poly(aryl-ether-ether-ketone) (PEEK) as monitored by pyrolysis-GC/MS and TG/MS, Journal of Analytical and Applied Pyrolysis, 18(1), 163–173, **1990**
- <sup>202</sup> G. Basseri, M. Mehrabi Mazidi, F. Hosseini, M.K. Razavi Aghjeh, Relationship among microstructure, linear viscoelastic behavior and mechanical properties of SBS triblock copolymer-compatible PP/SAN blend, Polymer Bulletin, 71(2), 465–486, **2014**
- <sup>203</sup> A. Arun, K. Dullaert, R.J. Gaymans, The melt rheological behavior of AB, ABA, BAB, and (AB)<sub>n</sub> block copolymers with monodisperse aramide segments, Polymer Engineering & Science, 50(4), 756–761, **2010**
- <sup>204</sup> M.P. Escudier, I.W. Gouldson, A.S. Pereira, F.T. Pinho, R.J. Poole, On the reproducibility of the rheology of shear-thinning liquids, Journal of Non-Newtonian Fluid Mechanics, 97(1), 99–124, **2001**
- <sup>205</sup> L.H. Perng, Thermal cracking characteristics of PEEK under different environments by the TG/FTIR technique, Journal of Polymer Science Part A-1: Polymer Chemistry, 37(1), 4582–4590, **1999**
- <sup>206</sup> M. Day, J.D. Cooney, D.M. Wiles, A kinetic study of the thermal decomposition of poly(aryl-ether-ether-ketone) (PEEK) in nitrogen, Polymer Engineering and Science, 29(1), 19–22, **1989**
- <sup>207</sup> A.S. Shabaev, A.A. Zhansitov, Z.I. Kurdanova, Investigation of thermal and thermo-oxidative degradation of poly(ether ether ketone) by gas chromatography, 色 谱, 36(4), 395–399, **2018**
- <sup>208</sup> S. Bakrani Balani, F. Chabert, V. Nassiet, A. Cantarel, C. Garnier, Toward improvement of the properties of parts manufactured by FFF (fused filament fabrication) through understanding the influence of temperature and rheological behaviour on the coalescence phenomenon, in: Proceedings of the 20th International Conference on Material Forming, Ireland, **2017**
- <sup>209</sup> J.D. Ferry, Viscoelastic properties of polymers, John Wiley & Sons, **1980**
- <sup>210</sup> J.E. Zanetto, Soudage par fusion des polymères thermoplastiques semi-cristallins, Doctorat Dissertations, École Polytechnique Fédérale de Lausanne, **2001**
- <sup>211</sup> K. Fuchs, C. Friedrich, J. Weese, Viscoelastic properties of narrow-distribution poly(methyl methacrylates), Macromolecules, 29(18), 5893–5901, **1996**
- <sup>212</sup> K.J. Laidler, The development of the Arrhenius equation, Journal of Chemical Education, 61(6), 494, **1984**
- <sup>213</sup> K.S. Cole, R.H. Cole, Dispersion and absorption in dielectrics. 1. Alternating current characteristics, The Journal of Chemical Physics, 9(4), 341–351, **1941**
- <sup>214</sup> W.W. Graessley, Linear viscoelasticity in entangling polymer systems, The Journal of Chemical Physics, 54(12), 5143–5157, **1971**
- <sup>215</sup> M. Coulson, L. Quiroga Cortés, E. Dantras, A. Lonjon, C. Lacabanne, Dynamic rheological behavior of poly(ether ketone ketone) from solid state to melt state, Journal of Applied Polymer Science, 135(27), 46456, **2018**
- <sup>216</sup> G. Régnier, C. Nicodeau, J. Verdu, F. Chinesta, V. Triquenaux, J. Cinquin, Welding of thermoplastic matrix composites: prediction of macromolecules diffusion at the interface, 1–4, **2018**
- <sup>217</sup> M. Vaezi, S. Yang, Extrusion-based additive manufacturing of PEEK for biomedical applications, Virtual and Physical Prototyping, 10(3), 123–135, **2015**
- <sup>218</sup> D. Ha, A study on recycling of waste polyamide 12 powder into 3D printing filaments, Bachelor, Arcada University of Applied Sciences, **2019**
- <sup>219</sup> D.J. Dijkstra, Guidelines for rheological characterization of polyamide melts, Pure and Applied Chemistry, 81(2), 339–349, **2009**
- <sup>220</sup> D. Drummer, F. Kühnlein, M. Drexler, Degradation behaviour of PA 12 powders in laser sintering, in: Proceedings of 4th International Conference on Advanced Technology & Sciences, Rome, Greece, **2012**
- <sup>221</sup> D. Drummer, F. Kühnlein, S. Meister, M. Drexler, Investigations on the degradation behaviour of PA 12 plastic powders influence of high temperatures on the molecular weight, in: Proceedings of 13th International Rapid Product Development Association of South Africa Conference, South Africa, **2012**
- <sup>222</sup> D. Drummer, K. Wudy, M. Drexler, Modelling of the aging behavior of polyamide 12 powder during laser melting process, in: Proceedings of the AIP Conference, AIP Publishing, 1–5, **2015**
- <sup>223</sup> K. Wudy, D. Drummer, F. Kühnlein, M. Drexler, Influence of degradation behavior of polyamide 12 powders in laser sintering process on produced parts, in: Proceedings of the 29th International Conference of the Polymer Processing Society, AIP Publishing, Nuremberg, Germany, 691–695, **2013**
- <sup>224</sup> J. Parameswaranpillai, S. Thomas, Y. Grohens, Polymer blends: state of the art, new challenges, and opportunities, in: Characterization of Polymer Blends: Miscibility, Morphology and Interfaces, Wiley-VCH Verlag, Germany, 1–5, **2014**

- <sup>225</sup> O. Olabis, L.M. Robeson, M.T. Shaw, Polymer-polymer miscibility, Academic Press, **1979**
- <sup>226</sup> W.J. MacKnight, F.E. Karasz, J.R. Fried, Solid state transition behavior of blends, in: Polymer Blends, Academic Press, 185–242, **1978**
- <sup>227</sup> P.R. Couchman, Compositional variation of glass-transition temperatures. 2. Application of the thermodynamic theory to compatible polymer blends, *Macromolecules*, 11(6), 1156–1161, **1978**
- <sup>228</sup> T.G. Fox, Influence of diluent and of copolymer composition on the glass temperature of a polymer system, *Bulletin of the American Physical Society*, 1(1), 123, **1956**
- <sup>229</sup> M. Gordon, J.S. Taylor, Ideal copolymers and the second-order transitions of synthetic rubbers. 1. Non-crystalline copolymers, *Journal of Applied Chemistry*, 2(9), 493–500, **1952**
- <sup>230</sup> M. Aubin, R.E. Prud'homme, Analysis of the glass transition temperature of miscible polymer blends, *Macromolecules*, 21(10), 2945–2949, **1988**
- <sup>231</sup> C. Harrats, S. Thomas, G. Groeninckx, Micro- and nanostructured multiphase polymer blend systems. Phase morphology and interfaces, 1st ed., CRC Press, Boca Raton, FL, USA, **2005**
- <sup>232</sup> Z. Starý, S. Thomas, Y. Grohens, P. Jyotishkumar, Thermodynamics and morphology and compatibilization of polymer blends, in: Characterization of Polymer Blends: Miscibility, Morphology and Interfaces, 93–126, **2014**
- <sup>233</sup> B.S. Hsiao, B.B. Sauer, Glass transition, crystallization, and morphology relationships in miscible poly(aryl ether ketone) and poly(ether imide) blends, *Journal of Polymer Science Part B: Polymer Physics*, 31(8), 901–915, **1993**
- <sup>234</sup> G. Crevecoeur, G. Groeninckx, Binary blends of poly(ether ether ketone) and poly(ether imide). Miscibility, crystallization behavior and semicrystalline morphology, *Macromolecules*, 24(5), 1190–1195, **1991**
- <sup>235</sup> S.D. Hudson, D.D. Davis, A.J. Lovinger, Semicrystalline morphology of poly(aryl ether ether ketone)/poly(ether imide) blends, *Macromolecules*, 25(6), 1759–1765, **1992**
- <sup>236</sup> H.L. Chen, R.S. Porter, Phase and crystallization behavior of solution-blended poly(ether ether ketone) and poly(ether imide), *Polymer Engineering and Science*, 32(24), 1870–1875, **1992**
- <sup>237</sup> U. Sundararaj, C.W. Macosko, Drop breakup and coalescence in polymer blends: the effects of concentration and compatibilization, *Macromolecules*, 28(8), 2647–2657, **1995**
- <sup>238</sup> W. Zhu, C. Yan, Y. Shi, S. Wen, J. Liu, Y. Shi, Investigation into mechanical and microstructural properties of polypropylene manufactured by selective laser sintering in comparison with injection molding counterparts, *Materials & Design*, 82(1), 37–45, **2015**
- <sup>239</sup> E. Schmachtenberg, T. Seul, Model of isothermic laser-sintering, in: Proceedings of the 60th Technical Conference of the Society of Plastic Engineers, San Francisco, CA, USA, **2002**
- <sup>240</sup> P. Peyre, Y. Rouchausse, D. Defauchy, G. Régnier, Experimental and numerical analysis of the selective laser sintering (SLS) of PA12 and PEKK semi-crystalline polymers, *Journal of Materials Processing Technology*, 225(1), 326–336, **2015**
- <sup>241</sup> J.M.R.C.A. Santos, J.T. Guthrie, Polymer blends: the PC–PBT case, *Journal of Materials Chemistry*, 16(3), 237–245, **2006**
- <sup>242</sup> D. Drummer, K. Wudy, F. Kühnlein, M. Drexler, Polymer blends for selective laser sintering: material and process requirements, *Physics Procedia*, 39 509–517, **2012**
- <sup>243</sup> X. Yu, Y. Zheng, Z. Wu, X. Tang, B. Jiang, Study on the compatibility of the blend of poly(aryl ether ether ketone) with poly(aryl ether sulfone), *Journal of Applied Polymer Science*, 41(1112), 2649–2654, **1990**
- <sup>244</sup> T.M. Malik, Thermal and mechanical characterization of partially miscible blends of poly(ether ether ketone) and polyethersulfone, *Journal of Applied Polymer Science*, 46(2), 303–310, **1992**
- <sup>245</sup> Z. Ni, The preparation, compatibility and structure of PEEK–PES blends, *Polymers for Advanced Technologies*, 5(9), 612–614, **1994**
- <sup>246</sup> A. Arzak, J.I. Eguiazabal, J. Nazabal, Phase behaviour and mechanical properties of poly(ether ether ketone)-poly(ether sulphone) blends, *Journal of Materials Science*, 26(21), 5939–5944, **1991**
- <sup>247</sup> B. Nandan, L.D. Kandpal, G.N. Mathur, Poly(ether ether ketone)/poly(aryl ether sulphone) blends: thermal degradation behaviour, *European Polymer Journal*, 39(1), 193–198, **2003**
- <sup>248</sup> J. Noolandi, Multiblock copolymers as polymeric surfactants: are “pancakes” better than “dumbbells”?, *Macromolecular Theory and Simulations*, 1(5), 295–298, **1992**
- <sup>249</sup> T. Hoffmann, D. Pospiech, L. Häussler, P. Pötschke, U. Reuter, P. Werner, J.K.W. Sandler, M. Döring, V. Altstädt, Properties of segmented block copolymers in PEEK/PSU blends, *High Performance Polymers*, 20(6), 601–614, **2008**
- <sup>250</sup> P. Mitschang, M. Blinzler, A. Wöginger, Processing technologies for continuous fibre reinforced thermoplastics with novel polymer blends, *Composites Science and Technology*, 63(14), 2099–2110, **2003**
- <sup>251</sup> Z. Zhang, H. Zeng, Morphology, crystallization kinetics and melting behaviour of the blends of poly(ether ether ketone) with poly(ether sulfone with cardo side group), *Polymer*, 34(19), 4032–4037, **1993**
- <sup>252</sup> 张海春, 陈天禄, 袁雅桂, Synthesis of new type polyether ether ketone with phthalein lateral group, CN85108751A, **1987**

- <sup>253</sup> G. Song, J. Li, J. Yu, Y. Wang, J. Zhu, Z. Hu, Preparation and characterization of PES-C/PVPP nanofibrous composite membranes via solution-blowing, in: Proceedings of the IOP Conference Series: Earth and Environmental Science, IOP Publishing, 1–7, **2018**
- <sup>254</sup> H. Jiang, T. Chen, S. Bo, J. Xu, Novel macrocyclic precursors of phenolphthalein poly(arylene ether ketone) and poly(arylene ether sulfone): synthesis and polymerization, *Macromolecules*, 30(23), 7345–7347, **1997**
- <sup>255</sup> R. Guo, O. Lane, D. VanHouten, J.E. McGrath, Synthesis and characterization of phenolphthalein-based poly(arylene ether sulfone) hydrophilic–hydrophobic multiblock copolymers for proton exchange membranes, *Industrial & Engineering Chemistry Research*, 49(23), 12125–12134, **2010**
- <sup>256</sup> S. Greiner, K. Wudy, L. Lanzl, D. Drummer, Selective laser sintering of polymer blends: bulk properties and process behavior, *Polymer Testing*, 64(1), 136–144, **2017**
- <sup>257</sup> R. Kleijnen, M. Schmid, K. Wegener, Production and processing of a spherical polybutylene terephthalate powder for laser sintering, *Applied Sciences*, 9(7), 1308, **2019**
- <sup>258</sup> Z. Wu, Y. Zheng, H. Yan, T. Nakamura, T. Nozawa, R. Yosomiya, Molecular aggregation of PEEK with PES blends and the block copolymers composed of PEEK and PES components, *Die Angewandte Makromolekulare Chemie*, 173(2876), 163–181, **1989**
- <sup>259</sup> B. Nandan, L.D. Kandpal, G.N. Mathur, Poly(ether ether ketone)/poly(aryl ether sulfone) blends: melt rheological behavior, *Journal of Polymer Science Part B: Polymer Physics*, 42(8), 1548–1563, **2004**
- <sup>260</sup> B. Nandan, L.D. Kandpal, G.N. Mathur, Polyetherether ketone/polyarylethersulfone blends: thermal and compatibility aspects, *Journal of Polymer Science Part B: Polymer Physics*, 40(14), 1407–1424, **2002**
- <sup>261</sup> A. Arzak, J.I. Eguiazabal, J. Nazabal, Compatibility in immiscible poly(ether ether ketone)/poly(ether sulfone) blends, *Journal of Applied Polymer Science*, 58(3), 653–661, **1995**
- <sup>262</sup> W.F. Hale, A.G. Farnham, R.N. Johnson, R.A. Clendinning, Poly(aryl ethers) by nucleophilic aromatic substitution. II. Thermal stability, *Journal of Polymer Science Part A-1: Polymer Chemistry*, 5(9), 2399–2414, **1967**
- <sup>263</sup> M.A. Beard, O.R. Ghita, J. Bradbury, S. Flint, K.E. Evans, Material characterisation of additive manufacturing components made from a polyetherketone (PEK) high temperature thermoplastic polymer, in: P.J. Bartolo, *Innovative Developments in Virtual and Physical Prototyping*, CRC Press, 329–332, **2011**
- <sup>264</sup> S. Berretta, K.E. Evans, O. Ghita, Processability of PEEK, a new polymer for high temperature laser sintering (HT-LS), *European Polymer Journal*, 68(1), 243–266, **2015**
- <sup>265</sup> L. Lü, J.Y.H. Fuh, Y.S. Wong, *Laser-induced materials and processes for rapid prototyping*, Springer Science & Business Media, New York, NY, USA, **2013**
- <sup>266</sup> N. Kumar, H. Kumar, J.S. Khurmi, Experimental investigation of process parameters for rapid prototyping technique (selective laser sintering) to enhance the part quality of prototype by Taguchi method, *Procedia Technology*, 23(1), 352–360, **2016**
- <sup>267</sup> G. Guan, M. Hirsch, Z.H. Lu, D.T.D. Childs, S.J. Matcher, R. Goodridge, K.M. Groom, A.T. Clare, Evaluation of selective laser sintering processes by optical coherence tomography, *Materials & Design*, 88(1), 837–846, **2015**
- <sup>268</sup> T. Laumer, T. Stichel, T. Bock, P. Amend, M. Schmidt, Characterization of temperature-dependent optical material properties of polymer powders, in: AIP Conference Proceedings, AIP Publishing, 160001-1–5, **2015**
- <sup>269</sup> S. Negi, S. Dhiman, R.K. Sharma, Determining the effect of sintering conditions on mechanical properties of laser sintered glass filled polyamide parts using RSM, *Measurement*, 68(1), 205–218, **2015**
- <sup>270</sup> P.K. Jain, P.M. Pandey, P.V.M. Rao, Experimental investigations for improving part strength in selective laser sintering, *Virtual and Physical Prototyping*, 3(3), 177–188, **2008**
- <sup>271</sup> M. Taufik, P.K. Jain, Role of build orientation in layered manufacturing: a review, *International Journal of Manufacturing Technology and Management*, 22(1), 47–73, **2014**
- <sup>272</sup> U. Ajoku, N. Hopkinson, M. Caine, Experimental measurement and finite element modelling of the compressive properties of laser sintered nylon-12, *Materials Science and Engineering: A*, 428(1–2), 211–216, **2006**
- <sup>273</sup> J. Goupy, L. Creighton, *Introduction aux plans d'expériences. Toutes les techniques nécessaires à la conduite d'une étude*, 5e ed., Dunod, Paris, France, **2013**
- <sup>274</sup> W.A.Y. Yusoff, A.J. Thomas, The effect of employing an effective laser sintering scanning strategy and energy density value on eliminating “orange peel” on a selective laser sintering part, in: Proceedings of the 17th International Association for Management of Technology, 1–16, **2008**
- <sup>275</sup> J.C. Lee, S.H. Ahn, Bulk density measurement of porous functionally graded materials, *International Journal of Precision Engineering and Manufacturing*, 19(1), 31–37, **2018**
- <sup>276</sup> S. Dupin, O. Lame, C. Barrès, J.Y. Charneau, Microstructural origin of physical and mechanical properties of polyamide 12 processed by laser sintering, *European Polymer Journal*, 48(9), 1611–1621, **2012**
- <sup>277</sup> ISO 2768-1, General tolerances. Part 1: tolerances for linear and angular dimensions without individual tolerance indications, **1989**



- <sup>278</sup> ISO 2768-2, General tolerances. Part 2: geometrical tolerances for features without individual tolerance indications, **1989**
- <sup>279</sup> K. Manetsberger, J. Shen, J. Muellers, Compensation of non-linear shrinkage of polymer materials in selective laser sintering, in: Proceedings of Solid Freeform Fabrication Symposium, Austin, TX, USA, 346–356, **2001**
- <sup>280</sup> R.D. Goodridge, R.J.M. Hague, C.J. Tuck, An empirical study into laser sintering of ultra-high molecular weight polyethylene (UHMWPE), *Journal of Materials Processing Technology*, 210(1), 72–80, **2010**
- <sup>281</sup> P. Dardenne, J.A. Fernández Pierna, A NIR data set is the object of a chemometric contest at ‘Chimimétrie 2004,’ *Chemometrics and Intelligent Laboratory Systems*, 80(2), 236–242, **2006**
- <sup>282</sup> C. Lesty, J. Pleau-Varet, M. Kujas, Geometric method and generalized linear models. Two opposite multiparametric approaches illustrated on a sample of pituitary adenomas, *Journal of Applied Statistics*, 31(2), 191–213, **2004**
- <sup>283</sup> S. Singh, V.S. Sharma, A. Sachdeva, S.K. Sinha, Optimization and analysis of mechanical properties for selective laser sintered polyamide parts, *Materials and Manufacturing Processes*, 28(2), 163–172, **2013**
- <sup>284</sup> J.P. Kruth, X. Wang, T. Laoui, L. Froyen, Lasers and materials in selective laser sintering, *Assembly Automation*, 23(4), 357–371, **2003**
- <sup>285</sup> J.D. Muller, Etude des changements de phase de polymères dans le procédé de rotomoulage: coalescence et cristallisation couplées à la thermique du procédé, Doctorat Dissertations, Institut National des Sciences Appliquées de Lyon, **2008**
- <sup>286</sup> D. Defauchy, G. Regnier, P. Peyre, I. Amran, A. Ammar, Direct manufacturing of thermoplastic parts by powder laser sintering: comparison of coalescence simulations and Frenkel based physical model, in: Proceedings of the 27th World Congress of the Polymer Processing Society, Marrakech, Morocco, 1–7, **2011**
- <sup>287</sup> D. Defauchy, G. Regnier, I. Amran, P. Peyre, A. Ammar, F. Chinesta, Towards a numerical simulation of direct manufacturing of thermoplastic parts by powder laser sintering, in: Proceedings of the Computational Plasticity XI. Fundamentals and Applications, CIMNE Publications, Barcelona, Spain, 688–699, **2011**
- <sup>288</sup> A. Korycki, C. Garnier, N. Rodier, F. Chabert, E. Laurent, V. Nassiet, Numerical and experimental analysis of the thermal profile of printed layers during selective laser sintering process of poly(etheretherketone), in: Proceedings of the 22nd International ESAFORM Conference on Material Forming, Vitoria-Gasteiz, Spain, 150005, **2019**
- <sup>289</sup> C. Garnier, M.L. Pastor, F. Eyma, B. Lorrain, The detection of aeronautical defects in situ on composite structures using non destructive testing, *Composite Structures*, 93(5), 1328–1336, **2011**
- <sup>290</sup> M. Szczepanik, J. Stabiak, G. Wróbel, Ł. Wiebrzycki, Wykorzystanie systemów termowizyjnych do badań materiałów polimerowych, *Modelowanie Inżynierskie*, 5(36), 279–286, **2008**
- <sup>291</sup> T. Chen, Y. Zhang, Thermal modeling of laser sintering of two-component metal powder on top of sintered layers via multi-line scanning, *Applied Physics A*, 86(2), 213–220, **2006**
- <sup>292</sup> J. Xing, W. Sun, R.S. Rana, 3D modeling and testing of transient temperature in selective laser sintering (SLS) process, *Optik*, 124(4), 301–304, **2013**
- <sup>293</sup> T.H.C. Childs, M. Berzins, G.R. Ryder, A. Tontowi, Selective laser sintering of an amorphous polymer-simulations and experiments, Proceedings of the Institution of Mechanical Engineers, Part B: Journal of Engineering Manufacture, 213(4), 333–349, **1999**
- <sup>294</sup> D. Dai, D. Gu, Thermal behavior and densification mechanism during selective laser melting of copper matrix composites: simulation and experiments, *Materials & Design*, 55(1), 482–491, **2014**
- <sup>295</sup> X. Ding, L. Wang, S. Wang, Comparison study of numerical analysis for heat transfer and fluid flow under two different laser scan pattern during selective laser melting, *Optik*, 127(22), 10898–10907, **2016**
- <sup>296</sup> H. Hu, X. Ding, L. Wang, Numerical analysis of heat transfer during multi-layer selective laser melting of AlSi10Mg, *Optik*, 127(20), 8883–8891, **2016**
- <sup>297</sup> I.A. Roberts, C.J. Wang, R. Esterlein, M. Stanford, D.J. Mynors, A three-dimensional finite element analysis of the temperature field during laser melting of metal powders in additive layer manufacturing, *International Journal of Machine Tools and Manufacture*, 49(12–13), 916–923, **2009**
- <sup>298</sup> G. Bugada Miguel Cervera, G. Lombera, Numerical prediction of temperature and density distributions in selective laser sintering processes, *Rapid Prototyping Journal*, 5(1), 21–26, **1999**
- <sup>299</sup> A.J. Favaloro, B. Brenken, E. Barocio, R.B. Pipes, Simulation of polymeric composites additive manufacturing using abaqus, *Science in the Age of Experience*, 1(1), 103–114, **2017**
- <sup>300</sup> X. Tian, G. Peng, M. Yan, S. He, R. Yao, Process prediction of selective laser sintering based on heat transfer analysis for polyamide composite powders, *International Journal of Heat and Mass Transfer*, 120(1), 379–386, **2018**
- <sup>301</sup> X. Liu, M. Boutaous, S. Xin, Scattering effect in radiative heat transfer during selective laser sintering of polymers, in: Proceedings of the 19th International ESAFORM Conference on Material Forming, AIP Publishing, Nantes, France, 110006-1–6, **2016**
- <sup>302</sup> D. Moser, S. Pannala, J. Murthy, Computation of effective thermal conductivity of powders for selective laser sintering simulations, *Journal of Heat Transfer*, 138(8), 082002, **2016**

- <sup>303</sup> L. Xin, M. Boutaous, S. Xin, D.A. Siginer, Numerical modeling of the heating phase of the selective laser sintering process, *International Journal of Thermal Sciences*, 120(1), 50–62, **2017**
- <sup>304</sup> J.A. Nelson, A.E.W. Rennie, T.N. Abram, G.R. Bennett, A.C. Adiele, M. Wood, G. Galloway, Effect of process conditions on temperature distribution in the powder bed during laser sintering of polyamide-12, *Journal of Thermal Engineering*, 1(3), 159–165, **2014**
- <sup>305</sup> P. Foteinopoulos, A. Papacharalampopoulos, P. Stavropoulos, On thermal modeling of additive manufacturing processes, *Center for International Relations and Politics Journal of Manufacturing Science and Technology*, 20(1), 66–83, **2018**
- <sup>306</sup> K. Zeng, D. Pal, B. Stucker, A review of thermal analysis methods in laser sintering and selective laser melting, in: *Proceedings of Solid Freeform Fabrication Symposium*, Austin, TX, USA, 796–814, **2012**
- <sup>307</sup> L. Dong, A. Makradi, S. Ahzi, Y. Remond, Three-dimensional transient finite element analysis of the selective laser sintering process, *Journal of Materials Processing Technology*, 209(2), 700–706, **2009**
- <sup>308</sup> W. Piekarska, M. Kubiak, Z. Saternus, Numerical modelling of thermal phenomena in laser beam and hybrid welding processes using Abaqus FEA, *Archives of Foundry Engineering*, 11(2), 185–190, **2011**
- <sup>309</sup> H.J. Zimmermann, K. Könnecke, Crystallization of poly(aryl ether ketones): 3. The crystal structure of poly(ether ether ketone ketone) (PEEKK), *Polymer*, 32(17), 3162–3169, **1991**
- <sup>310</sup> V.L. Rao, P. Sivasadan, Synthesis and properties of polyether ketones, *European Polymer Journal*, 30(12), 1381–1388, **1994**
- <sup>311</sup> A. Arzak, J.I. Eguiazábal, J. Nazábal, Effect of annealing on the properties of poly(ether ether ketone), *Polymer Engineering and Science*, 31(8), 586–591, **1991**
- <sup>312</sup> K.D. Kim, L.H. Sperling, A. Klein, B. Hammouda, Reptation time, temperature, and cosurfactant effects on the molecular interdiffusion rate during polystyrene latex film formation, *Macromolecules*, 27(23), 6841–6850, **1994**
- <sup>313</sup> ASTM C 1444-00, Standard test method for measuring the angle of repose of free-flowing mold powders, **2000**
- <sup>314</sup> ASTM D 1895-96, Standard test methods for apparent density, bulk factor, and pourability of plastic materials, **2010**
- <sup>315</sup> ISO 23145-1, Fine ceramics (advanced ceramics, advanced technical ceramics) - determination of bulk density of ceramic powders - part 1: tap density, **2006**
- <sup>316</sup> H.H. Hausner, Friction conditions in a mass of metal powder, *International Journal of Powder Metallurgy*, 3(4), 7–13, **1967**
- <sup>317</sup> 3D Production Printer sPro 230 SLS, 3D Systems, **2019**
- <sup>318</sup> S. Schmitt, La fabrication directe plastique avec les nouveaux systèmes. Matériaux de frittage sélectif par laser stéréolithographie., in: *3D Systems Users World Conference*, 248–256, **2008**
- <sup>319</sup> 3D Production Printer ProX 500 SLS. Facility Guide, **2019**

# ANNEXES

## A.1. Technical specification

### A.1.1. Duraform PA12



## DuraForm® PA Plastic

For use with all selective laser sintering (SLS) systems

PROPERTY	CONDITION	METRIC	U.S.
Heat Deflection Temperature	ASTM D 648 0.125 MPa	180 °C 95 °C	316 °F 203 °F
Coefficient of Thermal Expansion (µm/m·°C) (µin/in·°F)	ASTM E 831 140 °C	82.6 179.2	46.9 99.6
Specific Heat Capacity	ASTM E 289	1.64 J/g·°C	0.392 Btu/lb·°F
Thermal Conductivity	ASTM E 1225	0.70 W/m·K	4.86 BTU/in·hr·°F
Flammability	UL 94	HB	HB

PROPERTY	CONDITION	METRIC	U.S.
Volume Resistivity	ASTM D 257	5.0 X 10 <sup>10</sup> ohm·cm	5.0 X 10 <sup>10</sup> ohm·cm
Surface Resistivity	ASTM D 257	7.0 X 10 <sup>10</sup> ohm	7.0 X 10 <sup>10</sup> ohm
Dielectric Constant (1 kHz)	ASTM D 150	0.04	0.04
Dielectric Loss (1 kHz)	ASTM D 150	2.73	2.73
Dielectric Strength (kV/mm)	ASTM D 149	17.3 kV/mm	40 kV/in

Data was generated by building parts under typical build parameters. DuraForm® PA Plastic was processed on a base level of 110 µm with layer thickness of 110 µm and 110 µm. 200 individual test pieces were processed on a base level of 110 µm with layer thickness of 110 µm.

**3D SYSTEMS**  
www.3dsystems.com

Warranty/Disclaimer: The performance characteristics of these products may vary according to product and process operating conditions. Material properties are based on test results for 3D Systems SLS parts. All type names or logos are trademarks of their respective owners. All type names or logos are trademarks of their respective owners. © 2017 by 3D Systems, Inc. All rights reserved. Specifications subject to change without notice. 3D Systems, DuraForm, and Sinteration are trademarks of 3D Systems, Inc. and Sinteration is a trademark of 3D Systems, Inc.



## DuraForm® PA Plastic

Durable polyimide (nylon) material for real-world physical testing and functional use.

PROPERTY	CONDITION	METRIC	U.S.
Specific Gravity	ASTM D 792	1.09 g/cm <sup>3</sup>	1.09 g/cm <sup>3</sup>
Molecular Weight (Mn)	ASTM D 570	0.27%	0.07%

PROPERTY	CONDITION	METRIC	U.S.
Tensile Strength (Minimum) (MPa/PSI)	ASTM D 638	43	6237
Tensile Modulus (Minimum) (GPa/PSI)	ASTM D 638	1586	230
Elongation at Break (%)	ASTM D 638	14	14
Flexural Modulus (Minimum) (MPa/PSI)	ASTM D 790	48	6962
Flexural Modulus (Minimum) (GPa/PSI)	ASTM D 790	1387	201
Hardness (HRR)	ASTM D 2240	78	73
Impact Strength (Charpy) (kJ/m <sup>2</sup> )	ASTM D 256	32 J/m	0.6 ft·lb/in
Impact Strength (Charpy) (J/m <sup>2</sup> )	ASTM D 256	336 J/m	6.3 ft·lb/in
Gardner Impact (HRR)	ASTM D 5420	2.7 J	2.0 ft·lb

Data was generated by building parts under typical build parameters. DuraForm® PA Plastic was processed on a base level of 110 µm with layer thickness of 110 µm and 110 µm. 200 individual test pieces were processed on a base level of 110 µm with layer thickness of 110 µm.

### General Properties

PROPERTY	CONDITION	METRIC	U.S.
Specific Gravity	ASTM D 792	1.09 g/cm <sup>3</sup>	1.09 g/cm <sup>3</sup>
Molecular Weight (Mn)	ASTM D 570	0.27%	0.07%

### Features

- Excellent surface resolution and feature detail
- Easy to process
- Compliant with USP Class VI testing
- Compatible with autoclave sterilization
- Good chemical resistance and low moisture absorption

### Benefits

- Nickel-balanced mechanical properties and processability
- Build prototypes that withstand functional testing
- Produce durable end-use parts without tooling
- Create accurate and repeatable parts as developed by manufacturer
- Recyclable and paintable for demonstration parts

### Applications

- Complex, thin-wall ductwork
- Functional prototypes that approach end-use performance properties
- Appropriate for low- to mid-volume rapid manufacturing or biocompatibility
- Medical applications requiring USP Class VI compliance,
  - Motorsports
  - Aerospace
- Housing and enclosures
- Impellers and connectors
- Consumer sporting goods
- Vehicle dashboards and grilles
- Snap-fit designs
- Parts requiring machining or joining with adhesives

# A.1.2. DuraForm FR1200



## DuraForm® FR1200

A flame-retardant nylon 12 material with high accuracy and excellent surface finish. Ideally suited for direct 3D production in aerospace, transportation, and consumer goods applications where reliable fire retardancy and reduced smoke and toxicity are required.

### General Properties

MEASUREMENT	CONDITION	METRIC	U.S.
Shore D Hardness (g/cm <sup>3</sup> )	ASTM D792	1.62	117
Water Absorb. (g/cm <sup>3</sup> )	ASTM D570	0.29	0.18

### Mechanical Properties

MEASUREMENT	CONDITION	METRIC	U.S.
Tensile Strength (MPa)	ASTM D 638	41	6110
Tensile Modulus (GPa)	ASTM D 638	2540	366
Elongation @ Break (%)	ASTM D 638	5.9	11
Flexural Strength (MPa)	ASTM D 790	62	8940
Flexural Modulus (GPa)	ASTM D 790	1770	257
Hardness (HRR)	ASTM D2240	76	11
Impact Strength @ 13°C (J/m <sup>2</sup> )	ASTM D256	25	6.16
Unnotched Izod @ 23°C		233	1.1

### Thermal Properties

MEASUREMENT	CONDITION	METRIC	U.S.
Heat Deflection Temperature @ 1.82 MPa	ASTM D688	180 °C	316 °F
Heat Deflection Temperature @ 0.45 MPa	ASTM D688	94 °C	211 °F
Coef. of Thermal Expansion (ppm/°C)	ASTM E831	140	78
Specific Heat (J/g°C)	ASTM E1269	1.38	0.33
Thermal Conductivity (W/mK)	@ 23°C	0.18	0.043
	@ 150°C	0.18	0.043
	@ 190°C	0.21	0.05
Thermal Coefficient of Expansion (ppm/°C)	ASTM E1390	0.22	1.15

The parts used to illustrate the above data were generated by building parts using 100% virgin powder using default parameters on an HP® Z610 3D printer.

### Electrical Properties

MEASUREMENT	CONDITION	METRIC	U.S.
Volume Resistivity (ohm-cm)	ASTM D527	5.97 x 10 <sup>14</sup>	2.35 x 10 <sup>14</sup>
Surface Resistivity (ohm)	ASTM D527	2.56 x 10 <sup>14</sup>	2.56 x 10 <sup>14</sup>
Dielectric Constant, 1 kHz	ASTM D150	0.028	0.028
Dielectric Constant, 1 MHz	ASTM D150	3.0	3.0
Dielectric Strength (kV/mm)	ASTM D149	22.5	975

### Flammability Properties

MEASUREMENT	CONDITION	METRIC	U.S.
FAI 25.853 (a) or Appendix F Part I (b)(6) (mm 1H)	60 sec	43.0	0.15
FAI 25.853 (b) or Appendix F Part I (a)(1)(1) (mm 1H)	12 sec	2	0.08
ATM 2.00278 (Smoke Density Rating Model Non-Faming) (code)	12 sec	pass	pass
ATM 2.00278 (Smoke Density Rating Model Non-Faming) (code)	2 sec	pass	pass
ATM 3.0005 (Climbation Toxicity Rating Model Non-Faming) (code)		pass	pass
ATM 2.0006 (HRR) (ETU A-7) (mm 1H) (code)		141.3	12.44
Total Heat Release (J/g)	2 mm	103.2	9.26
Flammability (UL-94) (E69541)	UL 94V	pass	pass
HB @ 1.5 mm (D667)		pass	pass

The parts used to illustrate the above data were generated by building parts using 100% virgin powder using default parameters on an HP® Z610 3D printer.

## DuraForm® FR1200

A flame-retardant nylon 12 material with high accuracy and excellent surface finish. Ideally suited for direct 3D production in aerospace, transportation, and consumer goods applications where reliable fire retardancy and reduced smoke and toxicity are required.

### Features

- FAI 25.853 compliant
- Passes ATM smoke density and toxicity requirements
- High accuracy and repeatability needed for manufacturing
- Non halogenated formulation
- Excellent surface quality

### Benefits

- Reduces lead costs with weight optimized design enabled by additive manufacturing
- Accelerate change in color, designs for in service aircraft
- Eliminate tooling and minimize spare part stocking costs
- Excellent flame retardancy at 12 and 60 second exposures

### Applications

- Direct 3D production of aircraft interior parts
- Parts requiring flame retardancy
- Automotive and transportation related parts where fire safety may be needed
- Consumer electronics and other goods



www.3dsystems.com


Notes and Disclaimers: The performance characteristics of these products may vary according to product application, operating conditions, or as it varies. 3D Systems makes no warranty, express or implied, regarding the accuracy of the data, the reliability of the information, or the results of its use.

© 2018 by 3D Systems, Inc. All rights reserved. Specifications subject to change without notice. 3D Systems, the 3D Systems logo, and DuraForm are registered trademarks and used here as a trademark of 3D Systems, Inc.

03 | 18

A.1.3. ZYPEEK 330 PF and ZYPEEK 550 PF

吉林省中研高性能工程塑料股份有限公司  
 Jilin Zhongyan High Performance Plastic Co., Ltd.



**ZYPEEK®\_550PF**

Test Item	Test Method	Conditions	Units	Test Data
<b>Mechanical Data</b>				
Tensile Strength	ISO 527	Yield, 23°C	MPa	100
Tensile Elongation	ISO 527	Break, 23°C	%	25
Flexural Strength	ISO 178	Yield, 23°C	MPa	160
Flexural Modulus	ISO 178	23°C	GPa	4.1
Izod Impact Strength	ISO 180/A	Notched	kJ m <sup>-2</sup>	5.5
	ISO 180/C	Unnotched	kJ m <sup>-2</sup>	-
Mould Shrinkage	ISO 294-4	Along Flow	%	1
		Across Flow	%	1.3
<b>Thermal Data</b>				
Melting Point	ISO 11357	-	°C	343
Glass Transition (T <sub>g</sub> )	ISO 11357	Onset	°C	143
<b>Flow</b>				
Melt Index	ISO 1133	380°C, 5kg	g 10min <sup>-1</sup>	20
<b>Miscellaneous</b>				
Density	ISO 1183	Crystalline	g cm <sup>-3</sup>	1.3
Volume Density	ISO 1183	-	g cm <sup>-3</sup>	0.3
Average Particle Size (D50)	ISO 13320-1	-	µm	50.75

\*Result based on similar products

- 1 -

吉林省中研高性能工程塑料股份有限公司  
 Jilin Zhongyan High Performance Plastic Co., Ltd.



**ZYPEEK®\_330PF**

Test Item	Test Method	Conditions	Units	Test Data
<b>Mechanical Data</b>				
Tensile Strength	ISO 527	Yield, 23°C	MPa	100
Tensile Elongation	ISO 527	Break, 23°C	%	15
Flexural Strength	ISO 178	Yield, 23°C	MPa	170
Flexural Modulus	ISO 178	23°C	GPa	4.1
Izod Impact Strength	ISO 180/A	Notched	kJ m <sup>-2</sup>	4.5
	ISO 180/C	Unnotched	kJ m <sup>-2</sup>	-
Mould Shrinkage	ISO 294-4	Along Flow	%	1
		Across Flow	%	1.3
<b>Thermal Data</b>				
Melting Point	ISO 11357	-	°C	343
Glass Transition (T <sub>g</sub> )	ISO 11357	Onset	°C	143
<b>Flow</b>				
Melt Index	ISO 1133	380°C, 5kg	g 10min <sup>-1</sup>	80
<b>Miscellaneous</b>				
Density	ISO 1183	Crystalline	g cm <sup>-3</sup>	1.3
Volume Density	ISO 1183	-	g cm <sup>-3</sup>	0.3
Average Particle Size (D50)	ISO 13320-1	-	µm	50

\*Result based on similar products

- 1 -

## A.1.4. VESTAKEEP 2000 FP

Powder Information		Test method international	national	Unit	VESTAKEEP 2000FP
Property		ISO 60	DIN 53 468	g/dm <sup>3</sup>	280
App. bulk density			Milvern Mastersizer	µm	approx. 50
Average particle size	d50				

Application technology properties		Test method international	national	Unit	VESTAKEEP 2000FP
Property		ISO 1183	DIN EN ISO 1183	g/cm <sup>3</sup>	1.30
Density	23°C				
Tensile test		ISO 527-1	DIN EN ISO 527-1	MPa	100
Stress at yield		ISO 527-2	DIN EN ISO 527-2	%	5
Strain at yield				%	30
Strain at break					
Tensile modulus		ISO 527-1/2	DIN EN ISO 527-1/2	MPa	3700
CHARPY impact strength		ISO 179/1e0	DIN EN ISO 179/1e0	kJ/m <sup>2</sup>	NH
	23°C			kJ/m <sup>2</sup>	NH
	-30°C			kJ/m <sup>2</sup>	6 C <sup>u</sup>
CHARPY notched impact strength		ISO 179/1eA	DIN EN ISO 179/1eA	kJ/m <sup>2</sup>	6 C <sup>u</sup>
	23°C			kJ/m <sup>2</sup>	6 C <sup>u</sup>
	-30°C			kJ/m <sup>2</sup>	6 C <sup>u</sup>
Temperature of deflection under load		ISO 75-1	DIN EN ISO 75-1	°C	155
Method A		ISO 75-2	DIN EN ISO 75-2	°C	205
Method B	1.8 MPa				
Method B	0.45 MPa				
Vicat softening temperature		ISO 306	DIN EN ISO 306	°C	335
Method A	10 N			°C	310
Method B	50 N				
Melting range		ISO 11357		°C	approx. 340
DSC	2nd heating				
Melt volume-flow rate (MVR)		ISO 1133	DIN EN ISO 1133	cm <sup>3</sup> /10 min	70
	300°C/5 kg				
Flammability acc. UL 94	3.2 mm	IEC60695	UL 94		V-0


Pigmentation may affect values.

\*) C – Complete break, incl. huge break II  
N – No break

\* = registered trademark

This information and all technical data are based on Evonik's present knowledge and experience. Evonik assumes no liability for errors. Evonik reserves the right to make changes to the data without notice. Evonik does not accept any responsibility for the use of the data. Evonik disclaims all representations and warranties, whether express or implied, and shall have no liability for merchantability of the product or its fitness for a particular purpose (even if Evonik is aware of such purpose), or otherwise. Evonik shall not be responsible for consequential, indirect or special damages (including loss of profits) of any kind. To the extent of its sole responsibility to arrange for the use of the data, Evonik shall not be liable for any damages. Evonik does not imply that similar products could not be used.

Evonik Industries AG, High Performance Polymers, 45764 Marl, Germany  
Phone: +49 2305 49-9878 E-mail: [evonik-hp@evonik.com](mailto:evonik-hp@evonik.com)  
[www.vestakeep.com](http://www.vestakeep.com)



## Product Information

**VESTAKEEP® 2000FP**  
Unreinforced, medium-viscosity polyether ether ketone fine powder

VESTAKEEP 2000FP is an unreinforced, medium-viscosity polyether ether ketone fine powder. It can be used as a basic resin or in blends with different additives for manufacturing compression molding parts.

The semi-crystalline polymer features superior thermal and chemical resistance. VESTAKEEP 2000FP is self-extinguishing.

VESTAKEEP 2000FP is supplied as a powder in boxes with moisture-proof polyethylene liners.

For information about processing of VESTAKEEP 2000FP, please follow the general recommendations in our brochure "VESTAKEEP Polyether Ether Ketone."

**For further information, please contact us at [evonik-hp@evonik.com](mailto:evonik-hp@evonik.com).**

October 2011


VESTAKEEP® = registered trademark of the Evonik Degussa GmbH







A.1.6. VICTREX PEEK 450 G




## VICTREX® PEEK 450G

High performance thermoplastic material, unreinforced PolyEtherEtherKetone (PEEK), semi crystalline, granules for injection molding and extrusion, standard flow, FDA food contact compliant, colour natural beige.

**Typical Application Areas:**  
Applications for higher strength and stiffness as well as high ductility. Chemically resistant to aggressive environments, suitable for sterilisation for medical and food contact applications.

CONDITIONS	TEST METHOD	UNITS	TYPICAL VALUE
<b>Mechanical Data</b>			
Tensile Strength	ISO 527	MPa	98
Tensile Elongation	ISO 527	%	45
Tensile Modulus	ISO 527	GPa	2.9
Flexural Strength	ISO 178	MPa	125
At yield, 23°C			165
120°C			85
175°C			19
Flexural Modulus	ISO 178	GPa	12.5
Compressive Strength	ISO 604	MPa	125
Charpy Impact Strength	ISO 1791eA	kJ/m <sup>2</sup>	7.0
Unnotched, 23°C	ISO 1791eB	n/b	
Notched, 23°C	ISO 180/A	kJ/m <sup>2</sup>	8.0
Unnotched, 23°C	ISO 180/U	n/b	
<b>Thermal Data</b>			
Melting Point	ISO 11357	°C	343
Glass Transition (Tg)	ISO 11357	°C	143
<b>Coefficient of Thermal Expansion</b>			
Along flow below Tg	ISO 11359	ppm K <sup>-1</sup>	45
Average below Tg			55
Along flow above Tg			120
Average above Tg			140
Heat Deflection Temperature	ISO 75-F	°C	152
As moulded, 1.8 MPa			160
Thermal Conductivity	ISO 22007-4	W/m K	0.32
Along flow, 23°C			0.29
Average, 23°C			0.26
Relative Thermal Index	UL 746B	°C	240
Mechanical loss impact			240
Mechanical withstand			180
<b>Flow</b>			
Melt Viscosity	ISO 11443	Pa.s	350
<b>Miscellaneous</b>			
Density	ISO 1183	g cm <sup>3</sup>	1.30
Shore D hardness	ISO 868		84.5
Water Absorption by immersion	ISO 62-1	%	0.45
Saturated, 23°C			0.55
Saturated, 100°C			

VICTREX® HIGH PERFORMANCE PAEK POLYMERS 5042166-04-01 Rev.01 July 2014



PROPERTY	TEST METHOD	UNITS	TYPICAL VALUE
<b>Electrical Properties</b>			
Volume Resistivity	IEC 60093	Ω cm	10 <sup>16</sup>
Surface Resistivity	IEC 60093	Ω sq	10 <sup>16</sup>
Dielectric Strength	IEC 60093	kV mm <sup>-1</sup>	23
Dielectric Loss (tan δ)	IEC 60093		0.004
Dielectric Constant (ε)	IEC 60093		3.1
Volume Resistance	IEC 60093	Ω cm	10 <sup>16</sup>
Surface Resistance	IEC 60093	Ω sq	10 <sup>16</sup>
<b>Flammability</b>			
UL94	UL94		0.074
Flaming Time	UL94	min	0.15
Char Yield	UL94	%	0.22
<b>Thermal Properties</b>			
Melting Point	ISO 11357	°C	343
Glass Transition (Tg)	ISO 11357	°C	143
Coefficient of Thermal Expansion	ISO 11359	ppm K <sup>-1</sup>	45
Along flow below Tg			55
Average below Tg			120
Along flow above Tg			140
Average above Tg			152
Heat Deflection Temperature	ISO 75-F	°C	160
As moulded, 1.8 MPa			160
Thermal Conductivity	ISO 22007-4	W/m K	0.32
Along flow, 23°C			0.29
Average, 23°C			0.26
Relative Thermal Index	UL 746B	°C	240
Mechanical loss impact			240
Mechanical withstand			180
<b>Flow</b>			
Melt Viscosity	ISO 11443	Pa.s	350
<b>Miscellaneous</b>			
Density	ISO 1183	g cm <sup>3</sup>	1.30
Shore D hardness	ISO 868		84.5
Water Absorption by immersion	ISO 62-1	%	0.45
Saturated, 23°C			0.55
Saturated, 100°C			

**Important notes:**  
 1) Extrusion conditions similar to our standards are typical of those used in our processing laboratories. Extrusion conditions are subject to change for different applications. Flow data is highly dependent on part geometry, mold configuration, and extrusion conditions.  
 2) Data are applicable to standard test specimens. Mechanical and thermal properties are subject to change in accordance with the material composition. Flow and impact data are highly dependent on part geometry, mold configuration and processing conditions. Properties may also differ for along flow and across flow.  
 Details data available in our website www.victrex.com or upon request.

A.1.7. EOS PEEK HP3



EOS GmbH - Electro Optical Systems  
 Robert-Stirling-Ring 1  
 D-82152 Krailling / München  
 Telephone: +49 (0)89 / 893 36-0  
 Telefax: +49 (0)89 / 893 36-285  
 Internet: [www.eos.com](http://www.eos.com)

---

Material Data Sheet

**EOS PEEK HP3, the high-grade performer**


**Application:**  
 EOS provides the world-first high-performance polymer for the laser-sintering process - EOS PEEK HP3. Belonging to the group of Polyaryletherketone (PAEK), this semi-crystalline, thermoplastic material was developed for the use on the new high-temperature system EOSINT P 800.

The laser-sintered parts achieve a tensile strength up to 95 MPa and a Young's modulus up to 4400 MPa. These values are on an up to 100 percent higher level than the so far market dominating materials PA 12 and PA 11. The continuous use temperature ranges within 180 °C (mechanical dynamic), 240 °C (mechanical static) and 260 °C (electrical) depending on the field of application which could not be reached so far.


EOS-PEEK HP3 is characterized by an outstanding combination of properties like

- ┆ excellent high temperature performance
- ┆ high wear resistance
- ┆ outstanding chemical resistance
- ┆ best fire, smoke and toxicity performance
- ┆ good hydrolysis resistance
- ┆ potential biocompatibility
- ┆ sterilisability

Due to this exceptional combination of properties EOS PEEK HP3 is optimally suited for highest demanding applications e.g. in medicine, aerospace industry or motorsports. In medical applications the outstanding properties make this material an ideal replacement for stainless steel and titanium. And in aerospace and in motorsports where light weight and fire resistance are of largest importance, EOS PEEK HP3 has developed to an adequate metal replacement.



EOS GmbH - Electro Optical Systems  
 Robert-Stirling-Ring 1  
 D-82152 Krailling / München  
 Telephone: +49 (0)89 / 893 36-0  
 Telefax: +49 (0)89 / 893 36-285  
 Internet: [www.eos.com](http://www.eos.com)



EOS GmbH - Electro Optical Systems  
 Robert-Stirling-Ring 1  
 D-82152 Krailling / München

---

Material Data Sheet

**General Material Properties:**

Properties	Test method	Value	Unit
Average grain size	Laser diffraction	60	µm
Bulk density	DIN 53466	0.43 ± 0.01	g/cm³
Density of laser-sintered part	DIN EN ISO 1183	1.315 ± 0.01	g/cm³

**Mechanical Properties (x, y-direction):**


Properties	Test method	Value	Unit
Tensile modulus	ASTM D638	4250 ± 150	MPa
Tensile strength	ASTM D638	90 ± 5	MPa
Elongation at break	ASTM D638	2.8 ± 0.2	%

**Thermal Properties:**

Properties	Test method	Value	Unit
Melting point	DSC	372 (702)	°C (°F)
Glass transition temperature (T <sub>g</sub> )	DSC	164 (327)	°C (°F)
Heat deflection temperature (HDT)	ISO 75 (1.8 MPa)	165 (328)	°C (°F)
Continuous use temperature	electrical	266 (506)	
	mechanical w/o impact	240 (464)	°C (°F)
	mechanical w/impact	180 (356)	


The mechanical properties depend on the x-, y-, z-position of the test parts and on the exposure parameters used. The data are based on our latest knowledge and are subject to changes without notice. They do not guarantee properties for a particular part and in a particular application.

© 2008 EOS GmbH - Electro Optical Systems. All rights reserved.



EOS GmbH - Electro Optical Systems  
 Robert-Stirling-Ring 1  
 D-82152 Krailling / München  
 Telephone: +49 (0)89 / 893 36-0  
 Telefax: +49 (0)89 / 893 36-285  
 Internet: [www.eos.com](http://www.eos.com)

# A.1.8. ULTRASON E 1010 PESU



**ULTRASON® E 1010**  
Polyethersulfone (PESU)

**ULTRASON® E 1010**  
We create chemistry

Product Information  
Sep 2019

ULTRASON E 1010 is an unfilled, low viscosity injection molding PESU grade. It flows readily and offers outstanding heat resistance and dimensional stability.


Typical applications include automotive applications such as fuse encapsulation, connectors heating system and headlight components and household applications such as microwave dishes and other applications requiring high heat resistance.

Property	ISO Test Method	Property Value
<b>PHYSICAL</b>		
Density, g/cm <sup>3</sup>	1183	1.37
Mold Shrinkage, parallel, %	294-4	0.79
Mold Shrinkage, normal, %	294-4	0.82
Moisture, % (50% RH) (Saturation)	62	0.8
		2.2
<b>RHEOLOGICAL</b>		
Melt Volume Rate (350 C/10 Kg), cc/10min	1133	150
<b>Mechanical</b>		
Tensile Modulus, MPa	527	2,650
Tensile stress at yield, MPa	527	85
Tensile strain at yield, %	527	6.8
Ball Indentation, MPa	2035-1	154
<b>IMPACT</b>		
Izod Notched Impact, kJ/m <sup>2</sup>	180	7
-30C		6.5
Charpy Notched, kJ/m <sup>2</sup>	179	7
-30C		6.5
Charpy Unnotched, kJ/m <sup>2</sup>	170	N
-30C		N
<b>THERMAL</b>		
HDT A, C	75	203
Coeff of Linear Thermal Expansion, Parallel, mm/mm C		0.52 X10-4
<b>ELECTRICAL</b>		
Comparative Tracking Index	IEC 6011-2	125
Volume Resistivity (Ohm-m)	IEC 60093	>1E13

General Information: 800-BC-RESIN  
Technical Assistance: 800-527-TECH (734-324-5150)  
Web address: <http://www.plasticportal.com/usa>

BASF Corporation  
Engineering Plastics  
1659 Biddle Avenue  
Wyandotte, MI 48182

Page 1 of 2




**ULTRASON® E 1010**  
We create chemistry

**ULTRASON® E 1010**  
We create chemistry

Surface Resistivity (Ohm)
 IEC 60093 | >1E15 || Dielectric Constant (100 Hz) | IEC 60250 | 3.9 |
Dielectric Constant (1 MHz)	IEC 60250	3.8
Dissipation Factor (100 Hz), E-4	IEC 60250	17
Dissipation Factor (1 MHz), E-4	IEC 60250	140
Dielectric Strength, KV/mm	IEC 60243-1	37
**UL RATINGS**	**UL Test Method**	**Property Value**
Flammability Rating	UL94	V-1
Relative Temperature Index	UL746B	180
Mechanical w/ Impact, C		180
Electrical, C		180
Flammability Rating	UL94	V-0
Relative Temperature Index	UL746B	190
Mechanical w/ Impact, C		180
Electrical, C		180
**Processing Guidelines**		
Max. Water content: 0.02%		
Ultron pellets can absorb moisture very rapidly and must be dried before processing. A vacuum oven or a dry air stream operating at 130°C (266°F) is recommended. Cooling air flow and uniform drying are essential to prevent warpage. The maximum drying time should not exceed at least 4 hours. Further information concerning safe handling procedures can be obtained from the Safety Data Sheet. Alternatively, please contact your BASF representative.		
**Material Handling**		
Melt Temperature 310-330C (584-724F)		
Mold Temperature 140-190C (284-364F)		
Injection and Packing Pressure 35-125 bar (500-1500 psi)		
**Mold Temperatures**		
Injection pressure controls the filling of the part and should be applied for 90% of ram travel. Packing pressure affects the final part and can be used effectively in controlling sink marks and shrinkage. It should be applied and maintained until the gate area is completely frozen off.		
Back pressure can be utilized to provide uniform melt consistency and reduce trapped air and gas.		
**Pressures**		
Fast fill rates are recommended to ensure uniform melt delivery to the cavity and prevent premature freezing. Surface appearance is directly affected by injection rate.		
**Note**		
Although all statements and information in this publication are believed to be accurate and reliable, they are presented gratis and for guidance only, and no liability for results obtained by use of this information is assumed. The user assumes all responsibility for the proper use of this information. **WARRANTIES OF ANY KIND, EITHER EXPRESS OR IMPLIED, INCLUDING WARRANTIES OF MERCHANTABILITY OR FITNESS FOR A PARTICULAR PURPOSE, ARE MADE REGARDING PRODUCTS DESCRIBED OR DESIGNED. DATA OR INFORMATION SET FORTH, STATEMENTS OR SUGGESTIONS CONCERNING POSSIBLE USE OF THE PRODUCTS ARE MADE WITHOUT REPRESENTATION OR WARRANTY BY BASF. THE USER SHOULD NOT ASSUME THAT TOXICITY DATA AND SAFETY MEASURES ARE INDICATED OR THAT OTHER MEASURES MAY NOT BE REQUIRED.**		
General Information: 800-BC-RESIN Technical Assistance: 800-527-TECH (734-324-5150) Web address: <http://www.plasticportal.com/usa>		
BASF Corporation Engineering Plastics 1659 Biddle Avenue Wyandotte, MI 48182		
Page 2 of 2		

A.1.9. ULTRASON E 3010 PESU

**Product Information**  
Sep 2019



**BASF**  
We create Chemistry

**Ultron® E 3010 Polyethersulfone (PESU)**

Ultron E 3010 is an unreinforced, higher viscosity injection molding and extrusion PESU grade, tougher and with improved chemical resistance.


Product Description	ISO Test Method	Property Value
Density, g/cm <sup>3</sup>	1183	1.37
Mold Shrinkage, parallel, %	204-4	0.85
Mold Shrinkage, normal, %	204-4	0.9
Melting, % (50% RH)	62	0.8
(Separation)		2.2
RHEOLOGICAL	ISO Test Method	Property Value
Melt Volume Rate (300 CF/10), cc/10mm	1133	35
MECHANICAL	ISO Test Method	Property Value
Tensile Modulus, MPa	527	
23C		2,650
Tensile stress at yield, MPa	527	
23C		85
Tensile strain at yield, %	527	
23C		6.9
Ball Indentation, MPa	ISO Test Method	Property Value
154	2039-1	
IMPACT	ISO Test Method	Property Value
Izod Notched Impact, kJ/m <sup>2</sup>	180	
-30C		8
23C		8
Charpy Notched, kJ/m <sup>2</sup>	179	
-30C		8
23C		8
Charpy Unnotched, kJ/m <sup>2</sup>	179	
-30C		N
23C		N
THERMAL	ISO Test Method	Property Value
HDT A, C	75	
mm/mm C		0.52 X10-4
207		
ELECTRICAL	ISO Test Method	Property Value
Comparative Tracking Index	IEC 80112	125
Volume Resistivity (Ohm-m)	IEC 60093	>1E13
Surface Resistivity (Ohm)	IEC 60093	>1E15
Dielectric Constant (100 Hz)	IEC 60250	3.9
Dielectric Constant (1 MHz)	IEC 60250	3.8
Dissipation Factor (100 Hz), E-4	IEC 60250	17
Dissipation Factor (1 MHz), E-4	IEC 60250	140

**BASF Corporation**  
Engineering Plastics  
1609 Biddle Avenue  
Wyandotte, MI 48192

**General Information: 800-BC-RESIN**  
Technical Assistance: 800-527-TECH (734-324-5150)  
Web address: <http://www.plasticportal.com/usa>

Page 1 of 2

**Ultron® E 3010**



**BASF**  
We create Chemistry

UL RATINGS	UL Test Method	Property Value
Dielectric Strength, kV/mm	IEC 60243-1	34
Flammability Rating	UL94	V-0
Relative Temperature Index, 1.5mm	UL746B	190
Mechanical w/ Impact, C		180
Electrical, C		180
Flammability Rating, 3.0mm	UL94	V-0
Relative Temperature Index, 3.0mm	UL746B	190
Mechanical w/ Impact, C		180
Electrical, C		180

**Processing Guidelines**

**Material Handling**  
Melt Viscosity: 0.02%  
Ultron pellets can absorb moisture very rapidly and must be dried before processing. A vacuum or dry air oven operating at 130-150C (266-302F) is recommended. Circulating air ovens are unsuitable. Drying time is dependent on moisture level, however this materials must be dried at least 4 hours. Further information concerning safe handling procedures can be obtained from the Safety Data Sheet. Alternatively, please contact your BASF representative.

**Typical Profile**  
Melt Temperature: 340-360C (644-734F)  
Mold Temperature: 140-180C (284-356F)  
Injection and Packing Pressure: 35-125 bar (500-1800 psi)

**Mold Temperature**  
Injection pressure controls the filling of the part and should be applied for 80% of ram travel. Packing pressure affects the final part and can be used effectively in controlling sink marks and shrinkage. It should be applied and maintained until the gate area is completely frozen off.

Back pressure can be utilized to provide uniform melt consistency and reduce trapped air and gas.

**Processing**  
Fast fill rates are recommended to ensure uniform melt delivery to the cavity and prevent premature freezing. Surface appearance is directly affected by injection rate.

**Note**  
Although all statements and information in this publication are believed to be accurate and reliable, they are presented gratis and for guidance only, and risks and liability for results obtained by use of the products or application of the suggestions described are assumed by the user. NO WARRANTIES OF ANY KIND, EITHER EXPRESS OR IMPLIED, INCLUDING WARRANTIES OF MERCHANTABILITY, FITNESS FOR A PARTICULAR PURPOSE, OR NON-INFRINGEMENT, ARE MADE. THE USER ASSUMES ALL RISK OF INJURY OR DAMAGE TO PERSONS OR PROPERTY FROM THE USE OF THE PRODUCTS DESCRIBED OR DESIGNS, DATA OR INFORMATION SET FORTH. SUGGESTIONS OR RECOMMENDATIONS CONCERNING POSSIBLE USE OF THE PRODUCTS ARE MADE WITHOUT REPRESENTATION OR WARRANTY THAT ANY SUCH USE IS FREE OF PATENT INFRINGEMENT AND ARE NOT RECOMMENDATIONS TO INFRINGE ANY PATENT. THE USER SHOULD NOT ASSUME THAT TOXICITY DATA AND SAFETY MEASURES ARE INDICATED OR THAT OTHER MEASURES MAY NOT BE REQUIRED.

**BASF Corporation**  
Engineering Plastics  
1609 Biddle Avenue  
Wyandotte, MI 48192

**General Information: 800-BC-RESIN**  
Technical Assistance: 800-527-TECH (734-324-5150)  
Web address: <http://www.plasticportal.com/usa>

Page 2 of 2







A.1.12. EOSINT P800



## EOSINT P 800

**The first laser-sintering system world-wide operating at up to 380°C processing high performance polymers**

**The technology:**  
**Laser-sintering - the key to e-Manufacturing**  
 Laser-sintering is well known as the technology of choice for producing the earliest route from product idea to market launch. Innovative companies from a broad range of industries are using this technology for e-Manufacturing – the fast, flexible and cost-effective production directly from electronic data for every phase of the product life cycle.

**The system:**  
**e-Manufacturing with high performance polymers**  
 The system is based on the technically sophisticated and proven

developed to satisfy the requirements for exciting, fast-acting and flexible, yet already available, technologies. The requirements for high performance polymers are laser-sintered (EOSINT P 800) but, hitherto, the system is limited to 200°C, which allows the construction of parts with very good performance characteristics. All the conventional advantages of laser-sintering are retained. The material used, the necessary temperatures and the resulting product characteristics are, however, a lot (usually) lighter than that found with polyamides. The construction of fully functional, directly finished parts was further

developed to satisfy the requirements for exciting, fast-acting and flexible, yet already available, technologies. The requirements for high performance polymers are laser-sintered (EOSINT P 800) but, hitherto, the system is limited to 200°C, which allows the construction of parts with very good performance characteristics. All the conventional advantages of laser-sintering are retained. The material used, the necessary temperatures and the resulting product characteristics are, however, a lot (usually) lighter than that found with polyamides. The construction of fully functional, directly finished parts was further

developed to satisfy the requirements for exciting, fast-acting and flexible, yet already available, technologies. The requirements for high performance polymers are laser-sintered (EOSINT P 800) but, hitherto, the system is limited to 200°C, which allows the construction of parts with very good performance characteristics. All the conventional advantages of laser-sintering are retained. The material used, the necessary temperatures and the resulting product characteristics are, however, a lot (usually) lighter than that found with polyamides. The construction of fully functional, directly finished parts was further



## EOSINT P 800

**The technology:**  
**Laser-sintering - the key to e-Manufacturing**  
 Laser-sintering is well known as the technology of choice for producing the earliest route from product idea to market launch. Innovative companies from a broad range of industries are using this technology for e-Manufacturing – the fast, flexible and cost-effective production directly from electronic data for every phase of the product life cycle.

**The system:**  
**e-Manufacturing with high performance polymers**  
 The system is based on the technically sophisticated and proven

developed to satisfy the requirements for exciting, fast-acting and flexible, yet already available, technologies. The requirements for high performance polymers are laser-sintered (EOSINT P 800) but, hitherto, the system is limited to 200°C, which allows the construction of parts with very good performance characteristics. All the conventional advantages of laser-sintering are retained. The material used, the necessary temperatures and the resulting product characteristics are, however, a lot (usually) lighter than that found with polyamides. The construction of fully functional, directly finished parts was further

developed to satisfy the requirements for exciting, fast-acting and flexible, yet already available, technologies. The requirements for high performance polymers are laser-sintered (EOSINT P 800) but, hitherto, the system is limited to 200°C, which allows the construction of parts with very good performance characteristics. All the conventional advantages of laser-sintering are retained. The material used, the necessary temperatures and the resulting product characteristics are, however, a lot (usually) lighter than that found with polyamides. The construction of fully functional, directly finished parts was further

developed to satisfy the requirements for exciting, fast-acting and flexible, yet already available, technologies. The requirements for high performance polymers are laser-sintered (EOSINT P 800) but, hitherto, the system is limited to 200°C, which allows the construction of parts with very good performance characteristics. All the conventional advantages of laser-sintering are retained. The material used, the necessary temperatures and the resulting product characteristics are, however, a lot (usually) lighter than that found with polyamides. The construction of fully functional, directly finished parts was further

## A.2. Research methodology

### A.2.1. Morphology

#### A.2.1.1. Scanning electron microscopy (SEM images)

A scanning electron microscope is a type of electron microscope that produces images of a sample by scanning the surface with a focused beam of electrons.

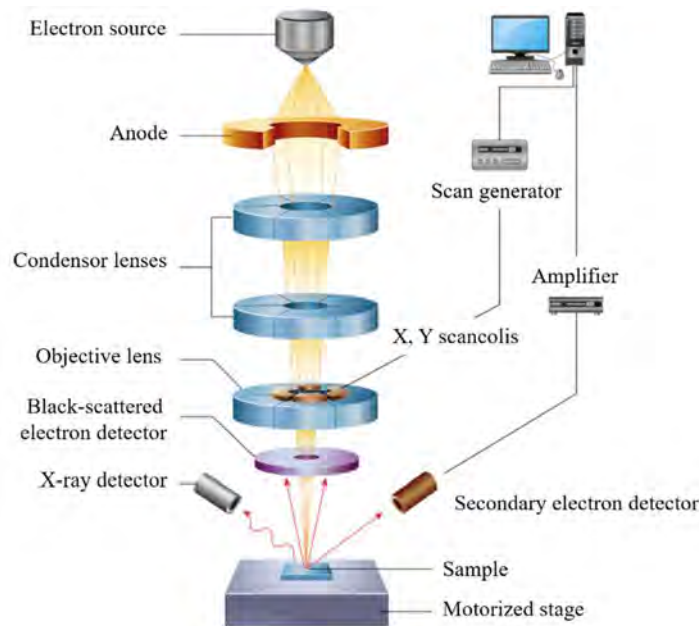


**Figure A.1. Scanning electron microscopy scheme**

The scanning electron microscopy examination of powder materials was performed with an EVO HD 15 LS by the ZEISS microscope. A small amount of powders was provided under the microscope to the pressurized chamber of 30 Pa. The electron secondary imaging was set with an accelerating voltage of 10 kV. Scanning electron microscopy creates magnified images of powders by scanning their surfaces with electrons, rather than light waves. A detector counts these electrons and sends the signals to an amplifier. The final image is built up from the number of electrons emitted from each spot on the sample.

#### A.2.1.2. ImageJ (circularity and shape ratio)

The shape analysis was carried out by using the image processing program ImageJ. The software is capable of evaluating the shape descriptors on specimen images. The SEM images were used and processed according to the following procedure:

- setting the scale from the original image (Figure A.2.a). It is defined with the tool line of the tool “Set Scale”. Then the contrast of the image is adjusted to bring out the grains and have a thinner histogram (Figure A.2.b);





The particles analysed were not overlapping and not lying on the edges of the image.

The particle shape analysis was carried out to quantitatively evaluate the shape of particles constituting selective laser sintering powders and potential new grades. Scanning electron microscopy images of the particles with the aid of the ImageJ software were used in this analysis. The circularity is obtained by the Equation A.1.

$$\text{Circularity} = \frac{4\pi A}{p^2} \quad (\text{A.1})$$

where:

- A - area of the analysed particle [ $\mu\text{m}^2$ ];
- p - perimeter of analysed particle [ $\mu\text{m}$ ].

The circularity is a dimensionless ratio between 0 and 1 characterizing the geometrical resemblance of a grain with a circle. It is possible to evaluate the morphological state of the particles, the closer it gets to 1, that means the particle is circular.

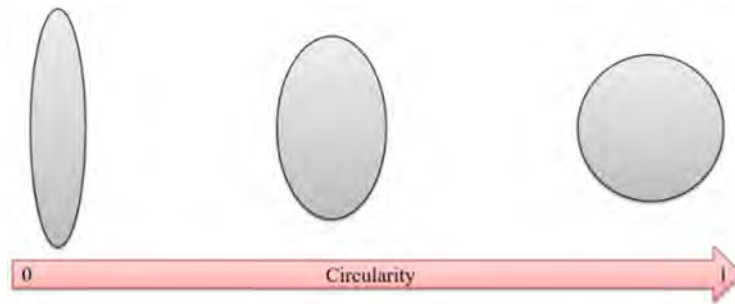


Figure A.3. Circularity of powder

The shape ratio is defined as the ratio between the maximal and minimal fiber diameters. The diameters of fiber are the diameters obtained by surrounding the grain by two parallel straight lines. When the lines are rotated around the grain, maximum value and minimum value are defined. This ratio of shape makes it possible to quantify the shape anisotropy of particle, that is to say if it is more or less elongated. The shape ratio is presented by Equation A.2.

$$\text{Shape ratio} = \frac{dF_{\max}}{dF_{\min}} \quad (\text{A.2})$$

where:

- $dF_{\max}$  - maximum Ferat diameter also called exo-diameter [ $\mu\text{m}$ ];
- $dF_{\min}$  - minimum Ferat diameter also called meso-diameter [ $\mu\text{m}$ ].

Values close to 1 indicate the presence of equated particles that can correspond to different shapes, such as circles, squares, overall circular polygons; while higher values identify highly elongated particles.

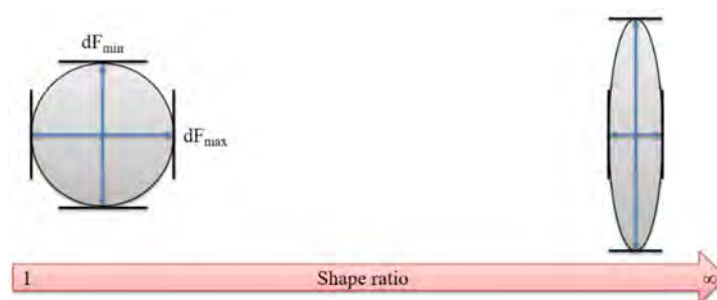


Figure A.4. Shape ratio of powder

Average values and standard deviations of main shape descriptors are reported along with their distribution.

#### A.2.1.3. Laser granulometry (particles size distribution)

Laser diffraction analysis is a technology that utilizes diffraction patterns of a laser beam passed through any object ranging from nanometers to millimetres in size to quickly measure geometrical dimensions of a particle. This process does not depend on the volumetric flow rate and the number of particles that pass through a surface over time.

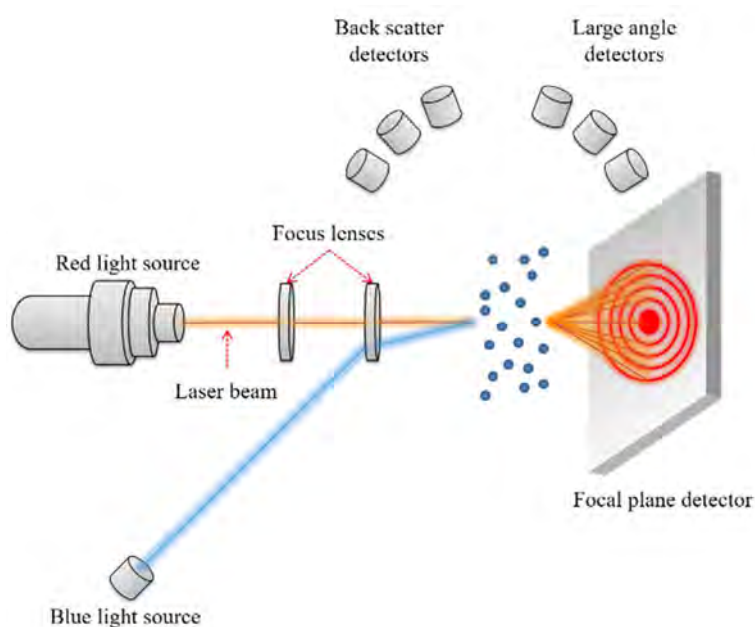


Figure A.5. Laser granulometry scheme

Laser granulometry measurements were therefore carried out using an apparatus LA-950V2 by HORIBA (Rhonatec - 3D Materials). The particle size detected ranges are from 100 nm to 3000  $\mu\text{m}$ . The process was carried out in water and ethanol as media with 1 min of

ultrasonic waves. It is well known that the fine powders can occur the problem of aggregation of fine particles and the granulometry data can reflect the aggregate size instead of particle size. The most widely used method to describe particle size is D values. The D<sub>10</sub>, D<sub>50</sub>, and D<sub>90</sub> are commonly used to represent the midpoint and range of particle size distribution of given powder.

#### **A.2.1.4. Wide-angle X-ray diffraction (WAXS)**

Wide-angle x-ray diffraction tests (WAXS) reveal the periodicities that may exist in a material. Thus, the x-ray diffraction spectrum of a semi-crystalline polymer exhibits diffraction lines, characteristic of the crystalline phase, superimposed on a diffuse halo, characteristic of the amorphous phase. The position of the lines allows us to deduce the crystalline structure. Their areas are equally interesting because they tell us about the degree of crystallinity given by the equation:

$$X_c = \frac{\text{Total area of crystalline peaks}}{\text{Area of crystalline lines} + \text{Area of diffuse halo}} \cdot 100 \% \quad (\text{A.3})$$

The analyses were carried out with a Philips PW 1700 diffractometer in reflection mode and for a CuK<sub>α</sub> radiation source.

The advantage of this method is that it is absolute, it is done without calibration. Besides, the analysis does not require heating, which makes it possible not to introduce hypothetical spherulite reorganizations during the measurement. However, the definition of the amorphous halo remains a factor of inaccuracy for the determination of the crystallinity rate.

### **A.2.2. Flowability**

#### **A.2.2.1. Angular measurement (angle of repose)**

The method is very simple, fast and has been the subject of standard ASTM C 1444 [313]. However, some modifications were introduced: as the powders did not flow through the funnel if the funnel was completely filled. Thus, the powder was added in a small amount, so that it could flow with small impact on the funnel, Figure A.6.a. At first, the dried powder was sieved with a sieve of 180 μm size, to avoid any agglomerate, and after the powder heap was put in the funnel, next it was released and allowed to flow freely to give a distance to a sheet of paper on the plate base (about 39 mm). The pile of powder forms and then collapses successively as the pouring takes place until the tip of the powder cone forming on the base plate enters the funnel nozzle.

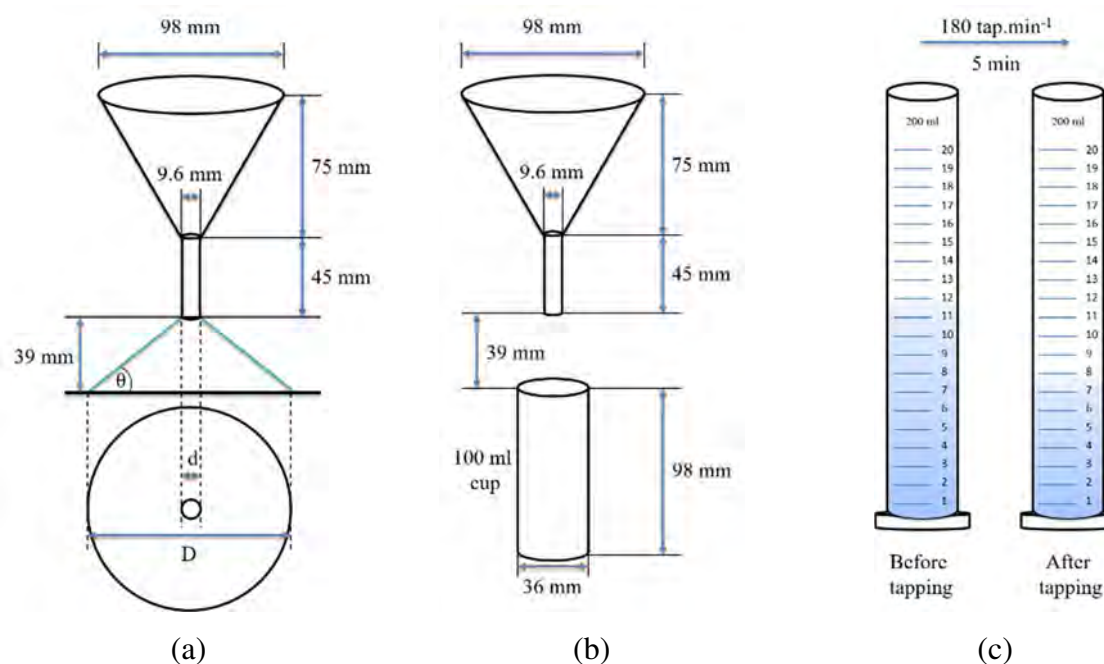


**Figure A.6. Measuring apparatus of (a) angle of repose (b) bulk density (c) tapped density**

The calculation of angle of repose was done with the Equation A.4.

$$\theta = \tan^{-1} \left( \frac{2H}{D - d} \right) \quad (\text{A.4})$$

where:

- $\theta$  - angle of repose [°];
- H - height of cone [cm];
- D - diameter of the pyramid [cm];
- d - internal diameter of funnel nozzle [cm].

The measurement was repeated at least three times to obtain the average value and standard deviation.

#### **A.2.2.2. Aptitude for settlement (Carr index and Hausner ratio)**

Both the Hausner ratio and the Carr index are correlated to the flowability of a powder.

The interparticle cohesion forces are possible to be described by measuring the capacity of the granular medium to density with a packing apparatus, according to standard ASTM D 1895-96 [314]. The bulk density is defined as the mass per unit volume of material, including the intergranular voids of material being tested. To measure it, the material used is shown in Figure A.6.b, it consists of a cylindrical vessel with a capacity of exactly 100 ml and the funnel with an opening diameter of 9.6 mm mounted at 39 mm above the measuring vessel.

The measurement procedure is as follows:

- clog the opening of the funnel with the hand or a sheet of paper and then pour a volume of 115 ml of powder. Release the opening and allow the powder to flow freely or with small impact into the cylindrical container;
- once all the powder has drained into the container, scrape the excess without stirring and weigh the amount of powder contained in the container. Finally, calculate the mass in grams of 1 cm<sup>3</sup> of the powder.

The tapped density is an increased bulk density attained after tapping a container containing the powder sample, according to standard ISO 23145-1 [315]. Tapped density is obtained by tapping (approximately 180 taps.min<sup>-1</sup>) a graduated measuring cylinder containing a packed powder, Figure A.6.c. After observing the initial powder volume, the measuring cylinder is tapped and volume readings are taken until little further volume change is observed. The tapping is achieved by raising the cylinder and allowing it to drop under its weight a specified distance.

The two analyses that were carried out to explain these results are those proposed by Carr [177] and Hausner [316]. To obtain more information from these successive densification measurements, it is possible to calculate in based on the bulk density and the tapped density, the Carr index, the Equation A.5.

$$CI = \left( \frac{\rho_{\text{tap}} - \rho_{\text{bulk}}}{\rho_{\text{tap}}} \right) \times 100 \% \quad (\text{A.5})$$

and the Hausner ratio, the Equation A.6.

$$HR = \frac{\rho_{\text{tap}}}{\rho_{\text{bulk}}} \quad (\text{A.6})$$

where:

- CI - compressibility index [%];
- HR - Hausner ratio [-];
- $\rho_{\text{tap}}$  - tapped density [g.cm<sup>-3</sup>];
- $\rho_{\text{bulk}}$  - bulk density [g.cm<sup>-3</sup>].

The measurement was repeated at least three times to obtain the average value and measurement error.



### A.2.3. Chemical analysis by Fourier transform infrared spectroscopy (FT-IR)

Fourier-transform infrared spectroscopy is a technique used to obtain an infrared spectrum of absorption or emission of a solid, liquid or gas. An infrared spectrometer simultaneously collects high-spectral-resolution data over a wide spectral range. This confers a significant advantage over a dispersive spectrometer, which measures intensity over a narrow range of wavelengths at a time.

All infrared transmission spectra were recorded using a PerkinElmer Fourier transform spectrometer in the 4000-650  $\text{cm}^{-1}$  range. The resolution was 4  $\text{cm}^{-1}$  with the maximal retardation of 0.25 cm, and 8 scans were accumulated for an improved signal to noise ratio. A powder was put on a beam of infrared light for the measurement. The test has been done three times for each sample. The infrared spectrum is essentially a graph of infrared light transmittance on the vertical axis versus wavelength on the horizontal axis.

### A.2.4. Thermal properties

#### A.2.4.1. Differential scanning calorimetry (DSC)

Differential scanning calorimetry is a thermoanalytical technique in which the difference in the amount of heat required to increase the temperature of a sample and reference is measured as a function of temperature. Both the sample and reference are maintained at nearly the same temperature throughout the experiment. Generally, the temperature program for a DSC analysis is designed such that the sample holder temperature increases linearly as a function of time.

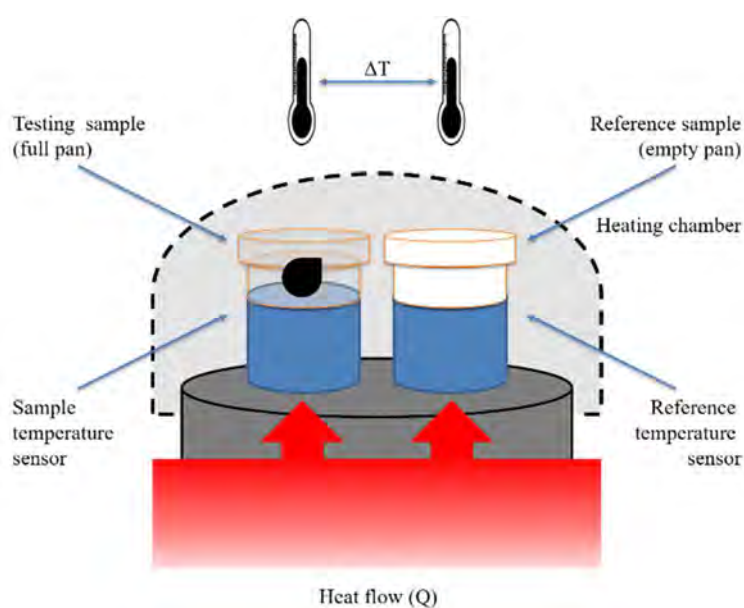


Figure A.7. Differential scanning calorimetry scheme

The apparatus used is the DSC Q200 from Thermal Analysis Instruments. It is equipped with an independent cooling unit (RCS) which allows the sequence of heating and cooling cycles. The measurements were carried out under nitrogen sweep  $50 \text{ ml}\cdot\text{min}^{-1}$  and for heating and cooling rates of  $10 \text{ }^\circ\text{C}\cdot\text{min}^{-1}$  from ambient temperature to  $300 \text{ }^\circ\text{C}$  for polyamide and  $450 \text{ }^\circ\text{C}$  for polyetheretherketone. The analyzes are carried out under inert gas to avoid any reaction of the material as well as the early ageing of the interior of the thermoregulated enclosure. A mass of 8 mg to 10 mg of the solid disc, powder in the molten state is placed in aluminium crucibles closed.

#### **A.2.4.2. Thermogravimetric analysis (TGA)**

The thermogravimetry is an analytical technique used for the study of thermal degradation phenomena on materials. The test shows the weight loss of the sample when exposed to a user-defined thermal program. The results can be interpreted versus time or temperature. The curves were obtained in the thermobalance, Shimadzu model TGA-50, using platinum crucibles under conditions of air, sample mass about 10-15 mg and heating rate at  $10 \text{ }^\circ\text{C}\cdot\text{min}^{-1}$  in the range from  $25 \text{ }^\circ\text{C}$  to  $630 \text{ }^\circ\text{C}$  and rate at  $20 \text{ }^\circ\text{C}\cdot\text{min}^{-1}$  in the range from  $630 \text{ }^\circ\text{C}$  to  $750 \text{ }^\circ\text{C}$ . The thermogravimetric analysis measures the amount and rate of change in the mass of the sample (remove coating layer of the surface) as a function of temperature or time in a controlled atmosphere.

#### **A.2.4.3. X-ray tomography (XRT)**

The X-ray tomography is a radiographic imaging technique that can produce images of the material internal structure at a spatial resolution better than  $1 \text{ }\mu\text{m}$ .

The X-ray tomography Easytom 150 by RX Solution was used to measure the volume fraction of air in the powder by taking about 600 tomographic section images. By combining them and comparing the different grey levels, the percentage of air is given for a certain density of powder.

#### **A.2.4.4. Hot disc (thermal conductivity and heat capacity)**

The thermal conductivity and heat capacity of plastic material is the measure of its ability to conduct heat. The absolute hot disk method with TPS 2500 S has been applied for calculation. This flexible method merely requires one or two pieces of the sample in question to test, each with no more than one flat surface where the sensor can be used. A probe composed of two nickel turns is placed between two samples of the same nature. The medium is considered almost infinite and isotropic.



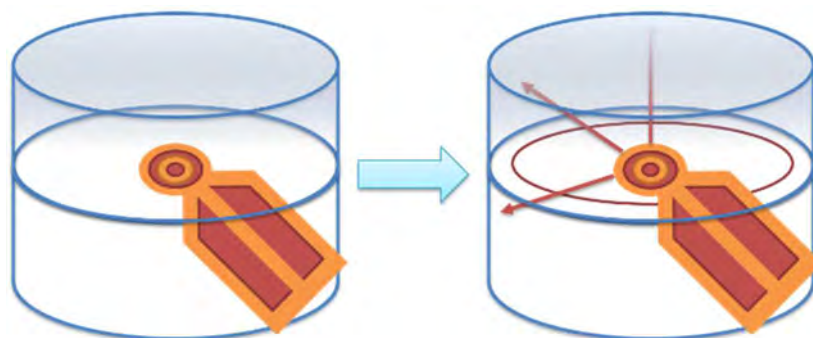


**Figure A.8. Experimental device for measuring conductivity**

During the test, an electric power is delivered for a given time. By Joule's effect, the probe emits heat that diffuses in both samples homogeneously. As the temperature increases, the electrical resistance of the probe may change over time. The increase of temperature and thus the variation of electrical resistance of probe depends, among other things, on the thermal conductivity of the sample. The resistance of probe according to time is determined as follows:

$$R(t) = R_0 [1 + \alpha \overline{\Delta T(\tau)}] \quad (\text{A.7})$$

with:

$$\tau = \sqrt{\frac{at}{d^2}} \quad (\text{A.8})$$

where:

- $R(t)$  - electrical resistance [ $\Omega$ ];
- $R_0$  - electrical resistance of probe at the start of a test [ $\Omega$ ];
- $\alpha$  - resistance coefficient of the probe [ $\text{K}^{-1}$ ];
- $\Delta T(\tau)$  - average value of temperature increase according to time [ $\text{K}^{-1}$ ];
- $\tau$  - temporal time [s];
- $a$  - thermal diffusivity of sample [ $\text{mm}^2 \cdot \text{s}^{-1}$ ];
- $d$  - diameter of the sample [mm].

The measurement was repeated at least three times to obtain the average value and measurement error.

This method allows for obtaining thermal conductivity and heat capacity of samples in powder or solid-state.

### A.2.5. Rheological and dynamic mechanical properties

The viscosity measurements were obtained by using an Anton Paar rheometer model MCR 302 or ARES LN2 rheometer. To perform the rheometric tests, the discs of 25 mm diameter and 2 mm thickness were used (Figure A.9.a). The disc is placed on the lower plate with the fixed temperature, such as 350 °C, 366 °C, 383 °C and 400 °C for PEEK and 200 °C, 220 °C and 240 °C for PA polymers. Once the polymer has been melted, a few minutes of waiting are necessary to allow a maximum of air trapped in the liquid to escape and come back to the stable temperature. To limit these diffusion and convection phenomena in time, small thickness of polymer is used and the measurements are carried out for a melted polymer thickness of approximately 2 mm.

To study the effect of recycled powder on prints, a mould was designed to create from fresh and recycled PA12 powders disks without the need for a 3D printer. The mould can create a disk of 25 mm in diameter and  $2.0 \pm 0.2$  mm in the thickness of the material. The heating temperature is at most 400 °C. The mould was created with Catia V5R19 software. To create a sample, a foil sheet is inserted between the holder and the ring. The foil prevents the sample from sticking to the support. Then the ring and the support are screwed together then the centre of the ring is filled with powder. Then a sheet of foil is put on the powder layer and the rod is put in place. The mould is then pressurized with a pressure of 5 t, this step allows to remove a maximum of air and reduce the number of residual air bubbles. The solid mould is put in an oven at 230 °C for 2 hrs. Before the temperature sweep test, the strain sweep test has been carried out to determine the linear viscoelastic domain of the PA and PEEK materials.

The rheology tests make it possible to identify two main values: the storage modulus ( $G'$ ) characterizing the elastic behaviour of sample and the loss modulus ( $G''$ ) characterizing the viscous behaviour of the polymer. With its two modules, the complex viscosity is calculated:

$$\eta^* = \frac{\sqrt{(G')^2 + (G'')^2}}{\omega} \quad (\text{A.9})$$

where:

- $\eta^*$  - complex viscosity [Pa.s];
- $G'$  - storage modulus [Pa];
- $G''$  - loss modulus [Pa];
- $\omega$  - angular frequency [rad.s<sup>-1</sup>].

To operate, the rheometer applies shear to the sample, the mechanical response of the sample is measured and the flow properties are thus deduced. Measures the mechanical properties of a sample as it is deformed over a range of stress, strain, time and temperature:

- can either apply stress (force) and measure strain (displacement), or apply strain and measure stress;
- determines the modulus of the material (stress/strain);
- controls the frequency (time) of the deformation to measure viscoelastic properties (storage modulus, loss modulus, loss factor);
- temperature-controlled in heating, cooling or isothermal modes.

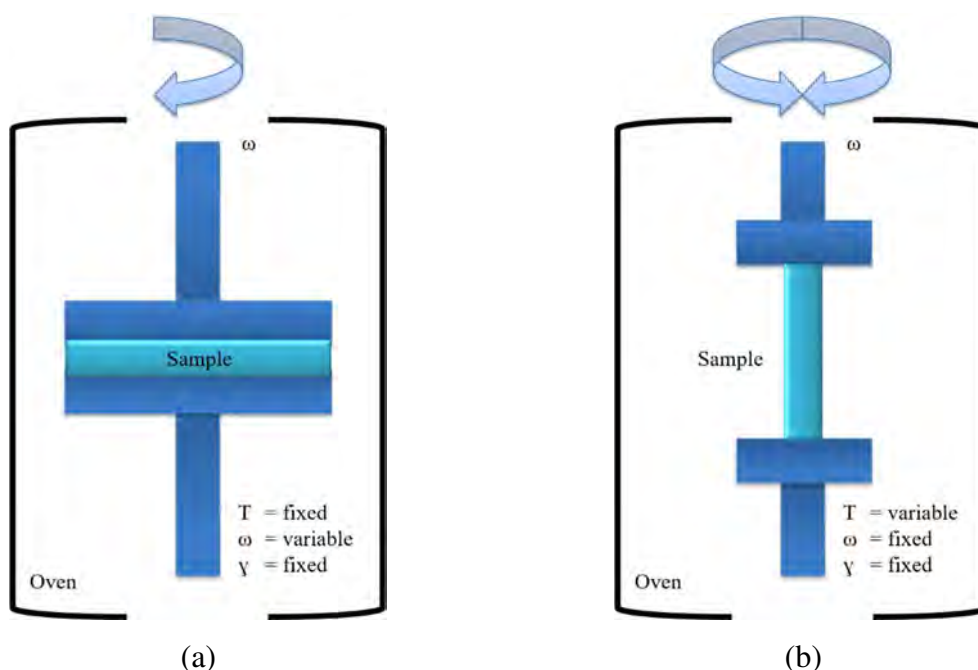


**Figure A.9. Schematization of rheometer and sample in (a) molten state (b) solid-state**

The thermo-mechanical properties were performed by dynamic mechanical thermal analysis using ARES LN2 rheometer. The plate specimens of 45 mm x 10 mm x 2 mm were prepared out of pressed moulded plates. The samples have been then tested in torsion mode at a frequency of 1 Hz and a heating rate of 3 °C.min<sup>-1</sup> over the temperature from 25 °C to 325 °C. These tests were carried out through rectangular scanning, that is to say, that the sample was fixed between two jaws, the lower part of which performs a slight rotation, which may represent the sinusoidal stress. The dynamic mechanical testing (Figure A.9.b) measures raw instrument signals such as force, displacement and stiffness:

$$\text{Stress [Pa]} = \frac{\text{Force [N]}}{\text{Area [m}^2\text{]}} \quad (\text{A.10})$$

Dimensions of the samples are recorded such as length, width and thickness:

$$\text{Strain} = \frac{\text{Deformation [m]}}{\text{Length [m]}} \quad (\text{A.11})$$

The software calculates mechanical parameters such as stress, strain and modulus:

$$\text{Modulus [Pa]} = \frac{\text{Stress [Pa]}}{\text{Strain}} \quad (\text{A.12})$$

The elastic (storage) modulus measures of elasticity of the material. The ability of the material to storage energy:

$$G'[\text{Pa}] = \left( \frac{\text{Stress [Pa]}}{\text{Strain}} \right) \cos\delta \quad (\text{A.13})$$

The viscous (loss) modulus is the ability of the material to dissipate energy. The energy lost as heat:

$$G''[\text{Pa}] = \left( \frac{\text{Stress [Pa]}}{\text{Strain}} \right) \sin\delta \quad (\text{A.14})$$

The loss factor measures of material damping such as vibration or sound damping:

$$\tan\delta = \left( \frac{G''}{G'} \right) \quad (\text{A.15})$$

Torsion and dynamic mechanical analysis geometries allow solid samples to be characterised in a temperature controlled environment.

### A.3. Preparation of blends

#### A.3.1. Process 11 parallel twin screw extruder

Created by Thermo Fischer Scientific (USA), a service company for science, researchers, clinical research, process engineers, and many other industrial and manufacturing sectors, the Process 11 is a unique and flexible twin-screw extruder, as seen on Figure A.10.



Figure A.10. Twin-screw extruder Process 11

This machine optimizes the expenditure of time, money and requires only a small amount of material to perform experiments and thus ensure the completion of many tests in an efficient and cost-effective manner. This type of device is mainly used in the fields of polymers, additives, adhesives, food or cosmetics. Below a list of few features of this extruder is presented:

- reduced use of sampling materials (20 g);
- performance range between 20 g.h<sup>-1</sup> and 2.5 kg.h<sup>-1</sup>;
- easily transportable, very small footprint;
- easy to use the touch screen with built-in power control;
- max rotation speed of screws is 1000 rpm;
- max temperature is 350 °C.

The general operation of Process 11 is quite simple. A volumetric feeder serves the material, granular or powder, in the extruder where the two screws are located. It may then be heated and driven, through these screws into the hopper to be finally extruded as a filament through the die.

There are a total of eight heating zones along with the screws, all adjustable at different temperatures, although in general the same temperature is applied for all zones. The screws are a width of 11 mm. They are composed of different elements assembled on a metal rod in a precise order, Figure A.11. The screws consist of two different zones: the conveying zones and the mixing zones. As its name indicates, the conveying zones are used to transport the material to the die. They do not require special mounting, unlike mixing zones. These areas are used to “grind” the material which has been already heated in the conveying areas located at the end of screws. The elements that constitute the mixing zones are called mixing elements. There are two different types of them, the mixing element  $0^\circ$  and the mixing element  $90^\circ$ . The arrangement of mixing elements may also be adapted to the type of material which is extruded.

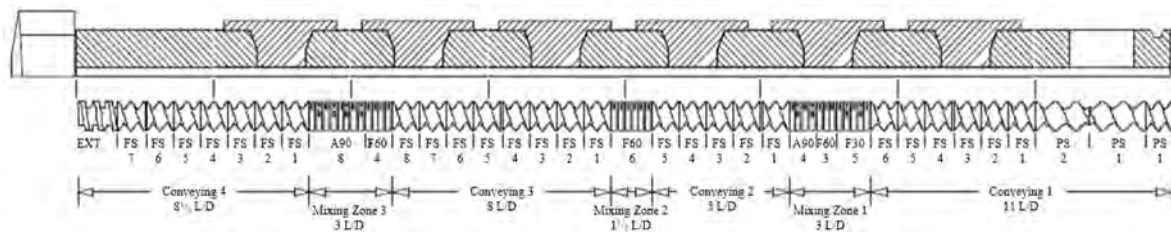


**Figure A.11. Screw arrangement for PEEK**

The representations of mixing elements on the mixing zones already indicate whether it is a  $0^\circ$  or  $90^\circ$  element. Then, the indications A90, F60 or F30 correspond to the angle between the different elements. An indication F30, for example, requires that when one element was put on the metal rod, the next one must be shifted by  $30^\circ$  relative to the previous one. Finally, once a first screw is properly completed the second one by putting all the elements at  $90^\circ$  is prepared. Once installed, the control panel allows them to turn on and adjust the speed of rotation.

The feeders are the devices that allow the material to enter the extruder. Process 11 consists of two feeders: a volumetric feeder and a weighted dispenser. The volumetric feeder is placed directly at the entrance of extruder. It can carry powders or granules and composed of feed hopper that can contain several hundred grams of material. The powder or granules are then transported and pushed into the hopper where the parallel-twin screw is located using the feed screw, operating in much the same manner as the conveying zones previously mentioned. The flow of this screw is directly adjustable on the control panel.

The gravimetric feeder is used for applications where small amounts of product need to be fed. Unlike the volumetric feeder, it works with a double screw system. The material is introduced into the hopper and from there it is fed into the agitator tank, where an agitator rotates vertically. The agitator allows an improved and more uniform filling ratio of the double

screw. These transport the material to the outlet of the device, where it falls freely into the extruder. The big advantage of weighing dispenser is that it can automatically calculate its flow rate according to the apparent density of the material and a given duration. It allows constant control of product weight and flows for precise dosing. To be able to calibrate this metering device, however, a large amount of material is needed.

The die is the element at the end of the extruder. Parallel twin screws may serve the material into the die, and extrude the polymer as a filament. It is also accompanied by a pressure sensor that connects to its upper end.

Finally, the last important element of Process 11 is the cooler. It is an indispensable device for the proper functioning of the extruder as well as for the safety of the user. As the name suggests, it takes care of cooling the electrical circuit present in the cabin. Requiring no water supply, it is easily transportable and filled directly by hand with distilled water.

### **A.3.2. Micro compounder 15 HT**

Micro-compounding refers to the mixing or processing of polymer formulations in the melt on a very small scale, typically several millilitres. It gives faster, yet reliable results with much smaller samples and at much fewer investment costs, thus speeding up the innovation process of polymer materials. The micro compounder has a capacity of 15 ml of material, it is the ease of use and robustness. It is a unique asset for you in the development of new material compound formulations: a full-fledged material processing instrument for plastic and rubber materials that fit on the laboratory bench or in the fume cupboard.



**Figure A.12. Micro compounder 15 HT**

Below a list of few features of this extruder is presented:

- double rotation speed of screws in a range from 1 rpm to 500 rpm (finer dispersion, better mixing, easier to scale up);
- more than double screw torque of 40 Nm at nearly all rpm (more stable extrusion rate);
- control over throughput improved the dimensional stability of spun filaments and cast films;
- stronger motor drive, the possibility of mixing higher viscous compounds;
- less than half the footprint, lower housing (easier to move and install in a fume hood);
- stiffer housing (less wear of screws and barrel, longer lifetime, less maintenance);
- easy to work with, to install add-ons (film or fiber line) and to maintain;
- the max operating temperature of 450 °C.

With 40 Nm of torque processing rubbers and elastomers becomes easy, even with fully intermeshing screws, which have better mixing capabilities than a tangential mixer, commonly used in rubber mixing. As a result, every volume has the same properties, as opposed to a tangential screw design.



## A.4. Print of specimens (machine/material pairs)

### A.4.1. The sPro230 SLS and Duraform PA12

The sPro230 SLS [317] machine shares a common architecture to produce high-resolution (layer thickness range of 0.08-0.15 mm) durable thermoplastic parts available in medium to large build volumes. It is a large and modern production printer that works in one of the most modern systems, such as digital imaging. The printer uses a digital imaging system to accurately build large parts, as the maximum build envelope capacity (X x Y x Z) is 550 mm x 550 mm x 750 mm with an inert atmosphere by nitrogen. The volume build rate is estimated at 3 l per hour.

The printer automatically feeds the powder and creates a model by laser sintering with a polyamide powder. Its unquestionable advantage is the fact that production control, from the beginning to the very end (Figure A.13.a), is carried out using intuitive software. The sPro230 SLS printer is widely used. It can be used both for printing individual guides for medical drills as well as for interior and prototypes in the automotive and aviation industry. It has also found its application in the production of consumer goods, more precisely in the printing of a series of casings for mobile devices.



Figure A.13. The sPro230 by 3D Systems

The breakout station presented in Figure A.13.b is used to remove the unsintered polymer powder from the required part. Then the powder is transported to the integrated recycling station and mixed with the fresh material. In this station, the fabricated part is well clean and can be given to the next modifications.

One of the most important elements of this system is the integrated recycling station and intelligent power cartridge (Figure A.13.c), performing the function of both mixing and dosing of material. It is an external (intermediate) system, the material is mixed outside the machine, in which the selective laser sintering process runs and is delivered continuously to the machine.

The mixing station has three storage bins in which there are: the storage tank with primary material, a storage tank with recycled material after the process, a third container with a ready mixture of primary and secondary material, in which they are mixed using a cyclone. The transport of material is forced by compressed air. The basic parameters are pressure  $p_1$  and  $p_2$ . The  $p_1$  value is constant and is responsible for maintaining the material in motion, whereas the  $p_2$  pressure, called high, initiates the movement of material in the form of small packages, which prevents clogging of the installation. The ready mixture is delivered to the production machine over a distance of up to 30 m.

It should be mentioned that one station can supply up to three production machines simultaneously. The advantage of this solution is the continuous supply of material, which allows the use of full production capacity of machines. The disadvantage is the low flexibility of system when it comes to material exchange and difficult control of basic processing parameter, for example: melt flow index, as well as the large inertia of the system, which in the case of a change in mass proportions of primary and secondary material during mixing has a negative impact on production quality [318].

Duraform PA12 is the material for real-world physical testing and functional use. This material has been investigated during this work and the results can be seen in the second chapter, characterization of powders available on the market: PEEK & PA.

#### **A.4.2. The ProX500 SLS and Duraform FR1200**

The ProX500 SLS [319] is a professional three-dimensional printer for selective laser sintering technology from the USA based manufacturer 3D Systems. This three-dimensional printing technique uses a laser as a power source to sinter powdered polymers that creates parts with greater precision, durability, and quality, compared to other printers of this class. Moreover, this machine is easy and economical to use. The compatible polymers are very durable engineering materials from tough nylon for production parts, to high-temperature resistant fibre-reinforced engineering plastic, to glass-filled engineering plastic for excellent stiffness. The compact printer works in tandem with the material Duraform ProX. Thanks to this configuration, the created models have a smoother surface, are more precise than elements produced on the same class of equipment and better than elements created by the spray method. Duraform ProX is 80 % recyclable, making the ProX500 SLS the most economical printer in its class. The machine is ideal for printing prototypes as well as low-volume production, including applications for space, automotive, medical or entertainment purposes, creates usable

parts and does not require additional assembly. Also, the machine is characterized by a high level of material recovery. Up to 95 % of powder can be used, which significantly reduces the cost of manufactured parts and wastes.

The printer is equipped with the print drivers and optional automated material handling module, that streamlines production and recycles of materials. The device has a working area of 381 mm x 330 mm x 457 mm and volume manufacturing speed of 2 l per hour. The large dimensions of the machine at the working area allow printing either large models, whose maximum size of one of the sides is over 40 cm or short series of smaller objects. The standard print mode is characterized by a scanning strategy which can be selected. This could be a “fill” or “fill and outline” option. In the recently developed strategy, the laser beam can scan the entire cross-section with  $12 \text{ m.s}^{-1}$  speed and the contour with a speed of  $3.5 \text{ m.s}^{-1}$ . The process becomes more flexible and better work on outline geometry can be done.



**Figure A.14. The ProX500 by 3D Systems (a) production machine (b) material quality control system**

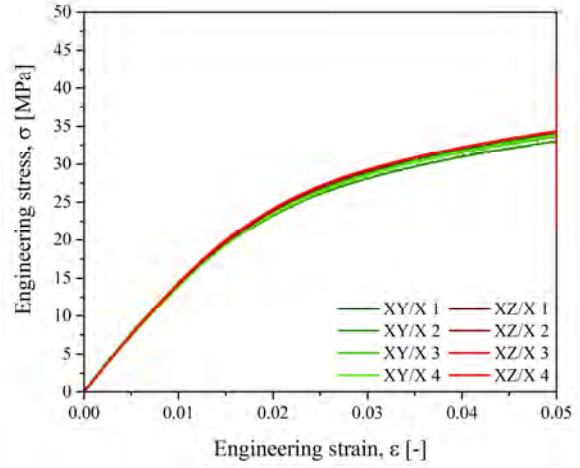
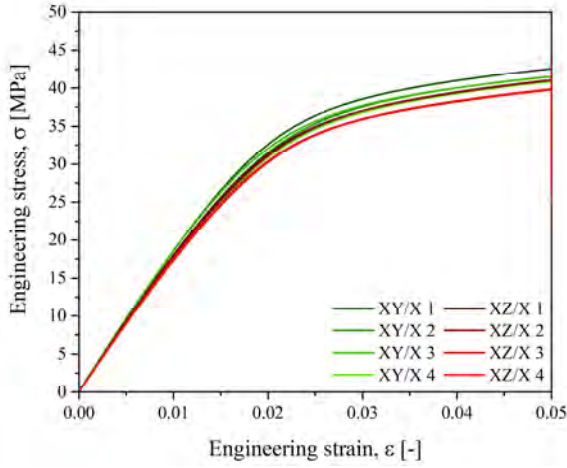
The laser sintering process can be divided into three parts. Warm-up stage preheats the entire bed of the machine in a nitrogen atmosphere just below the melting point of the material used in the process. After, in the build stage, the maximum temperature that ProX500 SLS can reach is  $290 \text{ }^{\circ}\text{C}$ . The  $\text{CO}_2$  laser, with the maximum power heat of 100 W, fuses the particles to produce the part. Then, the roller spreads a new very thin layer between  $80 \text{ }\mu\text{m}$  and  $150 \text{ }\mu\text{m}$  of new powder. The last cooling down stage starts when the process is completed and cools slowly the chamber to  $50 \text{ }^{\circ}\text{C}$ .

Duraform FR1200 delivers highly accurate flame retardant nylon parts with excellent surface quality for aerospace, transportation, and consumer goods applications. The safe smoke density and toxicity allow introducing direct three-dimensional production in aerospace to accelerate part delivery and reduce downtime. Duraform FR1200 is a non-halogenated polyamide 12 material.

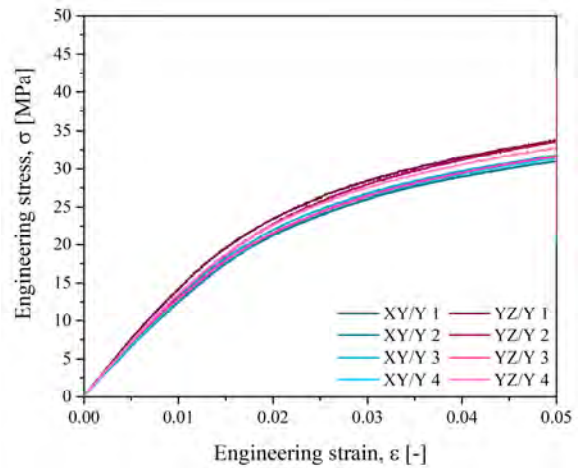
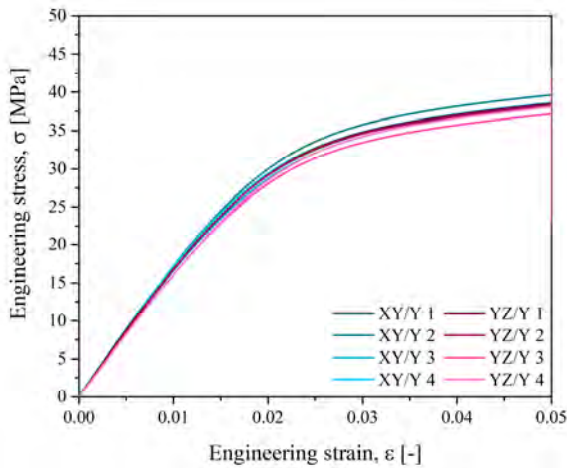
### A.5. Engineering stress-engineering strain curves

#### A.5.1. Diagrams for long and small specimens in each direction of printing

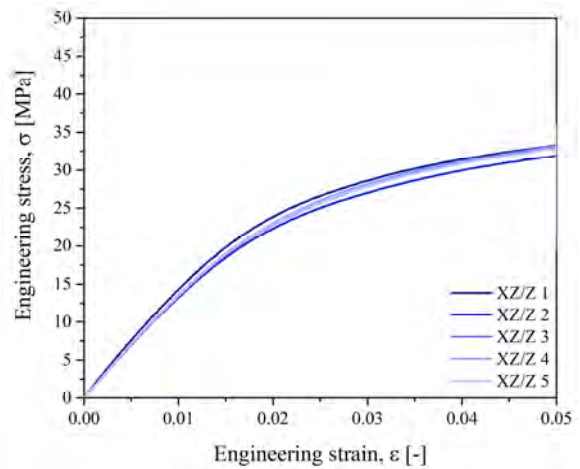
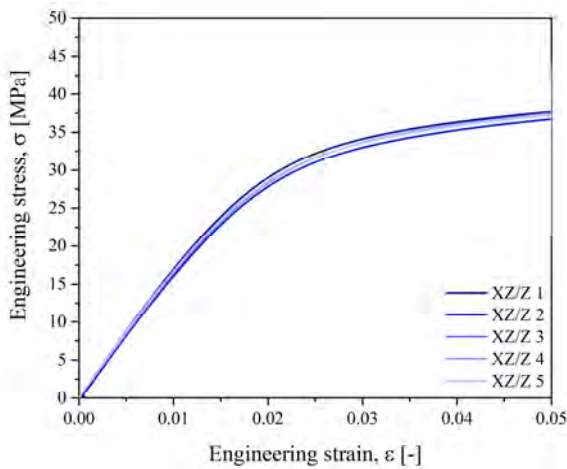
Axis-X



Axis-Y



Axis-Z

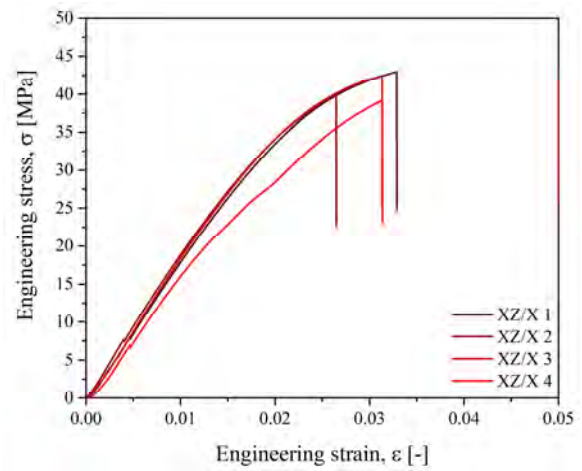
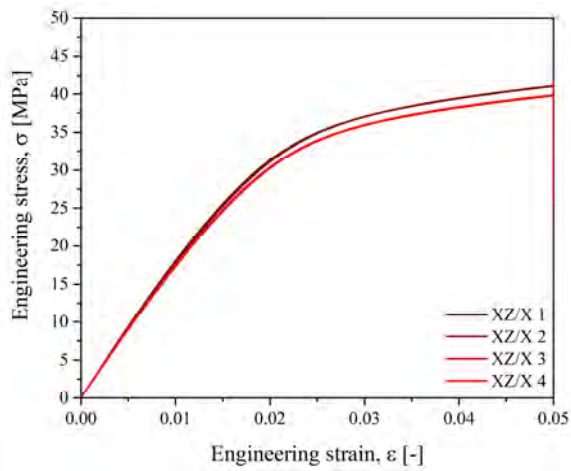


L = 170 mm

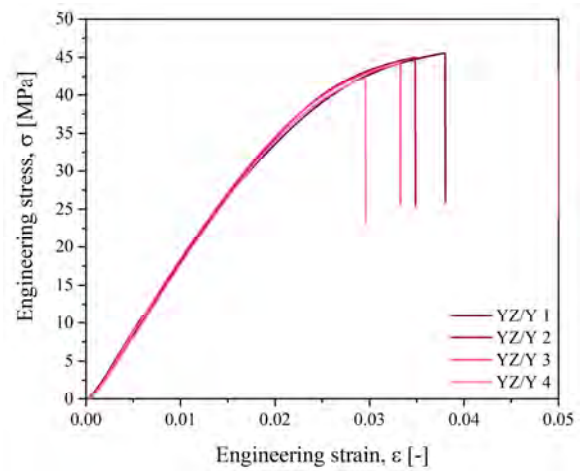
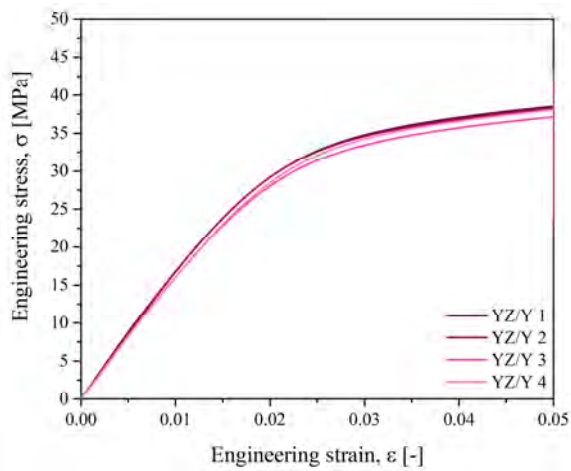
L = 85 mm

## A.5.2. Diagrams for pairs machine/material in each direction of printing

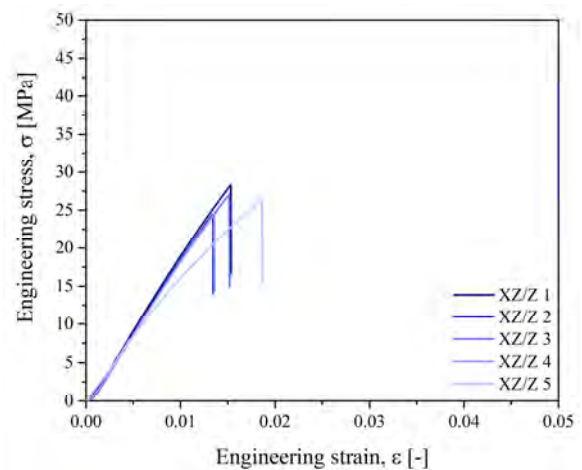
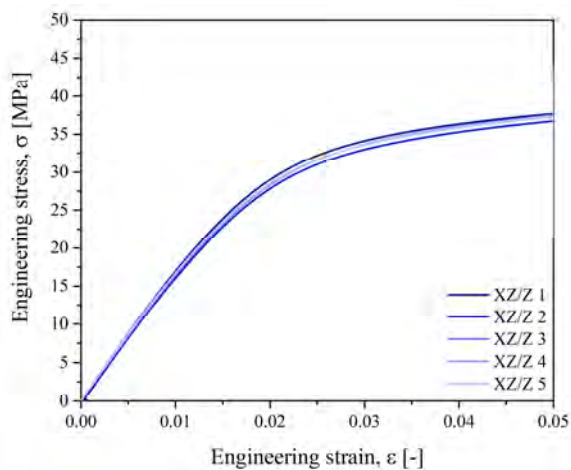
Axis-X



Axis-Y



Axis-Z



sPro230 / Duraform PA12

ProX500 / Duraform FR1200

## A.6. Iconography of correlations

### A.6.1. Positive (green) and negative (red) correlations of average data

A	B	R <sup>2</sup>
LPf	-SCf	0.92
LPf	-TensileS	0.76
SCf	tp	0.88
SCo	EDo	0.80
SS	-EDf	0.65
SS	-LSF	0.68
SS	VSF	0.61
EDo	-TSF	0.80
Dvol	Drel	0.96
Dvol	LSF	0.68
LSF	LST	0.73
TSF	WSF	0.77
TSF	TST	0.84
WSF	VSF	0.83
WSF	WST	0.75
VSF	-tp	0.73
TST	WST	0.70
WST	-tp	0.71
TensileM	-TensileE	0.54
Tc	-Tm	0.72

The isolated, variable without a link are: outline laser power, hydrostatic density, flexural modulus, flexural strength, glass transition temperature and crystallinity. These variables are considered by this method as not remarkable correlations.

**A.6.2. Positive (green) and negative (red) correlations of all the results**

A	B	R <sup>2</sup> in all the results analysis	R <sup>2</sup> in average analysis
LPf	-SCf	0.92	0.92
SCf	tp	0.88	0.88
SCo	EDo	0.80	0.80
SS	-EDf	0.65	0.65
SS	-LSF	0.64	0.68
EDo	-TSF	0.79	0.80
Dvol	FluxeralM	0.74	/
Dvol	FluxeralS	0.68	/
Dhyd	LSF	0.56	/
LSF	LST	0.51	0.73
TSF	WSF	0.60	0.77
TSF	TST	0.74	0.84
TSF	-tp	0.61	/
WSF	VSF	0.77	0.83
VSF	-tp	0.56	0.73
TST	WST	0.57	0.70
WST	-tp	0.59	0.71
FlexuralM	FluxeralS	0.69	/
FlexuralS	-TensileE	0.39	/
TensileM	TensileS	0.58	/
TensileM	Xc	0.47	/
Tc	-Tm	0.72	0.72

/ - the correlations that do not exist in average data

The isolated, variable without a link are outline laser power and glass transition temperature. Thus, the way to use unique value instead of averaging decreases the number of uncorrelated responses.

**A.6.3. Summary of CORICO and regression analysis**

Models of CORICO for 5 regressors	
EDf	$= 1.9 \cdot 10^{-2} + 1.6 \cdot 10^{-2} \text{LPf-SS} + 1.5 \cdot 10^{-2} \text{SCf} \text{]LPf} + 7.8 \cdot 10^{-3} \text{LPf\&-SS}$
<b>R<sup>2</sup></b>	<b>= 0.95</b>
EDo	$= 4.0 \cdot 10^{-3} + 3.1 \cdot 10^{-2} \text{LPo-SS} + 1.7 \cdot 10^{-2} \text{SCo} + 6.0 \cdot 10^{-3} \text{SCo} \text{]SS} - 4.2 \cdot 10^{-3} \text{SS\&-LPo}$
<b>R<sup>2</sup></b>	<b>= 0.99</b>
Dvol	$= 9.9 \cdot 10^{-1} - 3.5 \cdot 10^{-2} \text{LPf} \text{]SS} + 2.2 \cdot 10^{-2} \text{LPo} \{-\text{LPo}$
<b>R<sup>2</sup></b>	<b>= 0.36</b>
Dhyd	$= 1.0 + 2.9 \cdot 10^{-2} \text{LPf\#-SS} - 1.8 \cdot 10^{-2} \text{SCo} \cdot \text{SS}$
<b>R<sup>2</sup></b>	<b>= 0.46</b>
Drel	$= 94.0 + 2.6 \text{LPf\#-SS} - 1.6 \text{SCo} \cdot \text{SS}$
<b>R<sup>2</sup></b>	<b>= 0.46</b>
LSF	$= 2.0 \cdot 10^{-1} - 6.0 \cdot 10^{-1} \text{LPf} \{ \text{SS} - 3.3 \cdot 10^{-1} \text{SCo} \& \text{-SS} + 2.1 \cdot 10^{-1} \text{LPo} \{-\text{LPo} + 1.6 \cdot 10^{-1} \text{LPf} \& \text{SCf}$
<b>R<sup>2</sup></b>	<b>= 0.64</b>
TSF	$= -7.4 - 15.6 \text{SCo-SS} - 10.1 \text{LPo} + \text{SCo} + 7.7 \text{LPf} \{-\text{SCf} + 4.6 \text{LPf} \{ \text{SCo} + 4.4 \text{LPo} \{-\text{LPf}$
<b>R<sup>2</sup></b>	<b>= 0.77</b>
WSF	$= -1.1 - 3.5 \text{SCf-SS} - 2.1 \text{LPf-SS} - 1.9 \text{LPf} + \text{SCf} - 1.3 \text{LPo} \& \text{SCo}$
<b>R<sup>2</sup></b>	<b>= 0.44</b>
VSF	$= 6.5 \cdot 10^{-1} - 2.1 \text{SCf-SS} - 1.6 \text{LPf} + \text{SCf} - 1.3 \text{LPf} \cdot \text{LPf} + 6.3 \cdot 10^{-1} \text{SS} \text{]SS}$
<b>R<sup>2</sup></b>	<b>= 0.61</b>
LST	$= 3.6 \cdot 10^{-1} - 6.7 \cdot 10^{-1} \text{LPf} \text{]SS} - 3.7 \cdot 10^{-1} \text{SCo} \text{]SCf} + 3.0 \cdot 10^{-1} \text{LPf} + \text{SCf} + 2.8 \cdot 10^{-1} \text{LPo} \text{!SS} - 2.8 \cdot 10^{-1} \text{LPo} \text{]SS}$
<b>R<sup>2</sup></b>	<b>= 0.58</b>
TST	$= -4.9 - 13.2 \text{SCo} \& \text{-SS} - 6.8 \text{SCf} \wedge \text{LPo} - 5.0 \text{LPf} + \text{SCf}$
<b>R<sup>2</sup></b>	<b>= 0.59</b>
WST	$= -8.5 \cdot 10^{-1} - 4.0 \text{SCf-SS} - 3.0 \text{LPf} \& \text{SCf} + 2.5 \text{LPo} \# \text{-SS} - 2.3 \text{LPf} \text{]SCo}$
<b>R<sup>2</sup></b>	<b>= 0.54</b>
FlexuralM	$= 1888.5 + 163.8 \text{LPo} \{-\text{LPf} - 133.6 \text{SCf-SCo} + 131.3 \text{LPo} \text{'SS} + 97.6 \text{LPf} \{-\text{LPo}$
<b>R<sup>2</sup></b>	<b>= 0.22</b>
FlexuralS	$= 64.7 + 7.7 \text{SCo-SS}$
<b>R<sup>2</sup></b>	<b>= 0.31</b>
TensileM	$= 1995.1 - 304.7 \text{LPf} \{ \text{LPf} - 137.9 \text{SCo} \& \text{-LPo}$
<b>R<sup>2</sup></b>	<b>= 0.42</b>



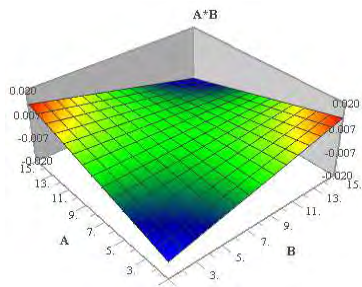
TensileS	= 40.9 – 7.5 LPf-SCf – 5.0 SCo-SS + 3.1 LPf!SS + 1.9 LPf#SS
R <sup>2</sup>	= 0.75
TensileE	= 4.1 – 1.1 SCf&SCo
R <sup>2</sup>	= 0.12
tp	= 51.4 + 93.2 SCf&-SS + 41.6 SCo-SS + 17.6 SS]SCf + 6.3 SCf&SCo – 5.4 LPo'SS
R <sup>2</sup>	= 0.99
Tg	= 69.9 – 6.2 LPo{-LPo – 5.3 LPfSS – 4.4 SS&-SCo
R <sup>2</sup>	= 0.32
Tc	= 147.2 – 3.6 LPo]SCo + 3.0 LPf#LPo – 3.0 SCo]SCf + 1.9 SS&-SS – 1.7 LPo{-SS
R <sup>2</sup>	= 0.42
Tm	= 189.9 – 6.3 LPf#LPo – 5.2 LPo*SCo
R <sup>2</sup>	= 0.17
Xc	= 26.7 – 3.0 LPf]LPf + 1.9 LPf!LPo – 1.6 LPo+SCo
R <sup>2</sup>	= 0.32

#### A.6.4. Interactions of CORICO method

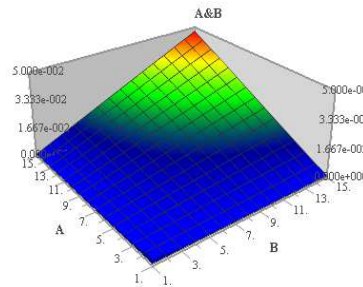
When the number of factors is large, the number of response surface graphs becomes prohibitive. CORICO replaces them with the symbols below, which will fit into the model equation.

Symbols used on CORICO diagram		
f(A,B)	Significance	The response Y is strong when...
A*B	A or-exclusive B	...A is strong and B weak or A is weak and B strong
A^B	A or B	...A is strong or B is strong
A^-B	A or not B	...A is strong or B is weak
A&B	A and B	...A and B are strong
A&-B	A and not B	...A is strong and B is weak
A]B	A modulated by B	...A is strong if B is strong
A]-B	A modulated by not B	...A is strong if B is weak
A}B	A modulated by B mean	...A is strong if B is mean
A'B	Neither A nor B (gen.)	... neither A nor B are extreme (they are mean)
A!B	Neither A nor B (str.)	... neither A nor B are extreme (they are str. mean)
A#B	A as B	...A varies as B
A+B	“A plus B”	...sum of A and B (centred-reduced) is strong
A-B	“A minus B”	...difference of A and B (centred-reduced) is strong

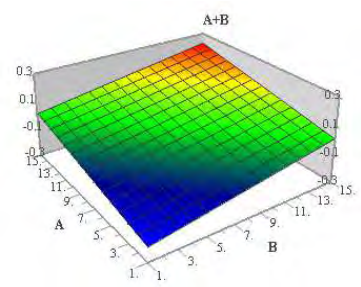
They correspond to the response surfaces of the figures below:



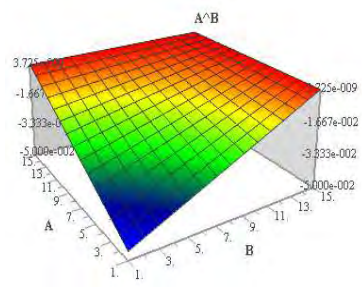
$A*B$  "A or exclusive B"



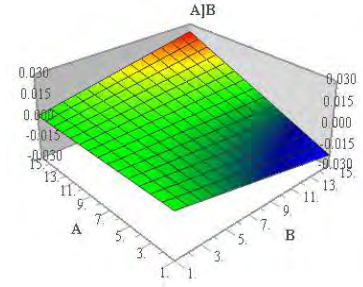
$A\&B$  "A and B"



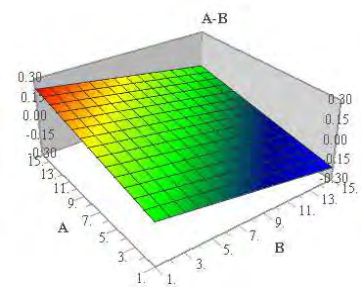
$A+B$



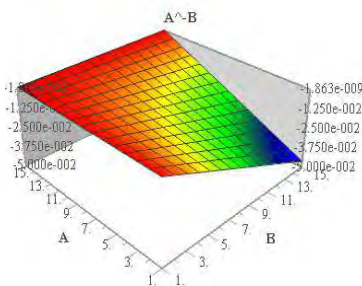
$A^B$  "A or B"



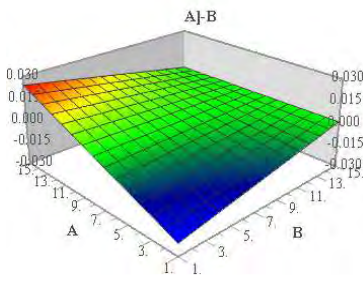
$A|B$  "A if B"



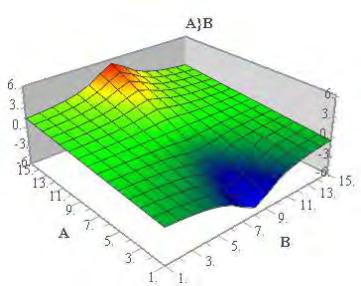
$A-B$



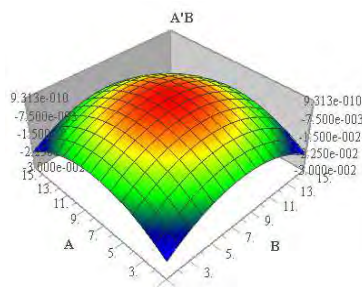
$A^-B$  "A or no B"



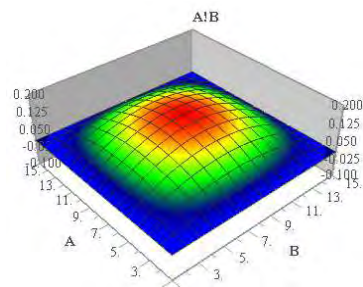
$A|^-B$  "A if no B"



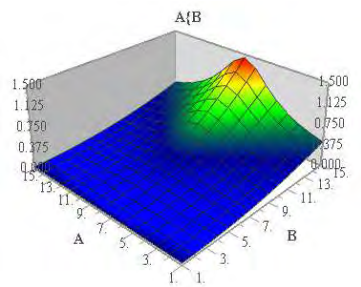
$A\}B$  "A if B average"



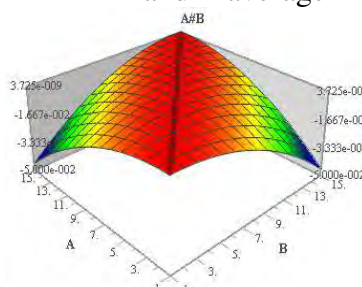
$A'B$  "A and B average"



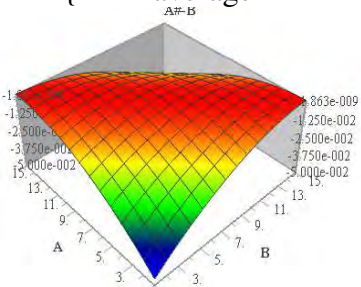
$A!B$  "A and B strictly average"



$A\{B$  "A average if B"



$A\#B$  "A as B"



$A\#^-B$  "A as no B"